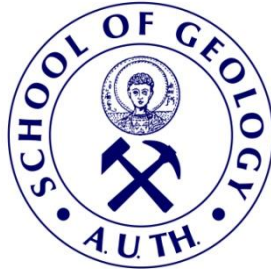




ARISTOTLE UNIVERSITY OF THESSALONIKI
FACULTY OF SCIENCES
SCHOOL OF GEOLOGY



CHRISTOS L. STERGIOU
Geologist, M.Sc.

CRITICAL AND RARE METALS IN TERTIARY MAGMATIC-
HYDROTHERMAL DEPOSITS AT THE SERBO-MACEDONIAN
METALLOGENIC PROVINCE IN GREECE (VATHI, GERAKARIO,
LAODIKINO, KOLCHIKO, ASPRA CHOMATA)

DISSERTATION THESIS

«This research was co-financed by Greece and the European Union (European Social Fund- ESF) through the Operational Programme «Human Resources Development, Education and Lifelong Learning» in the context of the project “Strengthening Human Resources Research Potential via Doctorate Research – 2nd Round” (MIS-5000432), implemented by the State Scholarships Foundation (IKY).»



Operational Programme
Human Resources Development,
Education and Lifelong Learning
Co-financed by Greece and the European Union



THESSALONIKI
2022





ΑΡΙΣΤΟΤΕΛΕΙΟ ΠΑΝΕΠΙΣΤΗΜΙΟ ΘΕΣΣΑΛΟΝΙΚΗΣ
ΣΧΟΛΗ ΘΕΤΙΚΩΝ ΕΠΙΣΤΗΜΩΝ
ΤΜΗΜΑ ΓΕΩΛΟΓΙΑΣ

ΧΡΗΣΤΟΣ Α. ΣΤΕΡΓΙΟΥ
MSc Γεωλόγος

ΤΑ ΚΡΙΣΙΜΑ ΚΑΙ ΣΠΑΝΙΑ ΜΕΤΑΛΛΑ ΣΕ ΤΡΙΤΟΓΕΝΗ
ΜΑΓΜΑΤΙΚΑ-ΥΔΡΟΘΕΡΜΙΚΑ ΚΟΙΤΑΣΜΑΤΑ
ΤΗΣ ΣΕΡΒΟ-ΜΑΚΕΔΟΝΙΚΗΣ ΜΕΤΑΛΛΟΓΕΝΕΤΙΚΗΣ ΕΠΑΡΧΙΑΣ
ΣΤΗΝ ΕΛΛΑΔΑ (ΒΑΘΗ, ΓΕΡΑΚΑΡΙΟ, ΛΑΟΔΙΚΗΝΟ, ΚΟΛΧΙΚΟ,
ΑΣΠΡΑ ΧΩΜΑΤΑ)

ΔΙΔΑΚΤΟΡΙΚΗ ΔΙΑΤΡΙΒΗ

«Το έργο συγχρηματοδοτείται από την Ελλάδα και την Ευρωπαϊκή Ένωση (Ευρωπαϊκό Κοινωνικό Ταμείο) μέσω του Επιχειρησιακού Προγράμματος «Ανάπτυξη Ανθρώπινου Δυναμικού, Εκπαίδευση και Διά Βίου Μάθηση», στο πλαίσιο της Πράξης «Ενίσχυση του ανθρώπινου ερευνητικού δυναμικού μέσω της υλοποίησης διδακτορικής έρευνας – 2^{ος} Κύκλος» (MIS-5000432), που υλοποιεί το Ίδρυμα Κρατικών Υποτροφιών (ΙΚΥ)»



Επιχειρησιακό Πρόγραμμα
Ανάπτυξη Ανθρώπινου Δυναμικού,
Εκπαίδευση και Διά Βίου Μάθηση
Με τη συγχρηματοδότηση της Ελλάδας και της Ευρωπαϊκής Ένωσης



ΘΕΣΣΑΛΟΝΙΚΗ
2022





CHRISTOS L. STERGIOU
MSc Geologist

CRITICAL AND RARE METALS IN TERTIARY MAGMATIC-
HYDROTHERMAL DEPOSITS AT THE SERBO-MACEDONIAN
METALLOGENIC PROVINCE IN GREECE (VATHI, GERA KARIO,
LAODIKINO, KOLCHIKO, ASPRA CHOMATA)

Carried out at the Department of Mineralogy, Petrology, Economic Geology, School of Geology,
Aristotle University of Thessaloniki
Submitted at the School of Geology A.U.Th., July/2022

Oral Examination Date: 23/05/2022

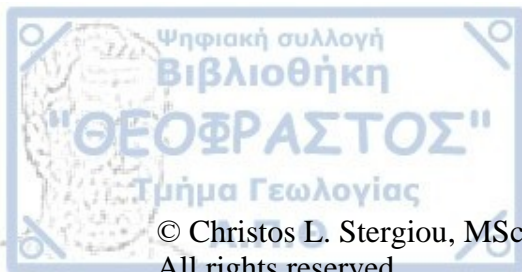
Annex Number of Scientific Annals of the School of Geology N°: 229

Three Member Committee

Assoc. Professor Vasilios Melfos, Supervisor
Professor Panagiotis Voudouris, Member
Assoc. Professor Lambrini Papadopoulou, Member

Examination Committee

Assoc. Professor Vasilios Melfos
Professor Panagiotis Voudouris
Assoc. Professor Lambrini Papadopoulou
Assoc. Professor Nikolaos Kantiranis
Assist. Professor Grogorios Aarne Sakellaris
Professor Irena Peytcheva
Assoc. Professor Ferenc Molnár



© Christos L. Stergiou, MSc Geologist, 2022

All rights reserved.

CRITICAL AND RARE METALS IN TERTIARY MAGMATIC-HYDROTHERMAL DEPOSITS AT THE SERBO-MACEDONIAN METALLOGENIC PROVINCE IN GREECE (VATHI, GERAkakario, LAODIKINO, KOLCHIKO, ASPRA CHOMATA). – *Ph.D. Thesis*

© Χρήστος Λ. Στεργίου, MSc Γεωλόγος, 2022

Με επιφύλαξη παντός δικαιώματος.

ΤΑ ΚΡΙΣΙΜΑ ΚΑΙ ΣΠΑΝΙΑ ΜΕΤΑΛΛΑ ΣΕ ΤΡΙΤΟΓΕΝΗ ΜΑΓΜΑΤΙΚΑ-ΥΔΡΟΘΕΡΜΙΚΑ ΚΟΙΤΑΣΜΑΤΑ ΤΗΣ ΣΕΡΒΟ-ΜΑΚΕΔΟΝΙΚΗΣ ΜΕΤΑΛΛΟΓΕΝΕΤΙΚΗΣ ΕΠΑΡΧΙΑΣ ΣΤΗΝ ΕΛΛΑΔΑ (ΒΑΘΗ, ΓΕΡΑΚΑΡΙΟ, ΛΑΟΔΙΚΗΝΟ, ΚΟΛΧΙΚΟ, ΑΣΠΡΑ ΧΩΜΑΤΑ). – *Διδακτορική Διατριβή*

Citation:

Στεργίου Χ. Λ., 2022. – Τα κρίσιμα και σπάνια μέταλλα σε Τριτογενή μαγματικά-υδροθερμικά κοιτάσματα της Σερβο-Μακεδονικής μεταλλογενετικής επαρχίας στην Ελλάδα (Βάθη, Γερακαριό, Λαοδικηνό, Κολχικό, Άσπρα Χώματα). Διδακτορική Διατριβή, Τμήμα Γεωλογίας, Α.Π.Θ., Αριθμός Παραρτήματος Επιστημονικής Επετηρίδας Τμ. Γεωλογίας No 229, σελ. 272.

Stergiou C. L., 2022. – Critical and rare metals in Tertiary magmatic-hydrothermal deposits at the Serbo-Macedonian metallogenic province in Greece (Vathi, Gerakario, Laodikino, Kolchiko, Aspra Chomata). Ph.D. Thesis, School of Geology, Aristotle University of Thessaloniki, Annex Number of Scientific Annals of the School of Geology No 229, 272 pp.

Any copying, storage and distribution of this work, in whole or part thereof for commercial purposes is forbidden. Reproduction, storage and distribution for non-profit, educational or research nature, are authorized, on the condition that the source and this message are indicated. Questions concerning the use of this work for profit should be addressed to the author.

The views and conclusions contained in this document reflect the author and should not be construed as reflecting official positions of AUTH.

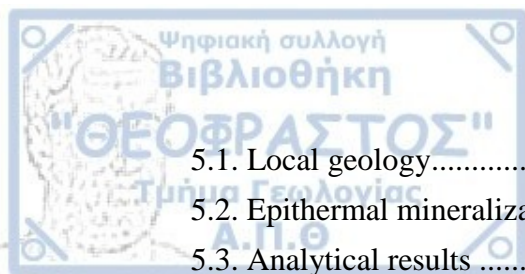


"One writes to teach, to move or to delight"
~ Rodolphus Agricola

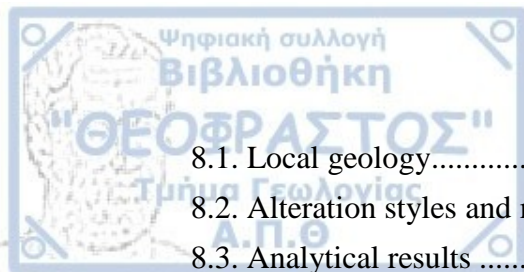


TABLE OF CONTENTS

TABLE OF CONTENTS.....	7
ABSTRACT.....	10
ΠΕΡΙΛΗΨΗ	13
PUBLICATIONS BASED ON THIS PHD THESIS	17
PREFACE	18
CHAPTER 1. INTRODUCTION	22
1.1. Critical and rare metals – Definition and management.....	22
1.2. Porphyry ore deposits and their satellite mineralization	28
1.2.1. Genetic model and metal sources.....	28
1.2.2. Anatomy – Ore mineralization – Critical and rare metals.....	31
1.2.3. Critical and rare metals - Mineral chemistry and nano-scale inclusions	36
1.3. Western Tethyan metallogenic belt: Serbo-Macedonian and Rhodope metallogenic provinces	39
1.4. Project rationale – Critical and rare metals under investigation	41
CHAPTER 2. GEOLOGICAL SETTING AND CENOZOIC MINERALIZATION.....	44
CHAPTER 3. METHODOLOGY	51
3.1. Fieldwork and sampling.....	51
3.2. Microscopy	52
3.3. Scanning electron microscope (SEM)	52
3.4. LA-ICP-MS.....	53
3.5. Bulk chemical analysis	54
CHAPTER 4. VATHI PORPHYRY Cu-Au±Mo DEPOSIT	55
4.1. Local geology.....	55
4.2. Mineralization stages and alteration styles	56
4.3. Analytical results	60
4.3.1. Bulk geochemical analysis.....	60
4.3.2. Pyrite and chalcopyrite - Mode of occurrence	62
4.3.3. Magnetite and titanite - Mode of occurrence	65
4.3.4. Critical and rare metals in pyrite and chalcopyrite (LA-ICP-MS)	66
4.3.5. Critical and rare metals in magnetite and titanite (LA-ICP-MS)	68
4.3.6. Statistical analysis of trace elements concentrations	72
4.4. Discussion.....	73
4.4.1. Mineral chemistry of pyrite and chalcopyrite and nano-scale inclusions.....	75
4.4.2. Mineral chemistry of magnetite and titanite and nano-scale inclusions.....	78
CHAPTER 5. GERAKARIO EPITHERMAL QUARTZ-STIBNITE VEIN MINERALIZATION	79



5.1. Local geology.....	79
5.2. Epithermal mineralization stage and alteration style	82
5.3. Analytical results	83
5.3.1. Bulk geochemical analysis	83
5.3.2. Stibnite - Mode of occurrence.....	84
5.3.3. Critical and rare metals in stibnite (LA-ICP-MS)	84
5.3.4. Statistical analysis of trace elements concentrations	85
5.4. Discussion	87
5.4.1. Mineral chemistry of stibnite and nano-scale inclusions.....	88
CHAPTER 6. METAMORPHIC- AND QUARTZ-HOSTED POLYMETALLIC VEIN MINERALIZATION AT LAODIKINO	91
6.1. Local geology.....	91
6.2. Mineralization and alteration styles	94
6.3. Analytical results	98
6.3.1. Bulk geochemical analysis	98
6.3.2. Pyrite and chalcopyrite - Mode of occurrence	100
6.3.3. Sphalerite and tetrahedrite - Mode of occurrence	102
6.3.4. Magnetite - Mode of occurrence	103
6.3.5. Critical and rare metals in pyrite and chalcopyrite (LA-ICP-MS)	104
6.3.6. Critical and rare metals in sphalerite and tetrahedrite (LA-ICP-MS).....	107
6.3.7. Critical and rare metals in magnetite (LA-ICP-MS)	108
6.3.8. Statistical analysis of trace elements concentrations	108
6.4. Discussion	111
6.4.1. Mineral chemistry of pyrite and chalcopyrite and nano-scale inclusions.....	116
6.4.2. Mineral chemistry of sphalerite and tetrahedrite and nano-scale inclusions	117
CHAPTER 7. METAMORPHIC- AND QUARTZ-HOSTED POLYMETALLIC VEIN MINERALIZATION AT KOLCHIKO	120
7.1. Local geology.....	120
7.2. Mineralization and alteration styles	125
7.3. Analytical results	127
7.3.1. Bulk geochemical analysis	127
7.3.2. Arsenopyrite and pyrite - Mode of occurrence	130
7.3.3. Chalcopyrite and sphalerite - Mode of occurrence.....	132
7.3.4. Critical and rare metals in arsenopyrite and pyrite (LA-ICP-MS)	134
7.3.5. Critical and rare metals in chalcopyrite and sphalerite (LA-ICP-MS)	137
7.3.6. Statistical analysis of trace elements concentrations	139
7.4. Discussion	140
7.4.1. Mineral chemistry of arsenopyrite and pyrite and nano-scale inclusions.....	144
7.4.2. Mineral chemistry of chalcopyrite and sphalerite and nano-scale inclusions	146
CHAPTER 8. ASPRA CHOMATA PORPHYRY-EPITHERMAL MINERALIZATION	148



8.1. Local geology.....	148
8.2. Alteration styles and mineralization stages.....	153
8.3. Analytical results	156
8.3.1. Bulk geochemical analysis.....	156
8.3.2. Pyrite and sphalerite - Mode of occurrence.....	160
8.3.3. Critical and rare metals in pyrite and sphalerite (LA-ICP-MS)	160
8.3.4. Statistical analysis of trace elements concentrations.....	162
8.4. Discussion.....	164
8.4.1. Mineral chemistry of pyrite and sphalerite and nano-scale inclusions.....	166
CHAPTER 9. DISCUSSION.....	169
CHAPTER 10. CONCLUSIONS	178
REFERENCES	187
SUPPLEMENT 1	213
SUPPLEMENT 2.....	223
SUPPLEMENT 3.....	250
SUPPLEMENT 4.....	260



ABSTRACT

The present doctoral thesis investigates the critical and rare metals distribution in selected Cenozoic deposits located in the Serbo-Macedonian and Rhodope metallogenic provinces in northeastern Greece. The study is focused on the deposits of Vathi, Gerakario, Laodikino, and Kolchiko (Kilkis ore district), as well as in Aspra Chomata (Kassandra mining district, NE Chalkidiki). The mineralogy, geochemistry and mineral chemistry of selected mineralized samples, reveal enrichment in critical and rare metals including Ag, Au, Bi, Ce, Co, Ga, Gd, Ge, In, La, Nb, Nd, Se, Sm, Ta, Te, Th, U and W. Emphasis is given on the distribution, abundance, and correlation of critical and rare metals among the different hydrothermal alteration styles and mineralization stages.

The Vathi porphyry Cu-Au±Mo deposit is mainly hosted in latite and quartz monzonite and is enriched in Ag, Au, Bi, Cd, Co, Ga, Ge, Hg, In, Nb, Sb, Se, Te, Th, V, W and rare earth elements (Ce, Gd, La, Nd, Sm). Pyrite and chalcopyrite are the most abundant ore minerals and are related to potassic, propylitic, and sericitic hydrothermal alterations (A- and D-veins), as well as to the late-stage epithermal overprint (E-veins). Magnetite and titanite are found mainly in M-veins and as disseminations in the potassic-calcic alteration of quartz monzonite. Disseminated magnetite is also present in the potassic alteration in latite, which is overprinted by sericitic alteration. Pyrite hosts pyrrhotite, galena, and Bi-telluride inclusions, and is enriched in Ag, Co, Sb, Se and Ti. Chalcopyrite incorporates bornite, sphalerite, galena, and Bi-sulfosalt inclusions, and is enriched with Ag, In and Ti. Inclusions of wittichenite, tetradymite, and cuprobismutite reflect enrichments of Te and Bi in the mineralizing fluids. Native gold is related to A- and D-type veins and is found as nano-inclusions in pyrite. Titanite inclusions characterize magnetite, whereas titanite is a major host of Ce, Gd, La, Nd, Sm, Th and W.

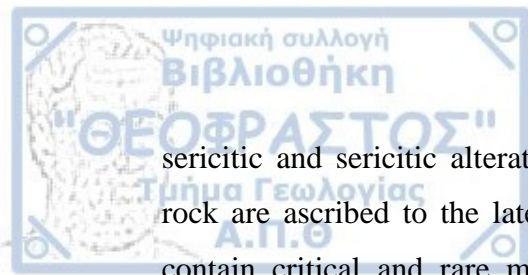
The Gerakario epithermal quartz-stibnite veins occur in the periphery of a Cu-Au porphyry deposit. The quartz-stibnite veins are enriched in Ag, Au, Bi, Ce, Co, Ga, La and Sb, and are depleted in Hg, Se and Te, reflecting the chemistry of the mineralizing fluids. Stibnite contains arsenopyrite inclusions and mainly incorporates As, Cu and Pb, as well as Sb, La and Ti.

The formation of the Laodikino and Kolchiko metamorphic- and quartz-hosted polymetallic vein mineralization includes several styles of mineralizing fluids

introduced mostly during the Mesozoic to Cenozoic tectono-metamorphic evolution of the broader region. At Laodikino, the massive and banded (stratiform-like) mineralization and the magnetite-rich pods are assumed to be of Mesozoic age, while a Cenozoic age is suggested for the polymetallic massive and quartz veins, as well as for the disseminations and aggregates found in hydrothermal halos. In the magnetite-rich pods, enrichments in Ce, Gd, La, Nd and Sm are associated with xenotime and bastnäsite. The polymetallic quartz veins are enriched in Ag and Sb, as well as in Au, Bi, Cd, Co, Hg, In and Se. Mineral chemistry indicates that initially pyrite was deposited from mineralizing fluids enriched in Co and depleted in Ag, Au, Bi, Hg and In. During the subsequent brecciation the mineralizing fluids, enriched in base (Cu, Zn, Pb), and critical metals (Ag, Au, Bi, Cd, Hg, In, Sb, Se), were introduced in the system at temperatures varying from 175 to 300 °C, and chalcopyrite, sphalerite, tennantite, and galena were deposited. Nano-inclusions of galena, tetrahedrite, and sphalerite are found in chalcopyrite. Tetrahedrite is also hosted in sphalerite.

Polymetallic massive and quartz veins, as well as pyrite-quartz veins and disseminations and aggregates are found at Kolchiko. Cenozoic regional metamorphism has overprinted the polymetallic massive veins, while the formation of the polymetallic quartz and quartz-pyrite veins is related to open space filling and to crack and seal textures, respectively. The polymetallic massive veins contain Au, Ce, La, U and W, the polymetallic quartz veins are more enriched in Ag, Bi, Cd, Co, Ga, Gd, In, Nd, Se, Sm, Te and Th, while the quartz-pyrite veins include moderate contents of Au, Bi, Sb and Te. Arsenopyrite from the polymetallic massive veins mainly incorporates Co, and is related to galenobismuthinite nano-inclusions. Pyrite at Kolchiko includes variable contents of critical and rare metals, and hosts galena, galenobismuthinite, and native bismuth as nano-inclusions. Chalcopyrite from the polymetallic quartz veins is the main host of Ag and Bi, and is associated with sphalerite and galenobismuthinite nano-inclusions. Sphalerite from the polymetallic quartz veins is the carrier of Cd, Hg and In, and accommodates chalcopyrite and galena as nano-inclusions. The mineralization styles in Kolchiko are associated with hydrothermal fluids including temperatures varying between 240 and 444 °C.

At Aspra Chomata the porphyry and the epithermal stages are hosted in the granodiorite porphyry, which is part of the Oligocene Stratoni granodiorite intruding the footwall of the Stratoni fault. Pyrite is the main metallic mineral in the potassic alteration that is overprinted by chloritic-sericitic alteration, as well as in the chloritic-



sericitic and sericitic alterations (D-veins). Bleaching and kaolinization of the host rock are ascribed to the late epithermal stage. Sericitic alteration and D-type veins contain critical and rare metals including Au, Co, In, Se, Te and W, while the epithermal veins are more enriched in Ag, Cd, Ga, Hg and Sb. Pyrite from the epithermal veins exhibits oscillatory zoning, which is related to elevated contents of As, Au and Ag. Bi, Hg, V and W preferentially precipitated in sphalerite, where Ag, Cd, Ga, Ge, In, Nb, Sb and Ti, also occur. Nano-inclusions of boulangerite are found both in pyrite and chalcopyrite.

The deliverables of this study promote the knowledge on the metallogenic framework of northern Greece by sharing new data on critical and rare metals distribution and emphasizing on Au-Bi-Te-metallogeny. In the Vertiskos Unit, the presence of Oligocene-Miocene porphyry-epithermal systems is ascribed to extensional tectonics, while the early Cenozoic (?) to Miocene veins hosted in metamorphic rocks are associated with transpressional to transtensional tectonics. Specific enrichments in critical and rare metals reflect varying physicochemical conditions during mineralizing processes.

Η παρούσα διδακτορική διατριβή διερευνά την παρουσία των κρίσιμων και σπάνιων μετάλλων σε επιλεγμένα Καινοζωικά κοιτάσματα τα οποία εντοπίζονται στις μεταλλογενετικές επαρχίες της Σερβο-Μακεδονικής και της Ροδόπης στην βορειοανατολική Ελλάδα. Η μελέτη επικεντρώνεται σε κοιτάσματα που εντοπίζονται στις περιοχές Βάθη, Γερακαριό, Λαοδικηνό και Κολχικό (κοιτασματολογική περιοχή του Κιλκίς) και στα Άσπρα Χώματα (μεταλλευτική περιοχή "Μεταλλεία Κασσάνδρας", ΒΑ Χαλκιδικής). Η ορυκτολογική, γεωχημική και ορυκτοχημική μελέτη επιλεγμένων δειγμάτων της κάθε μεταλλοφορίας αποκαλύπτει έναν εμπλουτισμό σε κρίσιμα και σπάνια μέταλλα όπως Ag, Au, Bi, Ce, Co, Ga, Gd, Ge, In, La, Nb, Nd, Se, Sm, Ta, Te, Th, U και W. Έμφαση δίνεται στην κατανομή, την αφθονία και την συσχέτιση μεταξύ των κρίσιμων και σπάνιων μετάλλων, των διαφορετικών σταδίων μεταλλοφορίας και των υδροθερμικών εξαλλοιώσεων.

Το πορφυριτικό κοίτασμα Cu-Au±Mo στη Βάθη φιλοξενείται κυρίως σε πετρώματα λατίτη και χαλαζιακού μονζονίτη Μειοκανικής ηλικίας και είναι εμπλουτισμένο σε Ag, Au, Bi, Cd, Co, Ga, Ge, Hg, In, Nb, Sb, Se, Te, Th, V και W, αλλά και σε σπάνιες γαίες (Ce, Gd, La, Nd και Sm). Ο σιδηροπυρίτης και ο χαλκοπυρίτης αποτελούν τα δύο πιο διαδεδομένα μεταλλικά ορυκτά, τα οποία σχετίζονται με την ποτασσική (Α-τύπου φλέβες), προπυλιτική και σερικιτική (D-τύπου φλέβες) υδροθερμική εξαλλοίωση, καθώς και με την επιθερμική επικάλυψη του συστήματος (E-τύπου φλέβες). Ο μαγνητίτης και ο τιτανίτης βρίσκονται κυρίως εντός των φλεβών M-τύπου και ως διασπορές στον χαλαζιακό μονζονίτη και σχετίζονται με την ποτασσική-ασβεστιούχο εξαλλοίωση. Διάσπαρτος μαγνητίτης εντοπίζεται επίσης στην ποτασσική εξαλλοίωση του λατίτη, η οποία υπερκαλύπτεται από σερικιτική εξαλλοίωση. Ο σιδηροπυρίτης φιλοξενεί εγκλείσματα μαγνητοπυρίτη, γαληνίτη και τελλουριδίων του βισμούθιου, και είναι εμπλουτισμένος σε Ag, Co, Sb, Se και Ti. Ο χαλκοπυρίτης εμπεριέχει εγκλείσματα βορνίτη, σφαλερίτη, γαληνίτη, και θειολάτων του βισμούθιου και είναι πλούσιος σε Ag, In και Ti. Εγκλείσματα βιττιτσενίτη, τετραδυμίτη και κυπροβισμούθιτη αντανakλούν τον εμπλουτισμό των μεταλλοφόρων διαλυμάτων σε Te και Bi. Ο αυτοφυής χρυσός σχετίζεται με τις φλέβες Α- και D-τύπου και βρίσκεται ως νανο-εγκλείσματα στον σιδηροπυρίτη. Εγκλείσματα τιτανίτη εντοπίζονται στον μαγνητίτη, ενώ ο τιτανίτης είναι ο κύριος ξενιστής των στοιχείων Ce, Gd, La, Nd, Sm, Th και W.

Οι επιθερμικές φλέβες χαλαζία-αντιμονίτη στην περιφέρεια του πορφυριτικού κοιτάσματος Cu-Au στο Γερακαριό είναι εμπλουτισμένες σε Ag, Au, Bi, Ce, Co, Ga, La και Sb, ενώ τα μέταλλα Hg, Se και Te απουσιάζουν, υποδηλώνοντας τη χημεία των μεταλλοφόρων διαλυμάτων. Ο αντιμονίτης περιέχει εγκλείσματα αρσеноπυρίτη και ενσωματώνει As, Cu, Pb, Sb, La και Ti.

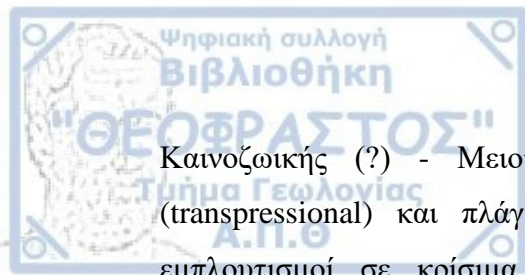
Ο σχηματισμός των πολυμεταλλικών μεταλλοφοριών που φιλοξενούνται σε μεταμορφωμένα πετρώματα και σε χαλαζιακές φλέβες στις περιοχές Λαοδικηνό και Κολχικό σχετίζονται με διάφορες φάσεις των μεταλλοφόρων διαλυμάτων, τα οποία ενεργοποιήθηκαν κατά τα τεκτονο-μεταμορφικά στάδια εξέλιξης της ευρύτερης περιοχής κατά το Μεσοζωικό και το Καινοζωικό. Στο Λαοδικηνό εντοπίζεται συμπαγής και στρωματόμορφη μεταλλοφορία και φακοί πλούσιοι σε μαγνητίτη, πιθανότατα Μεσοζωικής ηλικίας, καθώς και συμπαγείς πολυμεταλλικές και χαλαζιακές φλέβες, διασπορές και συγκεντρώσεις σιδηροπυρίτη-χαλκοπυρίτη εντός των ζωνών εξαλλοίωσης Καινοζωικής ηλικίας. Οι πλούσιοι σε μαγνητίτη φακοί της μεταλλοφορίας στην περιοχή του Λαοδικηνού έχουν σχετικά ψηλές περιεκτικότητες σε Ce, Gd, La, Nd και Sm που σχετίζονται με την παρουσία ξενότιμου και μπαστνασίτη. Οι πολυμεταλλικές χαλαζιακές φλέβες στο Λαοδικηνό είναι πλούσιες σε Ag και Sb, αλλά και σε Au, Bi, Cd, Co, Hg, In και Se. Η ορυκτοχημική μελέτη υποδηλώνει ότι τα μεταλλοφόρα διαλύματα εμπλουτισμένα σε Co και φτωχά σε Ag, Au, Bi, Hg και In, σχετίζονται με τον σχηματισμό του σιδηροπυρίτη. Ακολούθησε θραυστική παραμόρφωση των φλεβών και κυκλοφορία νέων μεταλλοφόρων διαλυμάτων, με θερμοκρασίες μεταξύ 175 και 300 °C, εμπλουτισμένων σε βασικά (Cu, Zn, Pb) και κρίσιμα μέταλλα (Ag, Au, Bi, Cd, Hg, In, Sb, Se). Ως συνέπεια, αποτέθηκαν τα ορυκτά χαλκοπυρίτης, σφαλερίτης, τετραεδρίτης και γαληνίτης. Νανο-εγκλείσματα γαληνίτη, τετραεδρίτη και σφαλερίτη βρίσκονται στον χαλκοπυρίτη. Ο τετραεδρίτης φιλοξενείται επίσης σαν εγκλείσμα στο σφαλερίτη.

Στο Κολχικό εντοπίζονται συμπαγείς πολυμεταλλικές και χαλαζιακές φλέβες, φλέβες χαλαζία-σιδηροπυρίτη, καθώς και διασπορές και συγκεντρώσεις σιδηροπυρίτη. Κατά το Καινοζωικό η μεταμόρφωση επηρέασε τις πολυμεταλλικές συμπαγείς φλέβες, ενώ ο σχηματισμός των πολυμεταλλικών χαλαζιακών φλεβών και των φλεβών χαλαζία-σιδηροπυρίτη χαρακτηρίζεται από πλήρωση κενών χώρων και ιστούς ρηγμάτωσης-επούλωσης, αντίστοιχα. Οι συμπαγείς πολυμεταλλικές φλέβες περιέχουν Au, Ce, La, U και W, οι πολυμεταλλικές χαλαζιακές φλέβες είναι εμπλουτισμένες σε Ag, Bi, Cd, Co, Ga, Gd, In, Nd, Se, Sm, Te και Th, ενώ οι φλέβες

χαλαζία-σιδηροπυρίτη περιλαμβάνουν συγκεντρώσεις Au, Bi, Sb και Te. Ο αρσеноπυρίτης των πολυμεταλλικών συμπαγών φλεβών ενσωματώνει Co και φιλοξενεί νανο-εγκλείσματα γαληνοβισμούθινιτη. Ο σιδηροπυρίτης από τα μεταλλοφόρα στάδια στο Κολχικό χαρακτηρίζεται από διαφορετικές συγκεντρώσεις κρίσιμων και σπάνιων μετάλλων και φιλοξενεί νανο-εγκλείσματα γαληνίτη, γαληνοβισμούθινιτη και αυτοφυούς βισμούθιου. Ο χαλκοπυρίτης από τις πολυμεταλλικές χαλαζιακές φλέβες είναι ο κύριος ξενιστής του Ag και του Bi, ενώ βρίσκεται με μορφή νανο-εγκλεισμάτων σφαλερίτη και γαληνοβισμούθινιτη. Ο σφαλερίτης από τις πολυμεταλλικές φλέβες είναι φορέας Cd, Hg και In, και φιλοξενεί νανο-εγκλείσματα χαλκοπυρίτη και γαληνίτη. Η μεταλλογενετική διαδικασία στο Κολχικό σχετίζεται με υδροθερμικά ρευστά με θερμοκρασίες που κυμαίνονται από 240 έως 444 °C.

Στα Άσπρα Χώματα το πορφυριτικό κοίτασμα Cu-Au και οι επιθερμικές φλέβες φιλοξενούνται σε γρανοδιοριτικό πορφύρη. Ο γρανοδιοριτικός πορφύρης αποτελεί τμήμα του γρανοδιορίτη Στρατωνίου Ολιγοκαινικής ηλικίας, ο οποίος διεισδύει στο κάτω τέμαχος (footwall) του ρήγματος Στρατωνίου. Ο σιδηροπυρίτης αποτελεί το κύριο μεταλλικό ορυκτό και σχετίζεται με την ποτασσική, τη χλωριτική-σερικιτική και τη σερικιτική εξαλλοίωση (D-τύπου φλέβες). Η καολινίωση και ο αποχρωματισμός του πορφυριτικού γρανοδιορίτη σχετίζονται με μεταγενέστερο επιθερμικό στάδιο. Η σερικιτική εξαλλοίωση και οι D-τύπου φλέβες περιέχουν κρίσιμα και σπάνια μέταλλα όπως Au, Co, In, Se, Te και W, ενώ οι επιθερμικές φλέβες περιλαμβάνουν Ag, Cd, Ga, Hg και Sb. Ο σιδηροπυρίτης στις επιθερμικές φλέβες χαρακτηρίζεται από ζωνώδη ανάπτυξη με υψηλές περιεκτικότητες σε As, Au και Ag. Τα χημικά στοιχεία Bi, Hg, V και W αποτέθηκαν κατά προτεραιότητα στον σφαλερίτη, όπου επίσης συμμετέχουν Ag, Cd, Ga, Ge, In, Nb, Sb και Ti. Νανο-εγκλείσματα βουλανζερίτη βρίσκονται τόσο στον σιδηροπυρίτη όσο και στον σφαλερίτη.

Τα αποτελέσματα της παρούσας μελέτης προωθούν την γνώση επί του μεταλλογενετικού πλαισίου στην βόρεια Ελλάδα προσθέτοντας νέα στοιχεία σχετικά με την παρουσία και την κατανομή των κρίσιμων και σπάνιων μετάλλων στις υπό μελέτη μεταλλοφορίες. Έμφαση δίνεται στην μεταλλογένεση του Au-Bi-Te. Στην Ενότητα Βερτίσκου, τα πορφυριτικά-επιθερμικά συστήματα Ολιγοκαινικής-Μειοκαινικής ηλικίας σχετίζονται με εκτατικές τεκτονικές διεργασίες, ενώ ο σχηματισμός των φλεβών που φιλοξενούνται σε μεταμορφωμένα πετρώματα Κάτω



Καινοζωικής (?) - Μειοκαινικής ηλικίας αποδίδεται σε πλάγια-συμπιεστική (transpressional) και πλάγια-εκτατική (transtensional) τεκτονική. Συγκεκριμένοι εμπλουτισμοί σε κρίσιμα και σπάνια μέταλλα αντανακλούν μεταβολές στις φυσικοχημικές συνθήκες που επικρατούσαν κατά τις μεταλλογενετικές διεργασίες.

PUBLICATIONS BASED ON THIS PHD THESIS

Peer-reviewed articles in journals

Stergiou C. L., Melfos V., Voudouris P., Spry P. G., Papadopoulou L., Chatzipetros A., Giouri K., Mavrogonatos C., Filippidis A., 2021a. The geology, geochemistry, and origin of the porphyry Cu-Au-(Mo) system at Vathi, Serbo-Macedonian Massif, Greece. *Applied Sciences*, 11, 479.

Stergiou, C. L., Melfos, V., Voudouris, P., Papadopoulou, L., Spry, P. G., Peytcheva, I., Dimitrova, D., Stefanova, E., Giouri, K., 2021b. Rare and critical metals in pyrite, chalcopyrite, magnetite, and titanite from the Vathi porphyry Cu-Au±Mo deposit, northern Greece, *Minerals*, 11, 630.

Stergiou, C.L., Melfos, V., Voudouris, P., Papadopoulou, L., Spry, P. G., Peytcheva, I., Dimitrova, D., Stefanova, E., 2022. A fluid inclusion and critical/rare metal study of epithermal quartz-stibnite veins associated with the Gerakario porphyry deposit, northern Greece. *Applied Sciences*, 12, 909.

Articles in international conferences

Stergiou, C. L., Melfos, V., and Voudouris, P., 2018. A review on the critical and rare metals distribution throughout the Vertiskos Unit, N. Greece. In: *Proceedings of the 1st International Electronic Conference on Mineral Science at Sciforum, Online. 16–31 July 2018, MDPI: Basel, Switzerland*.

Stergiou, C. L., Melfos, V., Voudouris, P., Papadopoulou, L., Spry, P. G., 2021c. Geology, mineralogy, and geochemistry of the intrusion-related polymetallic quartz veins at Laodikino, Serbo-Macedonian Massif, N. Greece. In: *Abstract volume of the SEG100: Celebrating a Century of Discovery, Whistler, Canada, September 14-17*.



PREFACE

Diachronically, human societies extensively explored and exploited their natural environment, the mineral raw materials it provided and their natural characteristics, experimenting upon their uses and applications (Stöllner 2003). Marble, base metals, and coal supported the welfare of human societies for centuries, while during the 20th century a great dependence on oil and steel emerged.

Today, mineral raw materials are subdivided into metals, industrial minerals and rocks, and energy minerals, and their availability critically affects the escalating development of human societies. Gradually this development challenged the sustainability of human societies by advancing their dependence on mineral raw materials (McMahon and Moreira 2014). As a result, conflicts rose between mineral raw materials exploitation, human societies, and natural environment (Sykes et al. 2016, Berman et al. 2017, Kivinen et al. 2020, Engels 2021). Under the social impacts of these conflicts, the developed countries throughout the past decades forwarded the decrease of domestic productions (Crowson 1996, High 2013, Sarra et al. 2019). This decision was based on the wide availability of these raw materials from several suppliers, as well as on secure and undisturbed supply networks (Chapman 2018). During the late 20th century, this perspective led to a decline of exploration and exploitation of minerals in the developed countries (e.g. member states of the European Union, the United States of America) (High 2013, Chapman 2018).

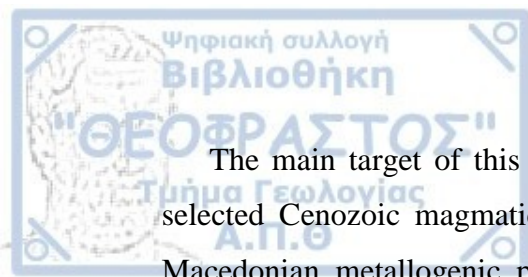
In more recent years, the rapidly developing economies of the world (e.g. the southeastern Asia countries: China, India) have incisively abrupt the supply and consumption of mineral raw materials (Mancheri 2015, Barakos et al. 2016, McNulty and Jowitt 2021). In addition, the Information Age, which succeeded the Industrial Age, revealed the importance of new metals and industrial minerals such as Be, Bi, Cd, Co, Cr, F, Ga, Ge, In, Li, Mg, Mn, Mo, Nb, Ni, Sb, Se, Sn, Sr, Ta, Te, Ti, V, W and Zr, as well as graphite, rare earth elements (REE) and platinum group elements (PGE) (Huston 2014). These commodities were defined as critical and rare to highlight their strategic role and significance for the modern high-technology industry (Moss et al. 2011). They are substantial to cutting-edge technological products; their natural availability is restricted and they exhibit a risk in supply (Girtan et al. 2021). Furthermore, the critical and rare metals are essential in the ongoing 4th industrial revolution held by the developed countries. This industrial and technological

transition targets to green technologies, including decarbonization and alternative energy solutions, to artificial intelligence (AI), and to 5G networks (Grandell et al. 2016, Kalantzakos 2020). During the last decade, the criticality, availability, and supply risk, have drove part of the developed countries (e.g. the EU, the USA, Canada, Australia) to support and invest in domestic exploration and exploitation of these mineral raw materials (Humphreys 2014, Goodenough et al. 2016, Granitto et al. 2020, McNulty and Jowitt 2021).

Economic Geology is a major discipline in the scientific study of the mineral raw materials (Pohl 2011). It contributes in the exploration for new mineral deposits, in economic and technical evaluations, in rational exploitation, in reducing environmental impact, and provides sufficient measurements of physical and chemical stabilization, recultivation and renaturalization during the rehabilitation of a mine (Pohl 2011, Ridley 2013).

Greece is characterized by a prolonged and systematic exploration and exploitation of mineral deposits which favored the development of the cultural and social life. Metals exploited and implemented in metallurgy are reported since the Late Neolithic (Bassiakos et al. 2018). Iron, lead, tin, gold, copper and silver were first systematically exploited during the Classical times (Ross et al. 2020, 2021). Famous mines of antiquity were located at Lavrion, Thassos, Pangaion, and Lakonis (Sanidas et al. 2016, Vaxevanopoulos et al. 2018, 2022, Ross et al. 2020, 2021). During the Byzantine (4th to 15th centuries CE) and the Ottoman periods (15th to 19th centuries CE) Ag, Au, Fe, Cu and Mn were put in more systematic production (Melfos and Voudouris 2017). Mines exploiting chromite, laterite, bauxite, iron-manganese, and carbonate-replacement deposits were operating in Greece during the 20th century producing Cr, Ni, Al, Mn, Fe, Pb, Zn, Cu, Au and Ag (Melfos and Voudouris 2017).

Galena, sphalerite, and gold-bearing pyrite and arsenopyrite are still mined actively in northern Greece, while the country constitutes a major producer of Ni-Fe, Al and Mg, within the European Union (Nerantzis 2016, Melfos and Voudouris 2017). Moreover, during the last two decades, exploration has revealed a significant potential for the exploitation of Au, Ag, Cu, Mo, Re, Sb, W, Te, Ga and REE (Arvanitidis 2010, Moss et al. 2011, Melfos and Voudouris 2012, Voudouris et al. 2013a, Tsirambides and Filippidis 2016, Melfos and Voudouris 2017, Voudouris et al. 2019a, 2022).

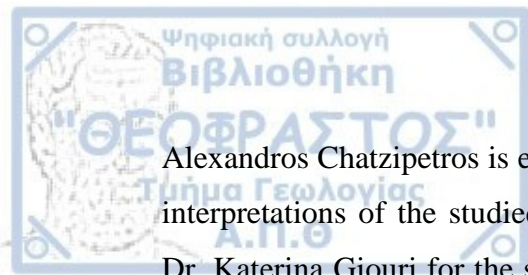


The main target of this thesis was to investigate the critical and rare metals of selected Cenozoic magmatic-hydrothermal ore mineralization hosted in the Serbo-Macedonian metallogenic province in Northern Greece. The Vathi porphyry Cu–Au±Mo deposit, the Gerakario porphyry Cu–Au and epithermal quartz–stibnite vein mineralization, the Laodikino metamorphic- and quartz-hosted polymetallic mineralization, the Kolchiko metamorphic- and quartz-hosted polymetallic vein mineralization, and the Aspra Chomata porphyry Cu–Au and epithermal vein mineralization were selected for this research. These mineralizations carry significant critical and rare metals, and are the most proper examples for targets of academic study and future exploitation.

This research was co-financed by Greece and the European Union (European Social Fund- ESF) through the Operational Programme "Human Resources Development, Education and Lifelong Learning" in the context of the project "Strengthening Human Resources Research Potential via Doctorate Research – 2nd Round" (MIS-5000432), implemented by the Greek State Scholarships Foundation (IKY). Furthermore, an initial preparatory part of the laboratory analysis was funded by the "2017 Society of Economic Geologists Canada Foundation (SEGCF) Fund", which supports research by students on mineral deposits or districts globally.

I am grateful for the support and patience of my supervisors throughout this research. I would like to acknowledge Associate Professor Vasilios Melfos for his valuable help, guidance, patience and motivation, which were crucial in completing the fieldwork, research and writing of the present thesis. Furthermore, Professor Panagiotis Voudouris and Associate Professor Lambrini Papadopoulou are especially thanked for sharing their insights, expertise and constructive comments on optical microscopy and scanning electron microscopy with energy dispersive spectroscopy (SEM-EDS) analysis. The discussions with them on the interpretation of the analytical results and on the reconstruction of the genetic models of the studied mineralization greatly assisted in completing this thesis.

Additional thanks should be addressed to Associate Professor Nikolaos Kantiranis and to Professors Antonios Koroneos and Andreas Georgakopoulos, as they facilitated laboratory work at the Department of Mineralogy-Petrology-Economic Geology, at the School of Geology of the Aristotle University of Thessaloniki, and supported the successful completion of this research. Associate Professor Nikolaos Kantiranis is also thanked for the implementation of XRD analysis. Associate Professor Nikolaos



Alexandros Chatzipetros is especially thanked for his insights on the structural control interpretations of the studied ore mineralizations. I would also like to acknowledge Dr. Katerina Giouri for the scientific discussions on various aspects of this work and her assistance in statistical analysis.

I would like to acknowledge and thank the expert staff of the Geological Institute of the Bulgarian Academy of Sciences for facilitating the laser ablation inductively coupled plasma mass spectroscopy (LA-ICP-MS) analysis in Sofia, Bulgaria. I am deeply grateful to Professor Irena Peytcheva and Assistant Professors Dimitrina Dimitrova and Elitsa Stefanova for their collaboration and assistance in obtaining and understanding the LA-ICP-MS analytical data.

Many thanks also go to all the colleagues who supported and aided me in my field work and in preparation of all sections respectively, namely Dimitris Mitropoulos, Evangelos Skoupras, Margarita Melfou, Nikolaos Kipouros and Aristeidis G. Stamatiadis.

Finally, I feel immensely grateful to my wife Eleni Tsirigoti, to my parents Lazaros and Konstantina, to my sister Galini, and to my grandmother Galini Stergiou as their unfailing support and patience greatly assisted in the integration effort of my doctorate studies, which tangible completion is this dissertation thesis. I would like to refer in particular my late grandfather Christos Th. Stergiou for urging me to continue with my postgraduate studies.

CHAPTER 1. INTRODUCTION

1.1. Critical and rare metals – Definition and management

Sufficient water supply, agricultural lands, energy resources, organic, and mineral raw materials diachronically operate as a solid base for a thriving human society. These factors are in interdependent affinity with a healthy natural and socio-economic environment (Sykes et al. 2016). Abruptions upon availability, supply, and access, to these factors challenge the physical existence of societies. As the population rises and the technology advances, the demand of raw materials grows even greater. As a result, new elements acquire more importance and are almost exclusively consumed in high-technology industry and in green technological applications. For example, bismuth (Bi) is used in medical and atomic research, lithium (Li) is needed in batteries, rhenium (Re) in superalloys and tellurium (Te) in solar cells (Moss et al. 2011, Graedel et al. 2014).

The earth's crust exhibits a wide variability of metals (Graedel et al. 2014). Major industrial metals, such as Fe, Al and Ti, exhibit crustal abundances on the order of weight percent (wt.%), while the crustal abundances of precious metals (e.g. Au, Pt, Os), REE, and other metals such as Se, In, Te and Re are usually on the order of parts per million (ppm) or parts per billion (ppb) (Graedel et al. 2014, Figure 1.1). Geologically, these metals are called "rare" as they are characterized by low concentrations in various rock types and deposits, resulting in scarce occurrences of economically valuable concentrations (Ayres and Peiro 2013, Watari et al. 2020). They include Be, Bi, Cd, Co, Cr, F, Ga, Ge, In, Li, Mg, Mn, Mo, Nb, Ni, Sb, Se, Sn, Sr, Ta, Te, Ti, V, W, Zr, REE and PGE (Huston 2014).

Ore deposits are formed under a combination of geological processes and circumstances (e.g. magmatism, thermal conductivity, fluid circulation, entrapment, weathering, diagenesis etc, Pohl 2011). They constitute areas of the earth's crust where one or more elements are concentrated in a relative abundance reaching economic levels (Pohl 2011). Nevertheless, besides geological factors there are more aspects controlling the exploitation and economic value of an ore deposit. They primarily include political, social, and environmental factors, as well as technical factors related to exploitation and production processes (Pohl 2011). The concept of "reserves and resources" is the result of the junction between the global metals market and the economic value. The term "resources" refers to a commodity, which is, or will

be, economic, while the term “reserves” highlights a part of the commodity resource, which has been fully geologically evaluated and its exploitation is commercially viable and legal (Pohl 2011, Ridley 2013).

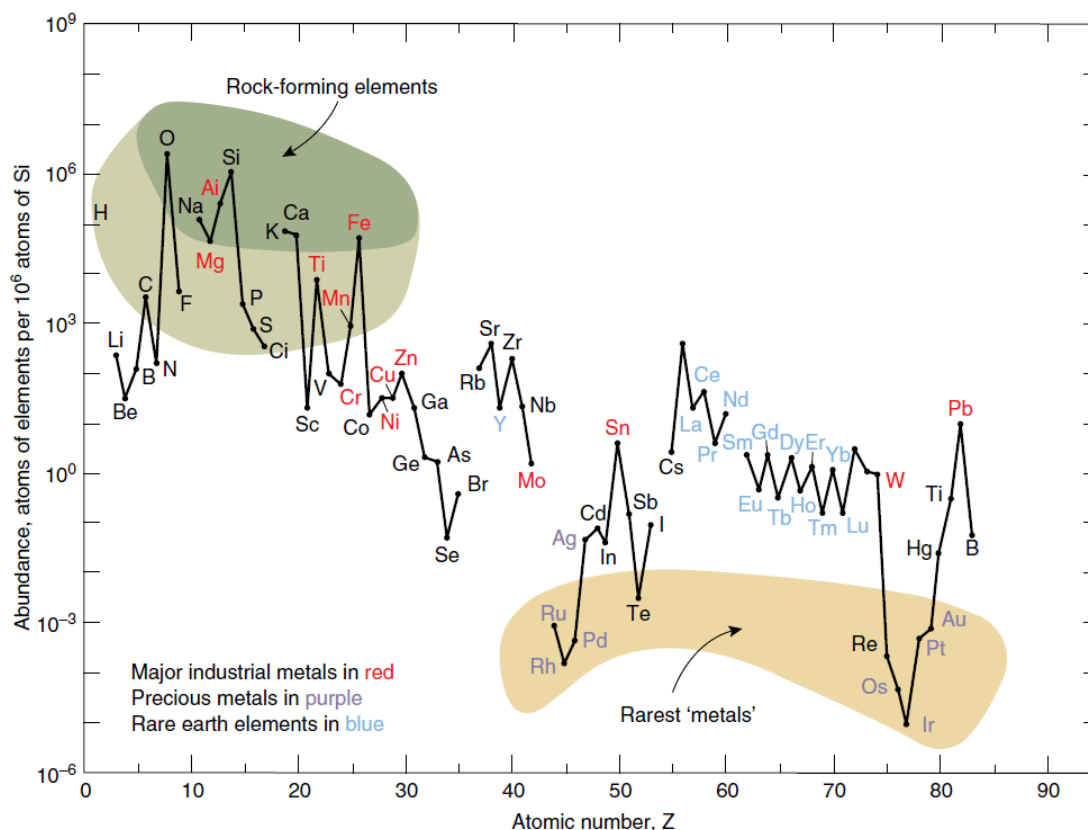


Figure 1.1. The abundances of industrial metals (red), precious metals (purple), and rare earth elements (blue) in the Earth’s upper continental crust as a function of atomic number (adapted from Graedel et al. 2014).

The formation of ore deposits is subjected to geological processes and their distribution exhibits a wide heterogeneity in a global scale (Sillitoe 2010, Verplanck and Hitzman 2016). This heterogeneity, when combined with political factors, may lead to production and export control and supply risk of a certain commodity (Mancheri 2015, Kalantzakos 2020). Subsequently, a key factor affecting the level of criticality of a mineral commodity is geo-politics (Chapman 2018).

The term “rare metals” is usually coupled with the terms “critical” or “strategic” metals (Ayres and Peiro 2013, Bertrand et al. 2016). Rarity is a prominent geological factor, while criticality reflects industrial and market values, and is defined by the importance of a specific metal to the high-technological industrial sector and by demand and supply (Watari et al. 2020). The list of critical metals is subject to

periodic assessment and review (Watari et al. 2020). In addition, it slightly varies among diverse countries (Table 1.1). The 2020 European Commission (EC) critical raw materials (CRM) list includes the following metals: Be, Bi, Co, Ga, Ge, Hf, In, Li, Nb, Sb, Sc, Sr, Ta, Ti, V, W, REE and PGE (European Commission 2020).

During the last decade, the EC has carefully focused on policies regarding the mineral resources exploration and exploitation. Taking into consideration economic and technical feasibility factors, the Member States of European Union (EU) should turn on exploring and developing their domestic mining potential, building a stronger economic society and securing the industrial future and independence (European Commission 2020). The EC has funded several projects examining the domestic potentials and the global challenges faced with respect to access to CRM (cf. Arvanitidis and Goodenough 2014, Goodenough et al. 2016, Sadeghi et al. 2020). The new growth strategy implemented by the EC under the name “European Green Deal” emphasizes the need of a sustainable supply of CRM by setting it as a pre-requisite (European Commission 2019). The supply strategy should be diversified and based both in primary and secondary sources (European Commission 2019). Economic geology can contribute in this task by advancing the knowledge concerning the distribution, host minerals, and enrichment mechanisms of critical metals in ore deposits. These factors are of major importance as they allow more efficient exploration and extraction. In addition, they reflect in the development of the domestic production, which subsequently downsizes supply risk and dependence on imports (Humphreys 2014, Figure 1.2.).

Table 1.1. Critical raw materials as defined by the EC and other countries. All entries are listed alphabetically.

Organization	Defined critical metals	Reference
European Commission	B, Ba, Be, Bi, Co, F, Ga, Ge, Hf, In, Li, Mg, Nb, Sb, Sc, Ta, V, W, REE and PGE, as well as bauxite, coking coal, natural graphite and rubber, phosphate rocks, phosphorus, silicon metal	European Commission (2020)
United States Department of the Interior, The White House	Al, As, Ba, Be, Bi, Co, Cr, Cs, F, Ga, Ge, He, Hf, In, Li, Mg, Mn, Nb, Rb, Re, Sc, Sn, Sr, Ta, Te, Ti, U, V, W, Zr, REE and PGE, as well as natural graphite, potash	Department of the Interior (2018), The White House (2021)
Geoscience Australia	Co, Cr, Ga, In, Li, Mg, Mn, Mo, Nb, Ni, Sb, Ta, Te, V, W, REE and PGE	Skirrow et al. (2013), Mudd et al. (2019)
People's Republic of China	Be, Co, Cs, Ga, Ge, Li, Nb, Ni, Rb, Re, Sc, Se, Sn, Ta, V, W, REE and PGE	Yan et al. (2021)
Government of the Russian Federation	Ag, Au, Be, Co, Cr, Cu, Ge, Li, Mn, Mo, Nb, Ni, Pb, Re, Sb, Sc, Sn, Ta, Ti, U, W, Zr, REE and PGE, as well as bauxite, diamonds and ultra-pure quartz	Chakhmouradian et al. (2015)



Figure 1.2. Major supplier countries of critical raw materials to the European Union (adapted from European Commission 2020).

Supply risk of raw materials has been a major concern of human societies since antiquity (Sykes et al. 2016). In modern era, criticality definition and assessment of raw materials was first attempted by the United States of America and the EU during the 1970s (Buijs and Sievers 2011, Graedel et al. 2014). Since then the developing needs of industry and technology, the changing geo-politics, and the progresses in mining technology advances have several times refreshed the enlisted critical metals (Buijs and Sievers 2011). As technology advances metals that used to be essential, become obsolete and the need of new metals is rising (Huston 2014). Lithium is considered a critical metal, as it is essential in the manufacturing of Li-ion batteries, which are used in high-technological apparatus. Lithium criticality in the battery industry has replaced the criticality of Ni, Pb and Zn, and is most certain that as technology advances Li will also be replaced (Chakhmouradian et al. 2015).

Back in 2008, the United States of America national research council applied a two-parameter model to assess mineral raw materials, while in 2010 the EC used the same model to produce its first report on CRM of the new technological age (European Commission 2010, Graedel et al. 2014). In this two-parameter model the investigated metals are scored according to both the impact and the risk of supply restriction (Graedel et al. 2014, Figure 1.3). The supply risk is defined by the political stability of the producing countries, the potential to substitute the metals, the environmental risks associated with mining, and the extent of recycling, whereas the

definition of supply restriction (or economic importance) includes the impact of supply disruption on European industry (European Commission 2010, Figure 1.3).

Criticality is affected also by the geographical area and the intended usage (Table 1.1). Regardless of the fact that the criticality assessment results may vary from country to country, the importance of metals such as Co, Ga, Ge, In, Li, Mg, Sb, Ta, Te, W, REE and PGE is profound (Table 1.1). The assessment of criticality is a complex matter and evolves processes in which data incorporation and expert judgments, especially in terms of supply risks and emerging technologies, are prerequisite (Mudd et al. 2019).

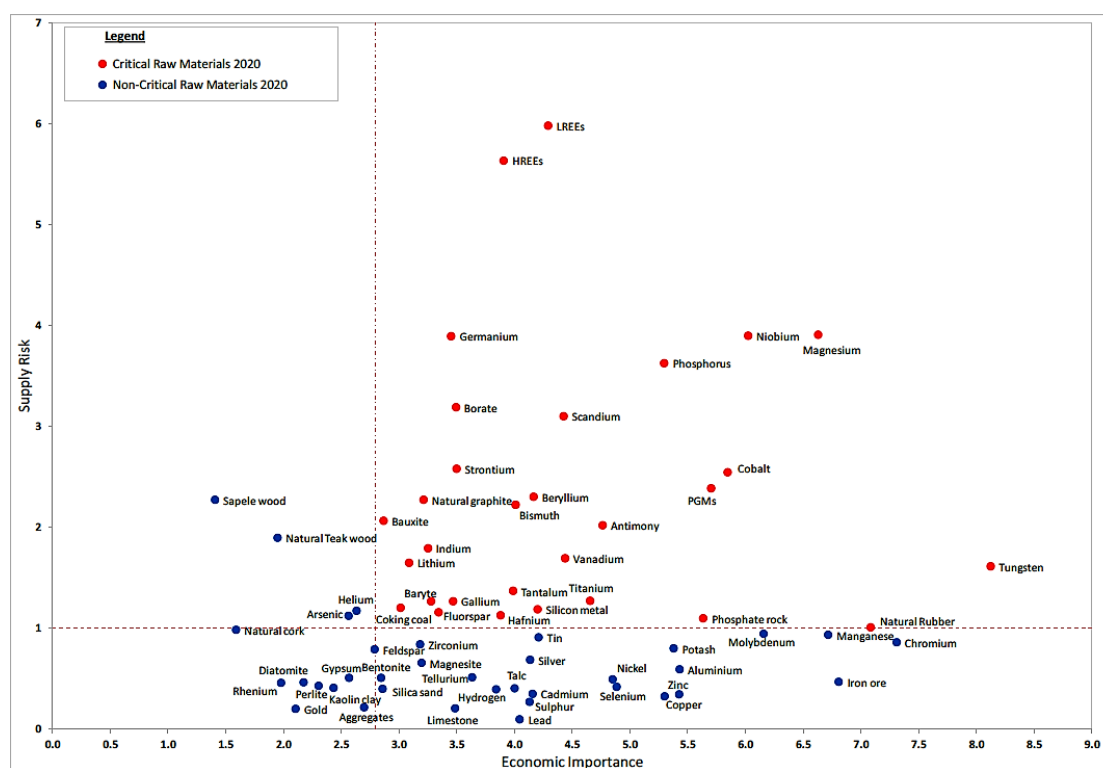


Figure 1.3. Criticality assessment results of 83 mineral raw materials (individual materials and groups e.g. LREEs, adapted from European Commission 2020).

Advances in substitution and recycling of certain CRM, as well as stockpiling, can diminish supply risks and overcome supply restrictions. However, these solutions bear new risks (Buijs and Sievers 2011, Graedel et al. 2014). Substitution may cause efficiency issues, recycling is energy consuming and cannot fully cover demand, while stockpiling affects market, intensifying the problem (Buijs and Sievers 2011, Graedel et al. 2014). Optimum exploration and mining methods, advanced metallurgical research targeting to more efficient extraction methods, and more

sustainable product manufacturing and productive recycling, can greatly serve in downsizing overall risks on CRM (Graedel et al. 2014).

Many CRM are co- or by-products of the production of industrial metals (Figure 1.1, 1.4). Bi, Te, Re and PGE can constitute co-products of copper and molybdenum found in magmatic-hydrothermal deposits (e.g. porphyry deposits), gallium is a co-product of aluminum production from bauxite, while some REEs are by-products in bauxite residue (McFall et al. 2018, Gamaletsos et al. 2019). The production of CRM as co- or by-products of the industrial metals production can add to the economic value of a mine. In addition, the secondary character of the production secures the mine life and operational stability against technological advances or market changes that may affect the supply demand of a certain CRM (Mudd et al. 2019).

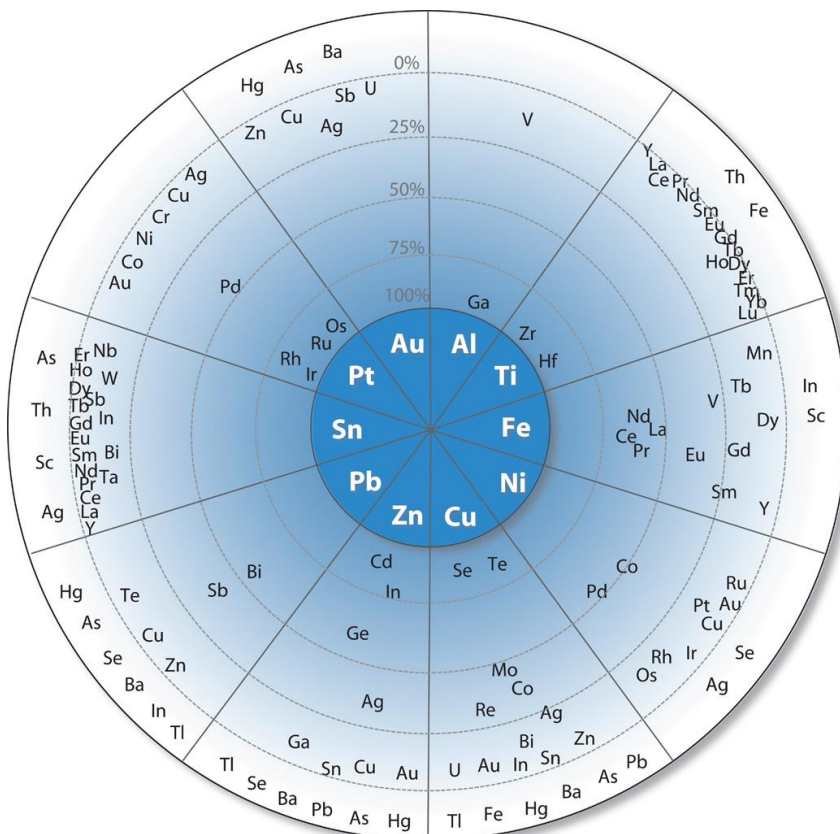


Figure 1.4. Wheel chart depicting metal companionability. Major industrial metals form the inner blue cycle. Minor metals and elements related to major metals appear in the outer space at distances proportional to the percentage (0 to 100%) of their primary production. The white outer circle includes elements for which the percentage of their production related to major metal is not yet determined (adapted from Nassar et al. 2015).

Consequently, operating mines producing industrial metals, such as Cu, Fe and Ni are ideal targets for research on CRM production potentials. Thus, the distribution of the CRM in the host minerals and their behavior during exploitation processes are of major interest. Nevertheless, these research topics are also of major significance in greenfield prospects and yet undeveloped deposits. The research on the source, distribution, and mineralogy of critical and rare metals participating in undeveloped prospects may support the future development of smart and small scale mines operating under the Green Deal agreement in the EU by adding to them additional value and production sustainability.

1.2. Porphyry ore deposits and their satellite mineralization

1.2.1. Genetic model and metal sources

Porphyry Cu deposits constitute voluminous ($10 - >100 \text{ km}^3$) and low grade magmatic-hydrothermal ore deposits (Sillitoe 2010). They are primarily associated with magmatic arcs constructed above active or ancient subduction zones at convergent plate margins (Sun et al. 2015, Figure 1.5a). In this setting, above batholiths and below volcanic chains, large volumes of hydrothermally altered rock centered on porphyry Cu stocks are found (Sinclair 2007, Seedorff et al. 2008, Sillitoe 2010, Richards 2011, Korges et al. 2020, Figure 1.5b). The magmatic rocks related to porphyry Cu systems mainly exhibit calc-alkaline affinities and felsic to intermediate compositions. Nevertheless, porphyry Cu deposits formed in post-subduction settings could also be described by alkaline affinities (Richards 2011, Figure 1.5c-e).

Partial melting of the hydrated mantle wedge beneath subduction related island-arc and back-arc settings, results in the formation of ultramafic to mafic cumulates in a zone described by melting, assimilation, storage and homogenization (MASH) processes (Sillitoe 2010, Sun et al. 2015). Magma produced in this zone is sulfur saturated and enriched in volatiles, silica, large-ion lithophile elements (LILE, e.g. Ba, K, Rb, Sr) deriving from the subducted slab, and in high field strength elements (HFSE, e.g. Hf, Nb, Ta, Th, U, Zr and REE) deriving from the mantle wedge (Sun et al. 2015). It forms diapirs that move upwards developing calc-alkaline batholiths of granitic to dioritic compositions and equigranular textures (Figure 1.5b, Richards 2011). These batholiths have a lifespan of between 100 Kyr to 30 Myr and are periodically rejuvenated by intermediate or mafic magma from the MASH zone (Rezeau et al. 2016). Later on, from these batholiths several porphyry intrusions are

impelled in shallow depths up to 5 km, towards the surface forming stocks (Seedorff et al. 2008, Sillitoe 2010). The batholiths can be associated with several porphyry deposits, whereas co-magmatic subaerial volcanic rocks are found at the surface slightly pre-dating the porphyry stocks formation (Sillitoe 2010). Usually, this volcanism is effusive, and not explosive, favoring the entrapment of the necessary magmatic volatiles needed in the development of the related epithermal style mineralization (Sillitoe 2010, Wang et al. 2019).

Copper, Ni and Au contents in arc magmas is ascribed primarily to mantle, as well as to pre-existing Cu-rich cumulates (Wilkinson 2013). In addition, ore deposits from an earlier subduction cycle may enhance magma fertility (Wilkinson 2013). In contrast, molybdenum is related to crustal assimilation (McFall et al. 2018). During MASH processes, chalcophile elements will partition strongly into sulfide phases relative to silicate melts, while siderophile elements will preferentially partition in the metallic phases, resulting in magmas depleted in metals (Richards 2011). Thus, a mechanism for metal enrichment in arc magmas was suggested, including magnetite crystallization in the oxidized magma chamber, the reduction of the melt, and the formation of an immiscible sulfide melt (Jenner et al. 2010). Reduced country rocks (e.g. shales, limestones) could also be assimilated in magma further enhancing this mechanism and metal fertility (Cloos 2001). Additionally, Nadeau et al. (2010) have suggested that Cu and Au fertility may be affected by the periodic injection of mafic magma into the batholith, the volatile exsolution and dissolution of sulfide into the volatile phase, and the transportation of these metals in reduced sulfur species. During the formation of the porphyry stocks, pressure reduction and/or mafic melt input exsolve these metals from the magma and subject them to hydrothermal transportation and precipitation in veins and potassic alteration (Sillitoe 2010). In these hydrothermal fluids Cu and precious metals are transported as sulfide complexes or chlorine ligands (Audétat et al. 2008). The final deposition of ore minerals includes mechanisms that include, temperature drop and solubility reduction of ore minerals, expansion of the magmatic vapor causing pressure changes, shifts in oxidation state of the fluid due to wall rock interaction, halite precipitation uncoupling Cl from metal bearing ligands, salt saturation, and reaction between shallow brines and magmatic vapor (Sillitoe 2010, Weis et al. 2012, Richards 2013, Lecumberri-Sanchez et al. 2015, Blundy et al. 2015).

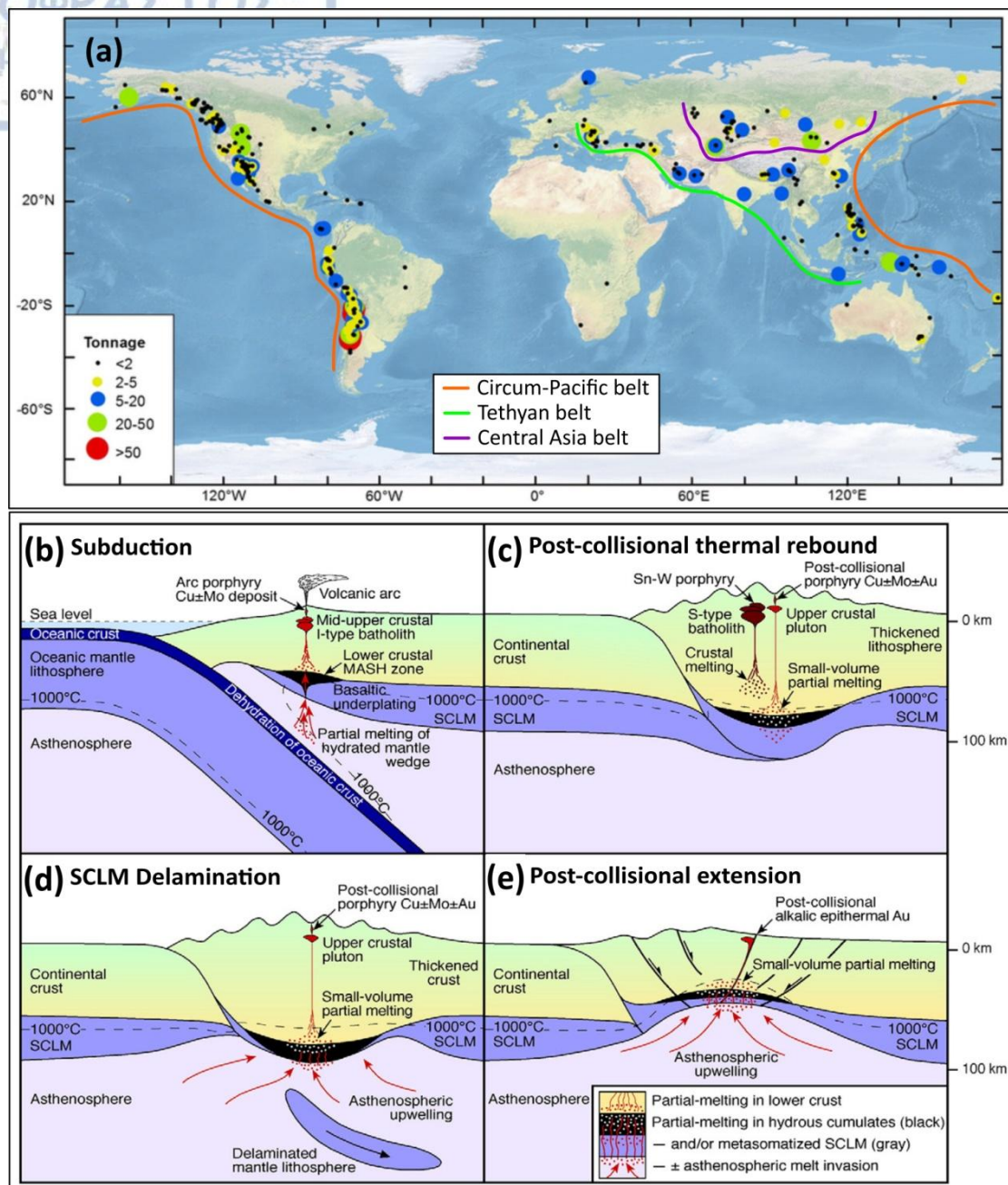


Figure 1.5. a. The worldwide distribution of major porphyry deposits, their tonnage, and major subduction zones are also shown (modified after Sun et al. 2015). b. The spatial and genetical connection between porphyry deposits and subduction (a) and post-subduction settings (c-e) (MASH = melting, assimilation, storage, and homogenization, SCLM = subcontinental lithospheric mantle, modified after Richards 2011).

Porphyry deposits are also associated with post-collisional settings, including lithospheric thickening and thermal rebound, subcontinental lithospheric mantle delamination, and lithospheric extension (Richards 2009, Richards 2011, Figure 1.5d,e). The parent rocks of mineralization are high-K (\pm Na) calc-alkaline to strongly

alkaline products of small volume magmas which are spatially isolated (Richards 2011). Regarding their formation, it is suggested that they derive by partial remelting of the metasomatized lithospheric roots and hydrous cumulate zones of former arc systems (Richards 2011). Furthermore, post-collisional extension may cause decompression melting in the upwelling, subduction-metasomatized asthenosphere. Thus, alkaline mafic magmas are formed, which can later ascend to upper crustal levels through trans-lithospheric extensional structures (i.e. detachment faults) (Richards et al. 2009, Moritz et al. 2016).

Magmas associated with post-subduction porphyry deposits are described by crustal radiogenic isotopic signatures, depletion in HFSE, and by high contents of LILE, inheriting these characteristics to the final porphyry intrusions (Richards 2009). These geochemical characteristics are related to extensive crustal assimilation and mixing with mantle derived magmas. In addition, post-subduction porphyries are characterized by Au enrichments, resulting in high Au/Cu ratios, and by elevated Ni and PGE concentrations (Richards 2009). Au, Ni and PGE exhibit a more siderophile than chalcophile affinity during the formation of the subduction related porphyry deposits producing Au-Ni-PGE enriched residual phases in the MASH zone (Richards 2009, Figure 1.5b). During the post-subduction stage these residual phases re-dissolve, enriching the ascending low-sulfur magma, which will finally produce porphyry and high to low-sulfidation epithermal mineralizations (Richards 2009, Wang et al. 2019).

1.2.2. Anatomy – Ore mineralization – Critical and rare metals

The porphyry deposits are subcategorized to porphyry Cu-Mo-Au, alkalic porphyry, and porphyry Sn (John et al. 2010, Sillitoe 2010, Richards 2009, 2011, 2013). They are hosted in small intrusions forming stocks or dikes, which are products of the underlying precursor pluton. The porphyry intrusions are I-type, calc-alkaline to alkaline in affinity and belong to the magnetite-series (Seedorff et al. 2008). The final porphyry deposit is usually hosted in multiple overprinting intrusions, which display typical porphyritic textures (Sillitoe 2010).

Hydrothermal alteration and mineralization occur within and at the periphery of the porphyry intrusions, exhibiting an outward cylindrical to oval zoned development (Sillitoe 2010, Halley et al. 2015, Figure 1.6a). Hydrothermal alterations commonly include: a) a centered potassic alteration with K-feldspar and biotite as key minerals,

b) a peripheral propylitic alteration comprising of chlorite, albite, calcite, epidote and hematite, and c) a sericitic alteration (also called phyllic) in the upper parts of the porphyry system, including mainly sericite, illite, chlorite, quartz and relic feldspar (Sillitoe 2010, Halley et al. 2015, Figure 1.6a). In the periphery and towards the lower limits of the ore zone of some porphyry deposits the sodic-calcic alteration is documented, including mainly albite, actinolite and magnetite (Sillitoe 2010). Centered to the potassic alteration and developed upwards towards the surface, the late intermediate argillic alteration is found including smectite, illite, kaolinite, chlorite and relic feldspar (Halley et al. 2015).

On the surface, above the porphyry system a lithocap is found associated with intermediate argillic (illite-chlorite-smectite-relic feldspar) and advanced argillic (pyrophyllite-alunite-topaz) alterations (Halley et al. 2015). These late alterations, as well as sericitic alteration, may also exhibit a strong overprint to earlier alterations. The formation of these hydrothermal alterations is the result of the progressive cooling by mixing of the magmatic fluids with meteoric water, starting from temperatures above 700 °C and reaching temperatures below 250 °C (Sillitoe 2010).

Eruptions forming phreatic breccias commonly occur during the latest stages of the porphyry deposits formation (Figure 1.6b). Mixing between magma and meteoric water may form these vertical columnar formations, reaching 2 km in depth and several meters in diameter (Sillitoe 2010, Figure 1.6b). These are usually slightly altered and depleted in metal content, but enriched in high-sulfidation Au mineralization (Sillitoe 2010).

In the hydrothermally altered host rocks the mineralization is found in structurally controlled veins, commonly forming stockworks, as well as disseminations (Sillitoe 2010, Halley et al. 2015). Multiphase porphyry stocks and dikes produce various vein types. Thus, vein paragenesis is very important in understanding the relation between veins and particular minerals and elements (Sillitoe 2010, Halley et al. 2015). Veins in porphyry deposits are divided in three categories including: (1) early M- and EB-types (potassic and sodic-calcic alterations, respectively), (2) intermineral A- and B-types (potassic alteration), and (3) late D-type veins (sericitic alteration, Sillitoe 2010).

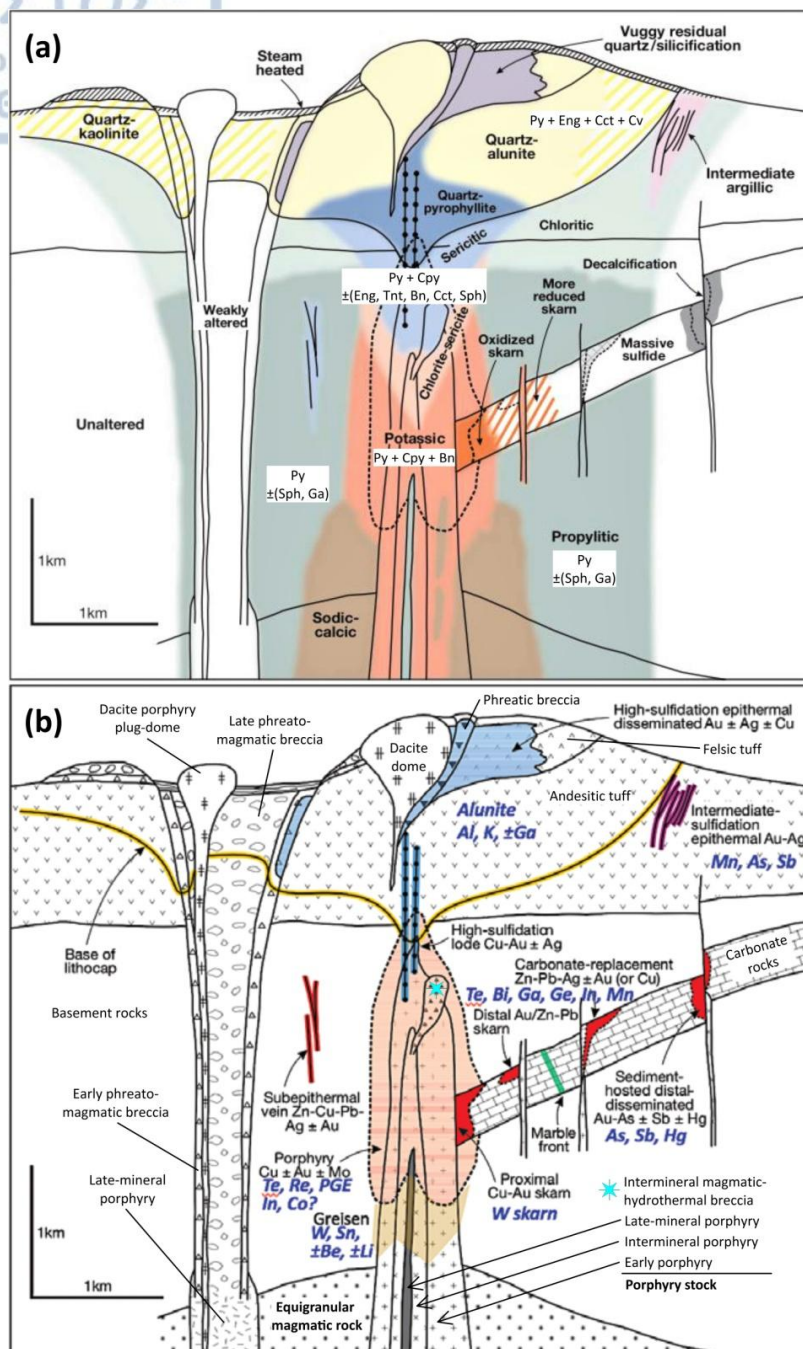


Figure 1.6. a. The distribution of hydrothermal alterations in a porphyry Cu deposit and associated key ore minerals (Bn = bornite, Cct = chalcocite, Cpy = chalcopyrite, Cv = covellite, Eng = enargite, Ga = galena, Py = pyrite, Sph = sphalerite, Tnt = tennantite, modified after Sillitoe 2010). b. The anatomy of a telescoped porphyry Cu system comprising a centrally located porphyry Cu-Mo-Au deposit. The mineralization styles occurring in the proximal or distal periphery of the porphyry deposits are also shown. Critical and rare metals, associated with the porphyry and their satellite mineralization, are highlighted in blue color (modified after Sillitoe 2010, Hofstra and Kreiner 2020).

Early veins are planar, do not contain quartz and sulfides, and lack alteration salvages (Arancibia and Clark 1996). Their mineralogy includes actinolite, magnetite (M-type), biotite (EB-type), plagioclase and K-feldspar (Sillitoe 2010, Arancibia and Clark 1996). The A- and B-type veins exhibit sinuous to planar shapes, ranging from stockworks to subparallel sheeted arrays with restricted alteration salvages. The A-type veins consist mainly of quartz, magnetite, chalcopyrite and bornite, while the B-type veins contain mostly quartz, molybdenite, chalcopyrite and pyrite (Sillitoe 2010). The D-type veins are planar in shape, enveloped in alteration salvages of various sizes, and host quartz, pyrite and chalcopyrite (Sillitoe 2010). Additionally, the E-type veins are described in several porphyry deposits (Pudack et al. 2009, Voudouris et al. 2013b, Mavrogonatos et al. 2020, Melfos et al. 2020). This type of veins occurs in the periphery of the porphyry system and is described by epithermal affinities (Pudack et al. 2009). Mineralogically they usually consist of enargite, famatinite, sphalerite and galena and they are commonly rimmed by quartz and calcite (Pudack et al. 2009).

Pyrite is the major Fe-mineral and is ubiquitous in the potassic, propylitic, and sericitic alterations related to disseminations and to vein-style mineralization (A, B, D and E types, Pudack et al. 2009, Sillitoe 2010). Chalcopyrite, bornite and chalcocite are the most important copper minerals, while Mo mainly occurs as molybdenite. Chalcopyrite is mined for Cu, but Ag is also extracted as a by-product (George et al. 2018). With respect to hydrothermal alterations and vein-style mineralization in porphyry systems, chalcopyrite exhibits a distribution similar to pyrite, with a more restricted presence in propylitic alteration (Sillitoe 2010). Molybdenite, when present, occurs deeper than the Cu-Au ore body or along the periphery of the intrusion (Ridley 2013). Native gold is hosted as small inclusions in bornite and chalcopyrite or as solid solutions in bornite (Sillitoe 2010). Pyrite distribution increases outwards the Cu ore body, and in large deposits may be traced for kilometers. Galena, sphalerite, tetrahedrite-tennantite, and Au-Bi-tellurides are associated with several porphyry ore assemblages (Sillitoe 2010).

Magnetite and titanite found in sodic-calcic and potassic alterations and in M-type veins are not considered as ore minerals, but their study serves as a potential exploration tool for Au-rich ore zones and can help discriminating barren from mineralized intrusions (Tiepolo et al. 2002, Cao et al. 2015, Nadoll et al. 2015, Huang et al. 2019, Mavrogonatos et al. 2019).

Despite their varied ore context, porphyry deposits have much lower grades than other ore types, and contain Cu from 0.2 to 1.3%, Mo from 50 to 300 g/t, and Au from 0.004 to 0.35 g/t (Sinclair 2007, John et al. 2010). However, the voluminous size of porphyry deposits makes them economically valuable. Thus, porphyry deposits are the main suppliers of the world's Cu and Mo production, while they are major sources of Au, Ag, Re, Pb and Zn (Cooke et al. 2014, Arndt et al. 2017). They are also important sources of the critical and rare metals: Bi, Co, In, Te, Se, Pd and Pt, which are mined as by-products (Sinclair 2007, John et al. 2010, Cooke et al. 2014, John and Taylor 2016, McFall et al. 2018).

The consolidation of the porphyry intrusions, the major alteration events, and the ore formation spans in time from 2000 to 100,000 years (Sillitoe 2010). Furthermore, the hydrothermal alteration and metal zonation may define kilometer scale haloes around the central ore zone (Sillitoe 2010). Consequently, in the periphery of the porphyry stocks a variety of satellite deposits may be developed including greisen, skarn, carbonate replacement, polymetallic veins, epithermal, and sediment-hosted (Figure 1.6b, Hedenquist et al. 2000, Sillitoe 2010, Wang et al. 2019). The term "intrusion-related" is commonly used to summarize these deposits (Sillitoe and Thompson 1998)

The criteria for the intrusion-related deposits according to Lang and Baker (2001) comprise: (1) subalkalic intrusions (metaluminous, intermediate to felsic compositions, near the boundary of ilmenite-magnetite series), (2) carbonatic hydrothermal fluids, (3) metal assemblage combining Au with Bi, W, As, Mo, Te, and/or Sb and restricted concentrations of base metals, (4) reduced mineral assemblage including arsenopyrite, pyrrhotite and pyrite with low sulfide mineral content (<5 vol%) and lack of magnetite and hematite, (5) very restricted and weak hydrothermal alteration, except in systems formed near the intrusions, (6) convergent tectonic system hosting magmatic rocks of alkalic, metaluminous, calc-alkalic, and peraluminous compositions, and (7) proximity to magmatic provinces comprising W and/or Sn deposits.

These satellite deposits may be proximal or distal to the porphyry stocks and they exhibit slight, yet distinctive in proportions, variations in metal endowment. Sillitoe and Thompson (1998) describe five probable transitional metal associations for the intrusion-related deposits including: Au-Fe oxide-Cu, Au-Cu-Mo-Zn, Au-As-Pb-Zn-Cu, Au-Te-Pb-Zn-Cu and Au-As-Bi-Sb. A spatial organization of these associations

includes the proximal Au-As \pm (Sn, W, Sb and base metals) and the distal Au-As-Sb-Hg \pm (Ag, Pb, Zn) deposits (Lang and Baker 2001). More recently, Hofstra and Kreiner (2020), based on the variable proportions of the same principal commodities (Cu, Zn, Pb, Ag, Au) and critical metals (Ge, Ga, In, Bi, Sb, As, W, Te) found in these deposits, used the overarching term "polymetallic S-R-V-IS" to collectively refer to skarn, replacement, vein, and intermediate sulfidation deposits (Table 1.2, Hofstra and Kreiner 2020).

Table 1.1. Deposit types related to porphyry Cu-Mo-Au systems and the principal, critical and rare metals hosted in them (modified from Hofstra and Kreiner 2020 and references therein).

Deposit types	Principal commodities	Critical and rare metals
Greisen	Mo, W, Sn	W, Sn
S-R-V tungsten	W	W, Bi, Mn
Porphyry/skarn molybdenum	Mo, W, Sn	W, Re, Bi
Porphyry/skarn copper	Cu, Au, Ag, Mo	PGE, Te, Re, Co, Bi, U
Skarn iron	Fe, Cu	Ge
Polymetallic S-R-V-IS	Cu, Zn, Cd, Pb, Ag, Au	Mn, Ge, Ga, In, Bi, Sb, As, W, Te
Distal disseminated silver-gold	Ag, Au	Sb, As
High-sulfidation gold-silver	Cu, Ag, Au	As, Sb, Te, Bi, Sn, Ga
Lithocap alunite and kaolinite	Al, K ₂ SO ₄ , Kaolin	Al, K ₂ SO ₄ , Ga

Abbreviations: S-R-V = skarn-replacement-vein, S-R-V-IS = skarn-replacement-vein-intermediate sulfidation.

1.2.3. Critical and rare metals - Mineral chemistry and nano-scale inclusions

During the past few years several works are investigating the trace elemental compositions of pyrite, chalcopyrite, magnetite and titanite by means of LA-ICP-MS (Deditius et al. 2011, Xu et al. 2015, George et al. 2018, Huang et al. 2019, Keith et al. 2020). A more restricted, yet advancing, literature was focused on arsenopyrite, sphalerite, tetrahedrite and stibnite geochemistry (Cook et al. 2009, 2013a, Frenzel et al. 2016, George et al. 2017, Li et al. 2019, Fu et al. 2020). The study of the trace element contents in these minerals contributes to the understanding of the ore-forming processes related to different ore deposit types and reveals the exploration and exploitation potentials of specific ore deposits in respect to critical and rare metals. Pyrite, chalcopyrite, arsenopyrite, sphalerite, tetrahedrite and stibnite are associated with varying amounts of critical and rare metals incorporated as: (1) solid solution or nanoparticles in crystal lattice, (2) nano-scale mineral inclusions, and (3) visible micro- to macro-scale mineral and fluid inclusions (Deditius et al. 2011, Cook et al. 2009, 2013a, George et al. 2017, 2018, Dmitrijeva et al. 2020, Keith et al. 2020, Fu et al. 2020). These inclusions can be formed through direct precipitation from the multi-

stage hydrothermal fluids into the minerals, or from processes such as overgrowth and recrystallization leading to exsolution, remobilization, and resorption of trace elements (Deditius et al. 2011, Cook et al. 2013a, George et al. 2018).

Pyrite (FeS_2) and chalcopyrite (CuFeS_2) are two common sulfide minerals found in most ore deposit types (Abraitis et al. 2004, Deditius et al. 2011, George et al. 2018). Ubiquity, a strong refractor character and stability under changing physicochemical conditions characterize pyrite (Deditius et al. 2011, Keith et al. 2020, Dmitrijeva et al. 2020). These aspects constitute pyrite a suitable mineral for the study of ore-forming processes (Abraitis et al. 2004, Deditius et al. 2011, Keith et al. 2020). Pyrite is an important host of several metals and metalloids including As, Hg and Tl in a weight percent (wt.%) level, and Co, Ni, Cu, As, Se, Mo, Ag, Sb, Te, Pb, Bi, Au and platinum group elements (PGE) in trace amounts (ppm levels, Keith et al. 2020, Dmitrijeva et al. 2020). These trace elements are found as solid solutions in pyrite and as complex nano-scale mineral inclusions (e.g. electrum, galena, tellurides, cinnabar) (Deditius et al. 2011, Keith et al. 2020).

Chalcopyrite may contain significant amounts of Ag, Se and Hg (in wt.% level) as well as a wide range of trace elements including Mn, Co, Zn, Ga, Cd, In, Sn, Sb, Tl, Pb and Bi (in ppm levels) (George et al. 2018, Reich et al. 2020, Marfin et al. 2020). In the absence of other co-crystallizing sulfides, chalcopyrite is characterized by an increasing ability to host lattice bound trace elements (George et al. 2018). Higher amounts of Ga and Sn in respect to other co-crystallizing sulfides are reported from chalcopyrite formed in high temperatures and/or pressures (George et al. 2018). Inclusions of other minerals and nanophases are commonly found in chalcopyrite, and mainly include sphalerite and micro-inclusions related to Zn-, As-, Pb- and Au-bearing mineral phases (George et al. 2018).

Arsenopyrite (FeAsS) is associated with trace elements including Co, Ni, Sb, Cu, Se and Te (in ppm to wt%. level), which are lattice bound and to Au, Ag, Pb and Bi (in ppm level) found as nanoparticles in growth zones or in cracks (Cook et al. 2013a, Li et al. 2019). Arsenopyrite commonly occurs in various magmatic-hydrothermal systems and is subjected to overgrowth and recrystallization resulting especially in gold (i.e. refractory or invisible form) enrichments.

Sphalerite (ZnS) incorporates a wide variety of trace elements in solid solution. Reported trace elements include Mn, Cd, In, Sn and Hg (in wt%. level) and Co, Ga, Ge, Mo, As and Tl (in ppm level) (Cook et al. 2009, Frenzel et al. 2016). Pb, Sb, Bi

and Au are mainly ascribed to nano- to micro- scale mineral inclusions, while Ag, Cu, Fe and Se may be related either to solid solution or mineral inclusions (Cook et al. 2009). Enrichments in Co and In are related to higher temperature ores, while Ga, Ge, Hg and Sn enrichments to lower temperature ores (Cook et al. 2009). In addition, when Ga and Ge are significantly incorporated in sphalerite, In content is depleted (Cook et al. 2009). Chalcopyrite, galena, native gold, tennantite-tetrahedrite, and a range of other sulfosalts and tellurides can be hosted as mineral inclusions in sphalerite (Cook et al. 2009). Principal component analysis conducted by Frenzel et al. (2016) demonstrates a positive correlation between Zn and Mn in sphalerite, and a negative correlation of Fe-Mn and Ge-Ga. Ag, Cu, Cd, Co and In contents are not correlated either to Fe-Mn or to Ge-Ga.

Tetrahedrite [(Cu,Fe,Zn,Ag)₁₂Sb₄S₁₃] is the Sb end member of the continuous solid solution series with the As-bearing tennantite. Tetrahedrite may contain significant amounts of Fe, Zn and Hg (in wt%. level), elevated values of Bi, Cd, Co and Mn, exceeding 1000 ppm, and minor amounts of Au, Ga, In, Mo, Ni, Te, Se, Sn and W (in ppm level, George et al. 2017). In co-crystallizing basic metal sulfides, tetrahedrite is enriched in Ag, As, Cu, Fe and Sb, and depleted in Ga, In and Sn (Hansen et al. 2003, George et al. 2017). Galena nano-scale inclusions are commonly found in tetrahedrite, while Sn enrichments may reflect stannite participating in solid solutions (George et al. 2017). In addition, other mineral members of the tetrahedrite-tennantite group may be incorporated in tetrahedrite or tennantite as solid solutions (i.e. freibergite, giraudite, goldfieldite, argentotennantite, argentotetrahedrite) (Hansen et al. 2003, George et al. 2017).

Stibnite (Sb₂S₃) trace elemental composition is not yet widely explored (Fu et al. 2020). Copper, Pb and As are mentioned as the main lattice bound substitutions for Sb in stibnite (in wt% level), whereas Au, Ag, Bi, In, Mo, Sn, Co, Cr, V, Zn, Ni, Ga, Ge, Rb, Sr, Pd, Cd and U can be incorporated in minor amounts (ppm level), related to nano-scale mineral inclusions (Fu et al. 2020). These inclusions comprise a range of low temperature sulfides, sulfosalts and arsenides (e.g. marcasite, chalcopyrite, löllingite, berthierite, galena) (Cook et al. 2013b). Stibnite may also be enriched in REE, especially in light REE such as Ce and La (Wang et al. 2012).

Magnetite and titanite are common accessory minerals in igneous and metamorphic rocks and in magmatic-hydrothermal ore deposits (Nadoll et al. 2014, Xu et al. 2015). Magnetite (Fe₃O₄) commonly contains trace elements including Ca,

Mg, Si and Ti (in wt.% level), and Ag, Al, As, Au, Co, Cr, Cu, Ga, Mg, Mn, Mo, Ni, Pb, V and Zn (in ppm level) (Nadoll et al. 2014, Deditius et al. 2018, Huang et al. 2019). Al, Co, Cr, Ga, Mg, Mn, Ni, Ti, V and Zn typically substitute primary cations in magnetite participating in the crystal lattice (Nadoll et al. 2014, Huang et al. 2019). Additionally, Al, Ca, Mg, Na, Si, Ti and V can be found as nanoparticles (i.e. nano-scale minerals, solid solutions) along growth or sector zones of magnetite (Deditius et al. 2018). Furthermore, high contents of P, Ti, V, Mn, Zr, Nb, Hf and Ta and low contents of Mg, Si, Co, Ni, Ge, Sb, W and Pb can distinguish igneous from hydrothermal (porphyry and skarn related) magnetite species (Nadoll et al. 2014, Huang et al. 2019). Overall igneous magnetite exhibits a more stable trace elemental signature than hydrothermal magnetite (Nadoll et al. 2014, Huang et al. 2019). This could be associated to the varying duration and temperatures of the multiple-fluid events resulting in the formation of hydrothermal magnetite (Deditius et al. 2018).

Titanite (CaTiSiO_5) incorporates significant amounts of Al, Fe, Na, K, U, Th, Sr, Y, Mn, Pb, Nb, Ta, Zr and REE (Xu et al. 2015). Al, Fe, Na, K and Mn are found in weight percent (wt.%) levels (Tiepolo et al. 2002, Cao et al. 2015). Chemical substitutions result in the enrichment of titanite in U, Th, Sr, Y, Nb, Ta, Zr and REE (Cao et al. 2015). Rare earth element concentrations, especially for Ce and Nd, can reach up to tens of thousands of parts per million (Xu et al. 2015). These elements are found structurally bound in titanite (Tiepolo et al. 2002, Cao et al. 2015).

1.3. Western Tethyan metallogenic belt: Serbo-Macedonian and Rhodope metallogenic provinces

The closure of the oceans of Paleotethys and Neotethys between middle Paleozoic and the present, have led to the formation of the Tethyan orogenic belt which stretches for more than 10,000 km from the Western Mediterranean to Southwestern Indonesia (Richards 2015, Wang et al. 2020). Tethyan metallogenic belt (TMB) is co-incident to the Tethyan orogen and is sub-divided into the Western and the Eastern Tethyan metallogenic belts (Figure 1.7, Richards 2015). Several small and mainly short-lived back-arc basins were formed between Mesozoic and Cenozoic along the Tethyan orogenic belt (late Jurassic to Miocene, Richards 2015). Thus, several major porphyry deposits are found along the TMB and during the last two decades 50 new Cu-deposits have been explored comprising more than 280 Mt of Cu ore (Zürcher et al. 2015, Wang et al. 2020).

The Serbo-Macedonian metallogenic province (SMMP) and the Rhodope metallogenic province (RMP) are part of the Western Tethyan metallogenic belt (Bertrand et al. 2014, Richards 2015, Melfos and Voudouris 2017, Figure 1.7). Furthermore, they constitute a continuous terrain comprising important deposits and prospects (e.g. the Trepça, Mavres Petres and Olympias skarn/carbonate replacement deposits, the Perama Hill and Sapes high-intermediate sulfidation epithermal deposits, the Allchar, Ada Tepe, and Kallyntirion Carlin-type deposits, and the Buchim, Skouries and Maronia porphyry deposits (Voudouris et al. 2011, Melfos and Voudouris 2012, 2017, Kołodziejczyk et al. 2015, McFall et al. 2018, Strmić Palinkas et al. 2018, Baker 2019, Melfos et al. 2020, Serafimovski et al. 2021).

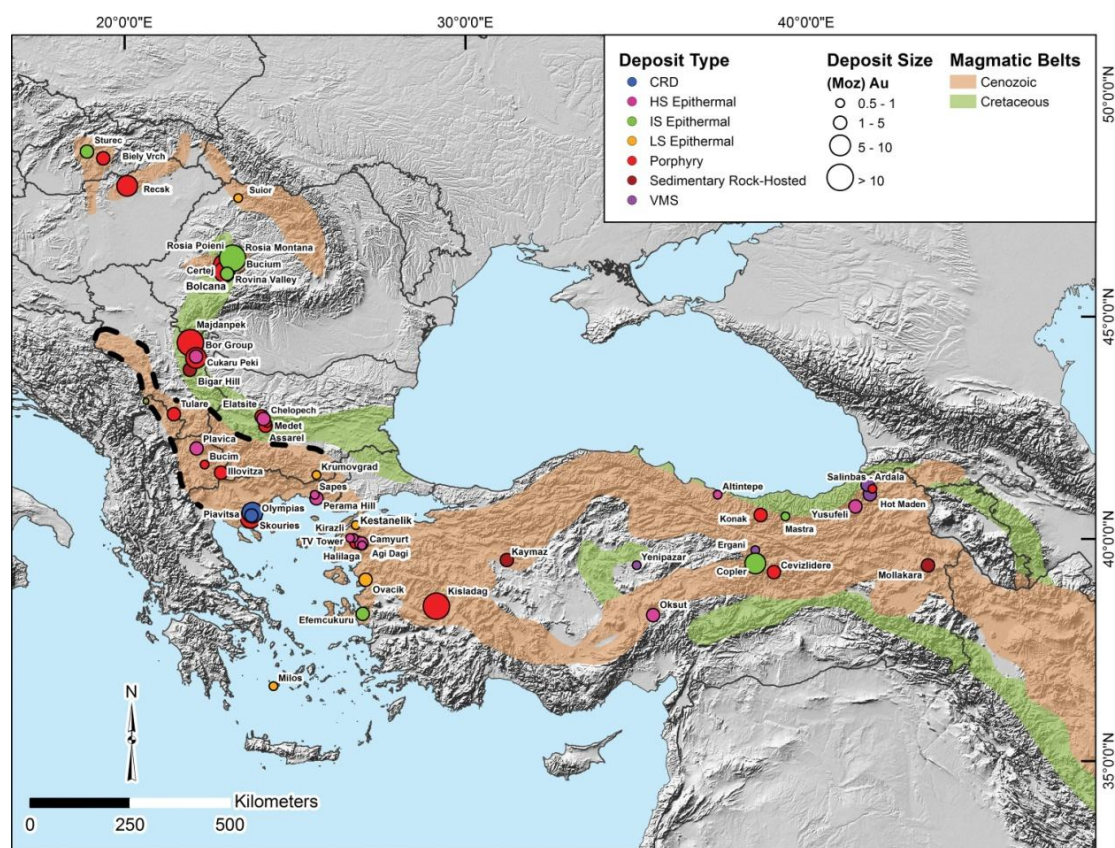


Figure 1.7. The Western Tethyan metallogenic belt and associated major Cretaceous and Cenozoic deposits in respect to gold endowment. The dashed black line highlights the location of the SMMP and RMP (CRD = carbonate replacement deposit, HS = high sulfidation, IS = intermediate sulfidation, LS = low sulfidation, VMS = volcanogenic massive sulfide, adapted and modified from Baker 2019).

In northeastern Greece, throughout the regions of Central-Eastern Macedonia and Thrace, the SMMP and the RMP, host major deposits and prospects including: 16

porphyry, 10 epithermal, 8 skarn/carbonate replacement, 9 intrusion-related polymetallic veins, and 2 reduced intrusion-related gold types which are grouped in 15 ore districts (Melfos and Voudouris 2017, Voudouris et al. 2019a).

1.4. Project rationale – Critical and rare metals under investigation

Major deposits of critical and rare metals are generally related to alkaline/peralkaline-carbonatite igneous rocks (e.g., carbonatites and granitic pegmatites), to sedimentary phosphorite and uranium ores, and to placer-type REE deposits (Dostal 2016, Sengupta and Van Gosen 2016, Verplanck and Hitzman 2016, Verplanck et al. 2016). However, deposits formed by magmatic-hydrothermal processes including porphyry Cu-Mo-Au and epithermal gold deposits related to alkaline igneous rocks, as well as Carlin-type and orogenic gold deposits, are also potential sources of rare metals, mainly as by-products (Goldfarb et al. 2016, Hofstra and Kreiner 2020, John and Taylor 2016, Kelley and Spry 2016, Velásquez et al. 2020).

Diversifying sources of critical and rare metals is of key significance. The exploitation of critical and rare metals mainly as by-products from porphyry systems could serve in source diversification (Goldfarb et al. 2016, John and Taylor 2016, Velásquez et al. 2020). Although, the enrichment processes of these metals and their distribution needs further understanding. Bulk geochemistry and mineral chemistry in respect to hydrothermal alterations and ore mineralization could assist in this direction. This knowledge could help in future exploration of critical and rare metals, as well as to unlock new exploitation potentials for producers.

The considerable potential in critical and rare metals of the deposits located in northern Greece has been previously emphasized (Arvanitidis 2010, Melfos and Voudouris 2012, Eliopoulos et al. 2014, Charalampides et al. 2013, Voudouris et al. 2013a, Cassard et al. 2015, Bertrand et al. 2016, Melfos and Voudouris 2017, Tsirambides and Filippidis 2019, Voudouris et al. 2019a). The present doctoral thesis aims to examine the critical and rare metals distribution in selected Cenozoic deposits located in the SMMP and RMP in NE Greece. The study is focused on the Vathi porphyry Cu-Au±Mo deposit, the Gerakario epithermal quartz-stibnite veins, the Laodikino metamorphic- and quartz-hosted polymetallic mineralization, the Kolchiko metamorphic- and quartz-hosted polymetallic veins, and the Aspra Chomata porphyry Cu-Au with the epithermal vein mineralization. The choice of these deposits was

based on previous publications highlighting their potential on critical and rare metals (e.g. Mposkos 1983, Thymiatis 1995, Melfos and Voudouris 2012, 2017, Toumanidou 2019, Tsirambides and Filippidis 2019, Voudouris et al. 2019a, Stergiou et al. 2018, 2021a-c).

Two exploration drilling projects have been held during the 1970s and 1980s at the Vathi deposit targeting the uranium and the porphyry-style mineralization (Stergiou et al. 2021a,b, advise Figure 2.1, 2.2). In addition, the tectonic setting, magmatism, hydrothermal alteration, ore mineralogy, and fluid inclusions of the Vathi deposit were previously studied by Filippidis et al. (1988), Frei (1992), and Stergiou et al. (2021a,b). Soil geochemical investigation was carried out by Kelepertsis et al. (1986). Rough estimations indicate 15 Mt of ore, grading 0.3 wt.% of Cu and 0.8 g/t of Au (Stergiou et al. 2016).

The Gerakario area has been explored for the porphyry Cu and Au, and the epithermal Sb mineralizations between the 1970s and the 1990s, and a review of the exploration workings is given by Toumanidou (2019) (advise Figure 2.1, 2.2). Kelepertsis et al. (1986) conducted a soil geochemical investigation in the area. Preliminary estimations report 9.6 Mt of ore with 0.35 wt.% Cu and up to 1.4 g/t Au (Toumanidou 2019). For the Laodikino area, Thymiatis (1995) mentions that the Institute of Geology and Mineral Exploration (IGME) carried out exploration workings, between 1978 and 1983, which included 8 drillings with a total length of 1,115 m (advise Figure 2.1, 2.2). In addition, Kelepertsis et al. (1987) conducted a stream and soil geochemical investigation.

At Kolchiko area, no exploration workings have ever been held (advise Figure 2.1, 2.2). Patsiouri (2017) examined the mineralogy and geochemistry of the polymetallic veins. The deposit is similar in terms of structural control and geochemistry with the adjacent Drakontio metamorphic- and quartz-hosted polymetallic vein mineralization (Vavelidis et al. 1999). The porphyry style deposit at Aspra Chomata is part of the Stratoní granodiorite stock, which has been systematically explored in previous years in the framework of the metallogenic study of the area (Siron et al. 2016, advise Figure 2.1, 2.2). A description of the mineralogy and geochemistry of the porphyritic stage and the adjacent base metal vein mineralization was first given by Gounaris (2017).

Geochemical investigations of bulk surface and core samples have revealed the enrichment of these deposits and prospects in critical and rare metals (Stergiou et al.

2018, 2021a-c). Furthermore, significant research was previously carried out regarding the ore mineral chemistry including scanning electron microscopy with energy dispersive spectroscopy (SEM-EDS) and electron probe micro analysis (EMPA) (e.g. Thymiatis 1995, Vavelidis et al., 1999, Melfos et al. 2001, Voudouris et al. 2007, Patsiouri 2017). However, the ore mineral chemistry by means of laser ablation inductively coupled plasma mass spectrometry (LA-ICP-MS) remains unexplored.

The investigation held during the previous years has substantially contributed in the discovery and exploration of several deposits in terms of ore geology, mineralogy, and bulk geochemistry. Furthermore, they have presented strong indications on critical and rare metals endowment. Nevertheless, the mineral chemistry and particular associations between specific minerals and trace metals need further investigation. For example, the distribution, abundance, and correlation of critical and rare metals among the different hydrothermal alteration styles and mineralization stages, especially for the porphyry deposits, is of major interest and have not been evaluated previously.

In the present study, emphasis is given to the distribution of the critical rare metals including Ag, Au, Bi, Ce, Co, Ga, Gd, Ge, In, La, Nb, Nd, Se, Sm, Ta, Te, Th, U and W in pyrite, chalcopyrite, magnetite and titanite from Vathi, in stibnite from Gerakario, in pyrite, chalcopyrite, sphalerite, tetrahedrite and magnetite from Laodikino, in pyrite, chalcopyrite, sphalerite and arsenopyrite from Kolchiko, and in pyrite and sphalerite from Aspra Chomata.

The deliverables of this project expand the scientific knowledge on the critical and rare metals endowment and their genetic associations in northern Greece. Moreover, they could promote and support the planning of new exploration and exploitation projects in the region by revealing the additional values of these deposits.

CHAPTER 2. GEOLOGICAL SETTING AND CENOZOIC MINERALIZATION

The area under investigation belongs to the Rhodope and the Serbo-Macedonian Massifs. The Rhodope Massif constitutes a deep-crustal nappe stack formed in close relation to Carpatho-Balkanides fold and thrust belt (Schmid et al. 2020). Between Eocene and Miocene, it was exhumed below the Carpatho-Balkanides orogen, the Serbo-Macedonian Massif (SMM) and the Circum-Rhodope Belt, and is now exposed as a giant core complex in southern Bulgaria and Greece (Schmid et al. 2020). This core complex is subdivided in the Northern Rhodope Core Complex, the Northern Rhodope Domain, and the Southern Rhodope Core Complex (Kydonakis et al. 2016). Five geotectonic units have been described including the lowermost Pangaion-Pirin Unit, the lower Arda-Byala Reka Unit, the middle Nestos suture zone Unit, the upper Kerdyllion-Madan Unit, and the uppermost Asenitsa-Thrace Unit (Schmid et al. 2020).

The Kerdyllion Unit belongs to the Southern Rhodope Core Complex and consists of Permian-Carboniferous mylonitic orthogneisses, micaschists and amphibolites, covered by marbles (Kydonakis et al. 2016, Figure 2.1). In the gneisses, a post-early Eocene metamorphic event of upper greenschist/lower amphibolite-facies is mentioned by Kydonakis et al. (2016). To the west, the Kerdyllion Unit borders to the Vertiskos Unit along the Kerdyllion detachment fault and the Stratonif fault (Figure 2.1).

The Vertiskos Unit constitutes the southern extension of the SMM in Greece. It is a NW-trending polytectonic and polymetamorphosed geotectonic and basement zone, stretching from the northern Greek borders to the Chalkidiki peninsula. It lies west of the Kerdyllion Unit along the Kerdyllion detachment fault, and east of the Circum-Rhodope Belt along a NW–SE trending dextral transpressional and transtensional fault zone (Kilias et al. 1999, Tranos et al. 1999, Brun et al. 2018, Schmid et al. 2020, Mposkos et al. 2021, Figure 2.1). The Chortiatiss Magmatic Suite and the Eastern Vardar Ophiolites are also found west of the SMM (Kydonakis et al. 2016). Vertiskos Unit consists of gneiss, schist and amphibolite intercalated with marble. Neoproterozoic to middle Ordovician granitoids, and Paleozoic to Triassic metagabbros-metadiabases and granites are also found (Kilias et al. 1999, Christofides et al. 2007, Abbo et al. 2019, Mposkos et al. 2021).

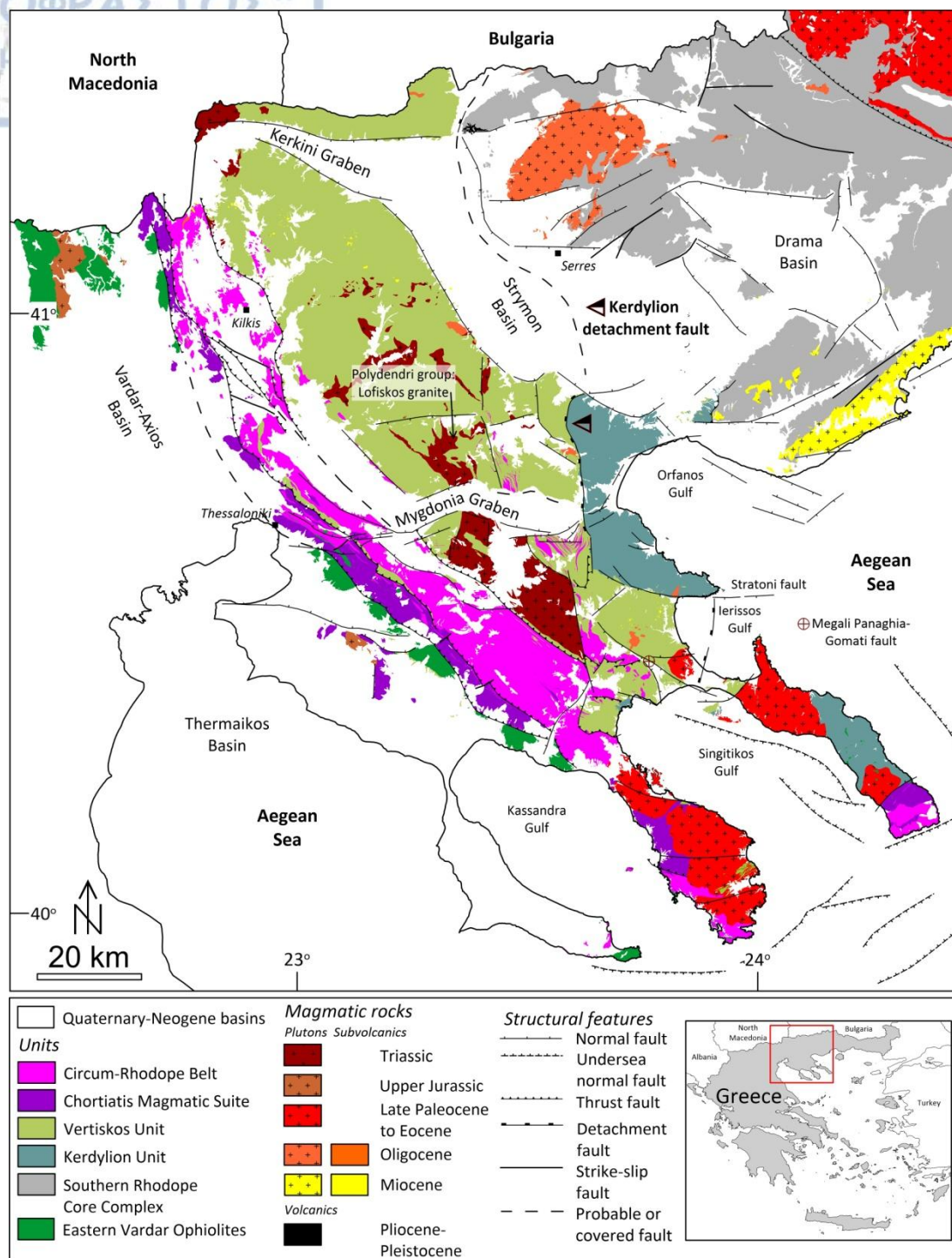


Figure 2.1. Geological map of the Vertiskos Unit in northern Greece. The adjacent Kerdyllion Unit, the Circum-Rhodope Belt, the Chortiatis Magmatic Suite, and the Eastern Vardar Ophiolites are also shown (modified after Kydonakis et al. 2016, Stergiou et al. 2018, 2021a,b).

According to Mposkos et al. (2021) the following metamorphic events describe the metamorphic history of the Vertiskos Unit (VOC=Vertiskos-Ograzden Complex (undifferentiated), SMM): (1) a Variscan ultrahigh pressure eclogite facies

metamorphism, (2) a Triassic low pressure and high temperature event, (3) a Jurassic-early Cretaceous prograde moderate to high-pressure epidote-amphibole to upper amphibolite facies metamorphism, and (4) a restricted late Cretaceous low pressure amphibolite facies event. It should also be mentioned that previous researchers studying the western part of the Vertiskos Unit in northern Greece highlight two pre-Mesozoic metamorphic events (HP-LT eclogite facies and HP-HT granulite facies and migmatite formation) and three Mesozoic to Cenozoic metamorphic events, including Jurassic to Cretaceous amphibolitic facies (~540-690°C, 0.5-0.8 GPa) followed by late Cretaceous to Eocene upper greenschist facies (MP-to-HP) and retrograde low greenschist facies events (Kourou 1991, Sidiropoulos 1991).

The Cenozoic igneous evolution of the Vertiskos and Kerdylion Units includes late Paleocene to Pliocene magmatic rocks subdivided in four magmatic pulses (Figure 2.1). These magmatic rocks include I-type plutonic, sub-volcanic, and volcanic rocks, associated with calc-alkaline to high-K calc-alkaline and shoshonitic affinities (Kockel et al. 1975, Frei 1992, Siron et al. 2018, Abbo et al. 2019, Figure 2.1). In the Southern Rhodope Core Complex, and in Kerdylion Unit, plutonic rocks exhibiting syn-tectonic fabrics occur, whereas in the Vertiskos Unit most magmatic rocks are late-stage intrusions (Eleftheriadis et al. 2001, Hahn et al. 2012, Siron et al. 2018). The mineralized intrusions are associated with the second and the third magmatic pulses (Oligocene-Miocene) and are located mainly in the Kilikis and the Chalkidiki ore districts (Melfos and Voudouris 2017, Siron et al. 2016, 2018, 2019, Stergiou et al. 2021a, Figure 2.2).

The Vertiskos Unit is located in the hanging wall of the Eocene-Oligocene Kerdylion first-order detachment fault, while another first-order structure of the region is the Miocene Strymon detachment fault exposed mainly in SW Bulgaria (Brun and Sokoutis 2018, Schmid et al. 2020, Figure 2.1). These two detachment faults are associated with an extensional regime, lasting from the late Cretaceous to the Miocene that resulted in the collapse of the Vertiskos Unit towards the SSW (Kydonakis et al. 2016, Brun and Sokoutis 2018). In the Vertiskos Unit, the extension is documented by ENE-WSW- and eastward-trending shear zones and related E-W-, NW-SE-, and NE-SW-trending normal to oblique faults and N-S-trending strike-slip faults (Kiliadis et al. 1999). The Cenozoic magmatic events and the formation of the Oligocene-Miocene mineralized intrusions were structurally controlled by these faults (Hahn et al. 2012, Siron et al. 2018, Stergiou et al. 2021a).

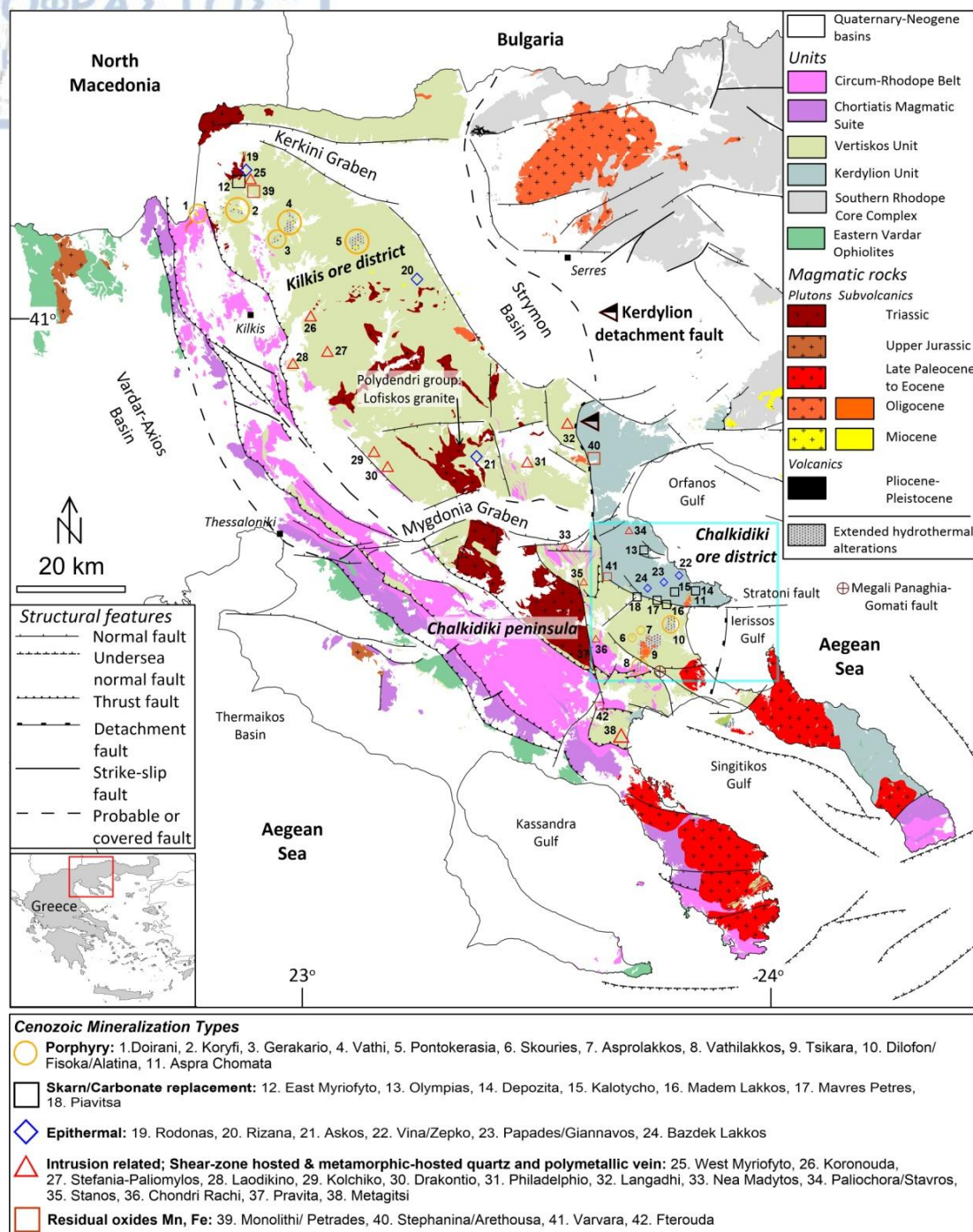


Figure 2.2. The geological setting of the Cenozoic magmatic rocks and related porphyry-type mineralization of the Vertiskos and Kerdylon Units (modified after Kydonakis et al. 2016, Melfos and Voudouris 2017, Siron et al. 2019, Stergiou et al. 2021a,b).

In the Vertiskos Unit, several deposits and prospects are located mainly along the Chalkidiki and the Kilgis ore districts (Voudouris et al. 2019a, Stergiou et al. 2021a,b). At the northern part of the Kilgis ore district, porphyry (Doirani, Koryfi, Gerakario, Vathi, Pontokerasia), skarn/carbonate replacement (East Myriofoyto), intrusion related (West Myriofoyto), epithermal (Rodonas), and residual oxides

(Monolithi, Petrades) deposits occur (Figure 2.2). The most important mineralization includes the Gerakario Cu-Au porphyry deposit hosted in a calc-alkaline syenite and a granodiorite intrusion, the Pontokerasia Cu-Mo-Au porphyry deposit associated with a calc-alkaline syenite intrusion, and the Vathi Cu-Au±Mo porphyry deposit associated with a high-K calc-alkaline monzonite (Stergiou et al. 2018, 2021a,b). Exploration projects held during the 1970s and the 1980s at Pontokerasia, Vathi and Gerakario indicated estimates of more than 258 Mt of ore with 0.40 wt.% Cu and 0.9 g/t Au (Tsirambides and Filippidis 2016).

Towards the south, mainly intrusion-related ore mineralization occurs, including shear-zone hosted and metamorphic- and quartz-hosted polymetallic veins (Koronouda, Stefania-Paliomylos, Laodikino, Kolchiko, Drakontio, Philadelphio, Langadhi) (Mposkos 1983, Thymiatis 1995, Vavelidis et al., 1999, Melfos et al. 2001, Stergiou et al. 2021a-c, Figure 2.2). A restricted occurrence of epithermal deposits is also documented at Rizana and Askos, while residual oxides (Fe, Mn) are found in Stephanina and Arethousa (Skoupras 2019, Stergiou et al. 2021a,b, Figure 2.2). Further to the south, in the Stanos-Nea Madytos ore district a shear-zone hosted Cu-Au-Bi-Te mineralization is located (Voudouris et al. 2013c, Bristol et al. 2015, Figure 2.2). Although magmatic intrusions are scarce in the region, there is evidence that these mineralizations are connected with magmatism (Voudouris et al. 2031c, Bristol et al. 2015).

The Chalkidiki ore district, also known as the Kassandra mining district, hosts several deposits and prospects that are actively explored and exploited since antiquity (Melfos and Voudouris 2017, Siron et al. 2018, 2019). The ore district spreads in both the Vertiskos and Kerdyllion Units (Figure 2.2). In the northern part, mainly carbonate replacement deposits (Olympias, Depozita, Kalotycho, Madem Lakkos, Maves Petres, Piavitsa) are found, whereas in the southern part porphyry deposits occur (Skouries, Asprolakkos, Vathilakkos, Tsikara, Dilofo, Fisoka, Alatina) (Melfos and Voudouris 2017, Voudouris et al. 2019a). Other deposits include the residual oxides (Mn, Fe) at Varvara and Fterouda and the intrusion related mineralization at Stavros, Paliochora, Pravita and Metagitsi (Figure 2.2).

The deposits found in the Kassandra mining district are mostly found in a narrow zone, set in an extensional regime and controlled by the southeastward extensions of the Kerdyllion detachment fault and of the Stratoni and Megali Panaghia-Gomati normal to oblique faults (Hahn et al. 2012, Siron et al. 2018, 2019, Figure 2.2). The

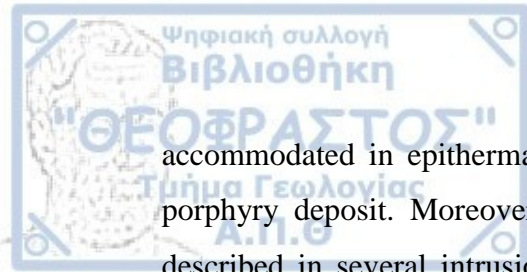
total measured and indicated resources comprise: 239.974 Mt of ore with 0.47 wt.% Cu and 0.65 g/t Au at Skouries Cu-Au porphyry deposit, 13.463 Mt of ore grading 4.8 wt.% Pb, 6.3 wt.% Zn, 8.07 g/t Au, and 145 g/t Ag at Olympias polymetallic carbonate replacement deposit, and 1 million Mt of ore with 6.2 wt.% Pb, 8.3 wt.% Zn, and 161 g/t Ag at Mavres Petres (Eldorado Gold Corporation 2021).

Most of the deposits and prospects located in the Kilgis ore district are poorly explored missing information on measured and indicated reserves and resources for base, critical and rare metals. Furthermore, a lack in knowledge of morphological and mineralogical characteristics is documented for some intrusion related deposits. Table 2.1 summarizes the deposits in the Vertiskos and Kerdylion Units that are enriched in critical and rare metals.

Table 2.1. Deposits enriched in critical and rare metals (modified after Melfos and Voudouris 2017, Stergiou et al. 2018).

Deposit	Ore district	Main commodities	Mineralization type	Critical and rare metals	References
Vathi	Kilkis	Cu, Au, Mo, U	Porphyry	W, Ga, Te, Bi, La, Ce, Nd, Gd, Au, Ag	Stergiou et al. (2021a,b)
Gerakario	Kilkis	Cu, Au	Porphyry	Sb	Toumanidou et al. (2019)
Skouries	Chalkidiki	Cu, Au, Mo	Porphyry	Pd, Pt, Ru, Re, Te, Bi	Eliopoulos et al. (2014), McFall et al. (2018)
Stanos	Stanos-Nea Madytos	Cu	Shear zone hosted	Au, Ag, Bi, Te	Bristol et al. (2015)
Laodikino	Kilkis	Cu, Fe, As, Zn, Pb, Ni	Metamorphic and quartz-hosted	Au, Te, Co, Sb, Bi	Thymiatis (1995)
Rizana	Kilkis	Sb, W	Epithermal	Sb, W	Skoupras (2019)
Stephania	Kilkis	Cu, Ni, As	Metamorphic and quartz hosted	Ag, Au, Bi, Te, Co	Melfos and Voudouris (2012)
Koronouda	Kilkis	Cu, Zn, Pb, Fe, As, Ni	Metamorphic and quartz hosted	Au, Ag, Co, Sb, Te, Bi	Bristol et al. (2015)

Platinum and Pd in the Skouries porphyry deposit are associated mainly with chalcopyrite, while Re is related to molybdenite (Eliopoulos et al. 2014, McFall et al. 2018). In the Vathi porphyry deposit significant enrichments in critical and rare metals (e.g. Au, Bi, Ce, La, Te) are attributed to hydrothermal alteration, ore mineralization, supergene enrichment and to phreatic breccia (Stergiou et al. 2021a,b). At the Rizana epithermal and shear-zone hosted deposit, stibnite and wolframite are the main Sb and W bearing minerals (Skoupras et al. 2019). Stibnite is also



accommodated in epithermal quartz veins found in the periphery of the Gerakario porphyry deposit. Moreover, telurides and a variety of Te- and Bi-sulfosalts are described in several intrusion-related deposits. Te and Bi are enriched in minerals such as tetradymite, bismuthinite, tellurobismuthite, aikinite, hessite, petzite, altaite and sylvanite (Thymiatis 1995, Voudouris et al. 2007, Patsiouri 2017).

CHAPTER 3. METHODOLOGY

3.1. Fieldwork and sampling

In this thesis, five deposits in the Region of Central Macedonia - Greece were studied in respect to critical and rare metal endowment. They are located in the areas of Vathi, Gerakario, Laodikino, Kolchiko, and Aspra Chomata. Surface mapping and sampling was held during the summer seasons of 2018 and 2019. During the field work, information on local geology, structural and vein relations were collected. Sampling was focused on the mineralization and the fresh and hydrothermally altered metamorphic and igneous rocks.

The Vathi porphyry Cu-Au±Mo deposit and the Gerakario stibnite vein mineralization are located approximately 16 km NE of Kilkis city, at the Public Mining Area of Vathi-Gerakario (Figure 2.2). The Vathi porphyry deposit (N41.1458°, E22.9639°) is located near the Vathi village, along Ragian Hills 1 and 2. Ten surface samples were collected, with a focus on hydrothermal alteration styles and mineralization stages. In addition, a set of 73 older surface samples and 16 polished sections from the legacy drill core samples were evaluated for further mineralogical and geochemical study. Eight polished sections studied here were from drill core H4 (43 to 166 m interval), and seven were from drill core H5 (53 and 73 m interval, please advise Figure 4.1). Description and characterization of the mineralogy and the alteration styles of the available drill cores can be found in Stergiou et al. (2021a).

The Gerakario stibnite vein mineralization (N41.114297°, E22.935334°) occurs at the SE part of the Gerakario Cu-Au porphyry deposit (Divouni Hills, N41.117023°, E22.929289°). Three samples were collected from a quartz-stibnite vein in an old underground mine.

The Laodikino metamorphic and quartz hosted polymetallic vein mineralization is located approximately 12 km SE of the Kilkis city (Figure 2.2). Polymetallic Cu-Au-Bi-Pb-Ag-Te±Au-bearing quartz and massive veins are hosted in a hilly area of approximately 6.6 km², located among the villages Laodikino, Chrysopetra, Fanari, Lipsidri and Akropotamia (N40.911088°, E22.972161°: coordinates centered to this area). Fieldwork was focused on local geology, as well as on vein and structural relations. Twenty-one samples were gathered originating from the mineralized quartz veins and the hydrothermally altered surrounding rocks.

The Kolchiko metamorphic- and quartz-hosted polymetallic vein mineralization is found approximately 22 km NE of Thessaloniki city (Figure 2.2). Polymetallic quartz (N40.769474°, E23.143515°) and massive (N40.772274°, E23.150227°) veins, enriched in As, Cu, Bi, Pb, Co, Ni, Ag and Au are found in a distance of approximately 5 km along the stream draining the area NE of the Kolchiko village. Fifteen samples were collected, and 8 more samples were adapted from the study of Patsiouri (2017). The Aspra Chomata porphyry deposit and epithermal vein mineralization is located approximately 75 km E of Thessaloniki city and 2 km N of Stratoni village in the Chalkidiki ore district (Figure 2.2). Twelve samples were collected, and 6 more samples were adapted from Gounaris (2017).

3.2. Microscopy

Optical microscopy study was held at the Department of Mineralogy-Petrology-Economic Geology, Aristotle University of Thessaloniki. In total, 73 polished and 30 thin-polished sections were prepared and studied under a Leitz LaborLux 11 Pol dual reflected-transmitted light polarizing microscope coupled with a Levenhuk M base series digital camera.

3.3. Scanning electron microscope (SEM)

A total of 50 selected polished sections were studied with a JEOL JSM-6390LV (Tokyo, Japan) scanning electron microscope (SEM) equipped with an OXFORD INCA 300 energy-dispersive system (EDS) (Oxford Instruments Ltd., Abingdon, UK) at the Faculty of Sciences, Aristotle University of Thessaloniki. The operating conditions were a 20 kV accelerating voltage and 0.4 mA probe current, 80s analysis time, and a beam diameter of ~1 μm , in the back-scattering electron (BSE) mode. SEM-EDS micro-analysis was targeted on the mineral chemistry of pyrite, chalcopyrite, titanite and magnetite from Vathi, of stibnite from Gerakario, of pyrite, chalcopyrite, sphalerite, tetrahedrite and magnetite from Laodikino, of pyrite, chalcopyrite, arsenopyrite and sphalerite from Kolchiko, and of pyrite and sphalerite from Aspra Chomata. The study focused on the detection of minerals found as micro-scale inclusions in the aforementioned minerals. Additionally, the determined iron, copper, zinc and titanium contents were used as internal standards in LA-ICP-MS analyses for pyrite, chalcopyrite, sphalerite, tetrahedrite, arsenopyrite, magnetite and

titanite. The tables with the average values of the conducted SEM-EDS analyses are given in Supplement 1.

3.4. LA-ICP-MS

A total of 22 polished sections were selected for the LA-ICP-MS analyses. Ten sections were from Vathi, two from Gerakario, three from Laodikino, five from Kolchiko, and two from Aspra Chomata. Trace element concentrations in pyrite, chalcopyrite, sphalerite, tetrahedrite, arsenopyrite, stibnite, magnetite and titanite were measured using a PerkinElmer ELAN DRC-e ICP mass spectrometer combined with a New Wave UP193-FX excimer laser ablation system at the Geological Institute, Bulgarian Academy of Sciences, Sofia, Bulgaria. The ablation was conducted in He medium. In order to maximize sensitivity, the ICP-MS was optimized daily with respect to the oxide production rate of ThO/Th (0.5%). Operating conditions of the laser system include: 5 Hz repetition rate, 20 to 50 μm spot size, and energy density on analyzed minerals and standards of 5.0 to 5.2 J/cm^2 (at 35 and 50 μm spot) and 4.5 to 5.0 J/cm^2 (at 25 and 20 μm spot). The nebulizer gas flow rate was 0.8 L/min, while auxiliary and make-up gas flows rates were 0.92 L/min. The analysis time was 100 s (background: 40 s, laser-on the sample: 60 s). The acquisition dwell time was set to 0.02 s for ^{74}Ge , ^{82}Se , ^{115}In , ^{125}Te , and ^{202}Hg , to 0.03 s for ^{107}Ag , to 0.04 s for ^{197}Au , and to 0.01 s for all other elements. The monitored isotopes include: ^{27}Al , ^{31}P , ^{34}S , ^{49}Ti , ^{51}V , ^{53}Cr , ^{55}Mn , ^{57}Fe , ^{59}Co , ^{60}Ni , ^{65}Cu , ^{66}Zn , ^{71}Ga , ^{73}Ge , ^{74}Ge , ^{75}As , ^{77}Se , ^{93}Nb , ^{95}Mo , ^{107}Ag , ^{111}Cd , ^{115}In , ^{118}Sn , ^{121}Sb , ^{125}Te , ^{139}La , ^{140}Ce , ^{146}Nd , ^{147}Sm , ^{157}Gd , ^{182}W , ^{185}Re , ^{197}Au , ^{202}Hg , ^{205}Tl , ^{208}Pb , ^{209}Bi , ^{232}Th and ^{238}U . The targeted areas in the polished sections were predefined to try to avoid mineral inclusions. Repeated external standardization was conducted by analyzing NIST SRM 610 and USGS GSD-1G glass standards, and the USGS Mass 1 sulfide standard.

Data reduction was performed by using the Fe contents of pyrite, chalcopyrite, arsenopyrite and magnetite, Zn contents of sphalerite, Cu contents of chalcopyrite, Ti contents of titanite, as well as Sb contents of stibnite measured by SEM-EDS as internal standards and the SILLS software (Guillong et al. 2008). During data reduction, peak-shaped fluctuations of the intensity signal of some isotopes were investigated in order to exclude the influence of other minerals on the chemical composition of the studied minerals. The full list of the LA-ICP-MS data, including elements ascribed to nano-scale mineral inclusions, is given in Supplement 2.

For the statistical analysis of the LA-ICP-MS analytical results, univariate analysis (minimum, maximum, standard deviation, and average) and bivariate analysis (Pearson's correlations, Supplement 3) were obtained with the SPSS statistics software (IBM). Statistical graphs and time-resolved analytical profiles of LA-ICP-MS analyses were plotted using the Grapher software (Golden Software LLC).

3.5. Bulk chemical analysis

Bulk geochemical analyses for major elements were conducted by lithium borate fusion and inductively coupled plasma emission spectrometry (ICP-ES), while trace elements, including REE, were determined in an ultra-trace level by Aqua Regia digestion and inductively coupled plasma atomic emission spectroscopy (ICP-AES). Aqua Regia digestion and ICP-ES finish was implied for overlimit analyses (detection limits: 1-1,500 ppm, ore grade) were conducted for As in Kolchiko samples, for Ag, Cd and Sb in Aspra Chomata samples, and for Sb in Laodikino samples. Overlimit Ag in Laodikino was determined by means of fire assay with gravimetric finish (detection limits: 50 - 10,000 ppm). All geochemical analyses of this research were carried out at MSALABS, Langley, Canada. The full dataset is given in Supplement 4. Previously published geochemical analyses by Stergiou et al. (2021a) and Gounaris (2017) which were considered in this study are also presented (Supplement 4). The statistical analysis of the bulk geochemical analyses included univariate and bivariate analysis (Supplement 3).

CHAPTER 4. VATHI PORPHYRY Cu-Au±Mo DEPOSIT

4.1. Local geology

Basement rocks at Vathi include Paleozoic two-mica gneisses and schists, intercalated with amphibolites, amphibolitic schists, and Mesozoic peridotites, which are intruded by unmineralized pegmatites and milky quartz veins (Figure 4.1, Stergiou et al. 2021a,b).

Cenozoic magmatic rocks at Vathi comprise subvolcanic stocks and dikes exhibiting porphyritic texture and barren granites that intruded the crystalline rocks (Stergiou et al. 2021a,b). These rocks occur in a graben bounded by faults with WNW-ESE and E-W trends (Stergiou et al. 2021a,b). Outcrops of the porphyry mineralization are located along Ragian 1 and 2 Hills (Figure 4.1). The mineralization is hosted by latite and is genetically associated with a quartz monzonite (18 ± 0.5 Ma and 17 ± 1 Ma, U-Pb zircon ages, Frei 1992), which intruded the crystalline basement rocks and the latite (Stergiou et al. 2021a,b, Figure 4.1). Both magmatic rocks are silica-saturated and exhibit calc-alkaline to slightly alkaline chemical affinities (Frei 1992, Stergiou et al. 2021a,b). A phreatic breccia crosscuts the latite and is genetically related to the quartz monzonite intrusion, whereas a latite cataclasite located in the northern part of Ragian Hill 1 is associated with a late epithermal event (Figure 4.1, Stergiou et al. 2021a,b). Old exploration drilling projects at Vathi revealed the development of an almost 100 m deep oxidation zone, and a narrow secondary enrichment zone (Stergiou et al. 2021a,b). Slightly altered and barren granites are found west and southwest of Ragian 1 and 2 Hills (Figure 2.1, Stergiou et al. 2021a).

Quartz monzonite outcrops are rare and are characterized by a weak potassic alteration, whereas the latite was affected by a local propylitization. An intense sericitic alteration overprinted these two alteration styles (Filippidis et al. 1988, Frei 1992, Stergiou et al. 2021a). Locally, a subsequent epithermal overprint is observed in the latite. Mineralization forms disseminations, aggregates, and veins (M, A and D types), while the metallic assemblage related to the epithermal overprint is accommodated in E-type veins (Stergiou et al. 2021a,b).

The porphyry-style mineralization was developed in a shallow (<2.6 km in depth) environment from hydrothermal fluids with moderate to high salinities at a minimum temperature of 311 °C. The late epithermal overprint was associated with less saline fluids (1.4-2.9 wt.% NaCl equiv.) and lower temperatures ranging from 205 to 259 °C

(Stergiou et al. 2021a). Surface samples contain as much as 9297 ppm Cu, 341 ppm Mo, 7 ppm Au, and 263 ppm U. In addition, an enrichment of La (up to 613 ppm), Ce (up to 894 ppm) and Nd (up to 211 ppm) is attributed to the formation of phreatic breccia (Stergiou et al. 2021a,b).

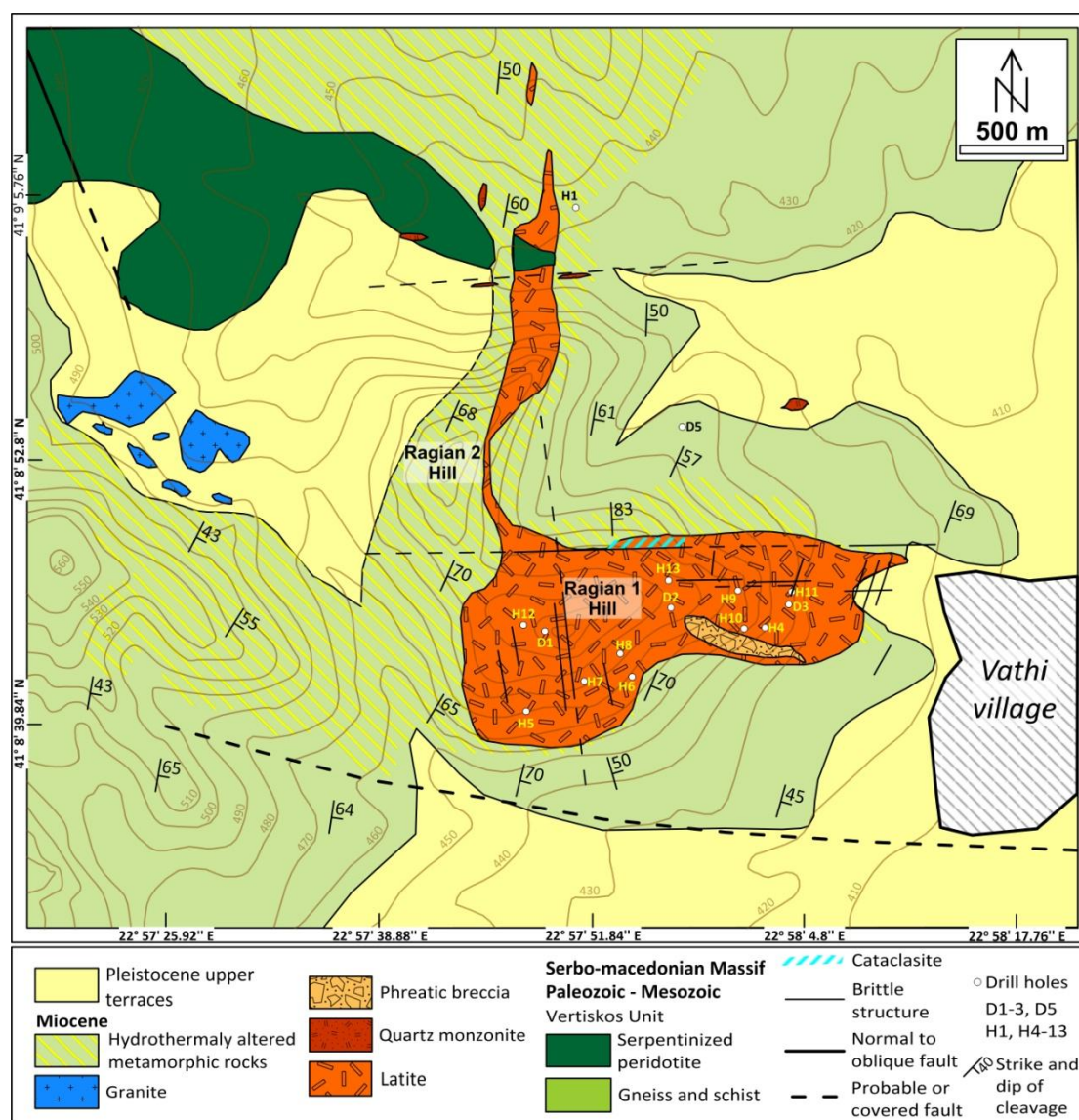


Figure 4.1. Geological map of the Vathi porphyry system. The legacy drill holes are also shown (modified after Stergiou et al. 2021a,b).

4.2. Mineralization stages and alteration styles

Early- to late-stage hydrothermal vein types at Vathi correspond to potassic-calcic (M-type), potassic (A-type), and sericitic (D-type) alterations (Stergiou et al. 2021b), whereas E-type veins are associated with the late epithermal overprinting (Figure 4.2a,b,d-g). Potassic alteration is overprinted by sericitic alteration (Table 4.1). The

following ore mineral assemblages are present: (1) magnetite associated with potassic-calcic alteration, (2) magnetite + pyrite + chalcopryrite \pm molybdenite \pm bornite related to potassic alteration, (3) pyrite + chalcopryrite associated with propylitic alteration, (4) pyrite + chalcopryrite + galena + sphalerite + native gold + tetradymite related to sericitic alteration, and (5) sphalerite + galena + arsenopyrite + pyrrhotite + pyrite + tetrahedrite \pm stibnite \pm tennantite associated with the epithermal overprint.

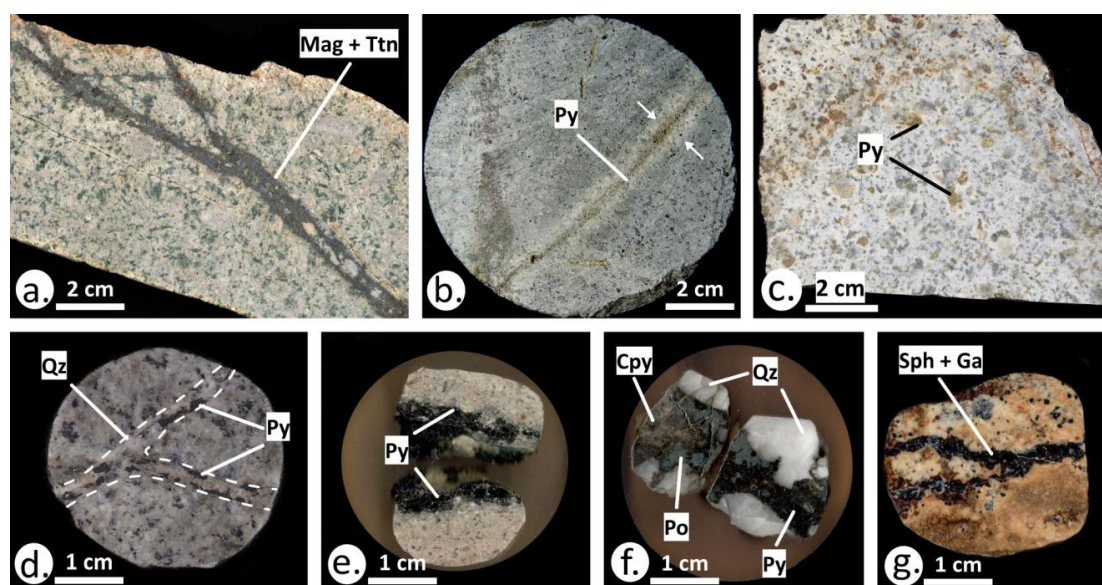


Figure 4.2. Mineralization stages from the Vathi porphyry Cu-Au \pm Mo system. a. Magnetite (Mag) and titanite (Ttn) in M-type vein crosscutting a quartz monzonite surface sample (potassic-calcic alteration). b. Pyrite (Py) in A-type vein crosscutting quartz monzonite drill core sample (potassic overprinted by sericitic alteration). Hydrothermal halo envelopes the vein (white arrows). c. Disseminations and aggregates of pyrite (Py) in a latite surface sample (sericitic alteration). d. Quartz (Qz) and pyrite (Py) in a D-type vein from a quartz monzonite surface sample (sericitic alteration). e. Pyrite (Py) in D-type vein from a latite drill core sample (sericitic alteration). f. Pyrite (Py), pyrrhotite (Po) and chalcopryrite (Cpy) in E-type vein from a latite drill core sample (epithermal overprint). g. Sphalerite (Sph) and galena (Gn) in E-type vein from a latite drill core sample (epithermal overprint).

Potassic-calcic alteration occurs in the quartz monzonite and is characterized by disseminations and M-type veins. These veins are up to 1 cm wide, continuous, sharp edged and branched (Figure 4.2a). They exhibit a massive texture and consist mainly of magnetite and titanite (Figure 4.3a). This hydrothermal alteration is characterized

by quartz, biotite, titanite, actinolite, rutile, and minor ilmenite and chlorite (Table 4.1).

Potassic alteration affected both the quartz monzonite and latite. A-type veins are up to 2 cm wide, continuous and enveloped by a hydrothermal halo (Figure 4.2b). They consist of pyrite, chalcopyrite (Figure 4.3b), native gold, and traces of bornite and galena (Stergiou et al. 2021b). In the latite, disseminated magnetite, pyrite and chalcopyrite, with minor bornite, molybdenite and pyrrhotite, are found. The alteration assemblage includes quartz, biotite, K-feldspar, and minor chlorite, sericite and rutile (Table 4.1).

Table 4.1. Typology, alteration and textural characteristics of the studied mineralization stages from the Vathi porphyry deposit (after Stergiou et al. 2021a,b).

Alteration style	Host rock	Mineralization stage	Metallic assemblage	Alteration assemblage
Potassic-calcic	Quartz monzonite	M-type veins Disseminated	Mag ± Ilm	Qz + Bt + Ttn + Act + Rt ± Chl
Potassic (overprinted by sericitic)	Quartz monzonite	A-type veins	Py + Cpy + Au ± Bn ± Gn	Qz + Bt + Kfs + Chl + Ser ± Rt
	Latite	Disseminated	Mag + Py + Cpy ± Bn ± Mol ± Po	
Sericitic	Quartz monzonite	D-type veins	Py + Cpy + Gn + Au + Ttd	Ser + Qz + Rt ± Dol ± Kln
		D-type veins	Py ± Cpy	
	Latite	Disseminated	Py + Cpy + Gn + Sph + Au ± Bn ± Mol ± Po ± Pn ± Tnt ± Ttr ± Wt ± Flt ± Cup ± Sch	
Propylitic	Quartz monzonite	Disseminated	Py	Chl + Qz ± Cal ± Ep
	Latite		Py ± Cpy	
Epithermal	Latite	E-type veins	Assemblage 1: Sph + Gn + Apy + Py + Cpy + Ttr ± Tnt ± Stb	Qz + Prl
			Assemblage 2: Py + Po + Cpy ± Gn	

Abbreviations: Act = actinolite, Apy = arsenopyrite, Au = native gold, Bn = bornite, Bt = biotite, Cal = calcite, Chl = chlorite, Cpy = chalcopyrite, Cup = cuprobismutite, Dol = dolomite, Ep = epidote, Flt = fletcherite, Gn = galena, Ilm = ilmenite, Kfs = K-feldspar, Kln = kaolinite, Mag = magnetite, Mol = molybdenite, Pn = pentlandite, Po = pyrrhotite, Prl = pyrophyllite, Py = pyrite, Qz = quartz, Rt = rutile, Ser = sericite, Sch = scheelite, Sph = sphalerite, Stb = stibnite, Ttn = titanite, Tnt = tennantite, Ttd = tetradymite, Ttr = tetrahedrite, W = wittichenite.

Sericitic alteration is associated with disseminations and D-type veins (Figure 4.2c). In the quartz monzonite, D-type veins are up to 1 cm wide continuous, sharp-edged and branched in shape (Figure 4.2d,e). They consist of pyrite, chalcopyrite and galena (Figure 4.3c). In minor amounts, native gold and tetradymite are found (Figure 4.3d). These minerals also occur as disseminations around the D-type veins. In the latite, the disseminated mineralization consists of pyrite, chalcopyrite, galena, sphalerite and native gold, and of traces of bornite, molybdenite, pyrrhotite,

pentlandite, tennantite, tetrahedrite, wittichenite, fletcherite, cuprobismutite and scheelite, while the D-type veins (< 5 cm in width) host pyrite and minor chalcopyrite (Table 4.1, Figure 4.3f,g). Sericitic alteration assemblage includes sericite, quartz, rutile, and minor dolomite and kaolinite (Table 4.1).

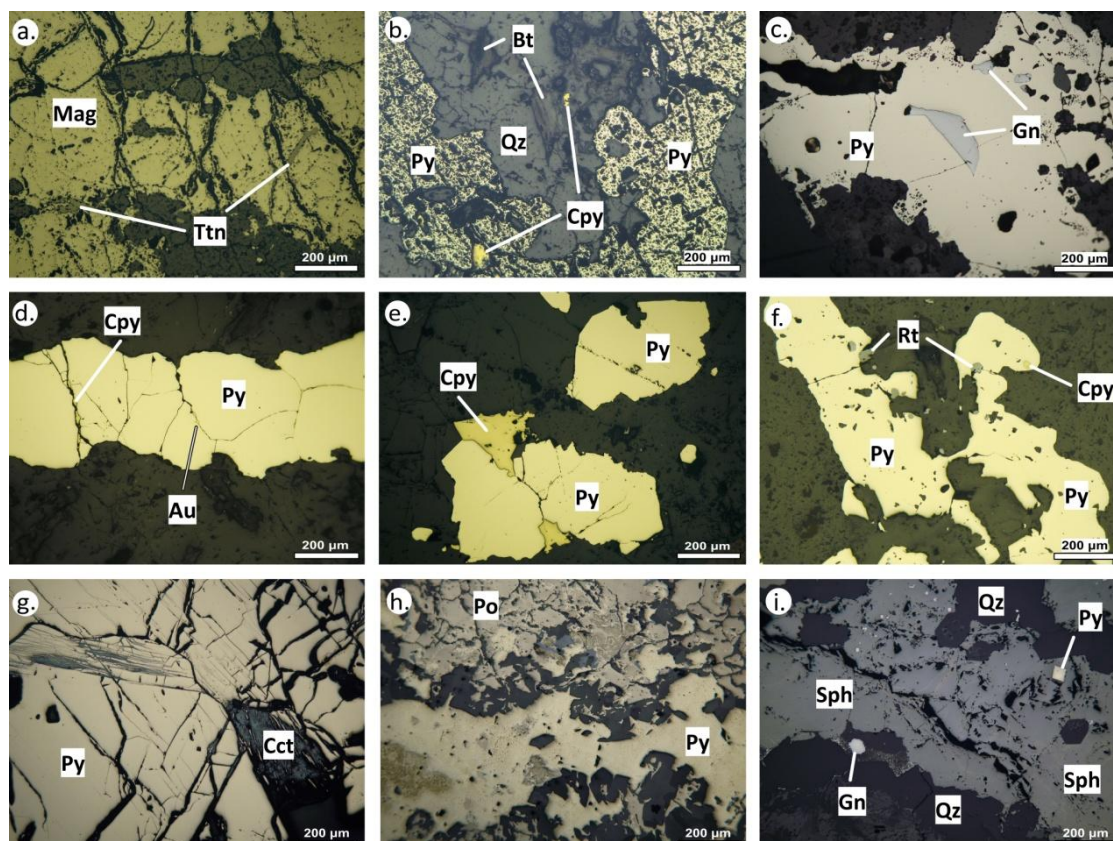


Figure 4.3. Photomicrographs (plane reflected light) of the hypogene mineralization in quartz monzonite (a-e) and latite (f-i). a. Magnetite (Mag) and titanite (Ttn) in M-type vein from potassic-calcic alteration. b. Pyrite (Py), chalcopyrite (Cpy), quartz (Qz) and biotite (Bt) in A-type vein from potassic alteration with sericitic overprint. c. Pyrite (Py) in a D-type vein and galena (Gn) filling interstices, disseminated mineralization with pyrite (Py) and galena (Gn) in sericitic alteration. d. Pyrite (Py), chalcopyrite (Cpy) and native gold (Au) in D-type vein in sericitic alteration. e. Disseminated mineralization with pyrite (Py) and chalcopyrite (Cpy) in the rock mass around a D-type vein (sericitic alteration). f. Pyrite (Py) aggregates with inclusions of chalcopyrite (Cpy) and rutile (Rt) in sericitic alteration. g. Pyrite (Py) and secondary chalcocite (Cct) in a D-type vein in sericitic alteration. h. Pyrrhotite (Po) and pyrite (Py) intergrowth in E-type vein (epithermal overprint). i. Sphalerite (Sph), galena (Gn) and euhedral pyrite (Py) in E-type vein rimmed by quartz (Qz) (epithermal overprint).

The epithermal overprint is characterized by E-type veins, which are continuous (<2 cm in width) and branched (Figure 4.2f,g). The E-type veins host two distinct metallic assemblages consisting of: (1) sphalerite, galena, arsenopyrite, pyrite, chalcopyrite and tetrahedrite, with minor stibnite and tennantite, and (2) pyrite, pyrrhotite, chalcopyrite and traces of galena (Table 4.1, Figure 4.3h,i). Quartz and pyrophyllite are the characteristic hydrothermal minerals associated with metallic mineralization (Table 4.1, Stergiou et al. 2021b).

4.3. Analytical results

4.3.1. Bulk geochemical analysis

Bulk geochemical analysis of mineralized samples was conducted in order to investigate their endowment in rare and critical metals. Eight surface samples were analyzed, five of which were from latite and three were from quartz monzonite. Among the latite samples, one was from propylitic alteration (Vath 42), and four were from sericitic alteration (Vath 34, Vath 38, Vath 40, Vath 45), whereas among the three samples from quartz monzonite; Vath 41 is relatively fresh, Vath 43 is from a D-type vein (sericitic alteration), and Vath 44 is from an M-type vein (potassic-calcic alteration). Table 4.2 includes the rare metal concentrations of these samples, and the average values for the same elements from previously published bulk geochemical analyses (Stergiou et al. 2021a).

Potassic-calcic alteration (Vath 44, quartz monzonite) is characterized by a depletion of rare metals (Figure 4.4). W (75 ppm) is the most enriched rare metal, while Ce (62 ppm), Th (42 ppm), Nd (27 ppm) and La (27 ppm) occur in decreasing concentrations (Table 4.2). Sericitic alteration is enriched with Au, Bi, Te, Co, Se and W (Figure 4.4). The quartz monzonite sample Vath 43 is enriched with Au (0.77 ppm) and Te (1.5 ppm). The latite samples (Vath 34 and Vath 45) exhibit the highest concentrations of Bi (14 ppm), Co (450 ppm), Se (8 ppm) and W (197 ppm) (Table 4.2).

Rare earth elements are highest in samples Vath 41 and Vath 42 (Figure 4.4). The relatively fresh quartz monzonite sample (Vath 41) contains significant amounts of Ce (153 ppm), Gd (7.8 ppm), La (83 ppm), Nd (85 ppm) and Sm (10 ppm). In addition, Ta (1.8 ppm) and Th (68 ppm) are more enriched in sample Vath 41 (Table 4.2). It is noteworthy that the highest values of Ag (4.6 ppm), Au (7 ppm) and Bi (239 ppm) are related to the D-type veins and the oxidized latite samples from sericitic alteration

(Figure 4.4, Supplement 4: Table S1-1, Stergiou et al. 2021). The highest concentrations of Ce (894 ppm), La (613 ppm), Nd (211 ppm) and Sm (23 ppm) are also related to sericitic alteration and are mainly concentrated in the phreatic breccia (Figure 4.4, Supplement 4: Table S1-1, Stergiou et al. 2021a).

Table 4.2. Bulk geochemical analyses of selected critical and rare metals from the Vathi porphyry system. The average values of these elements from previously analyzed samples by Stergiou et al. (2021a) are also given. For the full list of geochemical analyses, please advise Supplement 4, Table S1-1.

ppm	Host rock	Latite							Quartz monzonite			
	Alt.	Propylitic alt.		Sericitic alteration					Rel. Fresh	Pot.-calc. alt.	Sericitic alter.	
	Det. limit	Vath 42	AVG (n = 3)	Vath 34	Vath 38	Vath 40	Vath 45	AVG (n = 16)	Vath 41	Vath 44	Vath 43	AVG (n = 3)
Ag	0.01	0.45	0.58	0.32	0.48	0.10	0.04	1.1	0.12	0.05	0.89	0.42
Au	5x10 ⁻⁶	0.04	0.02	0.07	0.22	0.01	0.004	0.13	0.04	0.01	0.77	0.27
Bi	0.01	4.6	6.5	14.1	0.84	1.4	1.1	21	0.49	0.34	3.4	2.9
Cd	0.01	0.27	0.12	0.1	3.9	0.09	0.02	1.7	0.09	0.05	0.09	0.12
Ce	0.02	123	102	121	92	94	31	97	153	62	68	92
Co	0.1	38	13	17	18	48	450	35	23	13	30	45
Ga	0.05	9.4	16	2.2	1.7	1.9	5.1	15	6	7.7	8.5	15
Gd	0.05	6.6	5	4.5	4	4	2.3	5.1	7.8	4.1	3.9	4.7
Ge	0.05	0.24	0.24	0.13	0.11	0.11	0.09	0.11	0.18	0.20	0.19	0.19
Hg	0.005	0.21	0.2	0.42	0.32	0.22	0.1	0.19	0.19	0.11	0.19	0.17
In	0.005	0.01	0.11	0.08	0.08	0.05	b.d.l.	0.28	0.01	0.02	0.12	0.27
La	0.2	68	54	64	42	52	18	47	83	27	35	45
Nb	0.05	0.65	8.3	0.22	0.11	0.10	b.d.l.	8.6	1.2	0.6	1.2	5.3
Nd	0.1	46	38	47	35	33	12	40	85	27	28	39
Re	0.001	0.003	0.003	0.002	0.002	0.009	0.003	0.004	0.003	0.002	0.01	0.01
Sb	0.05	1.8	2.8	3.5	1.3	0.99	0.56	3.1	2.5	0.62	1.2	1.3
Se	0.2	1.2	1	b.d.l.	3.8	b.d.l.	7.9	3.8	1.2	b.d.l.	2.8	1.8
Sm	0.03	8.1	6.5	7.7	5.7	5.4	2.4	6.9	10	5	4.9	6.8
Ta	0.01	1.4	1.1	b.d.l.	b.d.l.	b.d.l.	b.d.l.	0.84	1.8	b.d.l.	b.d.l.	0.55
Te	0.01	0.49	0.3	0.01	b.d.l.	0.27	0.06	0.17	0.49	0.03	1.5	0.73
Th	0.2	44	45	39	40	36	24	38	68	42	47	46
Ti	50	1,900	2,403	90	b.d.l.	b.d.l.	b.d.l.	2,650	1,600	1,000	1,000	1,577
U	0.05	8.3	9.2	6.1	15	21	6.2	20	16	4.6	20	19
V	1	90	86	25	21	20	68	60	112	304	117	87
W	0.05	117	49	197	136	122	95	59	181	75	156	80

Abbreviations: alt. = alteration, AVG = average, b.d.l. = below detection limit, Det. limit = detection limit, n = number of analyses, n.a. = not analyzed, Pot.-calc. alt. = potassic-calcic alteration, Rel. Fresh = relatively fresh.

Pearson product-moment correlation coefficients and associated p-values were calculated for the bulk geochemical analyses conducted in this study along with previously published geochemical analyses (Table 4.2, Supplement 3: Table S4-1). Significant positive correlations ($p < 0.01$, values ≥ 0.8) were obtained for the

following elemental pairs: Ag-Au, Au-Se, Au-Te, Au-U, Ce-La, Ce-Nd, Ga-Nb, Gd-Nd, Gd-Sm, Nd-Sm, Se-Te, Se-U, Te-U (Supplement 3: Table S4-1). In addition, positive correlations ($p < 0.05$, values between 0.399 and 0.433) were defined for the elemental pairs: Cd-Hg, Cd-Te, Ce-Ta, Ga-Ta, Gd-Ta, Ge-V, Hg-Sb, La-Ta and Sm-Ta (Supplement 3: Table S4-1). Significant negative correlations ($p < 0.01$, values ≥ -0.586) occur for the pairs Ga-Ge, Ga-Hg, Ga-W, Ge-Nb, Hg-Nb and Nb-W (Supplement 3: Table S4-1).

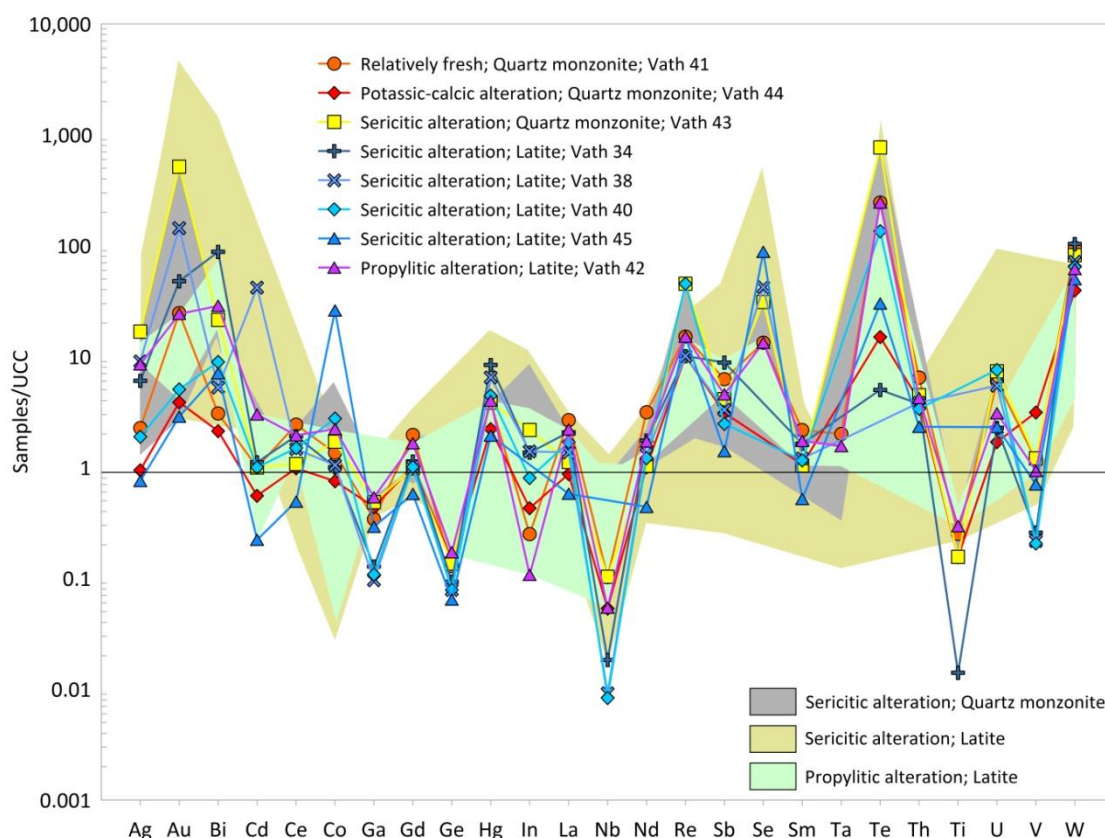


Figure 4.4. Upper continental crust (UCC) normalized logarithmic spider diagram of the eight analyzed samples presented here and the plot areas of previously analyzed samples by Stergiou et al. (2021a) corresponding to sericitic and propylitic alterations of quartz monzonite and latite (UCC normalized values after Rudnick and Gao 2003).

4.3.2. Pyrite and chalcopyrite - Mode of occurrence

Pyrite at Vathi is ubiquitous, especially in potassic and sericitic alterations. It is found as disseminations and aggregates, and in veins (Table 4.1). In the potassic alteration of the quartz monzonite, pyrite occurs in A-type veins crosscutting the host rock (Figure 4.3b). It is massive, filling the inner parts of the veins, and is intergrown

with chalcopyrite and bornite. Native gold and galena are found in the interstices of pyrite (Figure 4.5a). In the hydrothermal halo around the A-type veins, pyrite disseminations and aggregates vary in size from 100 to 500 μm . In the potassic alteration of the latite, pyrite (Py1) forms subhedral to euhedral disseminations and rounded aggregates (<1 mm in size, Figure 4.5b). It occurs along with magnetite, chalcopyrite, and traces of bornite, molybdenite and pyrrhotite (Figure 4.5b).

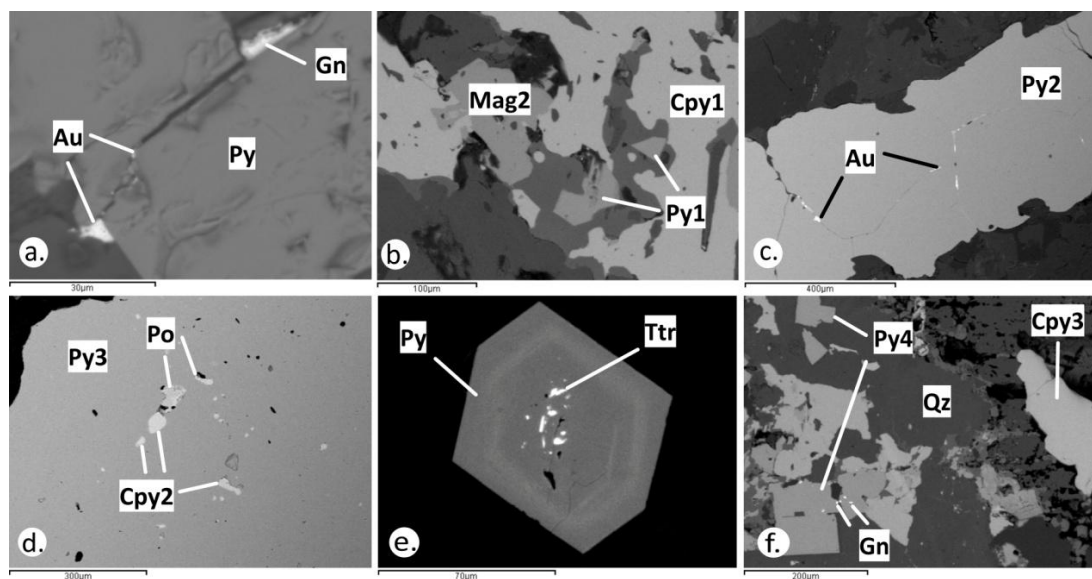


Figure 4.5. SEM back-scattered electron images of pyrite from different mineralization stages from the quartz monzonite (a-c) and the latite (d-f). a. Pyrite (Py), native gold (Au) and galena (Gn) in A-type vein (potassic alteration). b. Euhedral pyrite (Py1), chalcopyrite (Cpy1) and magnetite (Mag1, potassic alteration). c. Pyrite (Py2) in D-type vein and native gold (Au) in micro-cracks from sericitic alteration. d. Pyrite (Py3) bearing inclusions of chalcopyrite (Cpy2) and pyrrhotite (Po, sericitic alteration). e. Euhedral pyrite (Py) bearing tetrahedrite (Ttr) inclusions in E-type vein (epithermal overprint, assemblage 1). f. Euhedral pyrite (Py4) with galena (Gn) inclusions and chalcopyrite (Cpy3) in quartz (Qz) from E-type vein (epithermal overprint, assemblage 2).

In the sericitized quartz monzonite, pyrite (Py2) forms subhedral to euhedral disseminations and aggregates varying in size from 50 to 400 μm , and D-type veins (Figures 4.3c-e and 4.5c). Pyrite is intergrown with chalcopyrite, galena, native gold and tetradymite. Galena (<500 μm in size) is found in interstices or as replacements in disseminated pyrite, while chalcopyrite, native gold (Figures 4.3d and 4.5c) and tetradymite are found in micro-cracks and interstices in pyrite filling D-type veins.

The sericitic alteration of latite hosts disseminations and aggregates of pyrite as well as massive pyrite in D-type veins (Figure 4.3f,g). Disseminated pyrite (Py3) is intergrown with chalcopyrite and locally hosts inclusions (<100 μm in size) of galena and pyrrhotite (Figure 4.5d, Stergiou et al. 2021a). Pentlandite (<10 μm in size) was found in pyrrhotite. In D-type veins, massive pyrite is the dominant sulfide, while minor chalcopyrite inclusions are also found.

In the E-type veins related to the epithermal overprint, pyrite is a minor constituent in assemblage 1, and a major constituent in assemblage 2 (Table 4.1). In assemblage 1, euhedral pyrite (<80 μm in size) is found as inclusions in galena and sphalerite. Locally, it hosts tetrahedrite inclusions (<10 μm in size, Figure 4.5e). In assemblage 2, massive pyrite (Py4) is intergrown with pyrrhotite filling the inner parts of the veins (Figure 4.3h). Euhedral pyrite is found in the periphery of the veins and hosts inclusions of galena (Figure 4.5f).

Chalcopyrite is the second most abundant sulfide at Vathi (Table 4.1). In the potassic alteration of the quartz monzonite, chalcopyrite is found in A-type veins along with pyrite, native gold, and minor bornite and galena. In the hydrothermal halo around the A-type veins, chalcopyrite forms disseminations up to 200 μm in size (Figures 4.3b and 4.6a). In the potassic alteration of the latite, chalcopyrite (Cpy1, <1 mm in size) overgrows magnetite and coexists with pyrite, bornite, molybdenite and pyrrhotite (Figures 4.5b and 4.6b).

In the sericitically altered quartz monzonite, chalcopyrite appears as disseminations (<50 μm in size) and as aggregates along with pyrite (Figure 4.3e). Galena and tetradymite are found as inclusions (<100 μm in size) in chalcopyrite (Figure 4.6c). In the D-type veins, chalcopyrite occurs in fractures along pyrite (approximately <50 μm in width, Figures 4.3e and 4.6d). In the sericitic alteration of the latite, chalcopyrite (Cpy2) locally exhibits a more extensive distribution than pyrite and forms large aggregates reaching 1 cm in size. Chalcopyrite hosts inclusions of molybdenite, galena, sphalerite, bornite, pyrrhotite and pentlandite (<100 μm in size), as well as native gold, tennantite, tetrahedrite, wittichenite, fletcherite and cuprobismutite, which do not exceed 50 μm in size (Figure 4.6e,f). In D-type veins, crosscutting the sericitic alteration of latite, chalcopyrite is a minor constituent. It is found in pyrite as inclusions reaching up to 100 μm in size. In E-type veins, chalcopyrite occurs as nano-scale inclusions in sphalerite (i.e., chalcopyrite disease, assemblage 1, Table 4.1). In assemblage 2, chalcopyrite (Cpy3) is a minor constituent

filling interstices ($<100\ \mu\text{m}$) between pyrite, pyrrhotite and quartz (Table 4.1, Figure 4.5f).

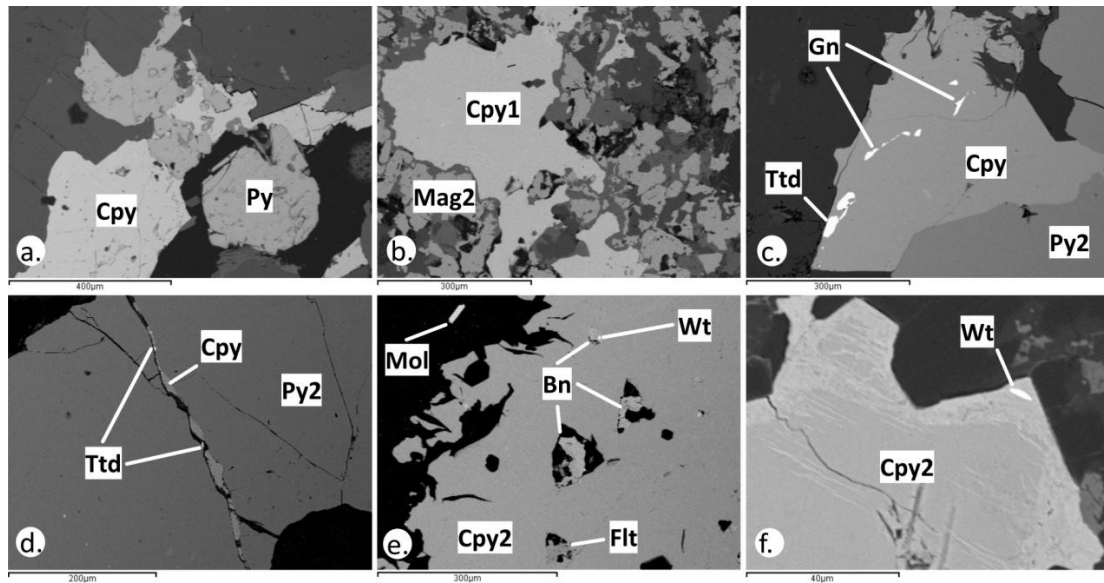


Figure 4.6. SEM back-scattered electron images of chalcopyrite from different mineralization stages from the quartz monzonite (a-d) and the latite (e-f). a. Chalcopyrite (Cpy) is intergrown with pyrite (Py) in A-type vein (potassic alteration). b. Chalcopyrite (Cpy1) overgrowth on magnetite (Mag2) aggregates (potassic alteration). c. Chalcopyrite (Cpy) is intergrown with pyrite (Py2) and bears inclusions of galena (Gn) and tetradymite (Ttd, sericitic alteration). d. Chalcopyrite (Cpy) and traces of tetradymite (Ttd) fill a crack running across a D-type vein with massive pyrite (Py2, sericitic alteration). e. Chalcopyrite (Cpy2) and euhedral inclusions of bornite (Bn), fletcherite (Flt), and molybdenite (Mol), with traces of wittichenite (Wt) are found in bornite (Bn, sericitic alteration). f. Chalcopyrite (Cpy2) and wittichenite (Wt, sericitic alteration).

4.3.3. Magnetite and titanite - Mode of occurrence

Magnetite occurs in the potassic-calcic alteration of the quartz monzonite and in the potassically altered latite (Table 4.1). In the potassic-calcic alteration, magnetite (Mag1) occurs as disseminations ($<400\ \mu\text{m}$ in size) and in M-type veins ($<1\ \text{cm}$ in width). It is intergrown with titanite and ilmenite ($<100\ \mu\text{m}$ in size, Figure 4.7a,b). In the M-type veins, massive magnetite is the dominant metallic mineral and includes titanite and ilmenite (Figures 4.3a and 4.7a,b). In the potassic alteration in latite, magnetite (Mag2) occurs as disseminations and aggregates ($<500\ \mu\text{m}$ in size, Figures

4.5b and 4.6b). It is overgrown by chalcopyrite and hosts minor inclusions of pyrrhotite (<40 μm in size).

Titanite (Ttn1) is found in the potassic-calcic alteration of the quartz monzonite as disseminations and in M-type veins (Figure 4.3a). Disseminated titanite (<100 μm in size) appears mainly as subhedral crystals, as intergrowths with ilmenite, and as overgrowths on magnetite. In M-type veins, titanite (<400 μm in size) is included in massive magnetite (Figure 4.7b).

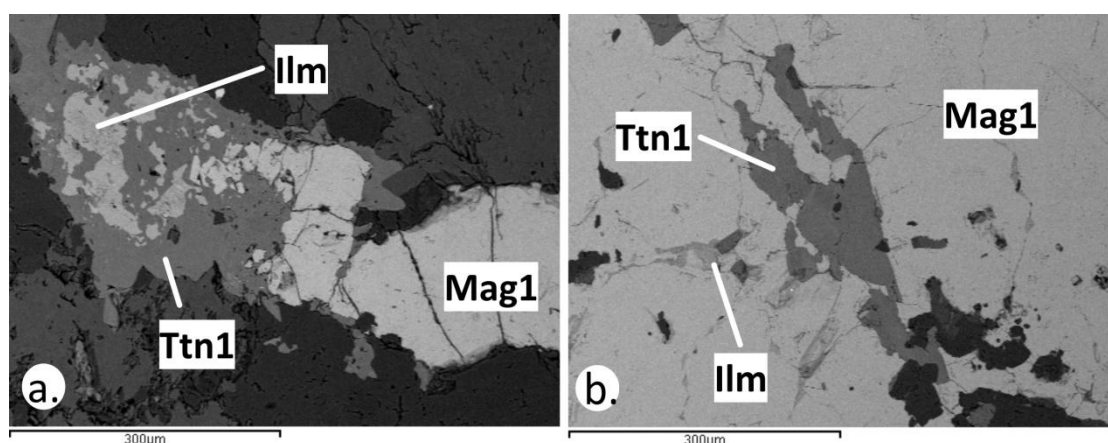


Figure 4.7. SEM back-scattered electron images of magnetite and titanite from the potassic-calcic alteration of the quartz monzonite (a,b). a. Disseminated magnetite (Mag1) is intergrown with titanite (Ttn1) and ilmenite (Ilm). b. Massive magnetite (Mag1) including titanite (Ttn1) and ilmenite (Ilm) in M-type vein.

4.3.4. Critical and rare metals in pyrite and chalcopyrite (LA-ICP-MS)

Trace elements in pyrite (Py1, Py2, Py3, Py4) and chalcopyrite (Cpy1, Cpy2, Cpy3) were measured by means of LA-ICP-MS. The trace element composition of pyrite and chalcopyrite exhibits notable variations between the different mineralization stages (Tables 4.3 and 4.4, Figure 4.8). In addition, ablation patterns reveal the occurrence of nano-scale mineral inclusions in pyrite. These inclusions are excluded from Tables 4.3 and 4.4. The complete analytical dataset for pyrite and chalcopyrite is given in Supplement 2 (Table S3-1).

Several base (As, Cr, Cu, Mn, Mo, Ni, Sn, Zn) and rare metals (Ag, Bi, Co, Hg, In, Sb, Se, Te, Ti, V, W) are incorporated in pyrite (Table 4.3, Figure 4.8). Of the four stages of pyrite, Py4 is the most enriched in trace elements, while Py2 is the most depleted one (Figure 4.8a). Cobalt is the most abundant rare metal, reaching 17,106 ppm in Py4 (Table 4.3). Ag (<6.6 ppm in Py4), Ti (<57 ppm in Py1), Se (<200 ppm in

Py1) and Sb (<10 ppm in Py3) are present in all pyrite stages (Table 4.3). V (<10 ppm) and Te (<41 ppm) were detected in Py1 and Py3, while In (<0.10 ppm) was found in Py1 and Py4. Hg (<0.7 ppm) occurs in Py3, while W (<27 ppm) and Bi (<1.0 ppm) were found in Py4 (Table 4.3, Figure 4.8a). Trace elements related to nano-scale mineral inclusions include Pb (<2,826 ppm in Py1, Supplement 2: Table S3-1). Rare metals related to nano-scale mineral inclusions comprise: Ag (<9.4 ppm), Cd (<48 ppm), In (<12 ppm), Au (<5.1 ppm) and Bi (<88 ppm) in Py1, gold (<2.2 ppm), Te (<1,237 ppm) and Bi (<1,771 ppm) in Py2, Ti (<57 ppm), V (<4 ppm), Co (<342 ppm), Bi (<6.3 ppm) and Th (<0.24 ppm) in Py3, and Ag (<3.7 ppm), Bi (<1.8 ppm) and U (<2.7 ppm) in Py4 (Supplement 2: Table S3-1).

Table 4.3. LA-ICP-MS analyses of pyrite from various mineralization stages. For the full dataset, see Supplement 2, Table S3-1.

Alteration	Potassic (overprinted by Sericitic)				Sericitic								Epithermal overprint			
Host rock	Latite				Quartz monzonite				Latite							
Mineralization stage	Py1, Disseminated (<i>n</i> = 9)				Py2, D-type veins (<i>n</i> = 9)				Py3, Disseminated (<i>n</i> = 19)				Py4, E-type veins, assemblage 2 (<i>n</i> = 7)			
Element	MIN	MAX	ST DEV	AVG	MIN	MAX	ST DEV	AVG	MIN	MAX	ST DEV	AVG	MIN	MAX	ST DEV	AVG
ppm																
Ag	2.2	2.2	n.a.	2.2	0.34	0.65	0.22	0.50	0.34	1.3	0.27	0.67	0.84	6.6	4.1	3.7
As	339	7,117	2,166	3,851	9.7	9.8	0.07	9.7	1.9	469	98	63	4.1	29	9.5	9.4
Au	b.d.l.	b.d.l.	n.a.	n.a.	b.d.l.	b.d.l.	n.a.	n.a.	b.d.l.	b.d.l.	n.a.	n.a.	b.d.l.	b.d.l.	n.a.	n.a.
Bi	b.d.l.	b.d.l.	n.a.	n.a.	b.d.l.	b.d.l.	n.a.	n.a.	b.d.l.	b.d.l.	n.a.	n.a.	1	1	n.a.	1
Co	17	1,341	409	201	11	93	33	33	0.73	8,700	1,391	1,931	2.3	17,106	7,954	4,736
Cr	27	47	7.9	38	36	46	4	41	31	54	3.8	42	30	42	3.9	35
Cu	b.d.l.	b.d.l.	n.a.	n.a.	12	16	1.5	14	4.3	425	139	65	59	59	n.a.	59
Hg	b.d.l.	b.d.l.	n.a.	n.a.	b.d.l.	b.d.l.	n.a.	n.a.	0.46	0.67	n.a.	0.56	b.d.l.	b.d.l.	n.a.	n.a.
In	0.09	0.09	n.a.	0.09	b.d.l.	b.d.l.	n.a.	n.a.	b.d.l.	b.d.l.	n.a.	n.a.	0.1	0.1	n.a.	0.1
Mn	48	91	16	61	53	59	2.3	56	48	76	2.7	55	48	53	2.5	50
Mo	b.d.l.	b.d.l.	n.a.	n.a.	b.d.l.	b.d.l.	n.a.	n.a.	2	2	n.a.	2	b.d.l.	b.d.l.	n.a.	n.a.
Ni	8.5	9,448	3,059	1,398	4.1	59	22	20	2.3	5,406	1,411	602	6.2	2,153	778	890
Pb	b.d.l.	b.d.l.	n.a.	n.a.	0.54	4.3	1.9	2.2	b.d.l.	b.d.l.	n.a.	n.a.	7	7	n.a.	7
Sb	0.34	10	4.8	3.1	2.1	3.23	0.43	2.6	0.45	1.6	0.02	0.96	0.96	1.2	0.2	1.1
Se	11	26	4.4	18	14	19	2.6	16	14	200	27	51	5.8	18	4.9	12
Sn	b.d.l.	b.d.l.	n.a.	n.a.	b.d.l.	b.d.l.	n.a.	n.a.	0.46	0.46	n.a.	0.46	b.d.l.	b.d.l.	n.a.	n.a.
Te	5.3	31	12	15	b.d.l.	b.d.l.	n.a.	n.a.	3	41	n.a.	18	b.d.l.	b.d.l.	n.a.	n.a.
Ti	20.3	39	6.7	29	26	34	2.8	30	20	57	2.6	31	21	41	7	28
Tl	0.62	0.67	0.03	0.64	b.d.l.	b.d.l.	n.a.	n.a.	b.d.l.	b.d.l.	n.a.	n.a.	1.2	1.2	n.a.	1.2
V	9.9	9.9	n.a.	9.9	b.d.l.	b.d.l.	n.a.	n.a.	4.2	4.2	n.a.	4.2	b.d.l.	b.d.l.	n.a.	n.a.
W	b.d.l.	b.d.l.	n.a.	n.a.	b.d.l.	b.d.l.	n.a.	n.a.	b.d.l.	b.d.l.	n.a.	n.a.	4.4	27	11	12
Zn	4.9	8.3	1.4	6.6	6	6.8	0.56	6.4	3.1	9.9	0.24	6.4	3.7	11	4.3	6.4

Abbreviations: AVG = average value, b.d.l. = below detection limit, MIN = minimum value, MAX = maximum value, n = number of analyses, n.a. = not analyzed, STDEV = standard deviation.

Chalcopyrite (Cpy1) from the potassic alteration of latite is most enriched with trace elements (Table 4.4, Figure 4.8b). Base (As, Cr, Mn, Ni, Pb, Sn, Zn) and rare (Ag, Bi, Co, Cd, Ge, Hg, In, Te, Ti, V, W) metals occur in chalcopyrite (Table 4.4). Ag (<519 ppm in Cpy2) is the most enriched rare metal and, along with Ti (<45 ppm in Cpy3) and In (<62 ppm in Cpy1), is incorporated in all chalcopyrite stages (Figure 4.8b). Co (<5.3 ppm) and Bi (<40 ppm) are associated with Cpy1 and Cpy2, while Ge

(<12 ppm) and Sb (<48 ppm) are found in Cpy2 and Cpy3 (Figure 4.8b). Cd (<45 ppm), V (<11 ppm) and Ga (<2.3 ppm) are related to Cpy1 (Table 4.4, Figure 4.8b). Se (<161 ppm), Te (<6.8 ppm) and Hg (<50 ppm) are present in Cpy2, whereas W (<2 ppm) is found in Cpy3 (Figure 4.8b). Nano-scale mineral inclusions in chalcopyrite chemistry are associated mainly with Pb and Bi. In Cpy2, Pb and Bi concentrations ascribed to inclusions reach 13,912 ppm and 3111 ppm, respectively (Supplement 2: Table S3-2). Additionally, Zn (<5,147 ppm), Ag (<9.4 ppm) and Cd (<48 ppm) were detected in Cpy1 (Supplement 2: Table S3-2).

Table 4.4. LA-ICP-MS analyses of chalcopyrite from various mineralization stages. For the full dataset, see Supplement 2, Table S3-2.

Alteration	Potassic (overprinted by Sericitic)				Sericitic				Epithermal overprint			
Host rock	Latite											
Mineralization stage	Cpy1, disseminated (<i>n</i> = 10)				Cpy2, disseminated (<i>n</i> = 12)				Cpy3, E-type veins, assemblage 2 (<i>n</i> = 2)			
Element	MIN	MAX	ST DEV	AVG	MIN	MAX	ST DEV	AVG	MIN	MAX	ST DEV	AVG
ppm												
Ag	6.8	17	3.4	10	8	519	103	47	134	407	193	271
As	56	83	8.9	67	4.8	25	5.6	12	b.d.l.	b.d.l.	n.a.	n.a.
Au	b.d.l.	b.d.l.	n.a.	n.a.	b.d.l.	b.d.l.	n.a.	n.a.	b.d.l.	b.d.l.	n.a.	n.a.
Bi	3	40	13	21	2.1	2.1	n.a.	2.1	b.d.l.	b.d.l.	n.a.	n.a.
Cd	4.4	45	15	14	b.d.l.	b.d.l.	n.a.	n.a.	b.d.l.	b.d.l.	n.a.	n.a.
Co	4.8	4.9	0.05	4.9	0.58	5.3	2.1	1.7	b.d.l.	b.d.l.	n.a.	n.a.
Cr	20	38	6.7	27	19	55	8.8	29	b.d.l.	b.d.l.	n.a.	n.a.
Ga	2.3	2.3	n.a.	2.3	b.d.l.	b.d.l.	n.a.	n.a.	b.d.l.	b.d.l.	n.a.	n.a.
Ge	b.d.l.	b.d.l.	n.a.	n.a.	4.9	12	5.1	8.5	9	9	n.a.	9
Hg	b.d.l.	b.d.l.	n.a.	n.a.	0.83	50	28	17	b.d.l.	b.d.l.	n.a.	n.a.
In	32	62	11	50	3.1	57	8.1	25	1	57	39	29
Mn	33	40	2.8	36	30	42	1.9	33	31	31	n.a.	31
Mo	b.d.l.	b.d.l.	n.a.	n.a.	b.d.l.	b.d.l.	n.a.	n.a.	b.d.l.	b.d.l.	n.a.	n.a.
Ni	5.1	6.2	0.8	5.7	4.1	7.5	2	5.3	b.d.l.	b.d.l.	n.a.	n.a.
Pb	5.4	14	6.1	9.7	4	4	n.a.	4	b.d.l.	b.d.l.	n.a.	n.a.
Sb	b.d.l.	b.d.l.	n.a.	n.a.	1.1	48	26	24	3.4	3.4	n.a.	3.4
Se	b.d.l.	b.d.l.	n.a.	n.a.	46	161	13	73	b.d.l.	b.d.l.	n.a.	n.a.
Sn	1.8	9	2.9	5.3	18	144	9	119	48	91	31	70
Te	b.d.l.	b.d.l.	n.a.	n.a.	3.9	6.8	1.7	5.1	b.d.l.	b.d.l.	n.a.	n.a.
Ti	11	41	9.6	24	12	31	6.1	17	45	45	n.a.	45
Tl	0.42	0.42	n.a.	0.42	38	38	n.a.	38	b.d.l.	b.d.l.	n.a.	n.a.
V	11	11	n.a.	11	b.d.l.	b.d.l.	n.a.	n.a.	b.d.l.	b.d.l.	n.a.	n.a.
W	b.d.l.	b.d.l.	n.a.	n.a.	b.d.l.	b.d.l.	n.a.	n.a.	2	2	n.a.	2
Zn	137	2,392	925	790	19	55	2.1	34	287	571	201	429

Abbreviations: AVG = average value, b.d.l. = below detection limit, MIN = minimum value, MAX = maximum value, n = number of analyses, STDEV = standard deviation.

4.3.5. Critical and rare metals in magnetite and titanite (LA-ICP-MS)

Magnetite (Mag1, Mag2) exhibits variations between the analyzed samples, while titanite (Ttn1) is characterized by distinctive geochemical patterns. Several rare metals were partitioned between coexisting magnetite and titanite, with titanite being a major host of REE (Table 4.5, Supplement 2: Tables S3-3 and S3-4).

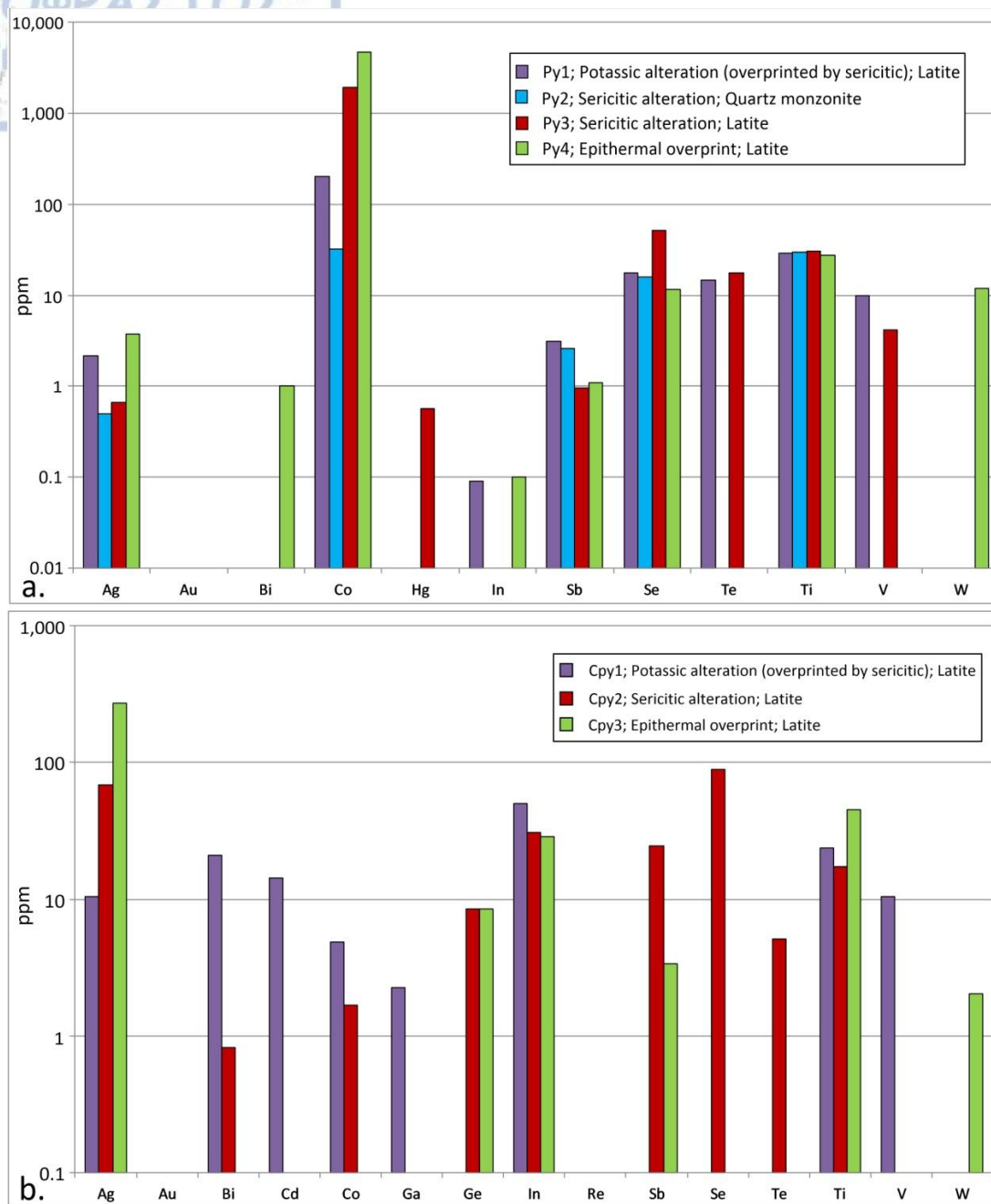


Figure 4.8. Average values of rare metal concentrations of (a) pyrite and (b) chalcopyrite from various mineralization stages. Local enrichments related to nano-scale mineral inclusions are excluded.

Magnetite (Mag2) is more enriched with trace elements than Mag1 (Table 4.5). Various base metals (e.g., Cr, Cu, Mn, Ni, Zn) and a restricted number of rare metals, including Ti, V, Co, Ga, Ge, Se and W, occur in magnetite (Table 4.5, Figure 4.9a). V (<4,176 ppm in Mag1) is the most enriched rare metal, followed by Ti (<2,468 ppm in Mag2, Table 4.5, Figure 4.9a). Co (<14 ppm) and Ga (<125 ppm) are more enriched in Mag1, whereas Ge (<16 ppm) is more enriched in Mag2. Se (<3.3 ppm) and W

(<13 ppm) were found in Mag1 and Mag2, respectively (Table 4.5, Figure 4.9a). Rare metals related to the presence of nanoparticles in magnetite (Mag1) include Ti (<3,553 ppm), Ag (<1.9 ppm), La (<4.3 ppm), Ce (<7.7 ppm), Bi (<0.92 ppm) and Th (<23 ppm, Supplement 2: Table S3-3). Sb (<2.6 ppm), Ce (<1.2 ppm), Bi (<6.4 ppm) and U (<5.6 ppm, Supplement 2: Table S3-4) were detected in Mag2. It should also be mentioned that Cu (<107 ppm) was detected in Mag1, and Pb (<46 ppm in Mag1) was found in Mag2.

Table 4.5. LA-ICP-MS analyses of magnetite and titanite from various mineralization stages. For the full dataset, see Supplement 2, Tables S3-3 and S3-4.

Mineral	Magnetite								Titanite			
Alteration	Potassic-calcic				Potassic (overprinted by sericitic)				Potassic-calcic			
Host rock	Quartz monzonite				Latite				Quartz monzonite			
Mineralization stage	Mag1, M-type veins (n = 7)				Mag2, disseminated (n = 9)				Ttn1, M-type veins (n = 5)			
Element	MIN	MAX	STDEV	AVG	MIN	MAX	STDEV	AVG	MIN	MAX	STDEV	AVG
ppm												
Ag	b.d.l.	b.d.l.	n.a.	n.a.	b.d.l.	b.d.l.	n.a.	n.a.	b.d.l.	b.d.l.	n.a.	n.a.
Al	1,062	3,161	873	1,966	943	4,076	1,576	2,416	4,505	5,002	209	4,741
As	43	60	12	52	b.d.l.	b.d.l.	n.a.	n.a.	39	146	40	104
Au	b.d.l.	b.d.l.	n.a.	n.a.	b.d.l.	b.d.l.	n.a.	n.a.	b.d.l.	b.d.l.	n.a.	n.a.
Bi	b.d.l.	b.d.l.	n.a.	n.a.	b.d.l.	b.d.l.	n.a.	n.a.	b.d.l.	b.d.l.	n.a.	n.a.
Cd	b.d.l.	b.d.l.	n.a.	n.a.	b.d.l.	b.d.l.	n.a.	n.a.	b.d.l.	b.d.l.	n.a.	n.a.
Ce	b.d.l.	b.d.l.	n.a.	n.a.	b.d.l.	b.d.l.	n.a.	n.a.	1,813	5,535	1487	4,047
Co	9.8	14	1.6	12	5	13	3.1	8.4	4	4	n.a.	4
Cr	39	282	96	112	63	2,043	738	372	b.d.l.	b.d.l.	n.a.	n.a.
Cu	36	36	n.a.	36	13	23	5.2	19	47	68	12	57
Ga	78	125	15	109	34	53	6.2	41	12	35	11	18
Gd	b.d.l.	b.d.l.	n.a.	n.a.	b.d.l.	b.d.l.	n.a.	n.a.	131	984	352	736
Ge	2.9	2.9	n.a.	2.9	5.5	16	6.2	3.7	24	40	7	35
In	b.d.l.	b.d.l.	n.a.	n.a.	b.d.l.	b.d.l.	n.a.	n.a.	4.9	10	2.1	7.8
La	b.d.l.	b.d.l.	n.a.	n.a.	b.d.l.	b.d.l.	n.a.	n.a.	576	1,369	343	1,020
Mn	564	734	69	644	467	786	118	660	311	713	156	498
Mo	b.d.l.	b.d.l.	n.a.	n.a.	b.d.l.	b.d.l.	n.a.	n.a.	7.6	11	1.6	8.6
Nb	n.a.	n.a.	n.a.	n.a.	b.d.l.	b.d.l.	n.a.	n.a.	n.a.	n.a.	n.a.	n.a.
Nd	n.a.	n.a.	n.a.	n.a.	b.d.l.	b.d.l.	n.a.	n.a.	872	4,215	1331	3,121
Ni	382	814	173	594	11	11	n.a.	11	b.d.l.	b.d.l.	n.a.	n.a.
P	125	364	169	245	b.d.l.	b.d.l.	n.a.	n.a.	365	984	299	617
Pb	b.d.l.	b.d.l.	n.a.	n.a.	b.d.l.	b.d.l.	n.a.	n.a.	b.d.l.	b.d.l.	n.a.	n.a.
Re	n.a.	n.a.	n.a.	n.a.	b.d.l.	b.d.l.	n.a.	n.a.	n.a.	n.a.	n.a.	n.a.
Sb	b.d.l.	b.d.l.	n.a.	n.a.	b.d.l.	b.d.l.	n.a.	n.a.	11	22	5.4	19
Se	3	3.3	n.a.	3.3	b.d.l.	b.d.l.	n.a.	n.a.	74	141	28	102
Sm	b.d.l.	b.d.l.	n.a.	n.a.	b.d.l.	b.d.l.	n.a.	n.a.	164	1,070	368	792
Sn	4.4	13	3.6	8.8	2.9	6	1.3	4.3	1286	2,503	496	1,988
Te	b.d.l.	b.d.l.	n.a.	n.a.	b.d.l.	b.d.l.	n.a.	n.a.	b.d.l.	b.d.l.	n.a.	n.a.
Ti	1,503	1,784	154	1,607	1074	2,468	542	1,718	189,900	203,100	4,731	195,660
Th	b.d.l.	b.d.l.	n.a.	n.a.	b.d.l.	b.d.l.	n.a.	n.a.	32	309	103	206
Tl	b.d.l.	b.d.l.	n.a.	n.a.	b.d.l.	b.d.l.	n.a.	n.a.	b.d.l.	b.d.l.	n.a.	n.a.
U	n.a.	n.a.	n.a.	n.a.	b.d.l.	b.d.l.	n.a.	n.a.	n.a.	n.a.	n.a.	n.a.
V	3,531	4,176	219	3,763	1831	2,832	327	2,381	1,164	2,620	568	2,136
W	b.d.l.	b.d.l.	n.a.	n.a.	2.7	13	4.8	6.8	11	81	34	31
Zn	37	59	7.9	51	59	137	33	92	38	63	11	50

Abbreviations: AVG = average value, b.d.l. = below detection limit, MIN = minimum value, MAX = maximum value, n = number of analyses, n.a. = not analyzed, STDEV = standard deviation.

Titanite (Ttn1) hosts base (As, Cu, Mn, Sn) and rare (e.g., V, Th, Se, W) metals and is enriched with REE (Table 4.5, Figure 4.9b). Rare metals comprise V (<2,620 ppm), Th (<309 ppm), Se (<141 ppm), W (<81 ppm), Ge (<40 ppm), Ga (<35 ppm),

Sb (<22 ppm), In (<10 ppm) and Co (<4 ppm, Figure 4.9b). Rare-earth elements in Ttn1 include Ce (<5,535 ppm), which is the most enriched trace element, followed by La (1,369 ppm), Sm (1,070 ppm), Nd (421 ppm) and Gd (986 ppm, Table 4.5, Figure 4.9b). Enrichments of rare metals related to nano-scale mineral inclusions were not detected in titanite.

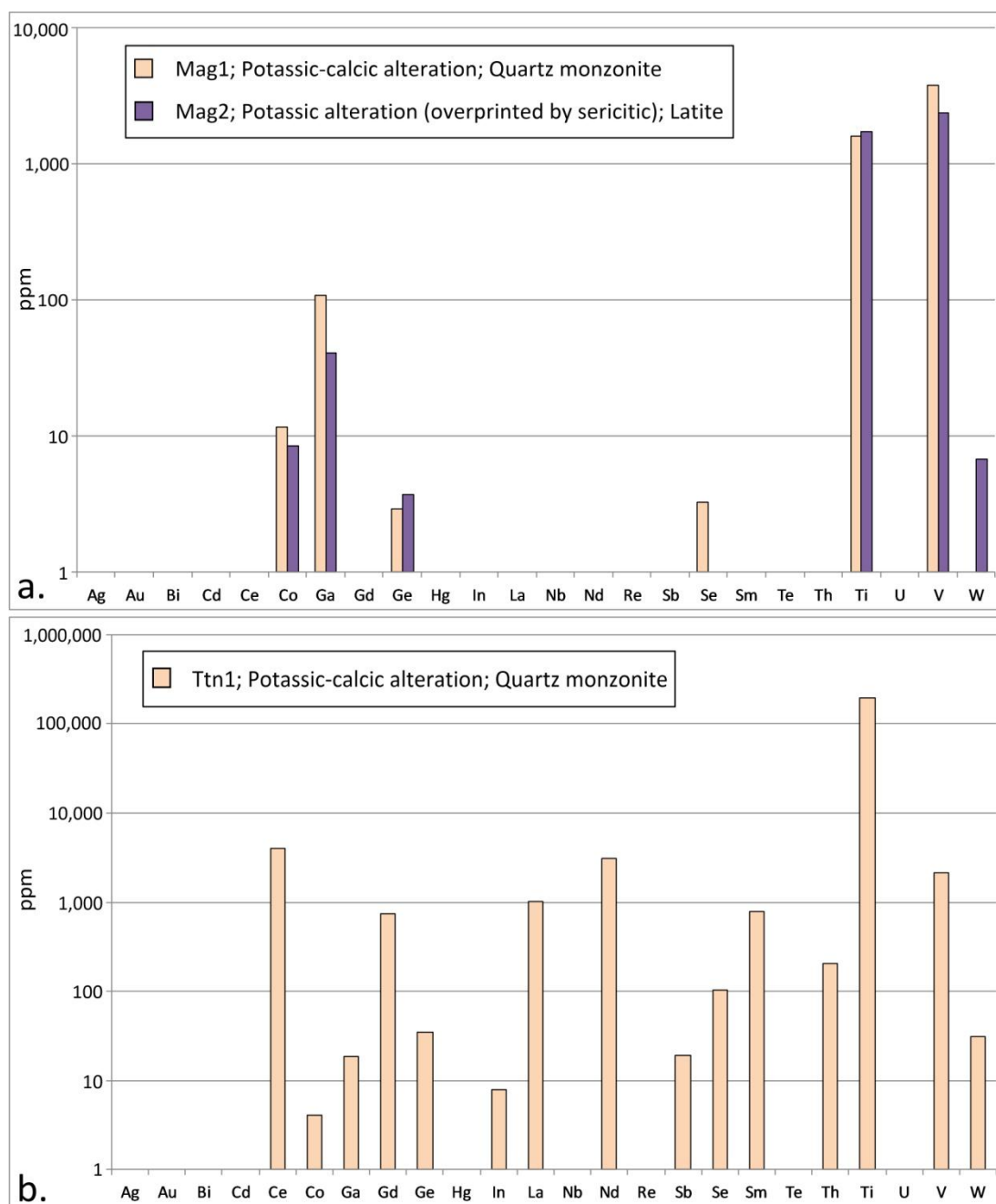


Figure 4.9. Average values of rare metal concentrations of (a) magnetite and of (b) titanite from various mineralization stages. Local enrichments related to nano-scale mineral inclusions are excluded.

4.3.6. Statistical analysis of trace elements concentrations

In order to further investigate the chemistry of pyrite, chalcopyrite, magnetite and titanite, and the geochemical association of the detected and measured rare metals, Pearson product-moment correlation coefficients and associated p-values were calculated for the LA-ICP-MS analyses. Heat maps of the Pearson correlation coefficient matrix for pyrite, chalcopyrite, magnetite and titanite are given in Tables S4-5 to S4-8 in Supplement 3. Based on data reduction and ablation patterns, trace element concentrations related to nano-scale mineral inclusions, or nanoparticles in the case of magnetite, were excluded before the statistical analyses.

Pearson product-moment correlation coefficients for pyrite are described by significant positive correlation ($p < 0.01$, value = 0.660) defined for the elemental pair Bi-Co (Supplement 3: Table S4-5). In addition, positive correlations ($p < 0.05$, value = 0.353) were defined for the pairs Hg-Te and Te-V (Supplement 3: Table S4-5). Negative correlations were not defined.

Significant positive correlations ($p < 0.01$, values ≥ 0.524) are noted for the elemental pairs Ag-Hg, Ag-Sb, Ag-W, Co-Hg, Co-Sb, Co-V, Hg-Sb, Hg-Se, Ti-V and for Ti-W in chalcopyrite (Supplement 3: Table S4-6). Positive correlation ($p < 0.05$, value = 0.513) occur between Sb and Se. Significant negative correlations ($p < 0.01$, values = -0.59) include the pair Ag-In, negative correlations ($p < 0.05$, values ≥ -0.409) are defined for the elemental pairs Bi-Se, Hg-In and In-W (Supplement 3: Table S4-6).

Magnetite is characterized by significant positive correlations ($p < 0.01$: values ≥ 0.844) for the pairs Ga-V and V-W, and by positive correlations ($p < 0.05$, value = 0.677) for the pair Co-V. Significant negative correlations were not detected for any elemental pairs (Supplement 3: Table S4-7).

Strong positive correlation coefficients ($p < 0.01$, values ≥ 0.960) occur for the elemental pairs Ce-La, Gd-Nd, Gd-Sm, Ge-Sb, Nd-Sm, Nd-V and Sm-V in titanite, while smaller positive correlations ($p < 0.05$, values ≥ 0.884) occur between Ce and Ge, Nd, Th and V, between Ge and La, Nd, Th and V, and for the pairs Ga-Th, Gd-V, Nd-Th, Sm-Th and Th-V (Supplement 3: Table S4-8). Significant negative correlations ($p < 0.01$, values ≥ -0.996) occur for the pairs Ge-W and Sb-W.

4.4. Discussion

At the Vathi deposit, the hydrothermal alteration, the porphyry and epithermal-related mineralization stages, the bulk geochemistry, and the mineral chemistry reveal specific mineralogical and geochemical relations to various rare metals (e.g. Ag, Au, Bi, Co, Se, Te and W, Table 4.2). The REE distribution and relative REE enrichment at Vathi are ascribed to monazite and titanite, and possibly to other rock-forming and alteration minerals (e.g., monazite, epidote, feldspar Stergiou et al. 2021a). The relatively fresh and unoxidized quartz monzonite (Vath 41) includes the highest concentrations of Ce, Gd, La, Nd and Sm, which are significantly correlated with each other (Figure 4.4, Supplement 3: Table S4-1). The comparison between the new and the previously published bulk geochemical analysis at Vathi emphasizes the effect of supergene processes on the enrichment of the rare metals (Table 4.2, Supplement 4: Table S1-1, Stergiou et al. 2021a).

The metallic and alteration assemblages related to potassic-calcic alteration and the complete absence of sulfide minerals suggest the highly oxidized nature of the initial fluids, as well as the high solubility of Fe and FeCl_2 (Table 4.1, Arancibia and Clark 1996). This type of alteration exhibits the lowest enrichment of rare metals (Table 4.2, Figure 4.4). W, Ce, Th, Nd and La are the most enriched rare metals at concentrations <75 ppm and are significantly correlated with each other (Supplement 3: Table S4-1). In Greece, M-type veins have been previously described from the Pagoni-Rachi, the Maronia, and the Stypsi porphyry deposits (Voudouris et al. 2013b, Voudouris et al. 2019b, Melfos et al. 2020). The M-type veins at Vathi are different in terms of metallic content and alteration assemblages and are not associated with the introduction of any hypogene mineralization, as is the case at Pagoni-Rachi (Voudouris et al. 2013b, Voudouris et al. 2019b, Melfos et al. 2020). The potassic alteration that was overprinted by sericitic alteration is associated with A-type veins in the quartz monzonite and with disseminations in the latite at Vathi (Table 4.1, Figures 4.3b, 4.5a and 4.6a). The formation of the A-type veins was a restricted event in terms of size and occurrence. According to Stergiou et al. (2021a), the formation of the A-type veins is related to boiling hydrothermal fluids at temperatures >390 °C (646 bars, <2.6 km in depth). The A-type veins are related to a restricted introduction of gold in the Vathi magmatic-hydrothermal system (Table 4.1, Figure 4.5a).

The sericitic alteration is characterized by D-type veins and disseminations in both the quartz monzonite and the latite (Table 4.1, Figure 4.2d,e). The sericitic alteration and the associated metallic and alteration assemblages formed at temperatures ranging between 311 and 392 °C, from a moderately saline (8.4-11.2 wt.% NaCl equiv.) fluid (Stergiou et al. 2021a). Tetradymite and native gold are spatially related to the mineralization of the quartz monzonite (Figures 4.5c and 4.6c,d). Bismuth tellurides, Bi-sulfosalts, and Au-Ag-tellurides have been previously reported from calc-alkaline to alkaline porphyry deposits in northern Greece (Voudouris et al. 2007). Tetradymite associated with sericitic alteration was recognized from the Koryfes porphyry deposit, whereas in the Papadokoryfi and Pagoni-Rachi porphyry deposits, tetradymite is found in the porphyry-epithermal transition environment (Voudouris et al. 2019a). The occurrence of pyrrhotite, pentlandite, wittichenite, fletcherite and cuprobismutite found in the latite at Vathi is uncommon or is rarely described for the sericitic alteration of the porphyry deposits found elsewhere in Greece (Voudouris et al. 2019a). At Vathi, pyrrhotite and pentlandite are found as inclusions along with chalcopyrite in pyrite disseminations and aggregates, while fletcherite, wittichenite and cuprobismutite occur as inclusions in chalcopyrite aggregates (Figures 4.5d and 4.6e). These textural characteristics suggest a Ni, Co, Bi and Ag enrichment and shifts in fO_2/fS_2 conditions for the mineralizing fluids of this stage. Shifts in sulfur fugacity caused by the interaction between the late-mineralizing fluids and carbonaceous wall rocks have been previously suggested for Vathi (Stergiou et al. 2021a).

Bulk geochemical analysis showed that rare metals are enriched in the sericitic alteration (Table 4.2, Figure 4.4). Au (0.8 ppm), Te (1.5 ppm) and Co (450 ppm) exhibit their highest enrichment in this alteration, while Se (2.8 ppm), Bi (3.4 ppm) and Ag (0.9 ppm) are also enriched (Table 4.2). In addition, Pearson's correlation coefficients suggested significant correlations for the pairs Ag-Au, Au-Se, Au-Te and Se-Te (Supplement 3: Table S4-1). These results verify the association among tetradymite and native gold. According to Voudouris et al. (2019a), the porphyry- and epithermal-style gold mineralization in Greece is classified as follows for deposits where: (a) native gold and Au-Ag-tellurides are associated with Bi-sulfosalts and oxidized-type Bi-sulfotellurides, (b) native gold is related to Bi-sulfosalts, and (c) native gold and Au-Ag-tellurides are only present. Using this classification scheme, it could be suggested that Vathi belongs to the first category.

The epithermal overprint occurs in the sericitic alteration of latite and is associated with E-type veins and cataclasite (Figures 4.1 and 4.2f,g). The epithermal stage, according to Stergiou et al. (2021a), developed between 205 and 259 °C, from a slightly saline (1.4-2.9 wt.% NaCl equiv.) fluid. Epithermal (E-type) veins related to the porphyry-epithermal transition environment have been previously described in Greece (e.g. Pagoni-Rachi, Stypsi, Maronia, Skouries) (Voudouris et al. 2019a, Melfos et al. 2020). At Vathi, the E-type veins host base metal sulfides only (Table 4.1).

4.4.1. Mineral chemistry of pyrite and chalcopyrite and nano-scale inclusions

The interpretation of the scanning electron microscopy and LA-ICP-MS analyses for pyrite and chalcopyrite at Vathi suggests that specific minerals occur as nano-inclusions. All the pyrite stages (Py1-4) at Vathi are enriched with Ag, Co, Sb, Se and Ti (Table 4.3, Figure 4.8a). In contrast, Hg, Te and V are elevated in Py1, Py2 and Py3, whereas Bi and W are present in Py4 of the late-stage epithermal overprint. In is associated with Py1 in the potassic alteration and the epithermal overprint (Py4, Figure 4.8a). It is suggested here that based on the ablation patterns, Co and Se are incorporated in pyrite as stoichiometric substitutions. Cobalt and Se are considered common stoichiometric substitutions for Fe and S, respectively (Abraitis et al. 2004). In addition, restricted amounts of Ag, Bi, Hg, In, Sb, Ti, V and W could be accommodated in the pyrite structure as solid solutions (Table 4.3, Abraitis et al. 2004, Deditius et al. 2011).

Based on the concentrations of some elements and the laser ablation patterns, several enrichments in trace elements of pyrite are attributed to nano-scale mineral inclusions (Supplement 2: Table S3-1, Figure 4.10). The rare metals related to inclusions comprise: Ag, Au, Bi, Cd and In in Py1, Au, Bi and Te in Py2, Bi, Co, Th, Ti and V in Py3, and Ag, Bi and U in Py4. Lead enrichment could be attributed to nano-scale inclusions of galena in Py2, Py3 and Py4. These trace elements could be associated with Bi-sulfosalts for Py1, with tetradymite for Py2, with pentlandite for Py3, and with galena for Py4 (Figure 4.10). Furthermore, based on the concentrations of Au and Cu, nano-inclusions of native gold are accommodated in Py1 and Py2, and chalcopyrite is hosted in Py2.

Chalcopyrite (Cpy1) (potassic alteration, latite) and Cpy2 (sericitic alteration, latite), as well as chalcopyrite (Cpy3) (E-type veins), contain enrichments of Ag, In

and Ti (Table 4.3). Cd, Ga and V are related to Cpy1, and Hg, Se and Te were found only in Cpy2, while Bi and Co are associated with Cpy1 and Cpy2. Ge and Sb were found in Cpy2 and Cpy3, while W was measured only in Cpy3 from the E-type veins. Based on the ablation patterns Ag, Bi, Cd, Co, Ga, Ge, Hg, In, Sb, Se, Te, Ti, V and W are accommodated in chalcopyrite in solid solutions (Figure 9.11a,b).

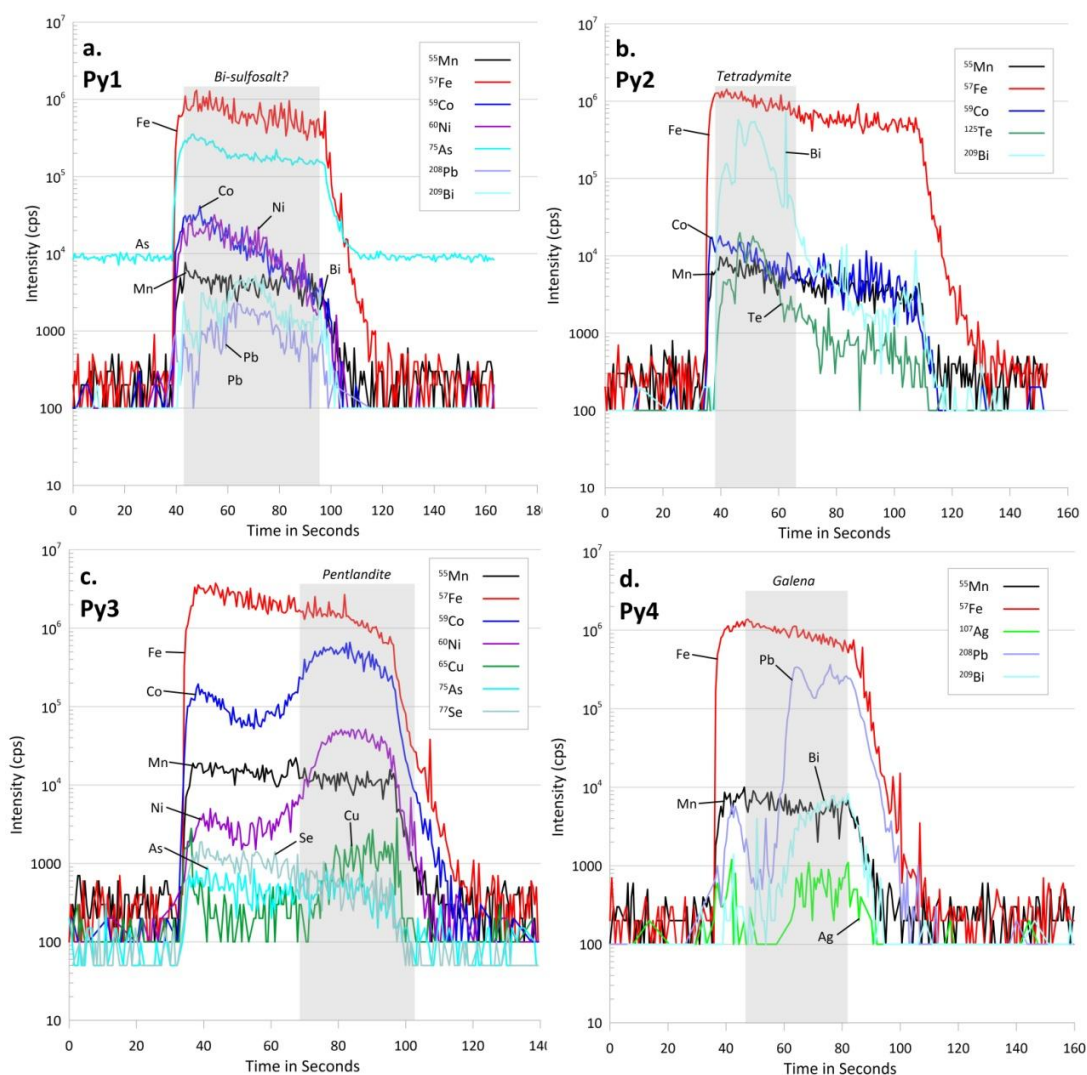


Figure 4.10. Selected time-resolved laser ablation ICP-MS depth profiles of pyrite (a-d) from the different groups and their associated inclusions (highlighted in gray). Manganese, Co, Ni and As, where present, exhibit similar distribution patterns to Fe, unless stated otherwise. a. In Py1, the distribution patterns of Bi and Pb could be related to nano-scale inclusions of Bi-sulfosalts. b. In Py2, the spiky patterns for Bi and Te could suggest the presence of nano-scale inclusions of tetradymite. c. In Py3, the similarly curved distribution patterns could be associated with the presence of pentlandite inclusions. d. In Py4, the spiky patterns of Pb, Bi and Ag could suggest the occurrence of galena inclusions.

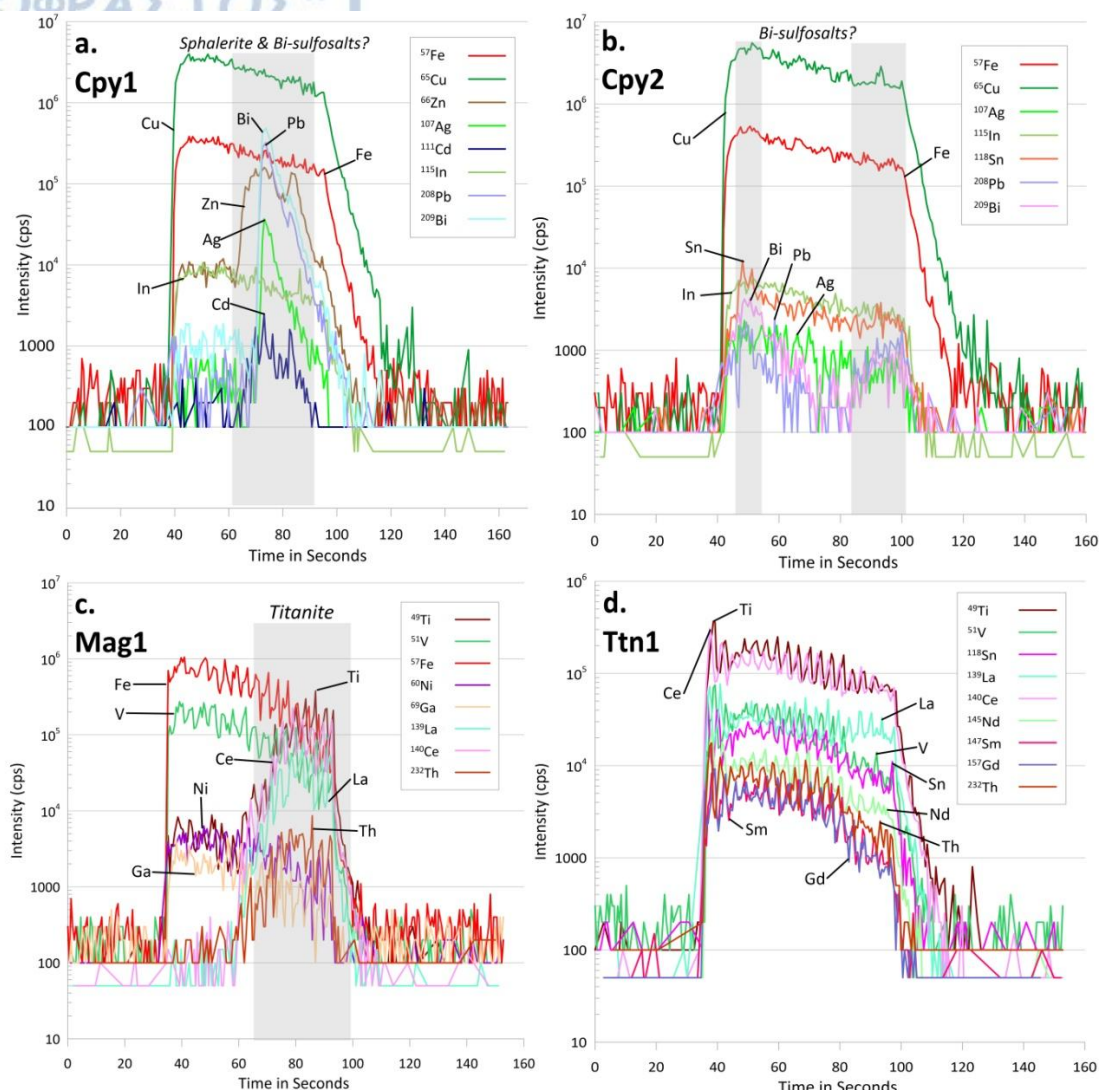


Figure 9.11. Selected time-resolved laser ablation ICP-MS depth profiles of chalcopyrite (a,b), magnetite (c) and titanite (d) and their associated inclusions (highlighted in gray). Iron, In, Ag and Sn, where present, exhibit similar distribution patterns to Cu, in Cpy1 and Cpy2. a. In Cpy1, the spiky patterns of Zn and Cd suggest the presence of sphalerite as nano-scale inclusions, while the more spiky patterns for Bi, Pb and Ag could be related to nano-scale inclusions of Ag-rich Bi-sulfosalts. b. In Cpy2, the curved patterns of Bi and Pb could be associated with Bi-sulfosalts found as nano-scale inclusions. c. In Mag1, V, Ni and Ga follow similar distribution patterns to iron, while the spiky patterns indicate a titanite inclusion in magnetite. In the titanite inclusion, La, Ce and Th follow the distribution patterns of Ti. d. In Ttn1, V, Sn, La, Ce, Nd, Sm, Gd and Th show similar distribution patterns.

Concentrations of trace elements ascribed to nano-scale mineral inclusions in chalcopyrite include mainly Bi and Pb, while Ag, Cd and Zn were attributed to inclusions in Cpy1 (Supplement 2: Table S3-2, Figure 9.11a,b). Zn and Cd

enrichments in Cpy1 are likely related to the presence of sphalerite nano-scale inclusions, while Bi and Pb (Cpy1, Cpy2), and Ag (Cpy1) are probably due the presence of Bi-sulfosalts (Figure 9.11a,b). Chalcopyrite (Cpy3) exhibits minor Pb enrichments, probably due to galena inclusions. It is noted that the presence of Bi-sulfosalts in Cpy2 is also supported by the presence of wittichenite and cuprobismutite (Figure 4.6e).

4.4.2. Mineral chemistry of magnetite and titanite and nano-scale inclusions

Magnetite (Mag1) from the M-type veins related to the potassic-calcic alteration in the quartz monzonite and magnetite (Mag2) from the potassic alteration in latite are associated with rare metals including Co, Ga, Ge, Ti and V, while W occurs in Mag2. These elements are likely incorporated as stoichiometric substitutions (Table 5, Figure 4.9a). Trace elements associated with nanoparticles include Ag, Bi, Ce, Cu, La, Pb, Th and Ti for Mag1, and Bi, Ce, Sb and U for Mag2 (Supplement 2: Table S3-3). Ablation patterns and SEM-EDS analysis support the concept that titanite is hosted as inclusions of various sizes in Mag1 (Figures 4.7b and 4.11c). The presence of Pb and S in Mag2 could be related to minor nano-scale galena inclusions.

Titanite (Ttn1) from the potassic-calcic alteration associated with quartz monzonite is enriched with Ce, Gd, La, Nd and Sm and hosts several rare metals including Co, Ga, Ge, In, Sb, Se, Th and V (Table 5). These elements constitute stoichiometric substitutions since nano-scale mineral inclusions were not detected (Figure 4.11d).

CHAPTER 5. GERAKARIO EPITHERMAL QUARTZ-STIBNITE VEIN MINERALIZATION

5.1. Local geology

Paleozoic to Mesozoic two-mica gneisses and serpentinized peridotites of the Vertiskos Unit form the basement rocks at Gerakario area (Figure 5.1). In vicinity, large amphibolite outcrops are found intercalated in two-mica gneisses, while to the west of the Gerakario area, rock units belonging to the Circum-Rhodope belt are obducted onto the two-mica gneisses of the Vertiskos Unit (Figure 2.2). Additionally, northwest of the Gerakario area, the Vathi Cu-Au±Mo porphyry deposit is located (Figure 5.1a,b).

Cenozoic magmatic rocks appear at Gerakario (Miggiros et al. 1990). They comprise granodiorite (34 ± 0.5 Ma, U-Pb zircon ages, Frei 1992), which appear as small stocks and is silica-saturated with calc-alkaline affinities (Miggiros et al. 1990), as well as stocks and dikes of syenite (22 ± 0.8 Ma, U-Pb zircon ages, Frei 1992) and diorite (24.7 ± 1.3 Ma, K-Ar whole rock, Tompouloglou 1981), which locally exhibit porphyritic textures. Syenite and diorite are slightly saturated to saturated and exhibit slightly alkaline affinities (Frei 1992). The diorite is reported from drill cores and is not found at the surface (Tompouloglou 1981). Outcrops of phreatic breccias are found in the broader area intruding the basement rocks (Toumanidou 2019). Local structures include NE-SW and E-W trending normal to oblique faults, which transcut the syenite (Miggiros et al. 1990, Figure 5.1a).

The granodiorite consists of quartz, plagioclase, hornblende, biotite, with minor K-feldspar, zircon, apatite and titanite (Frei 1992). The alteration assemblage includes biotite (weak potassic alteration), calcite, chlorite and epidote (propylitic alteration), and sericite (sericitic alteration) (Frei 1992). The syenite comprises quartz, plagioclase, K-feldspar, biotite and hornblende, and minor zircon, apatite, rutile and titanite (Frei 1992, Toumanidou 2019). The matrix contains quartz and K-feldspar (Frei 1992). Alteration assemblages include: biotite, magnetite and K-feldspar (potassic alteration), chlorite, allanite and calcite (propylitic alteration), and sericite and quartz (sericitic alteration) (Frei 1992). Hydrothermal alterations are extensively superimposed on each other and have significantly altered both the magmatic rocks and the surrounding metamorphic rocks (Toumanidou 2019).

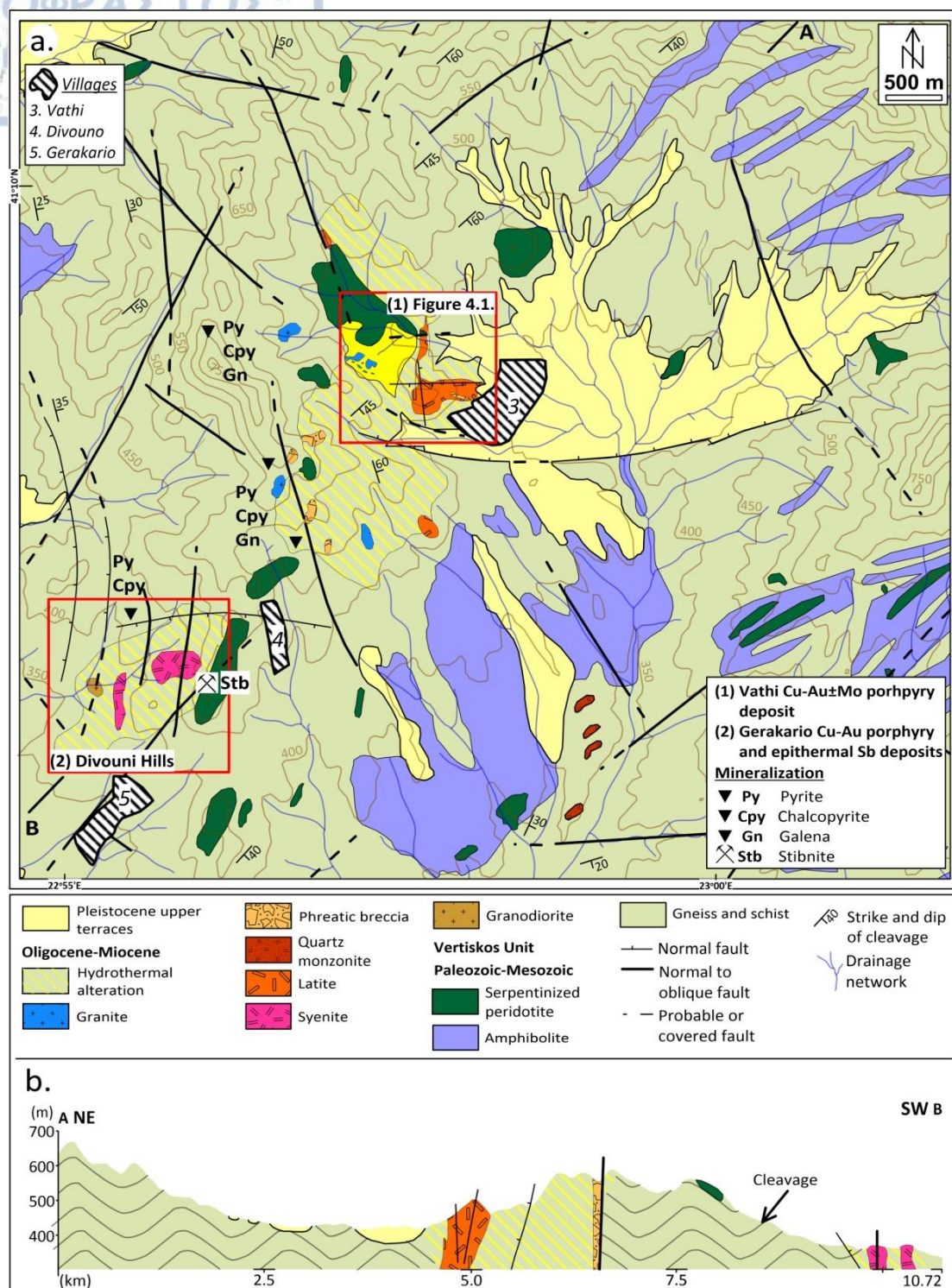


Figure 5.1. a. Geological map showing the Gerakario porphyry and epithermal system at the Divouni Hills (2) in respect to the Vathi porphyry deposit (1). b. Geological cross section of the study area. (modified after Miggiros et al. 1990, Stergiou et al. 2021a,b).

The porphyry mineralization outcrops at the Divouni hills and is genetically associated with the syenite. It is hosted in the syenite, the granodiorite, and the

metamorphic rocks (Toumanidou 2019). Ore textures include disseminations and veins (A-, B- and D-type) (Toumanidou 2019). At the eastern part of the porphyry system a stibnite mineralization is hosted in epithermal quartz veins crosscutting the two-mica gneiss (Figure 5.1a). The epithermal veins are continuous (<5cm in width), locally branched and filled with massive stibnite. In addition, other minor mineralization occurrences are found in the region consisting mainly of pyrite and chalcopyrite (\pm arsenopyrite, galena, stibnite) (Toumanidou 2019, Figure 5.1a). According to Frei (1992) metallic minerals related to porphyry mineralization include: pyrite-chalcopyrite (disseminations) and magnetite-pyrite-chalcopyrite (A- and B-type veins) found in the potassic alteration of the syenite. In addition, pyrite and minor chalcopyrite (disseminations), and pyrite in D-type veins are found in the sericitic alteration in the syenite, the granodiorite and the metamorphic rocks (Frei 1992, Toumanidou 2019). The metamorphic rocks found north of the Divouni hill in contact with the syenite are highly sheared and extensively hydrothermally altered (Toumanidou 2019). Near the surface, the porphyry mineralization is significantly oxidized. In the oxidation zone, pyrite is replaced by goethite, chalcopyrite by malachite and jarosite, and magnetite by hematite (Frei 1992, Toumanidou 2019).

Previous fluid inclusion studies revealed that the porphyry-style mineralization was developed at a maximum depth of 2 km, from magmatic-hydrothermal fluids with moderate to high salinities at a minimum temperature of 380 °C (Tompouloglou 2001, Toumanidou 2019). An early magmatic fluid was dissipated at 600 to 1000 °C and subsequently cooled at temperatures varying between 380 to 460 °C (Tompouloglou 2001, Toumanidou 2019, Stergiou et al. 2022). Boiling and fluid decomposition followed, resulting in a high saline aqueous fluid phase (35.7 to 45.6 wt% equiv. NaCl) and in a moderate saline gas phase (14.8 to 22.0 wt% equiv. NaCl) in the H₂O-NaCl-KCl system. The fluids were entrapped in A- and B-type veins at pressures ranging from 100 to 580 bar. Mixing of a high to moderate saline solution with meteoric waters resulted in the formation of the epithermal stage related to the stibnite vein mineralization at a depth between 600 and 1000 m. The mixture produced less saline fluids (7.9 to 10.4 wt% NaCl) with homogenization temperatures between 280 and 320 °C, and hydrostatic pressures ranging from 65 to 116 bar (Toumanidou 2019, Stergiou et al. 2022).

5.2. Epithermal mineralization stage and alteration style

The epithermal quartz-stibnite veins at Gerakario consist of the following ore mineral assemblage: stibnite + berthierite + native antimony + pyrite + arsenopyrite (Figure 5.2). Minor amounts of marcasite, pyrrhotite, chalcopyrite, löllingite and native gold are also present (Dimou et al. 1987). Gangue minerals include mainly quartz and minor calcite. Traces of valentinite (Sb_2O_3) are related to supergene oxidation.

Stibnite is the predominant ore mineral in the epithermal quartz veins (<5cm in width) (Figure 5.2b). Quartz is found on the walls of the epithermal veins along with calcite, and as veinlets (<2 cm in width) with traces of stibnite. Hydrothermal halos related to the epithermal mineralization are not observed in the surrounding two-mica gneiss, which is slightly affected by sericitic alteration.

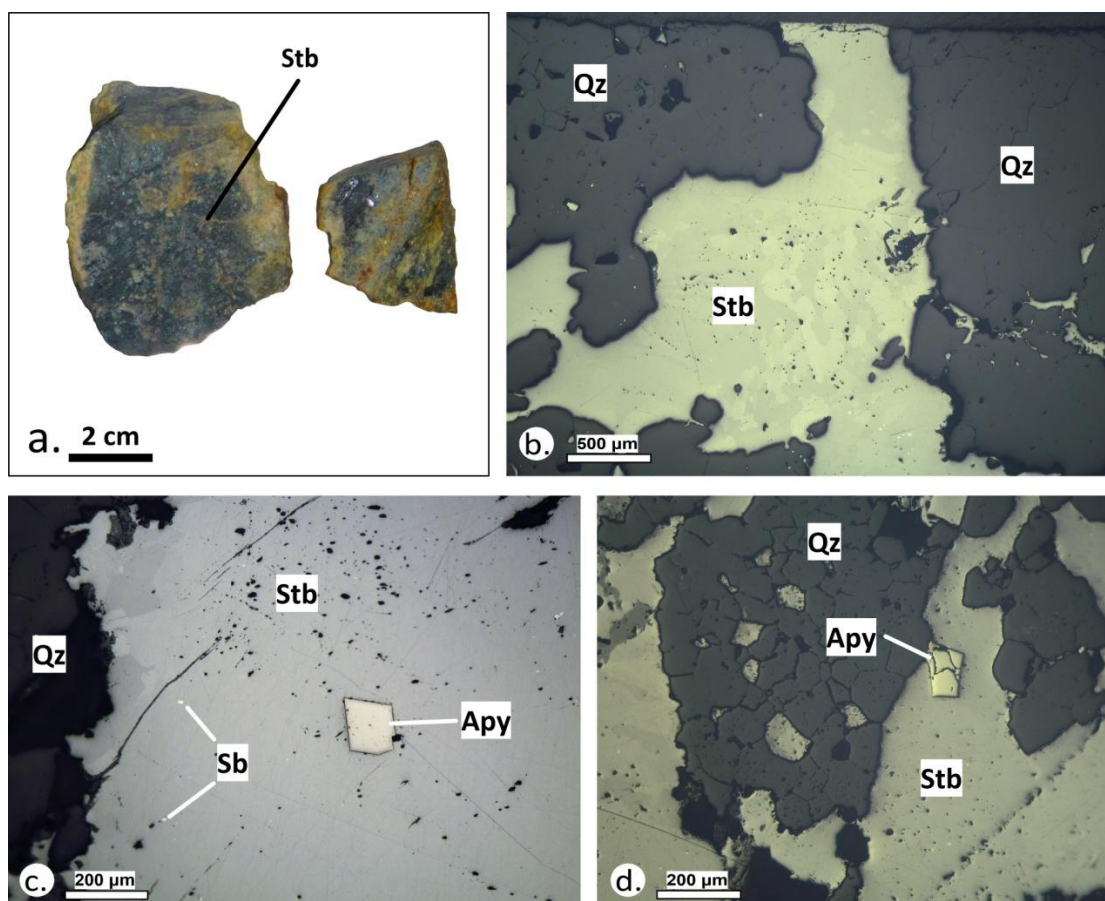


Figure 5.2. The epithermal quartz-stibnite veins at Gerakario (b-d: photomicrographs plane reflected light). a. Massive stibnite (Stb) from Gerakario. b. Stibnite (Stb) with quartz (Qz). c. Stibnite (Stb), euhedral arsenopyrite (Apy) and native antimony (Sb) in quartz (Qz). d. Euhedral arsenopyrite (Apy) in stibnite (Stb) and quartz (Qz).

5.3. Analytical results

5.3.1. Bulk geochemical analysis

Two bulk samples (Ger 3.1, Ger 05) from the quartz-stibnite vein mineralization were geochemically analyzed. Table 5.1 includes the critical and rare metal concentrations measured in these samples. The full geochemical dataset can be found in Supplement 1 (Table S1-2).

The quartz-stibnite veins are more enriched in Ag, Au, Bi, Cd and Sb in respect to upper continental crust (UCC) (Figure 5.3). In contrary, they are depleted in Ce, Co, Ga, La and U (Figure 5.3). The trace elements Gd, Ge, Hg, In, Nb, Nd, Re, Se, Sm, Ta, Te, Th, Ti, V and W exhibit concentrations below detection limits (Table 5.1, Figure 5.3).

Antimony in the quartz-stibnite veins reaches 574,000 ppm (57.4 wt.%), and it is followed by Co (up to 1.8 ppm), Ag (up to 1.2 ppm), Ga (up to 0.16 ppm), U (< 0.13 ppm), Au (up to 0.05 ppm), Cd (up to 0.05 ppm) and Bi (up to 0.03 ppm) (Table 5.1). The concentrations of Ce and La reach 0.12 ppm and 0.4 ppm, respectively (Table 5.1).

Table 5.1. Bulk geochemical analyses of selected critical and rare metals from the epithermal quartz-stibnite veins at Gerakario. For the full list of geochemical analyses please advise Supplement 4, Table S1-2.

	Host rock	Two-mica gneiss			Host rock	Two-mica gneiss	
	Alteration	Sericitic alteration			Alteration	Sericitic alteration	
ppm	Detection limit	Ger 3.1	Ger 05	ppm	Detection limit	Ger 3.1	Ger 05
Ag	0.01	0.98	1.2	Nd	0.1	b.d.l.	b.d.l.
Au	5x10 ⁻⁶	0.05	0.04	Re	0.001	b.d.l.	b.d.l.
Bi	0.01	0.02	0.03	Sb	0.01	326,000	574,000
Cd	0.01	0.05	0.04	Se	0.2	b.d.l.	b.d.l.
Ce	0.02	0.09	0.12	Sm	0.03	b.d.l.	b.d.l.
Co	0.1	1.8	0.9	Ta	0.01	b.d.l.	b.d.l.
Ga	0.05	0.16	0.07	Te	0.01	b.d.l.	b.d.l.
Gd	0.05	b.d.l.	b.d.l.	Th	0.2	b.d.l.	b.d.l.
Ge	0.05	b.d.l.	b.d.l.	Ti	50	b.d.l.	b.d.l.
Hg	0.005	b.d.l.	b.d.l.	U	0.05	0.09	0.13
In	0.005	b.d.l.	b.d.l.	V	1	b.d.l.	b.d.l.
La	0.2	0.4	0.4	W	0.05	b.d.l.	b.d.l.
Nb	0.05	b.d.l.	b.d.l.				

Abbreviation: b.d.l. = below detection limit.

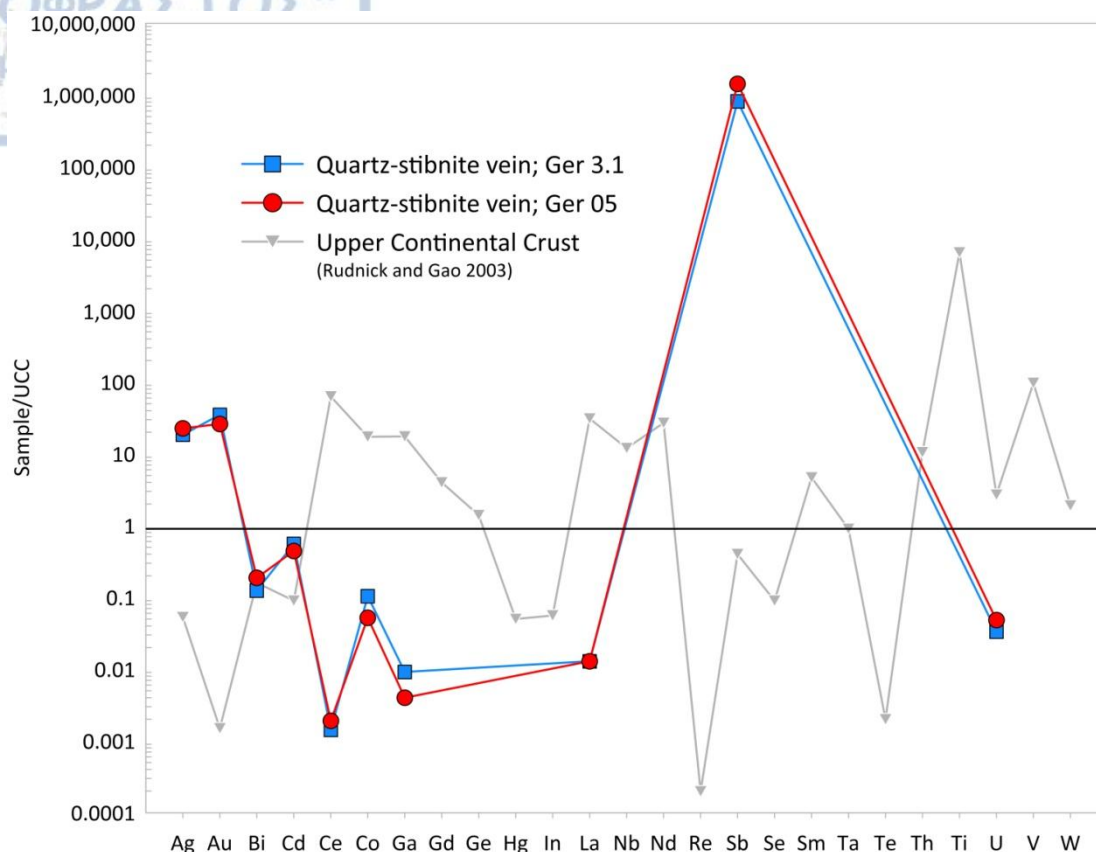


Figure 5.3. Upper continental crust (UCC) normalized logarithmic spider diagram of the two analyzed samples from the epithermal quartz-stibnite veins at Gerakario (UCC normalized values after Rudnick and Gao 2003).

5.3.2. Stibnite - Mode of occurrence

Stibnite in the epithermal veins (<5 cm in width) is massive and forms granular aggregates (Figure 5.2b). In some cases, stibnite inclusions (<100 μm in size) are found in quartz. Berthierite is commonly found as small inclusions in stibnite (Figure 5.4a) and locally as thin lamellae. Euhedral pyrite (<50 μm in size) and arsenopyrite (<200 μm in size) (Figures 5.2c,d and 5.4b,c), and ovoid inclusions of native antimony (<200 μm in size) (Figure 5.4a,d), occur scattered in stibnite. The oxidation of stibnite resulted in the formation of valentinite (<400 μm in size), near the walls of the veins (Figure 5.4b).

5.3.3. Critical and rare metals in stibnite (LA-ICP-MS)

Stibnite exhibits weak to moderate enrichments in trace elemental contents (Table 5.2, Figure 5.5). The full analytical dataset is given in Supplement 2 (Table S3-5). Base (As, Cu, Pb) and critical and rare metals (Ag, Bi, Ce, La, Re, Sm, Th, Ti, Tl) are hosted in stibnite (Table 5.1).

Lanthanum (up to 86 ppm) is the most enriched rare metal, followed by Ti (up to 18 ppm), Ag (up to 0.91 ppm), Tl (up to 0.56 ppm), Bi (up to 0.33 ppm), Ce (up to 0.32 ppm), Sm (up to 0.10 ppm) and Re (up to 0.03 ppm) (Table 5.2, Figure 5.5). The examination of ablation patterns reveals that critical and rare metals are incorporated into stibnite lattice and that nano-scale mineral inclusions are not present.

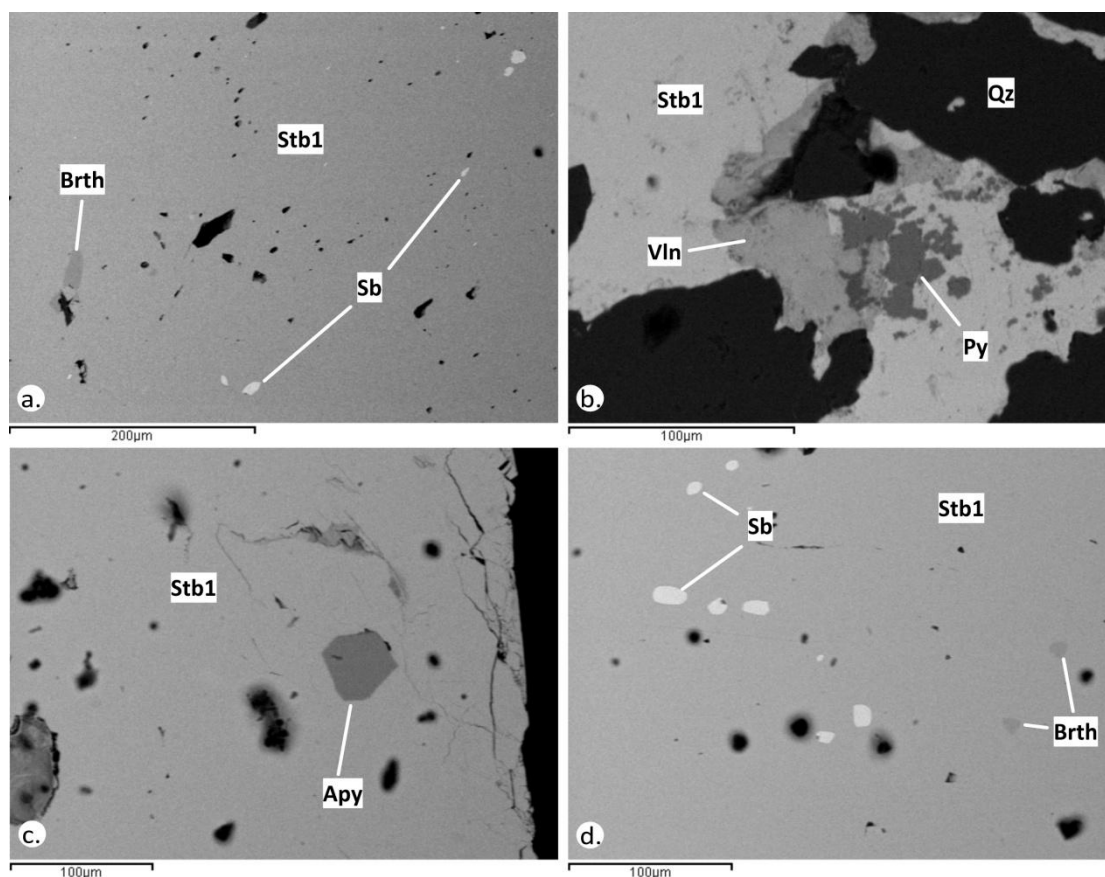


Figure 5.4. SEM back-scattered electron images of stibnite from the quartz-stibnite veins at Gerakario. a. Massive stibnite (Stb1) and minor inclusions of berthierite (Brth) and native antimony (Sb). b. Stibnite (Stb1), valentinite (Vln) and euhedral pyrite (Py) in quartz (Qz) interstices near the walls of the vein. c. Euhedral arsenopyrite (Apy) in massive stibnite (Stb1). d. Round-shaped inclusions of native antimony (Sb) and berthierite (Brth) in stibnite (Stb1).

5.3.4. Statistical analysis of trace elements concentrations

Pearson product-moment correlation coefficients for stibnite are described by significant positive correlation ($p < 0.01$, value = 0.919) defined for the elemental pair Ce-La (Supplement 3: Table S4-9). Positive correlations ($p < 0.05$, values: 0.563-0.589) were defined for the pairs Ce-Sb and La-Sb (Supplement 3: Table S4-9).

Negative correlation ($p < 0.05$, value: -0.564) was defined for the elemental pair Bi-Sb (Supplement 3: Table S4-9). Trace element concentrations related to nano-scale mineral inclusions were excluded before the statistical analyses.

Table 5.2. LA-ICP-MS analyses of stibnite from the epithermal quartz-stibnite veins at Gerakario. For the full dataset, see Supplement 2, Tables S3-5.

Alteration	Sericitic				Alteration	Sericitic			
Host rock	Two-mica gneiss				Host rock	Two-mica gneiss			
Mineralization stage	Stb1; Epithermal quartz-stibnite veins (n = 15)				Mineralization stage	Stb1; Epithermal quartz-stibnite veins (n = 15)			
Element	MIN	MAX	STDEV	AVG	Element	MIN	MAX	STDEV	AVG
ppm					ppm				
Ag	0.12	0.91	0.27	0.45	Nb	b.d.l.	b.d.l.	n.a.	n.a.
As	12	231	70	62	Nd	b.d.l.	b.d.l.	n.a.	n.a.
Au	b.d.l.	b.d.l.	n.a.	n.a.	Pb	98	165	23	122
Bi	0.15	0.33	0.05	0.2	Re	0.03	0.03	n.a.	0.03
Cd	b.d.l.	b.d.l.	n.a.	n.a.	Sb	710,800	716,500	1,611	711,827
Ce	0.09	0.32	0.08	0.2	Se	b.d.l.	b.d.l.	n.a.	n.a.
Co	b.d.l.	b.d.l.	n.a.	n.a.	Sm	0.10	0.10	n.a.	0.10
Cu	29	55	8.6	40	Te	b.d.l.	b.d.l.	n.a.	n.a.
Ga	b.d.l.	b.d.l.	n.a.	n.a.	Th	0.02	0.02	n.a.	0.02
Gd	b.d.l.	b.d.l.	n.a.	n.a.	Ti	9.7	18	2.3	13
Ge	b.d.l.	b.d.l.	n.a.	n.a.	Tl	0.35	0.56	0.11	0.48
Hg	b.d.l.	b.d.l.	n.a.	n.a.	U	b.d.l.	b.d.l.	n.a.	n.a.
In	b.d.l.	b.d.l.	n.a.	n.a.	V	b.d.l.	b.d.l.	n.a.	n.a.
La	24	86	28	44	W	b.d.l.	b.d.l.	n.a.	n.a.

Abbreviations: AVG = average value, b.d.l. = below detection limit, MIN = minimum value, MAX = maximum value, n = number of analyses, n.a. = not analyzed, STDEV = standard deviation.

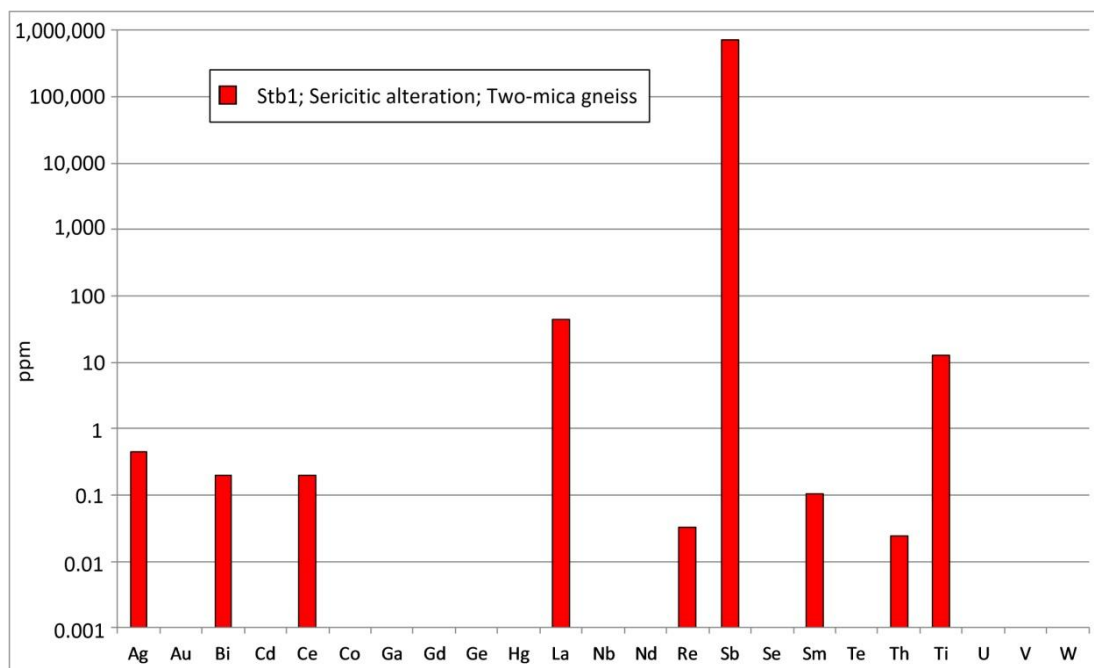


Figure 5.5. Average values of critical and rare metals concentrations of stibnite from the epithermal quartz-stibnite veins. Local enrichments related to nano-scale mineral inclusions are excluded.

5.4. Discussion

The quartz-stibnite vein type mineralization is satellite to the Miocene Gerakario Cu-Au porphyry deposit (Figure 5.1a). It was formed from a fluid of low to moderate salinity (7.9 to 10.4 wt% NaCl) at temperatures not exceeding 320 °C, and in a depth between 600 and 1000 m (Stergiou et al. 2022). A syenite stock (22 ± 0.8 Ma, U-Pb zircon ages, Frei 1992) is the main causative of the porphyry and epithermal mineralization at Gerakario, while a granodiorite stock and the surrounding metamorphics are the host rocks. The local structural setting (NE-SW and E-W trending normal to oblique faults) enhanced hydrothermal fluid circulation and mixing with meteoric water. As a result, base metal mineralization formed in the surrounding metamorphic rocks (Toumanidou 2019, Figure 5.1a).

The epithermal quartz-stibnite veins are hosted in the sericitically altered gneiss. They are mostly continuous and consist of stibnite + berthierite + native antimony + pyrite + arsenopyrite \pm (marcasite, pyrrhotite, chalcopyrite, löllingite, native gold) (Dimou et al. 1987, Toumanidou 2019, Stergiou et al. 2022, Figure 5.2a-d, 5.4a-d).

Bulk geochemical analysis revealed enrichments in Co (<1.8 ppm), Ag (<1.2 ppm), Ga (<0.16 ppm), Ce (<0.12 ppm), La (<0.4 ppm), Au (<0.05 ppm), Cd (<0.05 ppm) and Bi (<0.03 ppm) (Table 5.1). The depletion in Hg is profound (Table 5.1) and is in contrast to the Hg enriched character of the Sb ores located in SE China, where the formation of the epithermal deposits is ascribed to mineralizing fluids enriched in Sb-As-Hg-(Au-Tl-U) (Wang et al. 2012, Fu et al. 2020). Noteworthy are the relatively elevated concentrations of Ce (<0.32 ppm) and La (<86 ppm), as REE are not commonly incorporated in epithermal systems (Hofstra and Kreiner 2020, Table 1.2).

Hydrothermal carbonates (e.g. calcite) mainly host REE in the epithermal systems (Wang et al. 2012). In these cases, REE fractionation is depended upon the composition of the mineralizing fluids and the co-precipitating of other ore, gangue and alteration minerals (Wang et al. 2012). During precipitation of calcite, medium and heavy REEs are preferentially incorporated in its crystal lattice, while light REEs, especially La, are enriched in the residual fluid (Wang et al. 2012). Thus, significant contents of La and Ce, and rarely Pr, Nd and Sm are incorporated in stibnite, which formed after calcite (Wang et al. 2012). Leaching of carbonate wall rocks and of rock-forming minerals from the magmatic-hydrothermal fluids may introduce REEs to the

circulating hydrothermal system (Wang et al. 2012). A similar mechanism has been proposed for the REE enrichment detected in the oxidation zone of the adjacent Vathi porphyry Cu-Au±Mo deposit (Stergiou et al. 2021a, Figure 5.1). Furthermore, REE incorporation in minerals is related to specific physicochemical factors, including the structure of the lattice and complexation (i.e. the combination of individual atom groups, ions or molecules to create one large ion or molecule, Díaz-García and Badía-Laiño 2005), as well as sorption and desorption (Wang et al. 2012). Magmatic fluids are generally depleted in REE, while meteoric fluids are slightly enriched in light REE (Wood and Shannon 2003).

The anatomy of the quartz-stibnite veins at Gerakario, the ore assemblage, the bulk geochemistry, and the fluid inclusions study suggest that the ore mineralization was developed from intermediate to low sulfidation hydrothermal fluids, in a fault-induced epithermal stage set at the periphery of the Gerakario porphyry system. The same could be suggested for all the base metals vein sets found in the vicinity of the Gerakario porphyry system. Epithermal, high to low sulfidation veins are commonly found peripheral to porphyry systems and porphyritic intrusions (Sillitoe 2010, Wang et al. 2019). Epithermal veins are associated with several porphyry deposits in Greece (e.g., Pagoni Rachi, Maronia, Vathi) (Voudouris et al. 2019a, Melfos et al. 2020, Stergiou et al. 2021). However, the veins in these deposits do not host massive stibnite (Voudouris et al. 2019a). Epithermal veins with massive stibnite and realgar are found distal to porphyritic intrusions located at Chios island and the Agia area (Mavrovounio mountain). In those deposits, a zoning proximal to the intrusions containing Sn and Pb-Zn-Cu sulfides was identified by Voudouris et al. (2019a).

5.4.1. Mineral chemistry of stibnite and nano-scale inclusions

Stibnite (Stb1) at Gerakario is enriched in base metals (As, Cu, Pb) and bears weak to moderate contents of critical and rare metals (Ag, Bi, Ce, La, Re, Sm, Th, Ti, Tl) (Table 2, Figure 5.6). However, it is depleted in Au, Hg, Se and Te with concentrations below detection limits (Table 5.2). The depletion of Hg in stibnite contrasts to the Hg enrichment in stibnite from SE China (Fu et al. 2020). In addition, the depletion of Au^{+1} as solid solutions in stibnite and the presence of native gold in interstices of the quartz-stibnite veins (Dimou et al. 1987) indicate that Au precipitation slightly followed Sb precipitation. Thus, it could be suggested that the deposition of massive stibnite depleted the H_2S content of the mineralizing fluids, and

enhanced the precipitation of native gold (Au^0) in the quartz-epithermal veins (Zhou et al. 2021).

The concentrations of As, Cu and Pb in stibnite can be attributed to the stoichiometric substitutions of Sb ($2\text{Sb}^{3+} \leftrightarrow \text{Cu}^+ + \text{Pb}^{2+} + \text{As}^{3+}$), as well as, in some cases, to invisible nanoparticles or to higher incorporation of an element in a specific sector zone, as the LA-ICP-MS depth profiles locally consist of a series of peaks of slightly varying size (Figure 5.6a,b) (Fu et al. 2020). In addition, Cu and Pb exhibit a more consistent distribution in stibnite relatively to the As distribution (Table 5.2).

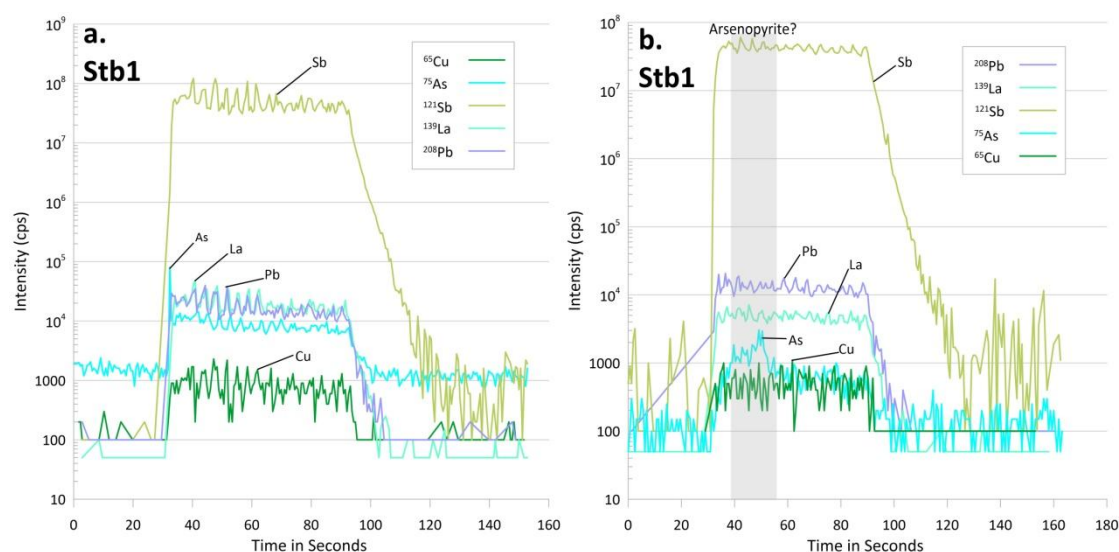
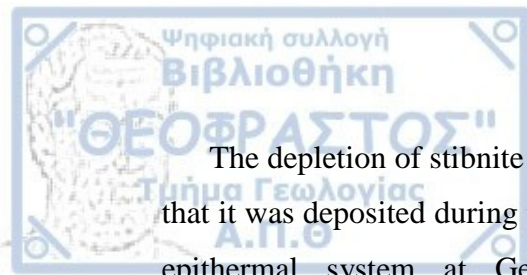


Figure 5.6. Selected time-resolved laser ablation ICP-MS depth profiles of stibnite from the epithermal quartz-stibnite veins at Gerakario. a. In Stb1, the distribution patterns of As, La, Pb, Cu and Sb are similar suggesting their affiliation with stibnite. b. In Stb1, the spiky pattern for As shows the presence of nano-scale inclusions of arsenopyrite in stibnite or that As is incorporated in higher amounts in a specific stibnite sector zone.

The depth profile of La exhibits a similar pattern to those of Sb, As, Cu and Pb (Figure 5.6a,b). The crystal lattice of stibnite does not include proper sites for REE accommodation, especially for La (Wang et al. 2012). Thus, following the suggestions of Wang et al. (2012), lanthanum in stibnite at Gerakario may occur in fluid inclusions or in lattice defects. The rest of the critical and rare metals, including Ag, Bi, Ce, Re, Th, Ti and Tl, which are detected in stibnite, display depth profiles close to background values. Regarding Ce and La contents, possible matrix-derived interferences (i.e., $^{121}\text{Sb}^{18}\text{O}(\pm\text{H})$ for La and Ce) could not be excluded and the distribution of these elements needs further investigation.



The depletion of stibnite in Hg, Se and Te, and the enrichment in La could suggest that it was deposited during the late stages of the mineralizing events in the porphyry-epithermal system at Gerakario. In addition, the other Fe-Cu-Pb-As vein mineralization found in the periphery of the porphyry system (Stergiou et al. 2022) (Figure 5.1a), and the enrichment of As, Cu and Pb in stibnite, indicate the predominance of base metals in the mineralizing fluids related to the epithermal stage.

CHAPTER 6. METAMORPHIC- AND QUARTZ-HOSTED POLYMETALLIC VEIN MINERALIZATION AT LAODIKINO

6.1. Local geology

The basement rocks at Laodikino consist mainly of Paleozoic two-mica gneiss and chlorite-muscovite schist, and in lesser amounts of biotite-, amphibole-, sericite- and garnet-gneiss belonging to the Vertiskos Unit (Thymiatis 1995, Figure 6.1a,b). Minor lenses of amphibolite and serpentinite-talc schist are intercalated in the basement gneisses and schists (Thymiatis 1995). These rocks were thrust towards W-SW on the rock units of the Circum-Rhodope belt (CRB, Spahic et al. 2019, Kiliass 2021). According to Kiliass et al. (1999) and Tranos et al. (1999), the SW-directed reverse faults, the NW-SE-trending kink bands, and the high-angle strike-slip faults found at the western part of the Vertiskos Unit document the local development of a NE-SW-trending contractional component related to thrusting. The SW-vergent thrusting probably occurred between late Oligocene and early Miocene (Kiliass et al. 1999).

The CRB includes Permian to late Triassic quartzite, volcano-sedimentary rocks and minor quartz- and calc-schists (CRB: Pyrgoto and Examili Formations), and middle to late Triassic limestone (CRB: Svoula Group) (Sidiropoulos 1991, Thymiatis 1995, Spahic et al. 2019, Figure 6.1a). According to Spahic et al. (2019), the metamorphic rocks of the broader Laodikino area belong to the late Devonian-early Carboniferous "Veles Series", which forms the eastern part of the CRB in the region. The "Veles Series" is a relic of the northern active margin of the old Paleotethys ocean-floor, while the Examili and Pyrgoto Formations document a Permian-early Triassic rifting (Spahic et al. 2019). According to Kougoulis et al. (1990), a barite mineralization enriched in Fe, Pb and Zn, is hosted in these rocks near Lipsidri village (Figure 6.1a). The barite mineralization is compact, stratiform and syngenetic to middle to late Triassic basic meta-tuffs belonging to the volcano-sedimentary rocks (Kougoulis et al. 1990, Asvesta 1992).

Four ductile deformation phases affected the Laodikino rocks, including the pre-Mesozoic to Mesozoic D1 to D3 phases, and the Cenozoic D4 phase, followed by brittle deformation (Kourou 1991, Thymiatis 1995). The D2 phase is the first event associated and is described by isoclinal folding of S1 fabric and by a penetrative S2 fabric.

The D3 event is characterized by tight isoclinal to recumbent folds and by a planar penetrative S3 fabric (Kourou 1991). The Cenozoic D4 event folded S3 fabric and produced open upright and kink folds and a planar S4 fabric (Kourou 1991, Thymiatis 1995). The D3 deformation event is associated with Jurassic to early Cretaceous amphibolite facies metamorphism, while the D4 deformation event is related to the late Cretaceous-Eocene upper greenschist and retrograde low greenschist facies metamorphism (Kourou 1991, Sidiropoulos 1991). Brittle deformation (early Oligocene-Miocene) is mainly characterized by NW- and NE-trending normal to oblique faults (Kilias 1999).

Several pegmatites, aplites and quartz veins occur parallel to the foliation of or intrude the metamorphic rocks at Laodikino. They are associated with the tectono-metamorphic evolution of the area and are divided in three groups. The first group includes dikes of pegmatites and aplites (<1 m in width), as well as quartz veins (<20 cm in width) almost parallel to the main schistosity of the two-mica gneiss. They are barren and their formation is attributed to the deep crustal retrogression during metamorphism (diafiorism) of the two-mica gneiss of the Vertiskos Unit (D2 deformation phase).

The second group of dikes comprises mainly pegmatites, and only sparsely aplites. They intrude the metamorphic rocks and crosscut the D3 deformation phase. These pegmatites form irregular stocks, sills and dikes (<100 m in length) and locally are intersected by hydrothermal quartz veins (fourth group). Along the pegmatites, minor lenses and veins (<20 cm in width) of oxidized mineralization are found, K-feldspar and plagioclase are altered to kaolinite and sericite, while the groundmass is dominated by sericite.

The third group includes milky quartz-chlorite veins (<20 cm in width, Figure 6.1a). These veins are found along planes of low-angle normal faults (N13W/69°ENE in average) developed in the hanging wall of reverse faults. Quartz is locally highly fragmented and vuggy, while chlorite forms foliated masses. Minor plagioclase and muscovite are also found. Plagioclase is slightly altered to sericite. Stains of Fe- and Mn- oxides appear in quartz fractures.

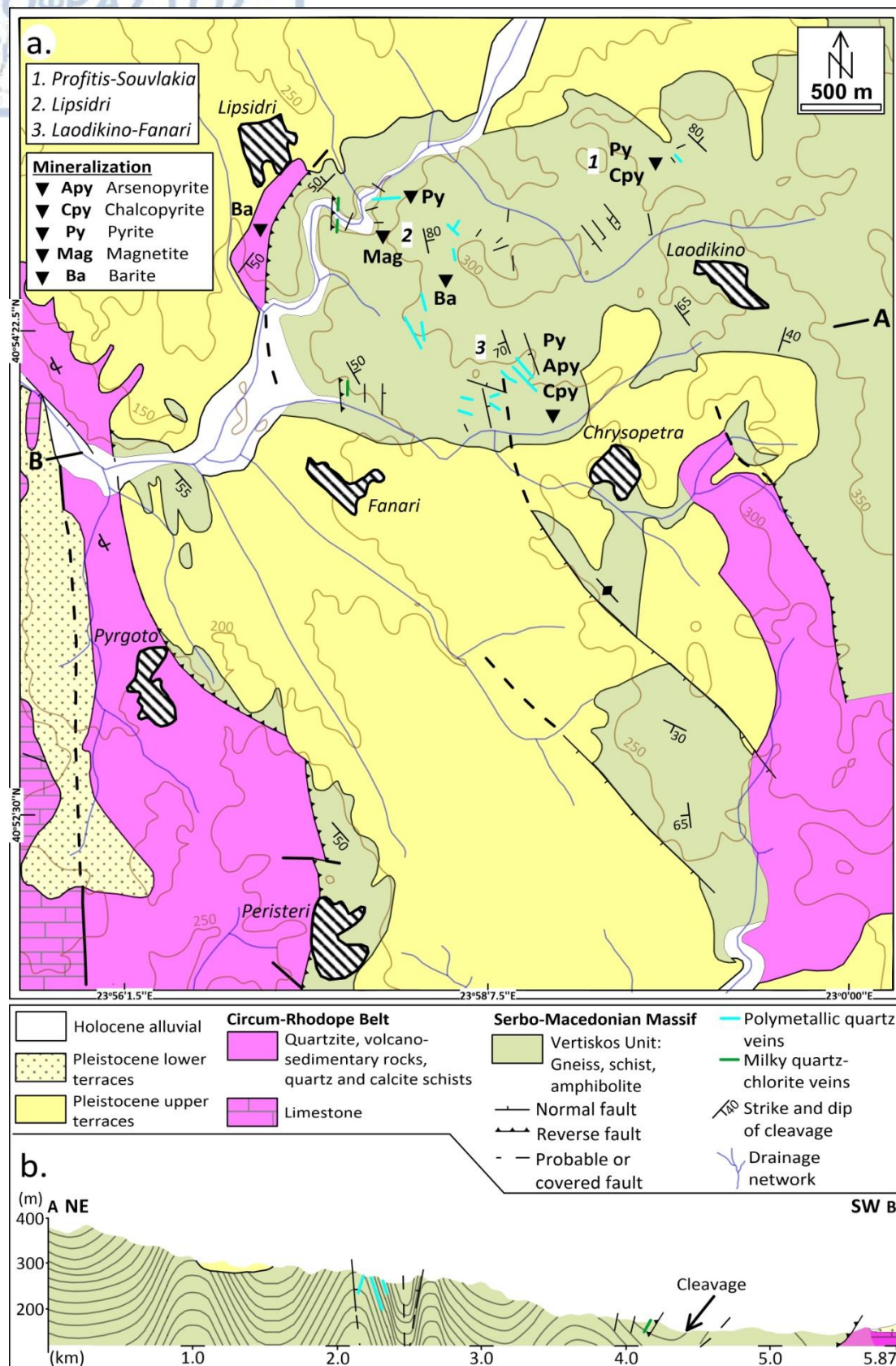


Figure 6.1. a. Geological map of the Laodikino metamorphic- and quartz-hosted polymetallic vein mineralization. b. Geological cross section of the study area (modified after Kockel and Ioannidis 1979a, Miggiros et al. 1990, Thymiatis 1995).

The forth group consists of hydrothermal quartz veins (<1 m in width) and polymetallic massive veins (~4 m in width). These two types of veins exhibit similar distribution and host Cu-Fe-As-Zn-Pb-Sb mineralization, which is enriched in Ag-Au-Bi-Cd-Co-Hg-In-Se-Te (Thymiatis 1995, Voudouris et al. 2007). They are mostly found at Profitis-Souvlakia, Lipsidri and Laodikino-Fanari (Figure 6.1a), where they intrude the D3 folds and are sub-parallel to or crosscut the D4 folds (Thymiatis 1995). Locally, along shear zones the polymetallic massive veins appear as lenses (i.e. boudin-like structures). They also appear in mylonitic zones (<2 m in width) of pre-existing normal or reverse fault zones (brittle deformation subsequent to D4 deformation phase). The largest veins are associated with NW-SE faults (N35W/73°NE in average), while smaller veins are found in accordance with NE-SW faults. Overall, the polymetallic quartz veins appear in higher angles than the polymetallic massive veins. In the Laodikino-Fanari area, restricted mineralization zones are found related to sub-parallel sets of veins and faults. Hydrothermal halos around the quartz veins are characterized by sericitization and chloritization. Due to supergene processes the mineralization in quartz and massive veins is oxidized.

6.2. Mineralization and alteration styles

Thymiatis (1995) was the first to describe in detail the metallic assemblages at Laodikino, and mentions three distinct assemblages occurring as massive and banded (stratiform-like, VMS-style) veins, massive veins, as well as disseminations. Based on Thymiatis (1995), Voudouris et al. (2007), and this study the metallic assemblages are revised as follows: 1) massive and banded (stratiform-like), 2) pods, 3) polymetallic massive veins, 4) polymetallic quartz veins, and 5) disseminations and aggregates in hydrothermal halos (Table 6.1). This study was focused on the mineralization hosted in the pods and in the polymetallic quartz veins.

The massive and banded (stratiform-like) metallic assemblage occurs only in drill core samples and was described by Thymiatis (1995). It is hosted in quartz- and calc-schists of the CRB reaching 2.5 m in width (Thymiatis 1995). Brown sphalerite is the main metallic mineral (>70 wt.% of the mineralization) followed by pyrite, galena, chalcopryrite, tetrahedrite, and minor amounts of boulangerite, bournonite, freibergite, jordanite, cosalite, ullmanite and berthierite (Thymiatis 1995, Table 6.1). Boulangerite, bournonite and jordanite mainly occur in calc-schist (Thymiatis 1995). Quartz and calcite are found as gangue minerals. Hydrothermal alteration includes

baritization and chloritization identified by the occurrence of barite, witherite and chlorite (Table 6.1).

The mineralized pods (<10 cm in width) are found along foliation in the biotite gneiss and are characterized by brecciated texture and chloritization (Figure 6.2a,b). They accommodate magnetite, pyrite, chalcopyrite, rutile, ilmenite, and traces of galena, arsenopyrite, xenotime and bastnäsite (Table 6.1, Figure 6.3a-c). Gangue minerals include quartz and calcite, while chlorite is related to alteration.

Table 6.1. Summary of the typology, alteration and textural characteristics of the mineralization at Laodikino.

Mineralization age	Mineralization style	Host rock	Alteration style	Metallic assemblage	Gangue and alteration assemblage	Reference
Mesozoic? (middle to late Triassic?)	Massive and banded (stratiform-like, VMS-style)	Quartz- and calc- schist	Baritization + chloritization	Sph + Py + Gn + Cpy + Ttr ± Boul ± Bnn ± Fr ± Jo ± Cos ± Ull ± Brth	Br + Wth + Chl Qz + Cal	Thymiatis (1995)
Pre-Cenozoic to early Cenozoic ?	Pods (magnetite-rich)	Biotite gneiss	Chloritization	Mag + Py + Cpy + Rt + Ilm ± Gn ± Apy ± Xtm ± Bsn	Cal + Chl + Qz	Thymiatis (1995), this study
Cenozoic? (early Oligocene-Miocene?)	Polymetallic massive veins	Two-mica gneiss + chlorite-muscovite schist	Sericitization + chloritization	Apy + Py + Cpy + Sph ± Ttr ± Gn ± Po ± Mag ± Ilm ± Rt ± Cob ± Alt Pils ± Elc ± Bi	Qz + Ser + Chl + Cal + Brt	Thymiatis (1995), Voudouris et al. (2007)
	Polymetallic quartz veins Disseminations and aggregates in hydrothermal halos			Py + Cpy + Ttr + Sph + Gn		Thymiatis (1995), this study
	Encrustations and masses		Oxidized mineralization	Py + Cpy		
				Hem + Gt + Mal + Azr + Cct + Cov + Cpr + Cu		

Abbreviations: Alt = altaite, Apy = arsenopyrite, Azr = azurite, Bi = native bismuth, Bnn = bournonite, Boul = boulangerite, Bsn = bastnäsite, Brt = barite, Brth = berthierite, Cal = calcite, Cct = chalcocite, Chl = chlorite, Cob = cobaltite, Cos = cosalite, Cov = covellite, Cpr = cuprite, Cpy = chalcopyrite, Cu = native copper, Elc = electrum, Fr = freibergite, Gt = goethite, Gn = galena, Hem = hematite, Ilm = ilmenite, Jo = jordanite, Mag = magnetite, Mal = malachite, Pils = pilsenite, Po = pyrrhotite, Py = pyrite, Qz = quartz, Rt = rutile, Ser = sericite, Sph = sphalerite, Ttn = titanite, Ttr = tetrahedrite, Ull = ullmenite, Wth = witherite, Xtm = xenotime.

The polymetallic massive veins (>80 wt.% of ore, <4 m in width, <600 m in length) are locally discontinuous and form lenses reflecting the overprint of the D4 deformation phase (i.e. late Cretaceous-Eocene upper greenschist to retrograde low greenschist facies metamorphism) on the textures of the mineralization. The polymetallic quartz veins (<1m in width) are locally related to fault zones (Figure 6.2c). They are planar and continuous, exhibiting comb and brecciated textures

(Figure 6.2d). Thymiatis (1995), based on drill core samples, mentions that the polymetallic massive and quartz veins, reach a depth of 200 m, forming hydrothermal halos and disseminations and aggregates of mineralization. The mineralization of the polymetallic massive veins includes arsenopyrite, pyrite, chalcopyrite, sphalerite, and minor tetrahedrite, galena, pyrrhotite, magnetite, ilmenite, rutile, cobaltite, altaite, pilsenite, electrum and native bismuth (Thymiatis 1995, Voudouris et al. 2007, this study, Table 6.1). The polymetallic quartz veins include pyrite, chalcopyrite, tetrahedrite, sphalerite and galena (Table 6.1, Figure 6.3d-f). Pyrite and chalcopyrite is found as disseminations and aggregates in the hydrothermal alteration halos.

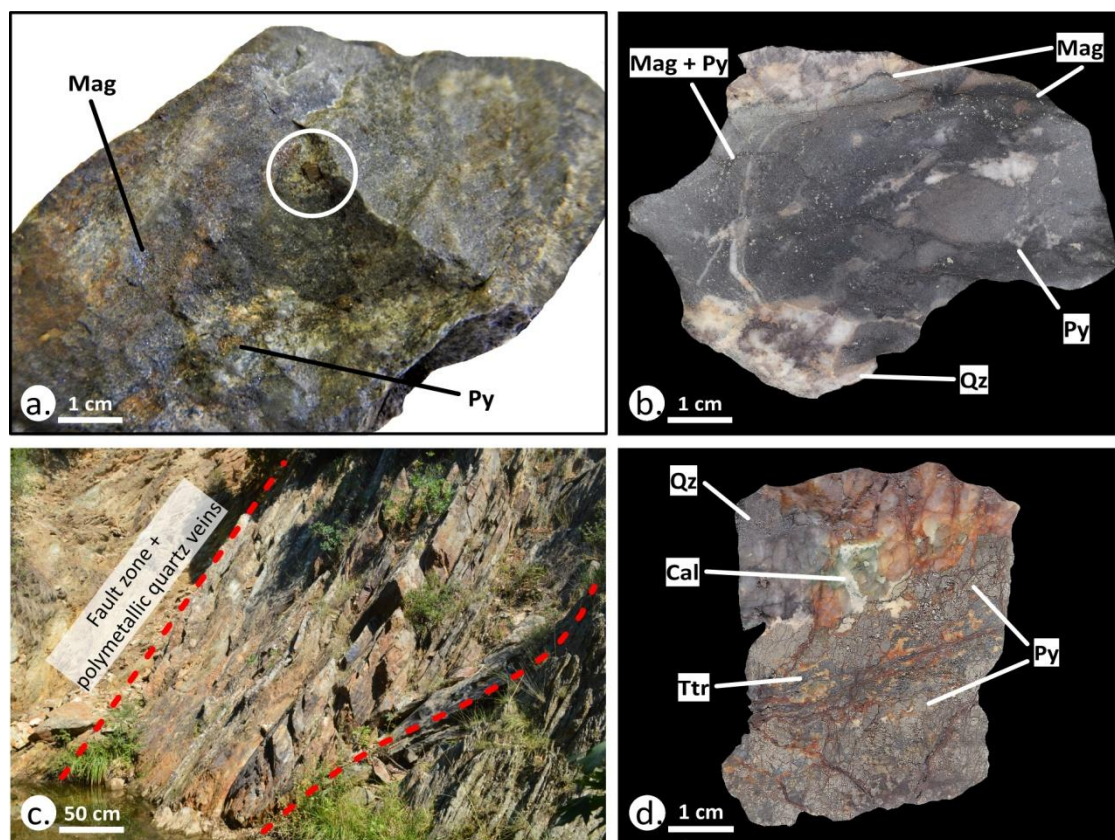


Figure 6.2. Mineralization at Laodikino. a. Bulk biotite gneiss with magnetite (Mag) and pyrite (Py). Euhedral pyrite is highlighted (white cycle). b. Quartz (Qz), magnetite (Mag) and pyrite (Py) from a brecciated pod. c. A fault zone containing oxidized polymetallic quartz veins. d. Pyrite (Py) and tetrahedrite (Ttr) rimmed by quartz (Qz) in a brecciated polymetallic quartz vein. Calcite (Cal) is found in quartz interstices.

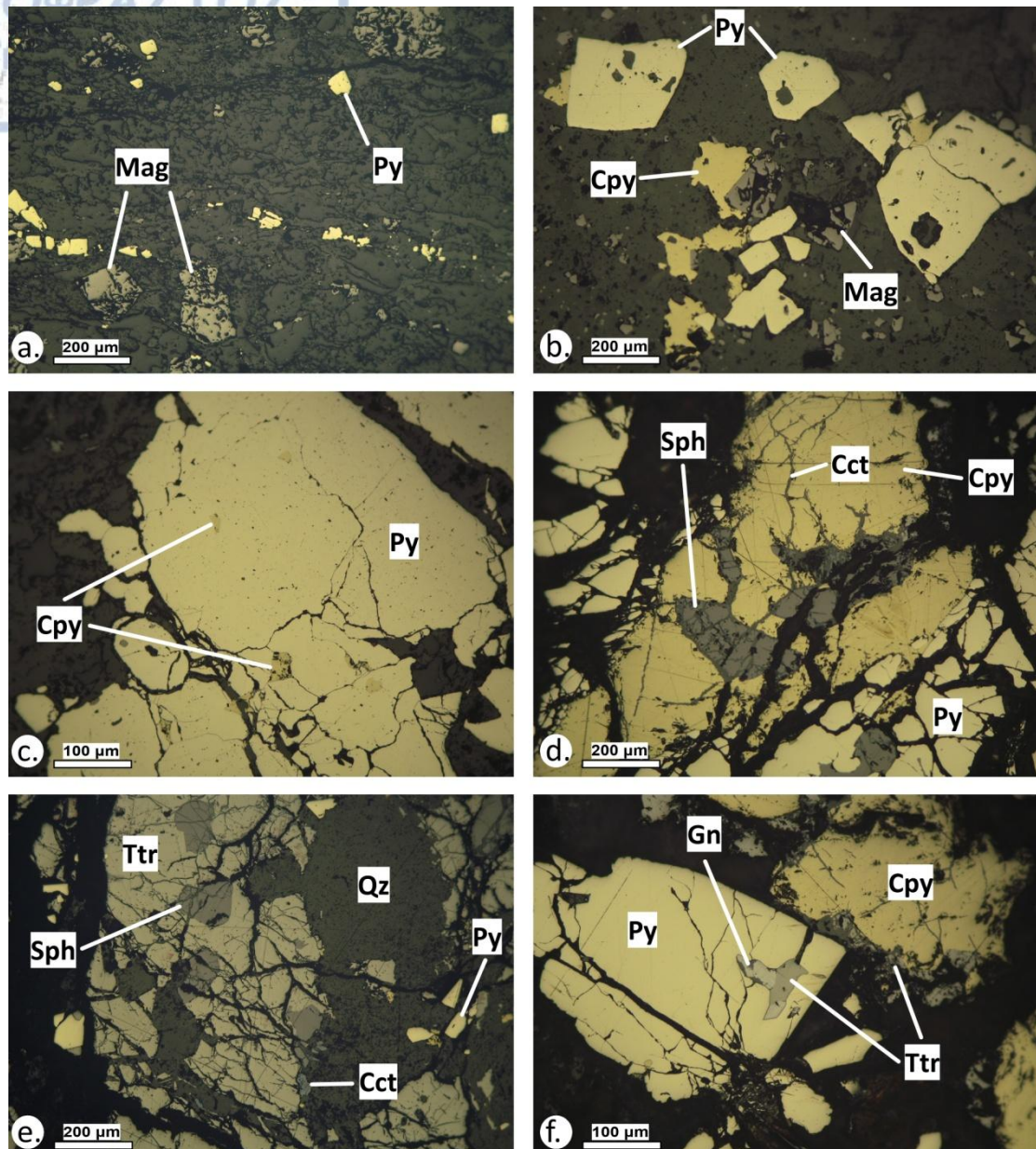


Figure 6.3. Photomicrographs (plane reflected light) of the hypogene mineralization in the pods (a-c) and in the polymetallic quartz veins (d-f). a. Euhedral pyrite (Py) and magnetite (Mag) set in quartz (Qz). b. Euhedral pyrite (Py) and magnetite (Mag) with minor chalcopyrite (Cpy) in interstices. c. Pyrite (Py) with inclusions of chalcopyrite (Cpy). d. Pyrite (Py) with cataclastic texture cemented by chalcopyrite (Cpy) and sphalerite (Sph). Chalcopyrite (Cpy1) and sphalerite (Sph1) are altered to chalcocite (Cct) along cracks. e. Euhedral sphalerite (Sph) partly replaced by chalcocite (Cct) and euhedral pyrite (Py), cemented by tetrahedrite (Ttr) and rimmed by quartz (Qz). f. Pyrite (Py) with cataclastic texture being replaced by galena (Gn) and tetrahedrite (Ttr) and cemented by chalcopyrite (Cpy).

Quartz and calcite are found as gangue minerals in the polymetallic massive and quartz veins. They are also found along with sericite and chlorite in hydrothermal halos associated with sericitization and chloritization. The oxidized metallic assemblage related to supergene processes forms encrustations and masses and consists of hematite, goethite, malachite, azurite, chalcocite, covellite, cuprite and native copper (Thymiatis 1995, this study, Table 6.1).

6.3. Analytical results

6.3.1. Bulk geochemical analysis

Eight surface mineralized samples from Laodikino were analyzed in order to examine the critical and rare metals endowment. Two samples were from the polymetallic quartz veins (LAO 08bi, LAO 08bii) and two were from the magnetite-rich pods (LAO 08, LAO 08a). Additionally, four samples from the hydrothermally altered and oxidized metamorphic rocks were also analyzed for background reference. The sample LAO 06a is from a quartz vein with chlorite and Fe-oxides impregnations related to the D2 deformation phase. The sample LAO 07 refers to a sericitically altered pegmatite associated with the D3 deformation phase, while the samples LAO 10 and LAO 11 come from a sericitized two-mica gneiss with goethite and malachite encrustations. Table 6.2 summarizes the critical and rare metals measured in the analyzed samples.

The polymetallic quartz veins exhibit major enrichments in Ag (<2,433 ppm), Au (<3 ppm), Bi (<83 ppm), Cd (<247 ppm), Hg (<187 ppm), In (<53 ppm), Sb (<70,500 ppm or 7.05 wt.%) and Se (<59 ppm, Table 6.2, Figure 6.4). In contrast, they are depleted in Ga, Ge, Nb, Te, Th, V, W and REE with concentrations not exceeding 10 ppm (Table 6.2). The magnetite-rich pods are depleted in critical and rare metals with distribution patterns similar to those of the hydrothermally altered and oxidized metamorphic rocks (Table 6.2, Figure 6.4). Au (<0.06 ppm), Bi (<0.83 ppm), Ga (<11 ppm) and In (<0.15 ppm) are slightly more enriched than the background reference (Table 6.2, Figure 6.4). The highest values of REE were analyzed in the samples from the magnetite-rich pods (Table 6.2, Figure 6.4). Ce (<58 ppm), Gd (<6.8 ppm), La (<30 ppm), Nd (<31 ppm) and Sm (<6.9 ppm), were the most enriched REE (Figure 6.4, Supplement 4: Table S1-3).

Table 6.2. Bulk geochemical analyses of selected critical and rare metals from Laodikino. For the full list of geochemical analyses advise Supplement 4, Table S1-3.

ppm	Host rock	Mineralization stages				Metamorphic rocks			
		Polymetallic quartz veins		Magnetite-rich pods		Quartz vein	Pegmatite	Two-mica gneiss	
		Sericitization		Chloritization		Chl.	Ser.	Sericitization and supergene oxidation	
	Det. limit	LAO 08bi	LAO 08bii	LAO 08	LAO 08a	LAO 06a	LAO 07	LAO 10	LAO 11
Ag	0.01	2,433	1,750	0.15	0.22	1.6	0.17	0.12	0.33
Au	5x10 ⁻⁶	3	2.2	0.06	0.03	0.01	0.003	0.002	0.02
Bi	0.01	83	77	0.83	0.65	0.04	0.02	0.2	0.16
Cd	0.01	247	207	0.39	0.41	1.7	0.16	b.d.l.	0.72
Ce	0.02	9	6.9	58	33	5.5	26	7.9	16
Co	0.1	166	81	11	8.5	4.3	2.1	0.47	1.9
Ga	0.05	1	1.2	11	8.5	4.3	2.1	0.47	1.9
Gd	0.05	1.4	1.3	6.8	4.7	0.95	3	0.28	2
Ge	0.05	0.16	0.29	0.3	0.23	0.15	b.d.l.	b.d.l.	0.14
Hg	0.005	187	171	0.05	0.05	0.2	0.06	0.82	0.53
In	0.005	53	53	0.1	0.15	0.01	b.d.l.	0.01	0.08
La	0.2	4.3	3.2	30	15	2.8	11	4.5	7.2
Nb	0.05	b.d.l.	0.12	0.12	0.14	0.09	0.19	0.08	0.14
Nd	0.1	4.6	3.9	31	18	3	13	2.7	7.4
Re	0.001	b.d.l.	b.d.l.	0.002	0.002	0.003	0.002	0.001	0.003
Sb	0.05	70,500	54,000	1.3	1.5	69	6.9	2.17	10
Se	0.2	24	59	0.8	0.5	b.d.l.	b.d.l.	b.d.l.	1.3
Sm	0.03	1.3	1.1	6.9	4.3	0.76	2.8	0.44	1.8
Ta	0.01	b.d.l.	b.d.l.	0.02	0.02	0.03	0.01	b.d.l.	b.d.l.
Te	0.01	0.03	0.03	0.07	0.06	0.01	b.d.l.	b.d.l.	0.33
Th	0.2	b.d.l.	0.3	4.3	3.4	0.4	10	0.7	2.4
Ti	50	b.d.l.	b.d.l.	0.02	0.01	0.02	0.01	b.d.l.	0.01
U	0.05	1.1	0.74	1.5	0.87	1	1	0.09	3.5
V	1	10	4	35	46	10	3	b.d.l.	10
W	0.05	b.d.l.	0.26	84	123	400	127	207	325

Abbreviations: alt. = alteration, b.d.l. = below detection limit, Chl. = chloritization, Det. limit = detection limit, Ser. = sericitization.

Pearson product-moment correlation coefficients and associated p-values were calculated for the bulk geochemical analyses (Supplement 3: Table S4-2). Significant positive correlations ($p < 0.01$, values ≥ 0.852) were obtained for the following elemental pairs: Ag-Au, Ag-Bi, Ag-Cd, Ag-Co, Ag-Hg, Ag-In, Ag-Sb, Au-Bi, Au-Cd, Au-Co, Au-Hg, Au-In, Au-Sb, Bi-Cd, Bi-Co, Bi-Hg, Bi-In, Bi-Sb, Bi-Se, Cd-Co, Cd-Hg, Cd-In, Cd-Sb, Cd-Se, Co-Hg, Co-In, Hg-In, Hg-Sb, Hg-Se, In-Sb, In-Se, Sb-Se, Ce-Ga, Ce-Gd, Ce-La, Ce-Nd, Ce-Sm, Ga-Cd, Ga-La, Ga-Nd, Ga-Sm, Gd-La, Gd-Nd, Gd-Sm, La-Nd, La-Sm, Nd-Sm, Re-Ti, Re-W, Ta-Ti and Te-U (Supplement 3: Table S4-2). Furthermore, positive correlations ($p < 0.05$, values between 0.708 and

0.826) were defined for the elemental pairs: Ag-Se, Au-Se, Co-Sb, Ce-V, Ga-Ti, Ga-V, Gd-V, La-V, Nb-Th, Nd-V and Sm-V (Supplement 3: Table S4-2). Significant negative correlations were not detected, while negative correlations ($p < 0.01$, values ≥ -0.771) include the elemental pairs Ag-Re, Au-Re, Bi-Re, Cd-Re, Co-Nd, Hg-Re, In-Re and Re-Sb (Supplement 3: Table S4-2).

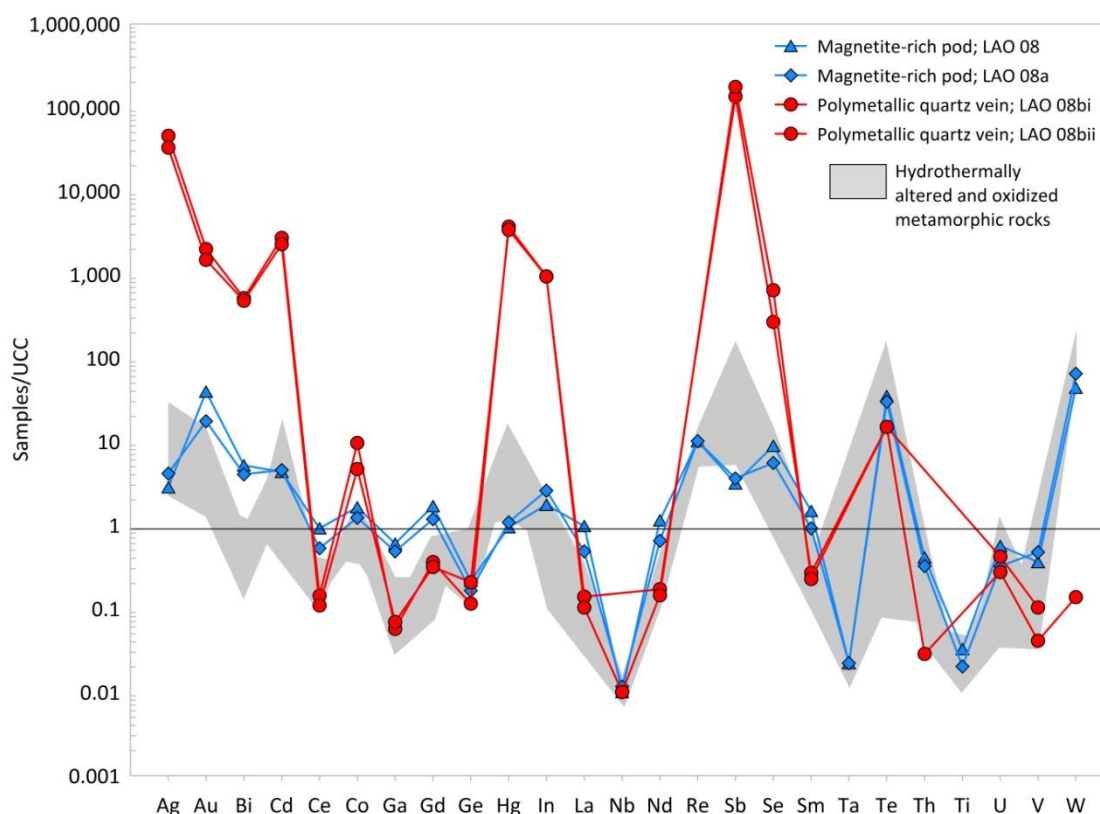


Figure 6.4. Upper continental crust (UCC) normalized logarithmic spider diagram of the four mineralized samples presented in comparison to the plot area of the hydrothermally altered and oxidized metamorphic rocks (UCC normalized values after Rudnick and Gao 2003).

6.3.2. Pyrite and chalcopyrite - Mode of occurrence

Pyrite at Laodikino is a major mineral in the polymetallic quartz veins and in the pods (Table 6.1). In the polymetallic quartz veins pyrite (Py1) forms massive bands (<1 cm in width) and exhibits wide cataclastic texture (Figure 6.2a, 6.3a,c, 6.5a). Chalcopyrite, tetrahedrite, sphalerite and galena are intercalated between the pyrite bands (Figure 6.3a-c). Rounded inclusions (<200 μm in width) consisting of chalcopyrite, galena, tetrahedrite, sphalerite and barite are found in pyrite (Figure 6.3c, 6.5a-d,f).

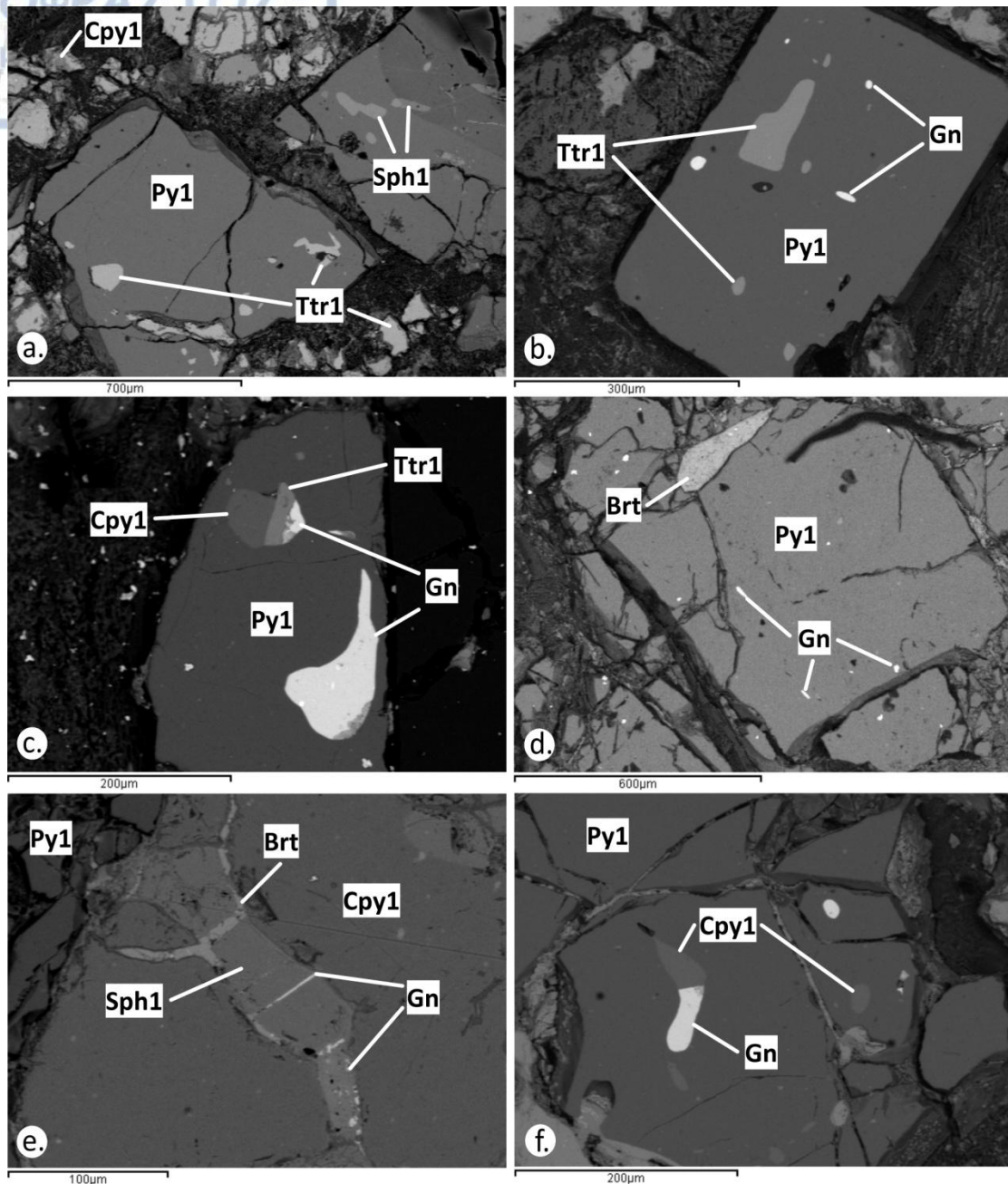


Figure 6.5. SEM back-scattered electron images of pyrite from the polymetallic quartz veins at Laodikino. a. Pyrite (Py1) with cataclastic texture containing tetrahedrite (Ttr1) and sphalerite (Sph1) inclusions, and cemented by chalcopyrite (Cpy1). b. Euhedral pyrite (Py1) with tetrahedrite (Ttr1) and galena (Gn) inclusions. c. Pyrite (Py1) with galena (Gn), tetrahedrite (Ttr1) and chalcopyrite (Cpy1) inclusions. d. Pyrite (Py1) with cataclastic texture, barite (Brt) and minor galena (Gn) inclusions. e. Massive chalcopyrite (Cpy1) intercalated with pyrite (Py1). Cracks in sphalerite (Sph1) are filled with barite (Brt) and galena (Gn). f. Pyrite (Py1) bears inclusions of chalcopyrite (Cpy1) and galena (Gn).

In the pods, pyrite (Py2) is found as subhedral to euhedral crystals (<1 mm in width), as well as aggregates of euhedral grains (<5 mm in width), set in a calcite-chlorite-quartz dominated matrix also hosting magnetite disseminations (<500 μm in width, Figure 6.3d, 6.6a). Locally, deformed aggregates consisting of subhedral to euhedral pyrite (<50 μm in width) fill the quartz-calcite intergranular space (Figure 6.6a). Pyrite (Py2) is overgrown by chalcopyrite (Figure 6.3e), and contains euhedral inclusions of magnetite (<80 μm in width), prismatic rutile-ilmenite intergrowths (<200 μm in width), prismatic arsenopyrite (<50 μm in width), and replacements of chalcopyrite and galena (<100 μm in width, Figure 6.6b,c). The rutile-ilmenite intergrowths are characterized by eroded rims and host xenotime inclusions, while in their periphery bastnäsite is found (Figure 6.6d).

Chalcopyrite (Cpy1) is the second most abundant sulfide mineral in the polymetallic quartz veins. It is intergrown with tetrahedrite, galena and sphalerite (Figure 6.3a-c, 6.5a,c). It mostly appears massive, cementing pyrite bands and also, in some cases, sphalerite. Locally, it is slightly altered to covellite (Figure 6.5e). It also occurs as rounded inclusions in pyrite (<200 μm in width), locally along with tetrahedrite and galena (Figure 6.5c,f). In the magnetite-rich pods, chalcopyrite (Cpy2) occurs as inclusions (<100 μm in width) in pyrite veinlets, along the cataclastic texture of pyrite, as well as overgrowths on pyrite (Figure 6.6b,c).

6.3.3. Sphalerite and tetrahedrite - Mode of occurrence

Sphalerite (Sph1) in the polymetallic quartz veins occurs as subhedral to euhedral inclusions (<400 μm in width), replaced by chalcocite along cracks and cemented by chalcopyrite or tetrahedrite (Figure 6.3a,b). It also appears as rounded inclusions (<200 μm in width) in pyrite (Figure 6.5a).

In the polymetallic quartz veins, tetrahedrite (Ttr1) abundance follows chalcopyrite. It occurs in bands cementing sphalerite grains (Figure 6.3b). Massive tetrahedrite is fragmented and is replaced by chalcocite along cracks (Figure 6.3b). Tetrahedrite forms rounded inclusions (<200 μm) in pyrite, locally along with chalcopyrite and galena (Figure 6.3c, 6.5b,c).

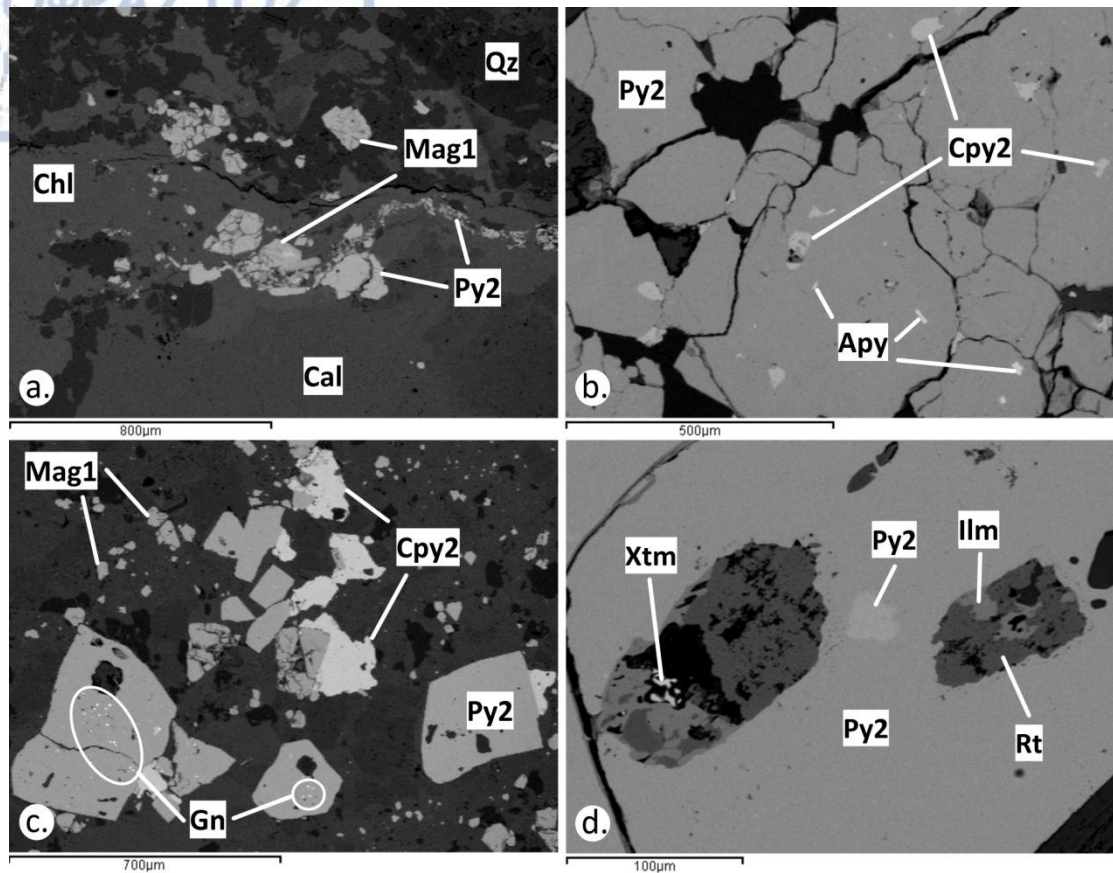


Figure 6.6. SEM back-scattered electron images of pyrite and chalcopyrite from the pods. a. Pyrite (Py2) as grains and in deformed aggregates in a calcite-chlorite-quartz matrix. Magnetite (Mag1) is also found. b. Pyrite (Py2) exhibiting cataclastic texture hosting chalcopyrite (Cpy2) and arsenopyrite (Apy) inclusions. c. Euhedral pyrite (Py2) grains with galena inclusions (white cycles), chalcopyrite (Cpy2) as overgrowths, and fine grained magnetite (Mag1). d. Rutile (Rt)-ilmenite (Ilm) intergrowths hosting xenotime (Xtm) in pyrite (Py2).

6.3.4. Magnetite - Mode of occurrence

Magnetite (Mag1) is widespread in the pods (Figure 6.3d,e). It occurs as subhedral to euhedral grains (<500 μm in width) with cataclastic textures, and as fine-grained disseminations (<200 μm in width) in the calcite-chlorite-quartz matrix (Figure 6.6a,c, 6.7a). The large euhedral grains locally contain ilmenite and chalcopyrite (Cpy2) inclusions (<20 μm in width, Figure 6.7b). The fine-grained disseminations are optically homogeneous, without any silicate or sulfide inclusions.

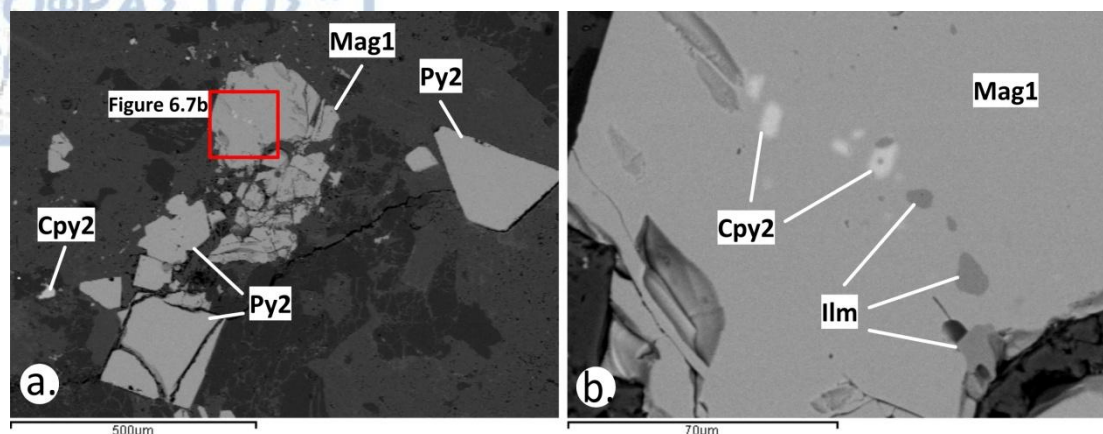


Figure 6.7. SEM back-scattered electron images of magnetite from the pods. a. Euhedral magnetite (Mag1) and pyrite (Py2) with cataclastic textures. b. Chalcopyrite (Cpy2) and ilmenite (Ilm) inclusions in magnetite (Mag1).

6.3.5. Critical and rare metals in pyrite and chalcopyrite (LA-ICP-MS)

Pyrite (Py1) in the polymetallic quartz veins exhibits weaker enrichment in critical and rare metals in respect to pyrite (Py2) hosted in the pods (Table 6.3, Figure 6.8a). The complete analytical dataset for pyrite is given in Supplement 2 (Table S3-6).

Table 6.3. LA-ICP-MS analyses of pyrite from the polymetallic quartz veins and the pods at Laodikino. For the full dataset, see Supplement 2, Tables S3-6.

Host rock	Two-mica gneiss and schist				Biotite gneiss			
Alteration	Sericitization				Chloritization			
Mineralization style	Py1, Polymetallic quartz veins (n = 10)				Py2, Magnetite-rich pods (n = 24)			
Element	MIN	MAX	ST DEV	AVG	MIN	MAX	ST DEV	AVG
ppm								
Ag	b.d.l.	b.d.l.	n.a.	n.a.	0.47	30	7.5	4.6
As	76	593	190	307	11	41,077	10,458	6,545
Au	b.d.l.	b.d.l.	n.a.	n.a.	0.52	21	8	9.0
Bi	b.d.l.	b.d.l.	n.a.	n.a.	0.37	3.5	1	1.2
Co	0.53	4,030	1,505	734	5.2	2,493	532	306
Cr	b.d.l.	b.d.l.	n.a.	n.a.	b.d.l.	b.d.l.	n.a.	n.a.
Cu	1.7	8.1	4.5	4.9	1.8	27	9	9
Hg	b.d.l.	b.d.l.	n.a.	n.a.	b.d.l.	b.d.l.	n.a.	n.a.
In	b.d.l.	b.d.l.	n.a.	n.a.	1.2	17	8	7.5
Mn	2.9	5.6	0.77	4.5	4.1	25	5.3	7.3
Mo	2.2	2.2	n.a.	2.2	b.d.l.	b.d.l.	n.a.	n.a.
Ni	31	464	147	202	4	1,000	223	145
Pb	0.21	0.57	0.18	0.39	0.72	4.8	1.5	2
Sb	0.56	1.8	0.62	1.1	0.59	29	12	16
Se	9.3	35	7.1	19	5.3	126	37	45
Sn	b.d.l.	b.d.l.	n.a.	n.a.	1	9.3	5.8	5.2
Te	b.d.l.	b.d.l.	n.a.	n.a.	4	4.6	0.46	4.3
Ti	11	20	2.7	16	9.1	25	4.4	14
Tl	b.d.l.	b.d.l.	n.a.	n.a.	0.25	3.4	2.2	1.8
V	0.27	0.27	n.a.	0.27	b.d.l.	b.d.l.	n.a.	n.a.
W	b.d.l.	b.d.l.	n.a.	n.a.	3.9	3.9	n.a.	3.9
Zn	b.d.l.	b.d.l.	n.a.	n.a.	4.5	4.5	n.a.	4.5

Abbreviations: AVG = average value, b.d.l. = below detection limit, MIN = minimum value, MAX = maximum value, n = number of analyses, n.a. = not analyzed, STDEV = standard deviation.

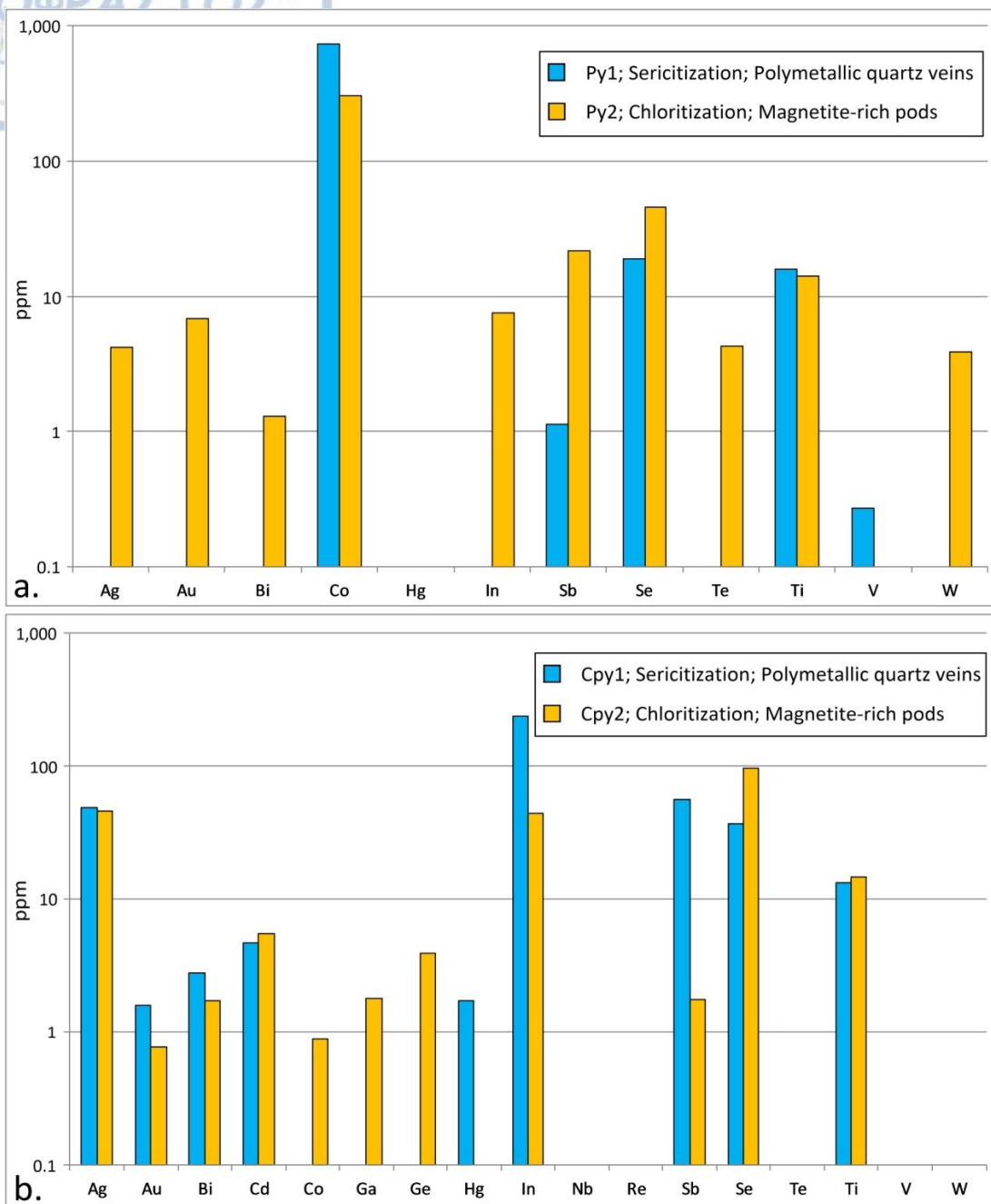


Figure 6.8. Average values of critical and rare metals concentrations of pyrite (a) and chalcopyrite (b) from the polymetallic quartz veins and the magnetite-rich pods. Local enrichments related to nano-scale mineral inclusions are excluded.

In Py1, base metals (As, Cu, Mn, Mo, Ni, Pb) and a restricted number of critical and rare metals (Co, Sb, Se, Ti, V) were measured (Table 6.3). Co (<4,030 ppm) is the most enriched trace element and is followed by Se (<35 ppm), Ti (<20 ppm), Sb (<1.8 ppm) and V (<0.27 ppm) (Table 6.3, Figure 6.8a). Pyrite (Py2), is characterized by slightly more enriched profiles in base (As, Cu, Mn, Ni, Pb, Sn), critical and rare metals (Table 6.3, Figure 6.8a). Critical and rare metals include Co (<2,493 ppm), Se

(<126 ppm), Ag (<30 ppm), Sb (<29 ppm), Ti (<25 ppm), Au (<21 ppm), In (<17 ppm), Te (<4.6 ppm), W (<3.9 ppm) and Bi (<3.5 ppm) (Table 6.3, Figure 6.8a).

Trace elements related to nano-scale mineral inclusions were not measured in Py1. In Py2, base metals related to nano-scale mineral inclusions include Cu (<7,943 ppm), Pb (<190 ppm), Sn (<0.78 ppm) and Zn (<1,747 ppm) (Supplement 2: Table S3-6). Critical and rare metals related to nano-scale mineral inclusions comprise: Sb (<293 ppm), Bi (<173 ppm), Ag (<13 ppm) and In (<7 ppm) (Supplement 2: Table S3-6).

Chalcopyrite (Cpy1) from the polymetallic quartz veins includes weaker enrichments in trace elements than Cpy2 from the magnetite-rich pods (Table 6.4, Figure 6.8b). The more enriched base metals include Pb, Sn and Zn (Table 6.4). Rare metals include Ag (<51 ppm), Au (<0.77 ppm), Bi (<3.6 ppm), Cd (<6.1 ppm), Co (<0.89 ppm), Ga (<1.8 ppm), Ge (<3.9 ppm), In (<51 ppm), Sb (<1.8 ppm), Se (<109 ppm) and Ti (<22 ppm) (Table 6.4, Figure 6.8b).

Table 6.4. LA-ICP-MS analyses of chalcopyrite from the polymetallic quartz veins and the pods at Laodikino. Advise also Supplement 2, Table S3-7.

Host rock	Two-mica gneiss and schist				Biotite gneiss			
Alteration	Sericitization				Chloritization			
Mineralization style	Cpy1, Polymetallic quartz veins (<i>n</i> = 10)				Cpy2, Magnetite-rich pods (<i>n</i> = 5)			
Element	MIN	MAX	ST DEV	AVG	MIN	MAX	ST DEV	AVG
ppm								
Ag	8.6	243	73	49	40	51	4.6	46
As	6.8	10	1.4	8.8	b.d.l.	b.d.l.	n.a.	n.a.
Au	0.78	2.9	0.9	1.6	0.77	0.77	n.a.	0.77
Bi	0.45	7.6	2.2	2.8	0.40	3.6	1.3	1.7
Cd	3.7	5.3	0.71	4.7	5	6.1	0.78	5.5
Co	b.d.l.	b.d.l.	n.a.	n.a.	0.89	0.89	n.a.	0.89
Cr	b.d.l.	b.d.l.	n.a.	n.a.	b.d.l.	b.d.l.	n.a.	n.a.
Ga	b.d.l.	b.d.l.	n.a.	n.a.	1.8	1.8	n.a.	1.8
Ge	b.d.l.	b.d.l.	n.a.	n.a.	3.9	3.9	n.a.	3.9
Hg	0.43	4.8	1.4	1.7	b.d.l.	b.d.l.	n.a.	n.a.
In	191	277	31	238	41	51	4	44
Mn	2.3	5.9	1.2	3.6	3.4	3.4	n.a.	3.4
Mo	b.d.l.	b.d.l.	n.a.	n.a.	b.d.l.	b.d.l.	n.a.	n.a.
Ni	5	5	n.a.	5	8	8	n.a.	8
Pb	7	68	27	30	0.83	35	15	8.6
Sb	8.8	76	27	56	1.8	1.8	n.a.	1.8
Se	19	45	8	37	90	109	7.7	96
Sn	51	62	2.9	55	36	48	5.7	43
Te	b.d.l.	b.d.l.	n.a.	n.a.	b.d.l.	b.d.l.	n.a.	n.a.
Ti	10	18	2.5	13	11	22	5.9	15
Tl	0.65	1.9	0.68	1.1	b.d.l.	b.d.l.	n.a.	n.a.
V	b.d.l.	b.d.l.	n.a.	n.a.	b.d.l.	b.d.l.	n.a.	n.a.
W	b.d.l.	b.d.l.	n.a.	n.a.	b.d.l.	b.d.l.	n.a.	n.a.
Zn	152	284	43	224	41	95	20	61
Cd:Zn	0.02	0.02	n.a.	0.02	n.a.	n.a.	n.a.	n.a.

Abbreviations: AVG = average value, b.d.l. = below detection limit, MIN = minimum value, MAX = maximum value, n = number of analyses, STDEV = standard deviation.

Trace elements in Cpy1 include the base metals As, Ni, Pb, Sn and Zn, and several rare metals (Table 6.4). The most enriched rare metal is In (<277 ppm), and it is

followed by Ag (<243 ppm), Sb (<76 ppm), Se (<45 ppm), Ti (<18 ppm), Bi (<7.6 ppm), Cd (<5.3 ppm) and Au (<2.9 ppm) (Table 6.4, Figure 6.8b).

Nano-scale mineral inclusions in chalcopyrite (Cpy1) are associated mainly with Pb and Sb. Pb attributed to mineral inclusions reach 492 ppm, while Sb is up to 469 ppm (Supplement 2: Table S3-7). Arsenic (<168 ppm) and Zn (<77 ppm) were also measured and are attributed to nano-inclusions (Supplement 2: Table S3-7). In Cpy2, concentrations of base and critical metals related to nano-scale mineral inclusions were not measured.

6.3.6. Critical and rare metals in sphalerite and tetrahedrite (LA-ICP-MS)

Sphalerite (Sph1) and tetrahedrite (Ttr1) from the polymetallic quartz veins are characterized by moderate enrichments in trace elements, including base, critical and rare metals (Table 6.5, Figure 6.9a,b). The complete analytical datasets for sphalerite and tetrahedrite are given in Supplement 2 (Table S3-8,9).

Table 6.5. LA-ICP-MS analyses of sphalerite and tetrahedrite from the polymetallic quartz veins at Laodikino. Advise also Supplement 2, Table S3-8,9.

Mineral	Sphalerite				Tetrahedrite			
Host rock	Two-mica gneiss and schist							
Alteration	Sericitization							
Mineralization style	Sph1, Polymetallic quartz veins (<i>n</i> = 10)				Ttr1, Polymetallic quartz veins (<i>n</i> = 10)			
Element	MIN	MAX	STDEV	AVG	MIN	MAX	STDEV	AVG
ppm								
Ag	0.84	54	23	13	5,649	7,185	495	6,239
As	6	9.2	2.2	7.6	28,968	41,510	3,979	34,721
Au	b.d.l.	b.d.l.	n.a.	n.a.	0.55	0.83	0.19	0.69
Bi	b.d.l.	b.d.l.	n.a.	n.a.	222	320	39	267
Cd	2,198	2,676	182	2,429	443	669	74	512
Co	0.46	0.88	0.23	0.61	0.29	0.79	0.25	0.51
Cr	b.d.l.	b.d.l.	n.a.	n.a.	b.d.l.	b.d.l.	-	-
Ga	b.d.l.	b.d.l.	n.a.	n.a.	0.59	0.73	0.1	0.66
Ge	1.7	1.7	n.a.	1.7	2	3.3	0.53	2.5
Hg	99	182	25	152	54	98	12	72
In	289	630	141	416	14	18	1.3	16
Mn	217	393	48	271	21	45	10	34
Mo	b.d.l.	b.d.l.	n.a.	n.a.	b.d.l.	b.d.l.	-	-
Ni	1.63	1.63	n.a.	1.63	2.6	2.6	-	2.6
Pb	3	6	2.1	4.5	1.3	121	39	27
Sb	0.49	30	16	12	234,400	277,613	14,411	255,615
Se	9.3	56	14	30	84	109	7.5	97
Sn	0.34	0.84	0.35	0.59	0.69	0.78	0.06	0.73
Te	b.d.l.	b.d.l.	n.a.	n.a.	b.d.l.	b.d.l.	-	-
Ti	3.4	8.8	1.9	6	5.1	13	2.7	7.7
Tl	b.d.l.	b.d.l.	n.a.	n.a.	0.25	0.52	0.12	0.35
V	0.49	0.49	n.a.	0.49	0.27	0.27	-	0.27
W	b.d.l.	b.d.l.	n.a.	n.a.	b.d.l.	b.d.l.	-	-
Zn	640,400	645,500	2,464	643,970	49,924	63,501	4,400	57,164
Cd:Zn	0.003	0.004	0.001	0.0035	n.a.	n.a.	n.a.	n.a.

Abbreviations: AVG = average value, b.d.l. = below detection limit, MIN = minimum value, MAX = maximum value, n = number of analyses, STDEV = standard deviation.

Trace elements in sphalerite (Sph1) include the base metals As, Cu, Fe, Mn, Ni and Sn (Table 6.5, Supplement 2: Table S3-8). Cd is the most enriched rare metal in Sph1 reaching 2,676 ppm, and is followed by In (<630 ppm), Hg (<182 ppm), Se (<56 ppm), Ag (<54 ppm), Sb (<30 ppm), Ti (<8.8 ppm), Ge (<1.7 ppm), Co (<0.88 ppm) and V (<0.49 ppm) (Table 6.5, Figure 6.9a).

Tetrahedrite (Ttr1) from the polymetallic quartz veins contains varying concentrations of base metals including As, Cu, Fe, Mn, Ni, Pb, Sn and Zn (Table 6.5, Supplement 2: Table S3-9). Critical and rare metals in Ttr1 comprise Sb (<277,613 ppm), Ag (<7,185 ppm), Cd (<669 ppm), Bi (<320 ppm), Se (<109 ppm), Hg (<98 ppm), In (<18 ppm), Ti (<13 ppm), Ge (<3.3 ppm), Au (<0.83 ppm), Co (<0.79 ppm), Ga (<0.73 ppm) and V (<0.27 ppm) (Table 6.5, Figure 6.9b).

Nano-scale mineral inclusions in sphalerite (Sph1) are related to Cu (<29,474 ppm), Pb (<6,678 ppm) and As (<1,605 ppm), as well as to critical and rare metals including Sb (<1,369 ppm), Ag (<814 ppm) and Bi (<3.3 ppm) (Supplement 2: Table S3-8). In tetrahedrite (Ttr1), concentrations of trace elements related to nano-scale mineral inclusions were not detected.

6.3.7. Critical and rare metals in magnetite (LA-ICP-MS)

Magnetite (Mag1) hosts several base metals and a limited number of critical and rare metals. The full analytical dataset is given in Supplement 2 (Table S3-10). Base metals in Mag1 include Cr, Cu, Mn, Mo, Ni, Pb and Zn (Table 6.6, Supplement 2: Table S3-10). The most enriched rare metal is V (<586 ppm), followed by Ti (<303 ppm), Ga (<14 ppm), Ge (<5.2 ppm), Co (<3.1 ppm), Ce (<0.52 ppm), Th (<0.19 ppm) and La (<0.12 ppm) (Table 6.6, Figure 6.10). Trace elements concentrations related to nanoparticles were not detected in magnetite (Mag1).

6.3.8. Statistical analysis of trace elements concentrations

Pearson product-moment correlation coefficients for pyrite, chalcopyrite, sphalerite, tetrahedrite and magnetite were calculated for Laodikino. Based on data reduction and ablation patterns, trace element concentrations related to nano-scale mineral inclusions or nanoparticles were excluded before the statistical analyses. In pyrite, correlation coefficients are characterized by significant positive correlations ($p < 0.01$, value > 0.549) defined for the elemental pairs Ag-In and Bi-Se (Supplement 3: Table S4-10). Negative correlations were not obtained.

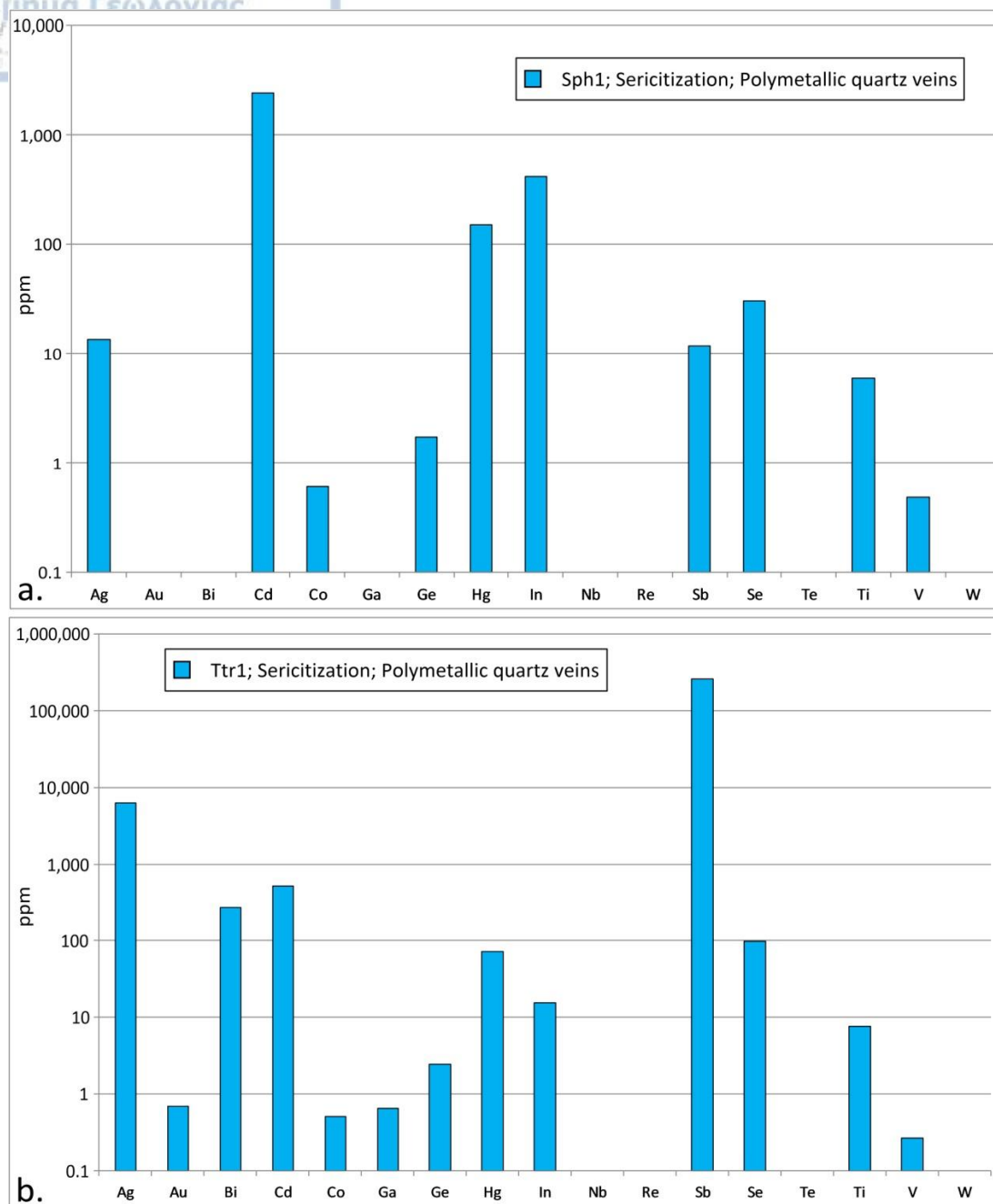


Figure 6.9. Average values of critical and rare metals concentrations of sphalerite (a) and tetrahedrite (b) from the polymetallic quartz veins. Local enrichments related to nano-scale mineral inclusions are excluded.

Chalcopyrite is characterized by significant positive correlations ($p < 0.01$, value > 0.839) for the elemental pair Au-Hg, and by positive correlations ($p < 0.05$, value > 0.609) for the elemental pairs Au-In and Hg-In (Supplement 3: Table S4-11). Significant negative correlations were defined for the elemental pairs Co-Ga and In-

Se ($p < 0.01$, value > -0.945), while negative correlation ($p < 0.05$, value > -0.578) was determined for the elemental pair Au-Se (Supplement 3: Table S4-11).

Table 6.6. LA-ICP-MS analyses of magnetite from the magnetite-rich pods at Laodikino. For the full dataset, see Supplement 2, Tables S3-5.

Host rock	Biotite gneiss									
Alteration	Chloritization									
Mineralization style	Mag1, Magnetite-rich pods ($n = 10$)									
Element	MIN	MAX	STDEV	AVG	Element	MIN	MAX	STDEV	AVG	
ppm					ppm					
Ag	b.d.l.	b.d.l.	n.a.	n.a.	Nd	b.d.l.	b.d.l.	n.a.	n.a.	
Al	123	1,176	305	333	Ni	31	92	21	62	
As	b.d.l.	b.d.l.	n.a.	n.a.	P	46	46	n.a.	46	
Au	b.d.l.	b.d.l.	n.a.	n.a.	Pb	0.96	5.1	2.2	2.7	
Bi	b.d.l.	b.d.l.	n.a.	n.a.	Re	b.d.l.	b.d.l.	n.a.	n.a.	
Cd	b.d.l.	b.d.l.	n.a.	n.a.	Sb	b.d.l.	b.d.l.	n.a.	n.a.	
Ce	0.15	0.52	0.26	0.34	Se	b.d.l.	b.d.l.	n.a.	n.a.	
Co	1.7	3.1	0.50	2.3	Sm	b.d.l.	b.d.l.	n.a.	n.a.	
Cr	46	208	114	127	Sn	b.d.l.	b.d.l.	n.a.	n.a.	
Cu	52	54	1.6	53	Te	b.d.l.	b.d.l.	n.a.	n.a.	
Ga	6.5	14	2.2	10	Ti	135	303	51	183	
Gd	b.d.l.	b.d.l.	n.a.	n.a.	Th	0.19	0.19	n.a.	0.19	
Ge	5.2	5.2	n.a.	5.2	Tl	0.63	0.63	n.a.	0.63	
In	b.d.l.	b.d.l.	n.a.	n.a.	U	b.d.l.	b.d.l.	n.a.	n.a.	
La	0.12	0.12	n.a.	0.12	V	424	586	65	497	
Mn	546	977	158	741	W	b.d.l.	b.d.l.	n.a.	n.a.	
Mo	2.9	2.9	n.a.	2.9	Zn	25	59	10	41	
Nb	b.d.l.	b.d.l.	n.a.	n.a.						

Abbreviations: AVG = average value, b.d.l. = below detection limit, MIN = minimum value, MAX = maximum value, n = number of analyses, STDEV = standard deviation.

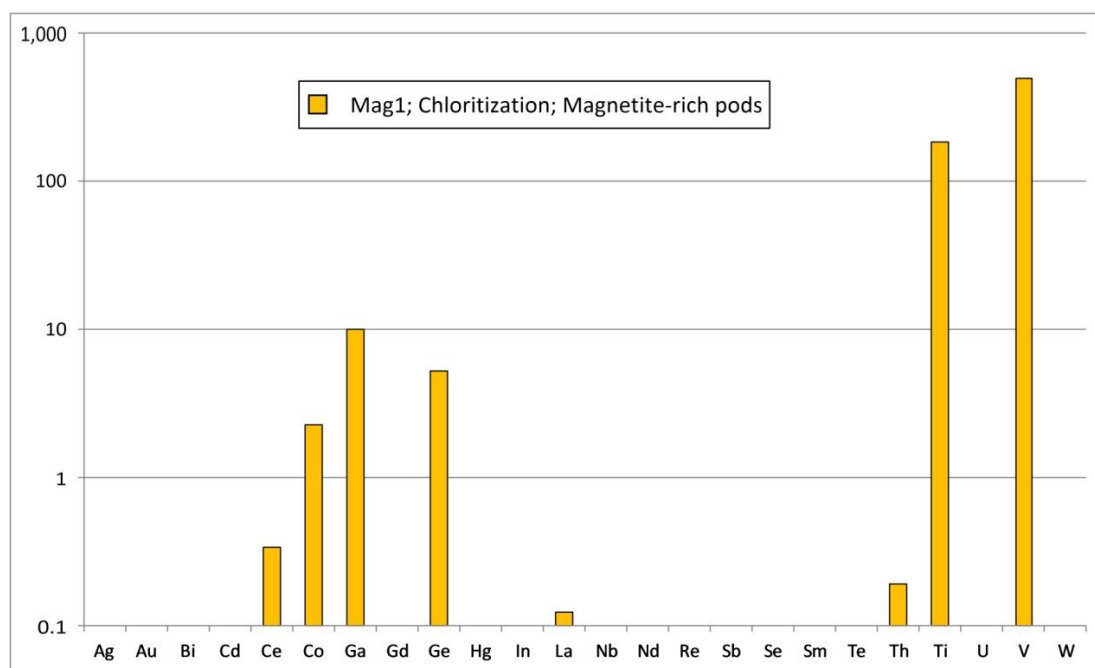


Figure 6.10. Average values of critical and rare metals concentrations of magnetite from the magnetite-rich pods.

Pearson product-moment correlation coefficients for sphalerite, revealed significant positive correlations ($p < 0.01$, value > 0.827) for the elemental pairs Ag-

Sb, Ag-V, Cd-In, Cd-Se and Sb-V (Supplement 3: Table S4-12). Positive correlations ($p < 0.05$, value > 0.638) were determined for the pairs Bi-Te, Cd-Hg, Cd-Ti, In-Se and In-Ti (Supplement 3: Table S4-12). Significant negative correlations ($p < 0.01$, value = -0.918), are ascribed to the elemental pair Ga-Te. Additionally, negative correlations ($p < 0.05$, value > -0.692) are related to the pairs Bi-Ga, Bi-Nb, Nb-Te and Te-W (Supplement 3: Table S4-12).

Significant positive correlations ($p < 0.01$, value > 0.769) in tetrahedrite were detected for the pairs Bi-Hg, Cd-Ga, Cd-In, Cd-Sb, Ga-Hg, Ga-In and In-Sb (Supplement 3: Table S4-13). Furthermore, positive correlations ($p < 0.05$, value > 0.644) were obtained for the elemental pairs Ag-In, Ag-Sb, Bi-Cd, Bi-Ga and Cd-Hg (Supplement 3: Table S4-13). Significant negative correlations ($p < 0.01$, value > -0.797) include the elemental pair Au-V and Bi-Co, while negative correlations ($p < 0.05$, value > -0.723) are defined for the pairs Co-Hg and Hg-Ti (Supplement 3: Table S4-13). Pearson product-moment correlation coefficients for magnetite were only defined for the elemental pair La-Th (significant positive correlations: $p < 0.01$, value = 1.000, Supplement 3: Table S4-14).

6.4. Discussion

Five mineralization styles occur at Laodikino (Table 6.1). Although geochronological data are missing, the interpretation of structural data could suggest that two mineralization styles are of pre-Cenozoic age, and 3 were formed during Cenozoic. Thus, it is suggested here that the massive and banded (stratiform-like) mineralization is of middle to late Triassic, the magnetite-rich pods are of pre-Cenozoic to early Cenozoic age, whereas the polymetallic massive and quartz veins, and the disseminations and aggregates in hydrothermal halos are of Cenozoic age (Kougoulis et al. 1990, Thymiatis 1995, this study, Table 6.1).

The massive and banded (stratiform-like) mineralization hosted in quartz and calcite schists shares similar textural characteristics with the barite mineralization described by Kougoulis et al. (1990). In addition, the alteration assemblage comprises barite, witherite, as well as chlorite, quartz and calcite (Table 6.1). It is suggested that both mineralizations are genetically associated and that are products of fumarolic activity related to submarine volcanism (VMS-style mineralization) (Kougoulis et al. 1990, Thymiatis 1995). This volcanism is characterized by island-arc mafic affinities and is ascribed to the rifting of the SMM during middle to late Triassic (Kougoulis et

al. 1990, Asvesta 1992). Thymiatis (1995) determined that the massive and banded (stratiform-like) mineralization equilibrated in temperatures below 400 °C.

The mineralized pods found in biotite gneiss are enriched in magnetite, followed by pyrite, chalcopyrite, rutile, ilmenite, and traces of galena, arsenopyrite, xenotime and bastnäsite (Table 6.1). Bulk geochemical analyses showed values close to those of the background hydrothermally altered and oxidized metamorphic rocks (Table 6.2, Figure 6.4).

The textural and mineralogical observations suggest that magnetite (Mag1) was formed first in the pods. It is subhedral to euhedral, forms aggregates with cataclastic texture, and overall is free of inclusions. These characteristics, coupled with the depleted (<1,000 ppm in average, Figure 6.5) geochemical profile in Al, Cr, Ti and V, could suggest that magnetite is metamorphic in origin (after Deditious et al. 2018). The biotite gneiss could be the source of iron, while the restricted and minor ilmenite and chalcopyrite inclusions (<20 µm in width) in magnetite could indicate recrystallization. Furthermore, the fine-grained, subhedral to euhedral magnetite (<200 µm in width) set in the calcite-chlorite-quartz matrix, exhibiting no inclusions or pressure shadows, support that its formation was not followed by any kinematic process related to the deformation of the biotite gneiss.

Textural characteristics for pyrite (Py2) suggest that it was formed after magnetite, and was subjected to recrystallization during regional metamorphism (Figure 6.3d,e, 6.6a-c). Recrystallization is related to the growth of euhedral pyrite crystals and of aggregates of euhedral pyrite forming porphyroblasts (Figure 6.2b). Mineral inclusions found in pyrite vary between grains, while are absent from the fine pyrite grains (Figure 6.6c). Euhedral magnetite, and prismatic rutile-ilmenite and arsenopyrite inclusions may be related to pyrite recrystallization and overgrowth (Figure 6.6b,d). Galena inclusions occurring in the central parts of the pyrite grains may be related to pyrite recrystallization and expulsion of lead (Figure 6.6c). Chalcopyrite (Cpy2) is not related to mineral inclusions and forms overgrowths on pyrite, suggesting that it was deposited after magnetite (Mag1) and pyrite (Py2) (Figure 6.3f, 6.6b,c).

Both pyrite (Py2) and chalcopyrite (Cpy2) host critical and rare metals (Tables 6.3, 6.4, Figure 6.8a,b). During pyrite recrystallization under amphibolite or greenschist facies metamorphism, the structurally compatible As, Co, Ni, Sb, Se and Tl, are not expelled from pyrite structure due to its refractory character (Conn et al.

2019). Expulsion of structurally compatible Ag, Au, Bi, Cu, Mo and Pb, as well as exsolution of mineral inclusions has been described for recrystallized pyrite resulting in the formation of sulfides, sulfosalts and native gold (George et al. 2018, Conn et al. 2019). This remobilization is restricted in space and usually does not exceeds few meters in length with the new minerals being deposited along pyrite boundaries, in fractures and rock interstices, as well as in veins (Marshall et al. 2000, Conn et al. 2019). In Py2, copper contents are depleted (9 ppm in average), while Ag, In and Se are more enriched in Cpy2. Thus, a restricted Cu remobilization during metamorphism could be associated with chalcopyrite precipitation in the magnetite-rich pods. Nevertheless, the deposition mechanism of chalcopyrite needs further investigation.

The rutile-ilmenite intergrowths are commonly related to replacement of rutile by ilmenite under acid-leaching and low temperatures approximately at 150 °C (Janssen et al. 2010). In addition, the replacement of Nb-rutile by ilmenite is related to Nb and REE(Y) exsolutions in Ditrau alkaline intrusive complex (Hirtopanu et al. 2014). In the magnetite-rich pods, the rutile-ilmenite intergrowths are found in pyrite, they have eroded rims and host xenotime (Figure 6.6d). In their periphery bastnäsite is found. Xenotime (YPO_4) and bastnäsite ($(\text{La}, \text{Ce}, \text{Y})\text{CO}_3\text{F}$) are major carriers of REE, while xenotime may also host Th and U (Kositcin et al. 2003, Berger et al. 2008). The enrichments in Ce, Gd, La, Nd and Sm measured in bulk samples from the magnetite-rich pods should be ascribed to xenotime and bastnäsite occurrence (Figure 6.4, Supplement 4: Table S1-3). A preliminary examination by means of SEM-EDS highlighted the absence of Nb and REE(Y) in rutile. Although, as the chemical composition of rutile needs further investigation by means of LA-ICP-MS, the formation of bastnäsite during hydrothermal alteration of rutile could not be excluded. In xenotime, dysprosium was the only REE detected. Thus, following suggestions made by Kositcin et al. (2003) the diagenetic origin of xenotime could be supported.

The hydrothermal polymetallic mineralization was formed in the two-mica gneiss, the chlorite-muscovite schists and in quartz veins in the Profitis, Lipsidri and Laodikino-Fanari areas (Thymiatis 1995, Voudouris et al. 2007). The mineralization is shear-zone related and includes polymetallic massive (~ 4 m in width) and quartz (<1 m in width) veins showing comb and brecciated textures, reaching 200 m in depth and developing minor hydrothermal halos (Thymiatis 1995).

Structurally the polymetallic massive and quartz veins share characteristics reflecting the imprint of the regional tectonics to the mineralization formation. In addition, regional metamorphism also affected the polymetallic massive veins. Thymiatis (1995), applying sphalerite and arsenopyrite geobarometry suggested that the polymetallic massive veins equilibrated in retrograde greenschist facies, at temperatures between 350 and 450 °C and at pressures ranging between 4.5 and 7.5 kbar. According to Kiliyas et al. (1999), the retrograde greenschist facies of the SMM developed between Eocene and early Oligocene. This metamorphic event is concurrent with the Eocene ductile deformation of the SMM, which was succeeded during early Oligocene by brittle deformation (Kiliyas et al. 1999).

The NW-trending faults correspond to the older brittle structures related to the fracturing of Vertiskos Unit (early Oligocene, Kiliyas et al. 1999). They are suggested as the kinematic link between ductile shearing (lower crust) and brittle faulting (upper crust) (Kiliyas et al. 1999), and probably it could have also favored the emplacement of the massive polymetallic veins. The conjugate NE-SW-trending normal to oblique and the N-S-trending strike-slip faults were developed during Oligocene-Miocene and enhanced fluid circulation (Kiliyas et al. 1999). The polymetallic quartz veins, exhibiting steeper angles than the polymetallic massive veins, may be related to the later stages of brittle faulting resulting in high-angle normal faults (Miocene to Pliocene, Kiliyas et al. 1999).

The polymetallic massive veins exhibit a rich mineral assemblage including base metal sulfides, tellurides (altaite), sulfosalts (tetrahedrite, altaite), electrum and native bismuth. According to Thymiatis (1995) and Voudouris et al. (2007) arsenopyrite and pyrite were first deposited in the polymetallic massive veins, while Cu, Zn and Pb along with Bi, Te and Au were introduced to the system during a later brecciating event.

In the polymetallic quartz veins, tetrahedrite is the only sulfosalt mineral, whereas tellurides and electrum are missing (Table 6.1). Pyrite (Py1) appears in massive bands exhibiting wide cataclastic textures (Figure 6.2a, 6.3a,c), while inclusions (<200 μm in width) of chalcopyrite, galena, tetrahedrite, sphalerite and barite are found in Py1 (Figure 6.3a-c, 6.5a-d,f). The shape and the occurrence of these inclusions could affiliate their presence to replacement of Py1. Most of the replacements include tetrahedrite and galena or exclusively galena (Figure 6.3c, 6.5b). Replacements comprising chalcopyrite-tetrahedrite-galena, chalcopyrite-galena, and exclusively

sphalerite or barite exhibit a more restricted occurrence (Figure 6.5a,c,d,f). In addition, euhedral sphalerite (Sph1) cemented by tetrahedrite (Ttr1) indicates the late deposition of tetrahedrite (Figure 6.3b).

The bulk geochemical analyses of the polymetallic quartz veins revealed enrichments in Ag (<2,433 ppm), followed by Cd (<247 ppm), Hg (<187 ppm), Bi (<83 ppm), Se (<59 ppm), In (<53 ppm) and Au (<3 ppm) (Figure 6.4). Sb abundance (<70,500 ppm or 7.05 wt.%, Table 6.2) is ascribed to tetrahedrite. Furthermore, antimony is significantly correlated with Ag, Cd, Hg, Bi, Se and In (Supplement 3: Table S4-2).

Mineral chemistry showed that tetrahedrite (Ttr1) is a major host of Ag (<7,185 ppm), Bi (<320 ppm), Sb (<277,163 ppm) and Se (<109 ppm), sphalerite (Sph1) accommodates Cd (<2,676 ppm), Hg (<182 ppm) and In (<630 ppm), and chalcopyrite (Cpy1) comprises up to 2.9 ppm Au (Table 6.4, 6.5). Sphalerite is more enriched in Co and In, relatively to Ga, Ge, Hg and Sn, suggesting that it was formed in temperatures ascribed to mesothermal ($T = 300\text{-}200\text{ }^{\circ}\text{C}$, Pohl 2011) rather than to epithermal ($T < 200\text{ }^{\circ}\text{C}$, Pohl 2011) mineralizing stages (after Cook et al. 2009). The Cd:Zn ratio in chalcopyrite is 0.02, while in sphalerite varies from 0.03 to 0.04 (Tables 6.4, 6.5). In addition, Ag, Bi, Cd, Hg, In, Sb and Se exhibit positive correlations in tetrahedrite and sphalerite (Supplement 3: Table S4-12,13). In contrast, pyrite is enriched in Co (<4,030 ppm), bears minor concentrations of Sb (<1.8 ppm) and Se (<35 ppm), and is depleted in Ag, Au, Bi, Hg and In (Table 6.3). Noteworthy is the overall depletion in Te in the analyzed pyrite, chalcopyrite, sphalerite and tetrahedrite from the polymetallic quartz veins (Figure 6.8a,b, 6.9a,b). According to George et al. (2015), galena could host Te in oscillatory and sector compositional zoning and in nano-scale mineral inclusions (e.g. altaite). Although the mineral chemistry of galena was not investigated in this study, the absence of other metallic minerals could ascribe the Te (<0.03 ppm) contents in the polymetallic quartz veins to galena (Table 6.2).

Consequently, following the classification of hydrothermal deposits proposed by Gebre-Mariam et al. (1995) and the suggestions made after Cook et al. (2009) on sphalerite chemistry, the polymetallic quartz veins at Laodikino were formed at epizonal conditions ($T = 150\text{-}300\text{ }^{\circ}\text{C}$, 0.5-1.5 kbar, <6 km depth). Pyrite enveloped by quartz was first deposited by mineralizing fluids enriched in Co and depleted in critical and rare metals (Figure 6.8a). Brittle deformation and pyrite cataclasis

followed introducing mineralizing fluids enriched in Cu, Zn and Pb, as well as in several critical and rare metals including Ag, Au, Bi, Cd, Hg, In, Sb and Se. Cd, Hg and In, were first preferentially precipitated along with Zn to form subhedral to euhedral sphalerite. George et al. (2018) suggested that co-crystallizing chalcopyrite and sphalerite are characterized by typically equal Cd:Zn ratios. The distinct differences in Cd:Zn_{Cpy} and Cd:Zn_{Sph} further support the argument that sphalerite was formed before chalcopyrite. Gold precipitated in massive chalcopyrite, while Ag, Bi and Se became more enriched in the residual mineralizing fluids and precipitated in tetrahedrite. The mineralizing process was terminated with the tetrahedrite and galena deposition.

The occurrence of cobaltite, altaite, pilsenite, electrum and native bismuth in the polymetallic massive veins suggests higher enrichments in Au, Bi, Co and Te for the mineralizing fluids. In contrary, the mineralizing fluids associated with the polymetallic quartz veins were significantly enriched in Ag. The polymetallic mineral assemblages at Laodikino share common characteristics in terms of geochemistry (enrichments in Ag-Au-Bi-Cd-Co-Hg-In-Se-Te), host rocks, and structural control with other Cu-Fe-As-Zn-Pb-Sb intrusion-related deposits located in the SMM (e.g. Stanos, Nea Madytos, Koronouda, Drakontio, Melfos and Voudouris 2017). According to Bristol et al. (2015), the ore mineralization in these ore deposits was formed during shearing at the upper greenschist-lower amphibolite facies metamorphism, appears to be genetically linked to distal or proximal buried intrusions, and to extension-related shear zones. This study suggests that similar conditions occurred also at Laodikino during Cenozoic and probably between Eocene and Miocene.

6.4.1. Mineral chemistry of pyrite and chalcopyrite and nano-scale inclusions

The interpretation of the scanning electron microscopy and laser ablation ICP-MS analyses indicate that specific minerals occur as nano-inclusions in pyrite and chalcopyrite at Laodikino (Figure 6.11a-b). Base metals including As, Cu, Mn, Mo, Ni and Pb are found in both Py1 and Py2 incorporated in crystal lattice. In Py2, base metals are slightly more enriched (Table 6.3). In addition, Py1 is less enriched in critical and rare metals in respect to Py2 (Figure 6.8a). Co Sb, Se, Ti and V, are the critical and rare metals found in Py1 and their distribution patterns suggest that they are incorporated as stoichiometric substitutions (Co, Sb, Se) or as nanoparticles (Ti,

V) in distorted areas of the pyrite lattice. Nano-scale mineral inclusions were not detected in pyrite (Py1). In Py2, Ag, Au, Bi, Co, In, Sb, Se, Te, Ti and W are found (Table 6.3, Figure 6.8a). Base and rare metals related to nano-scale mineral inclusions were detected in Py2. They mostly include Cu, Bi and Pb, and could be related to nano-scale inclusions of chalcopyrite based on the metallic assemblage hosted in the magnetite-rich pods (Figure 6.11a).

Base and rare metals are slightly more enriched in Cpy2 than in Cpy1 (Table 6.4, Figure 6.8b). Base metals include As, Ni, Pb, Sn and Zn in Cpy1 and Pb, Sn and Zn in Cpy2 (Table 6.4). Critical and rare metals comprise Ag, Au, Bi, Cd, In, Sb, Se and Ti for both Cpy1 and Cpy2, while additionally Co, Ga and Ge, are found in Cpy2 (Table 6.4, Figure 6.8b). The time-resolved laser ablation ICP-MS depth profiles for these trace elements suggest that they are lattice bound in chalcopyrite (Figure 6.11b). In Cpy1, arsenic, Pb, Sb and Zn were detected being associated with nano-scale inclusions of galena, tetrahedrite and sphalerite (Supplement 2: Table S3-7, Figure 6.11b). In Figure 6.11b, noteworthy is the spiky pattern of Ag ascribed to the presence of tetrahedrite. Nano-scale mineral inclusions were not detected in Cpy2. The absence of other co-crystallizing sulfide minerals (e.g. galena and/or sphalerite) and of nano-scale inclusions, and the slightly more enriched mineral chemistry of Cpy2 in respect to Cpy1, support the argument made by George et al. (2018) that these conditions increase the amount of lattice bound trace elements in chalcopyrite.

6.4.2. Mineral chemistry of sphalerite and tetrahedrite and nano-scale inclusions

Sphalerite and tetrahedrite at Laodikino accommodate several base metals and are significantly enriched in critical and rare metals (Table 6.5, Figure 6.9a,b). Scanning electron microscopy and LA-ICP-MS analyses indicate that tetrahedrite is found as inclusions in sphalerite. Sphalerite (Sph1) includes the base metals As, Cu, Fe, Mn, Ni and Sn, and the critical and rare metals Ag, Cd, Co, Ge, Hg, In, Se, Sb, Ti and V (Table 6.5, Figure 6.9a). The time-resolved laser ablation ICP-MS depth profiles for these elements suggest that they are hosted in sphalerite as solid solutions (Figure 6.11c). Nevertheless, based on the concentrations of some elements and the laser ablation patterns, several enrichments in Ag, As, Bi, Cu, Pb and Sb are attributed to nano- or micro-scale inclusions of tetrahedrite (Ttr1) (Supplement 2: Table S3-8, Figure 6.11c).

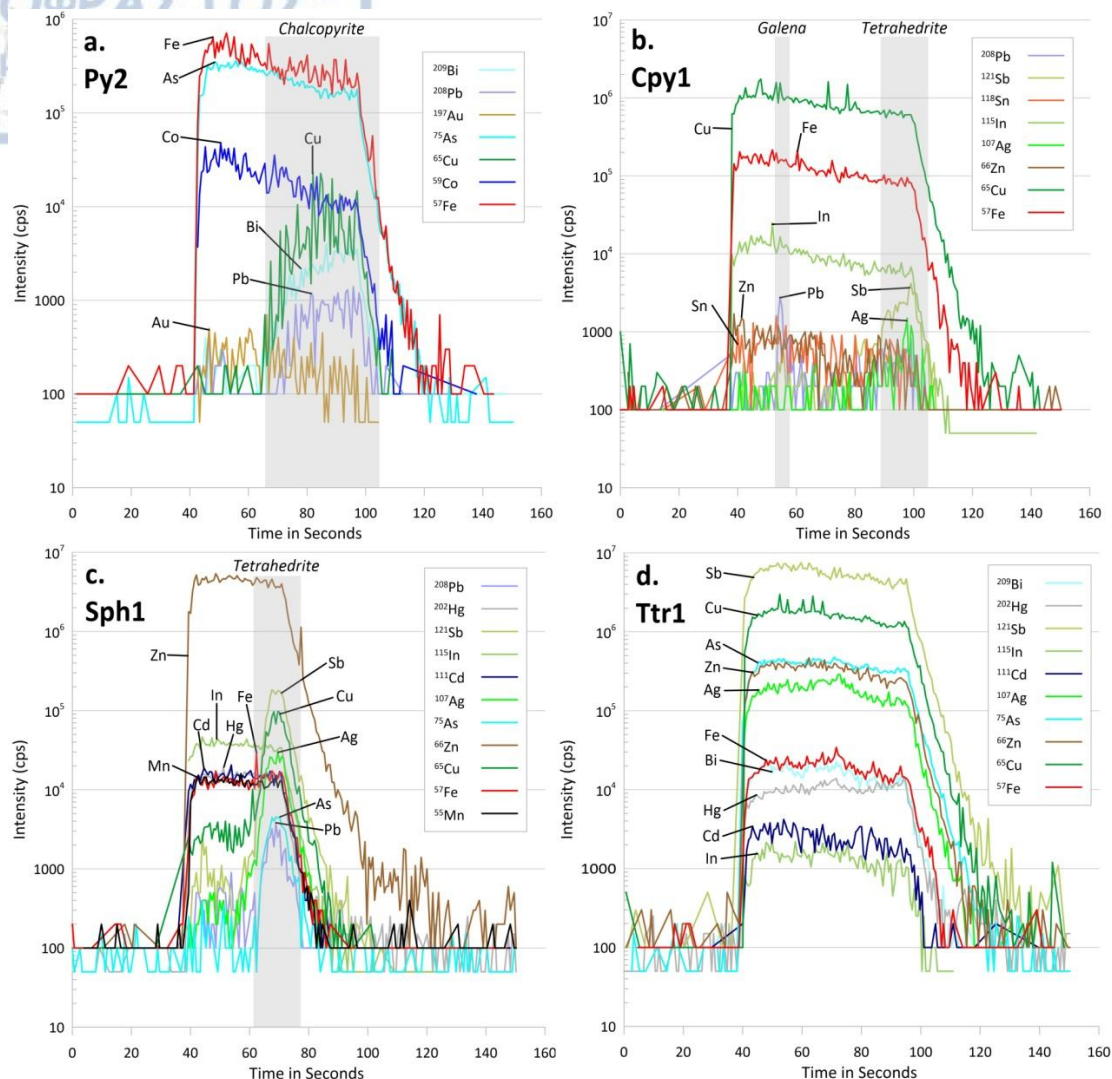
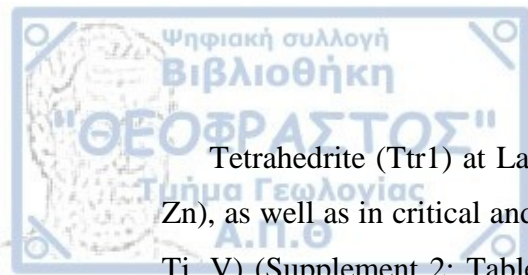


Figure 9.4. Selected time-resolved laser ablation ICP-MS depth profiles of pyrite (Py2), chalcopyrite (Cpy1), sphalerite (Sph1) and tetrahedrite (Ttr1) from the polymetallic quartz veins and the magnetite-rich pods at Laodikino. Associated nano-scale inclusions are highlighted in gray. a. In Py2, the distribution patterns of Fe, As, Co and Au are similar suggesting the incorporation of these elements in crystal lattice. The spiky patterns of Cu, Bi and Pb indicate that nano-scale inclusions of chalcopyrite are hosted in pyrite (Py2). b. In Cpy1, copper, Fe, In, Zn and Sn are incorporated as stoichiometric substitutions, while the spiky patterns for Pb, and for Sb and Ag suggest the occurrence of nano-scale inclusions of galena and tetrahedrite, respectively. c. In Sph1, the distribution patterns of Zn, In, Cd, Hg, Mn and Fe, support that these elements are incorporated as stoichiometric substitutions, whereas Sb, Cu, Ag, As and Pb spiky distributions patterns highlight the presence of tetrahedrite inclusions. d. In Ttr1, the distribution patterns of Sb, Cu, As, Zn, Ag, Fe, Bi, Hg, Cd and In suggest that these elements are accommodated as stoichiometric substitutions and/or as solid solutions.



Tetrahedrite (Ttr1) at Laodikino is enriched in base (As, Cu, Fe, Mn, Ni, Pb, Sn, Zn), as well as in critical and rare metals (Ag, Au, Bi, Cd, Co, Ga, Ge, Hg, In, Sb, Se, Ti, V) (Supplement 2: Table S3-9, Table 6.5, Figure 6.9b). The investigation of the trace elements concentrations and their time-resolved laser ablation ICP-MS depth profiles support that they are hosted in tetrahedrite as stoichiometric substitutions and/or as solid solutions. Solid solutions of the tetrahedrite-tennantite group are quite usually found in tetrahedrite (George et al. 2017). Thus, the series of minor spikes appearing in the time-resolved laser ablation ICP-MS depth profiles, especially for Ag, Bi, Fe and Hg could be related to solid solutions (Figure 6.11d). Nano-scale mineral inclusions were not detected in tetrahedrite (Ttr1).

CHAPTER 7. METAMORPHIC- AND QUARTZ-HOSTED POLYMETALLIC VEIN MINERALIZATION AT KOLCHIKO

7.1. Local geology

Metamorphic rocks at Kolchiko comprise mainly Paleozoic mica-schists and migmatite gneiss, with minor metasandstones and pegmatites of the Vertiskos Unit (Figure 7.1). Locally, amphibolite, eclogite, and chlorite-talc-schist are found as minor lenses or intercalated beds, while Paleozoic serpentinized peridotites and serpentinites occur east of the study area (Kourou 1991). The migmatite gneiss is characterized by leucosomes with parallel arrangement (layered migmatites) or forming boudins. Scarce outcrops of augen-gneiss are found mainly in lower topographies along streams and creeks (Figure 7.1). The migmatite gneiss is intercalated with mica schist and metasandstone (Kourou 1991). The migmatite gneiss and the mica schist (Kolchiko-Analipsi mica-schists after Kourou 1991) are genetically related.

The Triassic Lofiskos granite intrudes the metamorphic rocks north of the study area (Kourou 1991, Figure 2.2). It belongs to the group of the barren Triassic granites (also termed Polydendri group: S-type, syn-collisional granites), which intruded the central part of the Vertiskos Unit (Kourou 1991, Figure 2.2). Lofiskos granite is a large stock trending NW-SE and is also associated to several other minor and satellite stocks, sills and dikes of various sizes.

The pegmatites are subdivided in two groups. The first group is of metamorphic origin and is related with deep crustal retrogression. These pegmatites (<30 cm in width) are rare and are always parallel to the main schistosity of the migmatite gneiss. The second group includes large pegmatitic dikes (<50 m in width), related to the Triassic granites. They are coarse-grained and include euhedral quartz and perthite (<5 cm in length), which is slightly altered to sericite, as well as minor muscovite (Kourou 1991). Both pegmatite groups are barren.

The most recent rocks include dolerite dikes and younger milky quartz-chlorite veins and hydrothermal polymetallic quartz veins. Dolerite consists of hornblende and plagioclase, with traces of magnetite, ilmenite and hematite. It forms dikes (<1 m in width), which are hydrothermally altered (chloritization) with the alteration assemblage comprising chlorite, albite, zoisite, and minor quartz, sericite and calcite.

The doleritic dikes intrude the metamorphic rocks and are only slightly deformed due to the retrograde greenschist facies metamorphism (Kourou 1991).

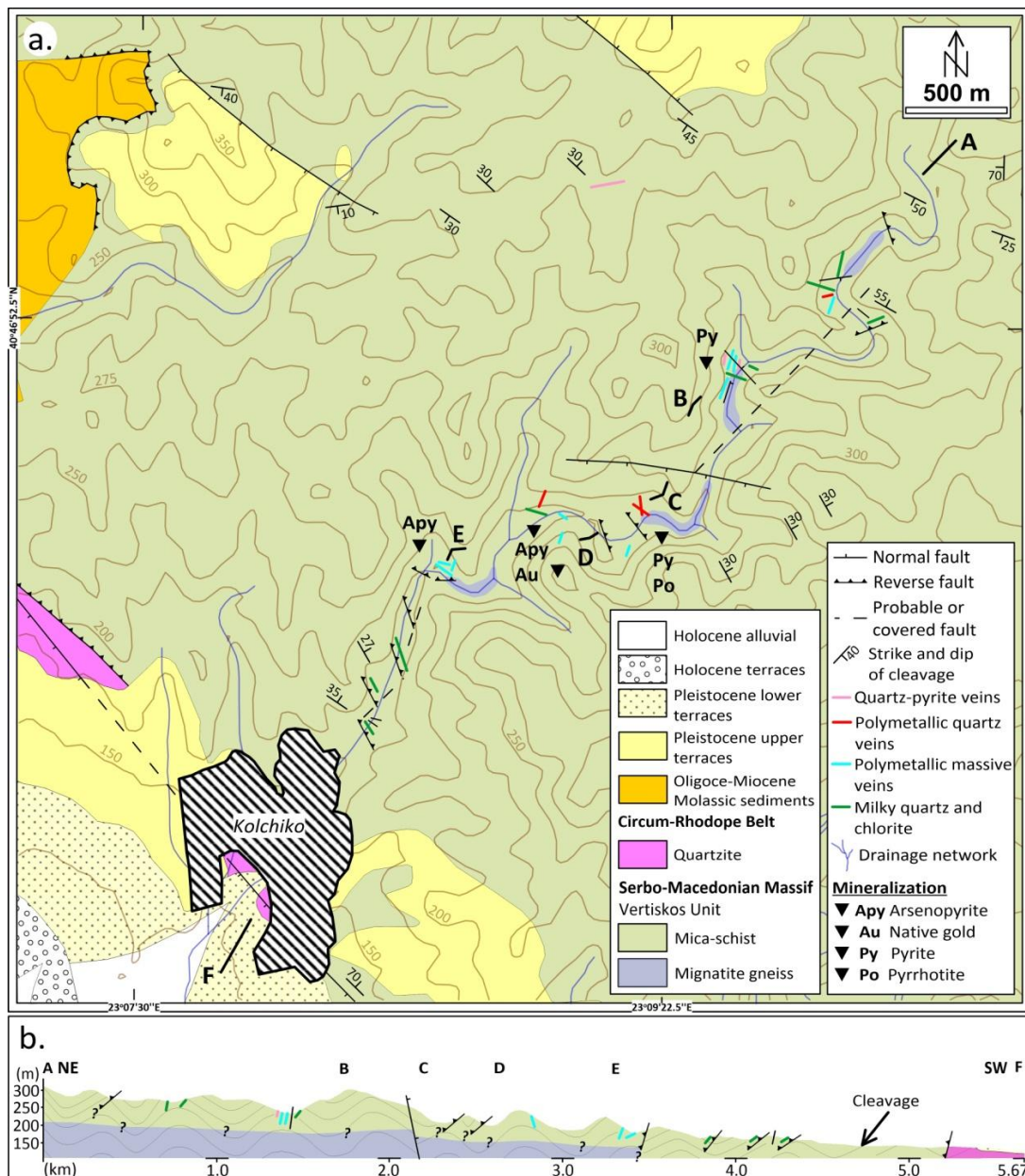


Figure 7.1. a. Geological map of the Kolchiko area, b. Geological cross section traversing the mineralization at Kolchiko (modified after Kockel et al. 1979b).

The milky quartz-chlorite veins (<20 cm in width) have a similar development to those found in the Laodikino area. They crosscut the migmatite gneiss and the mica-schist, and occur along planes of normal faults (N83W/68°NE in average) located in the hanging wall of reverse faults (Figure 7.1). They comprise quartz, plagioclase and minor biotite. Alteration assemblage includes mainly chlorite, with quartz, sericite and

calcite. Quartz is the predominant mineral and locally appears highly brecciated and vuggy. Chlorite is the second most abundant mineral. It occurs in open spaces forming foliated masses. Plagioclase intergrows with quartz and is slightly altered to sericite. Biotite appears in the intergranular space and is altered to chlorite. Sericite and calcite appear in thin veinlets (<300 μm in width) crosscutting the quartz-plagioclase intergrowths and the chlorite masses. Euhedral pyrite (<500 μm in width) is a minor component in these veins. It forms aggregates (<1 cm in width) along with biotite.

Three types of mineralized veins are found at Kolchiko: polymetallic massive veins (<10 cm in width), polymetallic quartz veins (<10 cm in width), and quartz-pyrite veins (<5 cm in width). These veins are of hydrothermal origin and crosscut the mica-schists (Figure 7.1, 7.2a-f). The polymetallic massive veins appear in low angles (N66W/30°NE in average) near the contact between the mica-schist and the migmatite. The polymetallic quartz veins occur in higher angles (N73W/47°NNE in average) in the mica-schist, while the quartz-pyrite veins crosscut the mica-schist in even higher angles (S13W/80°WNW in average). The occurrence of the polymetallic quartz and of the quartz-pyrite veins is associated with a set of conjugate NW- and SW-trending normal faults. All these veins are enveloped in restricted hydrothermal halos containing quartz, sericite and chlorite (sericitization). Locally, the mineralization is oxidized due to supergene processes.

These sets of dikes and veins is associated with the tectono-metamorphic history of the area (Kourou 1991). The metamorphic events at Kolchiko comprise: (1) early and restricted eclogitic event (M1) connected to the formation of eclogite from tholeiitic mafic protoliths, (2) subsequent metamorphism (M2: $T = 650-750\text{ }^{\circ}\text{C}$, $P = 3.5-8.5\text{ kb}$, Kourou 1991) related to partial melting and the formation of the migmatite gneiss, (3) amphibolite facies metamorphism (M3: $T = 500-640\text{ }^{\circ}\text{C}$, $P = 5-8\text{ kb}$, Kourou 1991), (4) upper greenschist facies metamorphism ($T = 440-520^{\circ}\text{C}$, $P = 5-6\text{ kb}$, Kourou 1991), and (5) retrograde greenschist facies metamorphism (M5: $T = 300-550\text{ }^{\circ}\text{C}$, $P < 5\text{ kb}$, Kourou 1991). Geothermometry on chlorite from the milky quartz-chlorite veins revealed formation temperatures varying between 304 and 328 $^{\circ}\text{C}$ (Patsiouri 2017).

The ductile deformation phases documented at Kolchiko include the pre-Mesozoic to Mesozoic D1 and D2 phases, the Mesozoic D3 phase related to the Alpine Orogeny, the D4 Cenozoic phase, and a later brittle deformation (Kourou 1991). The D1 deformation event and the S1 fabric, found in the layered migmatites and the

amphibolites, are related to the M2 metamorphic event (Kourou 1991). Folds were not developed during this event. The D2 event resulted in the isoclinal tight folding of the S1 fabric and to the development of the S2 penetrative fabric related to the axial planes of F2 folds (Kourou 1991). During this event, the boudinage texture was developed in the migmatite gneiss. Thus, Kourou (1991) suggested that D2 deformation phase was subsequent to the M2 metamorphic event and was related to the M3 metamorphic event.

The D3 event folded the S2 fabric, and created close to tight recumbent F3 folds and the S3 fabric that is the main penetrative fabric in the mica schists. Also, the S3 fabric is imposed on the Lofiskos granite (Polydendri group, Kourou 1991). The granites of the Polydendri group were formed during the D3 deformation event by the extensive melting of metasediments similar to the metasandstones exposed in the area. The second group of pegmatites in the area is exclusively related to the Lofiskos granite and to the Polydendri group. During the D3 event, they intruded the metamorphic rocks, mainly along the F3 limbs or parallel to F3 axial planes. The greenschist facies metamorphism (M4) started during the D3 deformation event and continued after it ended. Amphibolites and metasandstones remained unaffected by the D3 folding, whereas discrete shear zones, parallel to the S3 fabric, were developed in mica schists and migmatites (Kourou 1991).

Open, upright folds (F4) and kink folds were developed during the D4 deformation event. A coincident S4 fabric is not described by Kourou (1991). The retrograde M5 metamorphic event (Eocene and early Oligocene, Kiliass et al. 1999) is concurrent to the D4 deformation phase. Also, it is suggested that the dolerite dikes intruded during this event (Kourou 1991). The D4 deformation phase was succeeded during early Oligocene by the onset of the brittle deformation transecting the Vertiskos Unit (Kiliass et al. 1999). Northwest-trending normal faults, conjugate NE-SW-trending normal to oblique, as well as N-S-trending strike-slip faults were developed during Oligocene-Miocene (Kiliass et al. 1999). In addition, the development of a NE-SW-trending contractional component along the western ridge of the SMM between late Oligocene and early Miocene resulted in a SW-vergent thrusting (Kiliass et al. 1999). Thus, the metamorphic rocks of the Kolchiko area are thrust on the Permian-Lower Triassic quartzite of the CRB (Examili Fm, Kiliass 2021) and on the Oligocene-Miocene molassic sediments of the Mygdonia graben (Figure 2.1, 7.1). The younger set of faults (S43E/83°SW in average) at Kolchiko

transcut all the older structural features and is associated with the Miocene to Pliocene high angle normal faulting described by Kiliass et al. (1999).



Figure 7.2. Mineralization styles from the Kolchiko area. a. Arsenopyrite (Apy) and quartz (Qz) in a polymetallic massive vein. b. Arsenopyrite (Apy), pyrite (Py) and quartz (Qz) in a polymetallic massive vein. c. Pyrite (Py), minor arsenopyrite (Apy) and quartz (Qz) as a gangue mineral in a polymetallic massive vein. d. Arsenopyrite (Apy) and quartz (Qz) in a planar polymetallic massive vein. e. Pyrite (Py) and chalcopyrite (Cpy) in a polymetallic quartz vein. f. Pyrite (Py) along cracks and in quartz (Qz) interstices in a quartz-pyrite vein.

7.2. Mineralization and alteration styles

The metallic assemblage at Kolchiko is hosted in polymetallic massive and quartz veins, in quartz-pyrite veins, as well as disseminations in the mica schists (Patsiouri 2017, this study). The polymetallic massive (>80 wt.% of ore, <10 cm in width) and the quartz veins (<5 cm in width, Figure 7.2a-e), as well as the quartz-pyrite veins (<5 cm in width) are planar and continuous (Figure 7.2f). The depth of these veins is unknown.

Arsenopyrite and pyrite are the major metallic minerals filling up to 80% of the veins (Figure 7.2a-c). Locally, the ore texture in the polymetallic massive veins varies from massive to disseminate. Gangue minerals related to all types of veins include quartz in varying amounts (Figure 7.2a-f). Quartz may fill up to 60% of the polymetallic massive and quartz veins (Figure 7.2d,e) and up to 80% of the quartz-pyrite veins (Figure 7.2f).

The metallic minerals of the polymetallic massive veins include arsenopyrite, pyrite, chalcopyrite, galena, pyrrhotite, minor galenobismuthinite, native bismuth and gold, and traces of titanite, ilmenite, rutile and uraninite (Patsiouri 2017, this study, Table 7.1, Figure 7.2a-d, 7.3a-c). According to Patsiouri (2017), the occurrence of native gold in the massive veins is highly correlated with arsenopyrite, while uraninite is found as traces in pyrite along with zircon.

Table 7.1. Summary of the typology, alteration and textural characteristics of the mineralization stages found at Kolchiko.

Mineralization age	Mineralization style	Host rock	Alteration style	Metallic assemblage	Alteration assemblage	Reference
Pre to early Oligocene?	Polymetallic massive veins	Mica-schist	Sericitization	Apy + Py + Cpy + Gn + Po ± Gab ± Bi ± Au ± Ttn ± Ilm ± Rt ± Urn	Ser + Qz + Chl	Patsiouri (2017), this study
Late Oligocene-early Miocene?	Polymetallic quartz veins	Mica-schist	Sericitization	Py + Cpy + Apy + Gn + Sph + Po ± Bi ± Hes ± Tb	Ser + Qz + Chl	
	Quartz-pyrite veins	Mica-schist	Sericitization	Py ± Cpy	Ser + Qz + Chl	This study
	Disseminations and aggregates	Mica-schist	Sericitization	Py	Ser + Qz + Chl	
Post-mineralization	Encrustations and masses	Polymetallic veins	Oxidized mineralization	Gt + Scd + Cov + Hem + Ang + Bsm	-	

Abbreviations: Ang = anglesite, Apy = arsenopyrite, Au = native gold, Bi = native bismuth, Bsm = bismite, Chl = chlorite, Cov = covellite, Cpy = chalcopyrite, Gab = galenobismuthinite, Gn = galena, Gt = goethite, Hem = hematite, Hes = hessite, Ilm = ilmenite, Po = pyrrhotite, Py = pyrite, Qz = quartz, Rt = rutile, Scd = scorodite, Ser = sericite, Sph = sphalerite, Tb = tellurobismuthite, Ttn = titanite, Urn = uraninite.

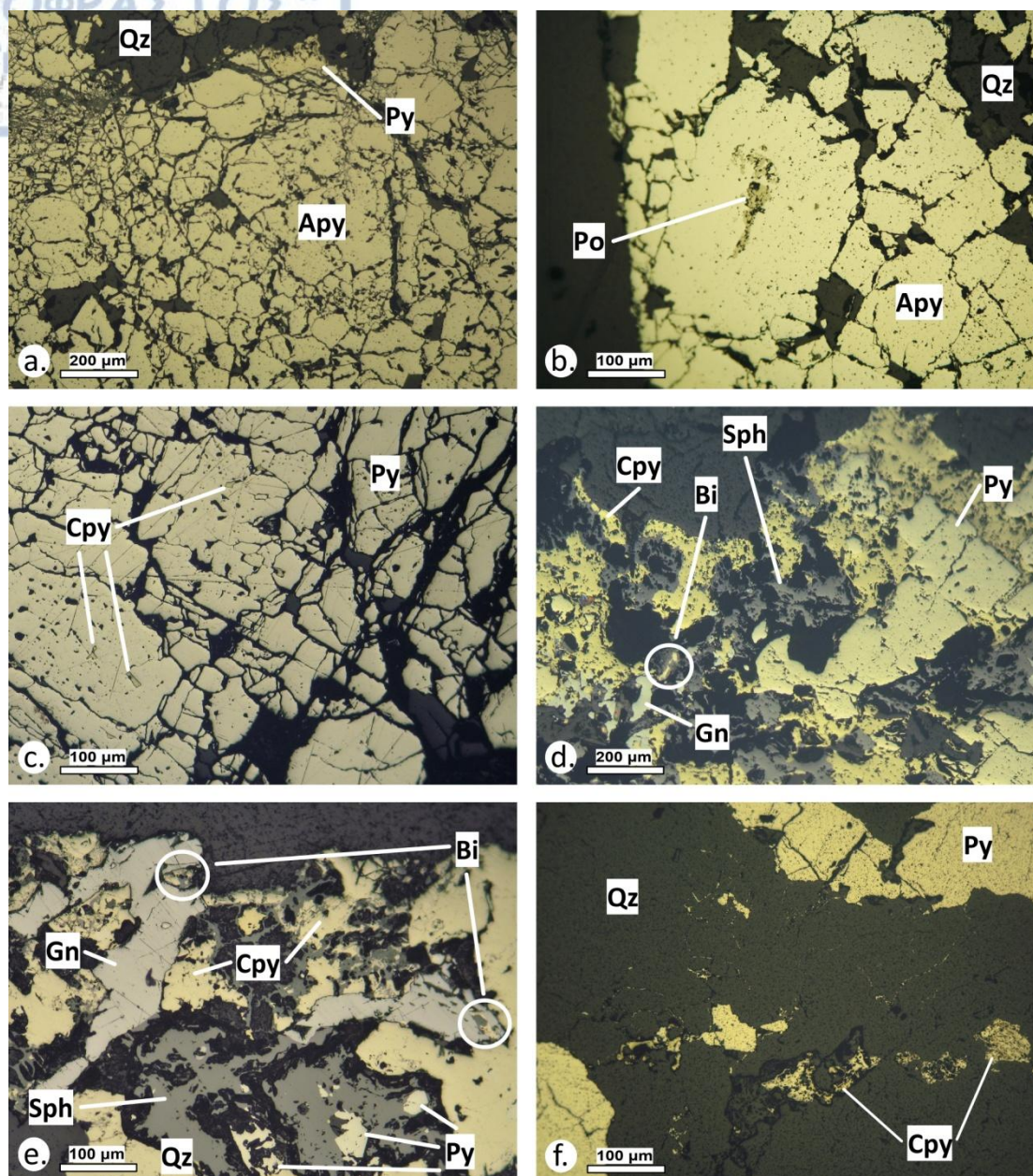


Figure 7.3. Photomicrographs (plane reflected light) of the hypogene mineralization in the polymetallic massive (a-c) and quartz (d-e) veins, as well as in the quartz-pyrite veins (f) at Kolchiko. a. Massive arsenopyrite (Apy) with quartz (Qz) and minor pyrite. b. Pyrrhotite (Po) hosted in massive arsenopyrite (Apy) and quartz (Qz). c. Massive pyrite (Py) and chalcopyrite (Cpy) inclusions. d. Euhedral pyrite (Py) cemented by chalcopyrite (Cpy), sphalerite (Sph) and galena (Gn), and native bismuth (Bi). e. Pyrite (Py) in sphalerite (Sph), and galena (Gn) with inclusions of native bismuth (Bi) cemented by chalcopyrite (Cpy). f. Pyrite (Py) with quartz (Qz) and minor chalcopyrite (Cpy).

The polymetallic quartz veins consist of pyrite, chalcopyrite, arsenopyrite, galena, sphalerite, pyrrhotite, and minor native bismuth, hessite and tellurobismuthite (Table

7.1, Figure 7.2e, 7.3d-e). In the quartz-pyrite veins, pyrite is the main metallic mineral, while chalcopyrite occurs in traces (Table 7.1, Figure 7.2f, 7.3f). Pyrite fills the cracks and the quartz interstices (Figure 7.2f). Furthermore, pyrite is found as disseminations and aggregates (<3 mm in width) in the alteration halos (sericitization) around the polymetallic massive and quartz veins (Table 7.1).

The various mineralization stages are enveloped by restricted hydrothermal halos. Alteration assemblage consists mainly of sericite, quartz and chlorite (Table 7.1). Goethite, scorodite and covellite in the polymetallic massive veins, as well as hematite, anglesite and bismite (Bi_2O_3) in the polymetallic quartz veins are related to supergene processes (Table 7.1).

7.3. Analytical results

7.3.1. Bulk geochemical analysis

Twelve surface mineralized samples from the Kolchiko area were analyzed in respect to their critical and rare metals endowment. Eight samples were from the polymetallic massive veins (KOLX 01a, KOLX 01bi, KOLX 01bii, KOLX 03a: arsenopyrite is the dominant metallic mineral, KOLX 02a, KOLX 02bi, KOLX 03c: pyrite is the dominant metallic mineral), and three samples were from the polymetallic quartz veins (KL 13i, KL 13ii, KL 13a) (Table 7.2, Figure 7.4). One sample was analyzed from the quartz-pyrite veins (KL 07) (Table 7.2, Figure 7.4). Additionally, one sample from a pegmatite (KL 06) related to the adjacent Triassic granite, and 2 samples from the milky quartz veins (KL 01, KL 02a), and 1 sample from the hydrothermally altered and oxidized metamorphic rocks (KL02b) were analyzed for comparison and background reference (Table 7.3, Figure 7.4).

The polymetallic massive and quartz veins exhibit similar geochemical profiles, whereas those of the quartz-pyrite and the pegmatite show distinct trends (Figure 7.4). The pyrite-dominated polymetallic massive veins are more enriched in critical and rare metals than the arsenopyrite-dominated polymetallic massive veins (Figure 7.4). The pyrite-dominated polymetallic massive veins are more enriched in Au (<9.2 ppm), Ce (<20 ppm) and W (<844 ppm), while the arsenopyrite-dominated polymetallic massive veins include higher contents in La (<12 ppm) and U (<2.5 ppm) (Table 7.2, Figure 7.4).

The polymetallic quartz veins incorporate the higher contents in Ag (<23 ppm), Bi (<995 ppm), Cd (<14 ppm), Co (<320 ppm), Ga (<2.4 ppm), Gd (<1.7 ppm), In

(<0.44 ppm), Nd (<6.2 ppm), Se (<38 ppm), Sm (<1.6 ppm), Te (<3 ppm) and Th (<15 ppm) (Table 7.2, Figure 7.4). Rare earth elements and Ge, Nb and Ti are depleted in the mineralized veins in respect to the metamorphic reference rocks.

Table 7.2. Bulk geochemical analyses of selected critical and rare metals from Kolchiko. For the full list of geochemical analyses advise Supplement 4, Table S1-3.

		Mineralization stages											
	Host rock	Polymetallic massive veins								Polymetallic quartz veins			Py-Qz veins
	Alt.	Sericitization											
ppm	Det. limit	KOLX 01a	KOLX 01bi	KOLX 01bii	KOLX 01c	KOLX 02a	KOLX 02bi	KOLX 03a	KOLX 03c	KL 13i	KL 13ii	KL 13a	KL 07
Ag	0.01	1.7	1.4	1.3	4.5	13	1.8	5.6	9.7	23	33	17	0.18
Au	5x10 ⁻⁶	1.1	2.1	2.4	0.35	0.34	9.2	0.66	0.3	0.35	0.13	0.53	0.32
Bi	0.01	262	466	504	181	390	693	190	425	995	694	739	30
Cd	0.01	0.05	0.03	0.06	1.9	0.55	0.01	0.24	0.15	3.2	14	12	0.11
Ce	0.02	14	5.4	18	0.32	0.41	20	9.3	1.2	16	15	7.9	2.1
Co	0.1	296	275	269	124	78	161	261	89	320	245	159	19
Ga	0.05	0.6	0.37	0.68	0.06	0.05	0.91	0.84	0.28	1.9	2.1	2.4	0.49
Gd	0.05	0.34	0.15	0.3	b.d.l.	b.d.l.	0.5	0.67	0.07	1.5	1.7	1.3	0.31
Ge	0.05	0.12	0.12	0.11	0.15	0.13	0.09	0.12	0.06	0.2	0.16	0.11	b.d.l.
Hg	0.005	0.04	0.05	0.07	0.09	0.10	0.04	0.05	0.16	0.1	0.25	0.12	0.008
In	0.005	0.01	b.d.l.	0.01	0.07	0.38	0.01	0.02	0.07	0.13	0.44	0.35	b.d.l.
La	0.2	12	4.1	17	b.d.l.	0.3	10	4.1	0.7	7.1	7.6	3.7	1.1
Nb	0.05	0.1	0.1	0.12	0.08	0.12	0.27	0.28	0.19	0.13	0.24	0.27	0.33
Nd	0.1	2.8	1.4	2.7	b.d.l.	0.1	4.9	3.9	0.4	6.2	5.6	4	1
Re	0.001	0.004	0.002	0.003	0.002	0.004	b.d.l.	0.002	0.01	0.002	0.002	b.d.l.	b.d.l.
Sb	0.05	58	54	39	23	2.5	42	35	0.61	13	13	11	183
Se	0.2	9.6	8.8	7	10	17	6	11	5.7	38	31	19	1
Sm	0.03	0.44	0.23	0.38	b.d.l.	b.d.l.	0.8	0.85	0.07	1.6	1.6	1.2	0.26
Ta	0.01	b.d.l.	0.01	0.02	b.d.l.	b.d.l.	b.d.l.	b.d.l.	b.d.l.	b.d.l.	b.d.l.	b.d.l.	0.01
Te	0.01	1.4	1.8	1.4	0.36	2	1.6	2.2	1.5	3	2.1	2.6	0.12
Th	0.2	1.3	0.5	0.6	b.d.l.	b.d.l.	1.5	1.1	0.3	6.5	15	6.8	0.5
Ti	50	b.d.l.	b.d.l.	b.d.l.	b.d.l.	b.d.l.	100	60	b.d.l.	b.d.l.	100	100	100
U	0.05	0.58	0.33	0.75	0.05	b.d.l.	0.3	2.5	0.07	0.56	1.2	0.64	0.08
V	1	9	9	8	8	7	9	7	4	7	6	2	b.d.l.
W	0.05	35	109	246	189	469	36	142	844	168	176	0.88	0.11

Abbreviations: alt. = alteration, b.d.l. = below detection limit, Det. limit = detection limit.

The pegmatite shows the highest enrichment in Sb (<648 ppm), followed by restricted contents of Ce (<5.9 ppm), Co (<4.4 ppm), La (<2.6 ppm) and Nd (<2.3 ppm) (Table 7.3). The milky quartz veins and the two-mica schist exhibit depleted geochemical profiles in critical and rare metals (Figure 7.4). The highest contents of critical and rare metals is the mica-schist are ascribed to Co (<53 ppm), while the milky quartz veins contain up to 108 ppm Bi and up to 53 ppm Sb (Table 7.3).

Table 7.3. Bulk geochemical analyses of selected critical and rare metals from pegmatite (KL 06), milky quartz veins (KL 01, KL 02a), and the mica schist (KL 02b) from Kolchiko. For the full list of geochemical analyses advise Supplement 4, Table S1-3.

	Host rock	Mica schist	Milky quartz veins		Pegmatite
	Alteration	Sericitization			
ppm	Detection limit	KL 02b	KL 01	KL 02a	KL 06
Ag	0.01	0.12	0.2	0.06	0.03
Au	5x10 ⁻⁶	0.01	0.04	0.002	0.003
Bi	0.01	3.5	108	1.2	0.19
Cd	0.01	0.17	b.d.l.	0.02	0.03
Ce	0.02	6.1	0.43	15	5.9
Co	0.1	53	2.7	4.4	4.4
Ga	0.05	3.6	0.64	3.4	1.1
Gd	0.05	1.3	b.d.l.	1.7	0.5
Ge	0.05	0.07	b.d.l.	b.d.l.	b.d.l.
Hg	0.005	b.d.l.	0.01	b.d.l.	0.01
In	0.005	0.03	b.d.l.	0.02	b.d.l.
La	0.2	3.4	0.3	7.2	2.6
Nb	0.05	1.8	0.16	0.31	0.09
Nd	0.1	4	0.2	6.8	2.3
Re	0.001	0.004	b.d.l.	b.d.l.	b.d.l.
Sb	0.05	7.4	53	9.5	648
Se	0.2	0.5	0.8	b.d.l.	b.d.l.
Sm	0.03	1	0.05	1.6	0.49
Ta	0.01	b.d.l.	b.d.l.	b.d.l.	b.d.l.
Te	0.01	0.04	0.2	0.02	b.d.l.
Th	0.2	0.6	0.3	4.9	b.d.l.
Ti	50	0.01	b.d.l.	0.06	b.d.l.
U	0.05	0.58	b.d.l.	1.5	0.23
V	1	5	b.d.l.	8	1
W	0.05	0.51	0.79	0.34	0.13

Abbreviations: b.d.l. = below detection limit.

Pearson product-moment correlation coefficients and associated p-values were calculated for the bulk geochemical analyses (Supplement 3: Table S4-3). Significant positive correlations ($p < 0.01$, values ≥ 0.625) were obtained for the elemental pairs: Ag-Bi, Ag-Cd, Ag-Co, Ag-Ge, Ag-Hg, Ag-In, Ag-Se, Ag-Te, Ag-Th, Bi-Co, Bi-Ge, Bi-Hg, Bi-Se, Bi-Te, Cd-Hg, Cd-In, Cd-Se, Cd-Th, Ce-La, Ce-Nd, Ce-Sm, Co-Ge, Co-Se, Co-Te, Ga-Gd, Ga-Nb, Ga-Nd, Ga-Sm, Ga-Ti, Gd-Nd, Gd-Sm, Gd-Th, Ge-Se, Ge-Te, Hg-In, Hg-Se, Hg-Th, In-Se, In-Th, Nd-Sm, Nd-Th, Nd-U, Re-W, Se-Te, Se-Th and Sm-Th (Supplement 3: Table S4-3).

Additionally, positive correlations ($p < 0.05$, values between 0.504 and 0.621) were defined for the elemental pairs: Ag-Gd, Ag-Sm, Au-Se, Bi-Cd, Bi-Th, Cd-Gd,

Cd-Sm, Ce-Gd, Ce-V, Co-La, Co-V, Ga-Th, Gd-Ti, Gd-U, Ge-Hg, Ge-V, La-Nd, La-Ta, La-V, Nd-Ti, Se-Sm, Sm-Ti and Sm-U (Supplement 3: Table S4-3). Negative correlations were not detected (Supplement 3: Table S4-3).

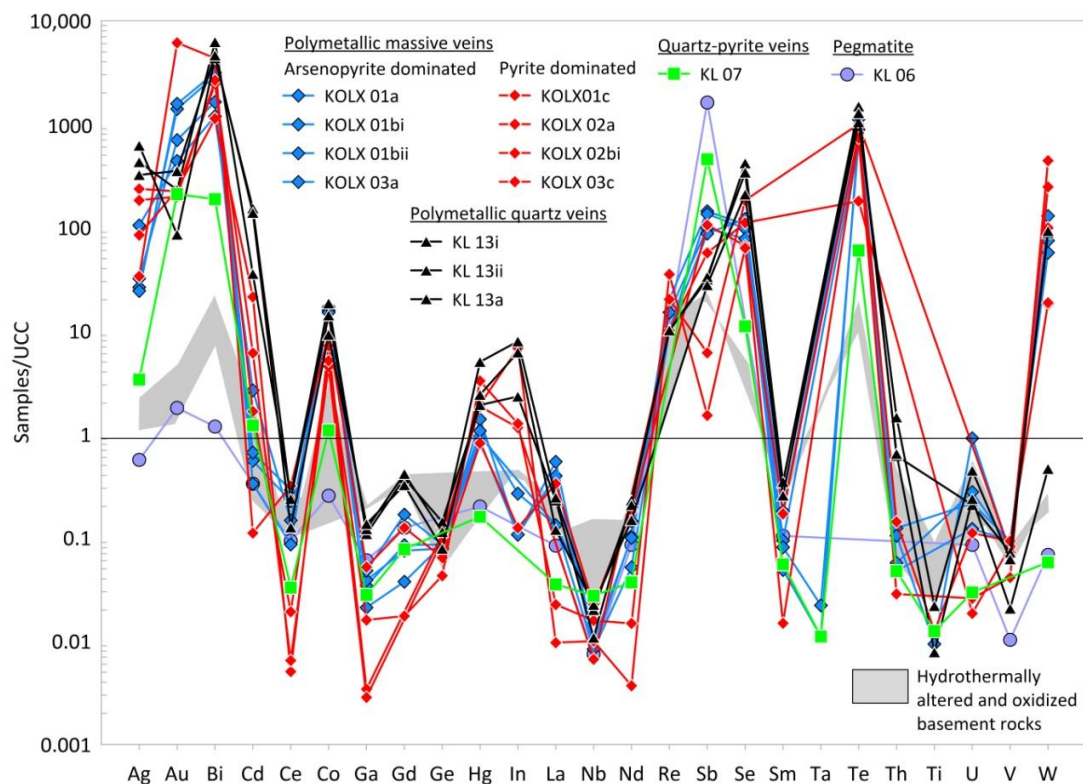


Figure 7.4. Upper continental crust (UCC) normalized logarithmic spider diagram of the analyzed samples from Kolchiko in comparison to the plot area of the hydrothermally altered and oxidized metamorphic rocks (UCC normalized values after Rudnick and Gao 2003).

7.3.2. Arsenopyrite and pyrite - Mode of occurrence

Arsenopyrite and pyrite are the dominant metallic minerals in the polymetallic massive and quartz veins at Kolchiko (Figure 7.5a-c). In the polymetallic massive veins, arsenopyrite (Apy1) is granular (<500 μm in width) to massive, and locally exhibits cataclastic texture (Figure 7.3a). It is intergrown with minor pyrite (Py1) (<300 μm in width) and hosts irregular inclusions of pyrrhotite (<400 μm in width) (Figure 7.3b, 7.5a). Native bismuth (<10 μm in width) rarely occurs in the intergranular space. Additionally, Patsiouri (2017) reports the occurrence of chalcopyrite and native gold (<200 μm in width) in the intergranular space. In the pyrite-dominated polymetallic massive veins, arsenopyrite is a minor component and occurs sparsely as euhedral grains (<200 μm in width).

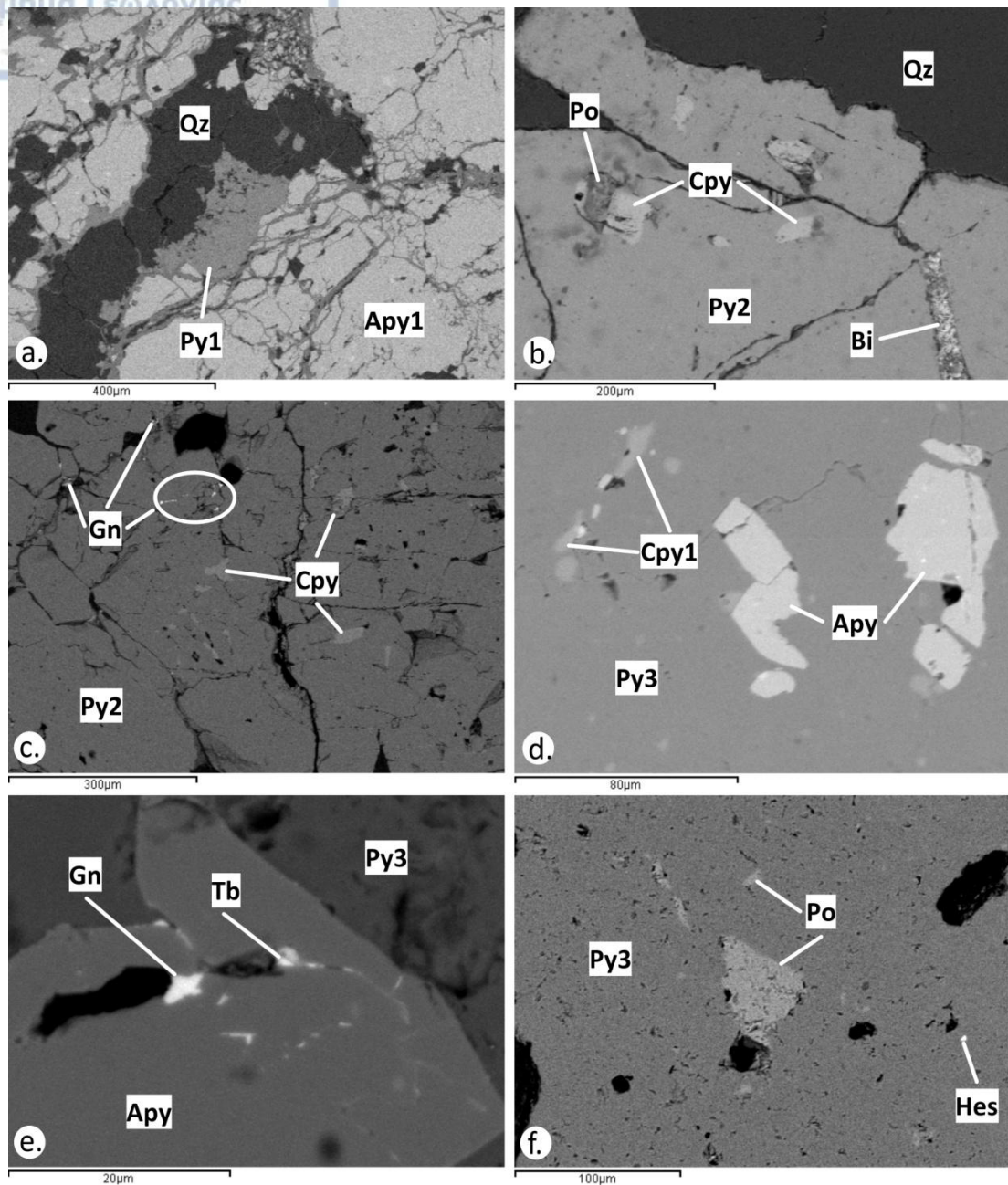


Figure 7.5. SEM back-scattered electron images of arsenopyrite and pyrite from the polymetallic massive veins (a-c) and from the polymetallic quartz veins (d-f). a. Arsenopyrite (Apy1) exhibiting cataclasis, minor pyrite (Py1) and quartz (Qz) as a gangue mineral. b. Subrounded inclusions of chalcopyrite (Cpy) and pyrrhotite (Po), and native bismuth (Bi) filling a veinlet in pyrite (Py2), and quartz (Qz) as a gangue mineral. c. Galena (Gn) in interstices and chalcopyrite (Cpy) inclusions in pyrite (Py2). d. Euhedral arsenopyrite (Apy) and chalcopyrite (Cpy1) in pyrite (Py3). e. Arsenopyrite (Apy), galena (Gn) and tellurobismuthite (Tb) in pyrite (Py3). f. Pyrrhotite (Po) and hessite (Hes) inclusions in pyrite (Py3).

In the polymetallic quartz veins, arsenopyrite rarely occurs. It is associated with euhedral grains ($<200\ \mu\text{m}$ in width) and with inclusions ($<100\ \mu\text{m}$ in width) in pyrite and chalcopyrite (Figure 7.5d). In arsenopyrite interstices, galena and tellurobismuthite are found (Figure 7.5e).

In the polymetallic massive veins, pyrite (Py1 and Py2) exhibits massive to granular textures and cataclasis (Figure 7.3c). In the arsenopyrite-dominated polymetallic massive veins, pyrite (Py1) is a minor component and appears as subhedral to euhedral grains ($<300\ \mu\text{m}$ in width). In the pyrite-dominated polymetallic massive veins, pyrite (Py2) appears as subhedral to euhedral grains ($<3\ \text{mm}$ in width) along with arsenopyrite, chalcopyrite, pyrrhotite, galena and native bismuth (Figure 7.5b,c). Chalcopyrite and pyrrhotite form subrounded inclusions ($<100\ \mu\text{m}$ in width) in Py2 grains, while galena and native bismuth occur along the boundaries of pyrite grains, and in Py2 interstices ($<20\ \mu\text{m}$ in width) (Figure 7.3b, 7.5b,c).

In the polymetallic quartz veins, pyrite (Py3) is subhedral to euhedral in shape ($<400\ \mu\text{m}$ in width), and cemented by chalcopyrite, sphalerite, galena and native bismuth. Inclusions of galena ($<200\ \mu\text{m}$ in width), arsenopyrite ($<100\ \mu\text{m}$ in width), chalcopyrite ($<30\ \mu\text{m}$ in width) and pyrrhotite ($<20\ \mu\text{m}$ in width) are found in pyrite (Figure 7.5f). Hessite, tellurobismuthite and native bismuth ($<70\ \mu\text{m}$ in width) are found in the intergranular space and as inclusions in galena. In the quartz-pyrite veins, pyrite (Py4) fills veinlets and forms aggregates ($<3\ \text{mm}$ in width) along cracks in quartz. Locally, it is intergrown with minor chalcopyrite (Figure 7.3f).

7.3.3. Chalcopyrite and sphalerite - Mode of occurrence

Chalcopyrite is found in all the mineralization stages related to veins (Table 7.1). In the polymetallic massive veins, chalcopyrite is a minor component. It is found in the intergranular space between arsenopyrite and pyrite ($<200\ \mu\text{m}$ in width), and as subrounded inclusions ($<100\ \mu\text{m}$ in width) in pyrite grains along with pyrrhotite ($<50\ \mu\text{m}$ in width) (Figure 7.3b, 7.5b). In the pyrite-dominated polymetallic massive veins, chalcopyrite inclusions in pyrite are locally overgrown by galena (Figure 7.6a).

In the polymetallic quartz veins, chalcopyrite (Cpy1) is the second most abundant metallic mineral after pyrite (Figure 5.3d,e). It cements pyrite, and is intergrown with sphalerite (Figure 7.6b). Furthermore, it hosts euhedral arsenopyrite, and inclusions of galena and native bismuth (Figure 7.3d,e, 7.6b,c).

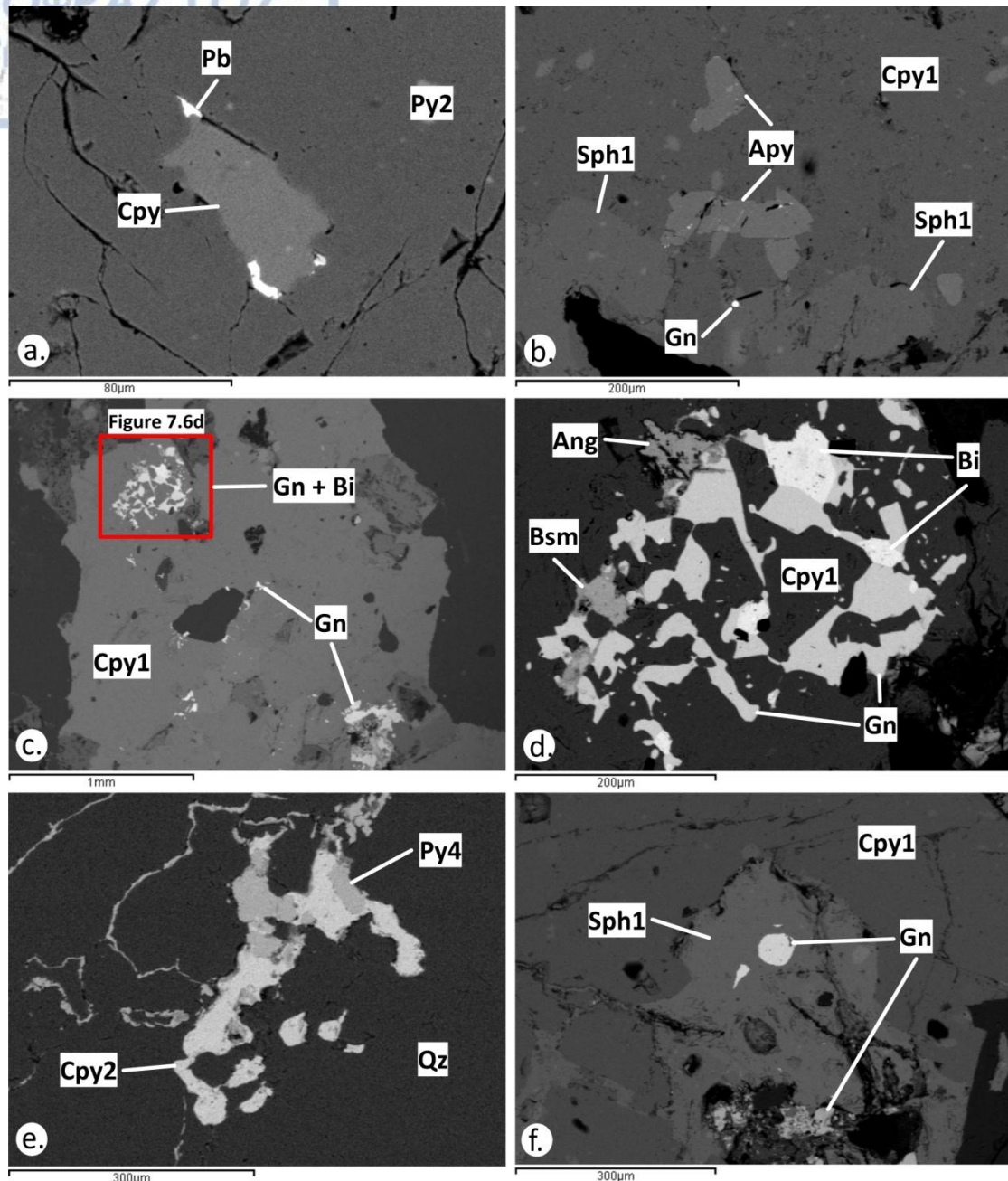


Figure 7.6. SEM back-scattered electron images of pyrite, chalcopyrite and sphalerite from Kolchiko (a = polymetallic massive veins: pyrite dominated, b-d, f = polymetallic quartz veins, e = quartz-pyrite veins). a. Chalcopyrite (Cpy) in pyrite (Py2) and galena (Gn) in interstices. b. Chalcopyrite (Cpy1) is intergrown with sphalerite (Sph1) and hosts inclusions of euhedral arsenopyrite (Apy). Galena (Gn) is found in sphalerite. c. Chalcopyrite (Cpy1) contains inclusions of galena (Gn) and native bismuth (Bi). d. Galena (Gn) and native bismuth (Bi) in chalcopyrite (Cpy1). Anglesite (Ang) and bismite (Bsm) occur due to the oxidation of galena and native bismuth, respectively. e. Pyrite (Py4) is intergrown with chalcopyrite (Cpy2) in cracks along quartz (Qz). f. Sphalerite (Sph1) is intergrown with chalcopyrite (Cpy1) and hosts galena (Gn) inclusions.

In the quartz-pyrite veins, chalcopyrite (Cpy2) is a minor constituent (Figure 7.3f). It is intergrown with pyrite along cracks in quartz (Figure 7.3f). Locally, quartz cracks are filled only by chalcopyrite.

Sphalerite (Sph1) is found only in the polymetallic quartz veins (Table 7.1). It is intergrown with chalcopyrite (Cpy2). It appears in irregular shape (<500 μm in width) and along with chalcopyrite it cements pyrite (Py3) (Figure 7.3d,e, 7.6b,f). Commonly, it is replaced by galena, which appears as irregular to rounded inclusions (<300 μm in width) in Sph1 (Figure 7.6f).

7.3.4. Critical and rare metals in arsenopyrite and pyrite (LA-ICP-MS)

Arsenopyrite (Apy1) exhibits depleted contents in base, critical and rare metals (Table 7.4, Figure 7.7a). The full analytical dataset for arsenopyrite is given in Supplement 2 (Table S3-11). Base metals concentrations include As (<295,377 ppm or 29.5 wt.%), Ni (<90 ppm), Cr (<20 ppm), Cu (<20 ppm), Mn (<5 ppm) and Pb (<3.1 ppm) (Table 7.4). Critical and rare metals include up to 627 ppm Co, up to 101 ppm Sb, up to 21 ppm Se, up to 15 ppm Ti, up to 13 ppm Te, up to 3.5 ppm Au, up to 2.4 ppm Ag, up to 1.6 ppm Hg and up to 0.30 ppm Tl (Table 7.4, Figure 7.7a). Elevated contents in Bi (<100 ppm) and Pb (<6.8 ppm) in Apy1 are related to nano-scale mineral inclusions and are excluded from Table 7.4 (Supplement 2: Table S3-11).

Table 7.4. LA-ICP-MS analyses of arsenopyrite from the polymetallic massive veins at Kolchiko. Advise also Supplement 2, Table S3-11.

Host rock	Mica-schist				Host rock	Mica-schist			
Alteration	Sericitization				Alteration	Sericitization			
Mineralization style	Apy1, Polymetallic massive veins (n = 10)				Mineralization style	Apy1, Polymetallic massive veins (n = 10)			
Element	MIN	MAX	STDEV	AVG	Element	MIN	MAX	STDEV	AVG
ppm					ppm				
Ag	2.4	2.4	-	2.4	Nb	b.d.l.	b.d.l.	-	-
As	196,291	295,377	31,071	231,425	Ni	23	90	20	35
Au	0.63	3.5	1.4	1.9	Pb	0.63	3.1	1.1	1.6
Bi	b.d.l.	b.d.l.	-	-	Re	b.d.l.	b.d.l.	-	-
Cd	b.d.l.	b.d.l.	-	-	Sb	57	101	16	75
Co	77	627	176	294	Se	9.2	21	3.8	15
Cr	20	20	-	20	Sn	b.d.l.	b.d.l.	-	-
Cu	20	20	-	20	Te	12	13	0.47	12
Ga	b.d.l.	b.d.l.	-	-	Ti	11	15	2.7	13
Ge	b.d.l.	b.d.l.	-	-	Tl	0.30	0.30	-	0.30
Hg	0.87	1.6	0.23	1.2	V	b.d.l.	b.d.l.	-	-
In	b.d.l.	b.d.l.	-	-	W	b.d.l.	b.d.l.	-	-
Mn	3.6	5	0.57	4.1	Zn	640,400	645,500	2,464	643,970
Mo	b.d.l.	b.d.l.	-	-					

Abbreviations: AVG = average value, b.d.l. = below detection limit, MIN = minimum value, MAX = maximum value, n = number of analyses, STDEV = standard deviation.

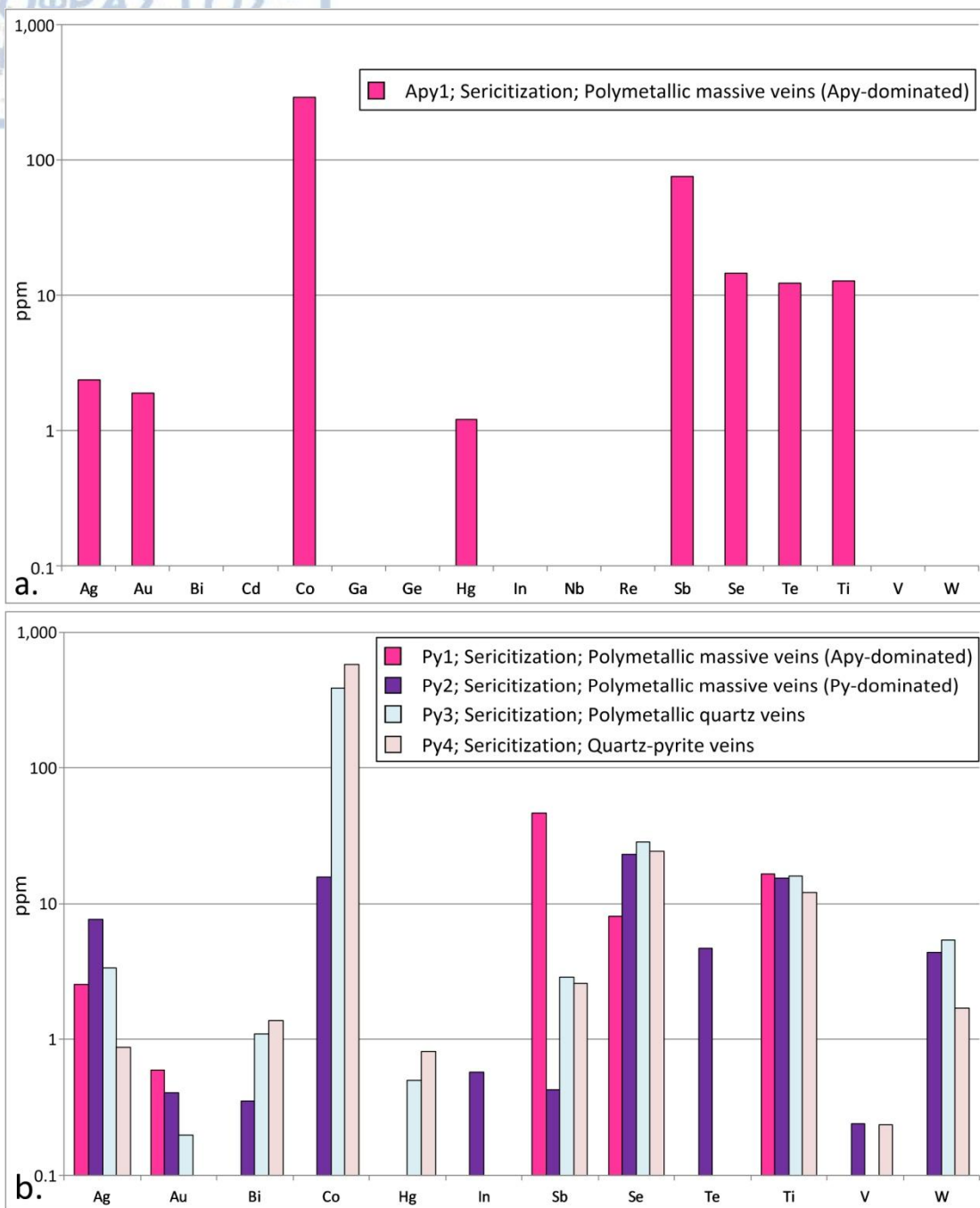


Figure 7.7. Average values of critical and rare metals concentrations of arsenopyrite (a) from the polymetallic massive veins and of pyrite (b) from the polymetallic massive and quartz veins and the quartz-pyrite veins. Local enrichments related to nano-scale mineral inclusions are excluded.

Pyrite (Py1-4) from the various mineralization styles at Kolchiko exhibits diversity in trace elements enrichments reflecting distinct geochemical profiles (Table 7.5, Figure 7.7b). The most enriched base metals include As (<18,820 ppm), Zn (<65 ppm) and Sn (<2.7 ppm) in Py2, Ni (<1,713 ppm), Pb (<120 ppm) and Cu (<95 ppm) in Py4, and Mn (<64 ppm) and Cr (<43 ppm) in Py3, while Mo contents are below

detection limit (Table 7.5). Pyrite (Py2) from the pyrite-dominated polymetallic massive veins is more enriched in Ag (<21 ppm), Au (<1.3 ppm), In (<2.2 ppm) and Te (<7 ppm), while pyrite (Py1) from the arsenopyrite-dominated polymetallic massive veins exhibits the highest contents in Sb (<55 ppm) (Table 7.5, Figure 7.7b). Pyrite (Py3) from the polymetallic massive veins is more enriched in Ti (<52 ppm). Pyrite (Py4) from the quartz-stibnite veins is characterized by enrichments in Co (<2,155 ppm), Se (<63 ppm), Bi (<4 ppm) and Hg (<0.81 ppm) (Table 7.5, Figure 7.7b). V (<0.24 ppm) exhibits similar enrichments in Py2 and Py4, as well as W (<10 ppm) for Py2 and Py3 (Table 7.5, Figure 7.7b).

Table 7.5. LA-ICP-MS analyses of pyrite from the mineralizing stages at Kolchiko. For the full dataset, see Supplement 2, Tables S3-12.

Host rock	Mica-schist															
Alteration	Sericitization															
Mineralization style	Py1, Apy-dominated polymetallic massive veins (n = 3)				Py2, Py-dominated polymetallic massive veins (n = 22)				Py3, Polymetallic quartz veins (n = 15)				Py4, Quartz-pyrite veins (n = 10)			
Element	MIN	MAX	ST DEV	AVG	MIN	MAX	ST DEV	AVG	MIN	MAX	ST DEV	AVG	MIN	MAX	ST DEV	AVG
ppm																
Ag	2	3.1	0.77	2.6	0.75	21	7.9	5.5	1.2	15	3.9	4.2	0.36	1.8	0.60	0.88
As	111	1,014	502	436	1.3	18,820	6,318	4,543	5.2	10	2.1	7.8	b.d.l.	b.d.l.	-	-
Au	0.59	0.59	-	0.59	0.22	1.3	0.33	0.47	0.20	0.20	-	0.20	b.d.l.	b.d.l.	-	-
Bi	b.d.l.	b.d.l.	-	-	0.22	0.4	0.1	0.34	0.49	2.1	0.72	1.1	0.23	4	1.6	1.4
Co	b.d.l.	b.d.l.	-	-	0.26	35	12	16	57	623	136	390	205	2,155	577	579
Cr	b.d.l.	b.d.l.	-	-	12	12	-	12	11	44	11	33	11	11	-	11
Cu	17	17	-	17	4.4	11	2.1	7.7	3.3	9.5	2.6	6.5	3.8	95	36	21
Hg	b.d.l.	b.d.l.	-	-	b.d.l.	b.d.l.	-	-	0.34	0.67	0.12	0.51	0.81	0.81	-	0.81
In	b.d.l.	b.d.l.	-	-	0.05	2.2	1.2	0.75	b.d.l.	b.d.l.	-	-	b.d.l.	b.d.l.	-	-
Mn	4.3	7	1.4	5.6	3.3	6.5	0.81	4.9	4.8	64	25	31	4.4	20	4.7	6.4
Mo	b.d.l.	b.d.l.	-	-	b.d.l.	b.d.l.	-	-	b.d.l.	b.d.l.	-	-	b.d.l.	b.d.l.	-	-
Ni	b.d.l.	b.d.l.	-	-	1.6	68	20	23	9.4	182	44	98	143	1,713	473	421
Pb	b.d.l.	b.d.l.	-	-	0.19	3.62	2	1.4	6.6	100	34	54	7.2	120	40	49
Sb	38	55	12	46	0.37	0.59	0.08	0.47	0.47	6	1.8	1.7	0.46	8.1	2.7	2.6
Se	15	15	-	15	8.1	62	14	23	7	46	9.9	28	9.8	63	16	25
Sn	b.d.l.	b.d.l.	-	-	2.7	2.7	-	2.7	b.d.l.	b.d.l.	-	-	0.42	0.43	0.007	0.43
Te	b.d.l.	b.d.l.	-	-	2.4	7	2.3	4.7	b.d.l.	b.d.l.	-	-	b.d.l.	b.d.l.	-	-
Ti	9.6	21	6.1	16	9.5	25	4	16	5.9	52	12	18	5.9	18	4	12
Tl	0.91	3.2	1.6	2.1	0.36	1.05	0.29	0.77	0.25	0.71	0.24	0.53	0.32	0.82	0.35	0.57
V	b.d.l.	b.d.l.	-	-	0.24	0.24	-	0.24	b.d.l.	b.d.l.	-	-	0.24	0.24	-	0.24
W	b.d.l.	b.d.l.	-	-	0.88	10	4	4.4	0.56	10	3.6	5.4	1.7	1.7	-	1.7
Zn	b.d.l.	b.d.l.	-	-	7.2	65	41	36	5.9	5.9	-	5.9	b.d.l.	b.d.l.	-	-

Abbreviations: Apy = arsenopyrite, AVG = average value, b.d.l. = below detection limit, MIN = minimum value, MAX = maximum value, n = number of analyses, n.a. = not analyzed, Py = pyrite, STDEV = standard deviation.

Trace elements related to nano-scale mineral inclusions include Bi (<196 ppm), Sb (<73 ppm), Pb (<44 ppm), Cu (<33 ppm) and Tl (<3 ppm) in Py1, As (<22,330 ppm), Cu (<1,847 ppm), Pb (<1,134 ppm), Bi (<366 ppm), Zn (<173 ppm), Ag (<21 ppm), Sb (<15 ppm), In (<12 ppm) and Sn (<11 ppm) in Py2, Pb (<456 ppm), Cu (<82 ppm), Sb (<26 ppm), Bi (<14 ppm), Ag (<13 ppm) and Zn (<4.3 ppm) in Py3, and Cu (<124 ppm) and Bi (<8.1 ppm) in Py4 (Supplement 2: Table S3-12).

7.3.5. Critical and rare metals in chalcopyrite and sphalerite (LA-ICP-MS)

Chalcopyrite (Cpy1) from the polymetallic quartz veins is more enriched in trace elements than Cpy2 from the quartz-pyrite veins (Table 7.6, Figure 7.8a). The full laser ablation ICP-MS analytical dataset is given in Supplement 2 (Table S3-13).

Table 7.6. LA-ICP-MS analyses of chalcopyrite from the polymetallic quartz veins and the pods at Laodikino. Advise also Supplement 2, Table S3-13,14.

Mineral	Chalcopyrite								Sphalerite			
Host rock	Mica-schist											
Alteration	Sericitization											
Mineralization style	Cpy1, Polymetallic quartz veins (n = 11)				Cpy2, Quartz-pyrite veins (n = 2)				Sph1, Polymetallic quartz veins (n = 10)			
Element	MIN	MAX	ST DEV	AVG	MIN	MAX	ST DEV	AVG	MIN	MAX	ST DEV	AVG
ppm												
Ag	34	106	22	83	2.3	2.3	-	2.3	8.5	59	15	20
As	11	18	3.7	15	b.d.l.	b.d.l.	-	-	b.d.l.	b.d.l.	-	-
Au	0.59	4.5	1.5	2.1	0.92	0.92	-	0.92	0.22	0.84	0.25	0.42
Bi	7.9	18	5.2	14	b.d.l.	b.d.l.	-	-	0.30	2.6	0.97	1.4
Cd	4.7	4.7	-	4.7	b.d.l.	b.d.l.	-	-	1,867	2,015	51	1,960
Co	2.8	5.5	0.83	4.2	11	64	38	37	133	151	5.4	141
Cr	17	21	1.8	19	b.d.l.	b.d.l.	-	-	b.d.l.	b.d.l.	-	-
Cu	309,550	388,071	29,278	342,903	346,400	346,400	-	346,400	75	1,060	345	333
Ga	0.73	0.73	-	0.73	b.d.l.	b.d.l.	-	-	0.71	0.81	0.05	0.76
Ge	6.3	6.3	-	6.3	8.6	8.6	-	8.6	b.d.l.	b.d.l.	-	-
Hg	0.59	1.4	0.4	1	b.d.l.	b.d.l.	-	-	11	20	2.3	15
In	0.35	4.4	1.6	2.9	0.72	0.72	-	0.72	15	20	1.5	17
Mn	3.1	30	12	11	b.d.l.	b.d.l.	-	-	656	737	24	688
Mo	b.d.l.	b.d.l.	-	-	b.d.l.	b.d.l.	-	-	b.d.l.	b.d.l.	-	-
Nb	b.d.l.	b.d.l.	-	-	b.d.l.	b.d.l.	-	-	b.d.l.	b.d.l.	-	-
Ni	b.d.l.	b.d.l.	-	-	4.3	43	28	24	b.d.l.	b.d.l.	-	-
Pb	9.1	17	3.8	12	b.d.l.	b.d.l.	-	-	0.54	5.7	2.2	3.3
Re	b.d.l.	b.d.l.	-	-	b.d.l.	b.d.l.	-	-	b.d.l.	b.d.l.	-	-
Sb	1.5	4.9	1.2	3.8	b.d.l.	b.d.l.	-	-	1.8	1.8	-	1.8
Se	7.9	64	18	35	8.9	22	9.3	15	18	42	7.4	32
Sn	3.1	9.3	2	6.8	2.7	12	6.6	7.4	b.d.l.	b.d.l.	-	-
Te	b.d.l.	b.d.l.	-	-	b.d.l.	b.d.l.	-	-	b.d.l.	b.d.l.	-	-
Ti	7	29	8.7	15	12	12	-	12	3.3	5.7	1.1	4.5
Tl	b.d.l.	b.d.l.	-	-	6.3	6.3	-	6.3	b.d.l.	b.d.l.	-	-
V	1.3	1.3	-	1.3	1.7	1.7	-	1.7	b.d.l.	b.d.l.	-	-
W	b.d.l.	b.d.l.	-	-	b.d.l.	b.d.l.	-	-	b.d.l.	b.d.l.	-	-
Zn	392	616	73	501	96	167	50	132	62,700	62,700	0	62,700
Cd:Zn	0.008	0.008	-	0.008	n.a.	n.a.	n.a.	n.a.	0.003	0.003	-	0.003

Abbreviations: AVG = average value, b.d.l. = below detection limit, MIN = minimum value, MAX = maximum value, n = number of analyses, STDEV = standard deviation.

The highest concentrations in base metals include up to 616 ppm Zn, up to 30 ppm Mn, up to 21 ppm Cr, up to 18 ppm As and up to 17 ppm Pb in Cpy1, as well as up to 43 ppm Ni and up to 12 ppm Sn in Cpy2 (Table 7.6). In Cpy1, Ag (<106 ppm), Au (<4.5 ppm), In (<4.4 ppm), Se (<64 ppm) and Ti (<29 ppm) are incorporated in higher contents, whereas chalcopyrite (Cpy2) is more enriched in Co (<64 ppm), Ge (<8.6 ppm) and V (<1.7 ppm) (Table 7.6, Figure 7.8a). Bismuth (<18 ppm), Cd (<4.7 ppm), Ga (<0.73 ppm), Hg (<1.4 ppm) and Sb (<4.9 ppm) are only contained in Cpy1 (Table

7.6, Figure 7.8a). Nb, Re, Te and W are characterized by contents below detection limits (Table 7.6, Figure 7.8a).

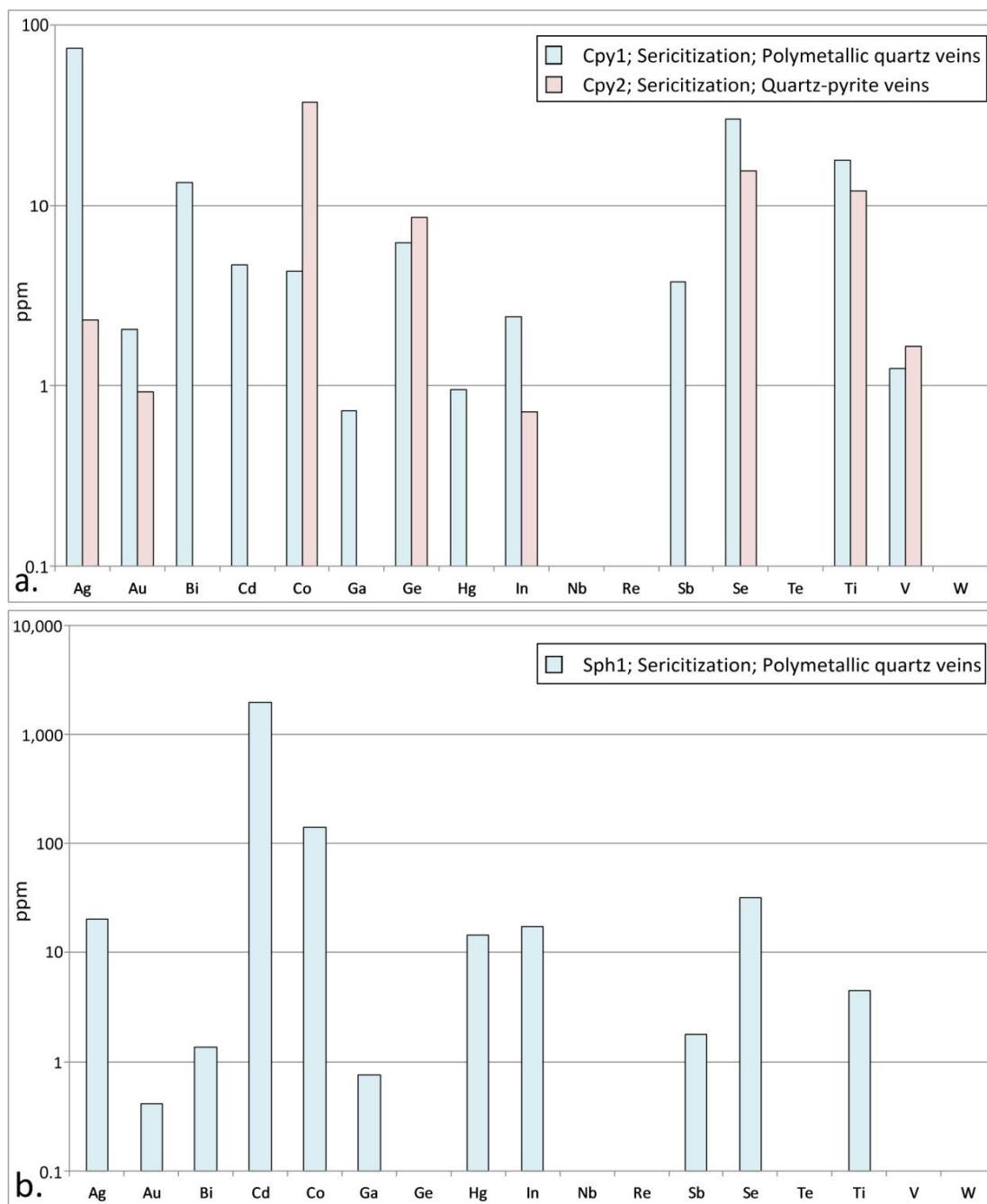


Figure 7.8. Average values of critical and rare metals contents of chalcopyrite (a) from the polymetallic quartz veins and the quartz-pyrite veins, and of sphalerite (b) from the polymetallic quartz veins. Local enrichments related to nano-scale mineral inclusions are excluded.

Contents of Zn (<746 ppm) and Pb (<23 ppm) in Cpy1 and of Pb (<1,697 ppm) and Mn (<1,063 ppm) in Cpy2 are ascribed to nano-scale mineral inclusions

(Supplement 2: Table S3-13). Critical and rare metals related to nano-scale mineral inclusions include Ag (<125 ppm), Bi (<25 ppm) and Sb (<2.8 ppm) in Cpy1, as well as Ag (<75 ppm), Bi (<229 ppm), Sb (<57 ppm), Th (<0.82 ppm) and U (<1.1 ppm) in Cpy2 (Supplement 2: Table S3-12).

Sphalerite (Sph1) from the polymetallic quartz veins exhibits enrichments in base metals including Cu (<1,060 ppm), Mn (<737 ppm) and Pb (<5.7 ppm) (Table 7.6). Critical and rare metals comprise Ag (<59 ppm), Au (<0.84 ppm), Bi (<2.6 ppm), Cd (<2,015 ppm), Co (<151 ppm), Ga (<0.81 ppm), Hg (<20 ppm), In (<20 ppm), Sb (<1.8 ppm), Se (<42 ppm) and Ti (<5.7 ppm) (Table 7.6, Figure 7.8b). Nano-scale mineral inclusions in Sph1 are related to Cu (<1,684 ppm), Pb (<128 ppm) and Bi (<15 ppm) (Supplement 2: Table S3-14).

7.3.6. Statistical analysis of trace elements concentrations

Pearson product-moment correlation coefficients for arsenopyrite, pyrite and chalcopyrite were calculated for Laodikino. Trace element concentrations related to nano-scale mineral inclusions were excluded before the statistical analyses.

Pearson product-moment correlation coefficients for arsenopyrite are defined by significant positive correlations ($p < 0.01$, value = 0.918) for the elemental pair Ag-Au (Supplement 3: Table S4-18). Positive correlations ($p < 0.05$, values > 0.665) include the pairs Ag-Co, Ag-Te and Au-Co (Supplement 3: Table S4-18). Negative correlations were not defined.

In pyrite, Pearson product-moment correlation coefficients are characterized by significant positive correlations ($p < 0.01$, values > 0.37) defined for the elemental pairs Au-Te, Bi-Hg and Co-Se (Supplement 3: Table S4-15). Positive correlations ($p < 0.05$, values > 0.304) were defined for Ag-Se and Hg-W, while negative correlations were not defined (Supplement 3: Table S4-15).

Chalcopyrite is described by significant positive correlations ($p < 0.01$, values > 0.749) including the elemental pairs Ag-In, Ag-Sb, Co-V, Hg-Ti, In-Sb, In-Se and Sb-Se (Supplement 3: Table S4-16). Positive correlations ($p < 0.05$, values > 0.564) were defined for the pairs Ag-Se, Bi-Sb and Bi-Se (Supplement 3: Table S4-16). Significant negative correlation ($p < 0.01$, value = -1.000) include the elemental pair Nb-W, and negative correlation ($p < 0.05$, value = -0.554) the pair In-V (Supplement 3: Table S4-16).

Sphalerite is characterized by significant positive correlations ($p < 0.01$, value = 0.792) defined for the elemental pair Ag-Au, and by positive correlation ($p < 0.05$, value = 0.633) for the pair Co-Sb (Supplement 3: Table S4-17). Significant negative correlations ($p < 0.05$, values > -0.803) for sphalerite include the elemental pairs Cd-V, Cd-W, Nb-W, Nb-W, Te-V and Te-W (Supplement 3: Table S4-17). Nevertheless, it should be mentioned that the Cd, V, W, Nb and Te contents are below detection limits in sphalerite.

7.4. Discussion

The polymetallic massive (>80 wt.% of ore, <10 cm in width) and quartz veins (<5 cm in width), as well as the quartz-pyrite veins (<5 cm in width) at Kolchiko are hosted in mica-schist (Table 7.1). The mineralization styles at Kolchiko were formed by various phases of hydrothermal fluids introduced in the region through distinct sets of faults, mainly between Eocene and Miocene, and under temperatures varying approximately between 240 and 444 °C. The mineralogical and textural characteristics of the polymetallic massive veins suggest that their formation initiated slightly before the onset of the retrograde greenschist facies metamorphism (M5 event: $T = 300-550$ °C, $P < 5$ kb, Kourou 1991, Kiliass et al. 1999). The formation of the polymetallic massive veins continued during the Eocene to early Oligocene post-collisional D4 deformation event under retrograde greenschist facies metamorphism and was coeval to the emplacement of the milky quartz-chlorite veins ($T = 304-328$ °C, chlorite geothermometry, Patsiouri 2017) and to the dolerite dikes (Kourou 1991). The dolerite dikes could have contributed in adjusting thermal conduits, forwarding hydrothermal fluid circulation, and the leaching and transportation of metals.

Later, the onset of the Oligocene-Miocene brittle deformation related to NW-trending normal faults, to NE-SW-trending normal to oblique, and to N-S-trending strike-slip faults induced hydrothermal fluids circulation and mixing with meteoric water, and created open spaces facilitating degassing, fluid pressure drop and mineral precipitation (Kiliass et al. 1999). Thus, the development of the polymetallic quartz veins and the quartz-pyrite veins could have been coeval with the onset of the late Oligocene to early Miocene dextral strike-slip fault zone along the western edge of the SMM. The development of this zone was associated with transpressional to transtensional tectonics and resulted in the SW-vergent thrusting of the Vertiskos Unit over the Permian-Lower Triassic quartzite of the CRB and the Oligocene-Miocene

molassic sediments of the Mygdonia graben (Kilias 2021, Figure 2.1, 7.1). Younger structures associated with Miocene to Pliocene normal faults (S43E/83°SW in average) are unrelated to mineralization and overprint all the previous mineralization stages and sets of faults. Thus, it is suggested that any significant mineralizing activity was terminated during Miocene. Similar formation conditions have been suggested for the adjacent Drakontio metamorphic- and quartz-hosted polymetallic vein mineralization and the Laodikino metamorphic and quartz hosted, shear-zone related, polymetallic vein mineralization (Thymiatis 1995, Vavelidis et al. 1999).

The textural characteristics of the polymetallic massive veins indicate the effect of metamorphism on the metallic minerals. Arsenopyrite and pyrite exhibit cataclastic textures and annealing (Figure 7.3a-c). Both minerals display 120° dihedral angles, while porphyroblasts are common. These textures are the simplest response of monomineralic masses of pyrite and arsenopyrite to thermal increase during metamorphism (Craig et al. 1998). In contrary, textures ascribed to metamorphism are absent from the metallic minerals accommodated in the polymetallic quartz veins and the quartz-pyrite veins (Figure 7.3d-f). The polymetallic quartz veins are characterized by open space filling textures as no directional relation is observed between quartz and metallic minerals (Figure 7.2e). Furthermore, the formation of the quartz-pyrite veins is associated with crack and seal processes as pyrite and minor chalcopyrite appear only along cracks in quartz and between quartz boundaries (Figure 7.2f, 7.3f). Locally, massive arsenopyrite is related to fracturing, opening and brecciation of pre-existing milky quartz veins (Figure 7.2d).

The average formation temperature for arsenopyrite is 398 °C ($T = 344$ °C to 444 °C after arsenopyrite geothermometry, Patsiouri 2017). High temperatures could favor the formation of cubanite, which instead is missing. According to Patsiouri (2017) the presence of chalcopyrite and pyrrhotite could be related to the transformation of cubanite under retrograde metamorphism. Lower temperatures varying between 235 and 271.5 °C are associated with the presence of galenobismuthinite and native bismuth (Patsiouri 2017). In addition, previous fluid inclusions study of quartz from the polymetallic massive veins held by Patsiouri (2017) revealed homogenization temperatures varying between 162 and 284 °C, with a maximum at 240 °C, and low salinities (5.1 to 14.2 wt.% NaCl equiv.). According to Patsiouri (2017) the nature of the studied fluid inclusions could not suggest the direct magmatic origin of the fluids associated with the ore assemblages in Kolchiko. Nevertheless, the absence of fluid

inclusions consisting of CO₂ and CH₄, also excludes the direct relation to metamorphic fluids (Patsiouri 2017). Similar homogenization temperatures with a maximum at 230 °C, and low salinities (4 to 12 wt.% NaCl equiv.) are also reported from the Stanos shear-zone hosted Cu-Au-Bi-Te mineralization (Bristol et al. 2015, Figure 2.2). At Stanos the ore mineralization is associated with proximal or distal intrusions and extension-related shearing set under upper greenschist to lower amphibolite facies metamorphism (Bristol et al. 2015).

The bulk geochemical analysis of the mineralized veins, the pegmatite, and the hydrothermally altered and oxidized metamorphic rocks reveal similar distribution patterns including specific enrichments (Figure 7.4). The hydrothermal fluids related to the formation of the polymetallic massive veins were initially saturated in As, Fe and S, resulting in the formation of arsenopyrite- and pyrite- dominated veins. This process was subjected to specific physico-chemical conditions. The absence of arsenic sulfides (e.g. realgar, orpiment) suggests that As massively precipitated along with Fe and S in temperatures exceeding 300 °C, and further complements the reported temperatures (Pokrovski et al. 2002, Patsiouri 2017). In continuous, the residual amount of As precipitated in arsenian pyrite in the pyrite-dominated polymetallic massive veins. Pyrite with As contents exceeding 1 wt.% is commonly referred to as arsenian pyrite with formation temperatures varying between 250 and 300 °C (Wells and Mullens 1973, Pokrovski et al. 2002, Stepanov et al. 2021).

The polymetallic massive veins are enriched in Au (<9.2 ppm), Ce (<20 ppm), La (<12 ppm), U (<2.5 ppm) and W (<844 ppm) (Table 7.2, Figure 7.4). Gold precipitation was significantly controlled by As precipitation. Arsenopyrite (Apy1) incorporates up to 3.5 ppm Au, pyrite (Py2) (arsenian pyrite) includes up to 1.3 ppm Au, while Py1 contains up to 0.59 ppm Au (Table 7.4, 7.5). Uranium is related to uraninite found along with zircon in pyrite from the polymetallic massive veins (Patsiouri 2017). Cerium and La are not associated to Apy1, Py1 and Py2, as REE were not detected in arsenopyrite and pyrite, and are not commonly hosted in these minerals (Deditius et al. 2011, Li et al. 2019, Figure 7.7). Thus, Ce and La contents could be ascribed to trace minerals, such as titanite (Xu et al. 2015). W is absent from Apy1 and may be related to Py2 (Figure 7.7).

The hydrothermal fluids associated with the polymetallic quartz veins mainly included Fe, Cu, As, Pb and Zn resulting in the precipitation of pyrite, chalcopyrite, arsenopyrite, galena and sphalerite. Pyrrhotite is found as inclusions in pyrite

reflecting shifts in fO_2/fS_2 conditions of the mineralizing fluids. The polymetallic quartz veins are more enriched in critical and rare metals compared to the polymetallic massive veins. Enrichments in Bi (<995 ppm), Ag (<23 ppm) and Te (<3 ppm) are ascribed to the occurrence of native bismuth, hessite and tellurobismuthite (Table 7.2, Figure 7.4). In a minor extent they are incorporated in pyrite (Py3), chalcopyrite (Cpy1) and sphalerite (Sph1) (Figure 7.7b, 7.8a,b). In addition, the Cd (<14 ppm), Co (<320 ppm), Ga (<2.4 ppm) and In (<0.44 ppm) could be related to pyrite and sphalerite mineral chemistry. Pyrite (Py3) contains up to 623 ppm Co, while sphalerite (Sph1) is a major host of Cd (<2,015 ppm), Ga (<0.81 ppm) and In (<20 ppm) (Table 7.5, 7.6).

The hydrothermal fluids related with the formation of the quartz-pyrite veins were mainly associated with Fe and minor Cu contents. Pyrite (Py4) is the main metallic mineral, while chalcopyrite occurs in traces (Figure 7.3f). The critical and rare metals contents are more depleted compared to those of the other mineralization styles (Figure 7.4). The spiky patterns for Au, Bi, Co, Hg, Sb and Te reported from bulk geochemistry are indicative of the nature of the mineralizing fluids (Figure 7.4). Pyrite (Py4) incorporates the highest concentrations of Bi (<4 ppm), Co (<2,155 ppm) and Hg (<0.81 ppm) among the examined pyrites (Figure 7.7b). The Sb (<183 ppm) content in the quartz-pyrite veins is the second most enriched among the analyzed samples, while Te (<0.12 ppm) is slightly more enriched than the background values of the hydrothermally altered and oxidized metamorphic rocks (Figure 7.4). Antimony (<8.1 ppm) is incorporated in Py4 and is missing from Cpy2, while Te is below detection limit in Py4 and Cpy2 (Table 7.5, 7.6).

Pitcrain et al. (2006) have shown that the mobility of trace elements including Au, Ag, As, Sb, Hg, Cd, Mo and W is affected by the grade of metamorphism. Under upper greenschist to amphibolite metamorphic facies they can be efficiently leached from the metamorphic rocks and mobilized for significant distance. In addition, Au, Cd, Hg and Sb can also be leached under low greenschist facies metamorphism (Pitcrain et al. 2006). Thus, the enrichment of these trace elements, especially in the polymetallic massive veins (e.g. Au, W), through metamorphic processes could not be excluded. Nevertheless, the metal association of Cu, Pb, Bi, Co, In, Se and Te support that intrusion-related hydrothermal fluids participated in the mineralizing fluids as this was documented in Stanos mineralization, which shares similar characteristics with Kolchiko (Voudouris et al. 2007, 2013c, Bristol et al. 2015).

In Greece, the telluride and bismuth sulfosalt mineralizations associated with gold are subdivided in three groups (Voudouris et al. 2007): a) Bi-sulfosalts and native gold without tellurides, b) Bi-tellurides accompany Bi-sulfosalts, native bismuth and gold, and c) Au-Ag-tellurides without Bi-tellurides and Bi-sulfosalts. The presence of galenobismuthinite, hessite, tellurobismuthite, as well as native bismuth and gold at Kolchiko, suggest that the mineralization belongs to the second category. Furthermore, tellurobismuthite (Bi_2Te_3 , $\text{Bi}:\text{Te}<1$) indicates oxidizing conditions during the formation of the polymetallic quartz veins (Voudouris et al. 2007).

7.4.1. Mineral chemistry of arsenopyrite and pyrite and nano-scale inclusions

Arsenopyrite (Apy1) is characterized by depleted contents of base (Cr, Cu, Mn, Ni, Pb), as well as of critical and rare metals (Co, Sb, Se, Ti, Te, Au, Ag, Hg, Tl), which may be lattice bound or incorporated as nanoparticles in growth zones (Table 7.4, Figure 7.7a). In addition, Pearson product-moment correlation coefficients support that the incorporation of Au-Co, as well as of Ag-Au, Ag-Co and Ag-Te is significantly coeval.

Nano-scale inclusions related to Bi and Pb are found in arsenopyrite (Supplement 2: Table S3-11). On the basis of the associated ore mineralogy they could be ascribed to galenobismuthinite (Table 7.1, Figure 7.9a).

Pyrite (Py1-4) from the various mineralization stages is associated with variable contents of base, critical and rare metals (Table 7.1, 7.5). Base metals include As, Zn and Sn in Py2, Mn and Cr in Py3, and Ni, Pb and Cu in Py4 (Table 7.5). Arsenic exceeding 1 wt.% reflects the presence of arsenian pyrite in Py2 from the pyrite-dominated polymetallic massive veins (Table 7.5). Critical and rare metals incorporated in pyrite lattice include Ag, Au, Sb, Se and Ti in Py1, Ag, Au, Bi, Co, In, Sb, Se, Te, Ti, V and W in Py2, Ag, Au, Bi, Co, Hg, Sb, Se, Ti and W in Py3, and Ag, Bi, Co, Hg, Sb, Se, Ti, V and W in Py4 (Table 7.5, Figure 7.7b). The arsenian pyrite from the Py2 group contains the highest concentrations of Au (<1.3 ppm) incorporated in crystal lattice (Table 7.5).

The concentrations of trace elements including Bi, Cu, Pb, Sb and Tl in Py1, Ag, As, Bi, Cu, In, Pb, Sb, Sn and Zn in Py2, Ag, Bi, Cu, Pb, Sb and Zn in Py3, and Bi and Cu in Py4, in comparison to their time-resolved laser ablation ICP-MS depth profiles indicate the presence of nano-scale mineral inclusions in pyrite from the various mineralization styles (Supplement 2: Table S3-12). It could be suggested that

these inclusions are mostly related to galena and native bismuth (Py1, Py3), and to galenobismuthinite (Py1, Py2) (Figure 7.9b-d). In Py4, nano-scale inclusions could be related to chalcopyrite.

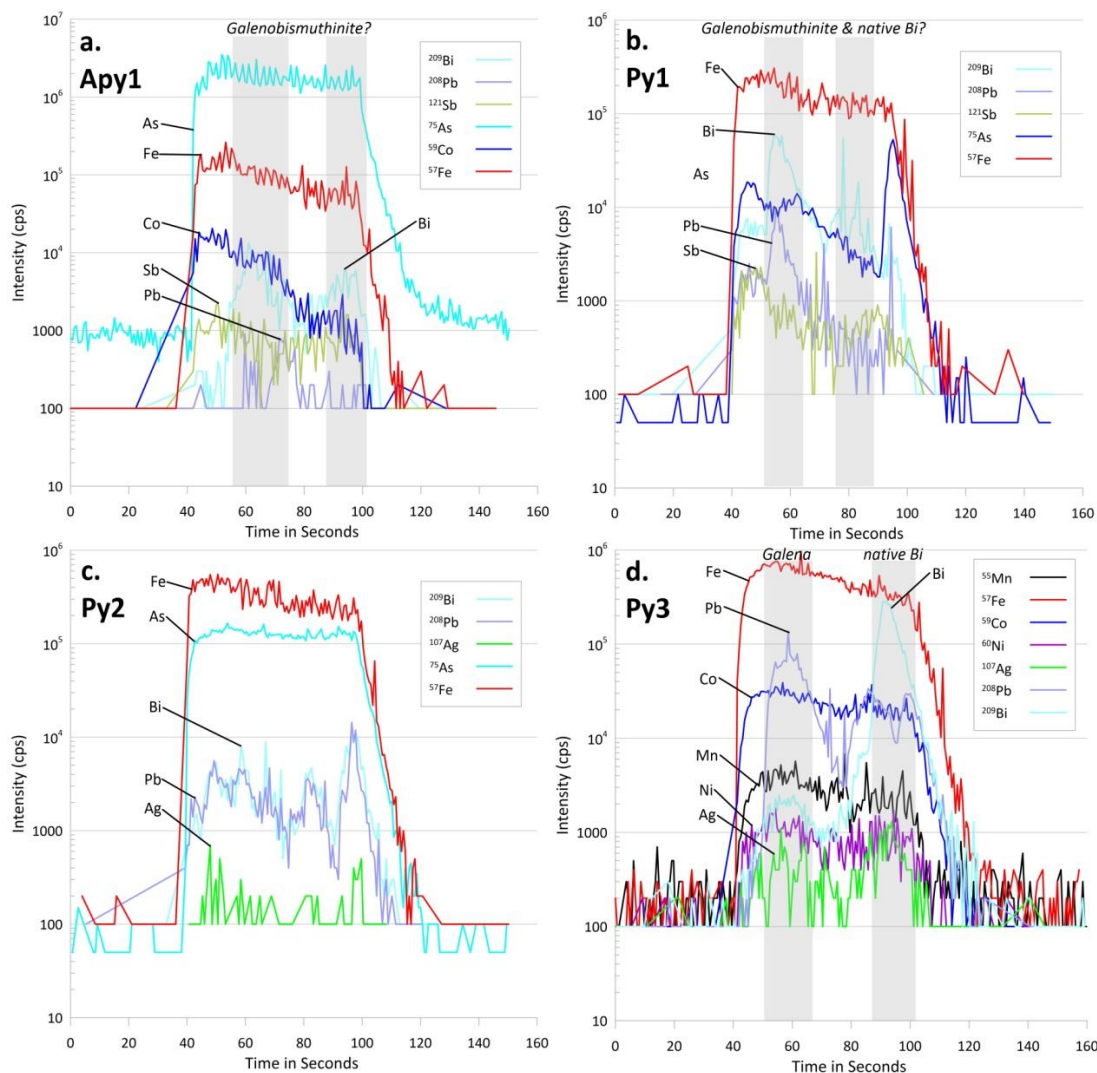


Figure 7.9. Selected time-resolved laser ablation ICP-MS depth profiles of arsenopyrite (Apy1) and pyrite (Py1, Py2, Py3) from the polymetallic massive and quartz veins at Kolchiko. Nano-scale mineral inclusions are highlighted in gray. a. In Apy1, the ablation patterns of Fe, Co and Sb exhibit similar distribution to Fe, while the ablation patterns of Bi and Pb suggest the occurrence of nano-scale inclusions in Apy1 most possibly related to boulangerite. b. In Py1, the spiky patterns of Bi and Pb indicate the presence of galenobismuthinite and/or native Bi. The ablation patterns of As and Sb are variable and locally spiky suggesting the variable incorporation of these trace elements in Py1. c. In Py2, the distribution patterns of Fe and As are similar highlighting the As-rich character of the pyrite. The ablation patterns of Bi, Pb and Ag are similarly variable across the plot area, supporting the occurrence of Ag-rich galenobismuthinite and/or galena nano-scale inclusions in Py2. d. In Py3, the

distribution patterns of Fe, Co, Mn and Ni are similar suggesting that these elements are hosted in the pyrite lattice. The distinct spiky patterns of Pb, Bi and Ag emphasize the occurrence of Ag-rich galena and native bismuth nano-scale inclusions.

7.4.2. Mineral chemistry of chalcopyrite and sphalerite and nano-scale inclusions

Base metals in chalcopyrite from Kolchiko include As, Cr, Mn, Pb and Zn in Cpy1, and Ni and Sn in Cpy2 (Table 7.6). In Cpy1, critical and rare metals comprise Ag, Au, Bi, Cd, Co, Ga, Ge, Hg, In, Sb, Se, Ti and V, whereas in Ag, Au, Co, Ge, In, Se, Ti and V are found in Cpy2 (Figure 7.8a). These elements are incorporated in chalcopyrite lattice.

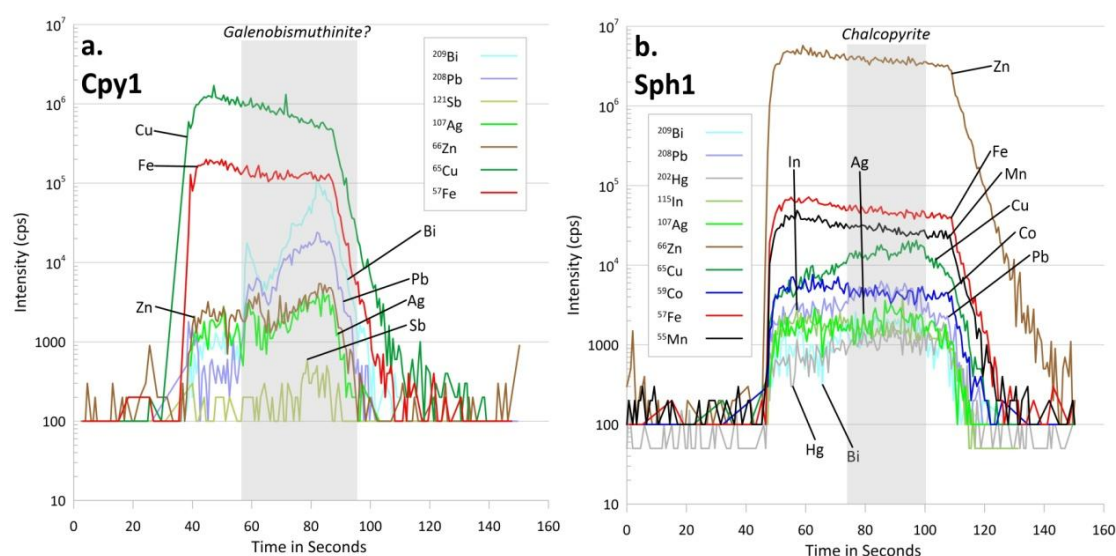
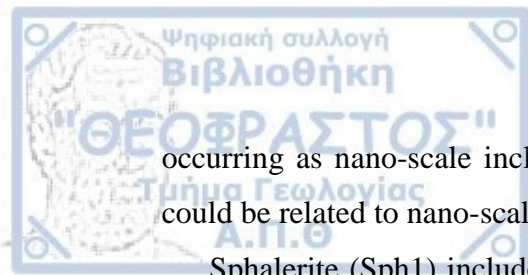


Figure 7.10. Selected time-resolved laser ablation ICP-MS depth profiles of chalcopyrite (Cpy1) and sphalerite (Sph1) from the polymetallic quartz veins at Kolchiko. Associated nano-scale inclusions are highlighted in gray. a. In Cpy1, the spiky distribution patterns Bi and Pb indicate the occurrence of galenobismuthinite nano-inclusions in chalcopyrite. Zinc, Ag and Sb are incorporated both in chalcopyrite and in galenobismuthinite. b. In Sph1, the distribution patterns of Cu, Fe, Mn, Co and In are similar suggesting that these elements are included in sphalerite. The curved patterns of Cu, Pb, Ag, Hg and Bi indicate that these elements are hosted both in Sph1 and in nano-scale inclusions of chalcopyrite.

In contrary, the concentrations of specific trace elements and their time-resolved laser ablation ICP-MS depth profiles suggest that chalcopyrite hosts nano-scale mineral inclusions (Supplement 2: Table S3-13). In Cpy1, variable contents of Zn, Pb, as well as of Ag, Bi and Sb are ascribed to sphalerite and galenobismuthinite



occurring as nano-scale inclusions (Figure 7.10a). In Cpy2, elevated contents of Pb could be related to nano-scale galena inclusions.

Sphalerite (Sph1) includes base metals (Cu, Mn, Pb), and critical and rare metals (Ag, Au, Bi, Cd, Co, Ga, Hg, In, Sb, Se, Ti) (Table 7.6, Figure 7.8b). The trace elements are incorporated in Sph1 as solid solutions. Nano-scale mineral inclusions are hosted in Sph1 and they are related to elevated contents of Cu, Pb and Bi suggesting the occurrence of chalcopyrite and galena (Supplement 2: Table S3-14, Figure 7.10b).

CHAPTER 8. ASPRA CHOMATA PORPHYRY-EPITHERMAL MINERALIZATION

8.1. Local geology

The Aspra Chomata porphyry-epithermal mineralization is associated with the Stratoni granodiorite (Figure 8.1). The Stratoni granodiorite is a NE-elongated magmatic intrusion located north of the Stratoni fault zone in NE Chalkidiki (Siron et al. 2016, Figure 8.1). The Stratoni fault zone (WNW-ESE-trending normal to oblique faults; approx. 12 km in length) is the major tectonic feature, which fragments the Chalkidiki block and separates the Kerdylion Unit (Rhodope Massif) to the north from the Vertiskos Unit (Serbo-Macedonian Massif) to the south (Kydonakis et al. 2016, Figure 8.1). Another regional major structure is the Megali Panaghia-Gomati fault (Figure 2.2).

The metamorphic rocks at the footwall of the Stratoni fault zone include mainly migmatitic gneiss, biotite gneiss, and granite gneiss, as well as intercalated lenses of marble and amphibolite belonging to the Kerdylion Unit (Siron et al. 2018, Figure 8.1). The hanging wall consists mainly of two-mica gneiss and schist, which are intercalated with amphibolite, calc-schists, and marble of the Vertiskos Unit (Siron et al. 2018, Figure 8.1). Along the Stratoni fault zone, as well as on the hanging wall, amphibolite, gabbro, and serpentized peridotite are found. These rocks are related to Triassic rifting that resulted in the opening of the Vardar Ocean (Thermes-Volvi-Gomati complex after Dixon and Dimitriadis 1984, Siron et al. 2016, Figure 8.1). These rocks were formed in an intracontinental rift or back-arc environment above an active subduction and were incorporated in the Vertiskos and Kerdylion Units during the later Alpine Orogeny (Dixon and Dimitriadis, 1984; Himmerkus et al. 2006).

Siron et al. (2018) describe three deformation events affecting the metamorphic rocks of the area. The D1 deformation event is characterized by a locally preserved compositional layering found in gneiss and marble at the northern part of the area. This layering is transformed to a penetrative S1 gneissosity affecting the late Paleocene to Eocene (58 Ma) granodiorites of the area (Siron et al. 2018, Figure 8.1). An amphibolite facies metamorphism is concurrent to the D1 deformation event (Siron et al. 2018). Pegmatites related to metamorphism occur parallel to the gneiss layering and as dikes crosscutting the metamorphic rocks (Siron et al. 2018). In addition, the D1 deformation event is related to the fold geometry occurring at the

footwall of the Stratoni fault zone, as well as to a broad anticlinorium at the hanging wall southwards of the fault zone (Siron et al. 2018).

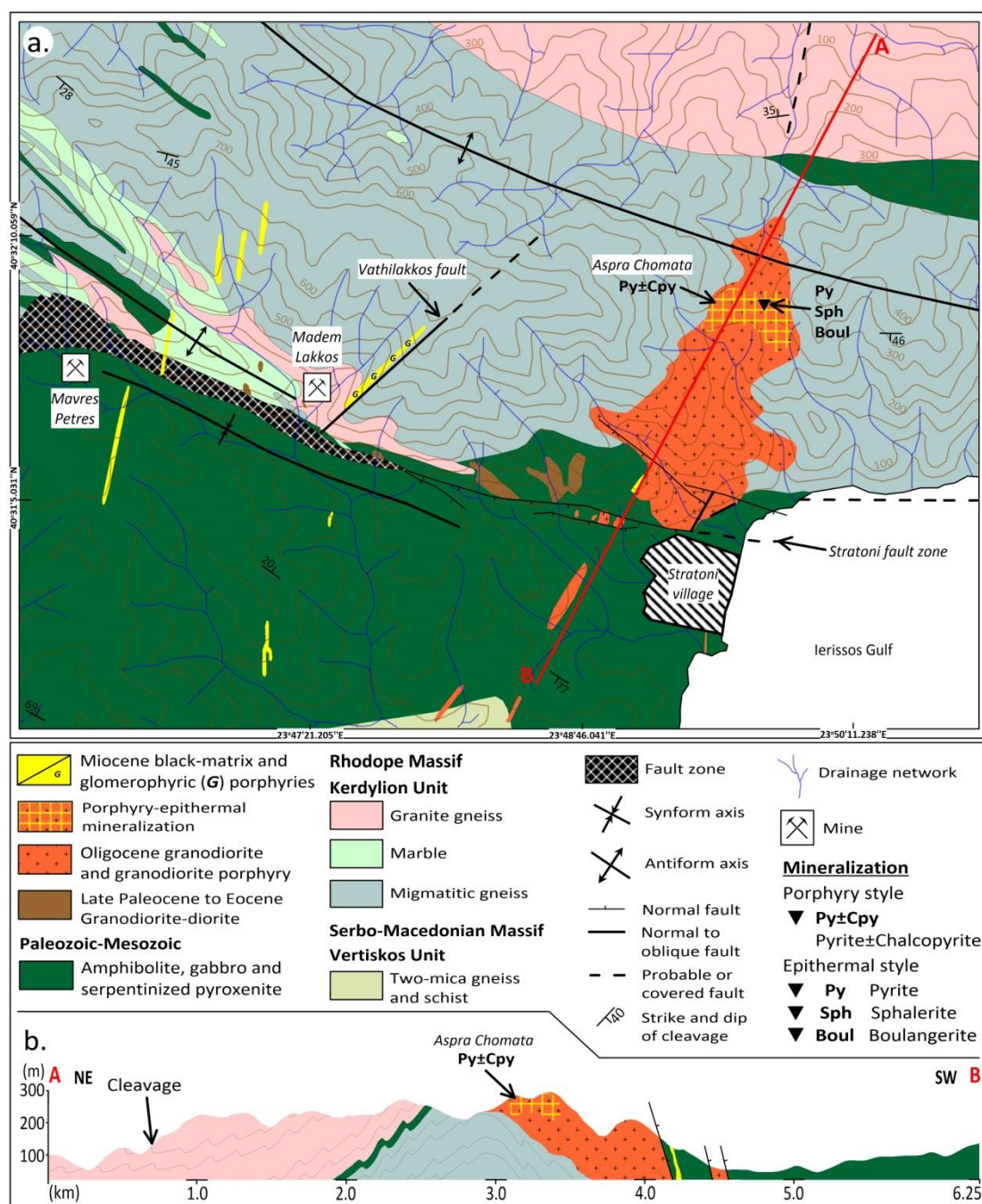


Figure 8.1. a. Geological map of the Stratoni and Mavres Petres area showing the location of the Aspra Chomata porphyry deposit and epithermal vein mineralization. b. Cross section of the Stratoni granodiorite and the Aspra Chomata deposit (modified after Siron et al. 2016, Siron et al. 2018).

The D2 deformation event overprinted the S1 foliation and developed the S2 ductile fabric under upper greenschist- to lower amphibolite-facies metamorphism

(Siron et al. 2018). Open to tight folds with inclined to near-recumbent axial planes are related to the D2 event (Siron et al. 2018). The D3 deformation event superimposed the S3 fabric related to pressure solution cleavage in marble and to cleavage domains wrapping S1 and S2 foliation and anastomosing fractures in schist and gneiss (Siron et al. 2018). Furthermore, the D3 event is associated with the local development of kink folds (Siron et al. 2018).

A subsequent event developing moderate- to shallow-dipping ductile mylonitic to protomylonitic shear zones is described by Siron et al. (2018). These mylonitic shear zones postdate S1 and S2 metamorphic fabrics and accommodate a greenschist-facies related mineral assemblage, including muscovite and chlorite (Siron et al. 2018). In addition, pegmatites and granite dikes and sills are found in the mylonitic shear zones (Siron et al. 2018). Two ductile kinematic phases have been described and include an older contractional event and a younger extensional event (Siron et al. 2018).

The Stratoni fault zone, initially acting as a mylonitic normal fault under SW-directed ductile extension, was later overprinted by synmineral semibrittle faults (Siron et al. 2018). During this stage, deformation rate was accelerated by hydrothermal fluids, which were introduced along the fault planes and developed a distinct shear-related foliation (Siron et al. 2018). Brittle deformation in the area includes the following sets of faults: 1) late Oligocene to early Miocene ENE-WSW-trending, synmineral, faults demonstrating E-W extension, 2) middle to late Miocene postmineral faults related to NE-SW-directed extension (e.g. Vathilakkos strike-slip fault, Figure 8.1), and 3) late Quaternary faults related to the N-S extension and active tectonism (Kilias et al. 1999, Pavlides et al. 2010, Siron et al. 2018).

Post-collisional Cenozoic magmatic rocks at NE Chalkidiki occur mainly along a NE-trending belt (<10 km in width) covering an area of approximately 484 km², which is outlined by the Stratoni and Megali Panaghia-Gomati fault zones (Gilg and Frei 1994, Hahn et al. 2012, Siron et al. 2016, 2018, 2019). Two Cenozoic igneous suites are identified in the area, reflecting two distinct post-collisional magmatic episodes, a late Oligocene and an early Miocene episode (Siron et al. 2018). The late Oligocene igneous suite, includes monzogabbros and granodiorites clustered in the Tsikara composite stock (27.0 ± 0.2 to 26.7 ± 0.3 Ma), and in the Stratoni granodiorite stock and the Fisoka porphyritic diorite stock (25.7 ± 0.4 to 24.5 ± 0.1 Ma) (Siron et al. 2016). The early Miocene igneous suite comprise the Skouries quartz monzonite porphyry stock (20.6 ± 0.5 Ma, Figure 2.2), the highly potassic glomerophyric

porphyry dikes crosscutting the Stratoni fault zone and the Olympias deposit (Figure 8.1), the barren Asprolakkos quartz monzonite porphyry (19.7 ± 0.1 Ma, Figure 2.2), the trachyandesite black-matrix porphyries crosscutting the Madem Lakkos deposit, and the glomerophytic dikes intruding the Vathilakkos fault (19.6 ± 0.1 Ma) (Gilg and Frei 1994, Hahn et al. 2012, Siron et al. 2016, 2018, 2019, Figure 8.1). Both igneous suites exhibit high-K calc-alkaline affinities. The igneous suite related to the early Miocene episode includes also a more evolved shoshonitic fragment (Kroll et al. 2002).

The Stratoni granodiorite outcrops in an area of approximately 1.5 km^2 and includes also a minor porphyritic phase at Aspra Chomata (Gilg and Frei 1994, Figure 8.2a). This porphyritic phase is exposed at the northern and topographically highest part of the intrusion and is characterized by granodiorite porphyry (Gilg and Frei 1994, Siron et al. 2016, Figure 8.1). The granodiorite stock intruded the footwall of the Stratoni fault zone along a south-dipping limb of an antiform (Siron et al. 2016). The metamorphic rocks include a sequence of biotite gneiss, amphibolite, and marble of the Kerdylion Unit (Siron et al. 2016). The contact between the granodiorite and metamorphic rocks is sharp and discordant to metamorphic foliation. The granodiorite is barren and a restricted calc-silicate skarn occurs at the western contact of the granodiorite within the gneiss (Siron et al. 2016).

The granodiorite has a crystallization age of 25.36 ± 0.15 Ma ($^{206}\text{Pb}/^{238}\text{U}$ zircon dating, Siron et al. 2016), while the granodiorite porphyry was dated at 24.53 ± 0.31 Ma ($^{206}\text{Pb}/^{238}\text{U}$ zircon dating, Siron et al. 2016). This porphyritic phase includes also zircons yielding an age of 25.78 ± 0.31 Ma ($^{206}\text{Pb}/^{238}\text{U}$ zircon dating), which are considered to be inherited by the granodiorite (Siron et al. 2016).

The Stratoni granodiorite is a fine to medium grained rock exhibiting equigranular to weakly porphyritic texture and including minor diorite phases (Kalogeropoulos et al. 1990, Siron et al. 2016). It consists of K-feldspar, plagioclase, biotite, and minor clinopyroxene, with accessory zircon, apatite, titanite and magnetite, set in a quartz-feldspar groundmass (Siron et al. 2016). The granodiorite porphyry consists of quartz, plagioclase, K-feldspar and biotite (Gounaris 2017).

In the Stratoni granodiorite the hydrothermal alteration mineral assemblage consists of chlorite, sericite, epidote, titanite and calcite (chloritic-sericitic alteration, advise also Table 8.1) (Siron et al. 2016). Metallic minerals include disseminations of pyrite and traces of chalcopyrite (Siron et al. 2016). At the southern part of the

granodiorite stock, near the Stratoni fault zone, mineralized veins with pyrite and galena are found (Siron et al. 2016).

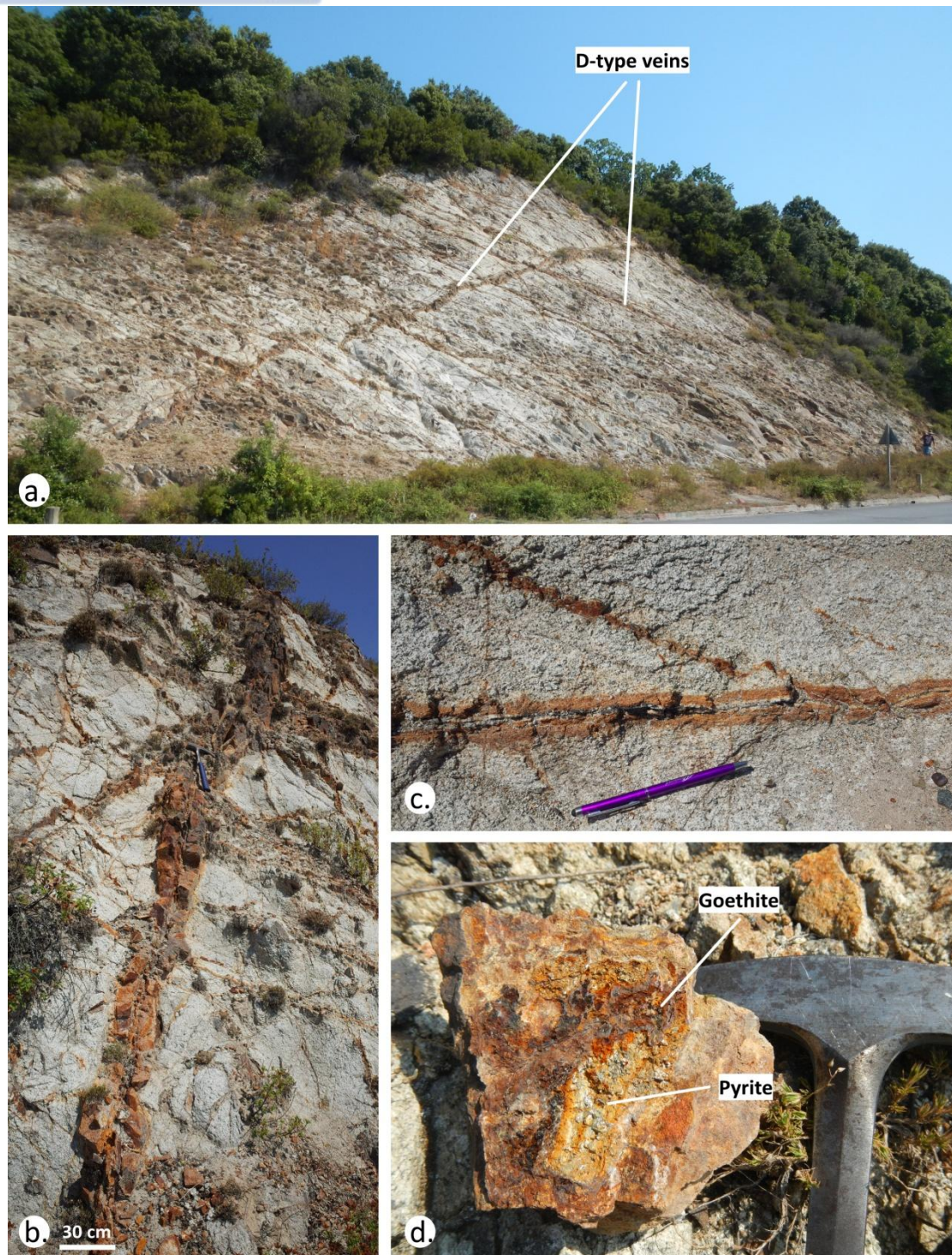


Figure 8.2. a. D-type veins with oxidized mineralization, crosscutting the hydrothermally altered granodiorite porphyry at Aspra Chomata. b. Intersecting D-type veins enveloped in alteration salvage. c. A branched D-type vein with quartz and oxidized mineralization in the inner part. d. Pyrite aggregate and goethite in a D-type vein.

8.2. Alteration styles and mineralization stages

Porphyry and epithermal mineralization stages occur at Aspra Chomata. The porphyry stage is related to potassic, chloritic-sericitic, and sericitic alterations, while the epithermal stage is associated with argillic alteration (Table 8.1). The potassic alteration at Aspra Chomata corresponds to an early and restricted hydrothermal stage, which was followed by chloritic-sericitic and sericitic (D-type veins) alterations (Figure 8.3a-c). The epithermal stage is associated to a late overprint (Gounaris 2017, Figure 8.3d). The ore mineral assemblages ascribed to these alterations include: (1) pyrite \pm chalcopyrite (potassic alteration), (2) pyrite (chloritic-sericitic and sericitic alterations), and (3) pyrite + sphalerite + boulangerite \pm arsenopyrite \pm galena \pm chalcopyrite \pm tetrahedrite (epithermal overprint) (Table 8.1).

Table 8.1. Summary of the typology, alteration and textural characteristics of the mineralization stages found at the Stratoní granodiorite stock and at Aspra Chomata.

Mineralization stage	Alteration style	Host rock	Mineralization texture	Metallic assemblage	Alteration assemblage	Reference
Porphyry	Potassic (overprinted by chloritic-sericitic)	Granodiorite porphyry	Disseminations	Py ± Cpy	Bt + Qz ± Rt	Gounaris (2017), this study
	Chloritic-sericitic	Granodiorite	Disseminations	Py ± Cpy	Chl + Ser + Ep + Ttn + Cal	Siron et al. (2018)
			Quartz veins	Py + Gn		
	Chloritic-sericitic	Granodiorite porphyry	Disseminations	Py	Chl + Ser + Qz + Rt + Cal	Gounaris (2017), this study
	Sericitic		Disseminations	Py	Ser + Qz	
D-type veins			Py	Ser + Qz		
Epithermal	Argillic	Granodiorite porphyry	Epithermal veins	Py + Sph + Boul ± Apy ± Gn ± Cpy ± Ttr	Kln	
Supergene oxidation	Oxidized mineralization		Encrustations and masses	Gt +Mal	-	

Abbreviations: Apy = arsenopyrite, Boul = boulangerite, Bt = biotite, Cal = calcite, Chl = chlorite, Cpy = chalcopyrite, Ep = epidote, Gn = galena, Kln = kaolinite, Py = pyrite, Qz = quartz, Rt = rutile, Ser = sericite, Sph = sphalerite, Ttn = titanite, Ttr = tetrahedrite.

Potassic alteration consists of secondary biotite, quartz, and minor chlorite, kaolinite and rutile (Figure 8.3a, 8.4a). The potassic alteration in the granodiorite porphyry is weak and includes pyrite disseminations (<200 μ m in length), with minor chalcopyrite (Gounaris 2017). Potassic alteration was overprinted by chloritic-sericitic alteration.

The chloritic-sericitic alteration includes chlorite, sericite, quartz, rutile and calcite (Figure 8.3b, 8.4b,c). In addition, epidote and titanite occur in the granodiorite (Table 8.1). The chloritic-sericitic alteration overprints the potassic alteration, and results in

the replacement of magmatic plagioclase by sericite and of hydrothermal biotite by chlorite and rutile. Pyrite is the only metallic mineral in the granodiorite porphyry, while minor chalcopyrite also occurs in the granodiorite. The chloritic-sericitic alteration is characterized by continuous quartz veins (<2 cm in width) with minor chlorite and calcite in the granodiorite (Figure 8.3b). Furthermore, quartz veins with pyrite and galena occur in the granodiorite (Siron et al. 2016).

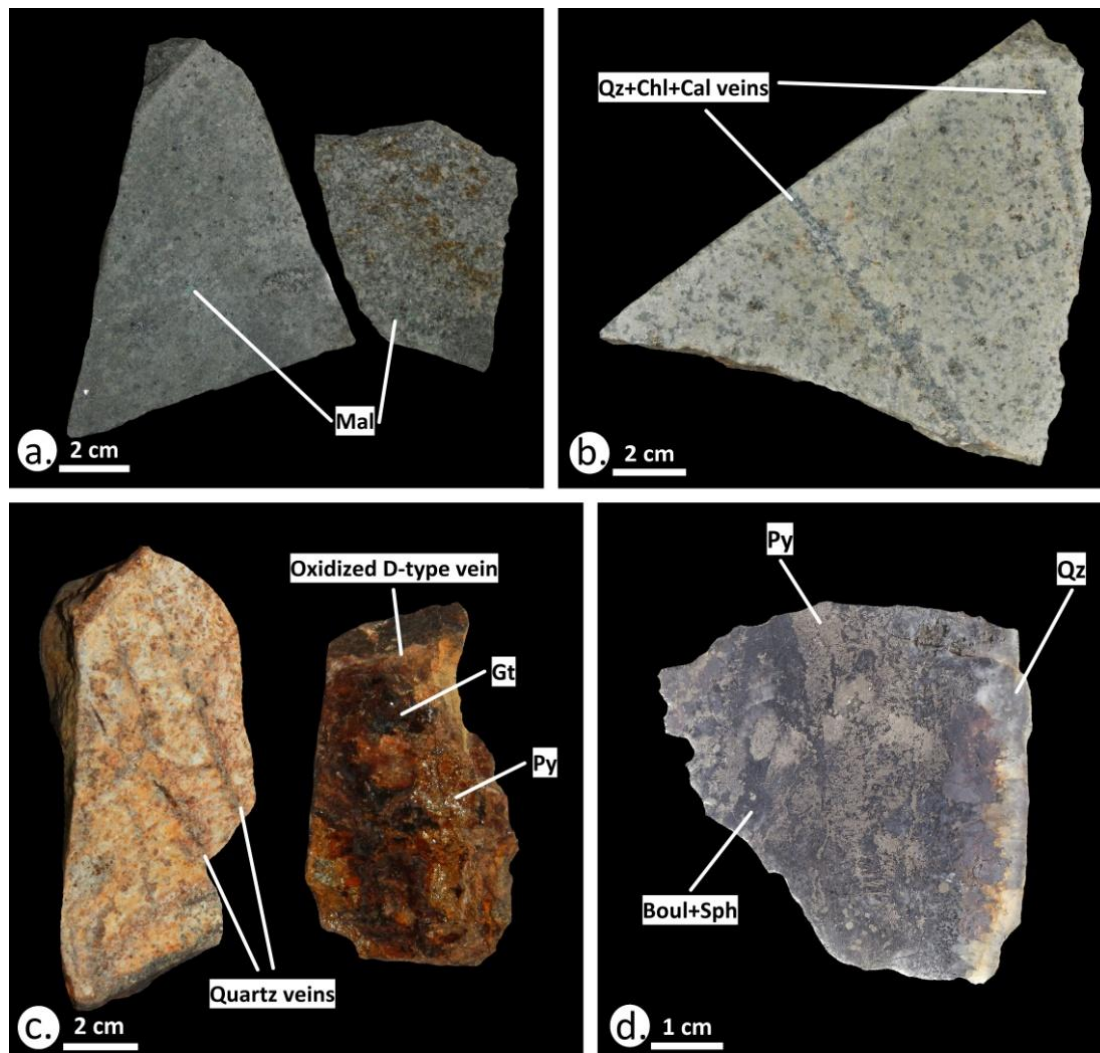


Figure 8.3. Mineralization stages and alteration styles from Aspra Chomata. a. Malachite impregnations in the granodiorite porphyry showing potassic overprinted by chloritic-sericitic alteration. b. Hydrothermal veins related to chloritic-sericitic alteration with quartz (Qz), chlorite (Chl), and calcite (Cal) crosscutting the granodiorite porphyry. c. Quartz D-type veins associated with sericitic alteration, with pyrite mineralization partly oxidized to goethite (Gt). d. Epithermal quartz (Qz) vein containing pyrite (Py), boulangerite (Boul), and sphalerite (Sph).

The sericitic alteration in the granodiorite porphyry comprises sericite and quartz (Gounaris 2017, this study, Figure 8.3c, 8.4d). Mineralization in sericitic alteration forms pyrite disseminations and aggregates (<1 cm in length), and D-type veins (Figure 8.2a-d). The D-type veins (<30 cm in width) are continuous, sharp-edged, mainly sheeted and sometimes perpendicular (Figure 8.2a,b), or form a network in the granodiorite porphyry (Figure 8.2b, 8.3c). At the northwestern part of the granodiorite porphyry the quartz and the D-type veins extend in the surrounding metamorphic rocks only for a few meters.

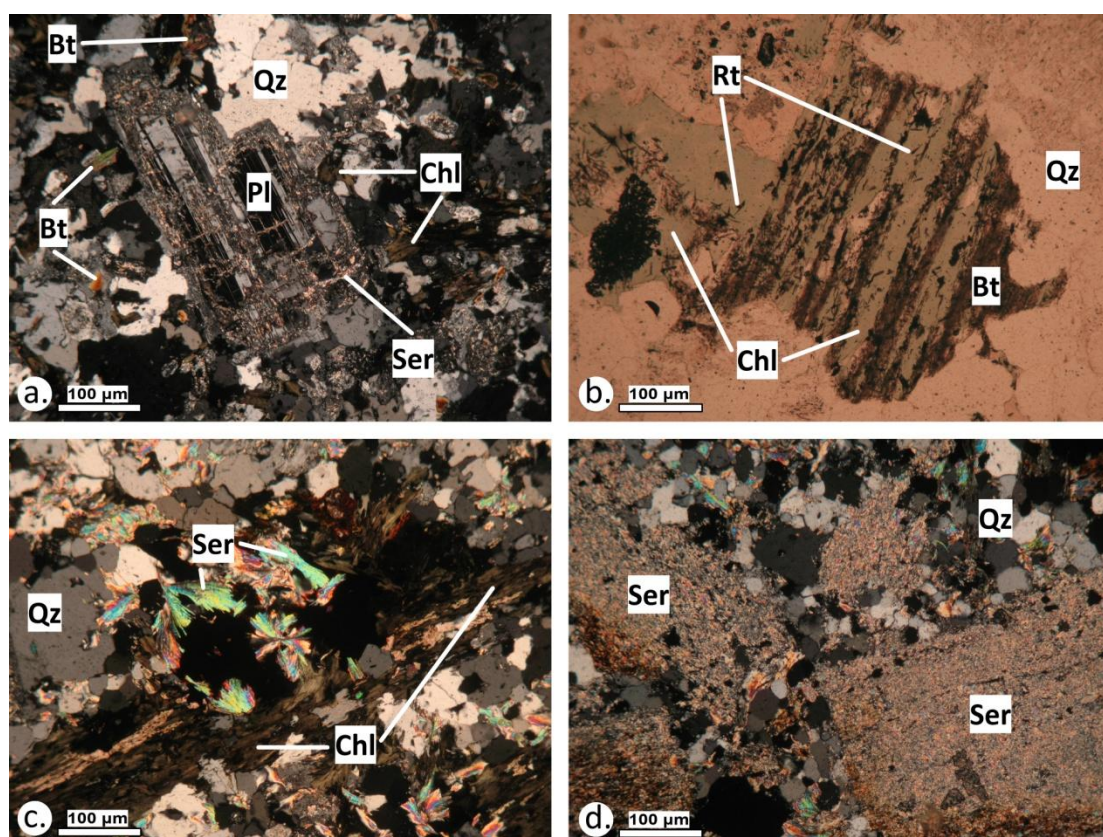


Figure 8.4. Photomicrographs of textures and minerals of the hydrothermal alterations in granodiorite from Aspra Chomata (cross polarized light: a,c,d, plane polarized light: b). a. Quartz (Qz), and plagioclase (Pl) replaced by sericite (Ser), and hydrothermal biotite (Bt) replaced by chlorite (Chl) from the potassic alteration overprinted by chloritic-sericitic alteration. b. Magmatic biotite (Bt) altered to chlorite (Chl) and rutile (Rt), from the chloritic-sericitic alteration. c. Quartz (Qz), chlorite (Chl) and sericite (Ser) in a hydrothermal vein from the chloritic-sericitic alteration. d. Sericite (Ser) in altered K-feldspars, and quartz (Qz) from the sericitic alteration.

The epithermal overprint is documented locally at the northern part of the porphyry system and includes base metal sulfide and quartz veins (Siron et al. 2016, Gounaris 2017, this study, Figure 8.1, 8.3d). Intense bleaching of the wall rocks and kaolinite are ascribed to argillic alteration. The epithermal stage is characterized by polymetallic quartz veins in the granodiorite porphyry. They are up to 10 cm in width, massive (>80 wt.% of ore), continuous, sharp-edged and branched in shapes (Figure 8.3d). The mineral assemblage contains pyrite, sphalerite, boulangerite, and minor arsenopyrite, galena, chalcopyrite and tetrahedrite (Table 8.1, Figure 8.5a-f). Quartz occurs as gangue mineral. It cements the ore minerals and forms combs on the walls of the veins (Table 8.1, Figure 8.3d, 8.5a-f).

The surface of the granodiorite porphyry affected by the hydrothermal alteration and supergene processes is clay-rich and the mineralization is oxidized. Malachite impregnations are usually found due to the oxidation of chalcopyrite (Figure 8.3a), while goethite and hematite are related to the oxidation of pyrite.

8.3. Analytical results

8.3.1. Bulk geochemical analysis

Six surface samples (Ach 01, Ach 04, Ach 07, Ach 12, Ach 08B1a, Ach 08B2b) from the Aspra Chomata porphyry-epithermal mineralization were analyzed in respect to their critical and rare metals endowment (Table 8.2). In addition, geochemical analysis (samples: Ach 02, Ach 05, Ach 08B2) conducted by Gounaris (2017) were adapted and co-evaluated in this research (Table 8.2). One sample (Ach 07) is from the potassic alteration overprinted by chloritic-sericitic alteration of the granodiorite porphyry. Five samples (Ach 01, Ach 02, Ach 04, Ach 11, Ach 12) are from the sericitic alteration of the granodiorite porphyry. One sample is from a D-type vein associated with the sericitic alteration affecting the granodiorite porphyry. Two samples (Ach 08B1a, Ach 08B2, Ach 08B2b) were selected from the epithermal veins (Table 8.2, Figure 8.6). The complete dataset of the bulk geochemical analysis is given in Supplement 4, Table S1-5.

The bulk geochemical profiles of the analyzed samples show spiky patterns reflecting distinct enrichments and depletions (Figure 8.6). In contrast, the geochemical profile of the analyzed samples from the potassic overprinted by chloritic-sericitic alteration of the granodiorite shows more flat patterns (Figure 8.6).

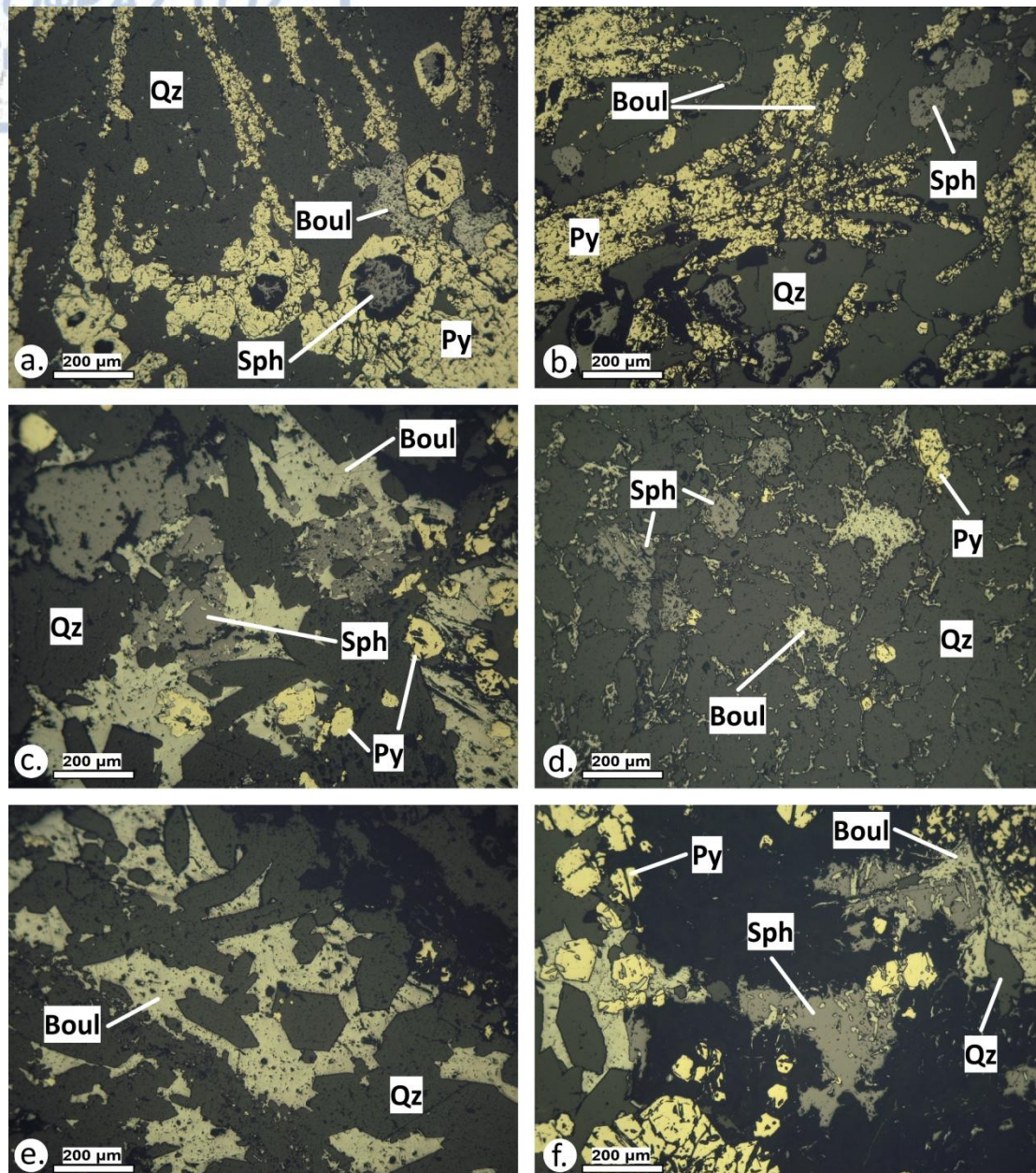


Figure 8.5. Photomicrographs (plane reflected light) of the epithermal vein mineralization at Aspra Chomata. a. Pyrite (Py) aggregates and overgrowths on sphalerite (Sph) and boulangerite (Boul) in quartz (Qz) interstices. b. Euhedral sphalerite (Sph), pyrite (Py) aggregates and boulangerite (Boul) in quartz (Qz). c. Sphalerite (Sph) and euhedral pyrite (Py) replaced by boulangerite (Boul) in quartz (Qz). d. Euhedral sphalerite (Sph), pyrite (Py), quartz (Qz) and boulangerite (Boul) in interstices. e. Boulangerite (Boul) cements euhedral quartz (Qz). f. Euhedral pyrite (Py) and quartz (Qz) cemented by sphalerite (Sph) and boulangerite (Boul).

Table 8.2. Bulk geochemical analyses of selected critical and rare metals from Aspra Chomata. Previously conducted geochemical analysis by Gounaris (2017) are also presented and marked with an asterisk. For the full list of geochemical analyses advise Supplement 4, Table S1-5.

	Mineralization stage	Porphyry							Epithermal		
	Host rock	Granodiorite porphyry									
	Alteration	Pot. alt.	Sericitic alteration					D-type vein	Argillic		
ppm	Detection limit	Ach 07	Ach 04	Ach 01	Ach 02*	Ach 11*	Ach 12	Ach 05*	Ach 08B1a	Ach 08B2*	Ach 08B2b
Ag	0.01	0.12	0.19	0.19	12	0.4	0.32	105	75	225	610
Au	5x10 ⁻⁶	0.03	0.02	0.02	13	0.01	0.01	13	3	3.1	2.5
Bi	0.01	n.a.	0.32	0.18	18	0.14	3.8	1.2	1.3	0.35	0.52
Cd	0.01	n.a.	0.12	2.9	1.2	0.53	0.05	67	10	>10 ³	1,180
Ce	0.02	68	46	33	43	35	20	14	9.2	1.9	5.9
Co	0.1	n.a.	18	22	74	21	5.6	221	27	91	8.6
Ga	0.05	18	7.3	6.9	14	7	0.75	8.1	0.75	12	19
Gd	0.05	4	2.9	2.4	n.a.	2.5	1.3	n.a.	0.37	n.a.	0.31
Ge	0.05	n.a.	0.16	0.1	0.54	0.13	b.d.l.	0.26	0.06	0.11	0.72
Hg	0.005	n.a.	0.02	0.03	n.a.	0.04	0.02	n.a.	3.1	n.a.	32
In	0.005	n.a.	0.01	0.01	0.09	b.d.l.	0.02	5	0.01	0.15	0.28
La	0.2	38	22	16	24	17	14	9.3	5.1	1.7	3.2
Nb	0.05	9.6	0.46	0.09	5.1	0.12	b.d.l.	0.4	0.12	0.1	b.d.l.
Nd	0.1	26	18	14	n.a.	15	7.3	n.a.	3.5	n.a.	2.4
Re	0.001	n.a.	0.002	0.05	0.02	0.002	0.002	0.03	0.004	0.02	0.01
Sb	0.05	n.a.	0.46	1.2	242	2.1	3	2,848	2,374	>10 ⁴	39,570
Se	0.2	n.a.	b.d.l.	0.5	5	0.2	1.4	46	2.2	1	2
Sm	0.03	4.7	3.4	2.6	n.a.	2.9	1.5	n.a.	0.57	n.a.	0.38
Ta	0.01	1.1	b.d.l.	b.d.l.	0.91	b.d.l.	b.d.l.	0.68	b.d.l.	0.29	b.d.l.
Te	0.01	n.a.	0.04	0.01	0.27	0.02	0.4	0.46	0.13	0.41	0.03
Th	0.2	25	24	28	23	25	21	1.7	1.7	1.9	b.d.l.
Ti	50	5,000	4,700	400	1,200	300	b.d.l.	b.d.l.	b.d.l.	b.d.l.	b.d.l.
U	0.05	8.6	6.6	10	3.8	6.6	25	23	0.62	1	3.1
V	1	115	70	58	60	69	9	8	4	4	5
W	0.05	3	103	181	482	188	72	1,411	378	1,029	15

Abbreviations: alt. = alteration, chl.-ser. = chloritic-sericitic, b.d.l. = below detection limit, Pot. alt. = potassic alteration overprinted by chloritic-sericitic alteration.

The D-type and the epithermal veins exhibit more enriched contents in critical and rare metals, while the granodiorite porphyry affected by potassic overprinted by chloritic-sericitic alteration is more enriched in Nb (<9.6 ppm), Ta (<1.1 ppm), Ti (<5,000 ppm), V (<115 ppm), as well as in REE including, Ce (<68 ppm), Gd (<4 ppm), La (<38 ppm), Nd (<26 ppm) and Sm (<4.7 ppm) (Table 8.2, Figure 8.6).

Samples from the potassic overprinted by chloritic-sericitic alteration of the granodiorite porphyry include lower amounts of critical and rare metals than those from the sericitic alteration (Figure 8.6). The sericitically altered granodiorite

porphyry is relatively more enriched in Bi (<18 ppm), Re (<0.05 ppm), Th (<28 ppm), U (<25 ppm) (Table 8.2, Figure 8.6). The D-type veins are more enriched in Ce, La, Nb, Re and U compared to the epithermal veins (Figure 8.6). The epithermal veins contain up to 39,570 ppm Sb, up to 1,180 ppm Cd, up to 610 ppm Ag, up to 32 ppm Hg, up to 3.1 ppm Au, while the D-type veins are more enriched in Au (<13 ppm), Co (<221 ppm), In (<5 ppm), Se (<46 ppm), Te (<0.46 ppm) and W (<1,411 ppm) (Table 8.2).

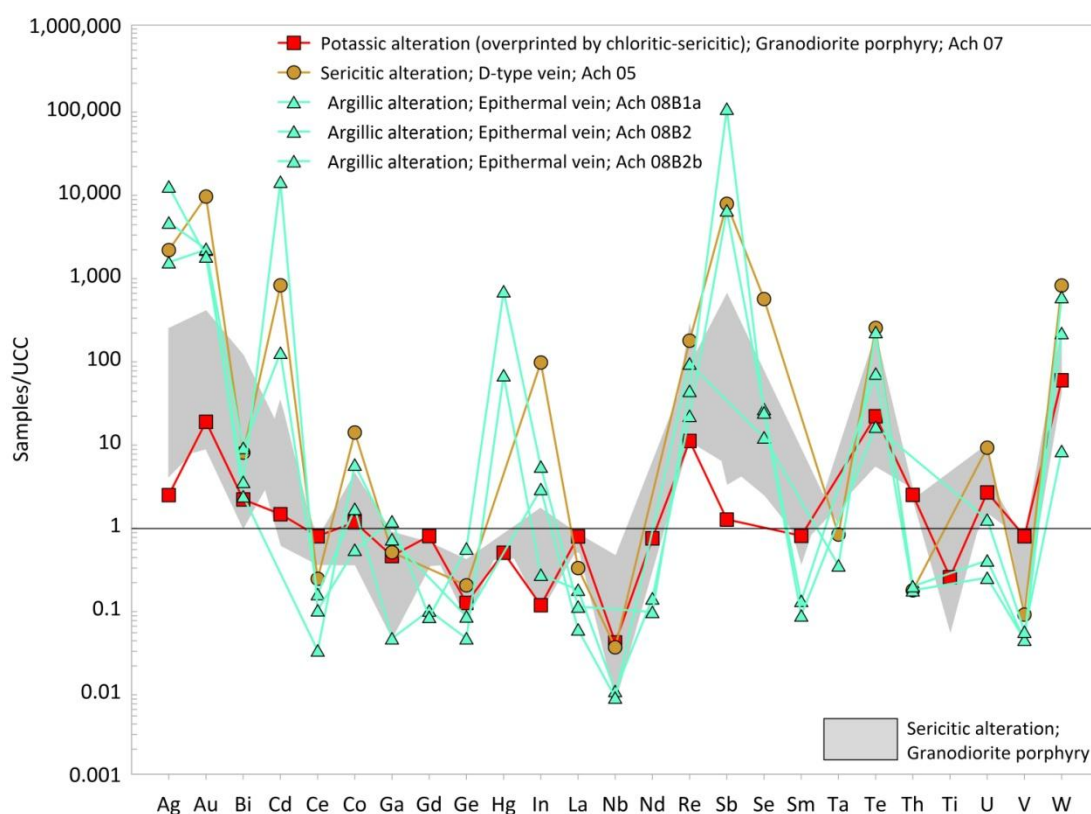


Figure 8.6. Upper continental crust (UCC) normalized logarithmic spider diagram of the analyzed samples from the Aspra Chomata porphyry deposit and epithermal vein mineralization (UCC normalized values after Rudnick and Gao 2003).

Pearson product-moment correlation coefficients and associated p-values were calculated for the bulk geochemical analyses (Supplement 3: Table S4-4). Significant positive correlations ($p < 0.01$, values ≥ 0.825) were obtained for the elemental pairs Ag-Cd, Ag-Hg, Ag-Sb, Bi-Nb, Cd-Hg, Cd-Sb, Ce-La, Ce-Th, Ce-Ti, Ce-V, Co-In, Co-Se, Co-W, Ga-Ge, Gd-Nd, Gd-Sm, Hg-Sb, In-Se, La-Th, La-Ti, La-V, Nd-Sm and Th-V (Supplement 3: Table S4-4). Positive correlations ($p < 0.05$, values between 0.685 and 0.785) were defined for the pairs Ag-Ga, Ag-Ge, Bi-Ta, Cd-Ga, Cd-Ge,

Co-Ta, Gd-Th, Gd-V, Ge-Hg, Ge-Sb, Nd-Ta, Nd-Th, Nd-V, Sm-Th, Sm-V and Ti-V (Supplement 3: Table S4-3). Negative correlations ($p < 0.05$, values between -0.678 and -0.681) include the elemental pairs Ag-La and Ag-Th (Supplement 3: Table S4-4).

8.3.2. Pyrite and sphalerite - Mode of occurrence

Pyrite and sphalerite are the dominant ore minerals in the epithermal veins associated with the porphyry deposit at Aspra Chomata. In this study only the pyrite (Py1) from the epithermal veins was analyzed by means of LA-ICP-MS. Pyrite (Py1) appears as euhedral grains ($< 200 \mu\text{m}$ in width) and as aggregates of euhedral grains ($< 1 \text{ cm}$ in width) (Figure 8.3d, 8.5a-d,f), which exhibit oscillatory zoning and are well-cemented by hydrothermal quartz (Figure 8.7a-c). In addition, it forms subhedral to euhedral overgrowths on sphalerite (Figure 8.5a, 8.7b). Commonly, needle-like crystals of boulangerite ($< 100 \mu\text{m}$ in width) are found in pyrite (Figure 8.7a-c), as well as in the intragranular space (Figure 8.7d). Locally, pyrite hosts inclusions of euhedral arsenopyrite ($< 50 \mu\text{m}$ in width) (Figure 8.7c). Traces of galena, chalcopyrite and tetrahedrite are found in pyrite and quartz interstices (Figure 8.7e).

Sphalerite (Sph1) occurs as subhedral to euhedral grains ($< 400 \mu\text{m}$ in width) (Figure 8.5a-d,f). It is intergrown with euhedral pyrite, and locally is overgrown by pyrite (Figure 8.5c,f, 8.7b). In addition, sphalerite is replaced by boulangerite needles ($< 100 \mu\text{m}$ in width), and cemented by hydrothermal quartz (Figure 8.7f).

8.3.3. Critical and rare metals in pyrite and sphalerite (LA-ICP-MS)

Pyrite (Py1) and sphalerite (Sph1) from the epithermal veins at Aspra Chomata incorporate varying contents of trace elements including base, critical and rare metals (Table 8.3, Figure 8.8a). The complete analytical datasets for pyrite and sphalerite are given in Supplement 2, Tables S3-15 and S3-16.

In Py1, the most enriched base metal is As ($< 43,671 \text{ ppm}$), and is followed by Cu ($< 2,569 \text{ ppm}$), Pb ($< 1,917 \text{ ppm}$) and Zn ($< 525 \text{ ppm}$) (Table 8.3). Critical and rare metals include up to 741 ppm Sb, up to 80 ppm Au, up to 60 ppm Ag, up to 41 ppm Ti, up to 0.16 ppm Co and up to 0.10 ppm In (Table 8.3, Figure 8.8a). Nano-scale mineral inclusions in Py1 are related to Pb ($< 5,360 \text{ ppm}$), Sb ($< 2,621 \text{ ppm}$), Zn ($< 150 \text{ ppm}$), Ag ($< 26 \text{ ppm}$), Cd ($< 7.2 \text{ ppm}$), Ge ($< 6.5 \text{ ppm}$), U ($< 0.62 \text{ ppm}$) and Th ($< 0.21 \text{ ppm}$) (Supplement 2: Table S3-15).

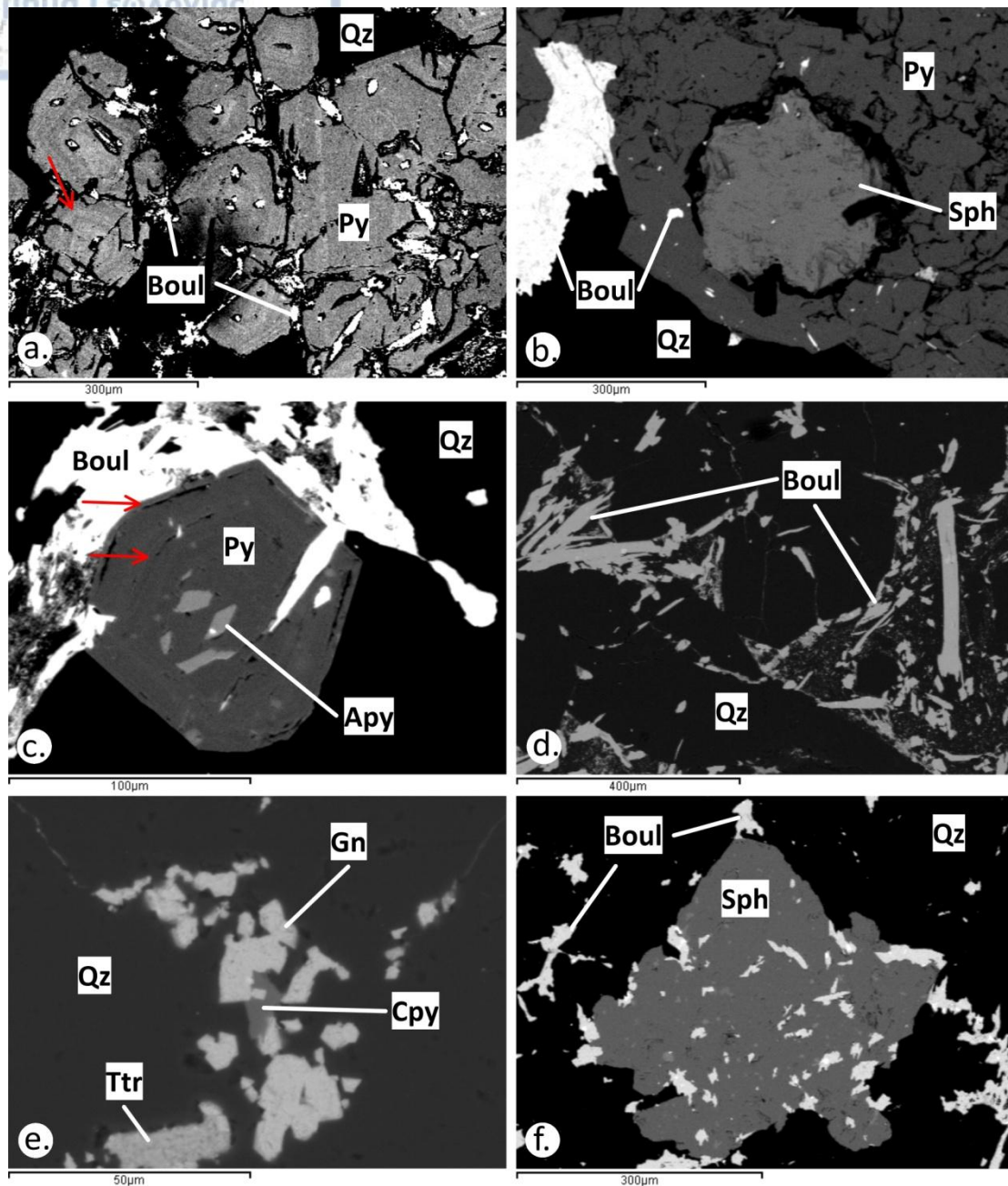


Figure 8.7. SEM back-scattered electron images of the epithermal vein mineralization from Aspra Chomata. (b-f: colors and brightness have been adjusted to highlight minerals and oscillatory zoning in pyrite). a. Pyrite (Py1) exhibiting oscillatory zoning (red arrow) replaced by boulangerite (Boul) and cemented by quartz (Qz). b. Pyrite (Py1) overgrows on sphalerite (Sph1) and is replaced by boulangerite (Boul) set in quartz (Qz). c. Euhedral arsenopyrite (Apy) in oscillatory-zoned (red arrows) euhedral pyrite (Py1) which is rimmed by boulangerite (Boul) and quartz (Qz). d. Boulangerite (Boul) needles in quartz (Qz). e. Galena (Gn), chalcopyrite (Cpy) and tetrahedrite (Ttr) in quartz interstices. f. Sphalerite (Sph1) replaced by boulangerite (Boul) and cemented by quartz (Qz).

Table 8.3. LA-ICP-MS analyses of pyrite and sphalerite from the epithermal veins at Aspra Chomata. For the full dataset, see Supplement 2, Tables S3-15 and S3-16.

Mineral	Pyrite				Sphalerite				
Mineralization stage					Epithermal				
Mineralization stage	Py1, (n = 7)				Sph1, (n = 21)				
Element	MIN	MAX	STDEV	AVG	Element	MIN	MAX	STDEV	AVG
Ag	6	60	25	32	Ag	0.99	52	12	9.2
As	31,727	43,671	4,084	39,187	As	5	23	9	10
Au	14	80	24	39	Au	b.d.l.	b.d.l.	-	-
Bi	b.d.l.	b.d.l.	-	-	Bi	0.04	0.14	0.07	0.09
Co	0.11	0.16	0.03	0.13	Cd	835	1,933	246	1,400
Cr	16	16	-	16	Co	b.d.l.	b.d.l.	-	-
Cu	818	2,569	604	1,278	Cr	b.d.l.	b.d.l.	-	-
Hg	b.d.l.	b.d.l.	-	-	Cu	61	809	244	292
In	0.06	0.10	0.02	0.07	Ga	15	44	7.3	25
Mn	5.4	15	3.2	7.7	Ge	0.0	13	2.9	1.8
Mo	b.d.l.	b.d.l.	-	-	Hg	11	37	8.1	21
Ni	0.87	0.87	-	0.87	In	0.14	1.4	0.30	0.40
Pb	110	1,917	1,277	1,013	Mn	681	7,253	1,729	2,322
Sb	51	741	488	396	Mo	0.37	0.51	0.09	0.44
Se	b.d.l.	b.d.l.	-	-	Nb	0.05	0.05	-	0.05
Sn	0.86	5.8	2.3	2.4	Ni	0.45	0.91	0.32	0.68
Te	b.d.l.	b.d.l.	-	-	Pb	0.11	4.6	1.9	1.5
Ti	25	42	6.9	33	Re	b.d.l.	b.d.l.	-	-
Tl	0.54	7.7	2.8	2.4	Sb	0.84	14	5	6
V	b.d.l.	b.d.l.	-	-	Se	b.d.l.	b.d.l.	-	-
W	b.d.l.	b.d.l.	-	-	Sn	8.6	128	38	55
Zn	82	525	313	303	Te	b.d.l.	b.d.l.	-	-
					Ti	7.1	18	2.9	11
					Tl	0.53	0.6	0.03	0.55
					V	0.71	0.71	-	0.71
					W	2.5	2.5	-	2.5
					Zn	616,800	639,400	8,379	627,667
					Cd:Zn	0.001	0.003	0.029	0.002

Sphalerite (Sph1) contains several base, critical and rare metals (Table 8.3, Figure 8.8b). Manganese (<7,253 ppm), Cu (<809 ppm) and Sn (<128 ppm) are the most enriched base metals (Table 8.3). Cadmium (<1,933 ppm) is the most enriched critical and rare metal, followed by Ag (<52 ppm), Ga (<44 ppm), Hg (<37 ppm), Ti (<18 ppm), Sb (<14 ppm), Ge (<13 ppm), W (<2.5 ppm), In (<1.4 ppm), V (<0.71 ppm), Bi (<0.14 ppm) and Nb (<0.05 ppm) (Table 8.3, Figure 8.8b).

Furthermore, Sph1 incorporates significant contents of base metals including Cu (<13,723 ppm), Pb (<7,168 ppm), As (<555 ppm) and of Sn (<371 ppm) in nano-scale mineral inclusions (Supplement 2: Table S3-16). Critical and rare metals are also found related to nano-scale mineral inclusions. They include up to 4,169 ppm Sb, up to 29 ppm Hg, up to 20 ppm Ag, up to 31 ppm Ti, up to 1.1 ppm Tl and up to 0.61 ppm In (Supplement 2: Table S3-16).

8.3.4. Statistical analysis of trace elements concentrations

Pearson product-moment correlation coefficients were defined for pyrite and sphalerite from Aspra Chomata. Following interpretations made after ablation

patterns, trace element concentrations related to nano-scale inclusions were excluded before the statistical analyses. Pyrite is characterized by significant negative correlation ($p < 0.01$, value = -0.949) for the elemental pair Ag-Ti (Supplement 3: Table S4-19). Sphalerite is associated with significant positive correlations ($p < 0.01$, values > 0.551) for the pairs Ag-V, Ag-W and Ge-Ti, with significant negative correlations ($p < 0.01$, values > -0.539) for the pairs Ti-V and Ti-W, and with negative correlation ($p < 0.01$, value = -0.438) for the pair Cd-Hg (Supplement 3: Table S4-20).

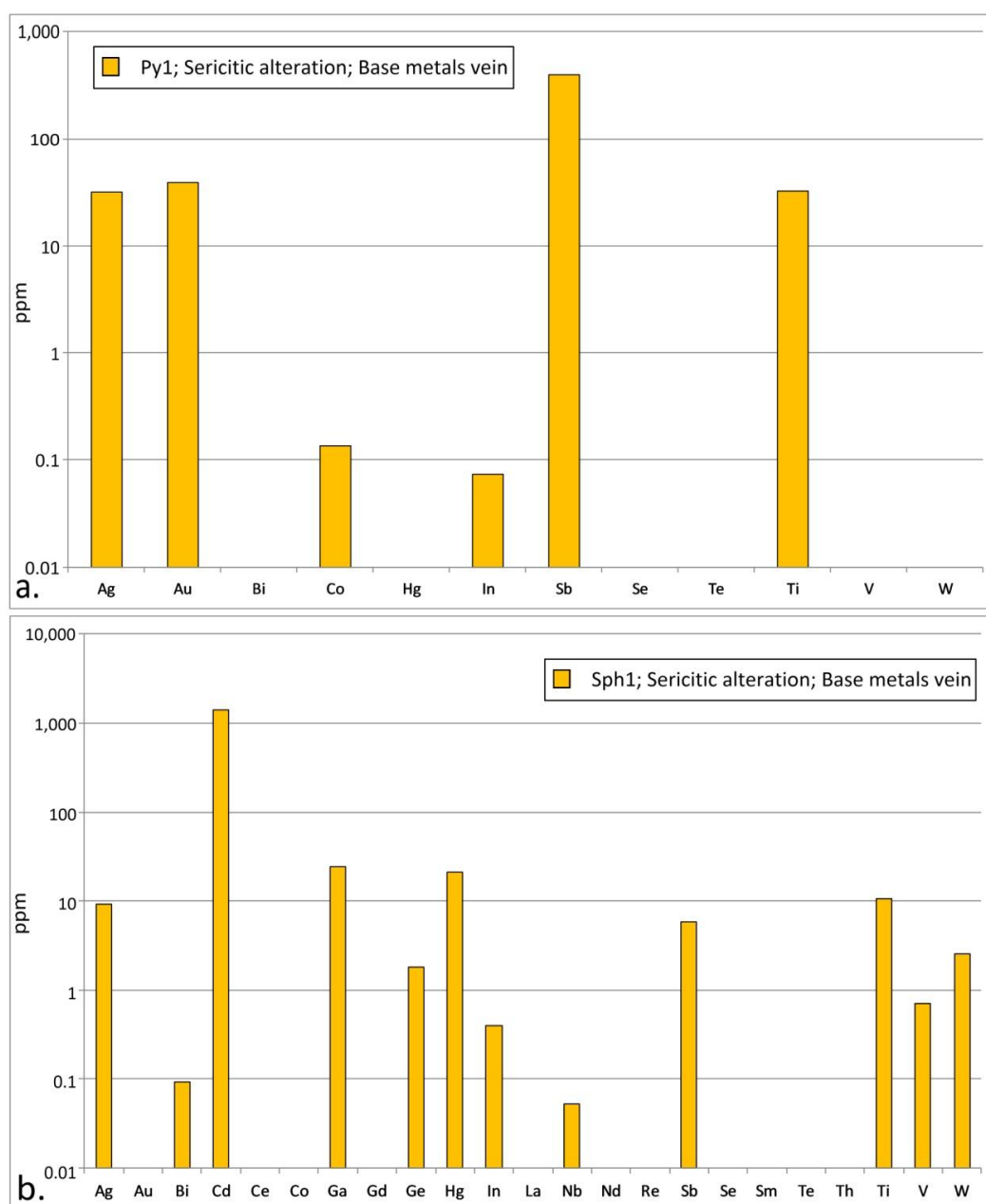


Figure 8.8. Average values of critical and rare metals contents of pyrite (a) and sphalerite (b) from the epithermal veins found in Aspra Chomata. Local enrichments related to nano-scale mineral inclusions are excluded.

8.4. Discussion

The Stratoni granodiorite is part of the late Oligocene igneous suite. Magma intruded the biotite gneiss, amphibolite, and marble of the Kerdylion Unit at the footwall of the Stratoni fault. As a result, the Stratoni granodiorite and minor diorite phases were formed at 25.36 ± 0.15 Ma ($^{206}\text{Pb}/^{238}\text{U}$ zircon dating, Siron et al. 2016). Magma differentiation resulted in the formation of a porphyritic phase at Aspra Chomata at 24.53 ± 0.31 Ma hosted in granodiorite porphyry ($^{206}\text{Pb}/^{238}\text{U}$ zircon dating, Siron et al. 2016). Also, Gilg and Frei (1994), reported a date of 25.0 ± 0.6 Ma for the sericitic alteration at Aspra Chomata. According to Siron et al. (2018), the age of the Stratoni granodiorite is coeval with the end of the synmineral, semibrittle deformation and related hydrothermal alteration along the Stratoni fault zone. In addition, Gounaris (2017) concluded that the evolution of the epithermal stage was coeval with the latest stages of Stratoni stock emplacement.

Locally, sheeted epithermal base metal sulfide veins overprint the porphyritic phase (Figure 8.3d). Intense bleaching and kaolinization of the wall rock are related to the epithermal mineralization stage (Gounaris 2017, Siron et al. 2018, Table 8.1). The metallic assemblage includes pyrite, sphalerite, boulangerite, and minor arsenopyrite, galena, chalcopyrite and tennantite (Table 8.1, Figure 8.5a-f). The widespread presence of euhedral pyrite and sphalerite suggests that they were first deposited, while pyrite overgrowths on sphalerite indicate that pyrite formation locally succeeded sphalerite crystallization (Figure 8.5a-d,f). Minor arsenopyrite occurs locally as euhedral crystals preceding pyrite crystallization, while galena, chalcopyrite and tennantite are found in pyrite and quartz interstices suggesting their late formation (Figure 8.7c,e). Pyrite exhibits oscillatory zoning with the euhedral, distinctly planar nature of the compositional layers indicating that crystals were not tightly cemented and maintained a faceted morphology throughout most of their growth history (Shore and Fowler 1996, Figure 8.7a,c). Boulangerite is commonly found in pyrite and sphalerite, as well as in the intragranular space highlighting its late crystallization from the hydrothermal fluids (Figure 8.7a-d).

Porphyry and epithermal stage mineralization, hydrothermal alteration and bulk geochemistry reveal distinct mineralogical and geochemical relations to various rare metals (Figure 8.6). The sericitically altered granodiorite porphyry contain up to 1,057 ppm Cu, up to 68 ppm Mo and up to 12 ppm Ag, while the D-type veins associated

with sericitic alteration include up to 1,712 ppm Cu, up to 175 ppm Mo and up to 105 ppm Ag. In addition, the sericitically altered granodiorite porphyry (Ach 02 = 13 ppm Au) and the D-type veins (Ach 05 = 13 ppm Au) are the major hosts of gold at Aspra Chomata (Table 8.2, Supplement 4: Table S1-5)

Cobalt, In, Se, Te and W contents are more enriched in the sericitic alteration rather than the potassic overprinted by chloritic-sericitic alteration affecting the granodiorite porphyry (Table 8.2, Figure 8.6). The D-type veins incorporate the highest contents of Co (<221 ppm), In (<5 ppm), Se (<46 ppm), Te (<0.46 ppm) and W (<1,411 ppm) (Table 8.2, Figure 8.6). The epithermal veins exhibit the higher enrichments in Ag (<610 ppm), Cd (<180 ppm), Ga (<19 ppm), Hg (<32 ppm) and Sb (<39,570 ppm) (Table 8.2, Figure 8.6).

The potassic overprinted by chloritic-sericitic alteration from the granodiorite porphyry exhibit the highest contents in REE, including Ce (<68 ppm), Gd (<4 ppm), La (<38 ppm), Nd (<26 ppm) and Sm (<4.7 ppm) (Table 8.2, Figure 8.6). The highest enrichments in Bi (<18 ppm), Nb (<9.6 ppm), Th (<28 ppm), Ti (<5,000 ppm), U (<25 ppm) and V (<115 ppm) are also related to the potassic overprinted by chloritic-sericitic alteration from the granodiorite porphyry (Table 8.2, Figure 8.6). These enrichments can be attributed to rock-forming and to hydrothermal alteration minerals (e.g. titanite, zircon, magnetite, feldspar) while variations in distribution could be related to the intense hydrothermal alteration and to supergene oxidation as it was also suggested for the Vathi porphyry deposit (Stergiou et al. 2021a).

According to Gounaris (2017), the elemental pairs Cu-Au and Pb-Zn exhibit strong positive linear correlations revealing their geochemical affiliation, while the pairs Au-Pb and Au-Zn show distinct negative linear correlations. In addition, Pearson product-moment correlation coefficients revealed significant positive correlations between specific elemental pairs (Supplement 3: Table S4-4). These elemental pairs can be summarized into groups, which include: 1) Ag-Cd-Hg-Sb, 2) Co-In-Se-W, 3) Ce-La-Th-Ti-V, and 4) Gd-Nd-Sm. By comparing correlations and relative contents of the analyzed trace elements it can be suggested that the rock-forming stage, as well as the potassic overprinted by chloritic-sericitic alteration, are related to REE, as well as Bi, Nb, Th, Ti, U and V. Co In, Se, Te and W were introduced during the sericitic alteration and the related D-type veins of the porphyry stage, while Ag, Cd, Ga, Hg and Sb are associated with the epithermal stage.

Similar geochemical enrichments in Ag, Au, Bi, Co, In, Se, Te and W, related to sericitic alteration and associated mineralizing stages, have been reported elsewhere in Greece including Maronia (Melfos et al. 2002, 2020), Pagoni-Rachi (Voudouris et al. 2013b), Fakos (Fornadel et al. 2012), and Vathi (Stergiou et al. 2021). Epithermal veins associated with the porphyry-epithermal transition environment occur in several porphyry deposits in Greece (e.g. Pagoni-Rachi, Stypsi, Voudouris et al. 2019a). According to Voudouris et al. (2019a), boulangerite occurs at epithermal-style deposits found at Pontokerasia (Melidonis 1972), Piavitsa (Siron et al. 2016), Panormos of Tinos isl. (Tombros et al. 2010), and Cape Evros of Mykonos isl. (Tombros et al. 2015). The epithermal mineralization at Aspra Chomata contains a simple mineralogy, mainly including pyrite, sphalerite and boulangerite (Table 8.1), but is more enriched in Ag (<610 ppm) compared to previously reported epithermal ores of Greece (i.e. epithermal-style ores: Mavrokoryfi (<16,943 ppb Ag), Perama Hill (<81,727 ppb Ag), Voudouris et al. 2019a).

The porphyritic stage at Aspra Chomata is enriched in Au (<13 ppm) and is overprinted by a Pb-Zn-Sb-Ag-As-epithermal stage. The formation of the porphyry stage may be ascribed to magma differentiation and to the entrapment of volatiles beneath the carapace of the Stratoni granodiorite. The associated sheeted and orthogonal quartz and D-type veins were formed following the carapace fracturing and a drop in lithostatic pressure. The minor extent of the quartz and the D-type veins in the metamorphic rocks, as observed at the northwestern part of the granodiorite porphyry, indicates that the formation of the porphyry stage was spatially restricted. Additionally, the kaolinization of the granodiorite porphyry around and closely to the epithermal veins indicates that the temperature of the hydrothermal fluids rapidly dropped below 300 °C or even 100 °C (Sillitoe 2010).

8.4.1. Mineral chemistry of pyrite and sphalerite and nano-scale inclusions

The joint interpretation of the scanning electron microscopy and LA-ICP-MS analysis for pyrite and sphalerite from the epithermal veins at Aspra Chomata indicates that specific trace elements are hosted as nano-scale mineral inclusions. Pyrite (Py1) is enriched with base (As, Cu, Pb, Zn), and critical and rare metals (Ag, Au, Co, In, Sb, Ti) (Table 8.3, Figure 8.8a, 8.9a). The ablation patterns indicate that these elements are incorporated as stoichiometric substitutions. Cobalt commonly substitutes for Fe in pyrite structure, while the incorporation mechanisms for Ag, As,

Au, Cu, In, Pb, Sb, Ti and Zn may include couple substitutions or incorporation of solid solutions in specific growth zones (Arbaitis et al. 2004, Deditius et al. 2011). Pyrite from the epithermal stage at Aspra Chomata is enriched in As (<43,671 ppm) and exhibits distinct oscillatory zoning (Figure 8.7a,c). According to Arbaitis et al. (2004), As and Au contents in pyrite are highly correlated, and both elements may be incorporated in pyrite lattice via coupled substitutions (i.e. Au^{3+} substitutes for Fe^{2+} and AsS^{3-} substitutes for the S_2^{2-} dianion). The same coupled substitution mechanism may be suggested for Ag^{3+} in pyrite. Furthermore, in As-rich pyrite with oscillatory zoning, the Pb, Sb and Zn contents are variable (Arbaitis et al. 2004). In Py1 of Aspra Chomata, a positive correlation between As and Pb, Sb and Zn is not documented, possibly suggesting the random incorporation of Pb, Sb and Zn as solid solutions in specific As enriched growth zones. It should be mentioned that according to the SEM-EDS analysis the higher Pb contents are ascribed to specific zones in Py1 (Figure 8.7a,c). Additionally, notable is the overall depletion in Hg, which is not a common aspect of As-rich pyrite (Arbaitis et al. 2004).

The elevated contents of Ag, Cd, Ge, Pb, Sb and Zn and the examined ablation patterns, suggest the presence of specific nano-scale mineral inclusions in pyrite (Py1) (Supplement 2: Tables S3-15 and S3-16, Figure 8.9a). Ag, Cd, Ge, Pb, Sb and Zn are possibly associated with boulangerite inclusions in pyrite (Figure 8.7a, 8.9a).

Sphalerite (Sph1) contains Mn, Cu and Sn, as well as variable concentrations of critical and rare metals (Ag, Bi, Cd, Ga, Ge, Hg, In, Nb, Sb, Ti, V, W) (Table 8.3, Figure 8.8b). The ablation patterns for these elements in Sph1 indicate that they are incorporated as solid solutions (Figure 8.9b). Sphalerite (Sph1) includes Ge, Ga, Hg and Sn, whereas it is free of Co and is depleted in In (<1.4 ppm), suggesting that it was precipitated under low temperatures (Cook et al. 2009, Table 8.3). In addition, by comparing pyrite and sphalerite mineral chemistry it is concluded that Bi, Hg, V and W preferentially precipitated in sphalerite (Figure 8.8a,b).

The concentrations of trace elements in sphalerite, including Ag, As, Cu, Hg, In, Pb, Sb, Sn, Ti and Tl, and their time-resolved laser ablation ICP-MS depth profiles reveal the affiliation to mineral inclusions (Supplement 2: Table S3-16, Figure 8.9b). Most of these elements are ascribed to boulangerite inclusions found in Sph1 (Figure 8.7f, 8.9b). In addition, Cu, Sn and In could be attributed to nano-scale inclusions of chalcopyrite (Supplement 2: Table S3-8).

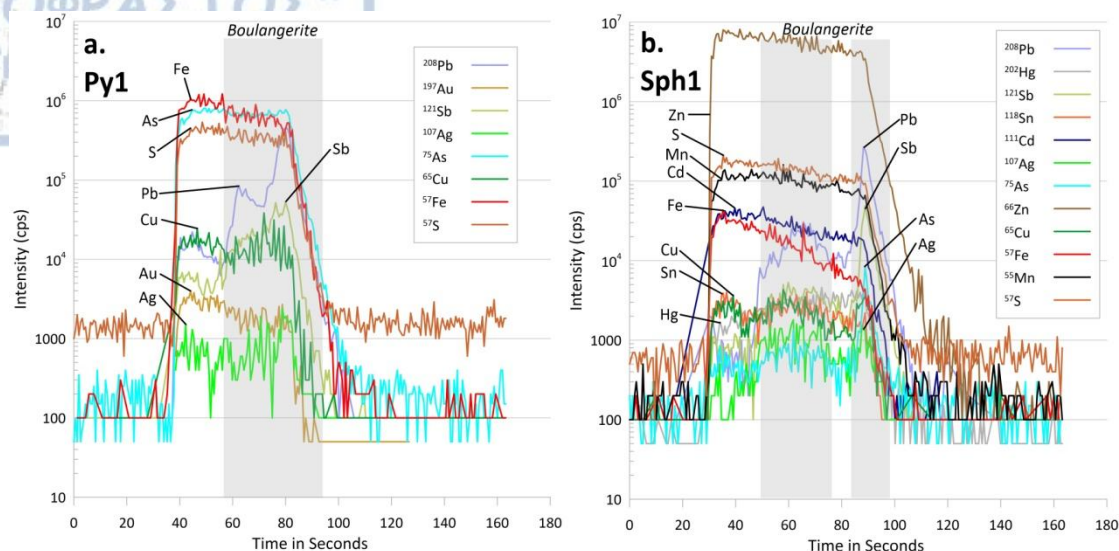


Figure 9.7. Selected time-resolved laser ablation ICP-MS depth profiles of pyrite (Py1) and sphalerite (Sph1) from the epithermal base metal veins at Aspra Chomata. Associated nano-scale inclusions are highlighted in gray. a. In Py1, the ablation patterns of Fe and S, are similar to those of As and Au indicating the incorporation of these elements in pyrite. The spiky patterns of Pb, Sb and Ag suggest that nano-scale inclusions of boulangerite are found in pyrite (Py1). Copper is associated both with pyrite (Py1) and boulangerite. b. In Sph1, the ablation patterns of Mn, Cd, Fe, are similar to those of Zn and S suggesting that these elements are hosted in sphalerite lattice. The distinct spiky patterns of Pb, Sb, As and Ag highlight the occurrence of boulangerite inclusions in sphalerite. Higher contents of Cu, Sn and Hg are related to boulangerite than sphalerite.

CHAPTER 9. DISCUSSION

Critical raw materials (CRM) are integral components of a strong and viable economy and society (Humphreys 2014, Huston 2014, Table 1.1). A sustainable supply of mineral raw materials needs accessible deposits and efficiently productive mines (Barakos et al. 2016). Advances in ore exploration further contribute in achieving this target. Commonly, land-use issues, social and environmental challenges, declining ore grades, and resource nationalism cause challenges in securing undisturbed and sustainable supplies (McNulty and Jowitt 2021). In addition, the ongoing shift towards a low-carbon society and the advance of new technologies emphasize the future demands on CRM (Grandell et al. 2016). Recently, EU has been emphatically committed to a more sustainable future under the "European Green Deal" agreement (European Commission 2019). In this agreement, the secure supply of CRM is set as a necessary condition in achieving the "Green Deal" targets. Although Europe has a long history in mineral raw materials exploitation, the EU largely rely on imports of CRM (Goodenough et al. 2016, Figure 1.2). Europe could be considered underexplored in particular with modern exploration methods, as good understanding on the genesis of particular deposits, as well as on their reserves and resources is missing (Moss et al. 2011, Cassard et al. 2015, Bertrand et al. 2016). The same applies in the case of mineral deposits in Northern Greece (Melfos and Voudouris 2017).

Metal enrichment to ore grade is the eventual conclusion of large-scale and long-term fractionation depleting specific geochemical reservoirs in the Earth's crust (Lehmann et al. 2000). Magmatism produced in collisional and post-collisional settings, controlled by thermal gradients, permeability, and structural processes, eventually produces, depending upon fluid input and metal concentrations, various mineralizations hosted in porphyry, skarn, epithermal and minor satellite deposits (Lehmann et al. 2000, Sillitoe 2010, Figure 1.6). Immiscible sulfide melts control metals transportation and concentration from the MASH cumulates to magma chambers, while sulfide complexes and chlorine ligands are carriers of metals in the mineralizing hydrothermal fluids at shallower depths (Audétat et al. 2008, Jenner et al. 2010). Chalcophile and siderophile affinity of the metals partitioning in magma controls metal distribution in the mineralizing systems and metal partitioning in the metallic minerals. Relations between specific metals are also manifested by metal

companionality (e.g. Se and Te affiliation to Cu, Cd and In affiliation to Zn, and Bi and Sb affiliation to Pb) (advise also Chapters 1.1, Figures 1.4 and 1.6b).

Porphyry Cu-Au-Mo deposits are reported as potential exploration and exploitation targets for rare metals, exhibiting enrichments of Re, Te, Co, Bi, U and PGE (Table 1.2, John and Taylor 2016, Hofstra and Kreiner 2020). The polymetallic assemblages found in the periphery of porphyry systems related to skarn, replacement, vein, and intermediate sulfidation epithermal mineralization types are enriched with Mn, Ge, Ga, In, Bi, Sb, As, W and Te (Kelley and Spry 2016, Goldfarb et al. 2016, Hofstra and Kreiner 2020, Table 1.2). In addition, low- to high-sulfidation mineralization associated with epithermal overprinting of porphyry systems may include Te, Bi, As, Sb, V and F (Goldfarb et al. 2016, Hofstra and Kreiner 2020). Several of these critical and rare metals are hosted in sulfide and non-sulfide minerals found in these deposits (i.e. Ag and Se in chalcopyrite, Te in pyrite, Bi in tetrahedrite and galena, REE in titanite, advise also Chapter 1.2.3). In addition, Te forms Au-Ag-tellurides, and several non-precious tellurides/sulfotellurides/tellurfates. Rare earth elements are hosted in minerals such as monazite, brockite and bastnäsite, while PGE reside in Pd-Pt arsenides and/or tellurides (Kelley and Spry 2016).

During Cenozoic, subduction and accretion of oceanic and continental domains, slab retreat and migration of magmatic activity towards the south, and exhumation of core complexes and plutonic rocks to the surface have controlled the geodynamic evolution in the Aegean domain (Jolivet et al. 2103, Schmid et al. 2020). Slab retreat, asthenospheric upwell, melting of the lower crust and mixing with mantle-derived melts, have been long suggested as the key factors driving the Oligocene-Miocene high-K calc-alkaline to shoshonitic magmatism across the Aegean (Pe-Piper et al. 2009, Ersoy and Palmer 2013, Jolivet et al. 2013). Lately, Schaarschmidt et al. (2021a) supported that the Oligocene-Miocene magmatic activity in the Aegean was primarily sourced by a very heterogeneous geochemical reservoir modified under low subduction rates, low melting degrees, and by various subducted Ba- and P-enriched sedimentary and continental rocks belonging to the Ionian and Gavrovo-Tripolitza blocks. According to the same authors, assimilation of crustal rocks during magma ponding in the MASH zone, and in magma chambers in the upper crust, was very restricted (Schaarschmidt et al. 2021a). In addition, McFall et al. (2018) highlighted the major role of immiscible Bi-Te melts in the collection and transportation of PGE

and other precious metals in high temperature hydrothermal systems, resulting in the formation of platinum group minerals without PGE fluid saturation.

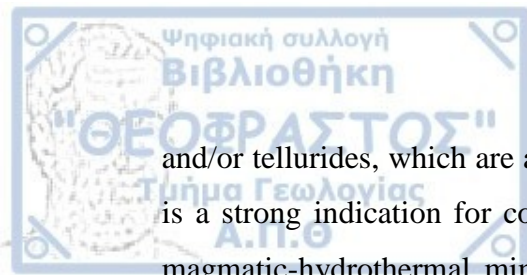
The numerous magmatic-hydrothermal mineralizations found in the Aegean domain manifest conditions related to shallow magmatic activity, rapid exhumation, and intense tectonic activity (Melfos and Voudouris 2017, Voudouris et al. 2019a, Schaarschmidt et al. 2021a). Across northern Greece, several porphyry mineralizations (e.g. Pagoni Rachi, Koryfes Hill, Konos Hill, Maronia, Melitena, Skouries, Vathi) are variably enriched in Ag, Au, Bi, Re, Te and PGE (McFall et al. 2018, Voudouris et al. 2019a). In addition, sub-epithermal/epithermal mineralizations (e.g. Sapes, Perama Hill, Pefka) are enriched in Ag, Au, Ga, Ge, In, Sn, Se and Te (Voudouris et al. 2019a, 2022). Sulfide minerals hosted in Cenozoic mineralizations across the Aegean domain incorporate amounts of metals (e.g. Au, As, Te) exsolved from magmatic intrusions at depth and transported by magmatic vapors (Voudouris et al. 2019a, Schaarschmidt et al. 2021b). In addition, sulfide minerals hosted in shallow hydrothermal systems contain enrichments of As, Bi, Hg, Mo and Tl (Voudouris et al. 2019a). Their incorporation in sulfide minerals is ascribed to fluid boiling and mixing with meteoric water, which produced a vapor phase able to transfer these metals (Schaarschmidt et al. 2021b).

The SMMP and RMP in northern Greece, belong to the Western Tethyan metallogenic belt, and constitute encouraging regions for future exploration projects in southeastern Europe (Melfos and Voudouris 2012, 2017, Tsirambides and Filippidis 2016, Baker 2019, Voudouris et al. 2019a, Figure 1.7). In the region of Central Macedonia in northern Greece, along the SMMP and the adjacent RMP, several deposits and prospects of Cenozoic age are enriched in base (Pb, Zn, Cu) and critical and rare metals (e.g. Sb, W, Te, Bi, Ga, Co, Ag, Au, REE and PGE, Voudouris et al. 2007, Melfos and Voudouris 2017, Tsirambides and Filippidis 2019, Stergiou et al. 2021a,b, Figure 2.2, Table 9.1). Oligocene to Miocene porphyry deposits (e.g. Vathi, Gerakario, Aspra Chomata) are clustered in the Kilkis and Chalkidiki ore districts, while several other deposits including skarn/carbonate, and epithermal are found proximal to the mineralized intrusions (e.g. Gerakario stibnite vein mineralization) (Stergiou et al. 2021b, 2022, Figure 2.2). Vein deposits hosted in metamorphic rocks are found at Laodikino and Kolchiko (Stergiou et al. 2021c, Figure 2.2).

At the Vertiskos Unit, the formation of the porphyry-epithermal systems and their satellite mineralization was set in an extensional tectonic regime, while the polymetallic massive and quartz veins hosted in metamorphic rocks and in shear zones were formed under transpressional to transtensional tectonics (Figure 9.1). Relative enrichments of critical and rare metals revealed in this study are grouped and presented in Figure 9.1, in respect to the mineralization styles incorporating them. The critical and rare metals are associated with: (1) stoichiometric substitutions, (2) solid solutions or nanoparticles in crystal lattice, (3) nano-scale mineral inclusions, and (4) visible micro- to macro-scale minerals.

The porphyry-epithermal systems are more enriched in Au-Bi-Co-Sb-Se-Te-W-REE. At Vathi, the presence of tetradymite in association with native gold as well as of wittichenite and cuprobismutite in the sericitic alteration, indicate enrichments of Au-Bi-Te-Se for the mineralizing fluids (Figure 4.5c, 4.6d,e, Table 9.1). Tetradymite, wittichenite and cuprobismuthite, and possibly other unidentified Bi-sulfosalts, are hosted as micro- and nano-scale inclusions in pyrite and chalcopyrite (Figure 4.6c,e,f, 4.10a,b, 4.11a,b). In addition, pyrite from the sericitic alteration at Vathi largely incorporates Co in crystal lattice (Figure 4.10a-c). Titanite in the potassic-calcic alteration of the quartz-monzonite at Vathi is a major host of rare metals, including W and REE, with Ce, La, Nd and Sm, incorporated as stoichiometric substitutions (Figure 4.9b, Table 9.1). Although the epithermal veins found around the porphyry systems mainly host base metals (e.g. Cu, Pb, Zn), the epithermal veins at Gerakario contain significant concentration of Sb as stibnite (Figure 5.2a, 5.3).

The metal association Ag-Au-Bi-Cd-Hg-In-Sb-Se-Te-W is ascribed to the veins hosted in metamorphic rocks (Figure 9.1). These metals are variably incorporated in the analyzed pyrite, chalcopyrite, sphalerite and tetrahedrite from Laodikino, and in arsenopyrite, pyrite, chalcopyrite and sphalerite from Kolchiko (Table 9.1). Tetrahedrite from the polymetallic quartz veins at Laodikino largely incorporates Ag either in solid solutions or as nanoparticles hosted in crystal lattice (Figure 6.11d). At Kolchiko, the presence of native bismuth and galenobismuthinite cementing pyrite and chalcopyrite in the polymetallic quartz veins (Figure 7.3d,e), as well as nano- to micro-scale inclusions in arsenopyrite, pyrite and chalcopyrite from the polymetallic massive and quartz veins, indicates relative enrichment in Bi of the mineralizing fluids. At Vertiskos Unit, the mineralization associated with the veins crosscutting the metamorphic rocks, include varying concentrations of Bi and Te as Bi-sulfosalts



and/or tellurides, which are also usually related to precious metals (e.g. Ag, Au). This is a strong indication for concealed proximal and/or distal magmatic intrusions and magmatic-hydrothermal mineralizing processes set along or near shear zones. This assumption has been previously suggested by Vavelidis et al. (1999), Voudouris et al. (2013c), Bristol et al. (2015), Melfos and Voudouris (2017), and Voudouris et al. (2019a).

Table 9.1. Geology, mineralogy, geochemistry, and mineral chemistry of the studied deposits and metallic minerals. For details on each deposit please advise the text and the Tables 4.1, 6.1, 7.1 and 8.1. (HR: Host Rock, MIN: Mineralization).

Deposit name	Geotectonic unit/ Ore district	Main commodities	Critical and rare metals	Deposit style/ Morphology of ore bodies	Host rocks	Age	Alteration style and assemblage	Mineralization stage	Metallic minerals	Studied metallic minerals	Critical and rare metals in the studied metallic minerals	Nano-scale mineral inclusions
Vathi	Vertiskos Unit/ Kilkis ore district	Cu-Au±Mo	Ag, Au, Bi, Cd, Co, Ga, Ge, Hg, In, Nb, Sb, Se, Te, Th, V, W and REE: Ce, Gd, La, Nd and Sm	Porphyry Sub-alkaline Cu-Au/ Stockwork, veins, disseminations	Qz-monzonite	HR: Miocene (18±0.5 Ma and 17±1 Ma, Frei 1992)	Potassic-calcic: Qz + Bt + Ttn + Act + Rt ± Chl	M-type veins Disseminated	Mag ± Ilm	Mag1	Co, Ga, Ge, Se, Ti, V	Ttn
										Ttn1	Ce, Co, Ga, Gd, Ge, In, La, Nd, Sb, Se, Sm, Th, Ti, V, W	None
							Sericitic: Ser + Qz + Rt ± Dol ± Kln	D-type veins	Py + Cpy + Gn + Au + Ttd	Py2	Ag, Co, Sb, Se, Ti	Ttd, Au, Cpy
					Latite	HR: Miocene?	Potassic (overprinted by sericitic): Qz + Bt + Kfs + Chl + Ser ± Rt	Disseminated	Mag + Py + Cpy ± Bn ± Mol ± Po	Mag2	Co, Ga, Ge, Ti, V, W	Gn
										Py1	Ag, Co, In, Sb, Se, Te, Ti, V	Bi-sulfosalts, Au
										Cpy1	Ag, Bi, Cd, Co, Ga, In, Ti, V	Sph, Bi-sulfosalts
							Sericitic: Ser + Qz + Rt ± Dol ± Kln	1) D-type veins 2) Disseminated	1) Py ± Cpy 2) Py + Cpy + Gn + Sph + Au ± Bn ± Mol ± Po ± Pn ± Tnt ± Ttr ± Wt ± Flt ± Cup ± Sch	Py3	Ag, Co, Hg, Sb, Se, Te, Ti, V	Po
										Cpy2	Ag, Bi, Co, Ge, In, Sb, Se, Te, Ti	Bi-sulfosalt (Wt, Cup?)
							Epithermal: Qz + Prl	E-type veins	Assemblage 2: Py + Po + Cpy ± Gn	Py4	Ag, Bi, Co, In, Sb, Se, Ti, W	Gn
										Cpy3	Ag, Ge, In, Sb, Ti, W	Gn

Abbreviations: Act = actinolite, Au = native gold, Bn = bornite, Bt = biotite, Chl = chlorite, Cpy = chalcopyrite, Cup = cuprobismutite, Dol = dolomite, Flt = fletcherite, Gn = galena, Ilm = ilmenite, Kfs = K-feldspar, Kln = kaolinite, Mag = magnetite, Mol = molybdenite, Pn = Pentlandite, Po = pyrrhotite, Prl = pyrophyllite, Py = pyrite, Qz = quartz, Rt = rutile, Ser = sericite, Sch = scheelite, Sph = sphalerite, Ttn = titanite, Tnt = tennantite, Ttd = tetradymite, Ttr = tetrahedrite, Wt = wittichenite.

Table 9.1. Continued.

Deposit name	Geotectonic unit/ Ore district	Main commodities	Critical and rare metals	Deposit style/ Morphology of ore bodies	Host rocks	Age	Alteration style and assemblage	Mineralization style or stage	Metallic minerals	Studied metallic minerals	Critical and rare metals in the studied metallic minerals	Nano-scale mineral inclusions
Gerakario	Vertiskos Unit/ Kilkis ore district	Sb	Ag, Au, Bi, Ce, Co, Ga, Sb and La	Epithermal satellite to porphyry sub-alkaline Cu-Au/ Veins	Two-mica gneiss	MIN: Miocene?	(HR) Sericitic: Ser + Qz	Epithermal stage: intermediate to low sulfidation veins with quartz	Stb + Brth + Sb + Py + Apy ± Mrc ± Po ± Cpy ± Lo ± Au	Stb1	Ag, Bi, Ce, La, Re, Sb, Sm, Th, Ti	Apy
Laodikino	Vertiskos Unit/ Kilkis ore district	Cu-Fe-As-Zn-Pb-Sb	Ag, Au, Bi, Sb, Cd, Co, Ga, Hg, In, Sb, Se and REE: Ce, Gd, Nd, Sm	Metamorphic and shear-zone hosted/ Veins, disseminated	Biotite gneiss	MIN: Mesozoic?	Chloritization: Cal + Chl + Qz	Pods (magnetite-rich)	Mag + Py + Cpy + Rt + Ilm ± Gn ± Apy ± Xtm ± Bsn	Mag1	Ce, Co, Ga, Ge, La, Th, Ti, V	None
										Py2	Ag, Au, Bi, Co, In, Sb, Se, Te, Ti, W	Cpy
										Cpy2	Ag, Au, Bi, Cd, Co, Ga, Ge, In, Sb, Se, Ti	None
					Two mica gneiss, chlorite-muscovite schist	MIN: Cenozoic? (early Oligocene-Miocene?)	Sericitization + chloritization: Qz + Ser + Chl + Cal + Brt	Polymetallic quartz veins	Py + Cpy + Ttr + Sph + Gn	Py1	Co, Sb, Se, Ti, V	None
										Cpy1	Ag, Au, Bi, Cd, Hg, In, Sb, Se, Ti	Gn, Sph, Ttr
										Sph1	Ag, Cd, Co, Ge, Hg, In, Sb, Se, Ti, V	Ttr
										Ttr1	Ag, Au, Bi, Cd, Co, Ga, Ge, Hg, In, Sb, Se, Ti, V	None

Abbreviations: Apy = arsenopyrite, Au = native gold, Bsn = bastnäsité, Brt = barite, Brth = berthierite, Cal = calcite, Chl = chlorite, Cpy = chalcopyrite, Gn = galena, Ilm = ilmenite, Lo = löllingite, Mag = magnetite, Mrc = marcasite, Po = pyrrhotite, Py = pyrite, Qz = quartz, Rt = rutile, Sb = native antimony, Ser = sericite, Sph = sphalerite, Stb = stibnite, Ttr = tetrahedrite, Xtm = xenotime.

Table 9.1. Continued.

Deposit name	Geotectonic unit/ Ore district	Main commodities	Critical and rare metals	Deposit style/ Morphology of ore bodies	Host rocks	Age	Alteration style and assemblage	Mineralization style or stage	Metallic minerals	Studied metallic minerals	Critical and rare metals in the studied metallic minerals	Nano-scale mineral inclusions
Kolchiko	Vertiskos Unit/Kilkis ore district	As-Fe-Cu-Zn-Pb	Ag, Au, Bi, Ce, Cd, Co, Ga, In, Sb, Se, Te, Th, U, W and REE: Gd, La, Nd, Sm	Metamorphic-hosted/ Massive, veins, disseminated	Mica-schist	MIN: pre-early Oligocene?	Sericitization: Ser + Qz + Chl	Polymetallic massive veins	Apy + Py + Cpy + Gn + Po ± Gab ± Bi ± Au ± Ttn ± Ilm ± Rt ± Urn	Apy1 (Apy-dominated)	Ag, Au, Co, Hg, Sb, Se, Te, Ti	Gab
										Py1 (Apy-dominated)	Ag, Au, Sb, Se, Ti	Gn, Bi, Gab
										Py2 (Py-dominated)	Ag, Au, Bi, Co, In, Sb, Se, Te, Ti, V, W	Gab
						MIN: late Oligocene-early Miocene?	Sericitization: Ser + Qz + Chl	Polymetallic quartz veins	Py + Cpy + Apy + Gn + Sph + Po ± Bi ± Hes ± Tb	Py3	Ag, Au, Bi, Co, Hg, Sb, Se, Ti, W	Gn, Bi
										Cpy1	Ag, Au, Bi, Cd, Co, Ga, Ge, Hg, In, Sb, Se, Ti, V	Sph, Gab
										Sph1	Ag, Au, Bi, Cd, Co, Ga, Hg, In, Sb, Se, Ti	Cpy, Gn
								Quartz-pyrite veins	Py ± Cpy	Py4	Ag, Bi, Co, Hg, Sb, Se, Ti, V, W	Cpy
										Cpy2	Ag, Au, Co, Ge, In, Se, Ti, V	Gn
Aspra Chomata	Kerdylion Unit/Chalkidiki ore district	Sb-Fe-Zn	Ag, Cd, Co, Ga, Hg, In, Sb, Se, Te, W	Epithermal overprinting porphyry high-K calc-alkaline Cu-Au/ Veins	Granodiorite porphyry	HR: 24.53±0.31 Ma	Argillic: Kln	Epithermal stage	Py + Sph + Boul ± Apy ± Gn ± Cpy ± Ttr	Py1	Ag, Au, Co, In, Sb, Ti	Boul
										Sph1	Ag, Bi, Cd, Ga, Ge, Hg, In, Nb, Sb, Ti, V, W	Boul, Cpy

Abbreviations: Apy = arsenopyrite, Au = native gold, Bi = native bismuth, Boul = boulangerite, Chl = chlorite, Cpy = chalcopyrite, Gab = galenobismuthinite, Gn = galena, Hes = hessite, Ilm = ilmenite, Kln = kaolinite, Po = pyrrhotite, Py = pyrite, Qz = quartz, Rt = rutile, Ser = sericite, Sph = sphalerite, Tb = tellurobismuthite, Ttn = titanite, Ttr = tetrahedrite, Urn = uraninite.

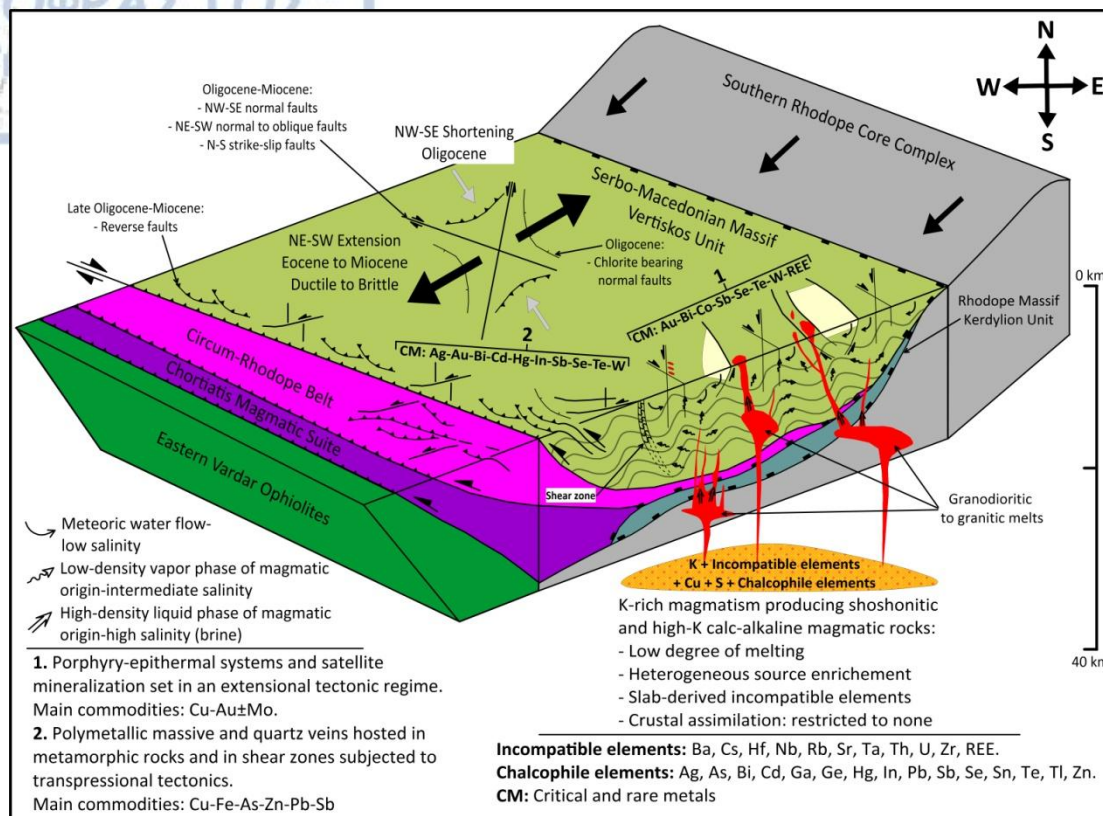


Figure 9.1. Schematic model showing magma emplacement and Oligocene-Miocene tectonic settings focusing on the central and the northern part of the Vertiskos Unit (Serbo-Macedonian Massif). The distribution of porphyry-epithermal systems, and the polymetallic massive and quartz veins hosted in metamorphic rocks is shown in respect to the associated critical and rare metals groups (with information from Kilias et al. 1999, Melfos and Voudouris, 2017, Voudouris et al. 2019a, Schaarschmidt et al. 2021a).

CHAPTER 10. CONCLUSIONS

Critical and rare metals are related to the subsistence of the high-tech industry. They are also associated with the ongoing transition towards a low-carbon society. Supply risk highly challenges the sustainability of the high-tech industry and the goals of the low-carbon society. Thus, the exploration of diversifying sources for critical and rare metals is a high priority. Under this perspective, the present study investigated selected Cenozoic deposits of the Serbo-Macedonian and Rhodope metallogenic provinces in northern Greece focusing on the critical and rare metals endowment. The mineralogy, geochemistry, and mineral chemistry of the deposits found at Vathi, Gerakario, Laodikino and Kolchiko (Kilkis ore district), as well as in Aspra Chomata (Kassandra mining district, NE Chalkidiki), were studied emphasizing on the distribution and abundance of Ag, Au, Bi, Ce, Co, Ga, Gd, Ge, In, La, Nb, Nd, Se, Sm, Ta, Te, Th, U and W. In addition, the correlation of these critical and rare metals with the different hydrothermal alteration styles and mineralization stages was explored, while the fluid inclusion study aims to clarify the formation conditions of the mineralizations located at Laodikino, Kolchiko and Aspra Chomata.

Vathi porphyry Cu-Au±Mo deposit occurs in the northern part of the Kilkis ore district in the Oligocene-Miocene SMMP. The porphyry style mineralization is mainly hosted in latite and is genetically associated with the intrusion of quartz monzonite (18 to 17 Ma). The quartz monzonite appears as fault-controlled, narrow, elongated stocks, while latite forms a plug-shaped body. These two rocks are silica-saturated and exhibit alkali calcic to slightly alkaline chemical affinities. A phreatic breccia crosscuts the latite and was likely formed during the intrusion of the quartz monzonite. The quartz monzonite and latite were affected by potassic and propylitic alteration that were subsequently overprinted by sericitic alteration. The potassic alteration is associated with the ore assemblage pyrite + chalcopyrite + bornite + molybdenite + magnetite in M- and A-type veins, and the propylitic alteration is related to pyrite + chalcopyrite, while the later sericitic alteration is associated with the assemblage pyrite + chalcopyrite + native gold ± tetradymite in D-type veins. The assemblage sphalerite + galena + arsenopyrite + pyrrhotite + pyrite ± stibnite ± tennantite is related to a subsequent epithermal overprinting event.

1) Bulk geochemistry shows enrichments in critical and rare metals including Ag, Au, Bi, Cd, Co, Ga, Ge, Hg, In, Nb, Sb, Se, Te, Th, V, W and REE (Ce, Gd, La, Nd and Sm).

2) Native gold occurs in A-type veins crosscutting the potassic alteration that is overprinted by sericitic alteration in quartz monzonite, and in D-type veins found in both the quartz monzonite and the latite. Native gold is more widespread in the sericitic alteration, where it occurs with tetradymite in the quartz monzonite, and with wittichenite and cuprobismutite in the latite.

3) Samples from the potassic and sericitic alterations show significant enrichments in rare metals including Ag, Au, Bi, Co, Se, Te and W. Rare-earth element enrichment is not related to the porphyry and epithermal mineralizing events, but is attributed mostly to rock-forming and supergene processes.

4) Pyrite at Vathi is enriched with Ag, Co, Sb, Se and Ti, while moderate and weak enrichments have been detected for Bi, Hg, Te, V and W, and for In, respectively. Chalcopyrite contains elevated concentrations of Ag, In and Ti and is moderately enriched with Bi, Cd, Co, Ga, Hg, Se, Te, V and W, and weakly enriched with Nb.

4) High concentrations of Co, Ga, Ge, Ti and V and low concentrations of Se and W occur in magnetite. Titanite is a major host of REE including Ce, Gd, La, Nd and Sm, as well as being a major host of Co, Ga, Ge, In, Sb, Se, Th and W.

5) Nano-scale mineral inclusions are likely related to the presence of Bi-sulfosalts and native gold in pyrite in the potassically altered latite. In addition, chalcopyrite, tetradymite and native gold in pyrite from the sericitic alteration in quartz monzonite, pentlandite in pyrite from the sericitic alteration in latite, and galena in pyrite in the epithermal overprint are also likely nano-inclusions. Nano-scale inclusions occur as sphalerite and Bi-sulfosalts in chalcopyrite from the potassic alteration in latite, and as Bi-sulfosalts in chalcopyrite from the sericitic alteration of the latite. Nano-scale inclusions of galena are accommodated in chalcopyrite from E-type veins. Inclusions of wittichenite, tetradymite and cuprobismutite reflect enrichments of Te and Bi in the mineralizing fluids associated with sericitic alteration.

6) Magnetite from the potassic-calcic alteration of the quartz monzonite hosts titanite inclusions, while minor amounts of nano-scale inclusions of galena likely occur in magnetite from the potassic alteration in latite. Titanite from the potassic-calcic alteration of the quartz monzonite contains no nano-inclusions.

The epithermal quartz-stibnite veins of Gerakario (Oligocene-Miocene, Kilkis ore district, SMMP) crosscut two-mica gneiss in the periphery of the Gerakario Cu-Au porphyry deposit, which is hosted mainly in a syenite intrusion of Miocene age. The formation of the veins is associated with a fault-induced epithermal stage and with intermediate to low sulfidation hydrothermal fluids.

1) The ore mineralogy includes stibnite, berthierite, native antimony, pyrite, arsenopyrite, and traces of marcasite, pyrrhotite, chalcopyrite, löllingite and native gold. Quartz and calcite appear as gangue minerals.

2) The bulk geochemistry of the quartz-stibnite veins revealed enrichments in critical and rare metals including Ag, Au, Bi, Ce, Co, Ga, La and Sb. The profound depletions in Hg and the incorporation of Ce and La contrast the geochemistry of the Sb ores found in SE China.

4) The laser ablation ICP-MS analysis of stibnite show elevated contents of As, Cu and Pb, and low to moderate enrichments in Ag, Bi, Ce, La, Re, Sm, Th, Ti and Tl. The depleted chemistry of stibnite in Hg, Se and Te further highlights the predominance of base metals in the mineralizing fluids. Correlation coefficients for the elemental pairs Ce-La, Ce-Sb and La-Sb in stibnite indicate positive correlations, while the pair Bi-Sb shows a negative correlation.

5) The contents of As, Cu and Pb, are attributed to stoichiometric substitutions, while As enrichments may be ascribed to arsenopyrite nano-scale inclusions. Lanthanum and Ce ablation patterns are similar to those of As, Cu, Pb and Sb, however their affiliation to stibnite remains ambiguous. La and Ce contents may be hosted in fluid inclusions or in lattice defects or may be the result of matrix-derived interferences.

6) Rare earth elements were sourced through leaching of carbonate wall rocks and rock-forming minerals from the magmatic-hydrothermal fluids. Contents of light REE may also be contributed by meteoric fluids. It is concluded that REE fractionation was controlled by the co-precipitation of calcite as a gangue mineral and it was subjected to physicochemical factors related to lattice structure, complexation, as well as sorption and desorption.

The Laodikino metamorphic-and quartz-hosted shear-zone related polymetallic vein mineralization occurs in the western part of the Oligocene-Miocene Kilkis ore district in the SMMP. Mineralization stages include massive and banded (stratiform-like) veins, pods, polymetallic massive and quartz veins, as well as disseminations and

aggregates, which are hosted in two mica gneiss, biotite gneiss, and chlorite-muscovite schist. The formation of the ore mineralization in Laodikino is ascribed to several stages of mineralizing fluids introduced through a wide network of folds and faults under the complex pre-Alpine to post-Alpine tectono-metamorphic evolution of the western part of the Vertiskos Unit. The massive and banded (stratiform-like) mineralization (VMS-style) was formed between middle and late Triassic under fumarolic activity set in an undersea environment related to rifting and island-arc mafic volcanism. The polymetallic massive and quartz veins are mainly controlled by NW-trending faults and secondarily by NE-trending structures suggesting that they were formed between early Oligocene and Miocene. The polymetallic massive veins crosscut the Alpine D3 folds and are sub-parallel to or crosscut the post-Alpine D4 folds, while along shear zones they occur as lenses. The polymetallic quartz veins appear discordant both to D3 and D4 folds. The magnetite-rich pods are locally brecciated and found parallel to foliation.

1) The polymetallic massive veins host arsenopyrite + pyrite + chalcopyrite + sphalerite \pm tetrahedrite \pm galena \pm pyrrhotite \pm magnetite \pm ilmenite \pm rutile \pm cobaltite \pm altaite \pm pilsenite \pm electrum \pm native bismuth. Arsenopyrite and pyrite were first precipitated, while Cu, Zn, Pb, Bi, Te and Au were later introduced following brecciation.

2) The polymetallic quartz veins accommodate pyrite + chalcopyrite + sphalerite + galena + tetrahedrite. Pyrite from the polymetallic quartz veins is characterized by irregular to ovoid replacements. Commonly, replacements consist of galena or tetrahedrite-galena, and rarely of chalcopyrite-tetrahedrite-galena, chalcopyrite-galena, or entirely of sphalerite or barite.

3) Alteration minerals associated with the polymetallic massive and quartz veins include quartz, sericite, chlorite and calcite, while the oxidation assemblage consists of hematite, goethite, malachite, azurite, chalcocite, covellite, cuprite and native copper.

4) Bulk geochemical analyses of the polymetallic quartz veins showed major enrichments in Ag and Sb, high contents in Cd, Hg, Bi, Se, In and Au, and moderate enrichment in Co. Antimony is correlated with Ag, Cd, Hg, Bi, Se and In.

5) In the polymetallic quartz veins, pyrite is enriched in Co, chalcopyrite incorporates Au, sphalerite contains Cd, Hg and In, while tetrahedrite hosts Ag, Bi, Sb and Se. Mineral chemistry suggests that pyrite was deposited from mineralizing fluids

enriched in Co and depleted in Ag, Au, Bi, Hg and In. Following brecciation, mineralizing fluids enriched in base (Cu, Zn, Pb), and critical metals (Ag, Au, Bi, Cd, Hg, In, Sb, Se) were introduced in the system in temperatures varying from 175 to 300 °C. The formation of euhedral sphalerite incorporating Cd, Hg and In, preceded the deposition of chalcopyrite where gold precipitated. Ag, Bi and Se, remained in the residual mineralizing fluids and were included in tetrahedrite and possibly galena concluding the ore deposition.

6) Altaite, cobaltite, electrum, pilsenite and native bismuth found in the polymetallic massive veins reflect mineralizing fluids enriched in Au, Bi, Co and Te. In contrary, the polymetallic quartz veins are characterized by Ag enrichment and they lack in Bi-sulfosalts, Bi-tellurides, Au-Ag-tellurides, native bismuth and gold.

7) In the polymetallic quartz veins, pyrite (Py1) contains base metals (As, Cu, Mn, Mo, Ni, Pb), as well as critical and rare metals Co, Sb, Se, Ti and V, which are incorporated in the crystal lattice. Nano-scale mineral inclusions are not found in Py1. In chalcopyrite (Cpy1), lattice bound base metals (As, Ni, Pb, Sn, Zn), and critical and rare metals (Ag, Au, Bi, Cd, In, Sb, Se, Ti) are present. Nano-scale mineral inclusions of galena, tetrahedrite and sphalerite are associated with Cpy1. Sphalerite (Sph1) includes As, Cu, Fe, Mn, Ni and Sn, as well as Ag, Cd, Co, Ge, Hg, In, Se, Sb, Ti and V, as solid solutions. Time-resolved laser ablation ICP-MS depth profiles support that Ag, As, Bi, Cu, Pb and Sb could also be related to nano- or micro-scale inclusions of tetrahedrite (Ttr1). In Ttr1, base metals (As, Cu, Fe, Mn, Ni, Pb, Sn, Zn), and critical and rare metals (Ag, Au, Bi, Cd, Co, Ga, Ge, Hg, In, Sb, Se, Ti, V) are found as stoichiometric substitutions and/or as solid solutions of the tetrahedrite-tennantite group. Nano-scale minerals do not occur in Ttr1.

8) The magnetite-rich pods accommodate magnetite + pyrite + chalcopyrite + rutile + ilmenite ± galena ± arsenopyrite ± xenotime ± bastnäsite. Calcite, chlorite and quartz are found as gangue and alteration minerals.

9) Bulk geochemical analysis of the magnetite-rich pods revealed that critical and rare metals (Au, Bi, Ce, Ga, Gd, In, La, Nd, Sm) contents are slightly more enriched compared to those from the hydrothermally altered and oxidized metamorphic rocks. Enrichments in Ce, Gd, La, Nd and Sm are ascribed both to xenotime and bastnäsite.

10) Textural characteristics and mineral chemistry indicate that magnetite was formed first and is metamorphic in origin. Pyrite formation followed and was subjected to recrystallization during regional metamorphism. Euhedral magnetite,

rutile-ilmenite and arsenopyrite, as well as rounded inclusions of galena are hosted in recrystallized pyrite. Chalcopyrite mainly forms overgrowths on pyrite and appears as replacements along fractures in pyrite. Galena and chalcopyrite occurrence may be related to Pb and Cu expulsion, respectively. Dysprosium is the only REE incorporated in xenotime suggesting its diagenetic origin.

11) In the magnetite-rich pods, pyrite (Py2) incorporates restricted amounts of As, Cu, Mn, Mo, Ni and Pb, and of critical and rare metals including Ag, Au, Bi, Co, In, Sb, Se, Te, Ti and W. Elevated contents of Cu, Bi and Pb are related to chalcopyrite nano-scale inclusions hosted in Py2. Chalcopyrite (Cpy2) includes Pb, Sn, Zn, as well as Ag, Au, Bi, Co, Cd, Ga, Ge, In, Sb, Se and Ti, in crystal lattice. Nano-scale mineral inclusions are not associated with Cpy2.

The Kolchiko metamorphic- and quartz-hosted polymetallic vein mineralization is located in the southern part of the Oligocene-Miocene Kilkis ore district in the SMMP. Mineralization styles include polymetallic massive and quartz veins, quartz-pyrite veins, and disseminations and aggregates. The metamorphic host rocks are mica-schists. Northwest trends characterize all the vein sets, while quartz-pyrite veins occur in high angles. The formation of the ore mineralization was controlled by several stages of tectono-metamorphic evolution and is similar to those described for Laodikino and Drakontio. Various phases of hydrothermal fluids, with temperatures varying between 240 and 444 °C, are associated with the mineralization deposition. The polymetallic massive veins are overprinted by the Eocene to early Oligocene retrograde greenschist facies metamorphism. Under these metamorphic conditions doleritic intrusions and milky quartz-chlorite veins were also emplaced at Kolchiko. The polymetallic quartz veins and the quartz-pyrite veins were developed under brittle deformation. Their formation is most probably related to development of the late Oligocene to early Miocene dextral strike-slip fault zone along the western edge of the SMM.

1) The polymetallic massive veins contain arsenopyrite + pyrite + chalcopyrite + galena + pyrrhotite ± galenobismuthinite ± native bismuth ± native gold ± titanite ± ilmenite ± rutile ± uraninite. They are subdivided into arsenopyrite- and pyrite-dominated. The polymetallic quartz veins include pyrite + chalcopyrite + arsenopyrite + galena + sphalerite + pyrrhotite ± native bismuth ± hessite ± tellurobismuthite. The quartz-pyrite veins accommodate pyrite ± chalcopyrite. Quartz is the gangue mineral in the mineralized veins.

2) Disseminations and aggregates of pyrite occur in sericitic hydrothermal halos. The alteration assemblage includes sericite, quartz and chlorite.

3) Oxidation related to supergene processes resulted in the formation of goethite, scorodite and covellite in the polymetallic massive veins, as well as of hematite, anglesite and bismite in the polymetallic quartz veins.

4) In the polymetallic massive veins arsenopyrite and pyrite form porphyroblasts and exhibit 120° dihedral angles related to annealing, suggesting response to metamorphism. In addition, cataclastic texture suggest brittle deformation.

5) Open space filling textures and crack and seal processes are ascribed to the formation of the polymetallic quartz veins and of the quartz-pyrite veins, respectively.

6) Fluid inclusion study of quartz from the polymetallic massive veins does not indicate direct magmatic origin of the mineralizing fluids and rejects the exclusive metamorphic origin. Homogenization temperatures have a maximum at 230 °C and low salinities (4 to 12 wt.% NaCl equiv.).

7) The polymetallic massive veins are enriched in Au, Ce, La, U and W, relative to the polymetallic quartz veins, which include higher contents of Ag, Bi, Cd, Co, Ga, In and Te, as well as of Gd, Nd, Se, Sm and Th. Arsenic and Au are significantly correlated in the polymetallic massive veins. The quartz-pyrite veins show enrichments in Au, Bi, Sb and Te.

8) Arsenopyrite (Apy1) from the arsenopyrite-dominated polymetallic massive veins incorporates restricted contents of Cr, Cu, Mn, Ni and Pb, as well as of Co, Sb, Se, Ti, Te, Au, Ag, Hg and Tl, which are found in crystal lattice or as nanoparticles in growth zones. Nano-scale inclusions of galenobismuthinite may occur in Apy1.

9) Pyrite (Py1) from the arsenopyrite-dominated polymetallic massive veins contains Ag, Au, Sb, Se and Ti, whereas As, Zn and Sn, as well as Ag, Au, Bi, Co, In, Sb, Se, Te, Ti, V and W, are found in Py2 from the pyrite-dominated polymetallic massive veins. In Py3 from the polymetallic quartz veins, Mn and Cr, as well as Ag, Au, Bi, Co, Hg, Sb, Se, Ti and W are incorporated. Pyrite (Py4) from the pyrite-quartz veins includes Ni, Pb, Cu, and Ag, Bi, Co, Hg, Sb, Se, Ti, V and W. These trace elements are lattice bound or related to nanoparticles. Nano-scale mineral inclusions may be related to galena and native bismuth in Py1 and Py3, and to galenobismuthinite in Py1 and Py2. Pyrite (Py4) is free of nano-scale mineral inclusions.

10) Chalcopyrite (Cpy1) from the polymetallic quartz veins hosts base metals (As, Cr, Mn, Pb, Zn), and critical and rare metals (Ag, Au, Bi, Cd, Co, Ga, Ge, Hg, In, Sb, Se, Ti, V), which are lattice bound. The same is concluded for base metals (Ni, Sn) and critical and rare metals (Ag, Au, Co, Ge, In, Se, Ti, V) included in Cpy2 from the pyrite-quartz veins. Nano-scale mineral inclusions are ascribed to sphalerite and galenobismuthinite in Cpy1, and to galena in Cpy2.

11) Sphalerite (Sph1) incorporates Cu, Mn and Pb, as well as Ag, Au, Bi, Cd, Co, Ga, Hg, In, Sb, Se and Ti, as solid solutions. Nano-scale inclusions of chalcopyrite and galena are related to Sph1.

The Aspra Chomata porphyry deposit and epithermal vein mineralization belong in the Kassandra mining district in NE Chalkidiki. The porphyritic stage is part of the Stratoni granodiorite, which intruded biotite gneiss, amphibolite, and marble at the footwall of the Stratoni fault during Oligocene. Magma differentiation during the crystallization of the granodiorite led to the development of the porphyritic phase, which is associated with distinct hydrothermal alterations. The potassic overprinted by chloritic-sericitic alteration is associated with the metallic assemblage pyrite + chalcopyrite, while the chloritic-sericitic and sericitic alterations are related to pyrite. In the late sericitic alteration pyrite is also hosted in D-type veins. The assemblage pyrite + sphalerite + boulangerite ± arsenopyrite ± galena ± chalcopyrite ± tennantite is associated with a subsequent overprinting event and is hosted in sheeted epithermal base metal sulfide veins. Bleaching and kaolinization of the granodiorite porphyry are ascribed to the epithermal stage. The porphyry stage mineralization appears oxidized at the surface.

1) Bulk geochemistry revealed that the sericitic alteration and the D-type veins are significantly enriched in Cu and Au, as well as in Pb, Zn, Mo and Ag. Critical and rare metals include Co, In, Se, Te and W, while the epithermal veins are relatively more enriched in Ag, Cd, Ga, Hg and Sb. The epithermal vein mineralization is depleted in Ce, La, Nb, Re and U compared to the D-type veins.

2) Bulk geochemistry and statistical analysis indicate that REE and Bi, Nb, Re, Ta, Th, Ti, U and V are related to rock-forming processes and to the potassic overprinted by chloritic-sericitic alteration, the introduction of Co, In, Se, Te and W is ascribed to sericitic alteration and related D-type veins, while Ag, Cd, Ga, Hg and Sb are associated with the epithermal stage.

3) In the epithermal vein mineralization, pyrite and sphalerite were first deposited. Pyrite crystallization continued resulting in overgrowths on sphalerite and in the development of oscillatory zoning. Minor euhedral arsenopyrite is found as inclusions in pyrite, while galena, chalcopyrite and tennantite appear in pyrite interstices. Boulangerite occurs as replacements in pyrite and sphalerite and between quartz grains.

4) Pyrite (Py1) from the epithermal veins incorporates base (As, Cu, Pb, Zn), and critical and rare metals (Ag, Au, Co, In, Sb, Ti) as stoichiometric substitutions or as solid solutions in specific growth zones. Py1 exhibiting oscillatory zoning incorporates significant contents of As which are correlated with Au and Ag contents. The uncorrelated contents of As and Pb, Sb and Zn indicate the random incorporation of these elements as solid solutions in specific growth zones enriched in As. In Py1, nano-scale minerals include boulangerite.

5) Sphalerite (Sph1) includes Mn, Cu and Sn, as well as Ag, Bi, Cd, Ga, Ge, Hg, In, Nb and W, which are hosted as solid solutions. The absence of Co and the In depletion, coupled with the Ga and Ge contents indicate that sphalerite was formed under low temperatures. Hg and W were precipitated in Sph1 rather than in co-crystallizing Py1. Nano-scale inclusions of boulangerite and chalcopyrite are related to sphalerite (Sph1).

The deliverables of this study add to the existing knowledge on the Au-Bi-Te metallogeny in the Serbo-Macedonian metallogenic province in northern Greece. Based on the relative abundances of the critical and rare metals two groups of Oligocene-Miocene deposits are outlined in respect also to local structural settings. The first group includes porphyry-epithermal and satellite mineralization set in an extensional tectonic regime and enriched in Au-Bi-Co-Sb-Se-Te-W-REE. The second group comprises veins hosted in metamorphic rocks ascribed to a stage of transpressional to transtensional tectonic activity and strike-slip faulting. These vein sets are enriched in Ag-Au-Bi-Cd-Hg-In-Sb-Se-Te-W.

REFERENCES

- Abbo, A., Avigad, D., and Gerdes, A., 2019. Crustal evolution of peri-Gondwana crust into present day Europe: The Serbo-Macedonian and Rhodope massifs as a case study. *Lithos*, 356, 105295.
- Abraitis, P. K., Patrick, R. A. D., and Vaughan, D. J., 2004. Variations in the compositional, textural and electrical properties of natural pyrite: A review. *International Journal of Mineral Processing*, 2004, 74, 41-59.
- Arancibia, O. N., and Clark, A. H., 1996. Early magnetite-amphibole-plagioclase alteration mineralization in the Island Copper porphyry copper-gold-molybdenum deposit, British Columbia. *Economic Geology*, 91, 402-438.
- Arndt, N. T., Fontboté, L., Hedenquist, J. W., Kesler, S. E., Thompson, J. F., and Wood, D. G., 2017. Future global mineral resources. *Geochemical Perspectives*, 6, 1-171.
- Arvanitidis, N., 2010. New metallogenetic concepts and sustainability perspectives for non-energy metallic minerals in Greece. *Bulletin of the Geological Society of Greece*, 43(5), 2437-2445.
- Arvanitidis, N., and Goodenough, K., 2014. Unlocking the potential of rare earth resources in Europe. *ERES2014: 1st European Rare Earth Resources Conference, 04-07 September 2014, Milos*.
- Asvesta, A., 1992. Magmatism and associated sedimentation during the first stage of the opening of the Vardar oceanic basin in Triassic times. *Aristotle University of Thessaloniki, Greece*, Ph.D. thesis, p. 439 (in Greek with English abstract).
- Audétat, A., Pettke, T., Heinrich, C. A., and Bodnar, R. J., 2008. The composition of magmatic-hydrothermal fluids in barren and mineralized intrusions. *Economic Geology*, 103(5), 877-908.
- Ayres, R. U., and Peiro, L. T., 2013. Material efficiency: rare and critical metals. *Philosophical Transactions of the Royal Society A: Mathematical, Physical and Engineering Sciences*, 371(1986), 20110563.

- Baker, T., 2019. Gold±copper endowment and deposit diversity in the Western Tethyan magmatic belt, southeast Europe: Implications for exploration. *Economic Geology*, 114(7), 1237-1250.
- Bakker, R. J., 2012. Package FLUIDS. Part 4: Thermodynamic modelling and purely empirical equations for H₂O-NaCl-KCl solutions. *Mineralogy and Petrology*, 105, 1-29.
- Barakos, G., Gutzmer, J., and Mischo, H., 2016. Strategic evaluations and mining process optimization towards a strong global REE supply chain. *Journal of Sustainable Mining*, 15(1), 26-35.
- Bassiakos, Y., Nerantzis, N., and Papadopoulos, S., 2018. Late Neolithic/Early Bronze Age metallurgical practices at Limenaria, Thasos: evidence for silver and copper production. *Archaeological and Anthropological Sciences*, 11(6), 2743-2757.
- Berger, A., Gnoss, E., Janots, E., Fernandez, A., and Giese, J., 2008. Formation and composition of rhabdophane, bastnäsite and hydrated thorium minerals during alteration: implications for geochronology and low-temperature processes. *Chemical Geology*, 254(3-4), 238-248.
- Berman, N., Couttenier, M., Rohner, D., and Thoenig, M., 2017. This mine is mine! How minerals fuel conflicts in Africa. *American Economic Review*, 107(6), 1564-1610.
- Bertrand, G., Cassard, D., Arvanitidis, N., and Stanley, G., 2016. Map of critical raw material deposits in Europe. *Energy Procedia*, 97, 44-50.
- Bertrand, G., Guillou-Frottier, L., and Loiselet, C., 2014. Distribution of porphyry copper deposits along the western Tethyan and Andean subduction zones: Insights from a paleotectonic approach. *Ore Geology Reviews*, 60, 174-190.
- Bristol, S. K., Spry, P. G., Voudouris, P. Ch., Melfos, V., Mathur, R. D., Fornadel, A. P., and Sakellaris, G. A., 2015. Geochemical and geochronological constraints on the formation of shear-zone hosted Cu–Au–Bi–Te mineralization in the Stanos area, Chalkidiki, northern Greece. *Ore Geology Reviews*, 66, 266-282.

- Brun, J. P., and Sokoutis, D., 2018. Core complex segmentation in North Aegean, a dynamic view. *Tectonics*, 37, 1797-1830.
- Brun, J. P., and Sokoutis, D., 2018. Core complex segmentation in North Aegean, a dynamic view. *Tectonics*, 37, 1797-1830.
- Blundy, J., Mavrogenes, J., Tattitch, B., Sparks, S., and Gilmer, A., 2015. Generation of porphyry copper deposits by gas-brine reaction in volcanic arcs. *Nature Geoscience*, 8(3), 235-240.
- Buijs, B., and Sievers, H., 2011. Resource Security Risks in Perspective Complexity and Nuance. *Polinares working paper*, 33, pp. 42.
- Cao, M. J., Qin, K. Z., Li, Q. M., Evans, N. J., and Jin, L. Y., 2015. In situ LA-(MC)-ICP-MS trace element and Nd isotopic compositions and genesis of polygenetic titanite from the Baogutu reduced porphyry Cu deposit, Western Junggar, NW China. *Ore Geology Reviews*, 65, 940-954.
- Cassard, D., Bertrand, G., Billa, M., Serrano, J. J., Tourlière, B., Angel, J. M., and Gaál, G., 2015. ProMine Mineral Databases: new tools to assess primary and secondary mineral resources in Europe. In: Weihed, P. (ed) *3D, 4D and Predictive Modeling of Major Mineral Belts in Europe*. Springer, Belrin, 9-58.
- Chakhmouradian, A. R., Smith, M. P., and Kynicky, J., 2015. From “strategic” tungsten to “green” neodymium: A century of critical metals at a glance. *Ore Geology Reviews*, 64(1), 455-458.
- Chapman, B., 2018. The geopolitics of rare earth elements: emerging challenge for US National Security and Economics. *Journal of Self-Governance and Management Economics*, 6(2), 50-91.
- Charalampides, G., Arvanitidis, N., Vatalis, K. I., and Platias, S., 2013. Sustainability perspectives in Greece as reflected by mineral deposits exploitation. *Procedia Economics and Finance*, 5, 143-151.

- Christofides, G., Koroneos, A., Liati, A., and Kral, J., 2007. The A-type Kerkini granitic complex in north Greece: geochronology and geodynamic implications. *Bulletin of the Geological Society of Greece*, 40, 700-711.
- Cloos, M., 2001. Bubbling Magma Chambers, Cupolas, and Porphyry Copper Deposits. *International Geology Review*, 43(4), 37-41.
- Conn, C. D., Spry, P. G., Layton-Matthews, D., Voinot, A., and Koenig, A., 2019. The effects of amphibolite facies metamorphism on the trace element composition of pyrite and pyrrhotite in the Cambrian Nairne Pyrite Member, Kanmantoo Group, South Australia. *Ore Geology Reviews*, 114, 103128.
- Cook, N. J., Ciobanu, C. L., Pring, A., Skinner, W., Shimizu, M., Danyushevsky, L., Saini-Eidukat, B., and Melcher, F., 2009. Trace and minor elements in sphalerite: A LA-ICPMS study. *Geochimica et Cosmochimica Acta*, 73(16), 4761-4791.
- Cook, N. J., Ciobanu, C. L., Meria, D., Silcock, D., and Wade, B., 2013a. Arsenopyrite-pyrite association in an orogenic gold ore: Tracing mineralization history from textures and trace elements. *Economic Geology*, 108(6), 1273-1283.
- Cook, N. J., Ciobanu, C. L., Giles, D., and Wade, B., 2013b. Correlating textures and trace elements in ore minerals. In: Jonsson, E., et al. (eds) *Mineral deposit research for a high-tech world*. Proceedings of the 12th Biennial SGA Meeting, Uppsala, Sweden, 288-291.
- Cooke, D. R., Hollings, P., Wilkinson, J. J., and Tosdal, R. M., 2014. Geochemistry of porphyry deposits. In: Holland, H. D., and Turekian, K. K., (eds) *Treatise on Geochemistry*, 2nd Edition, Elsevier, Amsterdam, 13, 357-381.
- Craig, J. R., Vokes, F. M., and Solberg, T. N., 1998. Pyrite: physical and chemical textures. *Mineralium Deposita*, 34(1), 82-101.
- Crowson, P., 1996. The European mining industry: What future? *Resources Policy*, 22(1-2), 99-105.

Deditius, A. P., Utsunomiya, S., Reich, M., Kesler, S. E., Ewing, R. C., Hough, R., and Walshe, J., 2011. Trace metal nanoparticles in pyrite. *Ore Geology Reviews*, 42(1), 32-46.

Deditius, A. P., Reich, M., Simon, A. C., Suvorova, A., Knipping, J., Roberts, M.P., Rubanov, S., Dodd, A., and Saunders, M., 2018. Nanogeochemistry of hydrothermal magnetite. *Contributions to Mineralogy and Petrology*, 173, 1-20.

Department of the Interior, U.S., 2018. Final List of Critical Minerals 2018. Office of the Secretary, US Department of Interior, pp. 2. <https://www.federalregister.gov/d/2018-10667> (Accessed online on 12/7/2021).

Díaz-García, M. E., and Badía-Laíño, R., 2005. Fluorescence, Derivatization. In Paul Worsfold, P., Townshend, A., Poole, C., (eds) *Encyclopedia of Analytical Science (Second Edition)*. Elsevier, Amsterdam, 138-148,

Dimou, E., Papastavrou, St., and Sermet, R., 1987. Antimony in Greece (3rd volume), Samos island, Gerakario Kilkis, Pefka Rhodope, Stagira Chalkidiki. IGME, Athens (in Greek), pp. 68.

Dixon, J.E., and Dimitriadis, S., 1984. Metamorphosed ophiolitic rocks from the Serbo-Macedonian massif near lake Volvi, north-east Greece. *Geological Society of London Special Publication*, 17, 603-618.

Dmitrijeva, M., Cook, N. J., Ehrig, K., Ciobanu, C. L., Metcalfe, A. V., Kamenetsky, M., Kamenetsky, V. S., and Gilbert, S., 2020. Multivariate statistical analysis of trace elements in pyrite: Prediction, bias and artefacts in defining mineral signatures. *Minerals*, 10, 61.

Dostal, J., 2016. Rare metal deposits associated with alkaline/peralkaline igneous rocks. In: Verplanck, P. L., Hitzman, M. W., (eds) *Rare Earth and Critical Elements in Ore Deposits*. Society of Economic Geologists Inc., Littleton, p. 33-54.

Driesner, T., 2007. The system H₂O-NaCl. Part II: Correlations for molar volume, enthalpy, and isobaric heat capacity from 0 to 1000 °C, 1 to 5000 bar, and 0 to 1 XNaCl. *Geochimica et Cosmochimica Acta*, 71, 4902-4919.

Driesner, T., and Heinrich, C. A., 2007. The system H₂O-NaCl. Part I: Correlations for molar volume, enthalpy, and isobaric heat capacity from 0 to 1000 degrees C, 1 to 5000 bar, and 0 to 1 X-NaCl. *Geochimica et Cosmochimica Acta*, 71, 4880-4901.

Eldorado Gold Corporation, 2021. Resources and Reserves. Available online: <https://www.eldoradogold.com/assets/resourcesand-reserves/default.aspx> (Accessed online on 2/8/2021).

Eleftheriadis, G., Frank, W., and Petrakakis, K., 2001. 40Ar/39Ar dating and cooling history of the Pangeon granitoids, Rhodope Massif (eastern Macedonia, Greece). *Bulletin of the Geological Society of Greece*, 34(3), 911-916.

Eliopoulos, D. G., Economou-Eliopoulos, M., and Zelyaskova-Panayiotova, M., 2014. Critical factors controlling Pd and Pt potential in porphyry Cu–Au deposits: evidence from the Balkan Peninsula. *Journal of Geosciences*, 4, 31-49.

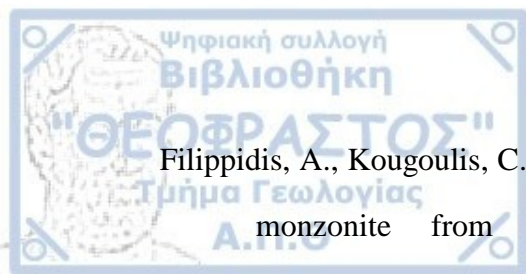
Engels, B., 2021. All good things come from below? Scalar constructions of the ‘local’ in conflicts over mining. *Political Geography*, 84, 102295.

Ersoy, E. Y., and Palmer, M. R., 2013. Eocene-Quaternary magmatic activity in the Aegean: Implications for mantle metasomatism and magma genesis in an evolving orogeny. *Lithos*, 180, 5-24.

European Commission, 2020. Study on the EU’s list of Critical Raw Materials – Final Report (2020). Brussels, pp. 158.

European Commission, 2019. The European Green Deal, COM(2019), 640final. pp. 24.

European Commission, 2010. Critical raw materials for the EU. Report of the Ad-hoc Working Group on defining critical raw materials, *Eucom*, 39, pp. 84.



Filippidis, A., Kougoulis, C., and Michailidis, K., 1988. Sr-bearing stilbite in a quartz monzonite from Vathi, Kilikis, Northern Greece. *Schweizerische Mineralogische und Petrographische Mitteilungen*, 68, 67-76.

Frei, R., 1992. Isotope (Pb, Rb-Sr, S, O, C, U-Pb) Geochemical Investigations on Tertiary Intrusives and Related Mineralizations in the Serbomacedonian Pb-Zn, Sb+Cu-Mo Metallogenic Province in Northern Greece. *Swiss Federal Institute of Technology (ETH) Zurich, Switzerland*, Ph.D. thesis, p. 231.

Frenzel, M., Hirsch, T., and Gutzmer, J., 2016. Gallium, germanium, indium, and other trace and minor elements in sphalerite as a function of deposit type-A meta-analysis. *Ore Geology Reviews*, 76, 52-78.

Fu, S., Hu, R., Bi, X., Sullivan, N. A., and Yan, J., 2020. Trace element composition of stibnite: Substitution mechanism and implications for the genesis of Sb deposits in southern China. *Applied Geochemistry*, 118, 104637.

Gamaletsos, P. N., Godelitsas, A., Philippidis, A., and Pontikes, Y., 2019. The rare earth elements potential of Greek bauxite active mines in the light of a sustainable REE demand. *Journal of Sustainable Metallurgy*, 5(1), 20-47.

Gebre-Mariam, M., Hagemann, S. G., and Groves, D. I., 1995. A classification scheme for epigenetic Archaean lode-gold deposits. *Mineralium Deposita*, 30(5), 408-410.

George, L., Cook, N. J., Ciobanu, C. L., and Wade, B. P., 2015. Trace and minor elements in galena: A reconnaissance LA-ICP-MS study. *American Mineralogist*, 100(2-3), 548-569.

George, L. L., Cook, N. J., and Ciobanu, C. L., 2017. Minor and trace elements in natural tetrahedrite-tennantite: Effects on element partitioning among base metal sulphides. *Minerals*, 7(2), 17.

George, L. L., Cook, N. J., Crowe, B. B., and Ciobanu, C. L., 2018. Trace elements in hydrothermal chalcopyrite. *Mineralogical Magazine*, 82, 59-88.

Gilg, H. A., and Frei, R., 1994. Chronology of magmatism and mineralization in the Kassandra mining area, Greece: The potentials and limitations of dating hydrothermal illites. *Geochimica et Cosmochimica Acta*, 58, 2107-2122.

Girtan, M., Wittenberg, A., Grilli, M. L., de Oliveira, D. P. S., Giosuè, C., and Ruello, M. L., 2021. The critical raw materials issue between scarcity, supply Risk, and unique Properties. *Materials*, 14(8), 1826.

Goldfarb, R. J., Hofstra, A. H., and Simmons, S. F., 2016. Critical elements in Carlin, epithermal, and orogenic gold deposits. In: Verplanck, P. L., and Hitzman, M. W. (eds) *Rare Earth and Critical Elements in Ore Deposits*. Society of Economic Geologists Inc., Littleton, 217-244.

Goodenough, K. M., Schilling, J., Jonsson, E., Kalvig, P., Charles, N., Tuduri, J., Deady, E. A., Sadeghi, M., Schiellerup, H., Müller, A., Bertrand, G., Arvanitidis, N., Eliopoulos, D. G., Shaw, R. A., Thrane, K., and Keulen, N., 2016. Europe's rare earth element resource potential: An overview of REE metallogenetic provinces and their geodynamic setting. *Ore Geology Reviews*, 72, 838–856.

Gounaris K., 2017. Petrographic, mineralogical and geochemical study of the porphyry mineralization at Aspra Chomata, NE Chalkidiki. *Aristotle University of Thessaloniki, Greece*, Diploma thesis, p. 64.

Graedel, T. E., Gunn, G., and Tercero Espinoza, L., 2014. Metal resources, use and criticality. In: Gunn, G., (ed) *Critical metals handbook*. John Wiley & Sons, New Jersey, pp.1-19.

Grandell, L., Lehtilä, A., Kivinen, M., Koljonen, T., Kihlman, S., and Lauri, L. S., 2016. Role of critical metals in the future markets of clean energy technologies. *Renewable Energy*, 95, 53-62.

Granitto, M., Emsbo, P., Hofstra, A. H., Orkild-Norton, A. R., Bennett, M. M., Azain, J. S., Koenig, A. E., and Karl, N.A., 2020. Global geochemical database of

critical minerals in archived mine samples: U.S. Geological Survey data release, <https://doi.org/10.5066/P9Z3XL6D>.

- Guillong, M., Meier, D. L., Allan, M. M., Heinrich, C. A., and Yardley, B. W. D., 2008. Appendix A6: SILLS: A MATLAB-based program for the reduction of laser ablation ICP-MS data of homogeneous materials and inclusions. In: Sylvester, P., (ed) *Laser Ablation ICP-MS in the Earth Sciences: Current Practices and Outstanding Issues*. Mineralogical Association of Canada Short Course 40, Vancouver, 328-333.
- Hahn, A., Naden, J., Treloar, P. J., Kiliyas, S. P., Rankin, A. H., and Forward, P., 2012. A new time frame for the mineralization in the Kassandra mine district, N Greece: deposit formation during metamorphic core complex exhumation. *Journal of Earth Sciences*, 96, 1079-1099.
- Hansen, M. K., Makovicky, E., and Karup-Møller, S., 2003. Exploratory studies on substitutions in tennantite-tetrahedrite solid solution. Part IV. Substitution of germanium and tin. *Neues Jahrbuch für Mineralogie - Abhandlungen*, 179, 43-71.
- Halley, S., Dilles, J. H., and Tosdal, R. M., 2015. Footprints: hydrothermal alteration and geochemical dispersion around porphyry copper deposits. *SEG Discovery*, 100, 1-17.
- Hedenquist, J. W., Arribas, A., and Gonzalez-Urien, E., 2000. Exploration for epithermal gold deposits. *Reviews in Economic Geology*, 13(2), 45-77.
- High, S., 2013. "The wounds of class": a historiographical reflection on the study of deindustrialization, 1973-2013. *History Compass*, 11(11), 994-1007.
- Himmerkus, F., Reischmann, T., and Kostopoulos, D.K., 2006. Late Proterozoic and Silurian basement units within the Serbo-Macedonian massif, northern Greece: the significance of terrane accretion in the Hellenides. *Geological Society of London Special Publication*, 260, 35-50.

Hirtopanu, P., Fairhurst, R. J., Jakab, G., and Andersen, C., 2015. Niobian rutile and its associations at Jolotca, Ditrau alkaline intrusive massif, east Carpathians, Romania. *Proceedings of the Romanian Academy, Series B*, 17, 39-55.

Hofstra, A. H., and Kreiner, D. C., 2020. Systems-Deposits-Commodities-Critical Minerals Table for the Earth Mapping Resources Initiative: U.S. Geological Survey Open-File Report 2020–1042, pp. 24.

Huang, X. W., Sappin, A. A., Boutroy, É., Beaudoin, G., and Makvandi, S., 2019. Trace element composition of igneous and hydrothermal magnetite from porphyry deposits: Relationship to deposit subtypes and magmatic affinity. *Economic Geology*, 114, 917-952.

Humphreys, D., 2014. The mining industry and the supply of critical minerals. In: Gunn, G. (ed). *Critical metals handbook*. John Wiley & Sons, New Jersey, 20-40.

Huston, D. L., 2014. New age metals: the geology and genesis of ores required for a changing economy and a carbon-constrained world – preface to a thematic issue on critical commodities. *Mineralium Deposita*, 49(8), 885-887.

Janssen, A., Putnis, A., Geisler, T., and Putnis, C. V., 2010. The experimental replacement of ilmenite by rutile in HCl solutions. *Mineralogical Magazine*, 74(4), 633-644.

Jenner, F. E., O'Neill, H. S. C., Arculus, R. J., and Mavrogenes, J. A., 2010. The magnetite crisis in the evolution of arc-related magmas and the initial concentration of Au, Ag and Cu. *Journal of Petrology*, 51(12), 2445-2464.

John, D. A., and Taylor, R. D., 2016. By-products of porphyry copper and molybdenum deposits. In: Verplanck, P. L., and Hitzman, M. W. (eds) *Rare Earth and Critical Elements in Ore Deposits*. Society of Economic Geologists Inc., Littleton, 137-164.

John, D. A., Ayuso, R. A., Barton, M. D., Blakely, R. J., Bodnar, R. J., Dilles, J. H., Gray, F., Graybeal, F. T., Mars, J. C., McPhee, D. K., Seal, R. R., Taylor, R.

- D., and Vikre, P. G., 2010. Porphyry copper deposit model, chap. B of Mineral deposit models for resource assessment. *U.S. Geological Survey, Scientific Investigations Report*, 2010–5070–B, pp. 169.
- Jolivet, L., Faccenna, C., Huet, B., Labrousse, L., Pourhiet, L., Lacombe, O., Lecomte, E., Burov, E., Denèle, Y., Brun, J. -J., Philippon, M., Paul, A., Salaün, G., Karabulut, H., Piromallo, C., Monié, P., Gueydan, F., Okay, A., Oberhänsli, R., Pourceau, A., Augier, R., Gadenne, L., and Driussi, O., 2013. Aegean tectonics: Strain localisation, slab tearing and trench retreat. *Tectonophysics*, 597, 1-33.
- Kalantzakos, S., 2020. The race for critical minerals in an era of geopolitical realignments. *The International Spectator*, 55(3), 1-16.
- Kalogeropoulos, S. I., Frei, R., Nikolaou, M., and Gerouki, F., 1990. Origin and metallogenetic significance of the Tertiary Stratoní "Granodiorite", Chalkidiki, N. Greece: isotopic and chemical evidence. *Bulletin of the Geological Society of Greece*, 26, 23-38.
- Keith, M., Smith, D. J., Doyle, K., Holwell, D. A., Jenkin, G. R. T., Barry, T. L., Becker, J., and Rampe, J., 2020. Pyrite chemistry: A new window into Au-Te ore-forming processes in alkaline epithermal districts, Cripple Creek, Colorado. *Geochimica et Cosmochimica Acta*, 274, 172-191.
- Kelepertsis, A. E., Reeves, R., and Andrulakis, J., 1986. Geochemical studies of porphyry type mineralization at Gerakario-Vathi of Kilikis area, northern Greece. *Mineral Wealth*, 42, 43-48.
- Kelepertsis, A. E., Karamanos, H., Andrulakis, J., and Polyzonis E., 1987. A stream and soil geochemical survey in metamorphic rocks of the Serbomacedonian Massif, Kilikis Province, Greece. *Chemie der Erde*, 47, 61-74.
- Kelley, K. D., and Spry, P. G., 2016. Critical elements in alkaline igneous rock-related epithermal gold deposits. In: Verplanck, P. L., and Hitzman, M. W.

(eds) *Rare Earth and Critical Elements in Ore Deposits*. Society of Economic Geologists Inc., Littleton, 195-216.

Kilias, A., 2021. The Hellenides: A Multiphase Deformed Orogenic Belt, its Structural Architecture, Kinematics and Geotectonic Setting during the Alpine Orogeny: Compression vs Extension the Dynamic Peer for the Orogen Making. A Synthesis. *Journal of Geology and Geoscience*, 5, 1-56.

Kilias, A., Falalakis, G., and Mountrakis, D., 1999. Cretaceous-Tertiary structures and kinematics of the Serbomacedonian metamorphic rocks and their relation to the exhumation of the Hellenic hinterland (Macedonia, Greece). *International Journal of Earth Sciences*, 88, 513-531.

Kockel, F., Mollat, H., and Gundlach, H., 1975. Hydrothermally altered and (copper) mineralized porphyritic intrusions in the Serbo-Macedonian Massif (Greece). *Mineralium Deposita*, 10, 195-204.

Kockel, F., and Ioannidis, K., 1979a. Geological map of Greece: Kilkis map sheet, 1:50.000. IGME, Athens.

Kockel, F., Mollat, H., Antoniadis, P., and Ioannidis, K., 1979b. Geological map of Greece: Lachanas map sheet, 1:50.000. IGME, Athens.

Kołodziejczyk, J., Pršek, J., Melfos, V., Voudouris, P. C., Maliqi, F., and Kozub-Budzyń, G., 2015. Bismuth minerals from the Stan Terg deposit (Trepça, Kosovo). *Neues Jahrbuch für Mineralogie Abhandlungen*, 192(3), 317-333.

Korges, M., Weis, P., and Andersen, C., 2020. The role of incremental magma chamber growth on ore formation in porphyry copper systems. *Earth and Planetary Science Letters*, 552, 116584.

Kositcin, N., McNaughton, N. J., Griffin, B. J., Fletcher, I. R., Groves, D. I., and Rasmussen, B., 2003. Textural and geochemical discrimination between xenotime of different origin in the Archaean Witwatersrand Basin, South Africa. *Geochimica et Cosmochimica Acta*, 67(4), 709-731.

Kougoulis, C., Veranis, N., and Kasoli-Fournaraki, A., 1990. Meta-volcanic rocks in the Examili Formation (north Greece). *Chemie der Erde*, 50, 67-79.

Kourou, A., 1991. Lithology, tectonics, geochemistry and metamorphism of a sector of the west part of the Vertiskos Group, The area NE of the lake Agios Vasilios (Koronia). *Aristotle University of Thessaloniki, Greece*, Ph.D. thesis, pp. 481, (in Greek with English abstract).

Kroll, T., Müller, D., Seifert, T., Herzig, P. M., and Schneider, A., 2002. Petrology and geochemistry of the shoshonite-hosted Skouries porphyry Cu-Au deposit, Chalkidiki, Greece. *Mineralium Deposita*, 37, 137-144.

Kydonakis, K., Brun, J. P., Poujol, M., Monié, P., and Chatzitheodoridis, E., 2016. Inferences on the Mesozoic evolution of the North Aegean from the isotopic record of the Chalkidiki blocks. *Tectonophysics*, 682, 65-84.

Lang, J. R., and Baker, T., 2001. Intrusion-related gold systems: the present level of understanding. *Mineralium Deposita*, 36(6), 477-489.

Lecumberri-Sanchez, P., Steele-MacInnis, M., Weis, P., Driesner, T., and Bodnar, R. J., 2015. Salt precipitation in magmatic-hydrothermal systems associated with upper crustal plutons. *Geology*, 43(12), 1063-1066.

Lehmann, B., Dietrich, A., and Wallianos, A., 2000. From rocks to ore. *International Journal of Earth Sciences*, 89(2), 284-294.

Li, W., Cook, N. J., Xie, G. Q., Mao, J. W., Ciobanu, C. L., Li, J. W., and Zhang, Z. Y., 2019. Textures and trace element signatures of pyrite and arsenopyrite from the Gutaishan Au–Sb deposit, South China. *Mineralium Deposita*, 54(4), 591-610.

Mancheri, N. A., 2015. World trade in rare earths, Chinese export restrictions, and implications. *Resources Policy*, 46, 262-271.

Marshall, B., Vokes, F. M., and Larocque, A. C. L., 2000. Regional metamorphic remobilization: upgrading and formation of ore deposits. In: Frank M. Vokes,

F. M., Marshall, B., and Spry, P. G. (eds) *Metamorphic and Metamorphogenic Ore Deposits. Reviews in Economic Geology*, 11, 19-38.

- Mavrogonatos, C., Voudouris, P., Berndt, J., Klemme, S., Zaccarini, F., Spry, P. G., Melfos, V., Tarantola, A., Keith, M., Klemm, R., and Haase, K., 2019. Trace elements in magnetite from the Pagoni Rachi porphyry prospect, NE Greece: Implications for ore genesis and exploration. *Minerals*, 9, 725.
- Mavrogonatos, C., Voudouris, P., Zaccarini, F., Klemme, S., Berndt, J., Tarantola, A., Melfos, V., and Spry, P. G., 2020. Multi-stage introduction of precious and critical metals in pyrite: A case study from the Konos Hill and Pagoni Rachi porphyry/epithermal prospects, NE Greece. *Minerals*, 10, 784.
- McFall, K. A., Naden, J., Roberts, S., Baker, T., Spratt, J., and McDonald, I., 2018. Platinum-group minerals in the Skouries Cu-Au (Pd, Pt, Te) porphyry deposit. *Ore Geology Reviews*, 99, 344-364.
- McMahon, G., and Moreira, S., 2014. The Contribution of the Mining Sector to Socioeconomic and Human Development. *Extractive industries for development series: n. 30*. World Bank, Washington, DC. pp. 72.
- McNulty, B. A., and Jowitt, S. M., 2021. Barriers to and uncertainties in understanding and quantifying global critical mineral and element supply. *Iscience*, 102809.
- Melfos V., Vavelidis M., and Arikas K., 2001. A new occurrence of argentopentlandite and gold from the Au-Ag-rich copper mineralisation in the Paliomylos area, Serbomacedonian Massif, Central Macedonia, Greece. *Bulletin of the Geological Society of Greece*, 34(3), 1065-1072.
- Melfos, V., Vavelidis, M., Christofides, G., and Seidel, E., 2002. Origin and evolution of the Tertiary Maronia porphyry copper-molybdenum deposit, Thrace, Greece. *Mineralium Deposita*, 37, 648-668.
- Melfos, V., and Voudouris, P., 2012. Geological, mineralogical and geochemical aspects for critical and rare metals in Greece. *Minerals*, 2, 300-317.

Melfos, V., and Voudouris, P., 2017. Cenozoic metallogeny of Greece and potential for precious, critical and rare metals exploration. *Ore Geology Reviews*, 89, 1030-1057.

Melfos, V., Voudouris, P., Melfou, M., Sánchez, M. G., Papadopoulou, L., Filippidis, A., Spry, P. G., Schaarschmidt, A., Klemm, R., Haase, K. M., Tarantola, A., and Mavrogenatos, C., 2020. Mineralogical constraints on the potassic and sodic-calcic hydrothermal alteration and vein-type mineralization of the Maronia porphyry Cu-Mo-Re-Au deposit in NE Greece. *Minerals*, 10, 182.

Miggiros, G., Ioannidis, K., and Kelepertsis, A., 1990. Geological map of Greece: Herson map sheet, 1:50.000. IGME, Athens.

Moritz, R., Rezeau, H., Ovtcharova, M., Tayan, R., Melkonyan, R., Hovakimyan, S., Ramazanov, V., Selby, D., Ulianov, A., Chiaradia, M., and Putlitz, B., 2016. Long-lived, stationary magmatism and pulsed porphyry systems during Tethyan subduction to post-collision evolution in the southernmost Lesser Caucasus, Armenia and Nakhichevan. *Gondwana Research*, 37, 465-503.

Moss, R. L., Tzimas, E., Kara, H., Willis, P., and Kooroshy, J., 2011. Critical metals in strategic energy technologies. JRC-Scientific and technical reports, Publications Office of the European Union, Luxembourg, pp. 164.

Mposkos, E., 1983. A mineralogical study of the Au–Ag–Bi–Te–Cu–Co–Ni–As–S ore mineralization in Macedonia. *Chemie der Erde*, 42, 281-296.

Mposkos, E., Krohe, A., and Baziotis, I., 2021. Deep tectonics in the Eastern Hellenides uncovered: The record of Variscan continental amalgamation, Permo-Triassic rifting, and Early Alpine collision in Pre-Variscan continental crust in the W-Rhodope (Vertiscos-Ograzden Complex, NGreece). *Tectonics*, 40, e2019TC005557.

Mudd, G. M., Werner, T. T., Weng, Z. -H., Yellishetty, M., Yuan, Y., McAlpine, S. R. B., Skirrow, R. G., and Czarnota, K., 2019. Critical Minerals in Australia:

A Review of Opportunities and Research Needs. Geoscience Australia, Canberra, pp. 58.

Nadeau, O., Williams-Jones, A. E., and Stix, J., 2010. Sulphide magma as a source of metals in arc-related magmatic hydrothermal ore fluids. *Nature Geoscience*, 3(7), 501-505.

Nadoll, P., Mauk, J. L., Leveille, R. A., and Koenig, A. E., 2015. Geochemistry of magnetite from porphyry Cu and skarn deposits in the southwestern United States. *Mineralium Deposita*, 50, 493-515.

Nassar, N. T., Graedel, T. E., and Harper, E. M., 2015. By-product metals are technologically essential but have problematic supply. *Science advances*, 1(3), e1400180.

Nerantzis, N., 2016. Pre-Industrial iron smelting and silver extraction in north-eastern Greece: an Archaeometallurgical Approach. *Archaeometry*, 58(4), 624-641.

Patsiouri, A., 2017. Mineralogy and geochemistry of ore occurrences in the metamorphic rocks of the Kolchiko area, Thessaloniki district. *Aristotle University of Thessaloniki, Greece*, M.Sc thesis, p. 126 (in Greek with English abstract).

Pavlidis, S., Caputo, R., Sboras, S., Chatzipetros, A., Papathanasiou, G., and Valkaniotis, S., 2010. The Greece catalogue of active faults and database of seismogenic sources. *Bulletin of the Geological Society of Greece*, 43, 486-494.

Pe-Piper, G., Piper, D. J., Koukouvelas, I., Dolansky, L. M., and Kokkalas, S., 2009. Postorogenic shoshonitic rocks and their origin by melting underplated basalts: The Miocene of Limnos, Greece. *Geological Society of America Bulletin*, 121(1-2), 39-54.

Pohl, W. L., 2011. Economic geology: principles and practice. John Wiley & Sons, pp. 663.

Pokrovski, G. S., Kara, S., and Roux, J., 2002. Stability and solubility of arsenopyrite, FeAsS, in crustal fluids. *Geochimica et cosmochimica acta*, 66(13), 2361-2378.

Pudack, C., Halter, W. E., Heinrich, C. A., and Pettke, T., 2009. Evolution of magmatic vapor to gold-rich epithermal liquid: The porphyry to epithermal transition at Nevados de Famatina, northwest Argentina. *Economic Geology*, 104, 449–477.

Reich, M., Román, N., Barra, F., and Morata, D., 2020. Silver-rich chalcopyrite from the active Cerro Pabellón geothermal system, northern Chile. *Minerals*, 10, 113.

Rezeau, H., Moritz, R., Wotzlaw, J., Tayan, R., Melkonyan, R., Ulianov, A., Selby, D., Abzac, F., and Stern, R. A., 2016. Temporal and genetic link between incremental pluton assembly and pulsed porphyry Cu-Mo formation in accretionary orogens. *Geology*, 44(8), 627–630.

Ridley, J., 2013. Ore deposit geology. Cambridge University Press, pp. 398.

Richards, J. P., 2009. Postsubduction porphyry Cu-Au and epithermal Au deposits: Products of remelting of subduction-modified lithosphere. *Geology*, 37(3), 247–250.

Richards, J. P., 2011. Magmatic to hydrothermal metal fluxes in convergent and collided margins. *Ore Geology Reviews*, 40, 1-26.

Richards, J. P., 2013. Giant ore deposits formed by optimal alignments and combinations of geological processes. *Nature Geoscience*, 6(11), 911-916.

Richards, J. P., 2015. Tectonic, magmatic, and metallogenic evolution of the Tethyan orogen: From subduction to collision. *Ore Geology Reviews*, 70, 323-345.

Ross, J., Voudouris, P., Melfos, V., and Vaxevanopoulos, M., 2020. Mines, Metals and money: Ancient world studies in science, archaeology and history. In: Sheedy, K. A., Davis, G. (eds) *Metallurgy in Numismatics*. Royal Numismatic Society Special Publication, London, 6, 9–21.

Ross, J., Voudouris, P., Melfos, V., Vaxevanopoulos, M., Soukis, K., and Merigot, K., 2021. The Lavrion silver district: Reassessing its ancient mining history. *Geoarchaeology*, 36(4), 617-642.

Rudnick, R. L., and Gao, S., 2003. The Composition of the Continental Crust. In: Holland, H. D., Turekian, K. K., (eds) *Treatise on Geochemistry, Vol. 3, The Crust*. Elsevier-Pergamon, Oxford, 1-64.

Sadeghi, M., Bertrand G., de Oliveira D., Arvanitidis, N., Decree, S., Gautneb H., Gloaguen E., Törmänen T. Reginiussen, Sievers, H., Quental, L., Ferreira, J., and Wittenberg, A., 2020. Prospectivity mapping of critical raw material at the continental scale- a part of the FRAME project. *EAGE Mineral Exploration Symposium, 17-18 Sept. 2020, online event*.

Sanidas, G. M., Bassiakos, Y., Georgakopoulou, M., Filippaki, E., Jagou, B., and Nerantzis, N., 2016. Polykmetos Sideros: à propos du fer en Grèce antique. *Revue archéologique*, (2), 279-301.

Sarra, A., Di Berardino, C., and Quaglione, D., 2019. Deindustrialization and the technological intensity of manufacturing subsystems in the European Union. *Economia Politica*, 36(1), 205-243.

Schaarschmidt, A., Haase, K. M., Voudouris, P. C., Melfos, V., and Klemd, R., 2021a. Migration of arc magmatism above mantle wedge diapirs with variable sediment contribution in the Aegean. *Geochemistry, Geophysics, Geosystems*, 22, e2020GC009565.

Schaarschmidt, A., Haase, K. M., Klemd, R., Keith, M., Voudouris, P. C., Alfieris, D., Strauss, H., and Wiedenbeck, M., 2021b. Boiling effects on trace element and sulfur isotope compositions of sulfides in shallow-marine hydrothermal systems: Evidence from Milos Island, Greece. *Chemical Geology*, 583, 120457.

Schmid, S. M., Fügenschuh, B., Kounov, A., Maţenco, L., Nievergelt, P., Oberhänsli, R., Pleuger, J., Schefer, S., Schuster, R., Tomljenović, B., and Ustaszewski,

K., 2020. Tectonic units of the Alpine collision zone between Eastern Alps and western Turkey. *Gondwana Research*, 78, 308-374.

Seedorff, E., Barton, M. D., Stavast, W. J. A., and Maher, D. J., 2008. Root zones of porphyry systems: Extending the porphyry model to depth. *Economic Geology*, 103, 939–956.

Sengupta, D., and Van Gosen, B. S., 2016. Placer-type rare earth element deposits. In: Verplanck, P. L., Hitzman, M. W., (eds) *Rare Earth and Critical Elements in Ore Deposits*. Society of Economic Geologists Inc., Littleton, 81-100.

Serafimovski, T., Dolenec, T., Tasev, G., Serafimovski, D., Rogan Šmuc, N., and Dolenec, M., 2021. Au-Pd and Bi-Se Bearing pyrite and chalcopyrite from the Buchim copper mine, Eastern Macedonia. *Materials and Technology*, 55(1), 71-76.

Shore, M., and Fowler, A. D., 1996. Oscillatory zoning in minerals; a common phenomenon. *The Canadian Mineralogist*, 34(6), 1111-1126.

Sidiropoulos, N., 1991. Lithology, geochemistry, tectonics and metamorphism of the northwestern part of the Vertiskos Group. The area of the Disoro (Krousia) Mountain, north of Kilkis. *Aristotle University of Thessaloniki, Greece*, Ph.D. thesis, pp. 592, (in Greek with English abstract).

Sillitoe, R. H., 2010. Porphyry copper systems. *Economic geology*, 105(1), 3-41.

Sillitoe, R. H., and Thompson, J. F., 1998. Intrusion–related vein gold deposits: types, tectono-magmatic settings and difficulties of distinction from orogenic gold deposits. *Resource Geology*, 48(4), 237-250.

Sinclair, W. D., 2007. Porphyry deposits. In: Goodfellow, W. D., (ed) *Mineral Deposits of Canada: A Synthesis of Major Deposit-Types, District Metallogeny, the Evolution of Geological Provinces, and Exploration Methods*. Geological Association of Canada, Mineral Deposits Division, Special Publication, 5, 223-243.

Siron, C. R., Thompson, J. F., Baker, T., Friedman, R., Tsitsanis, P., Russell, S., Randall, S., and Mortensen, J., 2016. Magmatic and metallogenic framework of Au-Cu porphyry and polymetallic carbonate-hosted replacement deposits of the Kassandra mining district, northern Greece. *Society of Economic Geologists*, Special Publication, 19, 29-55.

- Siron, C. R., Rhys, D., Thompson, J. F., Baker, T., Veligrakis, T., Camacho, A., Dalampiras, L., 2018. Structural controls on porphyry Au-Cu and Au-rich polymetallic carbonate-hosted replacement deposits of the Kassandra mining district, Northern Greece. *Economic Geology*, 113, 309-345.
- Siron, C. R., Thompson, J. F., Baker, T., Darling, R., and Dipple, G., 2019. Origin of Au-rich carbonate-hosted replacement deposits of the Kassandra mining district, northern Greece: Evidence for Late Oligocene, structurally controlled, and zoned hydrothermal systems. *Economic Geology*, 114, 1389-1414.
- Skirrow, R. G., Huston, D. L., Mernagh, T. P., Thorne, J. P., Dulfer, H., and Senior, A., 2013. Critical commodities for a high-tech world: Australia's potential to supply global demand. Geoscience Australia, Canberra, p. 118.
- Skoupras, E., 2019. Study of the stibnite ore mineralization in Rizana, Kilkis. *Aristotle University of Thessaloniki, Greece*, M.Sc thesis, p. 104 (in Greek with English abstract).
- Stein, H. J., Markey, R. J., Morgan, J. W., Hannah, J. L., and Scherstén, A., (2001). The remarkable Re–Os chronometer in molybdenite: how and why it works. *Terra Nova* 13, 479–486.
- Stepanov, A. S., Large, R. R., Kiseeva, E. S., Danyushevsky, L. V., Goemann, K., Meffre, S., Zhukova, I, and Belousov, I. A., 2021. Phase relations of arsenian pyrite and arsenopyrite. *Ore Geology Reviews*, 104285.
- Stergiou, C., Melfos, V., Voudouris, P., Michailidis, K., Spry, P., and Chatzipetros, A., 2016. Hydrothermal alteration and structural control of the Vathi porphyry Cu-Au- Mo-U ore system, Kilkis district, N. Greece. In: Kantiranis, N. (ed) *Scientific Annals of the School of Geology*. Aristotle University of Thessaloniki, Thessaloniki, 105, 69-74.
- Stergiou, C. L., Melfos, V., and Voudouris, P., 2018. A review on the critical and rare metals distribution throughout the Vertiskos Unit, N. Greece. In: *Proceedings of the 1st International Electronic Conference on Mineral Science at Sciforum, Online. 16–31 July 2018, MDPI: Basel, Switzerland*.

Stergiou C. L., Melfos V., Voudouris P., Spry P. G., Papadopoulou L., Chatzipetros A., Giouri K., Mavrogonatos C., and Filippidis A., 2021a. The geology, geochemistry, and origin of the porphyry Cu-Au-(Mo) system at Vathi, Serbo-Macedonian Massif, Greece. *Applied Sciences*, 11, 479.

Stergiou, C. L., Melfos, V., Voudouris, P., Papadopoulou, L., Spry, P. G., Peytcheva, I., Dimitrova, D., Stefanova, E., and Giouri, K., 2021b. Rare and Critical Metals in Pyrite, Chalcopyrite, Magnetite, and Titanite from the Vathi Porphyry Cu-Au±Mo Deposit, Northern Greece, *Minerals*, 11, 630.

Stergiou, C. L., Melfos, V., Voudouris, P., Papadopoulou, L., and Spry, P. G., 2021c. Geology, mineralogy, and geochemistry of the intrusion-related polymetallic quartz veins at Laodikino, Serbo-Macedonian Massif, N. Greece. In: *Abstract volume of the SEG100: Celebrating a Century of Discovery*, Whistler, Canada, September 14-17.

Stergiou, C.L., Melfos, V., Voudouris, P., Papadopoulou, L., Spry, P. G., Peytcheva, I., Dimitrova, D., and Stefanova, E., 2022. A Fluid Inclusion and Critical/Rare Metal Study of Epithermal Quartz-Stibnite Veins Associated with the Gerakario Porphyry Deposit, Northern Greece. *Applied Sciences*, 12, 909.

Stöllner, T. 2003. Mining and economy: a discussion of spatial organisations and structures of early raw material exploitation. In: Stöllner, Th., Körlin, G., Steffens, G., Cierny, J. (eds) *Man and Mining. Studies in honour of Gerd Weisgerber*. Der Anschnitt, Bochum, 16, 415-446.

Strmić Palinkas, S., Hofstra, A. H., Percival, T. J., Borojevic Sostaric, S., Palinkas, L., Bermanec, V., Pecskay, Z., and Boev, B., 2018. Comparison of the Allchar Au-As-Sb-Tl Deposit, Republic of Macedonia, with Carlin-Type Gold Deposits. *Reviews in Economic Geology*, 20, 335-363.

Sun, W., Huang, R. F., Li, H., Hu, Y. B., Zhang, C. C., Sun, S. J., Zhang, L. P., Ding, X., Li, C. Y., Zartman, R. E., and Ling, M. X., 2015. Porphyry deposits and oxidized magmas. *Ore Geology Reviews*, 65, 97-131.

Sykes, J., Wright, J., and Trench, A., 2016. Discovery, supply and demand: from Metals of Antiquity to critical metals. *Applied Earth Sciences*, 125(1), 3–20.

Thymiatis, G., 1995. The ore mineralization in Laodikino-Lipsidri area, Kilkis district, Macedonia, north Greece. *Aristotle University of Thessaloniki, Greece*, Ph.D. thesis, p. 260 (in Greek with English abstract).

Tiepolo, M., Oberti, R., and Vannucci, R., 2002. Trace-element incorporation in titanite: Constraints from experimentally determined solid/liquid partition coefficients. *Chemical Geology*, 191, 105-119.

The White House, U.S., 2021. Building resilient supply chains, revitalizing american manufacturing, and fostering broad-based growth, p. 250.

Tompouloglou, C., 1981. Les minéralisations tertiaires, type cuivre porphyrique, du massif Serbo-Macédonien (Macédoine, Grèce) dans leur context magmatique (avec un traitement géostatistique pour les données du prospect d'Alexia). *Ecole National Supérieure des Mines de Paris, France*, Ph.D. thesis, p. 204 (in French).

Tompouloglou, Ch., 2001. Etude d'inclusions fluides dans le context hydrothermal de mineralisations tertiaires, type cuivre porphyrique, du Massif Serbo-Mecadonien en Mecedoine, Grece. In: *Special Volume in honor of the Emeritus Professor Ioannis Papageorgakis*. Metsovion National Technical University, Athens, 225-261.

Toumanidou, O. C., 2019. Preliminary study of the porphyry system in Gerakario of Kilkis. *Aristotle University of Thessaloniki, Greece*, M.Sc thesis, p. 84 (in Greek with English abstract).

Tranos, M. D., Kiliass, A. A., and Mountrakis, D. M. 1999. Geometry and kinematics of the Tertiary post-metamorphic Circum Rhodope Belt Thrust System (CRBTS) Northern Greece. *Bulletin of the Geological Society of Greece*, 33, 5-16.

Tsirambides, A, and Filippidis, A., 2016. Gold metallogeny of the Serbomacedonian-Rhodope metallogenic belt (SRMB). *Bulletin of the Geological Society of Greece*, 50, 2037-2046.

Tsirambides, A., and Filippidis, A., 2019. Sb- Bi-bearing metallogeny of the SerboMacedonian-Rhodope Metallogenic Belt (SRMB). *Bulletin of the Geological Society of Greece*, 55(1), 34-64.

Vavelidis, M., Melfos, V., and Kiliass, A., 1999. The gold-bearing quartz veins in the metamorphic rocks at the Drakontio area, central Macedonia, northern Greece. In: Stanley, C. J., et al. (ed) *Mineral Deposits, Process to Processing. Proceedings of the Fifth Biennial SGA Meeting and the Tenth Quadrennial IAGOD Symposium, London, United Kingdom, 22–25 August 1999, Vols. 1 and 2*. Balkema, Rotterdam, 209-212.

Vaxevanopoulos, M., Vavelidis, M., Melfos, V., Malamidou, D., and Pavlides, S., 2018. Ancient mining in Gold-Silver-Copper ore deposits and metallurgical activity in Mavrokofi area, Mount Pangaeon (Northeast Greece). In: Ben-Yosef, E., (ed) *Mining for Ancient Copper - Essays in Memory of Beno Rothenberg*. Tel Aviv University, Sonia and Marco Nadler Institute of Archaeology, Monograph Series, 37, 386-398.

Vaxevanopoulos, M., Blichert-Toft, J., Davis, G., and Albarède, F., 2022. New findings of ancient Greek silver sources. *Journal of Archaeological Science*, 137, 105474.

Velásquez, G., Carrizo, D., Salvi, S., Vela, I., Pablo, M., Pérez, A., 2020. Tracking cobalt, REE and gold from a porphyry-type deposit by LA-ICP-MS: A geological approach towards metal-selective mining in tailings. *Minerals*, 10, 109.

Verplanck, P. L., and Hitzman, M. W., 2016. Introduction: Rare Earth and Critical Elements in Ore Deposits. In: Verplanck, P. L., Hitzman, M. W., (eds) *Rare Earth and Critical Elements in Ore Deposits*. Society of Economic Geologists Inc., Littleton, 1-4.

Verplanck, P. L., Mariano, A. N., and Mariano, A., Jr. 2016. Rare earth element ore geology of carbonatites. In: Verplanck, P. L., Hitzman, M. W., (eds) *Rare Earth and Critical Elements in Ore Deposits*. Society of Economic Geologists Inc., Littleton, 5-32.

- Voudouris, P., Spry, P. G., Melfos, V., and Alfieris, D., 2007. Tellurides and bismuth sulfosalts in gold occurrences of Greece: Mineralogical and genetic considerations. In: Kojonen, K. K., Cook, N. J., Ojala, V. J., (eds) *Gold Deposits in Finland*. Geological Survey of Finland: Espoo, 53, 85-94.
- Voudouris, P., Melfos, V., Spry, P. G., Moritz, R., Papavassiliou, K., Falalakis, G. 2011. Mineralogy and geochemical environment of formation of the Perama Hill high-sulfidation epithermal Au-Ag-Te-Se deposit, Petrota Graben, NE Greece. *Mineralogy and Petrology*, 103, 79-100.
- Voudouris, P., Melfos, V., Spry, P. G., Bindi, L., Moritz, R., Ortelli, M., and Kartal, T., 2013a. Extremely Re-rich molybdenite from porphyry Cu-Mo-Au prospects in northeastern Greece: mode of occurrence, causes of enrichment, and implications for gold exploration. *Minerals*, 3, 165–191.
- Voudouris, P. C., Melfos, V., Spry, P. G., Kartal, T., Schleicher, H., Moritz, R., and Ortelli, M., 2013b. The Pagoni Rachi/Kirki Cu-Mo±Re±Au deposit, northern Greece: Mineralogical and fluid inclusion constraints on the evolution of a telescoped porphyry-epithermal system. *The Canadian Mineralogist*, 51(2), 253-284.
- Voudouris, P., Spry, P. G., Mavrogonatos, C., Sakellaris, G.A., Bristol, S. K., Melfos, V., Fornadel, A. 2013c. Bismuthinite derivatives, lillianite homologues, and bismuth sulfotellurides as indicators of gold mineralization at the Stanos shear-zone related deposit, Chalkidiki, northern Greece. *Canadian Mineralogist*, 51, 119-142.
- Voudouris, P., Mavrogonatos, C., Spry, P. G., Baker, T., Melfos, V., Klemd, R., Haase, K., Repstock, A., Djiba, A., Bismayer, U., Tarantola, A., Scheffer, C., Moritz, R., Kouzmanov, K., Alfieris, D., Papavassiliou, K., Schaarschmidt, A., Galanopoulos, E., Galanos, E., Kołodziejczyk, J., Stergiou, C., and Melfou, M., 2019a. Porphyry and epithermal deposits in Greece: an overview, new

discoveries, and mineralogical constraints on their genesis. *Ore Geology Reviews*, 107, 654-691.

Voudouris, P., Mavrogonatos, C., Melfos, V., Spry, P. G., Magganas, A., Alfieris, D., Soukis, K., Tarantola, A., Periferakis, A., Kołodziejczyk, J., Scheffer, C., Repstock, A., and Zeug, M., 2019b. The geology and mineralogy of the Stypsi porphyry Cu-Mo-Au-Re prospect, Lesbos Island, Aegean Sea, Greece. *Ore Geology Reviews*, 112, 103023.

Voudouris, P., Repstock, A., Spry, P. G., Frenzel, M., Mavrogonatos, C., Keith, M., Tarantola, A., Melfos, V., Tombros, S., Zhai, D., Cook, N.J., Ciobanu, C.L., Schaarschmidt, A., Rieck, B., Kolitsch, U., and Falkenberg, J., 2022. Physicochemical constraints on indium-, tin-, germanium-, gallium-, gold-, and tellurium-bearing mineralizations in the Pefka and St Philippos polymetallic vein-and breccia-type deposits, Greece. *Ore Geology Reviews*, 104348.

Wang, J., Wen, H., Fan, H., and Zhu, J., 2012. Sm-Nd geochronology, REE geochemistry and C and O isotope characteristics of calcites and stibnites from the Banian antimony deposit, Guizhou Province, China. *Geochemical Journal*, 46(5), 393-407.

Wang, L., Qin, K. Z., Song, G. X., and Li, G. M., 2019. A review of intermediate sulfidation epithermal deposits and subclassification. *Ore Geology Reviews*, 107, 434-456.

Wang, R., Zhu, D., Wang, Q., Hou, Z., Yang, Z., Zhao, Z., and Mo, X., 2020. Porphyry mineralization in the Tethyan orogen. *Science China Earth Sciences*, 63, 2042-2067.

Watari, T., Nansai, K., and Nakajima, K., 2020. Review of critical metal dynamics to 2050 for 48 elements. *Resources, Conservation and Recycling*, 155, 104669.

Weis, P., Driesner, T., and Heinrich, C., 2012. Porphyry-copper ore shells form at stable pressure-temperature fronts within dynamic fluid plumes. *Science*, 338(6114), 1613-1616.

Wells, J. D., and Mullens, T. E., 1973. Gold-Bearing Arsenian Pyrite Determined by Microprobe Analysis, Cortez and Carlin Gold mines, Nevada. *Economic Geology*, 68, 187-201.

Wilkinson, J. J., 2013. Triggers for the formation of porphyry ore deposits in magmatic arcs. *Nature Geoscience*, 6(11), 917-925.

Wood, S. A., and Shannon, W. M., 2003. Rare-earth elements in geothermal waters from Oregon, Nevada, and California. *Journal of Solid State Chemistry*, 171(1-2), 246-253.

Xu, L., Bi, X., Hu, R., Tang, Y., Wang, X., and Xu, Y., 2015. LA-ICP-MS mineral chemistry of titanite and the geological implications for exploration of porphyry Cu deposits in the Jinshajiang-Red River alkaline igneous belt, SW China. *Mineralogy and Petrology*, 109, 181-200.

Yan, W., Wang, Z., Cao, H., Zhang, Y., and Sun, Z., 2021. Criticality assessment of metal resources in China. *iScience*, 24(6), 102524.

Zhou, Z., Yonezu, K., Imai, A., Tindell, T., Li, H., and Gabo-Ratio, J. A., 2021. Trace elements mineral chemistry of sulfides from the Woxi Au-Sb-W deposit, southern China. *Resource Geology*, 72, e12279.

Zürcher, L., Bookstrom A. A., Hammarstrom, J. M., Mars, J. C., Ludington, S., Zientek, M. L., Dunlap, P., and Wallis, J. C., with contributions from Drew, L. J., Sutphin, D. M., Berger, B. R., Herrington, R. J., Billa, M., Kuşçu, I., Moon, C. J., and Richards, J. P., 2015. Porphyry copper assessment of the Tethys region of western and southern Asia. U.S. Geological Survey, Reston, Scientific Investigations Report, 2010–5090–V, p. 232.

SUPPLEMENT 1

Supplement 1. Datasets of SEM-EDS analyses.

Table S1-1. The average values of the SEM-EDS analyses conducted on pyrite from Vathi. AVG = average value, b.d.l. = below detection limit, MAX = maximum value, MIN = minimum value, n. = number of analyses, n.a. = not applicable, STDEV = standard deviation.

Hydrothermal alteration	Potassic overprinted by sericitic				Sericitic							
Host rock	Latite				Quartz monzonite							
Mineralization style	Py1; Disseminated (n = 10)				Py2; Disseminated (n = 11)				Py2; D-type vein (n = 5)			
Element	MIN	MAX	STDEV	AVG	MIN	MAX	STDEV	AVG	MIN	MAX	STDEV	AVG
S	52.25	53.75	0.52	53.24	54.00	54.37	0.26	54.19	53.35	54.99	0.68	54.17
V	b.d.l.	b.d.l.	n.a.	n.a.	b.d.l.	b.d.l.	n.a.	n.a.	b.d.l.	b.d.l.	n.a.	n.a.
Fe	45.45	46.61	0.33	46.22	45.63	46.00	0.26	45.82	44.32	46.65	1.03	45.47
Co	b.d.l.	b.d.l.	n.a.	n.a.	b.d.l.	b.d.l.	n.a.	n.a.	b.d.l.	b.d.l.	n.a.	n.a.
Ni	b.d.l.	b.d.l.	n.a.	n.a.	b.d.l.	b.d.l.	n.a.	n.a.	b.d.l.	b.d.l.	n.a.	n.a.
Cu	b.d.l.	b.d.l.	n.a.	n.a.	b.d.l.	b.d.l.	n.a.	n.a.	b.d.l.	b.d.l.	n.a.	n.a.
As	b.d.l.	0.50	0.22	0.16	b.d.l.	b.d.l.	n.a.	n.a.	b.d.l.	b.d.l.	n.a.	n.a.
Ag	b.d.l.	b.d.l.	n.a.	n.a.	b.d.l.	b.d.l.	n.a.	n.a.	b.d.l.	b.d.l.	n.a.	n.a.
Te	b.d.l.	b.d.l.	n.a.	n.a.	b.d.l.	b.d.l.	n.a.	n.a.	b.d.l.	0.77	0.42	0.37
Au	b.d.l.	b.d.l.	n.a.	n.a.	b.d.l.	b.d.l.	n.a.	n.a.	b.d.l.	b.d.l.	n.a.	n.a.
Bi	b.d.l.	b.d.l.	n.a.	n.a.	b.d.l.	b.d.l.	n.a.	n.a.	b.d.l.	b.d.l.	n.a.	n.a.
Total	98.73	100.50	0.57	99.62	100.00	100.00	0.00	100.00	100.00	100.00	0.00	100.00

Table S1-1. Continued.

Hydrothermal alteration	Sericitic								Epithermal overprint			
Host rock	Latite											
Mineralization style	Py3; Disseminated (n = 55)				Py3; D-type vein (n = 9)				Py4; E-type vein, Assemblage 2 (n = 10)			
Element	MIN	MAX	STDEV	AVG	MIN	MAX	STDEV	AVG	MIN	MAX	STDEV	AVG
S	52.81	55.85	0.85	53.72	52.20	53.45	0.36	52.83	53.00	55.75	0.99	54.50
V	b.d.l.	0.12	0.05	0.01	b.d.l.	b.d.l.	n.a.	n.a.	b.d.l.	b.d.l.	n.a.	n.a.
Fe	43.21	46.54	1.07	45.72	46.17	47.59	0.43	46.51	43.23	46.40	1.18	44.60
Co	b.d.l.	0.60	0.17	0.03	b.d.l.	0.10	0.04	0.02	b.d.l.	0.70	0.29	0.23
Ni	b.d.l.	0.73	0.24	0.05	b.d.l.	b.d.l.	n.a.	n.a.	b.d.l.	0.40	0.16	0.08
Cu	b.d.l.	2.00	0.55	0.12	b.d.l.	b.d.l.	n.a.	n.a.	b.d.l.	0.70	0.23	0.08
As	b.d.l.	0.14	0.04	0.01	b.d.l.	b.d.l.	n.a.	n.a.	b.d.l.	1.53	0.61	0.64
Ag	b.d.l.	0.54	0.15	0.03	b.d.l.	b.d.l.	n.a.	n.a.	b.d.l.	1.04	0.40	0.20
Te	b.d.l.	0.71	0.20	0.02	b.d.l.	b.d.l.	n.a.	n.a.	b.d.l.	0.40	0.13	0.04
Au	b.d.l.	b.d.l.	n.a.	n.a.	b.d.l.	b.d.l.	n.a.	n.a.	b.d.l.	b.d.l.	n.a.	n.a.
Bi	0.00	0.80	0.24	0.41	b.d.l.	0.40	0.20	0.19	b.d.l.	b.d.l.	n.a.	n.a.
Total	100.00	100.88	0.35	100.11	98.69	100.55	0.58	99.56	98.45	101.38	0.91	100.37

Table S1-2. The average values of the SEM-EDS analyses conducted on chalcopyrite from Vathi. AVG = average value, b.d.l. = below detection limit, MAX = maximum value, MIN = minimum value, n. = number of analyses, n.a. = not applicable, STDEV = standard deviation.

Hydrothermal alteration	Potassic overprinted by sericitic				Sericitic				Epithermal overprint			
Host rock	Latite											
Mineralization style	Cpy1; Disseminated (n = 9)				Cpy2; Disseminated (n = 33)				Cpy3; E-type vein, Assemblage 2 (n = 5)			
Element	MIN	MAX	STDEV	AVG	MIN	MAX	STDEV	AVG	MIN	MAX	STDEV	AVG
S	33.72	36.00	0.74	34.74	32.68	36.38	1.00	34.66	33.64	35.50	0.72	34.25
V	b.d.l.	0.36	0.16	0.10	b.d.l.	0.22	0.06	0.02	b.d.l.	b.d.l.	n.a.	n.a.
Fe	28.55	31.44	0.89	30.23	25.76	33.20	1.57	29.82	29.21	30.49	0.58	29.91
Co	b.d.l.	b.d.l.	n.a.	n.a.	b.d.l.	0.90	0.24	0.13	b.d.l.	b.d.l.	n.a.	n.a.
Ni	b.d.l.	b.d.l.	n.a.	n.a.	b.d.l.	0.60	0.15	0.06	b.d.l.	b.d.l.	n.a.	n.a.
Cu	33.46	35.82	0.72	34.75	31.57	35.61	1.13	33.78	34.17	35.85	0.66	35.33
As	b.d.l.	0.35	0.15	0.09	b.d.l.	0.60	0.13	0.04	b.d.l.	b.d.l.	n.a.	n.a.
Ag	b.d.l.	0.30	0.15	0.14	b.d.l.	0.60	0.13	0.03	b.d.l.	0.37	0.18	0.17
Te	b.d.l.	b.d.l.	n.a.	n.a.	b.d.l.	0.40	0.09	0.02	b.d.l.	b.d.l.	n.a.	n.a.
Au	b.d.l.	b.d.l.	n.a.	n.a.	b.d.l.	b.d.l.	n.a.	n.a.	b.d.l.	b.d.l.	n.a.	n.a.
Bi	b.d.l.	b.d.l.	n.a.	n.a.	b.d.l.	3.50	1.22	1.88	b.d.l.	b.d.l.	n.a.	n.a.
Total	98.81	101.51	0.97	100.05	92.92	102.62	2.04	100.45	98.79	100.10	0.52	99.66

Table S1-3. The average values of the SEM-EDS analyses conducted on magnetite from Vathi. AVG = average value, b.d.l. = below detection limit, MAX = maximum value, MIN = minimum value, n. = number of analyses, n.a. = not applicable, STDEV = standard deviation.

Hydrothermal alteration	Potassic-calcic								Potassic overprinted by sericitic			
Host rock	Quartz monzonite								Latite			
Mineralization style	Mag1; Disseminated (n = 10)				Mag1; M-type vein (n = 5)				Mag2; Disseminated (n = 20)			
Element	MIN	MAX	STDEV	AVG	MIN	MAX	STDEV	AVG	MIN	MAX	STDEV	AVG
Mg	b.d.l.	b.d.l.	n.a.	n.a.	b.d.l.	b.d.l.	n.a.	n.a.	b.d.l.	1.15	0.35	0.11
Al	b.d.l.	0.43	0.18	0.11	b.d.l.	b.d.l.	n.a.	n.a.	b.d.l.	1.50	0.46	0.43
Si	b.d.l.	0.56	0.26	0.24	b.d.l.	b.d.l.	n.a.	n.a.	b.d.l.	2.20	0.72	0.41
Ca	b.d.l.	b.d.l.	n.a.	n.a.	b.d.l.	b.d.l.	n.a.	n.a.	b.d.l.	0.41	0.15	0.09
Ti	b.d.l.	b.d.l.	n.a.	n.a.	b.d.l.	b.d.l.	n.a.	n.a.	b.d.l.	0.59	0.23	0.16
V	0.32	0.59	0.11	0.49	0.32	0.48	0.08	0.40	b.d.l.	0.91	0.29	0.16
Cr	b.d.l.	b.d.l.	n.a.	n.a.	b.d.l.	b.d.l.	n.a.	n.a.	b.d.l.	b.d.l.	n.a.	n.a.
Mn	b.d.l.	0.10	0.04	0.03	b.d.l.	0.25	0.12	0.12	b.d.l.	0.76	0.23	0.08
Fe	71.44	75.82	1.66	73.64	72.12	73.96	0.78	72.71	70.00	77.05	1.78	74.57
Co	b.d.l.	b.d.l.	n.a.	n.a.	0.50	0.63	0.06	0.57	b.d.l.	1.59	0.65	0.50
Ni	b.d.l.	0.03	0.01	0.01	b.d.l.	0.33	0.17	0.17	b.d.l.	b.d.l.	n.a.	n.a.
Zn	b.d.l.	b.d.l.	n.a.	n.a.	b.d.l.	b.d.l.	n.a.	n.a.	b.d.l.	1.07	0.37	0.22
O	22.72	27.98	1.76	26.05	25.67	27.13	0.64	26.33	22.38	26.00	1.24	23.63
Total	99.50	101.38	0.54	100.56	100.00	100.94	0.42	100.29	98.84	105.58	1.34	100.36

Table S1-4. The average values of the SEM-EDS analyses conducted on titanite from Vathi. AVG = average value, b.d.l. = below detection limit, MAX = maximum value, MIN = minimum value, n. = number of analyses, n.a. = not applicable, STDEV = standard deviation.

Hydrothermal alteration	Potassic-calcic							
Host rock	Quartz monzonite							
Mineralization style	Ttn1; Disseminated (n = 10)				Ttn1; M-type vein (n = 10)			
Element	MIN	MAX	STDEV	AVG	MIN	MAX	STDEV	AVG
Mg	b.d.l.	b.d.l.	n.a.	n.a.	b.d.l.	b.d.l.	n.a.	n.a.
Al	0.26	0.70	0.15	0.49	0.33	0.70	0.12	0.51
Si	15.07	15.80	0.22	15.56	15.07	15.80	0.23	15.59
Ca	19.06	20.11	0.31	19.56	19.41	20.09	0.24	19.62
Ti	17.89	20.00	0.58	18.57	17.98	20.57	0.88	18.91
V	b.d.l.	0.85	0.28	0.32	b.d.l.	0.85	0.27	0.34
Mn	b.d.l.	b.d.l.	n.a.	n.a.	b.d.l.	b.d.l.	n.a.	n.a.
Fe	0.84	1.94	0.42	1.40	0.84	1.94	0.38	1.33
Nb	b.d.l.	b.d.l.	n.a.	n.a.	b.d.l.	b.d.l.	n.a.	n.a.
O	40.73	41.27	0.16	41.07	40.73	41.26	0.17	41.08
Total	96.04	98.43	0.72	96.96	96.06	98.43	0.75	97.22

Table S1-5. The average values of the SEM-EDS analyses conducted on stibnite from Gerakario. AVG = average value, b.d.l. = below detection limit, MAX = maximum value, MIN = minimum value, n. = number of analyses, n.a. = not applicable, STDEV = standard deviation.

Hydrothermal alteration	Sericitic			
Host rock	Two-mica gneiss			
Mineralization style	Stb1; Vein (n = 33)			
Element	MIN	MAX	STDEV	AVG
S	28.02	29.20	0.52	28.53
V	b.d.l.	b.d.l.	n.a.	n.a.
Fe	b.d.l.	0.18	0.08	0.11
Co	b.d.l.	b.d.l.	n.a.	n.a.
Ni	b.d.l.	b.d.l.	n.a.	n.a.
Cu	b.d.l.	0.20	0.09	0.13
Zn	b.d.l.	0.13	0.06	0.05
As	b.d.l.	0.23	0.10	0.12
Ag	0.08	1.33	0.57	0.50
Te	b.d.l.	b.d.l.	n.a.	n.a.
Sb	69.47	71.08	0.75	70.56
Total	97.57	102.36	2.17	100

Table S1-6. The average values of the SEM-EDS analyses conducted on pyrite and chalcopyrite from Laodikino. AVG = average value, b.d.l. = below detection limit, MAX = maximum value, MIN = minimum value, n. = number of analyses, n.a. = not applicable, STDEV = standard deviation.

Mineral	Pyrite								Chalcopyrite							
Hydrothermal alteration	Chloritization				Sericitization				Chloritization				Sericitization			
Host rock	Biotite schist				Two-mica gneiss and schist				Biotite schist				Two-mica gneiss and schist			
Mineralization style	Py1; Veins and lenses (n = 43)				Py2; Polymetallic quartz veins (n = 31)				Cpy1; Veins and lenses (n = 28)				Cpy2; Polymetallic quartz veins (n = 33)			
Element	MIN	MAX	STDEV	AVG	MIN	MAX	STDEV	AVG	MIN	MAX	STDEV	AVG	MIN	MAX	STDEV	AVG
S	53.96	54.84	0.45	54.35	53.24	54.88	1.16	54.06	53.96	54.84	0.45	54.35	33.29	34.59	0.92	33.94
V	b.d.l.	0.07	0.04	0.02	b.d.l.	b.d.l.	n.a.	n.a.	b.d.l.	0.07	0.04	0.02	b.d.l.	0.04	0.03	0.02
Fe	45.29	46.73	0.68	46.17	45.80	46.96	0.82	46.38	45.29	46.73	0.68	46.17	29.14	29.65	0.36	29.40
Co	b.d.l.	0.14	0.07	0.05	0.09	0.10	0.01	0.09	b.d.l.	0.14	0.07	0.05	0.09	0.11	0.01	0.10
Ni	b.d.l.	0.23	0.11	0.09	0.04	0.08	0.03	0.06	b.d.l.	0.23	0.11	0.09	b.d.l.	0.02	0.01	0.01
Cu	b.d.l.	0.18	0.08	0.11	0.02	0.08	0.04	0.05	b.d.l.	0.18	0.08	0.11	33.60	34.56	0.67	34.08
As	b.d.l.	0.54	0.26	0.16	0.04	0.19	0.11	0.12	b.d.l.	0.54	0.26	0.16	0.09	0.13	0.03	0.11
Ag	b.d.l.	0.35	0.18	0.15	b.d.l.	0.05	0.03	0.02	b.d.l.	0.35	0.18	0.15	b.d.l.	b.d.l.	n.a.	n.a.
Te	b.d.l.	0.12	0.06	0.05	0.07	0.23	0.11	0.15	b.d.l.	0.12	0.06	0.05	b.d.l.	0.06	0.05	0.03
Total	99.24	103.19	1.92	101.14	99.30	102.56	2.31	100.93	99.24	103.19	1.92	101.14	96.21	100.21	0.04	100.18

Table S1-7. The average values of the SEM-EDS analyses conducted on sphalerite from Laodikino. AVG = average value, b.d.l. = below detection limit, MAX = maximum value, MIN = minimum value, n. = number of analyses, n.a. = not applicable, STDEV = standard deviation.

Hydrothermal alteration	Sericitization			
Host rock	Two-mica gneiss and schist			
Mineralization style	Sph1; Polymetallic quartz veins (n = 17)			
Element	MIN	MAX	STDEV	AVG
S	33.10	34.05	0.67	33.58
Mn	b.d.l.	0.08	0.06	0.04
Fe	1.98	2.08	0.07	2.03
Ni	b.d.l.	b.d.l.	n.a.	n.a.
Zn	64.21	64.82	0.43	64.52
As	0.07	0.11	0.03	0.09
Se	0.11	0.14	0.02	0.13
Ag	b.d.l.	0.12	0.08	0.06
Cd	b.d.l.	0.13	0.09	0.07
Sn	b.d.l.	b.d.l.	n.a.	n.a.
Sb	0.07	0.10	0.02	0.09
Te	b.d.l.	b.d.l.	n.a.	n.a.
Pb	0.17	2.05	1.33	1.11
Bi	0.63	0.66	0.02	0.64
Total	100.34	104.33	2.82	102.33

Table S1-8. The average values of the SEM-EDS analyses conducted on tetrahedrite from Laodikino. AVG = average value, b.d.l. = below detection limit, MAX = maximum value, MIN = minimum value, n. = number of analyses, n.a. = not applicable, STDEV = standard deviation.

Hydrothermal alteration	Sericitization			
Host rock	Two-mica gneiss and schist			
Mineralization style	Ttr1; Polymetallic quartz veins (n = 54)			
Element	MIN	MAX	STDEV	AVG
S	24.86	25.72	0.44	25.25
Fe	10.10	11.08	0.51	10.68
Cu	30.77	31.71	0.48	31.30
Zn	1.96	2.20	0.13	2.06
As	1.70	1.77	0.04	1.74
Ag	0.36	0.45	0.04	0.40
Sb	28.87	29.73	0.45	29.22
Totals	98.62	102.67	2.09	100.65

Table S1-8. The average values of the SEM-EDS analyses conducted on magnetite from Laodikino. AVG = average value, b.d.l. = below detection limit, MAX = maximum value, MIN = minimum value, n. = number of analyses, n.a. = not applicable, STDEV = standard deviation.

Hydrothermal alteration	Chloritization			
Host rock	Biotite schist			
Mineralization style	Mag1; Veins and lenses (n = 18)			
Element	MIN	MAX	STDEV	AVG
Mg	b.d.l.	0.06	0.04	0.03
Al	b.d.l.	0.13	0.07	0.06
Si	0.13	0.32	0.08	0.24
Ca	b.d.l.	0.04	0.02	0.01
Ti	b.d.l.	0.32	0.14	0.13
V	b.d.l.	0.18	0.09	0.05
Cr	b.d.l.	0.29	0.14	0.09
Mn	b.d.l.	0.78	0.41	0.42
Fe	71.61	73.20	0.70	72.42
Co	b.d.l.	0.20	0.10	0.05
Ni	b.d.l.	0.14	0.07	0.06
Zn	b.d.l.	b.d.l.	n.a.	n.a.
O	25.56	27.69	0.98	26.86
Totals	97.30	103.34	2.84	100.42

Table S1-9. The average values of the SEM-EDS analyses conducted on pyrite from Kolchiko. AVG = average value, b.d.l. = below detection limit, MAX = maximum value, MIN = minimum value, n. = number of analyses, n.a. = not applicable, STDEV = standard deviation.

Hydrothermal alteration	Sericitization							
Host rock	Mica schist							
Mineralization style	Py1; Polymetallic quartz veins (n = 27)				Py2; Massive veins (n = 43)			
Element	MIN	MAX	STDEV	AVG	MIN	MAX	STDEV	AVG
S	53.10	54.73	0.62	53.77	52.23	54.00	0.69	53.22
V	b.d.l.	0.30	0.13	0.08	b.d.l.	0.29	0.13	0.12
Fe	44.39	46.42	0.79	45.47	44.84	46.50	0.61	45.86
Co	b.d.l.	1.18	0.49	0.37	b.d.l.	1.31	0.49	0.40
Ni	b.d.l.	0.44	0.21	0.15	b.d.l.	0.42	0.19	0.17
Cu	b.d.l.	0.57	0.24	0.27	b.d.l.	0.32	0.16	0.10
As	b.d.l.	b.d.l.	n.a.	n.a.	b.d.l.	0.39	0.13	0.21
Ag	b.d.l.	0.43	0.18	0.24	b.d.l.	0.57	0.23	0.17
Te	b.d.l.	0.54	0.21	0.25	b.d.l.	0.23	0.12	0.08
Total	97.49	104.62	2.88	100.60	97.07	104.01	2.75	100.34

Table S1-10. The average values of the SEM-EDS analyses conducted on chalcopyrite and arsenopyrite from Kolchiko. AVG = average value, b.d.l. = below detection limit, MAX = maximum value, MIN = minimum value, n. = number of analyses, n.a. = not applicable, STDEV = standard deviation.

Minerals	Chalcopyrite				Arsenopyrite			
Host rock	Sericitization							
Mineralization style	Mica schist							
Mineralization style	Cpy1; Polymetallic quartz veins (n = 19)				Apy1; Massive veins (n = 17)			
Element	MIN	MAX	STDEV	AVG	MIN	MAX	STDEV	AVG
S	34.01	34.97	0.41	34.56	20.33	20.87	0.24	20.64
V	b.d.l.	0.41	0.24	0.20	b.d.l.	0.07	0.03	0.02
Fe	29.37	30.79	0.58	30.05	31.73	33.58	0.79	32.84
Co	b.d.l.	0.53	0.26	0.21	b.d.l.	0.25	0.11	0.15
Ni	b.d.l.	0.43	0.18	0.18	b.d.l.	0.25	0.12	0.10
Cu	33.57	35.10	0.64	34.22	b.d.l.	0.25	0.12	0.10
As	b.d.l.	0.67	0.33	0.17	45.10	46.89	0.77	46.12
Ag	b.d.l.	0.56	0.28	0.14	b.d.l.	0.21	0.11	0.09
Te	b.d.l.	0.58	0.26	0.28	b.d.l.	0.15	0.09	0.07
Total	96.96	104.04	3.18	100.01	97.16	102.52	2.37	100.13

Table S1-11. The average values of the SEM-EDS analyses conducted on sphalerite from Kolchiko. AVG = average value, b.d.l. = below detection limit, MAX = maximum value, MIN = minimum value, n. = number of analyses, n.a. = not applicable, STDEV = standard deviation.

Host rock	Sericitization			
Mineralization style	Mica schist			
Mineralization style	Sph1; Polymetallic quartz veins (n = 5)			
Element	MIN	MAX	STDEV	AVG
S	33.24	33.24	0.56	33.24
Mn	b.d.l.	b.d.l.	n.a.	n.a.
Fe	2.71	2.71	0.32	2.71
Ni	0.15	0.15	0.25	0.15
Zn	63.65	63.65	0.43	63.65
As	b.d.l.	b.d.l.	n.a.	n.a.
Se	b.d.l.	b.d.l.	n.a.	n.a.
Ag	0.27	0.27	0.47	0.27
Cd	b.d.l.	b.d.l.	n.a.	n.a.
Sn	b.d.l.	b.d.l.	n.a.	n.a.
Sb	b.d.l.	b.d.l.	n.a.	n.a.
Te	b.d.l.	b.d.l.	n.a.	n.a.
Pb	0.70	0.70	0.70	0.70
Bi	b.d.l.	b.d.l.	n.a.	n.a.
Total	100.72	100.72	2.74	100.72

Table S1-12. The average values of the SEM-EDS analyses conducted on pyrite from Aspra Chomata. AVG = average value, b.d.l. = below detection limit, MAX = maximum value, MIN = minimum value, n. = number of analyses, n.a. = not applicable, STDEV = standard deviation.

Host rock	Sericitic alteration			
Mineralization style	Granodiorite porphyry			
Mineralization style	Py1; Base metals vein (n = 74)			
Element	MIN	MAX	STDEV	AVG
S	52.31	53.79	0.66	52.91
Fe	44.09	46.44	0.86	45.09
Cu	0.00	0.13	0.05	0.02
Zn	0.00	0.09	0.04	0.05
As	0.32	1.50	0.45	0.83
Se	0.00	0.17	0.07	0.04
Ag	0.00	0.10	0.04	0.03
Cd	0.00	0.22	0.07	0.11
Sb	0.09	0.49	0.15	0.19
Pb	0.30	2.50	0.90	1.67
Totals	97.12	105.44	3.30	100.92

Table S1-13. The average values of the SEM-EDS analyses conducted on sphalerite from Aspra Chomata. AVG = average value, b.d.l. = below detection limit, MAX = maximum value, MIN = minimum value, n. = number of analyses, n.a. = not applicable, STDEV = standard deviation.

Host rock	Sericitic alteration			
Mineralization style	Granodiorite porphyry			
Mineralization style	Sph1; Base metals veins (n = 27)			
Element	MIN	MAX	STDEV	AVG
S	32.91	34.28	0.58	33.53
Mn	0.07	0.30	0.11	0.23
Fe	0.00	2.35	1.12	0.86
Ni	0.00	0.27	0.13	0.07
Zn	62.32	64.29	0.96	63.49
As	0.00	0.30	0.15	0.13
Se	0.00	0.15	0.08	0.04
Ag	0.00	0.20	0.10	0.11
Cd	0.00	0.46	0.19	0.25
Sn	0.00	0.17	0.08	0.06
Sb	0.00	0.29	0.14	0.10
Te	0.00	0.22	0.11	0.06
Pb	0.00	2.50	1.06	0.99
Bi	0.60	1.60	0.50	0.85
Total	95.90	107.39	5.31	100.77

SUPPLEMENT 2

Supplement 2. Datasets of LA-ICP-MS analyses.

Table S2-1. The full list of the LA-ICP-MS data acquired from the analyzed pyrite from Vathi. b.d.l. = below detection limit, n. = number of analyses, n.a. = not analyzed.

		Hydrothermal alteration	Potassic overprinted by sericitic									
		Host rock	Latite									
		Sample	123									
		n.	1	2	3	4	5	6	7	8	9	10
		Mineralization style	Py1; Disseminated									
		Average detection limit										
³⁴ S	ppm	n.a.	563,875	585,384	561,337	610,758	594,502	562,381	603,442	598,476	616,559	689,644
⁴⁹ Ti	ppm	n.a.	25	90	31	11,460	27	26	20	109	32	39
⁵¹ V	ppm	0.77	b.d.l.	10.5	b.d.l.	110	3.1	b.d.l.	b.d.l.	10	b.d.l.	b.d.l.
⁵³ Cr	ppm	n.a.	36	47	41	46	38	30	46	46	29	27
⁵⁵ Mn	ppm	n.a.	56	84	50	73	67	49	56	90	48	51
⁵⁷ Fe	ppm	n.a.	465,500	465,500	464,800	458,000	458,000	458,000	458,000	458,000	458,000	458,000
⁵⁹ Co	ppm	0.46	57	100	1,341	42	17	289	25	92	19	31
⁶⁰ Ni	ppm	2.8	1,101	9,448	505	137	30	1,304	11	32	8.5	38
⁶⁵ Cu	ppm	4.3	68	199	b.d.l.	5.9	b.d.l.	7.6	b.d.l.	4.2	b.d.l.	b.d.l.
⁶⁶ Zn	ppm	5.4	b.d.l.	5,448	b.d.l.	8.3	7.1	b.d.l.	6.7	4.9	6.3	b.d.l.
⁷⁵ As	ppm	9	350	339	2,767	3,953	4,150	7,117	5,009	4,550	4,622	5,655
⁷⁷ Se	ppm	11	14	11	21	17	26	12	17	21	19	17
⁹⁵ Mo	ppm	1.2	b.d.l.	b.d.l.	b.d.l.	b.d.l.	b.d.l.	b.d.l.	b.d.l.	b.d.l.	b.d.l.	b.d.l.
¹⁰⁷ Ag	ppm	0.54	2.2	9.4	b.d.l.	b.d.l.	b.d.l.	b.d.l.	b.d.l.	b.d.l.	b.d.l.	b.d.l.
¹¹⁵ In	ppm	0.2	b.d.l.	12	b.d.l.	0.09	0.10	b.d.l.	b.d.l.	b.d.l.	b.d.l.	b.d.l.
¹¹⁸ Sn	ppm	0.64	b.d.l.	b.d.l.	b.d.l.	28	0.87	b.d.l.	b.d.l.	b.d.l.	b.d.l.	b.d.l.
¹²¹ Sb	ppm	0.97	10	1.3	b.d.l.	b.d.l.	b.d.l.	b.d.l.	b.d.l.	b.d.l.	0.46	0.34
¹²⁵ Te	ppm	2.3	b.d.l.	b.d.l.	30	7.9	5.3	b.d.l.	7.2	31	b.d.l.	8
¹⁸² W	ppm	0.63	16.22	b.d.l.	b.d.l.	2.9	b.d.l.	b.d.l.	b.d.l.	b.d.l.	b.d.l.	b.d.l.
¹⁹⁷ Au	ppm	0.44	b.d.l.	1.3	b.d.l.	2.1	0.68	5.1	0.66	2.3	1.1	1.4
²⁰² Hg	ppm	0.67	b.d.l.	b.d.l.	b.d.l.	b.d.l.	b.d.l.	b.d.l.	b.d.l.	b.d.l.	b.d.l.	b.d.l.
²⁰⁵ Tl	ppm	0.36	0.67	0.62	b.d.l.	b.d.l.	b.d.l.	b.d.l.	b.d.l.	b.d.l.	b.d.l.	b.d.l.
²⁰⁸ Pb	ppm	0.28	683	2827	b.d.l.	5.4	5.7	5.9	1.9	8.2	b.d.l.	0.56
²⁰⁹ Bi	ppm	0.22	32	88	b.d.l.	18	14	9.1	22	14	0.22	b.d.l.
²³² Th	ppm	0.14	b.d.l.	b.d.l.	b.d.l.	1.7	b.d.l.	b.d.l.	b.d.l.	b.d.l.	b.d.l.	b.d.l.
²³⁸ U	ppm	0.12	b.d.l.	b.d.l.	b.d.l.	9.2	b.d.l.	b.d.l.	b.d.l.	b.d.l.	b.d.l.	b.d.l.

Table S2-1. Continued.

		Hydrothermal alteration	Latite								
		Host rock	Quartz monzonite								
		Sample	Vath 43								
		n.	1	2	3	4	5	6	7	8	9
		Mineralization style	Py2; D-type vein						Py2; Disseminated		
		Average detection limit									
³⁴ S	ppm	n.a.	n.a.	n.a.	n.a.	n.a.	n.a.	n.a.	n.a.	n.a.	n.a.
⁴⁹ Ti	ppm	n.a.	31	26	34	32	30	29	33	29	26
⁵¹ V	ppm	0.77	b.d.l.	b.d.l.	b.d.l.	b.d.l.	b.d.l.	b.d.l.	b.d.l.	b.d.l.	b.d.l.
⁵³ Cr	ppm	n.a.	45	46	42	40	46	43	36	39	35
⁵⁵ Mn	ppm	n.a.	53	55	56	58	55	59	53	58	54
⁵⁷ Fe	ppm	n.a.	462,500	462,500	469,000	469,000	469,000	469,000	460,000	460,000	460,000
⁵⁹ Co	ppm	0.46	13	19	11	76	11	93	19	8	19
⁶⁰ Ni	ppm	2.8	5.3	b.d.l.	4.1	59	b.d.l.	33	11	28	9
⁶³ Cu	ppm	4.3	b.d.l.	13	14	16	b.d.l.	12	b.d.l.	b.d.l.	b.d.l.
⁶⁶ Zn	ppm	5.4	b.d.l.	b.d.l.	b.d.l.	6	b.d.l.	b.d.l.	b.d.l.	b.d.l.	6.8
⁷⁵ As	ppm	9	b.d.l.	9.7	b.d.l.	b.d.l.	b.d.l.	9.7	b.d.l.	b.d.l.	b.d.l.
⁷⁷ Se	ppm	11	b.d.l.	14	16	19	b.d.l.	14	b.d.l.	b.d.l.	b.d.l.
⁹⁵ Mo	ppm	1.2	b.d.l.	b.d.l.	b.d.l.	b.d.l.	b.d.l.	b.d.l.	b.d.l.	b.d.l.	b.d.l.
¹⁰⁷ Ag	ppm	0.54	b.d.l.	b.d.l.	b.d.l.	0.65	0.34	b.d.l.	b.d.l.	b.d.l.	b.d.l.
¹¹⁵ In	ppm	0.2	b.d.l.	b.d.l.	b.d.l.	b.d.l.	b.d.l.	b.d.l.	b.d.l.	b.d.l.	b.d.l.
¹¹⁸ Sn	ppm	0.64	b.d.l.	b.d.l.	b.d.l.	b.d.l.	b.d.l.	b.d.l.	b.d.l.	b.d.l.	b.d.l.
¹²¹ Sb	ppm	0.97	3.2	3.1	2	2.5	2.9	2.3	2.7	2.4	2.1
¹²⁵ Te	ppm	2.3	b.d.l.	184	15	1238	b.d.l.	557	b.d.l.	b.d.l.	b.d.l.
¹⁸² W	ppm	0.63	b.d.l.	b.d.l.	b.d.l.	b.d.l.	b.d.l.	b.d.l.	b.d.l.	b.d.l.	b.d.l.
¹⁹⁷ Au	ppm	0.44	b.d.l.	b.d.l.	b.d.l.	2.2	b.d.l.	2.1	b.d.l.	b.d.l.	b.d.l.
²⁰² Hg	ppm	0.67	b.d.l.	b.d.l.	b.d.l.	b.d.l.	b.d.l.	b.d.l.	b.d.l.	b.d.l.	b.d.l.
²⁰⁵ Tl	ppm	0.36	b.d.l.	b.d.l.	b.d.l.	b.d.l.	b.d.l.	b.d.l.	b.d.l.	b.d.l.	b.d.l.
²⁰⁸ Pb	ppm	0.28	b.d.l.	b.d.l.	b.d.l.	4.3	0.54	1.8	b.d.l.	b.d.l.	b.d.l.
²⁰⁹ Bi	ppm	0.22	b.d.l.	b.d.l.	b.d.l.	1771	b.d.l.	779	b.d.l.	b.d.l.	b.d.l.
²³² Th	ppm	0.14	b.d.l.	b.d.l.	b.d.l.	0.11	b.d.l.	b.d.l.	0.09	b.d.l.	b.d.l.
²³⁸ U	ppm	0.12	n.a.	n.a.	n.a.	n.a.	n.a.	n.a.	n.a.	n.a.	n.a.

Table S2-1. Continued.

		Hydrothermal alteration	Sericitic							
		Host rock	Latite							
		Sample	Vath 45					101		
		n.	1	2	3	4	5	1	2	3
		Mineralization style	Py3; Disseminated							
		Average detection limit								
³⁴ S	ppm	n.a.	n.a.	n.a.	n.a.	n.a.	n.a.	n.a.	n.a.	n.a.
⁴⁹ Ti	ppm	n.a.	23	24	35	26	26	57	31	30
⁵¹ V	ppm	0.77	b.d.l.	b.d.l.	b.d.l.	b.d.l.	b.d.l.	4.2	b.d.l.	b.d.l.
⁵³ Cr	ppm	n.a.	38	40	42	41	42	41	48	54
⁵⁵ Mn	ppm	n.a.	48	49	53	50	54	76	55	61
⁵⁷ Fe	ppm	n.a.	468,100	460,100	465,500	465,500	450,600	465,000	465,000	465,000
⁵⁹ Co	ppm	0.46	343	3,011	8,700	5,440	2,717	44	b.d.l.	b.d.l.
⁶⁰ Ni	ppm	2.8	55	650	53	433	5,406	41	30	207
⁶³ Cu	ppm	4.3	3.1	64	7.1	b.d.l.	76	13	b.d.l.	b.d.l.
⁶⁶ Zn	ppm	5.4	b.d.l.	3.3	4.6	3.1	3.6	9.9	b.d.l.	b.d.l.
⁷⁵ As	ppm	9	6.8	8.7	31	27	1.9	46	45	63
⁷⁷ Se	ppm	11	85	94	73	41	200	21	36	42
⁹⁵ Mo	ppm	1.2	b.d.l.	b.d.l.	b.d.l.	b.d.l.	b.d.l.	2	b.d.l.	b.d.l.
¹⁰⁷ Ag	ppm	0.54	b.d.l.	b.d.l.	b.d.l.	b.d.l.	b.d.l.	0.91	b.d.l.	b.d.l.
¹¹⁵ In	ppm	0.2	b.d.l.	b.d.l.	b.d.l.	b.d.l.	b.d.l.	b.d.l.	b.d.l.	b.d.l.
¹¹⁸ Sn	ppm	0.64	b.d.l.	b.d.l.	b.d.l.	b.d.l.	0.46	b.d.l.	b.d.l.	b.d.l.
¹²¹ Sb	ppm	0.97	b.d.l.	b.d.l.	1.6	b.d.l.	b.d.l.	0.70	0.58	b.d.l.
¹²⁵ Te	ppm	2.3	b.d.l.	b.d.l.	b.d.l.	b.d.l.	b.d.l.	b.d.l.	b.d.l.	b.d.l.
¹⁸² W	ppm	0.63	b.d.l.	b.d.l.	b.d.l.	b.d.l.	b.d.l.	b.d.l.	b.d.l.	b.d.l.
¹⁹⁷ Au	ppm	0.44	b.d.l.	b.d.l.	b.d.l.	b.d.l.	b.d.l.	b.d.l.	b.d.l.	b.d.l.
²⁰² Hg	ppm	0.67	b.d.l.	b.d.l.	0.56	b.d.l.	b.d.l.	b.d.l.	b.d.l.	b.d.l.
²⁰⁵ Tl	ppm	0.36	b.d.l.	b.d.l.	b.d.l.	b.d.l.	b.d.l.	b.d.l.	b.d.l.	b.d.l.
²⁰⁸ Pb	ppm	0.28	0.43	2.4	6.7	b.d.l.	2.3	17	b.d.l.	b.d.l.
²⁰⁹ Bi	ppm	0.22	0.18	0.19	0.18	b.d.l.	b.d.l.	0.76	b.d.l.	b.d.l.
²³² Th	ppm	0.14	0.24	0.17	b.d.l.	b.d.l.	b.d.l.	b.d.l.	b.d.l.	b.d.l.
²³⁸ U	ppm	0.12	n.a.	n.a.	n.a.	n.a.	n.a.	n.a.	n.a.	n.a.

Table S2-1. Continued.

		Hydrothermal alteration	Sericitic										
		Host rock	Latite										
		Sample	111					124					
		n.	1	2	3	4	5	1	2	3	4	5	6
		Mineralization style	Py3; Disseminated										
		Average detection limit											
³⁴ S	ppm	n.a.	n.a.	n.a.	n.a.	n.a.	n.a.	766,581	754,688	830,456	791,118	759,614	699,177
⁴⁹ Ti	ppm	n.a.	23	29	28	28	32	27	40	27	33	38	20
⁵¹ V	ppm	0.77	b.d.l.	b.d.l.	b.d.l.	b.d.l.	b.d.l.	b.d.l.	b.d.l.	b.d.l.	b.d.l.	b.d.l.	b.d.l.
⁵³ Cr	ppm	n.a.	36	52	70	54	31	45	40	50	39	46	45
⁵⁵ Mn	ppm	n.a.	57	60	58	58	59	54	55	53	54	50	54
⁵⁷ Fe	ppm	n.a.	460,200	463,900	463,900	454,400	463,900	461,200	461,200	460,200	460,700	460,700	457,100
⁵⁹ Co	ppm	0.46	0.73	54	567	b.d.l.	b.d.l.	717	532	620	1,357	419	117
⁶⁰ Ni	ppm	2.8	2.3	362	58	b.d.l.	b.d.l.	46	107	15	145	184	b.d.l.
⁶⁵ Cu	ppm	4.3	b.d.l.	425	16	b.d.l.	4.3	5	26	13	6,966	b.d.l.	3,704
⁶⁶ Zn	ppm	5.4	b.d.l.	b.d.l.	b.d.l.	b.d.l.	b.d.l.	b.d.l.	4.8	b.d.l.	b.d.l.	4.5	7.1
⁷⁵ As	ppm	9	469	12	6.4	374	200	19	27	14	21	19	15
⁷⁷ Se	ppm	11	13	30	21	19	21	28	61	15	26	25	19
⁹⁵ Mo	ppm	1.2	b.d.l.	1.9	b.d.l.	b.d.l.	b.d.l.	b.d.l.	b.d.l.	b.d.l.	b.d.l.	b.d.l.	b.d.l.
¹⁰⁷ Ag	ppm	0.54	b.d.l.	1.3	0.34	b.d.l.	b.d.l.	b.d.l.	b.d.l.	b.d.l.	0.40	b.d.l.	0.57
¹¹⁵ In	ppm	0.2	b.d.l.	b.d.l.	b.d.l.	b.d.l.	b.d.l.	b.d.l.	b.d.l.	b.d.l.	b.d.l.	b.d.l.	b.d.l.
¹¹⁸ Sn	ppm	0.64	b.d.l.	4.9	b.d.l.	b.d.l.	b.d.l.	b.d.l.	b.d.l.	b.d.l.	b.d.l.	b.d.l.	b.d.l.
¹²¹ Sb	ppm	0.97	0.76	b.d.l.	0.82	0.49	b.d.l.	0.47	0.60	0.50	0.45	0.88	0.62
¹²⁵ Te	ppm	2.3	19	b.d.l.	b.d.l.	38	41	b.d.l.	b.d.l.	b.d.l.	b.d.l.	2.9	b.d.l.
¹⁸² W	ppm	0.63	b.d.l.	b.d.l.	b.d.l.	b.d.l.	b.d.l.	b.d.l.	b.d.l.	b.d.l.	b.d.l.	b.d.l.	b.d.l.
¹⁹⁷ Au	ppm	0.44	b.d.l.	b.d.l.	b.d.l.	b.d.l.	b.d.l.	b.d.l.	b.d.l.	b.d.l.	b.d.l.	b.d.l.	b.d.l.
²⁰² Hg	ppm	0.67	b.d.l.	0.46	b.d.l.	0.67	b.d.l.	b.d.l.	b.d.l.	b.d.l.	b.d.l.	b.d.l.	b.d.l.
²⁰⁵ Tl	ppm	0.36	b.d.l.	b.d.l.	b.d.l.	b.d.l.	b.d.l.	b.d.l.	b.d.l.	b.d.l.	b.d.l.	b.d.l.	b.d.l.
²⁰⁸ Pb	ppm	0.28	b.d.l.	5.5	0.47	0.84	b.d.l.	b.d.l.	b.d.l.	b.d.l.	b.d.l.	b.d.l.	b.d.l.
²⁰⁹ Bi	ppm	0.22	b.d.l.	6.3	b.d.l.	1.3	b.d.l.	b.d.l.	b.d.l.	b.d.l.	b.d.l.	b.d.l.	b.d.l.
²³² Th	ppm	0.14	b.d.l.	b.d.l.	b.d.l.	b.d.l.	b.d.l.	b.d.l.	b.d.l.	b.d.l.	b.d.l.	b.d.l.	b.d.l.
²³⁸ U	ppm	0.12	b.d.l.	b.d.l.	b.d.l.	b.d.l.	b.d.l.	b.d.l.	b.d.l.	b.d.l.	b.d.l.	b.d.l.	b.d.l.

Table S2-1. Continued.

		Hydrothermal alteration	Epithermal overprint						
		Host rock	Latite						
		Sample	128						
		n.	1	2	3	4	5	6	7
		Mineralization style	Py4; E-type vein						
		Average detection limit							
³⁴ S	ppm	n.a.	n.a.	n.a.	n.a.	n.a.	n.a.	n.a.	n.a.
⁴⁹ Ti	ppm	n.a.	25	21	22	29	23	41	32
⁵¹ V	ppm	0.77	b.d.l.	b.d.l.	b.d.l.	b.d.l.	b.d.l.	b.d.l.	b.d.l.
⁵² Cr	ppm	n.a.	34	34	30	35	36	30	42
⁵⁵ Mn	ppm	n.a.	53	49	48	49	53	48	53
⁵⁷ Fe	ppm	n.a.	449,000	468,600	462,600	456,800	446,800	446,900	446,900
⁵⁹ Co	ppm	0.46	51	71	108	195	2.25	15,619	17,106
⁶⁰ Ni	ppm	2.8	691	961	1575	2,153	814	31	6.1
⁶³ Cu	ppm	4.3	4.5	3.3	7.8	2.4	6.9	b.d.l.	59
⁶⁶ Zn	ppm	5.4	b.d.l.	b.d.l.	b.d.l.	3.7	4.1	b.d.l.	11
⁷⁵ As	ppm	9	7.1	4.1	b.d.l.	4.7	6	29	6
⁷⁷ Se	ppm	11	6.6	10	15	18	5.8	b.d.l.	14
⁹⁵ Mo	ppm	1.2	b.d.l.	b.d.l.	b.d.l.	b.d.l.	b.d.l.	b.d.l.	b.d.l.
¹⁰⁷ Ag	ppm	0.54	b.d.l.	0.49	1.4	3.7	6.6	0.84	0.94
¹¹⁵ In	ppm	0.2	b.d.l.	b.d.l.	b.d.l.	b.d.l.	b.d.l.	b.d.l.	0.10
¹¹⁸ Sn	ppm	0.64	b.d.l.	b.d.l.	b.d.l.	b.d.l.	b.d.l.	b.d.l.	b.d.l.
¹²¹ Sb	ppm	0.97	b.d.l.	b.d.l.	b.d.l.	b.d.l.	2.9	1.2	0.96
¹²⁵ Te	ppm	2.3	b.d.l.	b.d.l.	b.d.l.	b.d.l.	b.d.l.	b.d.l.	b.d.l.
¹⁸² W	ppm	0.63	4.4	9.4	b.d.l.	27	6.5	b.d.l.	b.d.l.
¹⁹⁷ Au	ppm	0.44	b.d.l.	b.d.l.	b.d.l.	b.d.l.	b.d.l.	b.d.l.	b.d.l.
²⁰² Hg	ppm	0.67	b.d.l.	b.d.l.	b.d.l.	b.d.l.	b.d.l.	b.d.l.	b.d.l.
²⁰⁵ Tl	ppm	0.36	b.d.l.	b.d.l.	b.d.l.	b.d.l.	1.2	b.d.l.	b.d.l.
²⁰⁸ Pb	ppm	0.28	7	4.3	1.1	2.5	60	8	16.2
²⁰⁹ Bi	ppm	0.22	b.d.l.	b.d.l.	0.17	b.d.l.	0.88	1.7	1.0
²³² Th	ppm	0.14	b.d.l.	b.d.l.	b.d.l.	b.d.l.	b.d.l.	b.d.l.	b.d.l.
²³⁸ U	ppm	0.12	b.d.l.	2.6	1.9	2.0	0.18	b.d.l.	b.d.l.

Table S2-2. The full list of the LA-ICP-MS data acquired from the analyzed chalcopyrite from Vathi. b.d.l. = below detection limit, n. = number of analyses, n.a. = not analyzed.

		Hydrothermal alteration	Potassic overprinted by sericitic									
		Host rock	Latite									
		Sample	123									
		n.	1	2	3	4	5	6	7	8	9	10
		Mineralization style	Cpy1; Disseminated									
		Average detection limit										
³⁴ S	ppm	n.a.	354,503	390,531	462,803	410,091	435,432	438,820	416,233	442,934	452,809	427,203
⁴⁹ Ti	ppm	29	b.d.l.	30	28	41	26	b.d.l.	20	11	19	19
⁵¹ V	ppm	2.2	6.9	3.9	b.d.l.	10.51	b.d.l.	b.d.l.	b.d.l.	b.d.l.	b.d.l.	b.d.l.
⁵³ Cr	ppm	37	b.d.l.	38	b.d.l.	b.d.l.	26	30	34	20	23	21
⁵⁵ Mn	ppm	n.a.	5,183	93	284	1,115	57	37	36	40	33	888
⁵⁷ Fe	ppm	n.a.	304,200	304,200	304,200	304,200	304,200	304,200	304,200	304,200	304,200	304,200
⁵⁹ Co	ppm	1	4.9	b.d.l.	b.d.l.	4.9	b.d.l.	b.d.l.	b.d.l.	b.d.l.	b.d.l.	b.d.l.
⁶⁰ Ni	ppm	6	5.1	b.d.l.	b.d.l.	6.2	b.d.l.	b.d.l.	b.d.l.	b.d.l.	b.d.l.	b.d.l.
⁶⁵ Cu	ppm	n.a.	312,236	344,112	360,735	339,521	346,136	347,562	349,197	363,254	334,359	345,304
⁶⁶ Zn	ppm	11	137	5,147	518	201	946	704	265	158	2,392	239
⁷¹ Ga	ppm	2.5	b.d.l.	b.d.l.	b.d.l.	b.d.l.	b.d.l.	2.2	b.d.l.	b.d.l.	b.d.l.	b.d.l.
⁷³ Ge	ppm	7.6	b.d.l.	b.d.l.	b.d.l.	b.d.l.	b.d.l.	b.d.l.	1.5	b.d.l.	b.d.l.	b.d.l.
⁷⁵ As	ppm	14	62	56	73	75	71	83	72	60	58	59
⁷⁷ Se	ppm	15	b.d.l.	b.d.l.	b.d.l.	b.d.l.	b.d.l.	b.d.l.	b.d.l.	b.d.l.	b.d.l.	b.d.l.
⁹³ Nb	ppm	0.44	b.d.l.	0.26	b.d.l.	b.d.l.	0.25	b.d.l.	b.d.l.	b.d.l.	b.d.l.	b.d.l.
⁹⁵ Mo	ppm	3.5	b.d.l.	b.d.l.	b.d.l.	b.d.l.	b.d.l.	b.d.l.	b.d.l.	b.d.l.	b.d.l.	b.d.l.
¹⁰⁷ Ag	ppm	n.a.	9.7	12	6.8	7.6	8.1	7.4	17	15	10	9.7
¹⁵⁷ Cd	ppm	4.1	b.d.l.	45	5.7	b.d.l.	8.9	7.6	b.d.l.	4.4	15	b.d.l.
¹¹⁵ In	ppm	n.a.	39	52	57	54	59	59	52	32	62	36
¹¹⁸ Sn	ppm	1.7	b.d.l.	2.1	9	2.7	8.3	7.8	3	1.8	7.4	5.3
¹²¹ Sb	ppm	1.1	b.d.l.	b.d.l.	b.d.l.	b.d.l.	b.d.l.	b.d.l.	b.d.l.	b.d.l.	b.d.l.	b.d.l.
¹²⁵ Te	ppm	7.8	b.d.l.	b.d.l.	b.d.l.	b.d.l.	b.d.l.	b.d.l.	b.d.l.	b.d.l.	b.d.l.	b.d.l.
¹⁸² W	ppm	1.5	9.9	b.d.l.	b.d.l.	5.92	1	b.d.l.	b.d.l.	b.d.l.	b.d.l.	1.6
¹⁸⁵ Re	ppm	1	b.d.l.	b.d.l.	b.d.l.	b.d.l.	b.d.l.	b.d.l.	b.d.l.	b.d.l.	b.d.l.	b.d.l.
¹⁹⁷ Au	ppm	0.81	b.d.l.	b.d.l.	b.d.l.	b.d.l.	b.d.l.	b.d.l.	b.d.l.	b.d.l.	b.d.l.	b.d.l.
²⁰² Hg	ppm	1.3	b.d.l.	b.d.l.	b.d.l.	b.d.l.	b.d.l.	b.d.l.	b.d.l.	b.d.l.	b.d.l.	b.d.l.
²⁰⁵ Tl	ppm	0.87	b.d.l.	b.d.l.	b.d.l.	b.d.l.	b.d.l.	b.d.l.	0.42	b.d.l.	b.d.l.	b.d.l.
²⁰⁸ Pb	ppm	1.6	190	273	1.2	46	5.4	1.3	16	43	14	3.9
²⁰⁹ Bi	ppm	1.2	24	34	2.9	23	11	2.9	40	27	25	5.8
²³² Th	ppm	0.32	b.d.l.	b.d.l.	b.d.l.	b.d.l.	b.d.l.	b.d.l.	b.d.l.	b.d.l.	b.d.l.	b.d.l.
²³⁸ U	ppm	0.31	b.d.l.	b.d.l.	b.d.l.	b.d.l.	b.d.l.	b.d.l.	b.d.l.	b.d.l.	b.d.l.	b.d.l.

Table S2-2. Continued.

		Hydrothermal alteration	Sericite												Epithermal overprint			
		Host rock	Latite															
		Sample	101		105								128					
		n.	1	2	1	2	3	4	5	6	7	8	9	10	1	2		
		Mineralization style	Cpy2; Disseminated														Cpy3; E-type vein	
		Average detection limit																
³⁴ S	ppm	n.a.	n.a.	n.a.	n.a.	n.a.	n.a.	n.a.	n.a.	n.a.	n.a.	n.a.	n.a.	n.a.	n.a.	n.a.		
⁴⁹ Ti	ppm	29	15	b.d.l.	16	12	21	b.d.l.	b.d.l.	31	21	b.d.l.	15	19	45	b.d.l.		
⁵¹ V	ppm	2.2	b.d.l.	b.d.l.	b.d.l.	b.d.l.	b.d.l.	b.d.l.	b.d.l.	b.d.l.	b.d.l.	b.d.l.	b.d.l.	b.d.l.	b.d.l.	b.d.l.		
⁵³ Cr	ppm	37	27	26	22	25	27	b.d.l.	b.d.l.	55	b.d.l.	19	43	29	b.d.l.	b.d.l.		
⁵⁵ Mn	ppm	n.a.	30	30	37	32	35	42	32	38	34	34	34	32	31	322		
⁵⁷ Fe	ppm	n.a.	307,200	299,700	300,000	300,000	300,000	300,000	300,000	300,000	305,700	305,700	305,700	305,700	304,000	304,000		
⁵⁹ Co	ppm	1	b.d.l.	b.d.l.	0.58	b.d.l.	0.74	5.3	b.d.l.	b.d.l.	0.73	b.d.l.	1	b.d.l.	b.d.l.	b.d.l.		
⁶⁰ Ni	ppm	6	b.d.l.	b.d.l.	b.d.l.	b.d.l.	b.d.l.	b.d.l.	b.d.l.	b.d.l.	4.2	4.1	b.d.l.	7.5	b.d.l.	b.d.l.		
⁶⁵ Cu	ppm	n.a.	357,026	421,253	375,855	371,692	367,270	365,680	340,234	362,767	376,972	373,405	360,816	366,417	340,657	340,199		
⁶⁶ Zn	ppm	11	19	30	31	b.d.l.	49	1,313	35	1,208	55	74	39	54	571	287		
⁷¹ Ga	ppm	2.5	b.d.l.	b.d.l.	b.d.l.	b.d.l.	b.d.l.	b.d.l.	b.d.l.	b.d.l.	b.d.l.	b.d.l.	b.d.l.	b.d.l.	b.d.l.	b.d.l.		
⁷³ Ge	ppm	7.6	b.d.l.	b.d.l.	b.d.l.	b.d.l.	b.d.l.	b.d.l.	12	4.9	b.d.l.	b.d.l.	b.d.l.	b.d.l.	b.d.l.	8.5		
⁷⁵ As	ppm	14	12	25	7.2	b.d.l.	5.7	b.d.l.	b.d.l.	b.d.l.	b.d.l.	4.8	b.d.l.	b.d.l.	b.d.l.	b.d.l.		
⁷⁷ Se	ppm	15	46	54	92	105	98	161	70	83	86	77	97	91	b.d.l.	b.d.l.		
⁹³ Nb	ppm	0.44	n.a.	n.a.	b.d.l.	b.d.l.	b.d.l.	b.d.l.	b.d.l.	b.d.l.	b.d.l.	b.d.l.	b.d.l.	b.d.l.	b.d.l.	b.d.l.		
⁹⁵ Mo	ppm	3.5	b.d.l.	b.d.l.	b.d.l.	b.d.l.	b.d.l.	b.d.l.	b.d.l.	b.d.l.	b.d.l.	b.d.l.	b.d.l.	b.d.l.	b.d.l.	b.d.l.		
¹⁰⁷ Ag	ppm	n.a.	8	20	20	25	21	519	36	35	46	38	20	36	407	134		
¹⁵⁷ Cd	ppm	4.1	b.d.l.	b.d.l.	b.d.l.	b.d.l.	b.d.l.	b.d.l.	b.d.l.	b.d.l.	b.d.l.	b.d.l.	b.d.l.	b.d.l.	b.d.l.	b.d.l.		
¹¹⁵ In	ppm	n.a.	19	11	47	50	36	3.1	46	30	13	24	57	36	0.98	57		
¹¹⁸ Sn	ppm	1.7	144	113	126	120	122	18	101	123	126	123	102	141	91	48		
¹²¹ Sb	ppm	1.1	b.d.l.	1.1	b.d.l.	b.d.l.	b.d.l.	48	b.d.l.	b.d.l.	b.d.l.	b.d.l.	b.d.l.	b.d.l.	b.d.l.	3.4		
¹²⁵ Te	ppm	7.8	b.d.l.	b.d.l.	3.9	6.8	b.d.l.	b.d.l.	b.d.l.	b.d.l.	b.d.l.	4.4	4.3	6.1	b.d.l.	b.d.l.		
¹⁸² W	ppm	1.5	b.d.l.	b.d.l.	b.d.l.	b.d.l.	b.d.l.	b.d.l.	b.d.l.	b.d.l.	b.d.l.	b.d.l.	b.d.l.	b.d.l.	2	b.d.l.		
¹⁸⁵ Re	ppm	1	n.a.	n.a.	b.d.l.	b.d.l.	b.d.l.	b.d.l.	b.d.l.	b.d.l.	b.d.l.	b.d.l.	b.d.l.	b.d.l.	b.d.l.	b.d.l.		
¹⁹⁷ Au	ppm	0.81	b.d.l.	b.d.l.	b.d.l.	b.d.l.	b.d.l.	b.d.l.	b.d.l.	b.d.l.	b.d.l.	b.d.l.	b.d.l.	b.d.l.	b.d.l.	b.d.l.		
²⁰² Hg	ppm	1.3	b.d.l.	b.d.l.	0.83	b.d.l.	b.d.l.	50	b.d.l.	b.d.l.	0.99	b.d.l.	b.d.l.	b.d.l.	b.d.l.	b.d.l.		
²⁰⁵ Tl	ppm	0.87	b.d.l.	b.d.l.	b.d.l.	b.d.l.	b.d.l.	38	b.d.l.	b.d.l.	b.d.l.	b.d.l.	b.d.l.	b.d.l.	b.d.l.	b.d.l.		
²⁰⁸ Pb	ppm	1.6	9.2	9	3.9	7.5	11	13,912	b.d.l.	17	15	14	4.0	15	b.d.l.	27		
²⁰⁹ Bi	ppm	1.2	0.34	11	4.4	4.6	13	3,111	b.d.l.	4.6	1.8	1.4	2.1	5.5	b.d.l.	b.d.l.		
²³² Th	ppm	0.32	b.d.l.	b.d.l.	b.d.l.	b.d.l.	b.d.l.	b.d.l.	b.d.l.	b.d.l.	b.d.l.	b.d.l.	b.d.l.	b.d.l.	b.d.l.	b.d.l.		
²³⁸ U	ppm	0.31	n.a.	n.a.	b.d.l.	b.d.l.	b.d.l.	b.d.l.	b.d.l.	b.d.l.	b.d.l.	b.d.l.	b.d.l.	b.d.l.	b.d.l.	b.d.l.		

Table S2-3. The full list of the LA-ICP-MS data acquired from the analyzed magnetite from Vathi. b.d.l. = below detection limit, n. = number of analyses, n.a. = not analyzed.

		Hydrothermal alteration	Potassic-calcic							Potassic overprinted by sericitic								
		Host rock	Quartz monzonite							Latite								
		Sample	Vath 44							123								
		n.	1	2	3	4	5	6	7	1	2	3	4	5	6	7	8	9
		Mineralization style	Mag1; M-type vein							Mag2; Disseminated								
		Average detection limit																
²⁷ Al	ppm	n.a.	1,826	2,350	1,814	3,161	1,062	1,424	1,288	37,773	2,213	5,399	16,645	3,012	943	16,099	5,290	4,076
³¹ P	ppm	102	b.d.l.	b.d.l.	b.d.l.	b.d.l.	b.d.l.	125	364	b.d.l.	b.d.l.	b.d.l.	b.d.l.	b.d.l.	b.d.l.	b.d.l.	b.d.l.	b.d.l.
³⁴ S	ppm	866	n.a.	n.a.	n.a.	n.a.	n.a.	n.a.	n.a.	2595	b.d.l.	b.d.l.	3116	b.d.l.	b.d.l.	2571	b.d.l.	856
⁴⁹ Ti	ppm	n.a.	3,553	2,928	1,533	1,784	1,503	1,932	1,046	1,237	1,421	2,466	1,774	1,330	1,074	1,347	1,954	2,468
⁵¹ V	ppm	n.a.	3,657	3,576	3,531	3,725	3,804	4,176	3,875	2,735	2,516	2,006	2,587	1,830	2,832	2,304	2,351	2,263
⁵³ Cr	ppm	70	52	39	60	52	216	282	87	183	96	b.d.l.	117	64	2,043	88	63	66
⁵⁵ Mn	ppm	n.a.	734	563	583	590	628	698	711	1,476	591	525	672	467	786	680	680	763
⁵⁷ Fe	ppm	n.a.	723,600	723,600	723,600	723,600	722,200	722,200	721,800	723,600	723,600	723,600	723,600	723,600	723,600	723,600	723,600	723,600
⁵⁹ Co	ppm	n.a.	10	12	10	13	11	12	14	11	6	5	4	5	10	3	9	12
⁶⁰ Ni	ppm	14	712	720	649	814	383	495	382	68	b.d.l.	b.d.l.	b.d.l.	b.d.l.	11	b.d.l.	b.d.l.	b.d.l.
⁶⁵ Cu	ppm	11	b.d.l.	b.d.l.	b.d.l.	b.d.l.	b.d.l.	36	107	b.d.l.	b.d.l.	23	71	13	b.d.l.	68	16	23
⁶⁶ Zn	ppm	n.a.	50	59	48	59	48	37	56	182	61	88	146	69	59	137	95	107
⁷¹ Ga	ppm	n.a.	56	57	53	65	60	55	39	34	39	43	37	44	35	37	47	53
⁷³ Ge	ppm	n.a.	n.a.	n.a.	n.a.	n.a.	n.a.	n.a.	n.a.	b.d.l.	b.d.l.	b.d.l.	b.d.l.	12	b.d.l.	b.d.l.	16	b.d.l.
⁷⁵ As	ppm	31	b.d.l.	b.d.l.	b.d.l.	b.d.l.	b.d.l.	43	60	b.d.l.	b.d.l.	b.d.l.	b.d.l.	b.d.l.	b.d.l.	b.d.l.	b.d.l.	b.d.l.
⁷⁷ Se	ppm	40	3	b.d.l.	b.d.l.	b.d.l.	b.d.l.	b.d.l.	b.d.l.	b.d.l.	b.d.l.	b.d.l.	b.d.l.	b.d.l.	b.d.l.	b.d.l.	b.d.l.	b.d.l.
⁹³ Nb	ppm	1	n.a.	n.a.	n.a.	n.a.	n.a.	n.a.	n.a.	b.d.l.	b.d.l.	b.d.l.	b.d.l.	b.d.l.	b.d.l.	b.d.l.	b.d.l.	b.d.l.
⁹⁵ Mo	ppm	6.4	b.d.l.	b.d.l.	b.d.l.	b.d.l.	b.d.l.	b.d.l.	b.d.l.	b.d.l.	b.d.l.	b.d.l.	b.d.l.	b.d.l.	b.d.l.	b.d.l.	b.d.l.	b.d.l.
¹⁰⁷ Ag	ppm	2.5	b.d.l.	b.d.l.	b.d.l.	b.d.l.	b.d.l.	2	b.d.l.	b.d.l.	b.d.l.	b.d.l.	b.d.l.	b.d.l.	b.d.l.	b.d.l.	b.d.l.	b.d.l.
¹⁵⁷ Cd	ppm	9	b.d.l.	b.d.l.	b.d.l.	b.d.l.	b.d.l.	b.d.l.	b.d.l.	b.d.l.	b.d.l.	b.d.l.	b.d.l.	b.d.l.	b.d.l.	b.d.l.	b.d.l.	b.d.l.
¹¹⁵ In	ppm	0.72	b.d.l.	b.d.l.	b.d.l.	b.d.l.	b.d.l.	b.d.l.	b.d.l.	b.d.l.	b.d.l.	b.d.l.	b.d.l.	b.d.l.	b.d.l.	b.d.l.	b.d.l.	b.d.l.
¹¹⁸ Sn	ppm	4.6	10	11	6	13	4	2	b.d.l.	b.d.l.	3	5	b.d.l.	3	b.d.l.	4	5	6
¹²¹ Sb	ppm	3.2	b.d.l.	b.d.l.	b.d.l.	b.d.l.	b.d.l.	b.d.l.	b.d.l.	b.d.l.	b.d.l.	b.d.l.	b.d.l.	b.d.l.	b.d.l.	b.d.l.	3	b.d.l.
¹²⁵ Te	ppm	26	b.d.l.	b.d.l.	b.d.l.	b.d.l.	b.d.l.	b.d.l.	b.d.l.	b.d.l.	b.d.l.	b.d.l.	b.d.l.	b.d.l.	b.d.l.	b.d.l.	b.d.l.	b.d.l.
¹³⁹ La	ppm	0.78	b.d.l.	2	b.d.l.	3	1	1	4	b.d.l.	b.d.l.	b.d.l.	b.d.l.	b.d.l.	b.d.l.	b.d.l.	b.d.l.	b.d.l.
¹⁴⁰ Ce	ppm	0.84	b.d.l.	3	b.d.l.	6	1	1	8	b.d.l.	b.d.l.	1	b.d.l.	b.d.l.	b.d.l.	b.d.l.	1	1
¹⁴⁵ Nd	ppm	7.4	b.d.l.	b.d.l.	b.d.l.	b.d.l.	b.d.l.	b.d.l.	b.d.l.	b.d.l.	b.d.l.	b.d.l.	b.d.l.	b.d.l.	b.d.l.	b.d.l.	b.d.l.	b.d.l.
¹⁴⁷ Sm	ppm	4.1	b.d.l.	b.d.l.	b.d.l.	b.d.l.	b.d.l.	b.d.l.	b.d.l.	b.d.l.	b.d.l.	b.d.l.	b.d.l.	b.d.l.	b.d.l.	b.d.l.	b.d.l.	b.d.l.
¹⁵⁷ Gd	ppm	3.8	b.d.l.	b.d.l.	b.d.l.	b.d.l.	b.d.l.	b.d.l.	b.d.l.	b.d.l.	b.d.l.	b.d.l.	b.d.l.	b.d.l.	b.d.l.	b.d.l.	b.d.l.	b.d.l.
¹⁸² W	ppm	2.7	b.d.l.	b.d.l.	b.d.l.	b.d.l.	b.d.l.	b.d.l.	b.d.l.	13	b.d.l.	b.d.l.	7	b.d.l.	b.d.l.	3	4	b.d.l.
¹⁸⁵ Re	ppm	1.4	n.a.	n.a.	n.a.	n.a.	n.a.	n.a.	n.a.	b.d.l.	b.d.l.	b.d.l.	b.d.l.	b.d.l.	b.d.l.	b.d.l.	b.d.l.	b.d.l.
¹⁹⁷ Au	ppm	1.6	b.d.l.	b.d.l.	b.d.l.	b.d.l.	b.d.l.	b.d.l.	b.d.l.	b.d.l.	b.d.l.	b.d.l.	b.d.l.	b.d.l.	b.d.l.	b.d.l.	b.d.l.	b.d.l.
²⁰² Hg	ppm	n.a.	n.a.	n.a.	n.a.	n.a.	n.a.	n.a.	n.a.	n.a.	n.a.	n.a.	n.a.	n.a.	n.a.	n.a.	n.a.	n.a.
²⁰⁵ Tl	ppm	2.8	b.d.l.	b.d.l.	b.d.l.	b.d.l.	b.d.l.	b.d.l.	b.d.l.	b.d.l.	b.d.l.	b.d.l.	b.d.l.	b.d.l.	b.d.l.	b.d.l.	b.d.l.	b.d.l.
²⁰⁸ Pb	ppm	1.2	2	2	3	b.d.l.	8	59	46	33	b.d.l.	14	20	6	b.d.l.	23	11	14
²⁰⁹ Bi	ppm	0.93	b.d.l.	b.d.l.	b.d.l.	b.d.l.	b.d.l.	1	b.d.l.	4	b.d.l.	3	4	1	b.d.l.	6	b.d.l.	2
²³² Th	ppm	0.68	b.d.l.	b.d.l.	b.d.l.	b.d.l.	b.d.l.	1	23	b.d.l.	b.d.l.	b.d.l.	b.d.l.	b.d.l.	b.d.l.	b.d.l.	b.d.l.	b.d.l.
²³⁸ U	ppm	0.8	n.a.	n.a.	n.a.	n.a.	n.a.	n.a.	n.a.	b.d.l.	0	1	b.d.l.	b.d.l.	b.d.l.	1	b.d.l.	b.d.l.

Table S2-4. The full list of the LA-ICP-MS data acquired from the analyzed titanite from Vathi. b.d.l. = below detection limit, n. = number of analyses, n.a. = not analyzed.

		Hydrothermal alteration	Potassic-calcic				
		Host rock	Quartz monzonite				
		Sample	Vath 44				
		n.	1	2	3	4	5
		Mineralization style	Tm1; Disseminated				
		Average detection limit					
²⁷ Al	ppm	n.a.	5,002	4,672	11,513	4,505	4,785
³¹ P	ppm	237	b.d.l.	984	365	738	381
³⁴ S	ppm	n.a.	n.a.	n.a.	n.a.	n.a.	n.a.
⁴⁹ Ti	ppm	n.a.	195,000	195,000	189,900	195,300	203,100
⁵¹ V	ppm	n.a.	1,164	2,220	2,438	2,238	2,620
⁵³ Cr	ppm	74	b.d.l.	b.d.l.	b.d.l.	b.d.l.	b.d.l.
⁵⁵ Mn	ppm	n.a.	713	477	581	311	408
⁵⁷ Fe	ppm	n.a.	16,044	13,685	73,354	14,279	10,479
⁵⁹ Co	ppm	3.9	b.d.l.	b.d.l.	4	b.d.l.	b.d.l.
⁶⁰ Ni	ppm	20	b.d.l.	b.d.l.	130	b.d.l.	b.d.l.
⁶⁵ Cu	ppm	n.a.	68	47	167	66	47
⁶⁶ Zn	ppm	38	55	b.d.l.	63	44	38
⁶⁹ Ga	ppm	8	b.d.l.	13	35	12	14
⁷⁴ Ge	ppm	n.a.	24	40	39	33	40
⁷⁵ As	ppm	n.a.	39	146	122	107	106
⁷⁷ Se	ppm	49	b.d.l.	73	94	101	141
⁹³ Nb	ppm	n.a.	n.a.	n.a.	n.a.	n.a.	n.a.
⁹⁵ Mo	ppm	9.8	7.8	b.d.l.	7.6	b.d.l.	11
¹⁰⁷ Ag	ppm	2.8	b.d.l.	b.d.l.	b.d.l.	b.d.l.	b.d.l.
¹⁵⁷ Cd	ppm	19	b.d.l.	b.d.l.	b.d.l.	b.d.l.	b.d.l.
¹¹⁵ In	ppm	n.a.	7.2	10	4.9	8.9	7.8
¹¹⁸ Sn	ppm	n.a.	1727	2503	1286	2383	2039
¹²¹ Sb	ppm	3.4	b.d.l.	22	21	11	22
¹²⁵ Te	ppm	27	b.d.l.	b.d.l.	b.d.l.	b.d.l.	b.d.l.
¹³⁹ La	ppm	n.a.	576	1,010	1,343	803	1,369
¹⁴⁰ Ce	ppm	n.a.	1,813	4,065	5,239	3,584	5,535
¹⁴⁵ Nd	ppm	n.a.	872	3,078	3,956	3,485	4,215
¹⁴⁷ Sm	ppm	n.a.	164	778	941	1,009	1,070
¹⁵⁷ Gd	ppm	n.a.	131	749	840	984	974
¹⁸² W	ppm	5.3	b.d.l.	11	17	81	15
¹⁸⁵ Re	ppm	n.a.	n.a.	n.a.	n.a.	n.a.	n.a.
¹⁹⁷ Au	ppm	1.6	b.d.l.	b.d.l.	b.d.l.	b.d.l.	b.d.l.
²⁰² Hg	ppm	n.a.	n.a.	n.a.	n.a.	n.a.	n.a.
²⁰⁵ Tl	ppm	3.9	b.d.l.	b.d.l.	b.d.l.	b.d.l.	b.d.l.
²⁰⁸ Pb	ppm	n.a.	7.8	5.3	21	9.8	4
²⁰⁹ Bi	ppm	2	b.d.l.	2.1	2.9	2.8	3.4
²³² Th	ppm	n.a.	32	233	309	216	237
²³⁸ U	ppm	n.a.	n.a.	n.a.	n.a.	n.a.	n.a.

Table S2-5. The full list of the LA-ICP-MS data acquired from the analyzed stibnite from Gerakario. b.d.l. = below detection limit, n. = number of analyses, n.a. = not analyzed.

		Hydrothermal alteration	Sericitic alteration														
		Host rock	Two-mica gneiss														
		Sample	Ger 02					Ger 05									
		n.	1	2	3	4	5	1	2	3	4	5	6	7	8	9	10
		Mineralization style	Stb1; Vein														
		Average detection limit															
³⁴ S	ppm	n.a.	n.a.	n.a.	n.a.	n.a.	n.a.	325,100	326,461	312,332	323,054	306,726	298,248	287,051	291,923	285,300	272,881
⁴⁹ Ti	ppm	n.a.	12	16	13	9.7	14	13	13	11	12	11	18	14	16	11	11
⁵¹ V	ppm	0.52	b.d.l.	b.d.l.	b.d.l.	b.d.l.	b.d.l.	b.d.l.	b.d.l.	b.d.l.	b.d.l.	b.d.l.	b.d.l.	b.d.l.	b.d.l.	b.d.l.	b.d.l.
⁵³ Cr	ppm	6.8	b.d.l.	b.d.l.	b.d.l.	b.d.l.	b.d.l.	b.d.l.	b.d.l.	b.d.l.	b.d.l.	b.d.l.	b.d.l.	b.d.l.	b.d.l.	b.d.l.	b.d.l.
⁵⁵ Mn	ppm	1	b.d.l.	b.d.l.	b.d.l.	b.d.l.	b.d.l.	b.d.l.	b.d.l.	b.d.l.	b.d.l.	b.d.l.	b.d.l.	b.d.l.	b.d.l.	b.d.l.	b.d.l.
⁵⁷ Fe	ppm	33	b.d.l.	b.d.l.	b.d.l.	b.d.l.	b.d.l.	b.d.l.	b.d.l.	b.d.l.	b.d.l.	b.d.l.	b.d.l.	b.d.l.	b.d.l.	b.d.l.	b.d.l.
⁵⁹ Co	ppm	0.25	b.d.l.	b.d.l.	b.d.l.	b.d.l.	b.d.l.	b.d.l.	b.d.l.	b.d.l.	b.d.l.	b.d.l.	b.d.l.	b.d.l.	b.d.l.	b.d.l.	b.d.l.
⁶⁰ Ni	ppm	1.6	b.d.l.	b.d.l.	b.d.l.	b.d.l.	b.d.l.	0.43	b.d.l.	b.d.l.	b.d.l.	b.d.l.	b.d.l.	b.d.l.	b.d.l.	b.d.l.	b.d.l.
⁶⁵ Cu	ppm	n.a.	51	48	51	55	48	40	41	39	33	32	35	35	33	30	29
⁶⁶ Zn	ppm	4	b.d.l.	b.d.l.	b.d.l.	b.d.l.	b.d.l.	b.d.l.	b.d.l.	b.d.l.	b.d.l.	b.d.l.	b.d.l.	b.d.l.	b.d.l.	b.d.l.	b.d.l.
⁷¹ Ga	ppm	0.85	b.d.l.	b.d.l.	b.d.l.	b.d.l.	b.d.l.	b.d.l.	b.d.l.	b.d.l.	b.d.l.	b.d.l.	b.d.l.	b.d.l.	b.d.l.	b.d.l.	b.d.l.
⁷³ Ge	ppm	2.5	n.a.	n.a.	n.a.	n.a.	n.a.	b.d.l.	b.d.l.	b.d.l.	b.d.l.	b.d.l.	b.d.l.	b.d.l.	b.d.l.	b.d.l.	b.d.l.
⁷⁵ As	ppm	n.a.	231	117	198	40	33	111	51	33	26	21	22	14	12	13	12
⁷⁷ Se	ppm	5.8	b.d.l.	b.d.l.	b.d.l.	b.d.l.	b.d.l.	b.d.l.	b.d.l.	b.d.l.	b.d.l.	b.d.l.	b.d.l.	b.d.l.	b.d.l.	b.d.l.	b.d.l.
⁹³ Nb	ppm	0.08	n.a.	n.a.	n.a.	n.a.	n.a.	b.d.l.	b.d.l.	b.d.l.	b.d.l.	b.d.l.	b.d.l.	b.d.l.	b.d.l.	b.d.l.	b.d.l.
⁹⁵ Mo	ppm	0.81	b.d.l.	b.d.l.	b.d.l.	b.d.l.	b.d.l.	0.23	b.d.l.	b.d.l.	b.d.l.	b.d.l.	b.d.l.	b.d.l.	b.d.l.	b.d.l.	b.d.l.
¹⁰⁷ Ag	ppm	0.3	b.d.l.	0.58	b.d.l.	0.61	b.d.l.	0.70	0.91	b.d.l.	0.12	b.d.l.	0.22	0.62	0.37	0.14	0.22
¹¹¹ Cd	ppm	0.9	b.d.l.	b.d.l.	b.d.l.	b.d.l.	b.d.l.	b.d.l.	b.d.l.	b.d.l.	b.d.l.	b.d.l.	b.d.l.	b.d.l.	b.d.l.	b.d.l.	b.d.l.
¹¹⁵ In	ppm	0.06	b.d.l.	b.d.l.	b.d.l.	b.d.l.	b.d.l.	0.01	b.d.l.	b.d.l.	b.d.l.	b.d.l.	b.d.l.	b.d.l.	b.d.l.	b.d.l.	b.d.l.
¹¹⁸ Sn	ppm	0.57	b.d.l.	b.d.l.	b.d.l.	b.d.l.	b.d.l.	0.66	b.d.l.	0.64	b.d.l.	b.d.l.	b.d.l.	b.d.l.	b.d.l.	b.d.l.	b.d.l.
¹²¹ Sb	ppm	n.a.	716,500	712,700	714,600	710,800	710,800	711,200	711,200	711,200	711,200	711,200	711,200	711,200	711,200	711,200	711,200
¹²⁵ Te	ppm	1.6	b.d.l.	b.d.l.	b.d.l.	b.d.l.	b.d.l.	b.d.l.	b.d.l.	b.d.l.	b.d.l.	b.d.l.	b.d.l.	b.d.l.	b.d.l.	b.d.l.	b.d.l.
¹³⁹ La	ppm	n.a.	86	82	82	82	81	24	26	24	26	24	24	25	24	24	24
¹⁴⁰ Ce	ppm	n.a.	0.32	0.32	0.26	0.31	0.26	0.17	0.19	0.14	0.17	0.13	0.09	0.13	0.19	0.19	0.14
¹⁴⁵ Nd	ppm	0.56	b.d.l.	b.d.l.	b.d.l.	b.d.l.	b.d.l.	b.d.l.	b.d.l.	b.d.l.	b.d.l.	b.d.l.	b.d.l.	b.d.l.	b.d.l.	b.d.l.	b.d.l.
¹⁴⁷ Sm	ppm	0.33	b.d.l.	b.d.l.	b.d.l.	b.d.l.	b.d.l.	b.d.l.	b.d.l.	b.d.l.	0.10	b.d.l.	b.d.l.	b.d.l.	b.d.l.	b.d.l.	b.d.l.
¹⁵⁷ Gd	ppm	0.33	b.d.l.	b.d.l.	b.d.l.	b.d.l.	b.d.l.	b.d.l.	b.d.l.	b.d.l.	b.d.l.	b.d.l.	b.d.l.	b.d.l.	b.d.l.	b.d.l.	b.d.l.
¹⁸² W	ppm	0.33	b.d.l.	b.d.l.	b.d.l.	b.d.l.	b.d.l.	b.d.l.	b.d.l.	b.d.l.	b.d.l.	b.d.l.	b.d.l.	b.d.l.	b.d.l.	b.d.l.	b.d.l.
¹⁸⁵ Re	ppm	0.06	n.a.	n.a.	n.a.	n.a.	n.a.	0.03	b.d.l.	b.d.l.	b.d.l.	b.d.l.	b.d.l.	b.d.l.	b.d.l.	b.d.l.	b.d.l.
¹⁹⁷ Au	ppm	0.24	b.d.l.	b.d.l.	b.d.l.	b.d.l.	b.d.l.	b.d.l.	b.d.l.	b.d.l.	b.d.l.	b.d.l.	b.d.l.	b.d.l.	b.d.l.	b.d.l.	b.d.l.
²⁰² Hg	ppm	0.27	b.d.l.	b.d.l.	b.d.l.	b.d.l.	b.d.l.	b.d.l.	b.d.l.	b.d.l.	b.d.l.	b.d.l.	b.d.l.	b.d.l.	b.d.l.	b.d.l.	b.d.l.
²⁰⁵ Tl	ppm	0.32	b.d.l.	b.d.l.	b.d.l.	0.35	b.d.l.	b.d.l.	0.54	b.d.l.	b.d.l.	b.d.l.	b.d.l.	b.d.l.	0.56	b.d.l.	b.d.l.
²⁰⁸ Pb	ppm	n.a.	151	151	148	165	152	117	114	113	111	108	105	104	102	98	98
²⁰⁹ Bi	ppm	0.24	b.d.l.	0.20	b.d.l.	0.33	0.26	0.19	0.20	0.16	0.18	0.17	0.19	0.21	0.17	0.21	0.15
²³² Th	ppm	0.06	0.02	b.d.l.	b.d.l.	b.d.l.	b.d.l.	b.d.l.	b.d.l.	b.d.l.	b.d.l.	b.d.l.	b.d.l.	b.d.l.	b.d.l.	b.d.l.	b.d.l.
²³⁸ U	ppm	0.04	n.a.	n.a.	n.a.	n.a.	n.a.	b.d.l.	b.d.l.	b.d.l.	b.d.l.	b.d.l.	b.d.l.	b.d.l.	b.d.l.	b.d.l.	b.d.l.

Table S2-6. The full list of the LA-ICP-MS data acquired from the analyzed pyrite from Laodikino. b.d.l. = below detection limit, n. = number of analyses, n.a. = not analyzed.

		Hydrothermal alteration	Sericitization									
		Host rock	Two-mica gneiss and schist									
		Sample	LAO 08b									
		n.	1	2	3	4	5	6	7	8	9	10
		Mineralization style	Py1; Polymetallic quartz vein									
		Average detection limit										
⁴⁹ Ti	ppm	n.a.	18	11	20	17	16	14	13	18	16	16
⁵¹ V	ppm	0.6	b.d.l.	b.d.l.	b.d.l.	b.d.l.	b.d.l.	b.d.l.	0.27	b.d.l.	b.d.l.	b.d.l.
⁵³ Cr	ppm	14	b.d.l.	b.d.l.	b.d.l.	b.d.l.	b.d.l.	b.d.l.	b.d.l.	b.d.l.	b.d.l.	b.d.l.
⁵⁵ Mn	ppm	n.a.	4.3	4.2	4.7	5	2.9	4.5	3.9	5.3	5.6	5
⁵⁷ Fe	ppm	n.a.	466,200	466,800	466,800	463,100	463,100	460,600	460,600	460,600	460,600	460,600
⁵⁹ Co	ppm	n.a.	35	63	117	3,081	4,030	0.83	2.1	4.4	3.7	0.53
⁶⁰ Ni	ppm	1.5	411	266	190	85	48	31	164	249	464	109
⁶⁵ Cu	ppm	3.6	b.d.l.	b.d.l.	b.d.l.	b.d.l.	b.d.l.	b.d.l.	b.d.l.	8.1	b.d.l.	1.7
⁶⁶ Zn	ppm	8.3	b.d.l.	b.d.l.	b.d.l.	b.d.l.	b.d.l.	b.d.l.	b.d.l.	b.d.l.	b.d.l.	b.d.l.
⁷⁵ As	ppm	n.a.	474	242	180	506	593	76	118	274	487	123
⁷⁷ Se	ppm	5.1	26	19	19	18	9.3	13	19	15	17	35
⁹⁵ Mo	ppm	1.2	b.d.l.	2.2	b.d.l.	b.d.l.	b.d.l.	b.d.l.	b.d.l.	b.d.l.	b.d.l.	b.d.l.
¹⁰⁷ Ag	ppm	0.35	b.d.l.	b.d.l.	b.d.l.	b.d.l.	b.d.l.	b.d.l.	b.d.l.	b.d.l.	b.d.l.	b.d.l.
¹¹⁵ In	ppm	0.05	b.d.l.	b.d.l.	b.d.l.	b.d.l.	b.d.l.	b.d.l.	b.d.l.	b.d.l.	b.d.l.	b.d.l.
¹¹⁸ Sn	ppm	0.7	b.d.l.	b.d.l.	b.d.l.	b.d.l.	b.d.l.	b.d.l.	b.d.l.	b.d.l.	b.d.l.	b.d.l.
¹²¹ Sb	ppm	0.61	b.d.l.	b.d.l.	b.d.l.	1.8	b.d.l.	1.7	b.d.l.	1	0.56	0.56
¹²⁵ Te	ppm	2.4	b.d.l.	b.d.l.	b.d.l.	b.d.l.	b.d.l.	b.d.l.	b.d.l.	b.d.l.	b.d.l.	b.d.l.
¹⁸² W	ppm	0.6	b.d.l.	b.d.l.	b.d.l.	b.d.l.	b.d.l.	b.d.l.	b.d.l.	b.d.l.	b.d.l.	b.d.l.
¹⁹⁷ Au	ppm	0.29	b.d.l.	b.d.l.	b.d.l.	b.d.l.	b.d.l.	b.d.l.	b.d.l.	b.d.l.	b.d.l.	b.d.l.
²⁰² Hg	ppm	0.46	b.d.l.	b.d.l.	b.d.l.	b.d.l.	b.d.l.	b.d.l.	b.d.l.	b.d.l.	b.d.l.	b.d.l.
²⁰⁵ Tl	ppm	0.37	b.d.l.	b.d.l.	b.d.l.	b.d.l.	b.d.l.	b.d.l.	b.d.l.	b.d.l.	b.d.l.	b.d.l.
²⁰⁸ Pb	ppm	0.42	b.d.l.	b.d.l.	0.21	0.57	b.d.l.	0.51	b.d.l.	0.26	b.d.l.	b.d.l.
²⁰⁹ Bi	ppm	0.28	b.d.l.	b.d.l.	b.d.l.	b.d.l.	b.d.l.	b.d.l.	b.d.l.	b.d.l.	b.d.l.	b.d.l.
²³² Th	ppm	0.11	b.d.l.	b.d.l.	b.d.l.	b.d.l.	b.d.l.	b.d.l.	b.d.l.	b.d.l.	b.d.l.	b.d.l.
²³⁸ U	ppm	0.11	b.d.l.	b.d.l.	b.d.l.	b.d.l.	b.d.l.	b.d.l.	b.d.l.	b.d.l.	b.d.l.	b.d.l.

Table S2-6. Continued.

		Hydrothermal alteration	Chloritization											
		Host rock	Biotite gneiss											
		Sample	LAO 08ii											
		n.	1	2	3	4	5	6	7	8	9	10	11	12
		Mineralization style	Py2; Pods											
		Average detection limit												
⁴⁹ Ti	ppm	n.a.	667	13	10	17	10	9.1	13	25	20	16	17	15
⁵¹ V	ppm	0.6	1.4	b.d.l.	b.d.l.	b.d.l.	b.d.l.	b.d.l.	b.d.l.	b.d.l.	b.d.l.	b.d.l.	b.d.l.	b.d.l.
⁵³ Cr	ppm	14	b.d.l.	b.d.l.	b.d.l.	b.d.l.	b.d.l.	b.d.l.	b.d.l.	b.d.l.	b.d.l.	b.d.l.	b.d.l.	b.d.l.
⁵⁵ Mn	ppm	n.a.	25	4.7	4.2	19	6.3	4.4	18	6.9	5.6	86	259	6.1
⁵⁷ Fe	ppm	n.a.	462,500	462,500	462,500	462,500	462,500	463,500	463,500	463,500	463,500	461,900	462,500	462,500
⁵⁹ Co	ppm	n.a.	90	348	7	5.2	47	15	941	57	57	8.2	311	732
⁶⁰ Ni	ppm	1.5	371	1,000	200	20	188	17	22	10	97	96	101	30
⁶⁵ Cu	ppm	3.6	4.1	13	7,943	833	b.d.l.	188	951	324	212	1.8	3.9	1,898
⁶⁶ Zn	ppm	8.3	b.d.l.	b.d.l.	b.d.l.	b.d.l.	b.d.l.	b.d.l.	4.5	b.d.l.	b.d.l.	b.d.l.	b.d.l.	b.d.l.
⁷⁵ As	ppm	n.a.	444	757	148	20,896	704	11	1,292	1,069	120	435	341	14,429
⁷⁷ Se	ppm	5.1	106	88	6.9	b.d.l.	126	b.d.l.	13	5.3	b.d.l.	29	48	17
⁹⁵ Mo	ppm	1.2	b.d.l.	b.d.l.	b.d.l.	b.d.l.	b.d.l.	b.d.l.	b.d.l.	b.d.l.	b.d.l.	b.d.l.	b.d.l.	b.d.l.
¹⁰⁷ Ag	ppm	0.35	b.d.l.	0.55	4.6	1.1	b.d.l.	0.52	0.79	1.7	0.79	b.d.l.	b.d.l.	13
¹¹⁵ In	ppm	0.05	b.d.l.	b.d.l.	b.d.l.	b.d.l.	b.d.l.	b.d.l.	b.d.l.	b.d.l.	b.d.l.	b.d.l.	b.d.l.	b.d.l.
¹¹⁸ Sn	ppm	0.7	1.02	b.d.l.	b.d.l.	b.d.l.	b.d.l.	b.d.l.	b.d.l.	b.d.l.	b.d.l.	b.d.l.	b.d.l.	b.d.l.
¹²¹ Sb	ppm	0.61	0.71	b.d.l.	19	4.6	b.d.l.	17	23	17	29	b.d.l.	0.59	10
¹²⁵ Te	ppm	2.4	b.d.l.	4	b.d.l.	b.d.l.	b.d.l.	b.d.l.	b.d.l.	b.d.l.	b.d.l.	b.d.l.	b.d.l.	b.d.l.
¹⁸² W	ppm	0.6	3.9	b.d.l.	b.d.l.	b.d.l.	b.d.l.	b.d.l.	b.d.l.	b.d.l.	b.d.l.	b.d.l.	b.d.l.	b.d.l.
¹⁹⁷ Au	ppm	0.29	b.d.l.	b.d.l.	0.55	10	b.d.l.	b.d.l.	0.52	b.d.l.	b.d.l.	b.d.l.	b.d.l.	7.4
²⁰² Hg	ppm	0.46	b.d.l.	b.d.l.	b.d.l.	b.d.l.	b.d.l.	b.d.l.	b.d.l.	b.d.l.	b.d.l.	b.d.l.	b.d.l.	b.d.l.
²⁰⁵ Tl	ppm	0.37	b.d.l.	b.d.l.	b.d.l.	b.d.l.	b.d.l.	b.d.l.	b.d.l.	b.d.l.	b.d.l.	b.d.l.	0.25	b.d.l.
²⁰⁸ Pb	ppm	0.42	4.8	9.4	176	55	1.3	1.6	5.6	4.8	0.67	2.5	8.5	190
²⁰⁹ Bi	ppm	0.28	3.5	2.8	81	19	0.89	b.d.l.	6.5	12	1.4	0.96	13	173
²³² Th	ppm	0.11	b.d.l.	b.d.l.	b.d.l.	0.38	b.d.l.	b.d.l.	b.d.l.	b.d.l.	b.d.l.	b.d.l.	b.d.l.	b.d.l.
²³⁸ U	ppm	0.11	b.d.l.	b.d.l.	b.d.l.	0.14	b.d.l.	b.d.l.	0.14	b.d.l.	b.d.l.	b.d.l.	b.d.l.	b.d.l.

Table S2-6. Continued.

		Hydrothermal alteration	Chloritization											
		Host rock	Biotite gneiss											
		Sample	LA0 08aii											
		n.	1	2	3	4	5	6	7	8	9	10	11	12
		Mineralization style	Py2; Pods											
		Average detection limit												
⁴⁹ Ti	ppm	n.a.	10	13	12	40	18	12	9.4	14	13	22	9.6	14
⁵¹ V	ppm	0.6	b.d.l.	2.84	b.d.l.	b.d.l.	b.d.l.	b.d.l.	b.d.l.	b.d.l.	b.d.l.	b.d.l.	b.d.l.	b.d.l.
⁵³ Cr	ppm	14	b.d.l.	b.d.l.	b.d.l.	b.d.l.	b.d.l.	b.d.l.	b.d.l.	b.d.l.	b.d.l.	b.d.l.	b.d.l.	b.d.l.
⁵⁵ Mn	ppm	n.a.	6.1	135	5.8	307	4.5	5.8	6.1	5.5	6.1	7.4	6.1	4.1
⁵⁷ Fe	ppm	n.a.	463,000	463,000	463,000	463,000	463,000	463,000	463,000	463,000	463,000	469,800	463,000	463,000
⁵⁹ Co	ppm	n.a.	59	299	20	129	111	722	66	38	2,493	128	384	282
⁶⁰ Ni	ppm	1.5	30	51	90	211	431	b.d.l.	7.4	8.6	4	11	46	291
⁶⁵ Cu	ppm	3.6	982	635	543	27	b.d.l.	7.1	4,604	2,318	7.1	1,874	2,188	794
⁶⁶ Zn	ppm	8.3	336	109	1,747	b.d.l.	b.d.l.	b.d.l.	297	84	b.d.l.	128	166	b.d.l.
⁷⁵ As	ppm	n.a.	2,529	3,890	1,409	564	833	25,092	3,784	15,814	41,077	16,331	4,596	504
⁷⁷ Se	ppm	5.1	24	31	26	55	125	30	22	25	40	30	25	73
⁹⁵ Mo	ppm	1.2	b.d.l.	b.d.l.	b.d.l.	4.4	b.d.l.	b.d.l.	b.d.l.	b.d.l.	b.d.l.	b.d.l.	b.d.l.	b.d.l.
¹⁰⁷ Ag	ppm	0.35	1.1	4.4	30	b.d.l.	b.d.l.	b.d.l.	6.6	3.5	b.d.l.	3.9	5.4	0.47
¹¹⁵ In	ppm	0.05	1.2	1.6	17	b.d.l.	b.d.l.	b.d.l.	7.4	3	b.d.l.	5.1	4.7	b.d.l.
¹¹⁸ Sn	ppm	0.7	b.d.l.	0.78	9.28	b.d.l.	b.d.l.	b.d.l.	b.d.l.	0.58	b.d.l.	b.d.l.	b.d.l.	b.d.l.
¹²¹ Sb	ppm	0.61	29	28	292	b.d.l.	b.d.l.	b.d.l.	15	7	b.d.l.	4.8	5.6	b.d.l.
¹²⁵ Te	ppm	2.4	b.d.l.	b.d.l.	b.d.l.	b.d.l.	b.d.l.	b.d.l.	b.d.l.	b.d.l.	b.d.l.	b.d.l.	4.6	b.d.l.
¹⁸² W	ppm	0.6	b.d.l.	b.d.l.	b.d.l.	b.d.l.	b.d.l.	b.d.l.	b.d.l.	b.d.l.	b.d.l.	b.d.l.	b.d.l.	b.d.l.
¹⁹⁷ Au	ppm	0.29	0.88	2.8	0.60	b.d.l.	b.d.l.	12	2.6	7.1	21	12	3.7	b.d.l.
²⁰² Hg	ppm	0.46	b.d.l.	b.d.l.	b.d.l.	b.d.l.	b.d.l.	b.d.l.	b.d.l.	b.d.l.	b.d.l.	b.d.l.	b.d.l.	b.d.l.
²⁰⁵ Tl	ppm	0.37	b.d.l.	b.d.l.	3.4	b.d.l.	b.d.l.	b.d.l.	b.d.l.	b.d.l.	b.d.l.	b.d.l.	b.d.l.	b.d.l.
²⁰⁸ Pb	ppm	0.42	15	164	95	38	b.d.l.	1.1	94	32	b.d.l.	30	84	0.72
²⁰⁹ Bi	ppm	0.28	13	77	11	6.2	0.37	0.48	93	43	1.3	47	109	1.1
²³² Th	ppm	0.11	b.d.l.	b.d.l.	b.d.l.	b.d.l.	b.d.l.	b.d.l.	b.d.l.	b.d.l.	b.d.l.	b.d.l.	b.d.l.	b.d.l.
²³⁸ U	ppm	0.11	b.d.l.	b.d.l.	b.d.l.	b.d.l.	b.d.l.	b.d.l.	b.d.l.	b.d.l.	b.d.l.	b.d.l.	b.d.l.	b.d.l.

Table S2-7. The full list of the LA-ICP-MS data acquired from the analyzed chalcopyrite from Laodikino. b.d.l. = below detection limit, n. = number of analyses, n.a. = not analyzed.

		Hydrothermal alteration	Sericitization										Chloritization				
		Host rock	Two-mica gneiss and schist										Biotite gneiss				
		Sample	LAO 08b										LAO 08aii				
		n.	1	2	3	4	5	6	7	8	9	10	1	2	3	4	5
		Mineralization style	Cpy1; Polymetallic quartz vein										Cpy2; Pods				
		Average detection limit															
⁴⁹ Ti	ppm	8.1	15	13	15	b.d.l.	b.d.l.	10	13	b.d.l.	11	18	24	11	12	22	b.d.l.
⁵¹ V	ppm	0.9	b.d.l.	b.d.l.	b.d.l.	b.d.l.	b.d.l.	b.d.l.	b.d.l.	b.d.l.	b.d.l.	b.d.l.	5.6	b.d.l.	b.d.l.	b.d.l.	b.d.l.
⁵³ Cr	ppm	21	b.d.l.	b.d.l.	b.d.l.	b.d.l.	b.d.l.	b.d.l.	b.d.l.	b.d.l.	b.d.l.	b.d.l.	b.d.l.	b.d.l.	b.d.l.	b.d.l.	b.d.l.
⁵⁵ Mn	ppm	2.7	b.d.l.	5.9	3.2	2.9	2.7	b.d.l.	2.3	3.6	2.9	5	1,310	100	3.4	2	3
⁵⁷ Fe	ppm	n.a.	300,400	309,200	306,500	306,500	306,500	306,500	306,500	306,500	306,500	306,500	300,600	300,600	300,600	300,600	300,600
⁵⁹ Co	ppm	0.54	b.d.l.	b.d.l.	b.d.l.	b.d.l.	b.d.l.	b.d.l.	b.d.l.	b.d.l.	b.d.l.	b.d.l.	0.89	b.d.l.	b.d.l.	b.d.l.	b.d.l.
⁶⁰ Ni	ppm	3.4	b.d.l.	b.d.l.	b.d.l.	b.d.l.	b.d.l.	b.d.l.	b.d.l.	b.d.l.	b.d.l.	5	8	b.d.l.	b.d.l.	b.d.l.	b.d.l.
⁶⁵ Cu	ppm	n.a.	350,636	371,730	345,018	387,695	348,697	395,275	367,835	348,756	362,024	339,060	315,311	368,739	360,970	320,596	309,749
⁶⁶ Zn	ppm	n.a.	77	256	232	244	251	166	284	202	232	152	95	56	58	55	41
⁷¹ Ga	ppm	1.6	b.d.l.	b.d.l.	b.d.l.	b.d.l.	b.d.l.	b.d.l.	b.d.l.	b.d.l.	b.d.l.	b.d.l.	1.8	b.d.l.	b.d.l.	b.d.l.	b.d.l.
⁷⁴ Ge	ppm	3.5	b.d.l.	b.d.l.	b.d.l.	b.d.l.	b.d.l.	b.d.l.	b.d.l.	b.d.l.	b.d.l.	b.d.l.	b.d.l.	b.d.l.	b.d.l.	3.9	b.d.l.
⁷⁵ As	ppm	4	13	168	6.8	9.2	11	b.d.l.	10	9.1	b.d.l.	33	b.d.l.	b.d.l.	b.d.l.	b.d.l.	b.d.l.
⁷⁷ Se	ppm	n.a.	40	39	27	43	19	41	39	33	41	45	90	109	97	93	92
⁹³ Nb	ppm	0.27	b.d.l.	b.d.l.	b.d.l.	b.d.l.	b.d.l.	b.d.l.	b.d.l.	b.d.l.	b.d.l.	b.d.l.	b.d.l.	b.d.l.	b.d.l.	b.d.l.	b.d.l.
⁹⁵ Mo	ppm	2	b.d.l.	b.d.l.	b.d.l.	b.d.l.	b.d.l.	b.d.l.	b.d.l.	b.d.l.	b.d.l.	b.d.l.	b.d.l.	b.d.l.	b.d.l.	b.d.l.	b.d.l.
¹⁰⁷ Ag	ppm	n.a.	19	243	20	23	93	19	18	9	12	30	40	49	43	48	51
¹³⁷ Cd	ppm	2.2	b.d.l.	b.d.l.	b.d.l.	3.7	5.3	b.d.l.	b.d.l.	5	4.9	b.d.l.	b.d.l.	b.d.l.	6.1	b.d.l.	5
¹¹⁵ In	ppm	n.a.	219	272	274	260	234	277	232	224	202	191	43	51	46	42	41
¹¹⁸ Sn	ppm	n.a.	56	52	62	51	55	57	55	55	56	53	36	39	47	47	48
¹²¹ Sb	ppm	1.2	93	469	70	59	224	76	136	8.8	68	164	b.d.l.	1.8	b.d.l.	b.d.l.	b.d.l.
¹²⁵ Te	ppm	4.1	b.d.l.	b.d.l.	b.d.l.	b.d.l.	b.d.l.	b.d.l.	b.d.l.	b.d.l.	b.d.l.	b.d.l.	b.d.l.	b.d.l.	b.d.l.	b.d.l.	b.d.l.
¹⁸² W	ppm	0.98	b.d.l.	b.d.l.	b.d.l.	b.d.l.	b.d.l.	b.d.l.	b.d.l.	b.d.l.	b.d.l.	b.d.l.	b.d.l.	b.d.l.	b.d.l.	b.d.l.	b.d.l.
¹⁸⁵ Re	ppm	0.27	b.d.l.	b.d.l.	b.d.l.	b.d.l.	b.d.l.	b.d.l.	b.d.l.	b.d.l.	b.d.l.	b.d.l.	b.d.l.	b.d.l.	b.d.l.	b.d.l.	b.d.l.
¹⁹⁷ Au	ppm	0.47	0.83	2.4	0.78	2.7	2.9	1.6	0.96	0.92	b.d.l.	b.d.l.	b.d.l.	b.d.l.	b.d.l.	b.d.l.	0.77
²⁰² Hg	ppm	0.81	1.2	3.3	1.4	4.8	1.9	1.2	1.2	0.69	0.88	0.43	b.d.l.	b.d.l.	b.d.l.	b.d.l.	b.d.l.
²⁰⁵ Tl	ppm	0.54	b.d.l.	b.d.l.	b.d.l.	b.d.l.	0.86	b.d.l.	1.9	b.d.l.	b.d.l.	0.65	b.d.l.	b.d.l.	b.d.l.	b.d.l.	b.d.l.
²⁰⁸ Pb	ppm	n.a.	212	492	17	9.7	157	68	136	7	48	80	35	1.8	1.4	0.83	4.1
²⁰⁹ Bi	ppm	0.42	3.9	2.2	1.2	b.d.l.	7.6	0.45	2.5	b.d.l.	1.3	3.2	3.6	2.4	1.4	0.40	0.71
²³² Th	ppm	0.19	b.d.l.	b.d.l.	b.d.l.	b.d.l.	b.d.l.	b.d.l.	b.d.l.	b.d.l.	b.d.l.	b.d.l.	b.d.l.	b.d.l.	b.d.l.	b.d.l.	b.d.l.
²³⁸ U	ppm	0.18	b.d.l.	b.d.l.	b.d.l.	b.d.l.	b.d.l.	b.d.l.	b.d.l.	b.d.l.	b.d.l.	b.d.l.	0.56	b.d.l.	b.d.l.	b.d.l.	b.d.l.

Table S2-8. The full list of the LA-ICP-MS data acquired from the analyzed sphalerite from Laodikino. b.d.l. = below detection limit, n. = number of analyses, n.a. = not analyzed.

		Hydrothermal alteration	Sericitization									
		Host rock	Two-mica gneiss and schist									
		Sample	LAO 08b									
		n.	1	2	3	4	5	6	7	8	9	10
		Mineralization style	Sph1; Polymetallic quartz vein									
		Average detection limit										
⁴⁹ Ti	ppm	5.1	3.4	b.d.l.	7.3	b.d.l.	b.d.l.	5.2	8.8	6.8	b.d.l.	4.8
⁵¹ V	ppm	0.52	b.d.l.	b.d.l.	b.d.l.	b.d.l.	b.d.l.	b.d.l.	b.d.l.	0.49	b.d.l.	b.d.l.
⁵³ Cr	ppm	12	b.d.l.	b.d.l.	b.d.l.	b.d.l.	b.d.l.	b.d.l.	b.d.l.	b.d.l.	b.d.l.	b.d.l.
⁵⁵ Mn	ppm	n.a.	217	289	254	281	235	246	281	393	254	262
⁵⁷ Fe	ppm	n.a.	10,848	12,435	11,269	11,792	12,367	18,932	15,856	16,370	12,494	12,241
⁵⁹ Co	ppm	0.31	0.88	0.46	b.d.l.	b.d.l.	b.d.l.	b.d.l.	b.d.l.	b.d.l.	b.d.l.	0.48
⁶⁰ Ni	ppm	1.7	b.d.l.	1.6	b.d.l.	b.d.l.	b.d.l.	b.d.l.	b.d.l.	b.d.l.	b.d.l.	b.d.l.
⁶⁵ Cu	ppm	n.a.	299	8,117	467	2,137	392	29,474	7,868	2,491	455	311
⁶⁶ Zn	ppm	n.a.	645,500	640,400	645,500	640,400	640,400	645,500	645,500	645,500	645,500	645,500
⁷¹ Ga	ppm	0.86	b.d.l.	b.d.l.	b.d.l.	b.d.l.	b.d.l.	b.d.l.	b.d.l.	b.d.l.	b.d.l.	b.d.l.
⁷⁴ Ge	ppm	1.9	b.d.l.	b.d.l.	b.d.l.	b.d.l.	b.d.l.	b.d.l.	b.d.l.	b.d.l.	b.d.l.	1.7
⁷⁵ As	ppm	1.9	b.d.l.	92	13	45	6	1,605	170	9.2	4.1	b.d.l.
⁷⁷ Se	ppm	n.a.	28	22	17	24	24	45	40	40	9.3	56
⁹³ Nb	ppm	0.16	b.d.l.	b.d.l.	b.d.l.	b.d.l.	b.d.l.	b.d.l.	b.d.l.	b.d.l.	b.d.l.	b.d.l.
⁹⁵ Mo	ppm	1.2	b.d.l.	b.d.l.	b.d.l.	b.d.l.	b.d.l.	b.d.l.	b.d.l.	b.d.l.	b.d.l.	b.d.l.
¹⁰⁷ Ag	ppm	n.a.	1.1	135	5.7	42	2.1	814	161	54	9.4	0.84
¹³⁷ Cd	ppm	n.a.	2,198	2,301	2,290	2,390	2,292	2,596	2,676	2,638	2,289	2,621
¹¹⁵ In	ppm	n.a.	361	308	289	302	302	630	594	610	341	429
¹¹⁸ Sn	ppm	0.64	b.d.l.	0.34	b.d.l.	b.d.l.	b.d.l.	b.d.l.	b.d.l.	b.d.l.	0.84	b.d.l.
¹²¹ Sb	ppm	1.7	b.d.l.	180	33	69	5.2	1,369	884	30	22	0.49
¹²⁵ Te	ppm	2.2	b.d.l.	b.d.l.	b.d.l.	b.d.l.	b.d.l.	b.d.l.	b.d.l.	b.d.l.	b.d.l.	b.d.l.
¹⁸² W	ppm	0.59	b.d.l.	b.d.l.	b.d.l.	b.d.l.	b.d.l.	b.d.l.	b.d.l.	b.d.l.	b.d.l.	b.d.l.
¹⁸⁵ Re	ppm	0.15	b.d.l.	b.d.l.	b.d.l.	b.d.l.	b.d.l.	b.d.l.	b.d.l.	b.d.l.	b.d.l.	b.d.l.
¹⁹⁷ Au	ppm	0.24	b.d.l.	b.d.l.	b.d.l.	b.d.l.	b.d.l.	b.d.l.	b.d.l.	b.d.l.	b.d.l.	b.d.l.
²⁰² Hg	ppm	n.a.	99	152	148	130	151	150	182	163	165	182
²⁰⁵ Tl	ppm	0.33	b.d.l.	b.d.l.	b.d.l.	b.d.l.	b.d.l.	b.d.l.	b.d.l.	b.d.l.	b.d.l.	b.d.l.
²⁰⁸ Pb	ppm	0.71	b.d.l.	2.2	6.8	4.5	3	6,678	1,625	b.d.l.	6	b.d.l.
²⁰⁹ Bi	ppm	0.24	b.d.l.	b.d.l.	b.d.l.	0.35	b.d.l.	b.d.l.	3.3	b.d.l.	b.d.l.	b.d.l.
²³² Th	ppm	0.11	b.d.l.	b.d.l.	b.d.l.	b.d.l.	b.d.l.	b.d.l.	b.d.l.	b.d.l.	b.d.l.	b.d.l.
²³⁸ U	ppm	0.1	b.d.l.	b.d.l.	b.d.l.	b.d.l.	b.d.l.	0.41	0.42	b.d.l.	b.d.l.	b.d.l.

Table S2-9. The full list of the LA-ICP-MS data acquired from the analyzed tetrahedrite from Laodikino. b.d.l. = below detection limit, n. = number of analyses, n.a. = not analyzed.

		Hydrothermal alteration	Sericitization									
		Host rock	Two-mica gneiss and schist									
		Sample	LAO 08b									
		n.	1	2	3	4	5	6	7	8	9	10
		Mineralization style	Ttr1; Polymetallic quartz vein									
		Average detection limit										
⁴⁹ Ti	ppm	4.6	12	5.7	13	6.7	5.9	5.1	9.1	6.2	b.d.l.	6.6
⁵¹ V	ppm	0.46	b.d.l.	0.27	b.d.l.	b.d.l.	b.d.l.	b.d.l.	b.d.l.	0.38	b.d.l.	b.d.l.
⁵³ Cr	ppm	12	b.d.l.	b.d.l.	b.d.l.	b.d.l.	b.d.l.	b.d.l.	b.d.l.	b.d.l.	b.d.l.	b.d.l.
⁵⁵ Mn	ppm	n.a.	26	21	73	43	45	41	32	604	886	634
⁵⁷ Fe	ppm	n.a.	26,881	23,335	24,349	22,684	23,945	24,290	24,245	26,907	25,532	28,664
⁵⁹ Co	ppm	0.26	0.44	0.29	b.d.l.	0.79	b.d.l.	b.d.l.	b.d.l.	1.7	4.9	1.2
⁶⁰ Ni	ppm	1.6	2.6	b.d.l.	b.d.l.	b.d.l.	b.d.l.	b.d.l.	b.d.l.	4.2	3.8	3.4
⁶⁵ Cu	ppm	n.a.	347,300	347,300	347,300	347,300	343,200	343,200	346,300	343,200	343,200	344,200
⁶⁶ Zn	ppm	n.a.	59,039	58,404	61,419	56,625	51,775	52,705	49,924	58,230	63,501	60,018
⁷¹ Ga	ppm	0.93	b.d.l.	b.d.l.	b.d.l.	b.d.l.	b.d.l.	b.d.l.	b.d.l.	b.d.l.	0.73	0.59
⁷⁴ Ge	ppm	2.2	2.6	2.4	b.d.l.	2	b.d.l.	2	b.d.l.	b.d.l.	b.d.l.	3.3
⁷⁵ As	ppm	n.a.	30,778	35,141	37,099	31,635	33,270	28,968	32,662	36,748	39,403	41,510
⁷⁷ Se	ppm	n.a.	100	97	109	103	84	95	99	105	95	88
⁹³ Nb	ppm	0.16	b.d.l.	b.d.l.	b.d.l.	b.d.l.	b.d.l.	b.d.l.	b.d.l.	b.d.l.	b.d.l.	b.d.l.
⁹⁵ Mo	ppm	1	b.d.l.	b.d.l.	b.d.l.	b.d.l.	b.d.l.	b.d.l.	b.d.l.	b.d.l.	b.d.l.	b.d.l.
¹⁰⁷ Ag	ppm	n.a.	5,649	6,313	7,185	6,316	5,771	5,771	5,862	6,519	6,778	6,221
¹⁵⁷ Cd	ppm	n.a.	509	487	546	444	447	443	463	519	669	591
¹¹⁵ In	ppm	n.a.	15	16	17	15	14	15	15	16	18	17
¹¹⁸ Sn	ppm	0.58	b.d.l.	b.d.l.	0.78	b.d.l.	b.d.l.	b.d.l.	b.d.l.	b.d.l.	b.d.l.	0.69
¹²¹ Sb	ppm	n.a.	259,108	252,418	269,870	255,928	234,400	238,676	239,801	260,567	267,774	277,613
¹²⁵ Te	ppm	2.2	b.d.l.	b.d.l.	b.d.l.	b.d.l.	b.d.l.	b.d.l.	b.d.l.	b.d.l.	b.d.l.	b.d.l.
¹³⁹ La	ppm	n.a.	6.9	8.5	8.8	8.4	7.0	7.5	7.5	9.1	9.4	11
¹⁴⁰ Ce	ppm	0.06	b.d.l.	b.d.l.	b.d.l.	b.d.l.	0.05	b.d.l.	b.d.l.	2.4	4.6	4.4
¹⁴⁵ Nd	ppm	0.65	b.d.l.	b.d.l.	b.d.l.	b.d.l.	b.d.l.	b.d.l.	b.d.l.	1.6	2.2	2.5
¹⁴⁷ Sm	ppm	0.62	b.d.l.	b.d.l.	1.1	1.1	1	0.72	1.7	1.6	2	2.2
¹⁵⁷ Gd	ppm	0.38	b.d.l.	b.d.l.	b.d.l.	b.d.l.	b.d.l.	b.d.l.	b.d.l.	0.72	0.82	1.2
¹⁸² W	ppm	0.56	b.d.l.	b.d.l.	b.d.l.	b.d.l.	b.d.l.	b.d.l.	b.d.l.	b.d.l.	b.d.l.	b.d.l.
¹⁸⁵ Re	ppm	0.15	b.d.l.	b.d.l.	b.d.l.	b.d.l.	b.d.l.	b.d.l.	b.d.l.	b.d.l.	b.d.l.	b.d.l.
¹⁹⁷ Au	ppm	0.2	b.d.l.	b.d.l.	b.d.l.	b.d.l.	b.d.l.	b.d.l.	b.d.l.	0.83	0.55	b.d.l.
²⁰² Hg	ppm	n.a.	54	72	65	57	72	73	73	75	98	81
²⁰⁵ Tl	ppm	0.39	b.d.l.	b.d.l.	b.d.l.	b.d.l.	b.d.l.	0.25	0.52	b.d.l.	0.36	0.29
²⁰⁸ Pb	ppm	n.a.	1.3	4.3	3.4	15	3.1	7.5	5.8	39	121	67
²⁰⁹ Bi	ppm	n.a.	229	223	248	222	267	262	274	312	320	319
²³² Th	ppm	0.1	b.d.l.	b.d.l.	b.d.l.	b.d.l.	b.d.l.	b.d.l.	b.d.l.	b.d.l.	b.d.l.	b.d.l.
²³⁸ U	ppm	0.1	b.d.l.	b.d.l.	b.d.l.	b.d.l.	b.d.l.	b.d.l.	b.d.l.	0.91	1.4	1.4

Table S2-10. The full list of the LA-ICP-MS data acquired from the analyzed magnetite from Laodikino. b.d.l. = below detection limit, n. = number of analyses, n.a. = not analyzed.

		Hydrothermal alteration	Chloritization									
		Host rock	Biotite gneiss									
		Sample	LAO 08ii									
		n.	1	2	3	4	5	6	7	8	9	10
		Mineralization style	Mag1; Pods									
		Average detection limit										
²⁷ Al	ppm	n.a.	300	339	169	180	123	343	242	1,176	219	235
³¹ P	ppm	48	b.d.l.	b.d.l.	b.d.l.	b.d.l.	b.d.l.	b.d.l.	b.d.l.	b.d.l.	45.81	b.d.l.
⁴⁹ Ti	ppm	n.a.	186	303	182	135	138	142	222	143	179	201
⁵¹ V	ppm	n.a.	524	491	586	442	426	424	433	490	570	580
⁵³ Cr	ppm	52	b.d.l.	b.d.l.	b.d.l.	b.d.l.	b.d.l.	b.d.l.	b.d.l.	208	46	b.d.l.
⁵⁵ Mn	ppm	n.a.	623	718	604	582	546	924	977	935	727	770
⁵⁷ Fe	ppm	n.a.	723,500	723,500	723,500	723,500	723,500	723,500	723,500	723,500	723,500	723,500
⁵⁹ Co	ppm	2	2.7	2.1	2.5	b.d.l.	3.1	2.1	b.d.l.	b.d.l.	1.8	1.7
⁶⁰ Ni	ppm	n.a.	62	92	92	40	56	72	80	60	31	41
⁶³ Cu	ppm	13	b.d.l.	54.17	b.d.l.	b.d.l.	b.d.l.	b.d.l.	b.d.l.	51.95	b.d.l.	b.d.l.
⁶⁶ Zn	ppm	n.a.	25	36	38	37	37	59	45	30	48	50
⁷¹ Ga	ppm	n.a.	10	14	13	8.5	7.4	9.3	11	11	10	6.5
⁷⁴ Ge	ppm	6.8	b.d.l.	b.d.l.	b.d.l.	b.d.l.	b.d.l.	b.d.l.	b.d.l.	b.d.l.	b.d.l.	5.2
⁷⁵ As	ppm	7.3	b.d.l.	b.d.l.	b.d.l.	b.d.l.	b.d.l.	b.d.l.	b.d.l.	b.d.l.	b.d.l.	b.d.l.
⁷⁶ Se	ppm	4	b.d.l.	b.d.l.	b.d.l.	b.d.l.	b.d.l.	b.d.l.	b.d.l.	b.d.l.	b.d.l.	b.d.l.
⁹³ Nb	ppm	0.41	b.d.l.	b.d.l.	b.d.l.	b.d.l.	b.d.l.	b.d.l.	b.d.l.	b.d.l.	b.d.l.	b.d.l.
⁹⁵ Mo	ppm	3.1	b.d.l.	b.d.l.	b.d.l.	2.9	b.d.l.	b.d.l.	b.d.l.	b.d.l.	b.d.l.	b.d.l.
¹⁰⁷ Ag	ppm	1.5	b.d.l.	b.d.l.	b.d.l.	b.d.l.	b.d.l.	b.d.l.	b.d.l.	b.d.l.	b.d.l.	b.d.l.
¹³⁷ Cd	ppm	9.4	b.d.l.	b.d.l.	b.d.l.	b.d.l.	b.d.l.	b.d.l.	b.d.l.	b.d.l.	b.d.l.	b.d.l.
¹¹⁵ In	ppm	0.13	b.d.l.	b.d.l.	b.d.l.	b.d.l.	b.d.l.	b.d.l.	b.d.l.	b.d.l.	b.d.l.	b.d.l.
¹¹⁸ Sn	ppm	2.2	b.d.l.	b.d.l.	b.d.l.	b.d.l.	b.d.l.	b.d.l.	b.d.l.	b.d.l.	b.d.l.	b.d.l.
¹²¹ Sb	ppm	4.1	b.d.l.	b.d.l.	b.d.l.	b.d.l.	b.d.l.	b.d.l.	b.d.l.	b.d.l.	b.d.l.	b.d.l.
¹²⁵ Te	ppm	12	b.d.l.	b.d.l.	b.d.l.	b.d.l.	b.d.l.	b.d.l.	b.d.l.	b.d.l.	b.d.l.	b.d.l.
¹³⁹ La	ppm	0.24	b.d.l.	b.d.l.	b.d.l.	b.d.l.	b.d.l.	0.12	b.d.l.	b.d.l.	b.d.l.	b.d.l.
¹⁴⁰ Ce	ppm	0.18	b.d.l.	b.d.l.	b.d.l.	b.d.l.	b.d.l.	0.15	b.d.l.	0.52	b.d.l.	b.d.l.
¹⁴³ Nd	ppm	2.8	b.d.l.	b.d.l.	b.d.l.	b.d.l.	b.d.l.	b.d.l.	b.d.l.	b.d.l.	b.d.l.	b.d.l.
¹⁴⁷ Sm	ppm	1.2	b.d.l.	b.d.l.	b.d.l.	b.d.l.	b.d.l.	b.d.l.	b.d.l.	b.d.l.	b.d.l.	b.d.l.
¹⁵⁷ Gd	ppm	1.5	b.d.l.	b.d.l.	b.d.l.	b.d.l.	b.d.l.	b.d.l.	b.d.l.	b.d.l.	b.d.l.	b.d.l.
¹⁸² W	ppm	1.7	b.d.l.	b.d.l.	b.d.l.	b.d.l.	b.d.l.	b.d.l.	b.d.l.	b.d.l.	b.d.l.	b.d.l.
¹⁸⁵ Re	ppm	0.46	b.d.l.	b.d.l.	b.d.l.	b.d.l.	b.d.l.	b.d.l.	b.d.l.	b.d.l.	b.d.l.	b.d.l.
¹⁹⁷ Au	ppm	0.43	b.d.l.	b.d.l.	b.d.l.	b.d.l.	b.d.l.	b.d.l.	b.d.l.	b.d.l.	b.d.l.	b.d.l.
²⁰² Hg	ppm	2.2	b.d.l.	b.d.l.	b.d.l.	b.d.l.	b.d.l.	b.d.l.	b.d.l.	b.d.l.	0.63	b.d.l.
²⁰⁵ Tl	ppm	0.82	b.d.l.	0.96	b.d.l.	2	b.d.l.	b.d.l.	b.d.l.	5.1	b.d.l.	b.d.l.
²⁰⁸ Pb	ppm	1.2	b.d.l.	b.d.l.	b.d.l.	b.d.l.	b.d.l.	b.d.l.	b.d.l.	b.d.l.	b.d.l.	b.d.l.
²⁰⁹ Bi	ppm	0.25	b.d.l.	b.d.l.	b.d.l.	b.d.l.	b.d.l.	0.19	b.d.l.	b.d.l.	b.d.l.	b.d.l.
²³² Th	ppm	0.37	b.d.l.	b.d.l.	b.d.l.	b.d.l.	b.d.l.	b.d.l.	b.d.l.	b.d.l.	b.d.l.	b.d.l.
²³⁸ U	ppm	n.a.	300	339	169	180	123	343	242	1,176	219	235

Table S2-11. The full list of the LA-ICP-MS data acquired from the analyzed pyrite from Kolchiko. b.d.l. = below detection limit, n. = number of analyses, n.a. = not analyzed.

		Hydrothermal alteration	Sericitization																
		Host rock	Mica schist																
		Sample	KL 07i										KL 13ii						
		n.	1	2	3	4	5	6	7	8	9	10	1	2	3	4	5	6	7
		Mineralization style	Py1; Polymetallic quartz veins																
		Average detection limit																	
⁴⁹ Ti	ppm	n.a.	12	13	17	16	7.7	11	18	10	5.9	9.5	32	37	21	27	22	18	18
⁵¹ V	ppm	0.52	b.d.l.	b.d.l.	b.d.l.	b.d.l.	0.24	b.d.l.	b.d.l.	b.d.l.	b.d.l.	b.d.l.	b.d.l.	b.d.l.	b.d.l.	b.d.l.	b.d.l.	b.d.l.	b.d.l.
⁵³ Cr	ppm	13	b.d.l.	b.d.l.	b.d.l.	11	b.d.l.	b.d.l.	b.d.l.	b.d.l.	b.d.l.	b.d.l.	45	40	34	44	39	33	37
⁵⁵ Mn	ppm	n.a.	4.8	4.9	5.6	5.5	4.9	4.4	5	4.9	4.4	20	60	52	48	55	47	47	49
⁵⁷ Fe	ppm	n.a.	460,500	460,500	460,500	461,800	460,500	460,500	460,500	460,500	465,500	465,500	462,400	462,400	462,400	462,400	454,700	460,300	460,300
⁵⁹ Co	ppm	0.46	776	396	359	439	205	396	2,155	517	216	333	57	476	376	314	528	428	298
⁶⁰ Ni	ppm	2.6	612	275	249	310	143	216	1,713	318	147	228	9.4	140	98	76	122	88	172
⁶⁵ Cu	ppm	5	7	108	b.d.l.	6.5	124	b.d.l.	9.6	4.4	3.8	95	4.6	6.9	11	b.d.l.	4.6	27	82
⁶⁶ Zn	ppm	7.4	b.d.l.	b.d.l.	b.d.l.	b.d.l.	b.d.l.	b.d.l.	b.d.l.	b.d.l.	b.d.l.	b.d.l.	b.d.l.	b.d.l.	4.3	b.d.l.	b.d.l.	b.d.l.	b.d.l.
⁷⁵ As	ppm	1.1	b.d.l.	b.d.l.	b.d.l.	b.d.l.	b.d.l.	b.d.l.	b.d.l.	b.d.l.	b.d.l.	b.d.l.	b.d.l.	b.d.l.	b.d.l.	b.d.l.	b.d.l.	b.d.l.	b.d.l.
⁷⁷ Se	ppm	0.38	1	1.8	b.d.l.	0.38	b.d.l.	b.d.l.	0.80	b.d.l.	b.d.l.	0.36	0.87	1.9	0.90	1.2	13	5.6	8.7
⁹⁵ Mo	ppm	0.05	b.d.l.	b.d.l.	b.d.l.	b.d.l.	b.d.l.	b.d.l.	b.d.l.	b.d.l.	b.d.l.	b.d.l.	b.d.l.	b.d.l.	b.d.l.	b.d.l.	b.d.l.	b.d.l.	b.d.l.
¹⁰⁷ Ag	ppm	0.66	b.d.l.	b.d.l.	b.d.l.	b.d.l.	b.d.l.	0.43	0.42	b.d.l.	b.d.l.	b.d.l.	b.d.l.	b.d.l.	b.d.l.	b.d.l.	b.d.l.	b.d.l.	b.d.l.
¹¹⁵ In	ppm	0.49	0.79	1.3	0.55	b.d.l.	2.9	5	8.1	1.7	0.46	b.d.l.	22	6	3.6	26	1	b.d.l.	0.75
¹¹⁸ Sn	ppm	2.5	b.d.l.	b.d.l.	b.d.l.	b.d.l.	b.d.l.	b.d.l.	b.d.l.	b.d.l.	b.d.l.	b.d.l.	b.d.l.	b.d.l.	b.d.l.	b.d.l.	b.d.l.	b.d.l.	b.d.l.
¹²¹ Sb	ppm	0.68	b.d.l.	b.d.l.	b.d.l.	b.d.l.	b.d.l.	b.d.l.	b.d.l.	b.d.l.	b.d.l.	1.7	5.4	7.6	3	1.4	10	b.d.l.	b.d.l.
¹²⁵ Te	ppm	0.24	b.d.l.	b.d.l.	b.d.l.	b.d.l.	b.d.l.	b.d.l.	b.d.l.	b.d.l.	b.d.l.	b.d.l.	b.d.l.	b.d.l.	b.d.l.	b.d.l.	b.d.l.	b.d.l.	b.d.l.
¹⁸² W	ppm	0.60	b.d.l.	b.d.l.	b.d.l.	0.81	b.d.l.	b.d.l.	b.d.l.	b.d.l.	b.d.l.	b.d.l.	b.d.l.	0.42	0.44	0.67	0.67	b.d.l.	0.53
¹⁹⁷ Au	ppm	0.30	b.d.l.	0.82	b.d.l.	b.d.l.	0.32	b.d.l.	b.d.l.	b.d.l.	b.d.l.	b.d.l.	b.d.l.	b.d.l.	b.d.l.	b.d.l.	b.d.l.	b.d.l.	b.d.l.
²⁰² Hg	ppm	0.20	84	16	52	18	28	120	94	65	9.7	7.2	18	33	1.4	46	94	456	10
²⁰⁵ Tl	ppm	0.29	0.39	0.23	b.d.l.	4	8.1	0.32	1.1	0.84	0.27	3.4	b.d.l.	2.1	0.86	1.6	5.1	13	0.44
²⁰⁸ Pb	ppm	0.11	b.d.l.	b.d.l.	b.d.l.	b.d.l.	b.d.l.	b.d.l.	b.d.l.	b.d.l.	b.d.l.	b.d.l.	b.d.l.	b.d.l.	b.d.l.	b.d.l.	b.d.l.	b.d.l.	b.d.l.
²⁰⁹ Bi	ppm	0.11	b.d.l.	b.d.l.	b.d.l.	b.d.l.	b.d.l.	b.d.l.	b.d.l.	b.d.l.	b.d.l.	b.d.l.	b.d.l.	b.d.l.	b.d.l.	b.d.l.	b.d.l.	b.d.l.	b.d.l.
²³² Th	ppm	n.a.	12	13	17	16	7.7	11	18	10	5.9	9.5	32	37	21	27	22	18	18
²³⁸ U	ppm	0.52	b.d.l.	b.d.l.	b.d.l.	b.d.l.	0.24	b.d.l.	b.d.l.	b.d.l.	b.d.l.	b.d.l.	b.d.l.	b.d.l.	b.d.l.	b.d.l.	b.d.l.	b.d.l.	b.d.l.

Table S2-11. Continued.

		Hydrothermal alteration	Sericitization										
		Host rock	Mica schist										
		Sample	KL13iii								KOLX 01a		
		n.	1	2	3	4	5	6	7	8	1	2	3
		Mineralization style	Py1; Polymetallic quartz veins								Py2; Massive veins		
		Average detection limit											
⁴⁹ Ti	ppm	n.a.	8.4	8.6	18	52	15	11	5.9	12	21	9.6	18
⁵¹ V	ppm	0.52	b.d.l.	b.d.l.	b.d.l.	b.d.l.	b.d.l.	b.d.l.	b.d.l.	b.d.l.	b.d.l.	b.d.l.	b.d.l.
⁵³ Cr	ppm	13	11	b.d.l.	b.d.l.	b.d.l.	b.d.l.	b.d.l.	b.d.l.	b.d.l.	b.d.l.	b.d.l.	b.d.l.
⁵⁵ Mn	ppm	n.a.	5.1	5.5	5.4	64	4.8	4.9	4.9	6.2	7	4.3	5.4
⁵⁷ Fe	ppm	n.a.	465,000	465,000	465,000	465,000	463,200	463,200	463,200	463,200	458,800	458,800	458,800
⁵⁹ Co	ppm	0.46	428	532	258	467	373	312	623	381	b.d.l.	b.d.l.	b.d.l.
⁶⁰ Ni	ppm	2.6	113	68	72	92	92	84	182	62	b.d.l.	b.d.l.	b.d.l.
⁶⁵ Cu	ppm	5	b.d.l.	b.d.l.	b.d.l.	3.3	9.5	39	37	8.3	b.d.l.	17	33
⁶⁶ Zn	ppm	7.4	b.d.l.	b.d.l.	b.d.l.	5.9	b.d.l.	b.d.l.	b.d.l.	b.d.l.	b.d.l.	b.d.l.	b.d.l.
⁷⁵ As	ppm	1.1	b.d.l.	b.d.l.	b.d.l.	b.d.l.	b.d.l.	b.d.l.	b.d.l.	b.d.l.	b.d.l.	b.d.l.	b.d.l.
⁷⁷ Se	ppm	0.38	5.1	15	2.1	2.8	4.6	3	2	4.9	2	b.d.l.	3.1
⁹⁵ Mo	ppm	0.05	b.d.l.	b.d.l.	b.d.l.	b.d.l.	b.d.l.	b.d.l.	b.d.l.	b.d.l.	b.d.l.	b.d.l.	b.d.l.
¹⁰⁷ Ag	ppm	0.66	b.d.l.	b.d.l.	b.d.l.	b.d.l.	b.d.l.	b.d.l.	b.d.l.	b.d.l.	b.d.l.	b.d.l.	b.d.l.
¹¹⁵ In	ppm	0.49	1.4	1.3	2	0.55	0.55	0.71	0.78	0.47	55	38	73
¹¹⁸ Sn	ppm	2.5	b.d.l.	b.d.l.	b.d.l.	b.d.l.	b.d.l.	b.d.l.	b.d.l.	b.d.l.	b.d.l.	b.d.l.	b.d.l.
¹²¹ Sb	ppm	0.68	3.3	10	7.8	7.9	b.d.l.	0.56	b.d.l.	1.6	b.d.l.	b.d.l.	b.d.l.
¹²⁵ Te	ppm	0.24	0.20	b.d.l.	b.d.l.	b.d.l.	b.d.l.	b.d.l.	b.d.l.	b.d.l.	b.d.l.	b.d.l.	0.59
¹⁸² W	ppm	0.60	b.d.l.	0.47	0.54	b.d.l.	0.34	b.d.l.	b.d.l.	b.d.l.	b.d.l.	b.d.l.	b.d.l.
¹⁹⁷ Au	ppm	0.30	0.62	b.d.l.	b.d.l.	0.71	b.d.l.	0.25	b.d.l.	b.d.l.	3.2	0.91	2.8
²⁰² Hg	ppm	0.20	41	73	88	42	22	27	100	6.6	16	4.9	44
²⁰⁵ Tl	ppm	0.29	7	0.49	0.74	2.1	14	14	b.d.l.	1	15	5.1	196
²⁰⁸ Pb	ppm	0.11	b.d.l.	b.d.l.	b.d.l.	b.d.l.	b.d.l.	b.d.l.	b.d.l.	b.d.l.	b.d.l.	b.d.l.	b.d.l.
²⁰⁹ Bi	ppm	0.11	b.d.l.	b.d.l.	b.d.l.	b.d.l.	b.d.l.	b.d.l.	b.d.l.	b.d.l.	b.d.l.	b.d.l.	b.d.l.
²³² Th	ppm	n.a.	8.4	8.6	18	52	15	11	5.9	12	21	9.6	18
²³⁸ U	ppm	0.52	b.d.l.	b.d.l.	b.d.l.	b.d.l.	b.d.l.	b.d.l.	b.d.l.	b.d.l.	b.d.l.	b.d.l.	b.d.l.

Table S2-11. Continued.

		Hydrothermal alteration	Sericitization									
		Host rock	Mica schist									
		Sample	KOLX 02a									
		n.	1	2	3	4	5	6	7	8	9	10
		Mineralization style	Py3; Massive veins									
		Average detection limit										
⁴⁹ Ti	ppm	n.a.	17	14	25	14	19	16	16	12	11	12
⁵¹ V	ppm	0.52	b.d.l.	b.d.l.	b.d.l.	b.d.l.	b.d.l.	b.d.l.	b.d.l.	b.d.l.	b.d.l.	b.d.l.
⁵² Cr	ppm	13	b.d.l.	b.d.l.	b.d.l.	b.d.l.	b.d.l.	b.d.l.	b.d.l.	b.d.l.	b.d.l.	b.d.l.
⁵⁵ Mn	ppm	n.a.	4.7	6.2	5.1	4.3	4.5	6.5	4.8	3.8	5.4	3.3
⁵⁷ Fe	ppm	n.a.	463,600	463,600	463,600	463,600	463,600	463,600	463,600	463,600	463,600	463,600
⁵⁹ Co	ppm	0.46	12	7.2	23	22	0.26	4	32	17	31	27
⁶⁰ Ni	ppm	2.6	16	7.7	24	13	3.2	6.6	5.9	15	25	33
⁶⁵ Cu	ppm	5	b.d.l.	536	18	791	1,847	36	32	781	b.d.l.	b.d.l.
⁶⁶ Zn	ppm	7.4	b.d.l.	20	b.d.l.	65	173	b.d.l.	b.d.l.	37	b.d.l.	b.d.l.
⁷⁵ As	ppm	1.1	b.d.l.	b.d.l.	b.d.l.	b.d.l.	b.d.l.	b.d.l.	b.d.l.	b.d.l.	b.d.l.	b.d.l.
⁷⁷ Se	ppm	0.38	b.d.l.	11	2.4	10	15	6.8	21	4.5	b.d.l.	b.d.l.
⁹⁵ Mo	ppm	0.05	b.d.l.	1.4	b.d.l.	2.2	12	b.d.l.	b.d.l.	1.8	0.06	b.d.l.
¹⁰⁷ Ag	ppm	0.66	b.d.l.	2	b.d.l.	2.7	11	b.d.l.	b.d.l.	1.5	b.d.l.	b.d.l.
¹¹⁵ In	ppm	0.49	b.d.l.	12	1	1.3	15	0.76	0.36	2.1	b.d.l.	0.37
¹¹⁸ Sn	ppm	2.5	b.d.l.	b.d.l.	b.d.l.	b.d.l.	b.d.l.	b.d.l.	b.d.l.	b.d.l.	b.d.l.	b.d.l.
¹²¹ Sb	ppm	0.68	b.d.l.	b.d.l.	b.d.l.	b.d.l.	b.d.l.	b.d.l.	b.d.l.	b.d.l.	b.d.l.	b.d.l.
¹²⁵ Te	ppm	0.24	b.d.l.	b.d.l.	0.27	b.d.l.	0.29	0.22	b.d.l.	b.d.l.	b.d.l.	b.d.l.
¹⁸² W	ppm	0.60	b.d.l.	b.d.l.	b.d.l.	b.d.l.	b.d.l.	b.d.l.	b.d.l.	b.d.l.	b.d.l.	b.d.l.
¹⁹⁷ Au	ppm	0.30	b.d.l.	b.d.l.	b.d.l.	b.d.l.	b.d.l.	b.d.l.	b.d.l.	b.d.l.	b.d.l.	b.d.l.
²⁰² Hg	ppm	0.20	b.d.l.	761	41	223	1,134	189	158	191	0.25	b.d.l.
²⁰⁵ Tl	ppm	0.29	b.d.l.	366	95	171	333	134	250	102	0.39	b.d.l.
²⁰⁸ Pb	ppm	0.11	b.d.l.	b.d.l.	b.d.l.	b.d.l.	b.d.l.	b.d.l.	b.d.l.	b.d.l.	b.d.l.	b.d.l.
²⁰⁹ Bi	ppm	0.11	b.d.l.	b.d.l.	b.d.l.	b.d.l.	b.d.l.	b.d.l.	b.d.l.	b.d.l.	b.d.l.	b.d.l.
²³² Th	ppm	n.a.	17	14	25	14	19	16	16	12	11	12
²³⁸ U	ppm	0.52	b.d.l.	b.d.l.	b.d.l.	b.d.l.	b.d.l.	b.d.l.	b.d.l.	b.d.l.	b.d.l.	b.d.l.

Table S2-11. Continued.

		Hydrothermal alteration	Sericitization											
		Host rock	Mica schist											
		Sample	KOLX 03c											
		n.	1	2	3	4	5	6	7	8	9	10	11	12
		Mineralization style	Py3; Massive veins											
		Average detection limit												
⁴⁹ Ti	ppm	n.a.	18	23	16	10	11	17	9.5	22	14	16	17	12
⁵¹ V	ppm	0.52	b.d.l.	b.d.l.	b.d.l.	b.d.l.	b.d.l.	b.d.l.	b.d.l.	b.d.l.	0.24	b.d.l.	b.d.l.	b.d.l.
⁵³ Cr	ppm	13	b.d.l.	b.d.l.	b.d.l.	b.d.l.	b.d.l.	b.d.l.	b.d.l.	12	b.d.l.	b.d.l.	b.d.l.	b.d.l.
⁵⁵ Mn	ppm	n.a.	5.7	5.1	4.8	3.4	5.3	4.4	4.8	4.5	4.6	4.8	5.3	5.9
⁵⁷ Fe	ppm	n.a.	462,700	462,700	462,700	462,700	462,700	462,700	462,700	462,700	462,700	462,700	462,400	462,400
⁵⁹ Co	ppm	0.46	0.71	b.d.l.	14	0.84	3.8	27	35	0.83	27	27	b.d.l.	0.8
⁶⁰ Ni	ppm	2.6	b.d.l.	b.d.l.	28	3.1	7.6	50	53	b.d.l.	68	47	b.d.l.	1.6
⁶⁵ Cu	ppm	5	11	b.d.l.	44	107	b.d.l.	b.d.l.	b.d.l.	b.d.l.	7.9	6.8	4.4	8.1
⁶⁶ Zn	ppm	7.4	b.d.l.	b.d.l.	b.d.l.	b.d.l.	b.d.l.	b.d.l.	b.d.l.	b.d.l.	7.2	b.d.l.	b.d.l.	b.d.l.
⁷⁵ As	ppm	1.1	b.d.l.	b.d.l.	b.d.l.	b.d.l.	b.d.l.	b.d.l.	b.d.l.	b.d.l.	b.d.l.	b.d.l.	b.d.l.	b.d.l.
⁷⁷ Se	ppm	0.38	2.3	b.d.l.	1.3	5	1.3	0.75	1.1	3.6	1.1	0.83	1.9	6.4
⁹⁵ Mo	ppm	0.05	b.d.l.	b.d.l.	0.08	0.06	b.d.l.	b.d.l.	b.d.l.	b.d.l.	b.d.l.	b.d.l.	b.d.l.	0.05
¹⁰⁷ Ag	ppm	0.66	b.d.l.	b.d.l.	b.d.l.	b.d.l.	b.d.l.	b.d.l.	b.d.l.	b.d.l.	b.d.l.	b.d.l.	b.d.l.	b.d.l.
¹¹⁵ In	ppm	0.49	b.d.l.	b.d.l.	0.49	0.41	0.41	b.d.l.	b.d.l.	b.d.l.	b.d.l.	0.53	b.d.l.	0.59
¹¹⁸ Sn	ppm	2.5	b.d.l.	b.d.l.	4.7	2.4	b.d.l.	b.d.l.	b.d.l.	b.d.l.	b.d.l.	b.d.l.	b.d.l.	7
¹²¹ Sb	ppm	0.68	b.d.l.	b.d.l.	b.d.l.	b.d.l.	0.88	10	2.9	b.d.l.	b.d.l.	3.7	b.d.l.	b.d.l.
¹²⁵ Te	ppm	0.24	0.46	0.23	0.35	1.3	b.d.l.	b.d.l.	b.d.l.	0.40	b.d.l.	0.34	b.d.l.	0.80
¹⁸² W	ppm	0.60	b.d.l.	b.d.l.	b.d.l.	b.d.l.	b.d.l.	b.d.l.	b.d.l.	b.d.l.	b.d.l.	b.d.l.	b.d.l.	b.d.l.
¹⁹⁷ Au	ppm	0.30	b.d.l.	b.d.l.	b.d.l.	b.d.l.	b.d.l.	b.d.l.	1.1	0.83	b.d.l.	0.36	0.83	b.d.l.
²⁰² Hg	ppm	0.20	43	0.19	12	71	17	3.3	3.6	57	12	8.9	28	110
²⁰⁵ Tl	ppm	0.29	66	0.22	16	95	22	3	0.4	38	45	14	39	84
²⁰⁸ Pb	ppm	0.11	b.d.l.	b.d.l.	b.d.l.	b.d.l.	b.d.l.	b.d.l.	b.d.l.	b.d.l.	b.d.l.	b.d.l.	b.d.l.	b.d.l.
²⁰⁹ Bi	ppm	0.11	b.d.l.	b.d.l.	b.d.l.	b.d.l.	b.d.l.	b.d.l.	b.d.l.	b.d.l.	b.d.l.	b.d.l.	b.d.l.	b.d.l.
²³² Th	ppm	n.a.	18	23	16	10	11	17	9.5	22	14	16	17	12
²³⁸ U	ppm	0.52	b.d.l.	b.d.l.	b.d.l.	b.d.l.	b.d.l.	b.d.l.	b.d.l.	b.d.l.	0.24	b.d.l.	b.d.l.	b.d.l.

Table S2-12. The full list of the LA-ICP-MS data acquired from the analyzed chalcopyrite from Kolchiko. b.d.l. = below detection limit, n. = number of analyses, n.a. = not analyzed.

		Hydrothermal alteration	Sericitization												
		Host rock	Mica schist												
		Sample	KL 07i		KL 13ii			KL 13iii							
		n.	1	2	1	2	3	1	2	3	4	5	6	7	8
		Mineralization style	Cpy1; Polymetallic quartz veins												
		Average detection limit													
⁴⁹ Ti	ppm	6	b.d.l.	12	19	29	29	11	16	b.d.l.	7	b.d.l.	9.8	8.3	8.2
⁵¹ V	ppm	0.88	b.d.l.	1.7	1.3	b.d.l.	b.d.l.	b.d.l.	b.d.l.	b.d.l.	b.d.l.	b.d.l.	b.d.l.	b.d.l.	b.d.l.
⁵³ Cr	ppm	22	b.d.l.	b.d.l.	17	18	21	b.d.l.	b.d.l.	b.d.l.	b.d.l.	b.d.l.	b.d.l.	b.d.l.	b.d.l.
⁵⁵ Mn	ppm	1.8	51	1,063	30	28	28	3.1	3.5	3.8	3.4	3.1	b.d.l.	4.5	3.4
⁵⁷ Fe	ppm	n.a.	349,340	337,061	301,100	301,100	301,100	300,000	300,000	300,000	300,000	300,000	300,000	300,000	300,000
⁵⁹ Co	ppm	n.a.	11	64	5	5	4	2.8	3.8	4.4	3.3	5.5	4.3	4.6	3.4
⁶⁰ Ni	ppm	2.9	4.3	43	b.d.l.	b.d.l.	b.d.l.	b.d.l.	b.d.l.	b.d.l.	b.d.l.	b.d.l.	b.d.l.	b.d.l.	b.d.l.
⁶⁵ Cu	ppm	n.a.	346,400	346,400	381,050	388,071	382,153	317,277	309,550	334,540	336,607	310,927	327,617	327,931	356,214
⁶⁶ Zn	ppm	n.a.	96	167	392	429	616	501	504	546	560	396	533	530	746
⁷¹ Ga	ppm	1.5	b.d.l.	b.d.l.	b.d.l.	b.d.l.	b.d.l.	b.d.l.	b.d.l.	0.73	b.d.l.	b.d.l.	b.d.l.	b.d.l.	b.d.l.
⁷⁴ Ge	ppm	5.5	8.6	b.d.l.	n.a.	n.a.	n.a.	6.3	b.d.l.	b.d.l.	b.d.l.	b.d.l.	b.d.l.	b.d.l.	b.d.l.
⁷⁵ As	ppm	3.6	22	75	11	17	18	b.d.l.	b.d.l.	b.d.l.	b.d.l.	b.d.l.	b.d.l.	b.d.l.	b.d.l.
⁷⁷ Se	ppm	n.a.	22	8.9	10	12	37	64	34	41	43	7.9	46	45	44
⁹³ Nb	ppm	0.27	b.d.l.	b.d.l.	b.d.l.	b.d.l.	b.d.l.	b.d.l.	b.d.l.	b.d.l.	b.d.l.	b.d.l.	b.d.l.	b.d.l.	b.d.l.
⁹⁵ Mo	ppm	1.9	b.d.l.	b.d.l.	b.d.l.	b.d.l.	b.d.l.	b.d.l.	b.d.l.	b.d.l.	b.d.l.	b.d.l.	b.d.l.	b.d.l.	b.d.l.
¹⁰⁷ Ag	ppm	0.88	b.d.l.	2.3	65	90	125	77	89	97	92	34	86	97	106
¹³⁷ Cd	ppm	2.2	b.d.l.	b.d.l.	b.d.l.	b.d.l.	b.d.l.	b.d.l.	b.d.l.	b.d.l.	4.7	b.d.l.	b.d.l.	b.d.l.	b.d.l.
¹¹⁵ In	ppm	0.14	0.72	b.d.l.	0.6	0.47	3.1	4.4	4.2	3.9	3.5	0.35	4.2	3.5	3.5
¹¹⁸ Sn	ppm	n.a.	2.7	12	4.5	5	8.7	8.6	6.5	7.1	5.9	3.1	8	9.3	7.5
¹²¹ Sb	ppm	n.a.	17	57	1.3	2.2	2.8	4.9	4.5	1.5	4.1	2.1	2.9	4.2	4.3
¹²⁵ Te	ppm	3.8	b.d.l.	b.d.l.	b.d.l.	b.d.l.	b.d.l.	b.d.l.	b.d.l.	b.d.l.	b.d.l.	b.d.l.	b.d.l.	b.d.l.	b.d.l.
¹⁸² W	ppm	0.97	b.d.l.	b.d.l.	b.d.l.	b.d.l.	b.d.l.	b.d.l.	b.d.l.	b.d.l.	b.d.l.	b.d.l.	b.d.l.	b.d.l.	b.d.l.
¹⁸⁵ Re	ppm	0.29	b.d.l.	b.d.l.	b.d.l.	b.d.l.	b.d.l.	b.d.l.	b.d.l.	b.d.l.	b.d.l.	b.d.l.	b.d.l.	b.d.l.	b.d.l.
¹⁹⁷ Au	ppm	0.42	b.d.l.	0.92	b.d.l.	b.d.l.	2	3.2	b.d.l.	4.5	2.6	b.d.l.	0.59	0.94	0.61
²⁰² Hg	ppm	1.1	b.d.l.	b.d.l.	1.1	1.4	1.4	b.d.l.	b.d.l.	b.d.l.	0.63	0.59	b.d.l.	b.d.l.	b.d.l.
²⁰⁵ Tl	ppm	0.55	b.d.l.	6.3	b.d.l.	b.d.l.	b.d.l.	b.d.l.	b.d.l.	b.d.l.	b.d.l.	b.d.l.	b.d.l.	b.d.l.	b.d.l.
²⁰⁸ Pb	ppm	n.a.	303	1,697	6.2	11	17	17	13	11	23	23	9.1	11	14
²⁰⁹ Bi	ppm	n.a.	277	229	5.4	9.1	14	18	4	14	23	25	7.9	15	11
²³² Th	ppm	0.18	b.d.l.	0.82	b.d.l.	b.d.l.	0.15	b.d.l.	b.d.l.	b.d.l.	b.d.l.	b.d.l.	b.d.l.	b.d.l.	b.d.l.
²³⁸ U	ppm	0.17	b.d.l.	1.1	b.d.l.	0.12	b.d.l.	b.d.l.	b.d.l.	b.d.l.	b.d.l.	b.d.l.	b.d.l.	b.d.l.	b.d.l.

Table S2-13. The full list of the LA-ICP-MS data acquired from the analyzed sphalerite from Kolchiko. b.d.l. = below detection limit, n. = number of analyses, n.a. = not analyzed.

		Hydrothermal alteration	Sericitization									
		Host rock	Mica schist									
		Sample	KL 13iii									
		n.	1	2	3	4	5	6	7	8	9	10
		Mineralization style	Sph1; Polymetallic quartz veins									
		Average detection limit										
⁴⁹ Ti	ppm	4.6	5.1	b.d.l.	5.7	3.7	b.d.l.	b.d.l.	3.3	b.d.l.	b.d.l.	b.d.l.
⁵¹ V	ppm	0.5	b.d.l.	b.d.l.	b.d.l.	b.d.l.	b.d.l.	b.d.l.	b.d.l.	b.d.l.	b.d.l.	b.d.l.
⁵³ Cr	ppm	13	b.d.l.	b.d.l.	b.d.l.	b.d.l.	b.d.l.	b.d.l.	b.d.l.	b.d.l.	b.d.l.	b.d.l.
⁵⁵ Mn	ppm	n.a.	678	700	656	669	682	689	737	716	668	686
⁵⁷ Fe	ppm	n.a.	60,538	58,505	57,001	60,415	59,125	61,052	65,833	61,427	60,418	61,127
⁵⁹ Co	ppm	n.a.	133	137	142	143	136	139	144	151	140	147
⁶⁰ Ni	ppm	1.6	b.d.l.	b.d.l.	b.d.l.	b.d.l.	b.d.l.	b.d.l.	b.d.l.	b.d.l.	b.d.l.	b.d.l.
⁶³ Cu	ppm	n.a.	75	225	881	1,060	1,684	138	76	420	253	310
⁶⁶ Zn	ppm	n.a.	627,000	627,000	627,000	627,000	627,000	627,000	627,000	627,000	627,000	627,000
⁷¹ Ga	ppm	0.71	b.d.l.	b.d.l.	0.75	0.71	b.d.l.	b.d.l.	b.d.l.	0.81	b.d.l.	b.d.l.
⁷⁴ Ge	ppm	2	b.d.l.	b.d.l.	b.d.l.	b.d.l.	b.d.l.	b.d.l.	b.d.l.	b.d.l.	b.d.l.	b.d.l.
⁷⁵ As	ppm	2.3	b.d.l.	b.d.l.	b.d.l.	b.d.l.	b.d.l.	b.d.l.	b.d.l.	b.d.l.	b.d.l.	b.d.l.
⁷⁷ Se	ppm	n.a.	35	35	35	35	32	25	42	24	18	38
⁹³ Nb	ppm	0.13	b.d.l.	b.d.l.	b.d.l.	b.d.l.	b.d.l.	b.d.l.	b.d.l.	b.d.l.	b.d.l.	b.d.l.
⁹⁵ Mo	ppm	0.96	b.d.l.	b.d.l.	b.d.l.	b.d.l.	b.d.l.	b.d.l.	b.d.l.	b.d.l.	b.d.l.	b.d.l.
¹⁰⁷ Ag	ppm	n.a.	12	19	16	33	59	8.8	8.5	23	15	11
¹⁵⁷ Cd	ppm	n.a.	1,955	2,004	1,867	2,007	2,015	1,904	2,011	1,964	1,928	1,943
¹¹⁵ In	ppm	n.a.	18	15	17	20	17	19	18	16	17	16
¹¹⁸ Sn	ppm	0.7	b.d.l.	b.d.l.	b.d.l.	b.d.l.	b.d.l.	b.d.l.	b.d.l.	b.d.l.	b.d.l.	b.d.l.
¹²¹ Sb	ppm	0.74	b.d.l.	b.d.l.	b.d.l.	b.d.l.	b.d.l.	b.d.l.	b.d.l.	1.8	b.d.l.	b.d.l.
¹²⁵ Te	ppm	1.7	b.d.l.	b.d.l.	b.d.l.	b.d.l.	b.d.l.	b.d.l.	b.d.l.	b.d.l.	b.d.l.	b.d.l.
¹⁸² W	ppm	0.49	b.d.l.	b.d.l.	b.d.l.	b.d.l.	b.d.l.	b.d.l.	b.d.l.	b.d.l.	b.d.l.	b.d.l.
¹⁸⁵ Re	ppm	0.14	b.d.l.	b.d.l.	b.d.l.	b.d.l.	b.d.l.	b.d.l.	b.d.l.	b.d.l.	b.d.l.	b.d.l.
¹⁹⁷ Au	ppm	0.19	b.d.l.	b.d.l.	0.30	b.d.l.	0.84	b.d.l.	0.22	0.44	0.28	b.d.l.
²⁰² Hg	ppm	n.a.	20	14	15	15	13	15	11	13	14	16
²⁰⁵ Tl	ppm	0.32	b.d.l.	b.d.l.	b.d.l.	b.d.l.	b.d.l.	b.d.l.	b.d.l.	b.d.l.	b.d.l.	b.d.l.
²⁰⁸ Pb	ppm	n.a.	0.54	11	9.1	128	72	2.8	2.1	15	5.7	4.3
²⁰⁹ Bi	ppm	0.17	b.d.l.	3.4	3.2	12	15	0.97	0.3	7.5	2.6	1.6
²³² Th	ppm	0.09	b.d.l.	b.d.l.	b.d.l.	b.d.l.	b.d.l.	b.d.l.	b.d.l.	b.d.l.	b.d.l.	b.d.l.
²³⁸ U	ppm	0.09	b.d.l.	b.d.l.	b.d.l.	b.d.l.	b.d.l.	b.d.l.	b.d.l.	b.d.l.	b.d.l.	b.d.l.

Table S2-14. The full list of the LA-ICP-MS data acquired from the analyzed arsenopyrite from Kolchiko. b.d.l. = below detection limit, n. = number of analyses, n.a. = not analyzed.

		Hydrothermal alteration	Sericitization									
		Host rock	Mica schist									
		Sample	KOLX 01a									
		n.	1	2	3	4	5	6	7	8	9	10
		Mineralization style	Apy1; Massive veins									
		Average detection limit										
⁴⁹ Ti	ppm	10	15	b.d.l	11	b.d.l	b.d.l	b.d.l	b.d.l	b.d.l	b.d.l	b.d.l
⁵¹ V	ppm	1	b.d.l	b.d.l	b.d.l	b.d.l	b.d.l	b.d.l	b.d.l	b.d.l	b.d.l	b.d.l
⁵² Cr	ppm	22	b.d.l	b.d.l	b.d.l	b.d.l	b.d.l	b.d.l	b.d.l	b.d.l	20	b.d.l
⁵⁵ Mn	ppm	2.5	3.9	4.4	3.6	5.0	4.9	3.6	4.4	3.8	b.d.l	3.6
⁵⁷ Fe	ppm	n.a.	352,500	352,500	352,500	352,500	344,300	352,500	344,300	344,300	344,300	344,300
⁵⁹ Co	ppm	n.a.	312	366	414	334	417	175	135	627	77	81
⁶⁰ Ni	ppm	n.a.	27	24	23	36	46	29	25	90	29	25
⁶³ Cu	ppm	7.8	b.d.l	b.d.l	b.d.l	b.d.l	b.d.l	b.d.l	b.d.l	20	b.d.l	b.d.l
⁶⁶ Zn	ppm	13	b.d.l	b.d.l	b.d.l	b.d.l	b.d.l	b.d.l	b.d.l	b.d.l	b.d.l	b.d.l
⁷¹ Ga	ppm	1.9	b.d.l	b.d.l	b.d.l	b.d.l	b.d.l	b.d.l	b.d.l	b.d.l	b.d.l	b.d.l
⁷³ Ge	ppm	7	b.d.l	b.d.l	b.d.l	b.d.l	b.d.l	b.d.l	b.d.l	b.d.l	b.d.l	b.d.l
⁷⁵ As	ppm	n.a.	295,377	263,364	250,689	209,505	238,474	230,700	214,038	212,028	196,291	203,785
⁷⁷ Se	ppm	9.1	16	12	b.d.l	18.81	b.d.l	9.2	16	21	13.6	11
⁹² Nb	ppm	0.48	b.d.l	b.d.l	b.d.l	b.d.l	b.d.l	b.d.l	b.d.l	b.d.l	b.d.l	b.d.l
⁹⁵ Mo	ppm	2.6	b.d.l	b.d.l	b.d.l	b.d.l	b.d.l	b.d.l	b.d.l	b.d.l	b.d.l	b.d.l
¹⁰⁷ Ag	ppm	0.74	b.d.l	b.d.l	b.d.l	b.d.l	b.d.l	b.d.l	b.d.l	2.4	b.d.l	b.d.l
¹⁵⁷ Cd	ppm	2.1	b.d.l	b.d.l	b.d.l	b.d.l	b.d.l	b.d.l	b.d.l	b.d.l	b.d.l	b.d.l
¹¹⁵ In	ppm	n.a.	0.87	1.1	0.82	0.84	1.2	1.1	1	0.98	0.88	1.1
¹¹⁸ Sn	ppm	1.1	b.d.l	b.d.l	b.d.l	b.d.l	b.d.l	b.d.l	b.d.l	b.d.l	b.d.l	b.d.l
¹²¹ Sb	ppm	n.a.	101	67	71	67	78	98	70	88	57	57
¹²⁵ Te	ppm	5.5	b.d.l	b.d.l	b.d.l	b.d.l	b.d.l	12	b.d.l	13	b.d.l	b.d.l
¹⁸² W	ppm	1.4	b.d.l	b.d.l	b.d.l	b.d.l	b.d.l	b.d.l	b.d.l	b.d.l	b.d.l	b.d.l
¹⁸⁵ Re	ppm	0.38	b.d.l	b.d.l	b.d.l	b.d.l	b.d.l	b.d.l	b.d.l	b.d.l	b.d.l	b.d.l
¹⁹⁷ Au	ppm	0.57	1.6	0.63	b.d.l	b.d.l	b.d.l	b.d.l	b.d.l	3.5	b.d.l	b.d.l
²⁰² Hg	ppm	1.1	1.6	1.3	0.87	0.96	b.d.l	1.2	1.4	1.2	1.3	b.d.l
²⁰⁵ Tl	ppm	0.7	b.d.l	b.d.l	b.d.l	b.d.l	b.d.l	0.30	b.d.l	b.d.l	b.d.l	b.d.l
²⁰⁸ Pb	ppm	0.44	3.8	2.3	0.63	0.72	3.1	0.89	2.5	6.8	b.d.l	b.d.l
²⁰⁹ Bi	ppm	n.a.	35	101	9.7	27	48	14	42	48	6.9	18
²³² Th	ppm	0.29	b.d.l	b.d.l	b.d.l	b.d.l	b.d.l	b.d.l	b.d.l	b.d.l	b.d.l	b.d.l
²³⁸ U	ppm	0.27	b.d.l	b.d.l	b.d.l	b.d.l	b.d.l	b.d.l	b.d.l	b.d.l	b.d.l	b.d.l

Table S2-15. The full list of the LA-ICP-MS data acquired from the analyzed pyrite from Aspra Chomata. b.d.l. = below detection limit, n. = number of analyses, n.a. = not analyzed.

		Hydrothermal alteration	Sericitic alteration						
		Host rock	Granodiorite porphyry						
		Sample	Ach 08A2a						
		n.	1	2	3	4	5	6	7
		Mineralization style	Py1; Base metals vein						
		Average detection limit							
⁴⁹ Ti	ppm	n.a.	26	34	42	25	34	40	28
⁵¹ V	ppm	1	b.d.l.	b.d.l.	b.d.l.	b.d.l.	b.d.l.	b.d.l.	b.d.l.
⁵³ Cr	ppm	16	b.d.l.	b.d.l.	16	b.d.l.	b.d.l.	b.d.l.	b.d.l.
⁵⁵ Mn	ppm	n.a.	15	6.3	8.2	6.7	7.5	5.4	5.4
⁵⁷ Fe	ppm	n.a.	461,000	461,000	461,000	461,000	461,000	453,600	453,600
⁵⁹ Co	ppm	0.52	0.11	b.d.l.	0.16	b.d.l.	b.d.l.	b.d.l.	b.d.l.
⁶⁰ Ni	ppm	4.8	b.d.l.	b.d.l.	b.d.l.	b.d.l.	0.87	b.d.l.	b.d.l.
⁶⁵ Cu	ppm	n.a.	945	1,413	1,090	818	896	1,213	2,569
⁶⁶ Zn	ppm	25	525	123	82	54	150	b.d.l.	b.d.l.
⁷⁵ As	ppm	n.a.	31,727	39,472	35,774	41,082	41,036	41,546	43,671
⁷⁷ Se	ppm	12	b.d.l.	b.d.l.	b.d.l.	b.d.l.	b.d.l.	b.d.l.	b.d.l.
⁹³ Nb	ppm	0.3	b.d.l.	b.d.l.	b.d.l.	b.d.l.	b.d.l.	b.d.l.	b.d.l.
⁹⁵ Mo	ppm	2	b.d.l.	b.d.l.	b.d.l.	b.d.l.	b.d.l.	b.d.l.	b.d.l.
¹⁰⁷ Ag	ppm	n.a.	58	13	6.0	60	26	10	43
¹¹⁵ In	ppm	0.37	0.08	0.06	0.10	0.07	0.06	b.d.l.	b.d.l.
¹¹⁸ Sn	ppm	2	5.8	2.2	b.d.l.	0.91	0.86	b.d.l.	b.d.l.
¹²¹ Sb	ppm	n.a.	1,791	359	355	1,144	2,621	51	741
¹²⁵ Te	ppm	3.7	b.d.l.	b.d.l.	b.d.l.	b.d.l.	b.d.l.	b.d.l.	b.d.l.
¹⁸³ W	ppm	0.74	b.d.l.	b.d.l.	b.d.l.	b.d.l.	b.d.l.	b.d.l.	b.d.l.
¹⁹⁷ Au	ppm	n.a.	33	63	80	26	31	25	14
²⁰² Hg	ppm	0.85	b.d.l.	b.d.l.	b.d.l.	b.d.l.	b.d.l.	b.d.l.	b.d.l.
²⁰⁵ Tl	ppm	1.9	1.1	0.79	1.1	0.54	2.9	b.d.l.	7.7
²⁰⁸ Pb	ppm	n.a.	3,335	583.44	465.25	5,360	3,649	110	1,917
²⁰⁹ Bi	ppm	0.28	b.d.l.	b.d.l.	b.d.l.	b.d.l.	b.d.l.	b.d.l.	b.d.l.
²³² Th	ppm	0.26	0.05	b.d.l.	b.d.l.	b.d.l.	0.21	b.d.l.	b.d.l.
²³⁸ U	ppm	0.18	b.d.l.	b.d.l.	b.d.l.	0.05	0.62	b.d.l.	b.d.l.

Table S2-16. The full list of the LA-ICP-MS data acquired from the analyzed sphalerite from Aspra Chomata. b.d.l. = below detection limit, n. = number of analyses, n.a. = not analyzed.

		Hydrothermal alteration	Sericitic alteration									
		Host rock	Granodiorite porphyry									
		Sample	Ach 08A2a									
		n.	1	2	3	4	5	6	7	8	9	10
		Mineralization style	Sph1; Base metals veins									
		Average detection limit										
⁴⁹ Ti	ppm	7.4	9.7	9.7	7.8	31	11	12	18	15	7.9	7.1
⁵¹ V	ppm	0.59	b.d.l.	b.d.l.	b.d.l.	0.71	b.d.l.	b.d.l.	b.d.l.	b.d.l.	b.d.l.	b.d.l.
⁵³ Cr	ppm	12	b.d.l.	b.d.l.	b.d.l.	b.d.l.	b.d.l.	b.d.l.	b.d.l.	b.d.l.	b.d.l.	b.d.l.
⁵⁵ Mn	ppm	n.a.	3,316	4,372	4,349	2,732	2,651	2,191	4,739	7,253	1,228	1,273
⁵⁷ Fe	ppm	n.a.	86,917	97,815	99,312	78,919	69,998	59,932	111,736	92,771	29,924	45,889
⁵⁹ Co	ppm	0.29	b.d.l.	b.d.l.	b.d.l.	b.d.l.	b.d.l.	b.d.l.	b.d.l.	b.d.l.	b.d.l.	b.d.l.
⁶⁰ Ni	ppm	1.9	b.d.l.	b.d.l.	b.d.l.	b.d.l.	b.d.l.	b.d.l.	b.d.l.	b.d.l.	b.d.l.	b.d.l.
⁶⁵ Cu	ppm	n.a.	2,087	416	469	13,723	4,457	634	3,572	7,605	809	461
⁶⁶ Zn	ppm	n.a.	636,700	636,700	636,700	636,700	632,900	639,400	639,400	630,800	632,900	632,900
⁷¹ Ga	ppm	n.a.	20	18	17	21	19	22	15	16	26	23
⁷⁴ Ge	ppm	2	2.5	b.d.l.	b.d.l.	2.4	2.0	b.d.l.	6.4	3.6	b.d.l.	1.1
⁷⁵ As	ppm	5.8	b.d.l.	b.d.l.	b.d.l.	555	5.0	b.d.l.	5.6	b.d.l.	35	b.d.l.
⁷⁷ Se	ppm	6.6	b.d.l.	b.d.l.	b.d.l.	b.d.l.	b.d.l.	b.d.l.	b.d.l.	b.d.l.	b.d.l.	b.d.l.
⁹³ Nb	ppm	0.09	b.d.l.	b.d.l.	b.d.l.	0.05	b.d.l.	b.d.l.	b.d.l.	b.d.l.	b.d.l.	b.d.l.
⁹⁵ Mo	ppm	1	b.d.l.	0.51	b.d.l.	0.37	b.d.l.	b.d.l.	b.d.l.	b.d.l.	b.d.l.	b.d.l.
¹⁰⁷ Ag	ppm	n.a.	6.3	2.1	5.8	52	14	3.0	12	17	11	5.1
¹⁵⁷ Cd	ppm	n.a.	1,507	1,423	1,588	1,608	1,102	1,306	1,486	1,243	1,293	1,567
¹¹⁵ In	ppm	0.09	0.61	0.22	1.4	0.56	0.21	0.23	0.34	0.55	0.18	0.23
¹¹⁸ Sn	ppm	n.a.	196	88	371	119	51	61	100	124	14	56
¹²¹ Sb	ppm	0.71	8.4	4.6	0.84	4,169	11	3.6	7.8	9	965	2.8
¹²⁵ Te	ppm	2.2	b.d.l.	b.d.l.	b.d.l.	b.d.l.	b.d.l.	b.d.l.	b.d.l.	b.d.l.	b.d.l.	b.d.l.
¹⁸² W	ppm	0.42	b.d.l.	b.d.l.	b.d.l.	2.5	b.d.l.	b.d.l.	b.d.l.	b.d.l.	b.d.l.	b.d.l.
¹⁸⁵ Re	ppm	0.12	b.d.l.	b.d.l.	b.d.l.	b.d.l.	b.d.l.	b.d.l.	b.d.l.	b.d.l.	b.d.l.	b.d.l.
¹⁹⁷ Au	ppm	0.28	b.d.l.	b.d.l.	b.d.l.	b.d.l.	b.d.l.	b.d.l.	b.d.l.	b.d.l.	b.d.l.	b.d.l.
²⁰² Hg	ppm	n.a.	11	15	15	12	17	17	23	12	29	20
²⁰⁵ Tl	ppm	0.49	b.d.l.	b.d.l.	b.d.l.	b.d.l.	b.d.l.	b.d.l.	b.d.l.	b.d.l.	1.1	b.d.l.
²⁰⁸ Pb	ppm	0.49	3.6	6.9	3.3	7,168	5.2	1.4	7.7	6.4	1,993	2.6
²⁰⁹ Bi	ppm	0.19	b.d.l.	b.d.l.	b.d.l.	b.d.l.	b.d.l.	b.d.l.	b.d.l.	b.d.l.	b.d.l.	0.04
²³² Th	ppm	0.05	b.d.l.	b.d.l.	b.d.l.	b.d.l.	b.d.l.	b.d.l.	b.d.l.	b.d.l.	b.d.l.	b.d.l.
²³⁸ U	ppm	0.06	b.d.l.	b.d.l.	b.d.l.	b.d.l.	0.04	b.d.l.	b.d.l.	b.d.l.	b.d.l.	b.d.l.

Table S2-16. Continued.

		Hydrothermal alteration	Sericitic alteration										
		Host rock	Granodiorite porphyry										
		Sample	Ach 08A2b										
		n.	1	2	3	4	5	6	7	8	9	10	11
		Mineralization style	Sph1; Base metals veins										
		Average detection limit											
⁴⁹ Ti	ppm	7.4	14	13	11	7.9	9.1	8.7	9.4	14	b.d.l.	11	8.7
⁵¹ V	ppm	0.59	b.d.l.	b.d.l.	b.d.l.	b.d.l.	b.d.l.	b.d.l.	b.d.l.	b.d.l.	b.d.l.	b.d.l.	b.d.l.
⁵³ Cr	ppm	12	b.d.l.	b.d.l.	b.d.l.	b.d.l.	b.d.l.	b.d.l.	b.d.l.	b.d.l.	b.d.l.	b.d.l.	b.d.l.
⁵⁵ Mn	ppm	n.a.	1,016	1,441	681	1,638	1,069	3,621	710	1,485	755	1,453	795
⁵⁷ Fe	ppm	n.a.	34,412	12,134	25,918	72,764	40,238	10,544	20,847	69,606	19,481	68,409	23,041
⁵⁹ Co	ppm	0.29	b.d.l.	b.d.l.	b.d.l.	b.d.l.	b.d.l.	b.d.l.	b.d.l.	b.d.l.	b.d.l.	b.d.l.	b.d.l.
⁶⁰ Ni	ppm	1.9	b.d.l.	0.45	b.d.l.	b.d.l.	b.d.l.	0.91	b.d.l.	b.d.l.	b.d.l.	b.d.l.	b.d.l.
⁶⁵ Cu	ppm	n.a.	582	222	197	223	2,668	144	129	3,772	61	96	64
⁶⁶ Zn	ppm	n.a.	629,000	624,900	624,900	619,800	616,800	618,500	618,400	618,400	618,400	618,400	618,400
⁷¹ Ga	ppm	n.a.	44	27	35	24	34	20	30	33	26	19	30
⁷⁴ Ge	ppm	2	2.9	b.d.l.	4.5	b.d.l.	b.d.l.	b.d.l.	b.d.l.	b.d.l.	b.d.l.	b.d.l.	b.d.l.
⁷⁵ As	ppm	5.8	23	26	b.d.l.	b.d.l.	6.9	b.d.l.	b.d.l.	b.d.l.	b.d.l.	b.d.l.	b.d.l.
⁷⁷ Se	ppm	6.6	b.d.l.	b.d.l.	b.d.l.	b.d.l.	b.d.l.	b.d.l.	b.d.l.	b.d.l.	b.d.l.	b.d.l.	b.d.l.
⁹³ Nb	ppm	0.09	b.d.l.	b.d.l.	b.d.l.	b.d.l.	b.d.l.	b.d.l.	b.d.l.	b.d.l.	b.d.l.	b.d.l.	b.d.l.
⁹⁵ Mo	ppm	1	b.d.l.	b.d.l.	b.d.l.	b.d.l.	b.d.l.	b.d.l.	b.d.l.	b.d.l.	b.d.l.	b.d.l.	b.d.l.
¹⁰⁷ Ag	ppm	n.a.	7.0	20	3.5	2	15	2	3.0	11	0.99	1.7	1.3
¹⁵⁷ Cd	ppm	n.a.	1,330	1,198	1,800	1,500	1,385	835	1,242	1,933	1,211	1,613	1,233
¹¹⁵ In	ppm	0.09	0.53	0.54	0.21	0.32	0.26	0.62	0.14	0.62	b.d.l.	0.14	0.33
¹¹⁸ Sn	ppm	n.a.	29	61	69	31	56	90	28	128	16	25	8.6
¹²¹ Sb	ppm	0.71	37	59	7	0.90	14	61	0.84	7.4	b.d.l.	b.d.l.	b.d.l.
¹²⁵ Te	ppm	2.2	b.d.l.	b.d.l.	b.d.l.	b.d.l.	b.d.l.	b.d.l.	b.d.l.	b.d.l.	b.d.l.	b.d.l.	b.d.l.
¹⁸² W	ppm	0.42	b.d.l.	b.d.l.	b.d.l.	b.d.l.	b.d.l.	b.d.l.	b.d.l.	b.d.l.	b.d.l.	b.d.l.	b.d.l.
¹⁸⁵ Re	ppm	0.12	b.d.l.	b.d.l.	b.d.l.	b.d.l.	b.d.l.	b.d.l.	b.d.l.	b.d.l.	b.d.l.	b.d.l.	b.d.l.
¹⁹⁷ Au	ppm	0.28	b.d.l.	b.d.l.	b.d.l.	b.d.l.	b.d.l.	b.d.l.	b.d.l.	b.d.l.	b.d.l.	b.d.l.	b.d.l.
²⁰⁵ Hg	ppm	n.a.	12	35	16	21	26	37	28	16	33	23	30
²⁰⁵ Tl	ppm	0.49	0.53	0.57	b.d.l.	b.d.l.	b.d.l.	b.d.l.	b.d.l.	b.d.l.	b.d.l.	b.d.l.	b.d.l.
²⁰⁸ Pb	ppm	0.49	33	160	1.5	0.72	4.6	72	0.25	2.3	0.21	b.d.l.	0.11
²⁰⁹ Bi	ppm	0.19	b.d.l.	b.d.l.	b.d.l.	0.14	b.d.l.	b.d.l.	b.d.l.	b.d.l.	b.d.l.	b.d.l.	b.d.l.
²³² Th	ppm	0.05	b.d.l.	b.d.l.	b.d.l.	b.d.l.	b.d.l.	b.d.l.	b.d.l.	b.d.l.	b.d.l.	b.d.l.	b.d.l.
²³⁸ U	ppm	0.06	b.d.l.	b.d.l.	b.d.l.	b.d.l.	b.d.l.	b.d.l.	b.d.l.	b.d.l.	b.d.l.	b.d.l.	b.d.l.

SUPPLEMENT 3

Supplement 3. Heatmaps of Pearson's correlation coefficients.

Table S3-1. Heatmap of Pearson's correlation coefficients of the studied critical and rare metals detected in the bulk geochemical analyses from Vathi.

Correlations																									
	Ag	Au	Bi	Cd	Ce	Co	Ga	Gd	Ge	Hg	In	La	Nb	Nd	Re	Sb	Se	Sm	Ta	Te	Th	Ti	U	V	W
Ag	1																								
Au	0.536	1																							
Bi	0.008	0.116	1																						
Cd	0.345	0.683	0.65	1																					
Ce	-0.283	-0.274	0.262	0.009	1																				
Co	-0.179	0.003	-0.094	-0.090	-0.295	1																			
Ga	0.096	-0.256	0.071	-0.219	0.075	-0.346	1																		
Gd	-0.031	0.017	0.764	0.544	0.627	-0.203	0.029	1																	
Ge	-0.340	-0.112	-0.159	-0.188	0.029	0.181	-0.719	-0.009	1																
Hg	0.317	0.794	-0.114	0.461	-0.205	0.084	-0.704	-0.128	0.346	1															
In	-0.231	-0.212	-0.134	-0.343	0.062	-0.227	0.629	-0.272	-0.396	-0.375	1														
La	-0.312	-0.251	0.008	-0.163	0.933	-0.227	0.005	0.362	0.109	-0.112	0.085	1													
Nb	0.273	-0.224	0.364	0.082	0.192	-0.353	0.802	0.372	-0.753	-0.647	0.179	0.005	1												
Nd	-0.245	-0.194	0.584	0.246	0.85	-0.260	0.034	0.874	0.056	-0.203	-0.070	0.656	0.267	1											
Re	-0.243	-0.082	-0.143	-0.246	-0.008	0.130	-0.433	-0.186	0.509	0.148	-0.140	0.122	-0.461	-0.122	1										
Sb	0.364	0.608	-0.095	0.227	0.013	-0.110	0.060	-0.210	-0.207	0.451	0.169	0.163	-0.128	-0.183	0.045	1									
Se	0.565	0.932	-0.090	0.555	-0.337	0.129	-0.255	-0.146	-0.154	0.755	-0.230	-0.246	-0.231	-0.337	-0.105	0.612	1								
Sm	-0.147	-0.141	0.724	0.386	0.752	-0.240	0.097	0.958	-0.036	-0.229	-0.101	0.492	0.385	0.941	-0.193	-0.241	-0.306	1							
Ta	0.192	-0.247	0.057	-0.140	0.459	-0.294	0.427	0.43	-0.160	-0.393	-0.070	0.399	0.551	0.508	-0.322	-0.137	-0.197	0.42	1						
Te	0.533	0.87	-0.131	0.433	-0.217	-0.022	-0.255	-0.053	0.028	0.707	-0.248	-0.146	-0.269	-0.219	0.175	0.565	0.85	-0.201	-0.140	1					
Th	0.291	0.589	-0.097	0.275	0.111	-0.298	-0.173	0.055	0.123	0.535	-0.101	0.197	-0.251	0.108	-0.011	0.578	0.528	-0.031	0.144	0.611	1				
Ti	-0.246	-0.284	-0.207	-0.495	0.132	-0.219	0.639	-0.145	-0.137	-0.42	0.535	0.185	0.290	0.022	-0.092	0.102	-0.331	-0.061	0.369	-0.248	0.052	1			
U	0.54	0.949	-0.050	0.578	-0.289	-0.032	-0.192	-0.074	-0.198	0.737	-0.175	-0.252	-0.191	-0.251	-0.146	0.585	0.908	-0.218	-0.191	0.865	0.583	-0.288	1		
V	-0.294	-0.267	-0.036	-0.307	-0.042	-0.044	0.048	0.017	0.408	-0.279	-0.042	-0.079	-0.068	0.043	0.000	-0.244	-0.327	0.014	0.036	-0.219	-0.025	0.281	-0.287	1	
W	-0.404	-0.100	0.179	0.016	0.263	0.188	-0.684	0.218	0.732	0.336	-0.288	0.287	-0.586	0.347	0.554	-0.200	-0.187	0.257	-0.217	-0.049	-0.048	-0.210	-0.242	0.030	1

**. Correlation is significant at the 0.01 level (2-tailed).

*. Correlation is significant at the 0.05 level (2-tailed).

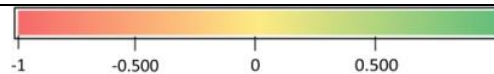


Table S3-2. Heatmap of Pearson's correlation coefficients of the studied critical and rare metals detected in the bulk geochemical analyses from Laodikino.

Correlations																										
	Ag	Au	Bi	Cd	Ce	Co	Ga	Gd	Ge	Hg	In	La	Nb	Nd	Re	Sb	Se	Sm	Ta	Te	Th	Ti	U	V	W	
Ag	1																									
Au	1.000	1																								
Bi	0.99	0.991	1																							
Cd	0.996	0.997	0.998	1																						
Ce	-0.411	-0.400	-0.416	-0.420	1																					
Co	0.95	0.948	0.904	0.925	-0.347	1																				
Ga	-0.431	-0.420	-0.430	-0.434	0.858	-0.322	1																			
Gd	-0.328	-0.317	-0.330	-0.335	0.98	-0.261	0.899	1																		
Ge	0.283	0.301	0.342	0.317	0.411	0.279	0.589	0.521	1																	
Hg	0.991	0.992	1.000	0.999	-0.423	0.907	-0.438	-0.338	0.332	1																
In	0.984	0.986	0.999	0.995	-0.422	0.889	-0.434	-0.336	0.350	0.999	1															
La	-0.388	-0.377	-0.393	-0.397	0.993	-0.319	0.863	0.964	0.445	-0.400	-0.399	1														
Nb	-0.598	-0.592	-0.533	-0.561	0.418	-0.717	0.248	0.410	-0.068	-0.538	-0.513	0.337	1													
Nd	-0.373	-0.362	-0.375	-0.380	0.997	-0.309	0.88	0.988	0.468	-0.383	-0.381	0.993	0.391	1												
Re	-0.758	-0.759	-0.772	-0.765	0.244	-0.598	0.380	0.240	-0.108	-0.771	-0.771	0.213	0.462	0.228	1											
Sb	0.943	0.948	0.981	0.968	-0.424	0.812	-0.428	-0.337	0.396	0.98	0.988	-0.401	-0.427	-0.382	-0.762	1										
Se	0.804	0.813	0.882	0.852	-0.389	0.614	-0.381	-0.307	0.467	0.877	0.898	-0.368	-0.233	-0.347	-0.689	0.956	1									
Sm	-0.343	-0.332	-0.346	-0.351	0.992	-0.276	0.892	0.996	0.504	-0.354	-0.352	0.984	0.388	0.997	0.227	-0.354	-0.322	1								
Ta	-0.472	-0.470	-0.478	-0.475	0.338	-0.339	0.703	0.393	0.270	-0.482	-0.480	0.346	0.094	0.369	0.593	-0.474	-0.437	0.376	1							
Te	-0.209	-0.206	-0.213	-0.211	0.085	-0.106	-0.008	0.080	0.089	-0.212	-0.212	0.064	0.228	0.059	0.499	-0.210	-0.174	0.077	-0.249	1						
Th	-0.451	-0.451	-0.456	-0.457	0.538	-0.498	0.230	0.497	-0.302	-0.457	-0.456	0.459	0.795	0.504	0.290	-0.448	-0.405	0.487	0.055	-0.042	1					
Ti	-0.573	-0.567	-0.580	-0.577	0.555	-0.417	0.804	0.580	0.329	-0.584	-0.582	0.568	0.218	0.577	0.708	-0.576	-0.524	0.576	0.937	-0.025	0.186	1				
U	-0.161	-0.158	-0.179	-0.171	0.169	-0.021	0.063	0.177	0.125	-0.178	-0.182	0.145	0.247	0.151	0.581	-0.197	-0.193	0.170	-0.118	0.943	0.088	0.130	1			
V	-0.269	-0.260	-0.281	-0.281	0.744	-0.156	0.912	0.826	0.595	-0.288	-0.290	0.729	0.154	0.765	0.243	-0.303	-0.299	0.798	0.531	0.083	0.111	0.579	0.083	1		
W	-0.663	-0.670	-0.678	-0.669	-0.236	-0.531	-0.027	-0.280	-0.389	-0.674	-0.676	-0.235	0.127	-0.258	0.824	-0.667	-0.607	-0.274	0.435	0.369	-0.084	0.441	0.353	-0.145	1	
**. Correlation is significant at the 0.01 level (2-tailed).																										
*. Correlation is significant at the 0.05 level (2-tailed).																										

**. Correlation is significant at the 0.01 level (2-tailed).

*. Correlation is significant at the 0.05 level (2-tailed).



Table S3-3. Heatmap of Pearson's correlation coefficients of the studied critical and rare metals detected in the bulk geochemical analyses from Kolchiko.

Correlations																										
	Ag	Au	Bi	Cd	Ce	Co	Ga	Gd	Ge	Hg	In	La	Nb	Nd	Re	Sb	Se	Sm	Ta	Te	Th	Ti	U	V	W	
Ag	1																									
Au	-0.199	1																								
Bi	0.715	0.362	1																							
Cd	0.819	-0.169	0.54	1																						
Ce	0.192	0.513	0.478	0.178	1																					
Co	0.410	0.225	0.672	0.254	0.553	1																				
Ga	0.191	-0.182	-0.009	0.355	0.375	-0.135	1																			
Gd	0.505	-0.164	0.269	0.564	0.535	0.129	0.9	1																		
Ge	0.66	0.061	0.72	0.419	0.305	0.813	-0.093	0.188	1																	
Hg	0.868	-0.111	0.632	0.731	0.086	0.404	-0.062	0.210	0.588	1																
In	0.844	-0.221	0.505	0.805	-0.027	0.131	0.158	0.353	0.477	0.757	1															
La	0.007	0.451	0.361	0.032	0.899	0.598	0.157	0.248	0.264	0.030	-0.136	1														
Nb	-0.168	-0.097	-0.306	-0.061	-0.055	-0.261	0.641	0.358	-0.195	-0.259	-0.102	-0.098	1													
Nd	0.355	0.183	0.355	0.364	0.81	0.310	0.768	0.902	0.225	0.090	0.138	0.527	0.217	1												
Re	0.106	-0.188	0.060	-0.187	-0.194	0.188	-0.201	-0.261	0.210	0.365	0.078	-0.006	0.187	-0.305	1											
Sb	-0.289	-0.103	-0.380	-0.188	-0.142	-0.356	-0.128	-0.150	-0.441	-0.336	-0.266	-0.146	-0.153	-0.147	-0.334	1										
Se	0.908	-0.097	0.815	0.651	0.314	0.648	0.093	0.439	0.86	0.703	0.682	0.155	-0.252	0.386	0.058	-0.330	1									
Sm	0.527	-0.024	0.377	0.547	0.655	0.253	0.824	0.979	0.266	0.228	0.322	0.347	0.246	0.958	-0.301	-0.163	0.504	1								
Ta	-0.254	0.147	0.063	-0.189	0.236	0.264	-0.235	-0.253	-0.010	-0.099	-0.253	0.526	-0.131	-0.149	0.026	-0.009	-0.157	-0.241	1							
Te	0.692	0.193	0.872	0.472	0.358	0.767	-0.096	0.203	0.769	0.607	0.536	0.264	-0.321	0.287	0.180	-0.413	0.813	0.316	-0.013	1						
Th	0.84	-0.132	0.532	0.865	0.449	0.317	0.504	0.769	0.419	0.677	0.684	0.226	-0.057	0.651	-0.200	-0.226	0.704	0.782	-0.203	0.434	1					
Ti	-0.103	-0.102	-0.302	0.001	0.299	-0.339	0.661	0.594	-0.344	-0.198	-0.047	0.124	0.215	0.574	-0.258	-0.151	-0.216	0.546	-0.149	-0.345	0.292	1				
U	0.159	-0.098	-0.021	0.180	0.462	0.345	0.412	0.539	0.160	0.069	0.027	0.320	0.089	0.625	-0.137	-0.194	0.161	0.591	-0.036	0.256	0.368	0.449	1			
V	0.026	0.419	0.304	-0.157	0.528	0.621	-0.047	0.052	0.579	0.119	-0.051	0.551	-0.103	0.305	0.248	-0.477	0.245	0.146	0.136	0.351	0.042	0.168	0.298	1		
W	0.276	-0.112	0.233	-0.079	-0.281	0.065	-0.414	-0.346	0.188	0.559	0.244	-0.188	-0.217	-0.385	0.8	-0.271	0.167	-0.349	0.034	0.303	-0.112	-0.252	-0.194	0.118	1	
**. Correlation is significant at the 0.01 level (2-tailed).																										
*. Correlation is significant at the 0.05 level (2-tailed).																										

**. Correlation is significant at the 0.01 level (2-tailed).

*. Correlation is significant at the 0.05 level (2-tailed).



Table S3-4. Heatmap of Pearson's correlation coefficients of the studied critical and rare metals detected in the bulk geochemical analyses from Aspra Chomata.

Correlations																									
	Ag	Au	Bi	Cd	Ce	Co	Ga	Gd	Ge	Hg	In	La	Nb	Nd	Re	Sb	Se	Sm	Ta	Te	Th	Ti	U	V	W
Ag	1																								
Au	0.208	1																							
Bi	-0.227	-0.164	1																						
Cd	0.989	0.064	-0.186	1																					
Ce	-0.643	-0.484	0.418	-0.545	1																				
Co	-0.036	0.202	0.094	-0.178	-0.229	1																			
Ga	0.699	0.203	0.264	0.719	-0.074	0.127	1																		
Gd	-0.460	-0.337	-0.371	-0.328	0.651	-0.523	-0.342	1																	
Ge	0.685	-0.195	0.423	0.766	-0.031	0.069	0.879	-0.421	1																
Hg	0.926	-0.139	-0.164	0.994	-0.425	-0.265	0.628	-0.261	0.744	1															
In	0.036	-0.103	-0.107	-0.037	-0.237	0.909	0.026	-0.369	0.085	-0.092	1														
La	-0.678	-0.499	0.519	-0.593	0.983	-0.171	-0.108	0.560	-0.028	-0.465	-0.183	1													
Nb	-0.220	-0.140	0.971	-0.185	0.495	0.157	0.366	-0.315	0.472	-0.172	-0.069	0.564	1												
Nd	-0.444	-0.349	-0.385	-0.314	0.641	-0.540	-0.349	0.996	-0.414	-0.240	-0.380	0.545	-0.324	1											
Re	-0.104	0.045	-0.036	-0.129	0.017	0.409	0.112	-0.019	-0.028	-0.178	0.369	0.002	0.027	-0.087	1										
Sb	0.994	0.082	-0.190	0.999	-0.574	-0.170	0.703	-0.355	0.759	0.996	-0.030	-0.623	-0.190	-0.338	-0.138	1									
Se	-0.007	-0.134	-0.020	-0.078	-0.202	0.919	0.015	-0.402	0.099	-0.125	0.995	-0.137	0.014	-0.414	0.367	-0.070	1								
Sm	-0.461	-0.345	-0.376	-0.332	0.646	-0.535	-0.360	0.998	-0.429	-0.259	-0.376	0.555	-0.321	0.999	-0.070	-0.357	-0.410	1							
Ta	-0.120	0.086	0.734	-0.189	0.134	0.733	0.366	-0.599	0.391	-0.248	0.512	0.227	0.778	-0.619	0.272	-0.189	0.573	-0.612	1						
Te	-0.100	0.426	0.251	-0.277	-0.383	0.674	-0.120	-0.639	-0.150	-0.348	0.528	-0.239	0.154	-0.664	0.064	-0.272	0.550	-0.642	0.581	1					
Th	-0.681	-0.375	0.261	-0.549	0.887	-0.424	-0.237	0.764	-0.257	-0.468	-0.414	0.881	0.272	0.731	0.105	-0.585	-0.393	0.75	-0.114	-0.372	1				
Ti	-0.401	-0.246	0.472	-0.306	0.861	-0.162	0.164	0.423	0.162	-0.270	-0.260	0.825	0.590	0.434	-0.120	-0.325	-0.226	0.425	0.244	-0.309	0.604	1			
U	-0.311	-0.325	-0.074	-0.273	0.040	0.348	-0.415	0.078	-0.275	-0.275	0.558	0.160	-0.192	0.036	0.203	-0.289	0.555	0.066	0.101	0.503	0.164	-0.233	1		
V	-0.541	-0.340	0.245	-0.420	0.937	-0.279	0.037	0.729	-0.037	-0.360	-0.317	0.87	0.368	0.72	0.082	-0.449	-0.301	0.72	0.016	-0.554	0.861	0.785	-0.164	1	
W	-0.023	0.471	0.023	-0.250	-0.382	0.947	0.076	-0.587	-0.074	-0.330	0.77	-0.335	0.078	-0.601	0.368	-0.236	0.774	-0.596	0.658	0.73	-0.518	-0.265	0.190	-0.384	1

**. Correlation is significant at the 0.01 level (2-tailed).

*. Correlation is significant at the 0.05 level (2-tailed).



Table S3-5. Heatmap of Pearson's correlation coefficients of selected critical and rare metals detected in pyrite from Vathi after LA-ICP-MS analyses.

Correlations											
	Ag	Bi	Co	Hg	In	Sb	Se	Te	Ti	V	W
Ag	1										
Bi	-0.039	1									
Co	-0.037	0.660	1								
Hg	-0.016	-0.037	0.105	1							
In	0.039	0.023	0.054	0.037	1						
Sb	0.169	-0.025	-0.050	-0.056	0.069	1					
Se	-0.125	-0.060	0.108	0.086	0.048	-0.184	1				
Te	-0.105	-0.060	-0.121	0.353	-0.043	-0.178	-0.091	1			
Ti	-0.091	0.048	0.216	0.035	-0.029	-0.043	0.037	-0.106	1		
V	-0.014	-0.030	-0.068	-0.049	0.030	-0.083	-0.035	0.353	0.040	1	
W	0.144	-0.036	-0.080	-0.060	0.036	-0.111	-0.097	-0.097	-0.115	-0.048	1

**. Correlation is significant at the 0.01 level (2-tailed).
*. Correlation is significant at the 0.05 level (2-tailed).

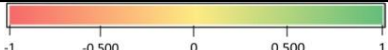


Table S3-6. Heatmap of Pearson's correlation coefficients of selected critical and rare metals detected in chalcopyrite from Vathi after LA-ICP-MS analyses.

Correlations															
	Ag	Bi	Cd	Co	Ga	Ge	Hg	In	Nb	Sb	Se	Te	Ti	V	W
Ag	1														
Bi	-0.209	1													
Cd	-0.142	-0.021	1												
Co	0.384	0.281	-0.145	1											
Ga	-0.090	-0.068	0.059	-0.086	1										
Ge	0.020	-0.168	-0.111	-0.129	-0.066	1									
Hg	0.765	-0.113	-0.074	0.59	-0.044	-0.066	1								
In	-0.59	0.266	0.305	-0.153	0.229	0.160	-0.409	1							
Nb	-0.089	-0.112	0.089	-0.086	-0.043	-0.066	-0.044	0.231	1						
Sb	0.773	-0.120	-0.079	0.585	-0.047	-0.039	0.998	-0.399	-0.047	1					
Se	0.322	-0.471	-0.317	0.150	-0.188	0.015	0.525	-0.401	-0.188	0.513	1				
Te	-0.088	-0.185	-0.124	-0.136	-0.073	-0.111	-0.074	0.082	-0.073	-0.079	0.385	1			
Ti	0.268	0.072	-0.097	0.175	-0.117	-0.177	-0.117	-0.083	0.177	-0.126	-0.338	-0.175	1		
V	-0.090	0.301	-0.073	0.524	-0.043	-0.066	-0.044	0.177	-0.043	-0.047	-0.188	-0.073	0.558	1	
W	0.577	-0.112	-0.073	-0.086	-0.043	-0.066	-0.044	-0.431	-0.043	-0.047	-0.188	-0.073	0.648	-0.043	1

**. Correlation is significant at the 0.01 level (2-tailed).
*. Correlation is significant at the 0.05 level (2-tailed).

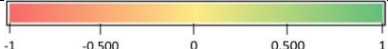


Table S3-7. Heatmap of Pearson's correlation coefficients of selected critical and rare metals detected in magnetite from Vathi after LA-ICP-MS analyses.

Correlations						
	Co	Ga	Ge	Ti	V	W
Co	1					
Ga	0.538	1				
Ge	-0.634	0.049	1			
Ti	0.410	0.027	0.099	1		
V	0.677	0.844	-0.281	-0.393	1	
W	^a	-0.553	-0.370	-0.473	0.956	1

* Correlation is significant at the 0.01 level (2-tailed).
* Correlation is significant at the 0.05 level (2-tailed).
a. Cannot be computed because at least one of the variables is constant.

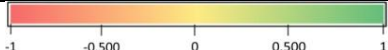


Table S3-8. Heatmap of Pearson's correlation coefficients of selected critical and rare metals detected in titanite from Vathi after LA-ICP-MS analyses.

Correlations														
	Ce	Ga	Gd	Ge	In	La	Nd	Sb	Se	Sm	Th	Ti	V	W
Ce	1													
Ga	0.510	1												
Gd	0.820	-0.254	1											
Ge	0.928	0.311	0.815	1										
In	-0.203	-0.908	0.137	0.085	1									
La	0.979	0.569	0.686	0.884	-0.324	1								
Nd	0.945	0.413	0.96	0.898	-0.062	0.861	1							
Sb	0.730	0.295	-0.541	1	-0.198	0.793	0.265	1						
Se	0.606	-0.141	0.792	0.066	-0.267	0.493	0.843	0.082	1					
Sm	0.865	-0.009	0.995	0.836	0.058	0.747	0.981	-0.293	0.897	1				
Th	0.901	0.983	0.869	0.925	-0.121	0.839	0.935	0.463	-0.127	0.89	1			
Ti	0.207	-0.680	0.221	0.122	0.388	0.172	0.187	0.146	0.768	0.223	-0.135	1		
V	0.95	0.271	0.953	0.935	0.018	0.867	0.993	0.520	0.851	0.971	0.933	0.225	1	
W	-0.678	-0.306	0.612	-0.997	0.174	-0.752	-0.191	-0.996	0.005	0.373	-0.475	-0.081	-0.447	1

** Correlation is significant at the 0.01 level (2-tailed).

* Correlation is significant at the 0.05 level (2-tailed).

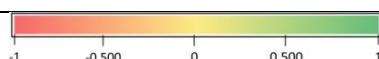


Table S3-9. Heatmap of Pearson's correlation coefficients of selected critical and rare metals detected in stibnite from Gerakario after LA-ICP-MS analyses.

Correlations																	
	Ag	Bi	Cd	Ce	Co	Ga	Ge	Hg	In	La	Nb	Sb	Se	Te	Ti	V	W
Ag	1																
Bi	0.413	1															
Cd	0.250	0.317	1														
Ce	0.094	0.231	-0.309	1													
Co	-0.113	0.163	0.252	0.153	1												
Ga	0.102	0.223	0.283	0.332	0.431	1											
Ge	-0.066	0.146	0.263	0.159	0.985	0.459	1										
Hg	-0.035	0.259	0.144	0.268	0.853	0.289	0.814	1									
In	-0.367	-0.004	-0.174	0.123	0.443	0.327	0.437	0.378	1								
La	-0.055	0.212	-0.446	0.919	0.107	0.299	0.097	0.203	0.191	1							
Nb	0.062	-0.224	0.455	-0.913	-0.107	-0.289	-0.095	-0.200	-0.189	-0.999	1						
Sb	-0.241	-0.564	-0.492	0.563	-0.087	0.031	-0.057	-0.024	0.108	0.589	-0.569	1					
Se	-0.093	0.258	0.132	0.238	0.837	0.252	0.769	0.982	0.371	0.196	-0.196	-0.061	1				
Te	0.234	0.419	0.099	-0.072	-0.075	-0.259	-0.078	-0.024	0.156	-0.016	0.012	-0.241	-0.024	1			
Ti	0.170	-0.169	-0.083	-0.059	-0.062	0.290	-0.118	0.083	0.010	0.038	-0.038	0.079	0.132	-0.270	1		
V	0.234	0.419	0.099	-0.072	-0.075	-0.259	-0.078	-0.024	0.156	-0.016	0.012	-0.241	-0.024	1	-0.270	1	
W	0.222	0.438	0.138	-0.045	-0.075	-0.271	-0.080	-0.002	0.136	-0.005	0.001	-0.244	-0.002	0.995	-0.283	0.995	1

** Correlation is significant at the 0.01 level (2-tailed).

* Correlation is significant at the 0.05 level (2-tailed).

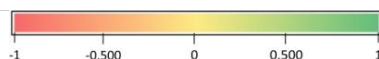


Table S3-10. Heatmap of Pearson's correlation coefficients of selected critical and rare metals detected in pyrite from Laodikino after LA-ICP-MS analyses.

Correlations												
	Ag	Au	Bi	Co	Hg	In	Sb	Se	Te	Ti	V	W
Ag	1											
Au	-0.038	1										
Bi	-0.160	0.172	1									
Co	-0.136	0.290	0.045	1								
Hg	-0.185	-0.206	0.030	0.002	1							
In	0.94	-0.085	-0.105	-0.084	-0.208	1						
Sb	-0.043	-0.139	-0.164	-0.159	-0.202	-0.057	1					
Se	-0.107	-0.005	0.549	-0.120	0.176	-0.059	-0.302	1				
Te	0.061	-0.088	-0.114	-0.017	0.077	0.166	-0.107	0.148	1			
Ti	-0.071	0.114	-0.294	0.089	-0.122	-0.057	0.126	-0.309	-0.072	1		
V	-0.012	0.091	-0.553	0.070	-0.173	0.061	0.105	-0.267	0.065	0.544	1	
W	-0.062	-0.058	0.853	-0.065	0.172	-0.040	-0.062	0.391	-0.043	-0.379	-0.695	1

** Correlation is significant at the 0.01 level (2-tailed).

* Correlation is significant at the 0.05 level (2-tailed).



Table S3-11. Heatmap of Pearson's correlation coefficients of selected critical and rare metals detected in chalcopyrite from Laodikino after LA-ICP-MS analyses.

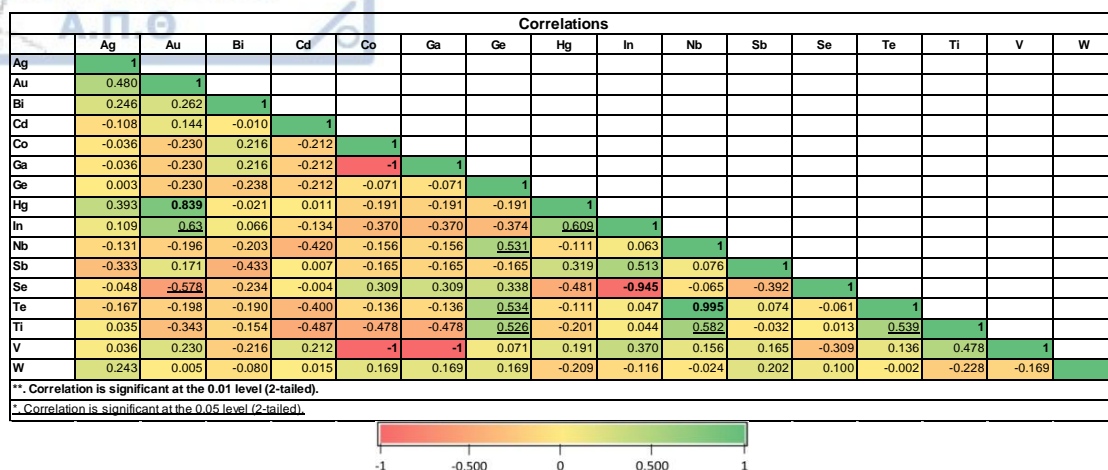


Table S3-12. Heatmap of Pearson's correlation coefficients of selected critical and rare metals detected in sphalerite from Laodikino after LA-ICP-MS analyses.

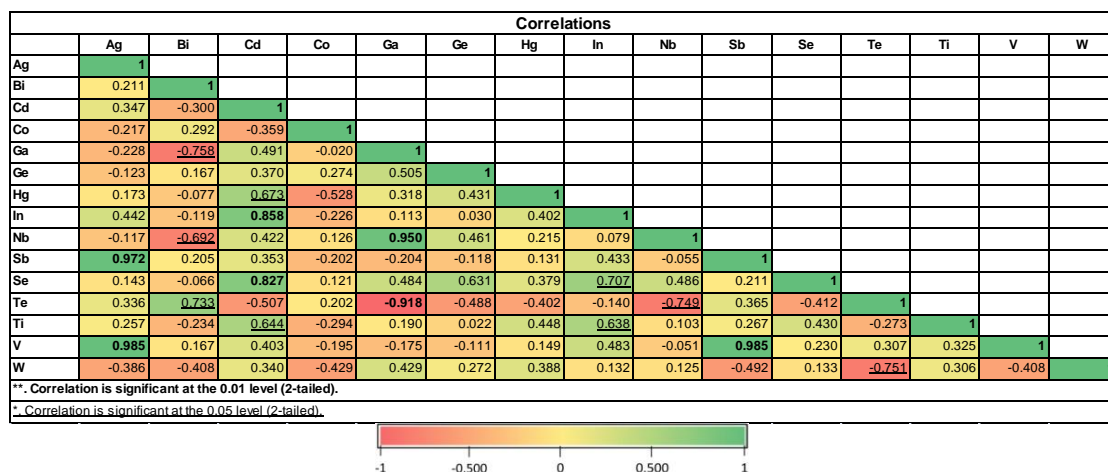


Table S3-13. Heatmap of Pearson's correlation coefficients of selected critical and rare metals detected in tetrahedrite from Laodikino after LA-ICP-MS analyses.

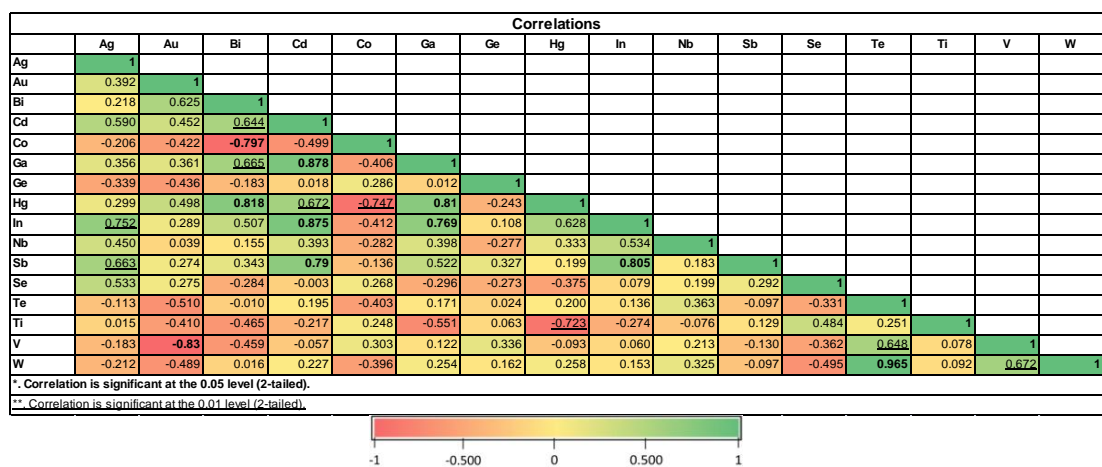


Table S3-14. Heatmap of Pearson's correlation coefficients of selected critical and rare metals detected in magnetite from Laodikino after LA-ICP-MS analyses.

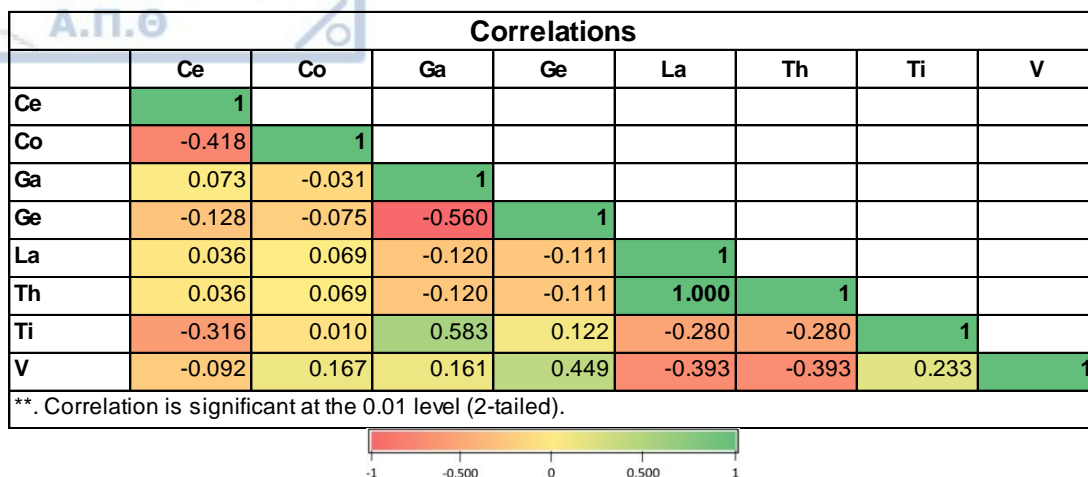


Table S3-15. Heatmap of Pearson's correlation coefficients of selected critical and rare metals detected in pyrite from Kolchiko after LA-ICP-MS analyses.

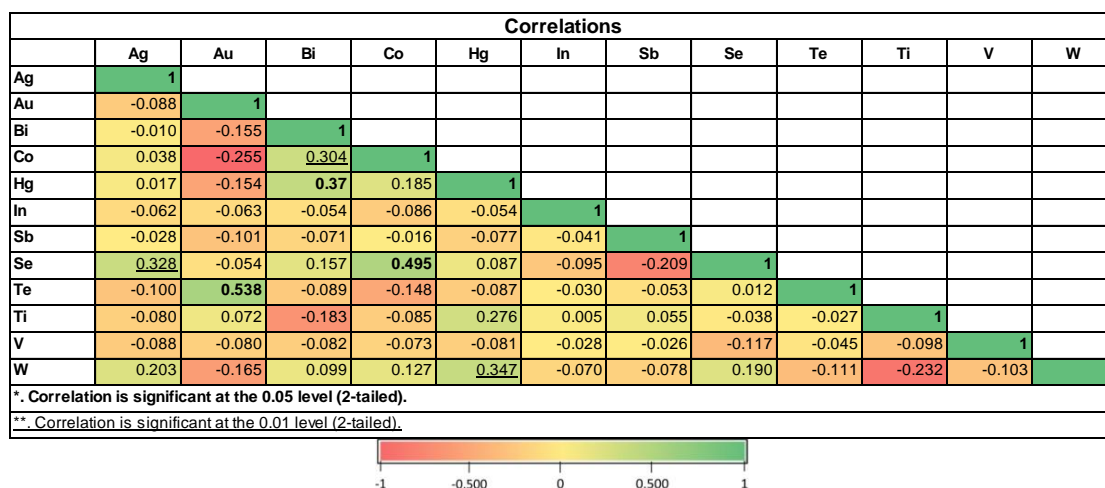


Table S3-16. Heatmap of Pearson's correlation coefficients of selected critical and rare metals detected in chalcopyrite from Kolchiko after LA-ICP-MS analyses.

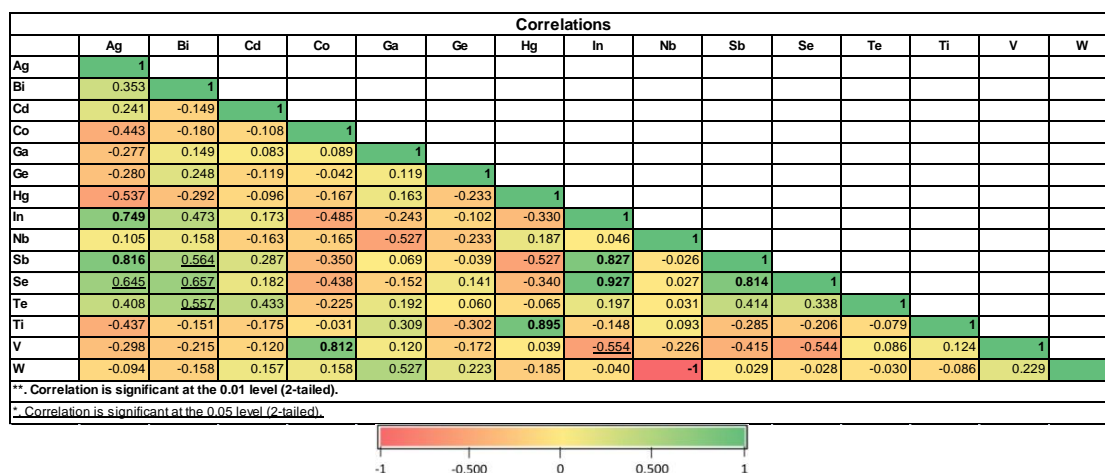


Table S3-17. Heatmap of Pearson's correlation coefficients of selected critical and rare metals detected in sphalerite from Kolchiko after LA-ICP-MS analyses.

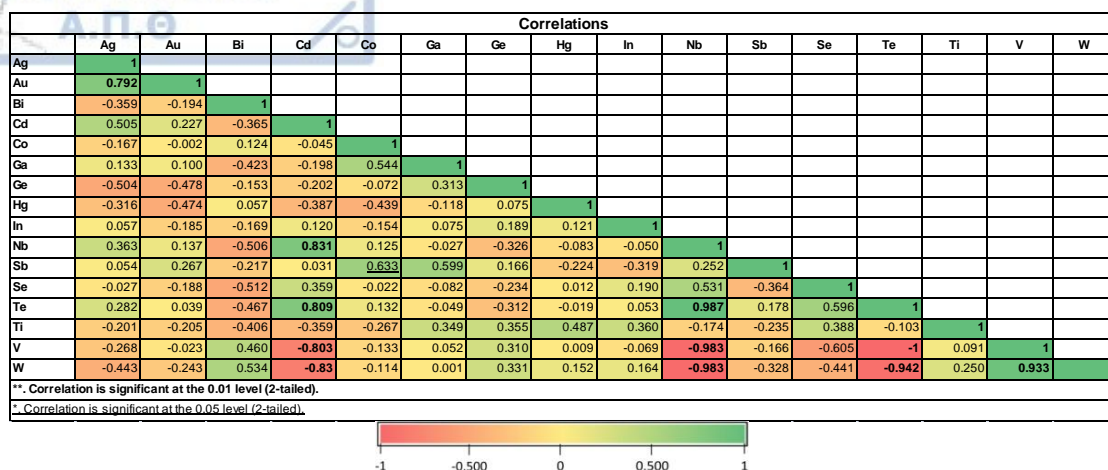


Table S3-18. Heatmap of Pearson's correlation coefficients of selected critical and rare metals detected in arsenopyrite from Kolchiko after LA-ICP-MS analyses.

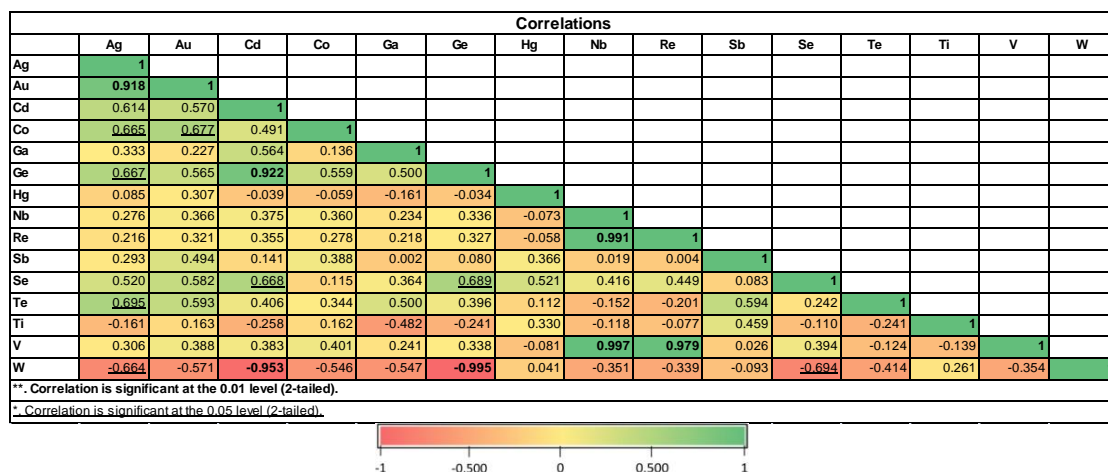


Table S3-19. Heatmap of Pearson's correlation coefficients of selected critical and rare metals detected in pyrite from Aspra Chomata after LA-ICP-MS analyses.

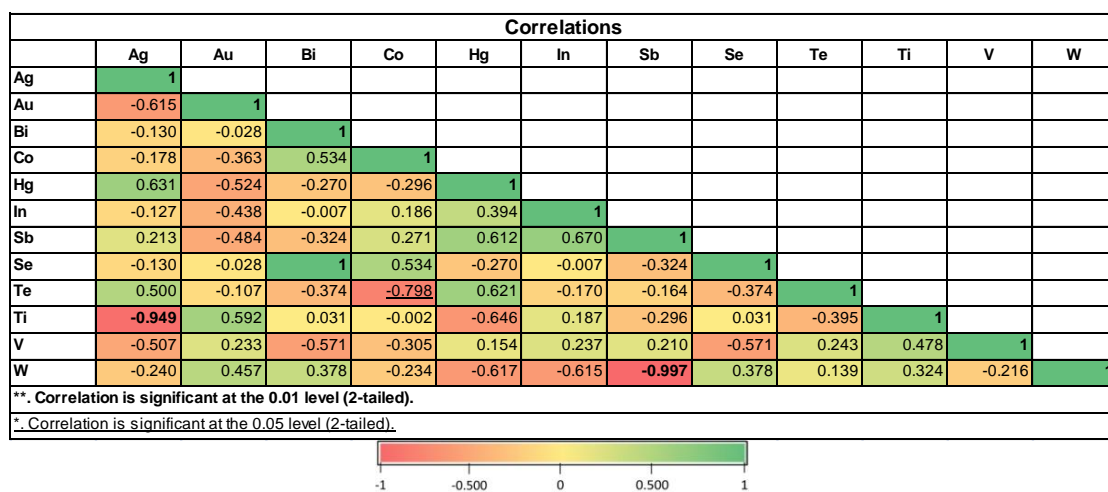


Table S3-20. Heatmap of Pearson's correlation coefficients of selected critical and rare metals detected in sphalerite from Aspra Chomata after LA-ICP-MS analyses.

Correlations														
	Ag	Bi	Cd	Co	Ga	Ge	Hg	In	Sb	Se	Te	Ti	V	W
Ag	1													
Bi	-0.031	1												
Cd	0.166	-0.061	1											
Co	0.206	-0.016	-0.079	1										
Ga	-0.054	0.023	0.121	0.226	1									
Ge	0.227	-0.045	0.276	0.057	-0.154	1								
Hg	-0.291	0.011	-0.438	0.223	0.089	-0.119	1							
In	0.248	0.052	0.072	0.246	-0.047	-0.011	0.026	1						
Sb	0.220	0.047	0.028	0.163	0.100	0.250	0.099	-0.019	1					
Se	0.206	-0.016	-0.079	1	0.226	0.057	0.223	0.246	0.163	1				
Te	-0.206	0.016	0.079	-1	-0.226	-0.057	-0.223	-0.246	-0.163	-1	1			
Ti	-0.339	0.054	0.026	0.018	0.055	0.551	-0.025	0.041	0.291	0.018	-0.018	1		
V	0.879	0.002	0.151	0.358	-0.023	0.065	-0.101	0.221	-0.057	0.358	-0.358	-0.539	1	
W	0.875	0.007	0.186	0.071	-0.095	0.052	-0.177	0.159	-0.112	0.071	-0.071	-0.582	0.956	1

**. Correlation is significant at the 0.01 level (2-tailed).

*. Correlation is significant at the 0.05 level (2-tailed).

-1

-0.500

0

0.500

1

SUPPLEMENT 4

Supplement 4. Datasets of bulk geochemical analyses.

Table S4-1. Bulk geochemical analyses of major, trace and rare earth elements of analyzed samples from Vathi. Geochemical analysis previously published by Stergiou et al. (2021) are also given. b.d.l. = below detection limit; n.a. = not analyzed.

	Latite																			
	Propylitic alteration			Sericitic alteration																
	Vath 10	Vath 19	Vath 42	Vath 01	VTH 3	VTH 4	Vath 05	Vath 07	VTH 11	VTH 12	Vath 12a	VTH 14	Vath 17	Vath 20	Vath 27b	Vath 34	Vath 38	Vath 40	Vath 45	
	Stergiou et al. 2021			Stergiou et al. 2021																
Major oxides (wt.%)																				
SiO ₂	66.73	n.a.	61.57	71.99	56.83	55.79	n.a.	n.a.	59.58	63.82	n.a.	56.93	67.09	n.a.	69.35	67.87	n.a.	n.a.	n.a.	
Al ₂ O ₃	16.35	n.a.	15.85	15.91	13.05	13.08	n.a.	n.a.	14.27	15.03	n.a.	13.56	14.80	n.a.	16.88	16.75	n.a.	n.a.	n.a.	
Fe ₂ O ₃	3.38	n.a.	5.68	2.67	19.22	20.95	n.a.	n.a.	10.98	5.65	n.a.	0.69	8.26	n.a.	2.40	3.01	n.a.	n.a.	n.a.	
CaO	0.26	n.a.	2.63	0.05	0.05	0.09	n.a.	n.a.	0.29	0.13	n.a.	0.09	0.03	n.a.	0.16	0.2	n.a.	n.a.	n.a.	
MgO	0.32	n.a.	2.82	0.53	0.29	0.50	n.a.	n.a.	0.28	0.27	n.a.	0.25	0.59	n.a.	0.51	0.32	n.a.	n.a.	n.a.	
Na ₂ O	0.36	n.a.	4.38	0.14	0.07	0.10	n.a.	n.a.	0.70	0.42	n.a.	0.25	0.09	n.a.	0.15	0.73	n.a.	n.a.	n.a.	
K ₂ O	8.79	n.a.	2.67	5.12	4.10	4.55	n.a.	n.a.	5.90	7.69	n.a.	5.19	5.22	n.a.	4.94	0.39	n.a.	n.a.	n.a.	
MnO	0.02	n.a.	0.04	0.01	0.01	0.03	n.a.	n.a.	0.01	b.d.l.	n.a.	b.d.l.	0.02	n.a.	b.d.l.	0.01	n.a.	n.a.	n.a.	
TiO ₂	0.48	n.a.	0.49	0.48	0.38	0.40	n.a.	n.a.	0.41	0.44	n.a.	0.44	0.42	n.a.	0.54	0.44	n.a.	n.a.	n.a.	
Trace elements (ppm)																				
Ag	0.60	0.70	0.45	3	0.80	1	1.1	0.77	0.30	2.4	0.39	4.6	0.10	0.94	0.80	0.32	0.48	0.10	0.04	
As	2.7	4	30	5.4	2.9	2.4	7.8	3.7	2.4	1.4	3	8.4	3.3	183	2.3	1.9	1	11	5.4	
B	n.a.	n.a.	n.a.	n.a.	n.a.	n.a.	n.a.	n.a.	n.a.	n.a.	n.a.	n.a.	n.a.	n.a.	n.a.	b.d.l.	b.d.l.	b.d.l.	b.d.l.	
Ba	1219	1330	189	159	341	99	89	719	1266	1876	927	5043	78	158	478	120	38	39	25	
Be	3	4	0.57	5	3	1	4	4	1	5	4	b.d.l.	5	5	5	0.56	0.74	1.7	1.2	
Bi	12	2.9	4.6	6.8	4.5	239	13	12	3	8	5.5	1.2	9.0	9.3	4.6	14.1	0.84	1.4	1.1	
Cd	0.06	0.02	0.27	b.d.l.	0.80	7.7	0.68	0.18	2.4	2.5	b.d.l.	b.d.l.	b.d.l.	b.d.l.	0.21	0.10	3.8	0.09	0.02	
Ce	107	78	123	13	75	139	91	141	101	119	74	94	122	160	76	121	92	94	31	
Co	0.90	0.70	38	0.90	1.6	2.5	0.50	1	3.4	0.60	1	1.1	3.3	2.8	2.5	17	18	48	450	
Cr	4	4	79	4	n.a.	n.a.	5	6	n.a.	n.a.	5	n.a.	4	5	5	2	1	2	5	
Cs	8.1	7	4.7	8.6	7.9	5.4	6.7	6.4	11	7.7	5.6	7.8	5.6	6.9	10	2.6	2.4	3.2	2.8	

Cu	85	88	117	404	1450	1277	1274	1073	9297	> 10,000	341	> 10,000	1502	143	612	59	3674	120	27
Dy	3.2	3.2	4.4	2.1	3.4	10	3.5	3.7	5.8	6.4	1.9	3.4	1.9	2.2	2.6	2.0	3	2.6	2.0
Er	1.8	1.8	2.9	1	2.1	5.1	1.8	2	3.8	3.9	1.3	1.7	0.90	1	1.8	0.78	1.5	1.2	0.87
Eu	1.7	1.2	1.6	0.50	1.4	3.6	2.4	2.2	2.0	2.0	1	1.2	1.9	1.8	1.1	1.6	1.2	1.1	0.93
Ga	20	20	9.4	22	15	15	24	21	16	15	21	15	20	19	21	2.2	1.7	1.9	5.1
Gd	4.1	4.3	6.6	2	4.4	14	6	5.5	6.5	7.4	3.6	5.0	3.8	4.1	4	4.5	4.1	4.0	2.3
Ge	n.a.	n.a.	0.24	n.a.	n.a.	n.a.	n.a.	n.a.	n.a.	n.a.	n.a.	n.a.	n.a.	n.a.	n.a.	0.13	0.11	0.11	0.09
Hf	2.5	2.5	0.16	2	4.6	4.3	2.1	2.7	5	4.9	2.4	5.7	1.8	2.4	2.1	0.19	0.17	0.26	0.11
Hg	n.a.	n.a.	0.20	n.a.	0.01	b.d.l.	n.a.	n.a.	0.01	b.d.l.	n.a.	0.11	n.a.	n.a.	n.a.	0.42	0.32	0.22	0.10
Ho	0.60	0.70	0.95	0.40	0.60	1.9	0.60	0.70	1.2	1.4	0.40	0.60	0.40	0.40	0.60	0.29	0.52	0.43	0.33
In	0.19	0.1	0.01	0.20	n.a.	n.a.	0.56	0.33	n.a.	n.a.	0.42	n.a.	0.63	0.29	0.21	0.08	0.08	0.05	b.d.l.
La	59	35	68	5.5	31	46	32	74	54	53	38	43	65	98	36	64	42	52	18
Li	11	14	11	9.6	n.a.	n.a.	6.5	12	n.a.	n.a.	12	n.a.	10	17	24	0.50	0.70	1.1	15
Lu	0.30	0.2	0.43	0.20	0.35	0.61	0.30	0.30	0.51	0.60	0.20	0.29	0.20	0.20	0.30	0.11	0.22	0.17	0.09
Mn	75	58	232	90	n.a.	n.a.	96	70	n.a.	n.a.	68	n.a.	191	46	49	93	41	4878	238
Mo	1.9	5.2	0.36	319	49	1.9	5	146	57	39	46	62	30	48	21	0.56	6.3	1.7	0.50
Nb	11	13	0.65	9.5	9.7	16	11	9.7	12	11	8.8	15	5.9	8.1	13	0.22	0.11	0.10	b.d.l.
Nd	39	30	46	8.4	37	93	44	49	41	46	30	39	46	46	32	47	35	33	12
Ni	2	1.7	40	2	6.7	6.3	1.8	3.3	5.7	2.3	2.6	1.2	4.2	9.1	5.6	1.1	2	40	162
P	n.a.	n.a.	n.a.	n.a.	n.a.	n.a.	n.a.	n.a.	n.a.	n.a.	n.a.	n.a.	n.a.	n.a.	n.a.	863	604	1113	809
Pb	51	307	117	93	24	41	76	29	40	99	82	89	11	139	99	29	29	41	22
Pr	13	8.7	13	1.7	9.1	20	13	15	11	13	8.2	11	14	16	9.1	13	10	9.5	3.3
Rb	287	261	64	420	241	339	406	345	170	267	292	190	367	244	213	42	32	24	36
Sb	3.8	2.9	1.8	5.4	0.10	0.30	6.6	3.4	0.20	0.10	1.7	0.20	3.5	19	2.4	3.5	1.3	0.99	0.56
Sc	4.8	6.7	7.6	4.3	9	9	7	6.1	6	7	4.6	7	5.2	4.9	6.2	2.5	1.8	2.2	4.4
Se	0.50	1.4	1.2	0.60	0.70	b.d.l.	0.60	b.d.l.	11	0.50	3.9	8.3	0.50	4.9	b.d.l.	b.d.l.	3.8	b.d.l.	7.9
Sm	6.2	5	8.1	2.2	6	17	8.7	8.1	7.5	8.7	5.2	6.9	6.5	6.3	4.9	7.7	5.7	5.4	2.4
Sn	7.3	7.6	4.2	15	8	32	16	10	9	5	4.3	5	8.3	11	13	5.3	1.5	b.d.l.	0.20
Sr	196	208	55	28	62	11	11	200	291	269	237	321	10	233	150	19	11	20	16
Ta	0.90	1	1.4	0.60	0.80	0.80	0.70	0.90	0.90	0.90	0.70	1.6	0.50	0.70	1	b.d.l.	b.d.l.	b.d.l.	b.d.l.
Tb	0.40	0.5	0.84	0.20	0.60	2.0	0.60	0.60	1	1.1	0.30	0.69	0.30	0.30	0.40	0.47	0.55	0.51	0.35
Te	b.d.l.	0.1	0.49	0.09	b.d.l.	b.d.l.	b.d.l.	0.09	b.d.l.	b.d.l.	0.27	b.d.l.	0.05	0.51	b.d.l.	0.01	b.d.l.	0.27	0.06
Th	46	44	44	37	37	37	42	43	39	40	21	39.7	37	53	41	39	40	36	24
Tl	5.7	4.6	0.83	5.4	0.90	0.90	4.3	4.6	0.60	0.80	4.5	0.60	4.2	3.5	4.1	0.56	0.44	0.35	0.41
Tm	0.30	0.3	0.39	0.20	0.33	0.77	0.30	0.30	0.54	0.59	0.20	0.27	0.20	0.20	0.30	0.10	0.22	0.17	0.11
U	9.6	9.8	8.3	9.4	71	14	32	28	20	32	12	14	12	11	11	6.1	15	21	6.2



V	82	85	90	52	91	72	68	102	42	46	66	62	72	56	101	25	21	20	68
W	8.2	23	117	12	11	124	24	14	6.2	8.9	119	4.7	10	>200	7.7	197	136	122	95
Y	15	16	27	13	20	54	13	15	31	36	11	16	7.5	9.9	14	8.1	14	13	9.2
Yb	1.9	1.8	2.8	1.2	2.1	3.8	1.8	2	3.5	3.9	1.2	1.7	1.4	1.5	1.8	0.66	1.4	1.1	0.63
Zn	22	20	54	54	115	212	19	28	38	28	16	9	37	108	67	14	20	82	19
Zr	64	65	184	7.8	176	162	52	65	176	192	58	193	45	59	54	7.1	6.4	11	5.7
Trace elements (ppb)																			
Au	8	6	36	20	103	1170	118	7.2	135	98	21	26	30	33	4	72	216	7.6	4.3
Re	b.d.l.	3	3	b.d.l.	n.a.	n.a.	b.d.l.	b.d.l.	n.a.	n.a.	3	n.a.	b.d.l.	5	b.d.l.	2	2	9	3

Table S4-1. Continued.

	Quartz monzonite					Oxidized mineralization	Phreatic breccia	Cataclasite
	Potassic-calcic alteration	Sericitic alteration			Relatively fresh	Sericitic alteration		
	Vath 44	Vath 30	Vath 32	Vath 43	Vath 41	VTH6	Vath 15	Vath 33
		Stergiou et al. 2021				Stergiou et al. 2021		
Major oxides (wt.%)								
SiO ₂	n.a.	n.a.	69.69	n.a.	63.05	7.58	n.a.	66.70
Al ₂ O ₃	n.a.	n.a.	15.67	n.a.	16.13	4.45	n.a.	16.67
Fe ₂ O ₃	n.a.	n.a.	3.14	n.a.	5.09	73.31	n.a.	3.34
CaO	n.a.	n.a.	0.05	n.a.	3.13	0.07	n.a.	1.11
MgO	n.a.	n.a.	0.50	n.a.	1.78	0.17	n.a.	1.85
Na ₂ O	n.a.	n.a.	0.15	n.a.	4.01	b.d.l.	n.a.	3.06
K ₂ O	n.a.	n.a.	6.84	n.a.	4.69	0.80	n.a.	4.22
MnO	n.a.	n.a.	0.01	n.a.	0.12	0.02	n.a.	0.03
TiO ₂	n.a.	n.a.	0.48	n.a.	0.51	0.05	n.a.	0.84
Trace elements (ppm)								
Ag	0.05	0.30	0.07	0.89	0.12	4.2	3.5	0.30
As	16	132	4.8	4.1	3.6	473	61	4.8
B	b.d.l.	n.a.	n.a.	b.d.l.	n.a.	n.a.	n.a.	n.a.
Ba	80	59	208	210	144	74	176	1645
Be	0.27	5	4	0.84	1.1	2	3	2
Bi	0.34	2.4	2.7	3.4	0.49	5.8	18	0.41
Cd	0.05	0.15	b.d.l.	0.09	0.09	6.9	b.d.l.	0.03
Ce	62	145	64	68	153	40	894	69
Co	13	103	1.9	30	23	42	1	6.8
Cr	32	7	5	5	81	n.a.	18	69
Cs	0.51	6.4	7.6	3.4	2.9	3	13	6.3
Cu	317	17	15	2577	54	> 10,000	722	109
Dy	2.8	4.1	1.3	2.9	4.8	5.4	5.5	3.8
Er	1.4	1.8	0.70	1.5	2.8	3.1	2.1	1.8
Eu	0.84	2.3	1	0.80	2.4	0.95	5.1	1.1
Ga	7.7	19	19	8.5	6.0	5.8	23	24
Gd	4.1	7.2	2.9	3.9	7.8	3.9	13	5.7
Ge	0.20	n.a.	n.a.	0.19	0.18	n.a.	n.a.	n.a.
Hf	0.12	2.2	2.4	0.11	0.30	0.80	1.5	0.02
Hg	0.11	n.a.	n.a.	0.19	0.19	0.86	n.a.	n.a.
Ho	0.48	0.80	0.30	0.50	0.98	1.1	0.90	0.80
In	0.02	0.19	0.49	0.12	0.01	n.a.	0.81	0.04
La	27	68	33	35	83	23	613	34
Li	1.7	7.2	11	6.9	4.8	n.a.	17	13
Lu	0.19	0.30	0.20	0.23	0.44	0.45	0.30	0.20
Mn	329	6798	93	400	427	n.a.	61	165
Mo	0.40	2.2	5.0	5.7	1.2	> 2000	341	1.8
Nb	0.64	10	4.7	1.2	1.2	0.20	3.8	5.7
Nd	27	61	26	28	85	14	211	33
Ni	151	92	3.9	12	4.9	47	3.7	41
P	2063	n.a.	n.a.	1402	n.a.	n.a.	n.a.	n.a.
Pb	20	137	18	33	51	977	28	20
Pr	6.9	18	7.4	7.6	16	3.7	79	8.8
Rb	3	318	89	52	31	63	321	159
Sb	0.62	1.1	1.7	1.2	2.5	19	11	0.52
Sc	2.1	6.1	6.4	4.6	2.2	7	10	17
Se	b.d.l.	0.40	2.3	2.8	1.2	47	b.d.l.	b.d.l.
Sm	5.0	11	4.5	4.9	10	2.9	23	6.2
Sn	4.9	8.4	2	2	1.8	3	8.3	3.6
Sr	30	131	128	506	58	64	47	187
Ta	b.d.l.	0.80	0.30	b.d.l.	1.8	0.10	0.30	0.50
Tb	0.53	0.80	0.10	0.53	1	0.80	1.3	0.60
Te	0.03	0.49	0.17	1.5	0.49	3	0.09	0.09



Th	42	34	55	47	68	75	36	13
Tl	0.07	4.4	5.2	0.39	0.21	0.30	4.3	2.4
Tm	0.19	0.30	0.10	0.21	0.44	0.52	0.40	0.30
U	4.6	15	21	20	16	263	41	2.7
V	304	81	64	117	112	b.d.l.	205	148
W	75	73	12	156	181	14	44	6.4
Y	14	21	6.7	14	15	29	27	22
Yb	1.2	1.7	0.90	1.4	2.8	3.3	2.2	1.6
Zn	15	156	19	29	39	39	34	33
Zr	3.6	52	59	2.6	6.2	26	38	1.1
Trace elements (ppb)								
Au	5.8	20	4	774	37	6996	724	7
Re	2	b.d.l.	b.d.l.	9	3	n.a.	3	b.d.l.

Table S4-2. Bulk geochemical analyses of major, trace and rare earth elements of analyzed samples from Gerakario. b.d.l. = below detection limit; n.a. = not analyzed.

	Two-mica gneiss				
	Sericitic alteration				
	Quartz-stibnite veins				
	Ger 3.1		Ger 05		
Major elements (wt.%)					
Al					
Ca	0.04			0.01	
Fe	0.33			0.46	
K	0.36			0.2	
Mg	0.02			b.d.l.	
Na	b.d.l.			b.d.l.	
S	0.02			0.03	
	16			19	
S	b.d.l.			b.d.l.	
Ti					
	Ger 3.1	Ger 05		Ger 3.1	Ger 05
Trace elements (ppm)					
Ag	0.98	1.2	Pb	22	20
As	6.2	4.6	Pr	b.d.l.	b.d.l.
Au	0.05	0.04	Rb	0.9	0.4
B	12	28	Re	b.d.l.	b.d.l.
Ba	b.d.l.	b.d.l.	Sb	326,000	574,000
Be	b.d.l.	b.d.l.	Sc	b.d.l.	b.d.l.
Bi	0.02	0.03	Se	b.d.l.	b.d.l.
Cd	0.05	0.04	Sm	b.d.l.	b.d.l.
Ce	0.09	0.12	Sn	0.5	0.6
Co	1.8	0.9	Sr	17	22
Cr	202	97	Ta	b.d.l.	b.d.l.
Cs	0.15	0.18	Tb	b.d.l.	b.d.l.
Cu	27	31	Te	b.d.l.	b.d.l.
Dy	b.d.l.	b.d.l.	Th	b.d.l.	b.d.l.
Er	b.d.l.	b.d.l.	Ti	b.d.l.	b.d.l.
Eu	b.d.l.	b.d.l.	Tl	0.81	0.86
Ga	0.16	0.07	Tm	b.d.l.	b.d.l.
Gd	b.d.l.	b.d.l.	U	0.09	0.13
Ge	b.d.l.	b.d.l.	V	b.d.l.	b.d.l.
Hf	b.d.l.	b.d.l.	W	b.d.l.	b.d.l.
Hg	b.d.l.	b.d.l.	Y	0.16	0.13
Ho	b.d.l.	b.d.l.	Yb	b.d.l.	b.d.l.
In	b.d.l.	b.d.l.	Zn	6	b.d.l.
La	0.4	0.4	Zr	b.d.l.	b.d.l.
Li	0.1	b.d.l.			
Lu	b.d.l.	b.d.l.			
Mn	33	20			
Mo	0.12	0.09			
Nb	b.d.l.	b.d.l.			
Nd	b.d.l.	b.d.l.			
Ni	5.9	3.6			
P	12	14			
Pb	22	20			
Pr	b.d.l.	b.d.l.			

Table S4-3. Bulk geochemical analyses of major, trace and rare earth elements of analyzed samples from Laodikino. b.d.l. = below detection limit; n.a. = not analyzed.

	Polymetallic quartz veins		Magnetite-rich pods		Quartz vein	Pegmatite	Two mica gneiss	
	Sericitization		Chloritization		Chloritization	Sericitization	Sericitization and supergene oxidation	
	LAO 08bi	LAO 08bii	LAO 08	LAO 08a	LAO 06a	LAO 07	LAO 10	LAO 11
Major elements (wt.%)								
SiO ₂	n.a.	n.a.	n.a.	n.a.	n.a.	60.8	68.02	n.a.
Al ₂ O ₃	n.a.	n.a.	n.a.	n.a.	n.a.	20.73	17.26	n.a.
Fe ₂ O ₃	n.a.	n.a.	n.a.	n.a.	n.a.	2.77	2.48	n.a.
CaO	n.a.	n.a.	n.a.	n.a.	n.a.	0.29	0.01	n.a.
MgO	n.a.	n.a.	n.a.	n.a.	n.a.	1.22	1.2	n.a.
Na ₂ O	n.a.	n.a.	n.a.	n.a.	n.a.	3.3	0.38	n.a.
K ₂ O	n.a.	n.a.	n.a.	n.a.	n.a.	5.57	5.94	n.a.
MnO	n.a.	n.a.	n.a.	n.a.	n.a.	0.04	0.04	n.a.
TiO ₂	n.a.	n.a.	n.a.	n.a.	n.a.	0.19	0.07	n.a.
P ₂ O ₅	n.a.	n.a.	n.a.	n.a.	n.a.	0.13	b.d.l.	n.a.
BaO	n.a.	n.a.	n.a.	n.a.	n.a.	0.11	0.07	n.a.
Cr ₂ O ₃	n.a.	n.a.	n.a.	n.a.	n.a.	0.02	b.d.l.	n.a.
SrO	n.a.	n.a.	n.a.	n.a.	n.a.	b.d.l.	b.d.l.	n.a.
Major elements (ppm)								
Al	0.12	0.14	3.1	1.6	1.4	0.62	0.16	0.79
Ca	3.8	3.5	12	8.6	0.03	0.14	0.01	0.03
Fe	19	23	8.6	8.8	4.1	0.36	0.25	4.5
K	0.02	0.01	0.04	0.02	0.1	0.53	0.23	0.11
Mg	0.11	0.14	2.3	1.4	0.96	0.06	0.01	0.37
Na	b.d.l.	0.01	b.d.l.	b.d.l.	b.d.l.	0.05	b.d.l.	0.02
S	31	32	1.1	0.69	0.04	0.01	0.07	b.d.l.
Ti	b.d.l.	b.d.l.	0.02	0.01	0.02	0.01	b.d.l.	0.01
Trace elements (ppm)								
Ag	2,433	1,750	0.15	0.22	1.6	0.17	0.12	0.33
As	2,497	6,334	50	24	19	3.8	2	184
Au	3	2.2	0.06	0.03	0.01	0.003	0.002	0.02
B	b.d.l.	31	12	b.d.l.	b.d.l.	b.d.l.	b.d.l.	b.d.l.
Ba	b.d.l.	13	15	43	68	120	43	43
Be	b.d.l.	b.d.l.	0.55	0.38	0.24	0.3	0.11	0.27
Bi	83	77	0.83	0.65	0.04	0.02	0.2	0.16
Cd	247	207	0.39	0.41	1.7	0.16	b.d.l.	0.72
Ce	9	6.9	58	33	5.5	26	7.9	16
Co	166	81	28	21	33	6.1	9.8	30
Cr	1	106	26	18	242	96	b.d.l.	252
Cs	b.d.l.	b.d.l.	0.08	0.06	0.69	0.24	0.23	0.25
Cu	98,350	75,890	115	197	32	3.2	1.4	4,488
Dy	1.4	1.16	4.6	4.1	1	3.5	0.12	2.1
Er	0.74	0.57	1.96	1.95	0.7	2	0.05	1.2
Eu	0.28	0.27	1.7	1.1	0.18	0.32	0.05	0.32
Ga	1	1.2	11	8.5	4.3	2.1	0.47	1.9
Gd	1.4	1.3	6.8	4.7	0.95	3	0.28	2
Ge	0.16	0.29	0.3	0.23	0.15	b.d.l.	b.d.l.	0.14
Hf	b.d.l.	b.d.l.	0.02	b.d.l.	b.d.l.	0.02	b.d.l.	b.d.l.
Hg	187	171	0.05	0.05	0.2	0.06	0.82	0.53
Ho	0.25	0.21	0.71	0.68	0.21	0.65	0.02	0.39
In	53	53	0.1	0.15	0.01	b.d.l.	0.01	0.08
La	4.3	3.2	30	15	2.8	11	4.5	7.2
Li	0.3	0.4	14	8.1	10	2.2	0.8	2.2
Lu	0.12	0.08	0.39	0.41	0.24	0.27	b.d.l.	0.22
Mn	1,759	860	26,090	22,802	2,381	115	10	313
Mo	0.11	0.42	0.98	0.66	1.6	1	0.11	1.49
Nb	b.d.l.	0.12	0.12	0.14	0.09	0.19	0.08	0.14

Nd	4.6	3.9	31	18	3	13	2.7	7.4
Ni	62	78	29	27	39	3.1	0.3	18
P	b.d.l.	b.d.l.	190	174	70	623	23	604
Pb	3,279	7,463	8.3	9.3	224	25	2.9	40
Pr	1.1	0.96	7.5	4.3	0.71	3.2	0.8	1.8
Rb	0.6	0.3	2.4	1.3	9.3	22	10	5.5
Re	b.d.l.	b.d.l.	0.002	0.002	0.003	0.002	0.001	0.003
Sb	70,500	54,000	1.3	1.5	69	6.9	2.17	10
Sc	0.4	0.8	12	12	0.7	0.7	b.d.l.	0.5
Se	24	59	0.8	0.5	b.d.l.	b.d.l.	b.d.l.	1.3
Sm	1.3	1.1	6.9	4.3	0.76	2.8	0.44	1.8
Sn	1.4	2.8	0.3	0.3	0.4	0.2	3.1	0.6
Sr	79	46	439	506	5.3	3.8	3.3	13
Ta	b.d.l.	b.d.l.	0.02	0.02	0.03	0.01	b.d.l.	b.d.l.
Tb	0.23	0.19	0.94	0.74	0.16	0.52	0.03	0.32
Te	0.03	0.03	0.07	0.06	0.01	b.d.l.	b.d.l.	0.33
Th	b.d.l.	0.3	4.3	3.4	0.4	10	0.7	2.4
Tl	0.28	0.21	0.04	0.03	0.3	0.14	0.08	0.07
Tm	0.11	0.07	0.29	0.29	0.12	0.29	b.d.l.	0.19
U	1.1	0.74	1.5	0.87	1	1	0.09	3.5
V	10	4	35	46	10	3	b.d.l.	10
W	b.d.l.	0.26	84	123	400	127	207	325
Y	7.5	5.2	22	20	6.8	18	0.47	9.8
Yb	0.7	0.5	2	2.2	0.94	1.8	0.04	1.3
Zn	43,200	40,000	109	112	313	31	b.d.l.	125
Zr	b.d.l.	b.d.l.	0.9	0.6	b.d.l.	b.d.l.	b.d.l.	b.d.l.

Table S4-4. Bulk geochemical analyses of major, trace and rare earth elements of analyzed samples from Kolchiko. b.d.l. = below detection limit; n.a. = not analyzed.

	Mica schist	Pegmatite	Milky quartz veins		Polymetallic massive veins								Polymetallic quartz veins			Quartz-pyrite vein
	Sericitization															
	KL 02b	KL 06	KL 01	KL 02a	KOLX 01a	KOLX 01bi	KOLX 01bii	KOLX 01c	KOLX 02a	KOLX 02bi	KOLX 03a	KOLX 03c	KL 13i	KL 13ii	KL 13a	KL 07
Major elements (wt.%)																
Al	0.45	0.33	0.06	0.99	0.03	0.02	0.06	0.01	b.d.l.	0.15	0.16	0.05	0.19	0.33	0.46	0.07
Ca	2.3	0.11	0.12	0.18	0.01	0.01	0.01	0.01	b.d.l.	0.01	0.02	b.d.l.	0.05	0.09	0.07	0.28
Fe	9.4	0.59	2.2	1.7	31	30	24	27	25	23	21	9.4	21	16	13	2.7
K	0.15	0.28	0.03	0.5	0.06	0.04	0.06	b.d.l.	b.d.l.	0.06	0.08	0.05	0.11	0.25	0.36	0.03
Mg	0.35	0.02	0.03	0.44	b.d.l.	b.d.l.	b.d.l.	b.d.l.	b.d.l.	b.d.l.	0.05	0.02	0.02	0.07	0.05	0.02
Na	0.02	0.07	0.01	0.08	b.d.l.	b.d.l.	b.d.l.	b.d.l.	b.d.l.	b.d.l.	b.d.l.	b.d.l.	0.02	0.01	0.02	0.01
S	0.6	0.02	0.56	0.15	>10	>10	9.3	>10	>10	6.6	9.1	9.9	>10	>10	11	2.2
Ti	0.01	b.d.l.	b.d.l.	0.06	b.d.l.	b.d.l.	b.d.l.	b.d.l.	b.d.l.	0.01	0.006	b.d.l.	b.d.l.	0.01	0.01	0.01
Trace elements (ppm)																
Ag	0.12	0.03	0.2	0.06	1.7	1.4	1.3	4.5	13	1.8	5.6	9.7	23	33	17	0.18
As	4266	1.9	17	284	370,900	356,300	285,300	1686	870	294,900	259,400	908	4308	5551	1729	1.1
Au	0.01	0.003	0.04	0.002	1.1	2.1	2.4	0.35	0.34	9.18	0.66	0.3	0.35	0.13	0.53	0.32
B	17	b.d.l.	b.d.l.	b.d.l.	21	23	21	23	15	17	15	b.d.l.	12	15	17	b.d.l.
Ba	18	76	b.d.l.	76	b.d.l.	b.d.l.	b.d.l.	b.d.l.	b.d.l.	16	13	11	b.d.l.	13	21	11
Be	0.17	0.5	b.d.l.	0.31	b.d.l.	b.d.l.	b.d.l.	b.d.l.	b.d.l.	b.d.l.	b.d.l.	b.d.l.	0.15	0.18	0.19	b.d.l.
Bi	3.5	0.19	108	1.2	262	466	504	181	390	693	190	425	995	694	739	30
Cd	0.17	0.03	b.d.l.	0.02	0.05	0.03	0.06	1.9	0.55	0.01	0.24	0.15	3.2	14	12	0.11
Ce	6.1	5.9	0.43	15	14	5.4	18	0.32	0.41	20	9.3	1.2	16	15	7.9	2.1
Co	53	4.4	2.7	4.4	296	275	269	124	78	161	261	89	320	245	159	19
Cr	6092	226	606	237	b.d.l.	b.d.l.	b.d.l.	b.d.l.	b.d.l.	2	b.d.l.	b.d.l.	b.d.l.	b.d.l.	271	503
Cs	0.82	0.15	b.d.l.	1.5	0.1	b.d.l.	0.1	0.05	b.d.l.	0.17	0.55	0.14	0.13	0.47	0.23	0.06
Cu	80	9.7	29	36	142	85	138	713	643	128	156	600	1159	615	1462	128
Dy	1.4	0.55	b.d.l.	1.8	0.19	0.09	0.15	b.d.l.	b.d.l.	0.26	0.5	0.07	1.4	1.7	1.5	0.39
Er	0.88	0.28	0.03	0.94	0.08	0.04	0.06	b.d.l.	b.d.l.	0.1	0.23	0.04	0.7	0.87	0.83	0.29
Eu	0.33	0.17	b.d.l.	0.25	0.08	0.04	0.06	b.d.l.	b.d.l.	0.13	0.19	b.d.l.	0.28	0.25	0.23	0.08
Ga	3.6	1.1	0.64	3.4	0.6	0.37	0.68	0.06	0.05	0.91	0.84	0.28	1.9	2.1	2.4	0.49
Gd	1.3	0.5	b.d.l.	1.7	0.34	0.15	0.3	b.d.l.	b.d.l.	0.5	0.67	0.07	1.5	1.7	1.3	0.31
Ge	0.07	b.d.l.	b.d.l.	b.d.l.	0.12	0.12	0.11	0.15	0.13	0.09	0.12	0.06	0.2	0.16	0.11	b.d.l.
Hf	b.d.l.	b.d.l.	b.d.l.	0.03	b.d.l.	b.d.l.	b.d.l.	b.d.l.	b.d.l.	b.d.l.	b.d.l.	b.d.l.	b.d.l.	b.d.l.	b.d.l.	0.03



Hg	b.d.l.	0.01	0.01	b.d.l.	0.04	0.05	0.07	0.09	0.10	0.04	0.05	0.16	0.1	0.25	0.12	0.008
Ho	0.28	0.1	b.d.l.	0.34	0.03	0.01	0.03	b.d.l.	b.d.l.	0.04	0.09	0.01	0.26	0.32	0.29	0.09
In	0.03	b.d.l.	b.d.l.	0.02	0.01	b.d.l.	0.01	0.07	0.38	0.01	0.02	0.07	0.13	0.44	0.35	b.d.l.
La	3.4	2.6	0.3	7.2	12	4.1	17	b.d.l.	0.3	10	4.1	0.7	7.1	7.6	3.7	1.1
Li	5.3	1	0.4	4.6	b.d.l.	0.2	0.2	0.3	b.d.l.	0.3	0.6	0.4	0.9	1.4	2.4	0.5
Lu	0.18	0.03	b.d.l.	0.12	0.02	b.d.l.	0.01	b.d.l.	b.d.l.	0.03	0.03	b.d.l.	0.12	0.14	0.12	0.04
Mn	2175	150	83	217	14	11	13	25	17	12	25	17	45	64	60	98
Mo	15	0.88	1	0.75	1.2	0.95	0.78	0.37	0.18	1.15	1.4	0.46	1.1	1	1.5	0.88
Nb	1.8	0.09	0.16	0.31	0.1	0.1	0.12	0.08	0.12	0.27	0.28	0.19	0.13	0.24	0.27	0.33
Nd	4	2.3	0.2	6.8	2.8	1.4	2.7	b.d.l.	0.1	4.9	3.9	0.4	6.2	5.6	4	1
Ni	141	7.3	12	6.9	36	32	24	50	39	24	27	12	46	34	30	20
P	414	423	38	672	52	32	146	b.d.l.	b.d.l.	77	66	22	187	501	369	26
Pb	11	35	84	3	50	37	61	480	229	3.7	130	315	2286	2900	1538	51
Pr	0.96	0.64	0.06	1.8	1.1	0.5	1.2	b.d.l.	0.04	1.8	1.1	0.12	1.8	1.6	1.1	0.27
Rb	9.9	8.2	1.2	27	0.7	0.5	0.8	0.4	0.1	2.3	5.6	2	4.4	12	14	1.5
Re	0.004	b.d.l.	b.d.l.	b.d.l.	0.004	0.002	0.003	0.002	0.004	b.d.l.	0.002	0.01	0.002	0.002	b.d.l.	b.d.l.
Sb	7.4	648	53	9.5	58	54	39	23	2.5	42	35	0.61	13	13	11	183
Sc	0.5	0.2	b.d.l.	1	0.2	0.1	0.2	b.d.l.	b.d.l.	0.3	0.2	b.d.l.	0.1	0.3	0.3	0.1
Se	0.5	b.d.l.	0.8	b.d.l.	9.6	8.8	7	10	17	6	11	5.7	38	31	19	1
Sm	1	0.49	0.05	1.6	0.44	0.23	0.38	b.d.l.	b.d.l.	0.8	0.85	0.07	1.6	1.6	1.2	0.26
Sn	5.2	0.3	0.4	3.2	0.2	b.d.l.	b.d.l.	1.2	0.4	0.4	0.8	0.6	0.3	0.7	1	0.4
Sr	35	7.6	3.3	4	5.1	1.8	8.5	0.7	0.4	11	2.6	1.8	2.5	3.1	2.4	3.9
Ta	b.d.l.	b.d.l.	b.d.l.	b.d.l.	b.d.l.	0.01	0.02	b.d.l.	b.d.l.	b.d.l.	b.d.l.	b.d.l.	b.d.l.	b.d.l.	b.d.l.	0.01
Tb	0.21	0.08	b.d.l.	0.29	0.04	0.02	0.03	b.d.l.	b.d.l.	0.06	0.1	0.01	0.26	0.3	0.24	0.05
Te	0.04	b.d.l.	0.2	0.02	1.4	1.8	1.4	0.36	2	1.6	2.2	1.5	3	2.1	2.6	0.12
Th	0.6	b.d.l.	0.3	4.9	1.3	0.5	0.6	b.d.l.	b.d.l.	1.5	1.1	0.3	6.5	15	6.8	0.5
Tl	0.08	0.05	0.04	0.19	0.1	0.08	0.06	0.18	0.35	0.05	0.4	0.13	0.35	0.21	0.2	0.05
Tm	0.13	0.04	b.d.l.	0.12	0.01	b.d.l.	0.01	b.d.l.	b.d.l.	0.02	0.03	b.d.l.	0.11	0.13	0.11	0.04
U	0.58	0.23	b.d.l.	1.5	0.58	0.33	0.75	0.05	b.d.l.	0.3	2.5	0.07	0.56	1.2	0.64	0.08
V	5	1	b.d.l.	8	9	9	8	8	7	9	7	4	7	6	2	b.d.l.
W	0.51	0.13	0.79	0.34	35	109	246	189	469	36	142	844	168	176	0.88	0.11
Y	8.3	2.6	0.25	8.8	0.93	0.41	0.7	0.18	0.1	0.64	2.1	0.43	5.7	7.3	5.5	2.5
Yb	1	0.23	0.04	0.81	0.08	0.03	0.07	b.d.l.	b.d.l.	0.13	0.2	0.04	0.67	0.82	0.78	0.3
Zn	13	3	2	26	3	3	4	30	7	6	6	3	964	5119	4112	6
Zr	0.6	b.d.l.	b.d.l.	0.7	b.d.l.	b.d.l.	b.d.l.	b.d.l.	b.d.l.	b.d.l.	b.d.l.	b.d.l.	b.d.l.	b.d.l.	b.d.l.	b.d.l.

Table S4-5. Bulk geochemical analyses of major, trace and rare earth elements of analyzed samples from Aspra Chomata. b.d.l. = below detection limit; n.a. = not analyzed; Pot. alt. = potassic alteration overprinted by chloritic-sericitic alteration.

	Granodiorite porphyry							Epithermal base-metals sulfide veins		
	Pot. alt.	Sericitic alteration								
	Ach 07	Ach 04	Ach 01	Ach 02*	Ach 11	Ach 12	Ach 05*	Ach 08B1a	Ach 08B2*	Ach 08B2b
Major oxides (wt.%)										
SiO ₂	65.21	66.31	n.a.	n.a.	68.29	n.a.	n.a.	n.a.	n.a.	n.a.
Al ₂ O ₃	16.19	16.4	n.a.	n.a.	15.48	n.a.	n.a.	n.a.	n.a.	n.a.
Fe ₂ O ₃	4.53	4.24	n.a.	n.a.	3.58	n.a.	n.a.	n.a.	n.a.	n.a.
CaO	1.88	2.69	n.a.	n.a.	1.54	n.a.	n.a.	n.a.	n.a.	n.a.
MgO	2.69	1.84	n.a.	n.a.	1.55	n.a.	n.a.	n.a.	n.a.	n.a.
Na ₂ O	3.16	3.32	n.a.	n.a.	3.23	n.a.	n.a.	n.a.	n.a.	n.a.
K ₂ O	3.36	3.44	n.a.	n.a.	3.7	n.a.	n.a.	n.a.	n.a.	n.a.
MnO	0.04	0.04	n.a.	n.a.	0.04	n.a.	n.a.	n.a.	n.a.	n.a.
TiO ₂	0.5	0.47	n.a.	n.a.	0.41	n.a.	n.a.	n.a.	n.a.	n.a.
P ₂ O ₅	0.16	0.17	n.a.	n.a.	0.14	n.a.	n.a.	n.a.	n.a.	n.a.
BaO	0.09	0.09	n.a.	n.a.	0.2	n.a.	n.a.	n.a.	n.a.	n.a.
Cr ₂ O ₃	0.03	0.02	n.a.	n.a.	0.04	n.a.	n.a.	n.a.	n.a.	n.a.
SrO	0.06	0.07	n.a.	n.a.	0.05	n.a.	n.a.	n.a.	n.a.	n.a.
Major elements (wt.%)										
Al	n.a.	1.8	1.7	7	1.6	0.30	0.49	0.12	0.08	0.05
Ca	n.a.	0.46	0.96	0.04	0.23	0.02	0.03	0.01	b.d.l.	0.01
Fe	n.a.	2.7	2.2	5.5	2.6	3.7	3.3	1.2	7.4	8.2
K	n.a.	0.31	0.26	2.8	0.21	0.17	0.17	0.08	0.02	0.02
Mg	n.a.	1.2	1.3	0.42	1.3	0.02	0.02	b.d.l.	b.d.l.	b.d.l.
Na	n.a.	0.08	0.05	0.14	0.04	0.02	0.04	b.d.l.	b.d.l.	0.01
S	n.a.	b.d.l.	0.17	0.75	0.02	0.13	0.64	1.2	>10	>10
Ti	n.a.	0.15	0.04	0.12	0.03	b.d.l.	b.d.l.	b.d.l.	b.d.l.	b.d.l.
Trace elements (ppm)										
Ag	n.a.	0.12	0.19	12	0.4	0.32	105	75	225	610
As	n.a.	4	2.2	531	3.4	24	3,359	507	6572	5,191
Au	n.a.	0.03	0.02	13	0.01	0.01	13	3	3.1	2.5
B	n.a.	b.d.l.	b.d.l.	n.a.	b.d.l.	b.d.l.	n.a.	b.d.l.	n.a.	b.d.l.
Ba	865	163	637	1254	264	91	94	b.d.l.	b.d.l.	b.d.l.
Be	n.a.	0.37	0.5	1.7	0.44	2.4	0.61	0.21	0.29	0.75
Bi	n.a.	0.32	0.18	18	0.14	3.8	1.2	1.3	0.35	0.52
Cd	n.a.	0.12	2.9	1.2	0.53	0.05	67	10	>1000	1,180
Ce	68	46	33	43	35	20	14	9.2	1.9	5.9
Co	n.a.	18	22	74	21	5.6	221	27	91	8.6
Cr	222	103	7	7	9	1	7	333	1	141
Cs	4.2	2.6	3.1	8.6	1.3	0.82	0.94	0.47	0.12	0.09
Cu	n.a.	513	725	566	382	1,057	1,712	64	2,702	4,432
Dy	3.1	2.4	1.9	n.a.	1.9	1.2	n.a.	0.16	n.a.	0.31
Er	2.1	1.2	0.97	n.a.	0.92	0.61	n.a.	0.06	n.a.	0.16
Eu	1.1	0.51	0.6	n.a.	0.57	0.4	n.a.	0.25	n.a.	0.1
Ga	18	7.3	6.9	14	7	0.75	8.1	0.75	12	19
Gd	4	2.9	2.4	n.a.	2.5	1.3	n.a.	0.37	n.a.	0.31
Ge	n.a.	0.16	0.1	0.54	0.13	b.d.l.	0.26	0.06	0.11	0.72
Hf	4.3	b.d.l.	b.d.l.	0.4	b.d.l.	b.d.l.	b.d.l.	b.d.l.	b.d.l.	b.d.l.
Hg	n.a.	0.02	0.03	n.a.	0.04	0.02	n.a.	3.1	n.a.	32
Ho	0.68	0.43	0.34	n.a.	0.33	0.2	n.a.	0.02	n.a.	0.05
In	n.a.	0.01	0.01	0.09	b.d.l.	0.02	5	0.01	0.15	0.28
La	38	22	16	24	17	14	9.3	5.1	1.7	3.2
Li	n.a.	15	11	15	17	0.30	24	0.4	7.9	0.1
Lu	0.35	0.17	0.14	n.a.	0.13	0.12	n.a.	b.d.l.	n.a.	0.03
Mn	n.a.	326	204	783	376	35	117	79	580	703
Mo	n.a.	0.79	11	68	0.69	32	175	4.4	1.6	1.5
Nb	9.6	0.46	0.09	5.1	0.12	b.d.l.	0.4	0.12	0.1	b.d.l.

Nd	26	18	14	n.a.	15	7.3	n.a.	3.5	n.a.	2.4
Ni	n.a.	7.6	5.4	2.5	5.7	0.6	3.1	6.7	0.7	2.8
P	n.a.	704	642	595	745	820	1,916	176	213	941
Pb	n.a.	18	15	1,096	21	60	20,850	9,550	62,849	105,200
Pr	7	5	3.7	n.a.	4.2	2.2	n.a.	1	n.a.	0.7
Rb	161	34	25	234	21	12	9.8	7	1.4	1.4
Re	n.a.	0.002	0.05	0.02	0.002	0.002	0.03	0.004	0.02	0.01
Sb	n.a.	0.46	1.2	242	2.1	3	2,848	2,374	>10,000	39,570
Sc	n.a.	5.2	3.7	6	4.4	0.4	0.8	0.2	0.5	0.9
Se	n.a.	b.d.l.	0.5	5	0.2	1.4	46	2.2	1	2
Sm	4.7	3.4	2.6	n.a.	2.9	1.5	n.a.	0.57	n.a.	0.38
Sn	b.d.l.	0.8	0.4	9.2	0.2	b.d.l.	47	4.4	41	69
Sr	586	69	43	30	29	61	58	14	8.1	32
Ta	1.1	b.d.l.	b.d.l.	0.91	b.d.l.	b.d.l.	0.68	b.d.l.	0.29	b.d.l.
Tb	0.55	0.42	0.34	n.a.	0.34	0.19	n.a.	0.04	n.a.	0.05
Te	n.a.	0.04	0.01	0.27	0.02	0.4	0.46	0.13	0.41	0.03
Th	25	24	28	23	25	21	1.7	1.7	1.9	b.d.l.
Tl	n.a.	0.3	0.29	3.4	0.2	0.12	0.59	7.1	80	87
Tm	0.32	0.17	0.14	n.a.	0.13	0.1	n.a.	b.d.l.	n.a.	0.02
U	8.6	6.6	10	3.8	6.6	25	23	0.62	1	3.1
V	115	70	58	60	69	9	8	4	4	5
W	3	103	181	482	188	72	1,411	378	1,029	15
Y	20	12	10	4.1	9.4	4.3	2.5	0.65	1.6	1.6
Yb	2	1.1	0.85	n.a.	0.8	0.73	n.a.	0.04	n.a.	0.16
Zn	n.a.	53	114	159	124	4	417	1,619	16,0557	17,5100
Zr	157	0.7	b.d.l.	4.3	b.d.l.	b.d.l.	0.8	b.d.l.	b.d.l.	b.d.l.

* Trace elements for these samples were adapted from Gounaris (2017).